Solar Flares and Coronal Physics Using P/OF as a Research Tool

Edited by
Einar Tandberg-Hanssen
Robert M. Wilson
NASA George C. Marshall Space Flight Center
Huntsville, Alabama

Hugh S. Hudson
University of California, San Diego
La Jolla, California

NΛSΛ

National Aeronautics
and Space Administration

Scientific and Technical
Information Branch

1986

TABLE OF CONTENTS

PREFACE

The Pinhole/Occulter Facility (P/OF), whose science and technology are discussed at length in these proceedings, has recently undergone a Phase A study carried out at the NASA Marshall Space Flight Center. (For an overview of study results, see the bibliography which concludes this section.) In anticipation of the succeeding Phase B study, the time appeared ripe to bring together solar physicists from around the world to re-examine and discuss P/OF as a research tool. About 60 observers, experimenters, and theorists from across the United States and from Brazil, France, Japan, the Netherlands, and the United Kingdom gathered in Huntsville, Alabama, May 8-10, 1985, for a three-day working conference entitled "Workshop on Solar High-Resolution Astrophysics Using the Pinhole/Occulter Facility." The resulting 25 invited and contributed papers, plus reports on the subpanel discussions, form the basis for this NASA Conference Publication. The editors would like to thank the participants for giving the interesting papers that created a stimulating workshop.

BIBLIOGRAPHY

"Large-Scale Telescopes for X-ray and Gamma-ray Astronomy," H. S. Hudson and R. P. Lin, 1978, Space Science Instrumentation, Vol. 4, p. 101.

"The Pinhole/Occulter Facility: Executive Summary," J. R. Dabbs, E. A. Tandberg-Hanssen, and H. S. Hudson, 1982, NASA Technical Paper 2089.

"The Pinhole/Occulter Facility," 1983, edited by E. A. Tandberg-Hanssen, H. S. Hudson, J. R. Dabbs, and W. A. Baity, NASA Technical Paper 2168.

"Pinhole Occulter Facility, Phase A Study," 1984, NASA/MSFC Program Development.

LIST OF WORKSHOP PARTICIPANTS

C.-H. An	(NRC/MSFC)	D. Neidig	(NSO Sacramento Peak)
T. Bai	(Stanford)	M. Pick	(Meudon Observatory, France)
P. Bornmann	(NSO Sacramento Peak)	T. Prince	(Caltech)
J. Brown	(Glasgow, UK)	D. Rabin[1]	(MSFC)
R. Canfield	(UCSD)	R. Ramaty	(GSFC)
C. Crannell	(GSFC)	E. Reichmann	(MSFC)
J. Dabbs	(MSFC)	D. Roalstad	(BASD)
C. de Jager	(Utrecht)	R. Rosner	(CFA)
B. Dennis	(GSFC)	N. Sheeley	(NRL)
K. Dere	(NRL)	S. Srinivas	(Teledyne Brown)
C. de Sanctis	(MSFC)	D. Smith	(BRA)
J. Dowdy	(MSFC)	J. Smith	(NOAA)
G. Dulk	(U. Colorado)	D. Spicer	(NASA HQ)
G. Emslie	(UAH)	S. Suess	(MSFC)
E. Fenimore	(LASL)	Z. Svestka	(Utrecht)
G. Gary	(MSFC)	E. Tandberg-Hanssen	(MSFC)
M. Green	(UAH)	F. van Beek	(Utrecht)
M. Hagyard	(MSFC)	R. Vondrak	(Lockheed)
E. Hildner	(HAO)	H. Waites	(MSFC)
G. Holman	(GSFC)	A. White	(MSFC)
J. Howell	(MSFC)	R. Wilson	(MSFC)
H. Hudson	(UCSD)	G. Withbroe	(CFA)
G. Hurford	(Caltech)	K. Wood	(NRL)
J. Ionson	(SDI)	S.-T. Wu	(UAH)
S. Kane	(UCB)		
P. Kaufmann	(INPE, Brazil)		
T. Kosugi	(U. Tokyo, Japan)		
M. Kundu	(U. Maryland)		
H.-A. Lin	(UCB)		
R. Lin	(UCB)		
R. MacQueen	(HAO)		
J. Middleditch	(LASL)		
R. Moore	(MSFC)		
R. Munro	(HAO)		

1. Presently, NOAO/NSO, Tucson, Arizona.

Wednesday, May 8 (Day 1)

J. Kingsbury	Welcoming Address
E. Tandberg-Hanssen	Day 1 Opening Remarks
R. Rosner	Solar Fine Structure
R. Canfield	Optical Imaging Spectroscopy
G. Withbroe	Corona and Solar Wind
N. Sheeley	SOLWIND Coronal Observations During 1979-1985
B. Dennis	Results from the Solar Maximum Mission
C. de Jager	X-Ray Imaging of Flare Impulsive Phase
Z. Svestka	X-Ray Imaging of Flare Loops and Coronal Arches
R. Ramaty	Indirect Evidence for Localization of Gamma-Ray Sources
G. Emslie	Theoretical Considerations for Hard X-Ray Imaging
R. Lin	Microflares, Coronal Flares, and Interplanetary Electrons

Thursday, May 9 (Day 2)

H. Hudson	Day 2 Opening Remarks
M. Pick	Solar Radio Corona
G. Dulk	Radio Imaging of Flares
G. Hurford	High Resolution Solar Microwave Observations
K. Wood	The P/OF as a Tool for X-Ray Astronomy
H. Hudson	P/OF Technical Concept
J. Dabbs/J. Howell	P/OF Engineering Study
H. Waites	Ground Simulation Testing for P/OF
S. Srinivas	Integration Support
D. Spicer/H. F. van Beek/D. Neidig/R. MacQueen (Moderator)	
	Future Missions Panel Discussions
E. Hildner	Symposium Summary

Friday, May 10 (Day 3)

R. Lin (Chairman)	X-Ray Subpanel Session
R. Munro (Chairman)	Coronal Subpanel Session
E. Tandberg-Hanssen (Chairman)	
	Subpanel Reports/Joint Discussion/Closing Remarks

INTRODUCTION

Hugh S. Hudson,[1] Einar Tandberg-Hanssen,[2] Robert M. Wilson,[2] and Joseph R. Dabbs[2]

The study of solar activity has progressed through several generations of observing capability, originating long ago in visual telescopic observations of sunspots (Galileo) and solar flares (Carrington). As we have progressed in this sequence of observational capability, we have had a typical mixture of older problems being solved, along with new questions being raised by the novel new data. Today many crucial questions remain: for example, is the excess energy needed to drive the phenomena of activity stored in the corona, or below the photosphere? This question remains unanswered but of real interest wherever in the Universe magnetic energy release creates observable astrophysical phenomena.

The Pinhole/Occulter Facility (P/OF) represents revolutionary improvements in solar observational capability. For X-radiation, crucial to studies of solar activity because of high-temperature phenomena and ubiquitous particle acceleration, the chief benefits will be in providing imaging at resolutions better than 1 arc s for hard X-ray and gamma-ray photons. For visible and EUV observations the P/OF represents a second generation of space experiments. The large telescope apertures that P/OF makes possible will give much better resolution and sensitivity. The P/OF concept creates these advantages not so much from sophisticated new technology, as simply from exploiting space to increase the distance between the observing instruments and the pinhole/occulter structure. The baseline separation is 50 m in the "strawman" configuration often mentioned in the papers published in these proceedings.

The papers below combine science with "advocacy." In these proceedings, authors were asked to consider the fields of science relevant to P/OF and to help the Science Working Group to reconsider the details of the strawman payload, originally chosen before the Solar Maximum Mission and Hinotori results became available. The advertising aspects of the advocacy are less important, because there is general community agreement that P/OF should be developed as soon as it can be fitted into the NASA program.

It is sometimes difficult to predict the results of new observational capability. There is usually a solid, anticipated result that justifies the development – in the case of the 5-m Hale telescope, the detection of individual stars in external galaxies was important. But there are also unexpected and often even more interesting results – perhaps the discovery of the quasars in the case of the Hale telescope. The analogous "expected" results for the P/OF X-ray imaging would be in the structure of the solar-flare impulsive phase, where we expect to find small structures that will require at least the angular resolution achievable by the initial P/OF. De Jager's paper in these proceedings discusses the physics of the impulsive phase.

In the papers presented here, the authors have made some substantial efforts to extrapolate from our present knowledge into the P/OF domain. On the X-ray side, there is much recent emphasis on rapid bursts and "microflares." There is a striking example of simultaneous rapid bursting in hard X rays and millimeter waves shown by Kaufmann et al.; see also the example of a physically large but rapidly variable radio source shown by Dulk. The radio observations act in some cases as a guide to our anticipated X-ray and coronal observations, and several papers in these proceedings review and comment upon the physics arising from the radio observations (see first Pick's article). The P/OF observations will have enormously greater power if simultaneous radio observations – over the whole radio spectrum – can be made simultaneously.

---

1. UCSD.
2. NASA Marshall Space Flight Center.

The ground-based optical spectrum offers a similar example of how observations at different wavelengths can work together well in studying the complex physics of solar activity. Canfield's article in these proceedings describes the modern developments in spatially-resolved H-α spectroscopy, which has been very productive in flare research in the past solar maximum. The development of numerical models for the heterogeneous structures of solar activity, linking the tenuous corona with the denser layers, has accompanied technological developments in ground-based observation. These have re-established the central role of ground-based observations of the optical spectra of solar flares.

The pioneering X-ray imaging observations from the Solar Maximum Mission and from the Hinotori spacecraft have given us some further knowledge upon which to base our expectations from P/OF. In Svestka's article there are probably examples of several new dynamical effects in the low corona visible through X-ray emission.

Finally, we should point out that the P/OF concept is changing in the light of recent data and theories. Before the past maximum, we had little knowledge of the solar gamma-ray spectrum. The gamma rays (and neutrons as well) turn out to be very detectable and quite interesting physically. The P/OF concept works well for these radiations, and we can anticipate making arc second images of gamma-ray and neutron sources in solar flares. The community of high-energy astrophysicists is only beginning to think about the implications of this possibility.

We attempted in this workshop to allow for this evolution by having two subpanel discussions on high-energy (Lin and Dennis) and low-energy (Munro) instrumentation, respectively. Because of the restricted time available for these discussions, they are somewhat incomplete – for example, the potential of gamma-ray and neutron imaging is not really discussed in these proceedings at all. We can only hope that these subjects, as well as the non-solar astrophysics enabled by P/OF (see an excellent summary paper by Wood on P/OF X-ray astronomy), will be given their proper attention as the enabling facility becomes available.

INTRODUCTORY PAPERS

X-RAY CAMERA

X-RAY SOURCE — APERTURE — RECORDED PICTURE — COMPUTER DECODING PROCEDURE — RECONSTRUCTED IMAGE
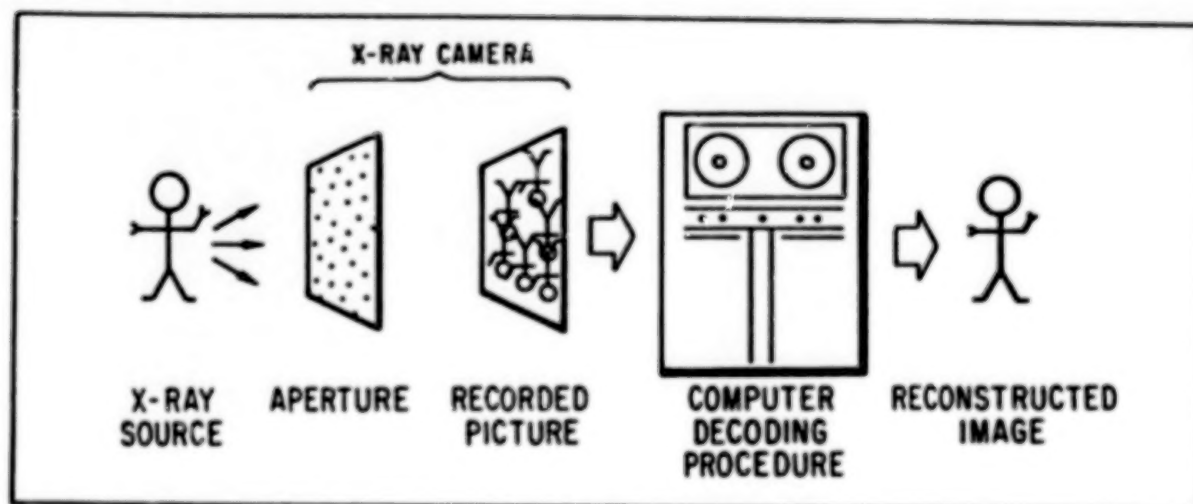
THE CONCEPT OF THE PINHOLE/OCCULTER FACILITY
(Invited)

Hugh S. Hudson

CASS C-011, UCSD, La Jolla, CA 92093 U.S.A.

ABSTRACT

The Pinhole/Occulter Facility is based upon a simple idea for obtaining high angular resolution in astronomical X-ray observations, for example for solar flares at energies >10 keV. The scheme uses a coded aperture device (multiple pinhole camera) with a large separation between the aperture encoder and the detector. Such an imaging device can have an angular resolution much better than 1 arc s if desired.

A large structure would also make it possible to have a large external occulter, which would have powerful applications, notably for high-sensitivity observations of the corona in EUV and white light. This capability leads to the definition of the Pinhole/Occulter Facility, which combines both X-ray and coronal observations. The present concept is based upon a 35-m deployable boom, erected in the cargo bay of the Space Shuttle and pointed in the solar direction by the Instrument Pointing System of Spacelab.

I. INTRODUCTION

It is possible to make images of high-energy radiations − X rays, γ-rays, and material particles − by using the coded-aperture method. If the aperture is a large distance from the detector, such images can have excellent angular resolution, limited only by diffraction if problems of fabrication and deployment be solved. The simplest example of such a coded-aperture telescope is the pinhole camera, which forms a real inverted image on any plane behind the pinhole. More complex aperture patterns can also be used, with a great increase in image brightness. Hudson and Lin (1978) described the application of these ideas to high-energy astrophysics.

The idea for a Pinhole/Occulter Facility (P/OF) began during studies of methods for observing solar hard X-ray emission with high angular resolution. These studies aimed at producing instruments to be deployed from the Space Shuttle. A Facility Definition Team for Hard X-Ray Imaging assessed the technology available for such observations, and in the course of these studies realized that very high angular resolution could be achieved.

This paper reviews the concept of the Pinhole/Occulter Facility from the point of view of its capability for X-ray observations; the other "half" of the instrumentation planned at present for P/OF aims at making revolutionary new EUV and visible-light observations of the corona. Further information appears elsewhere in this volume on the science in these areas of P/OF (Withbroe, 1985) and from the important phenomena that need both X-ray and coronal observations.

The non-solar capability of a large-area X-ray detector array with sub-arc-second imaging capability is great. This aspect too will not be discussed here, but is the subject of a separate paper by Wood (1985).

II. SCIENTIFIC OBJECTIVES

When dynamical phenomena occur in the magnetized plasma of the solar atmosphere, particle acceleration results. The mechanisms of this particle acceleration are interesting in themselves, but the particles also give us information about the energy release -- its timing, geometry, modality, and magnitude. Thus, since the initial hard X-ray observations of solar flares (Peterson and Winckler, 1959; for a review, see Kane et al., 1980), we have known that sensitive imaging observations of the hard X-ray bremsstrahlung production by the accelerated electrons would make the next major observational step in flare research.

The Pinhole/Occulter Facility takes major steps in improving the angular resolution and the sensitivity over prior observations. In angular resolution, P/OF will give 0.3 arc s as opposed to the 8 arc s of the Solar Maximum Mission (Van Beek et al., 1980); in sensitivity, P/OF has a total area of 1.5 m^2, far larger than any previous solar instrument, or any non-solar hard X-ray instrument for that matter. Its sensitivity will be great enough to observe many cosmic X-ray sources as they transit through the solar corona, and thus P/OF will observe solar phenomena at low flux levels never before observed.

The first major scientific objective is illustrated in Figure 1, which shows microwave and hard X-ray observations from a flare of November 5, 1980 (Duijveman and Hoyng, 1983). These data can only suggest relationships between the hard X-ray emissions and the microwave and Hα observations but certainly reinforce our ideas about the close relationship between the accelerated particles and the flare effects that occur at all levels of the flaring atmosphere.

In the corona the situation remains even more obscure. We know that dramatic effects take place: the launching of coronal mass ejections, the acceleration of "solar cosmic rays," and rearrangements of the magnetic field that require large amounts of energy. Figure 2 shows the Hinotori observations of a coronal hard X-ray source accompanying a flare of May 13, 1981, from which little impulsive emission occurred. Thus it seems as though the coronal particle acceleration can take place semi-independently of the acceleration on the compact, closed magnetic loops that flare up in the impulsive phase. The observational requirement here is for sensitivity, rather than high resolution particularly since the coronal plasma is more tenuous and thus produces bremsstrahlung more weakly.

III. CODED-APERTURE IMAGING

The basic idea of coded-aperture imaging for high-energy astrophysics was proposed independently in different forms by Oda (1965; the modulation collimator) and by Dicke (1968; the random aperture γ-ray imager). A general discussion of these imaging techniques had already been given by Mertz (1965), but the first practical application of the methods in astrophysics was with Oda's ideas: modulation collimators mounted on rocket-borne X-ray detectors succeeded in locating the bright cosmic X-ray source Sco X-1 well enough so that ground-based telescopes could identify its optical counterpart (Sandage et al., 1966), the first identified stellar X-ray source beyond the Sun.

We can now identify three classes of coded-aperture imagers, which have many, two, and one aperture masks, respectively:

1. Grid collimators (Soller collimators) in which several grids are placed at specific distances in front of a detector to define a narrow field of view. The HXIS instrument from the Solar Maximum Mission (Van Beek et al., 1980) is the most sophisticated example of this type.

2. Modulation collimators (Oda, 1965) in which two grids — one at the front, and one at the detector at the back of the instrument — cause shadow bands to sweep across the sky with the motion of the telescope. Recent variants of this, which we call "Fourier Transform Telescopes," do not require scanning motion (Makishima et al., 1978; Hurford and Hudson, 1985).

3. Coded-aperture imagers (Mertz, 1965; Dicke, 1968) in which a single aperture mask at the front of the instrument makes an intermediate image on a position-sensitive detector. The final image is produced by deconvolution, essentially by a correlation analysis. There are specific aperture codes that result in flat sidelobes (Gunson and Polychronopulos, 1976; Fenimore and Cannon, 1978), so that complete image information can be obtained.

These three approaches each have merit in specific applications. The third type has the advantages of high throughput and complete image formation, but its angular resolution is limited by the position resolution of the detector and by the mask-detector separation.

IV. X-RAY CAPABILITY OF THE PINHOLE/OCCULTER FACILITY

The Pinhole/Occulter Facility incorporates two hard x-ray imaging systems: a coded-aperture imager for sensitive observations of the whole Sun, with moderate angular resolution (8 arc s FWHM); and a Fourier-transform imager for high-resolution observations on the smallest scales (0.3 arc s FWHM). Both imagers use tungsten grids (aperture-encoding masks) with precise patterns of holes used to create the image on a position-sensitive detector.

Table 1 summarizes the tentative parameters of these two X-ray imagers on the Pinhole/ Occulter Facility. We describe each instrument briefly here:

Fourier-Transform Imager. The Fourier-transform approach to image formation divides the total area of detector into "subcollimators," each one of which measures one Fourier component of the source angular structure. To make a complete image requires a large number Fourier components; on the other hand, for a given detector area, the area per subcollimator drops as the number increases. This presents a tradeoff problem: sensitivity versus image completeness. Unfortunately this tradeoff depends upon the source angular structure itself, and also is hard to analyze, so the optimization of the number of subcollimators will require numerical modeling. Figure 3 shows how the subcollimators produce individual Fourier scans of the source angular structure.

The field of view decreases as the number of subcollimators increases and their dimensions decrease. For the 100-subcollimator layout given in Table 1, the field of view is only sufficient to image a single active region at high resolution. This implies that an "image motion compensator," an X-Y translation of the detector or of the grids, is required to image a given solar active region.

Coded-Aperture Imager. The simple coded aperture requires only a single grid, and then relies upon the position-sensing capability of the detector to form an image. If the pattern of the aperture code is physically large enough, the field of view can cover the whole Sun. The angular resolution is limited by the ratio of position resolution in the detector to mask distance, which corresponds in the data of Table 1 to about 4 arc s (FWHM, assuming oversampling by a factor of two and a position resolution of 0.5 mm). Figure 4 shows the hole pattern of a typical "uniformly redundant array" (Fenimore and Cannon, 1978).

V. CORONAL CAPABILITY OF THE PINHOLE/OCCULTER FACILITY

The existence of an occulter at some great distance from a telescope has real advantages for the observation of faint objects (e.g., the corona) in the presence of bright objects (e.g., the solar photosphere). The improvement in the diffraction pattern relative to that of a normal external occulter makes it possible to observe closer to the limb of the Sun. Even more important, the large shadow of the distant occulter makes it possible to have large-aperture optics; all previous space-borne coronagraphs have had small apertures with resulting poor angular resolution and low sensitivity. The Pinhole/Occulter Facility includes one coronal telescope – essentially an all-reflecting coronagraph – and an EUV spectrometer capable of imaging resonance-scattered solar light in various EUV emission lines.

VI. OTHER APPLICATIONS

The Pinhole/Occulter Facility has its own scientific program, but there are other potential applications of the basic idea – the use of large structures in space (or no structures at all) to create new observational capabilities. For interest, we review some of these ideas here with the caveat that none of them might have any relationship to the Pinhole/Occulter Facility.

Sun-Grazing Comets. The successful detection of Sun-grazing comets by coronagraphs (Michels et al., 1982; Sheeley et al., 1982) represents an interesting application of sensitive photometry of diffuse objects near the solar limb. The low diffracted light level of a remote external occulter not only reduces the diffuse background light, but also allows one to observe closer to the limb of the Sun. Both advantages should aid in the detection of comets that approach or strike the solar surface.

Planetary Detection. A remote external occulter provides a sharp Fresnel diffraction pattern, and this can aid in suppressing a bright stellar image in a search (for example) for a planet orbiting a nearby star. Spitzer (1962) may have proposed this originally in the context of space astronomy, having in mind an independent occulter subsatellite navigating around the Space Telescope. Elliot (1978) has given an analysis of grazing lunar occultation as a realization of this idea.

Solar Occultation. Elliot (private communication) has pointed out that sufficient control of scattered and diffracted light levels, together with high-resolution, stable stellar images from space, should permit observations of the actual occultation of a star by the outer layers of the solar atmosphere. This would provide a totally new means for studying atmospheric structure and also give high resolution.

Interferometric Detection of Gravitational Radiation. The deformation of large structures in space, or else perturbations of the relative positions of two independent satellites, might provide a means of detecting gravitational radiation via precise geometrical measurements (Faller and Bender, 1984).

Stellar Interferometry. At present there are ideas for multiple-component optical interferometers in space that would use one or more subsatellites (e.g., Stachnik et al., 1984; Labeyrie et al., 1984). The control of these subsatellites for interferometry resembles the control problem for X-ray imaging, but is much more demanding since position information at some small fraction of an optical wavelength would be required.

VII. EVOLUTION OF THE P/OF CONCEPT

A reasonable plan for developing the Pinhole/Occulter Facility would use Spacelab as a stepping-stone to an eventual deployment on the Space Station. The great sensitivity of P/OF means that it can obtain interesting results even in its initial brief observations, but the major fruits will come only from systematic observations as the Sun displays its whole range of phenomena. Non-solar observations naturally are limited only by the total number of photons detected, so that the long exposures possible from the Space Station will be essential.

The key technology needed for making coded-aperture telescopes of high resolution lies in stably defining the geometrical geometric relationship between the components of the instrument. A rigid structure can do this, as it does in a classical telescope. Relying on a rigid structure may pose problems for the highest resolution, however, since any structure will exhibit geometrical instability at some level. In "conventional" telescopes such as AXAF (the Advanced X-Ray Astrophysics Facility), one now finds designs in which some structural flexibility can be tolerated; essentially the motions of the image are reconstructed and removed after its detection by using accurate knowledge of the image motion.

In the initial formulation of the Pinhole/Occulter approach we envisioned the use of separate subsatellites, one carrying the coded aperture and the other carrying the detectors. Each subsatellite would carry components of a system for determining the pointing direction of the telescope. This information then would provide the precise knowledge needed to restore the image after the detection process. The use of such subsatellites in near-Earth orbit would require considerable maneuvering capability because of the need to maintain non-Keplerian orbits for a given view direction. This is analogous to the use of subsatellites for optical interferometry mentioned above, but with less severe requirements on relative position information.

The basic concept of the Pinhole/Occulter Facility offers us a chance to make revolutionary observations in important areas of solar observation without the need for very much technology development. In a sense the P/OF concept is a "brute force" solution to the problem of improving observations in this area, simply by having a very long "focal" length. This kind of idea can be considered in an era when large-scale construction can be done in space. The structures required are not massive ones, and their alignment is not particularly critical in view of the possibility of reconstructing an image photon-by-photon in the presence of substantial pointing jitter. Nevertheless, active damping control by the IPS would be necessary to stabilize the boom adequately.

On Spacelab, the deployment of the P/OF structure would be by use of a self-extending boom. On the Space Station, the longer time in orbit and access to the astronauts' aid in assembling a large structure make it possible to think more imaginatively. A permanent three-dimensional structure with excellent rigidity but low mass could easily be designed and assembled in orbit. This should make it possible to have a simpler pointing-control actuator than the IPS. Finally, one should look forward to the eventual evolution of this concept to include a maneuverable subsatellite capable of circulating around the detector array mounted on the Space Station. Such a facility would make it possible to achieve angular resolution well below 0.1 arc s.

REFERENCES

Dicke, R., 1968, *Astrophys J. (Lett.)*, 153, L101.

Duijveman, A. and Hoyng, P., 1983, *Solar Phys.*, 86, 279.

Elliot, J. L., 1978, *Icarus*, 35, 156.

Faller, J. E. and Bender, P. L., in Taylor, B. N., and Phillips, W. D. (eds.), 1984, *Precise Measurements and Fundamental Constants II*, NBS Special Publication 617, p. 689.

Fenimore, E. E. and Cannon, T. M., 1978, *Appl. Opt.*, 17, 337.

Gunson, J. and Polychronopulos, B., 1976, *M. N. R. A. S.*, 177, 485.

Hudson, H. S. and Lin, R. P., 1978, *Space Sci. Inst.*, 4, 101.

Hurford, G. H. and Hudson, H. S., 1985, in preparation.

Kane, S. R., and 10 co-authors, 1980, in P. A. Sturrock (ed.), *Solar Flares* (Boulder, Colorado), p. 187.

Labeyrie, A., Authier, B., Boit, J. L., De Graauw, T., Kibblewhite, E., Koechlin, L., Rabout, P., and Weigelt, G., 1984, *Bull. Am. Ast. Soc.*, 16, 828.

Makishima, K., and 6 co-authors, 1978, in Van der Hucht, K., and Vaiana, G. (eds.), *New Instrumentation for Space Astronomy* (New York, Pergamon), p. 277.

Mertz, L., 1965, *Transformations in Optics* (New York, Wiley).

Michels, D. J., Sheeley, N. R., Jr., Howard, R. A., and Koomen, M. J., 1982, *Science*, 215, 1097.

Oda, M., 1965, *Appl. Opt.*, 4, 143.

Peterson, L. E. and Winckler, J., 1959, *J. Geophys. Res.*, 64, 697.

Sandage, A. R., and 11 co-authors, 1966, *Astrophys. J.*, 146, 316.

Sheeley, N. R., Jr., Howard, R. A., Koomen, M. J., and Michels, D. J., 1982, *Nature*, 300, 239.

Spitzer, L., Jr., 1962, *Am. Sci.*, 50, 473.

Stachnik, R. V., Ashlin, K., and Hamilton, S., 1984, *Bull. Am. Ast. Soc.*, 16, 818.

Tsuneta, S., and 7 co-authors, 1983, *Solar Phys.*, 86, 313.

Van Beek, H. F., Hoyng, P., Lafleur, B., and Simnett, G. M., 1980, *Solar Phys.*, 65, 39.

Withbroe, G., 1985, these proceedings.

Wood, K., 1985, these proceedings.

TABLE 1. X-RAY IMAGING SYSTEMS FOR P/OF

Fourier-Transform Imager

Angular Resolution	0.3 arc s
Field of View	4 arc min
Total Area	3000 cm^2
Energy Range	2 – 120 keV
Number of Subcollimators	100
Time Resolution	< 1 ms

Coded-Aperture Imager

Angular Resolution	4 arc s
Field of View	whole Sun
Total Area	12 000 cm^2
Energy Range	2 – 50 keV
Time Resolution	< 1 ms
Sensitivity @ 5 keV	0.03 μJy

40 "
~30 000 km

$T_B = 2.0 \times 10^8$ K

$T_B = 6.3 \times 10^8$ K
$T_{B,L} = 5.4 \times 10^8$ K
$T_{B,R} = 9.4 \times 10^8$ K

VLA 15 GHz

HXIS 16-30 keV
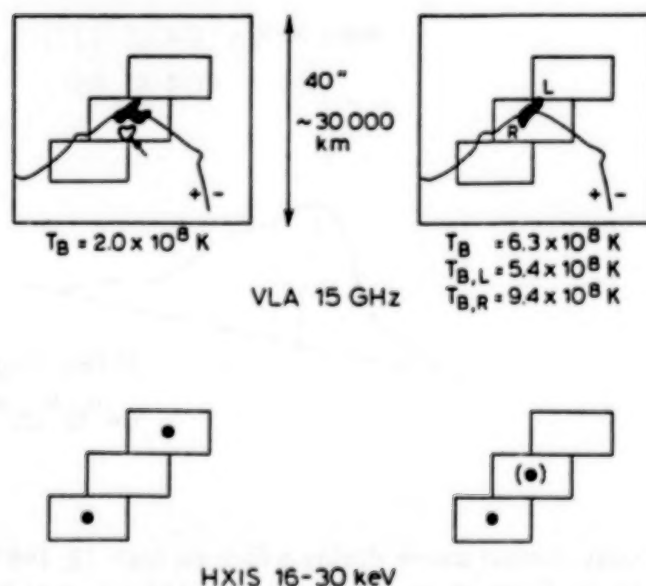
Figure 1. Observations of hard X rays (lower panels) and microwaves (upper panels) from a flare of November 5, 1980 (Duijveman and Hoyng, 1983). The two epochs in the flare represent (left) an impulsive spike, and (right) the peak of gradual hard X-ray emission. The dots in the rectangular pixels (8 arc s X 16 arc s) indicate that the spectrum in those pixels deviated significantly from a single-temperature thermal fit. Thus, this observation shows – at a marginal level of image quality – that the foot-points of the flux tube shown by the microwave source tend to show thick-target hard X-ray emission.

11
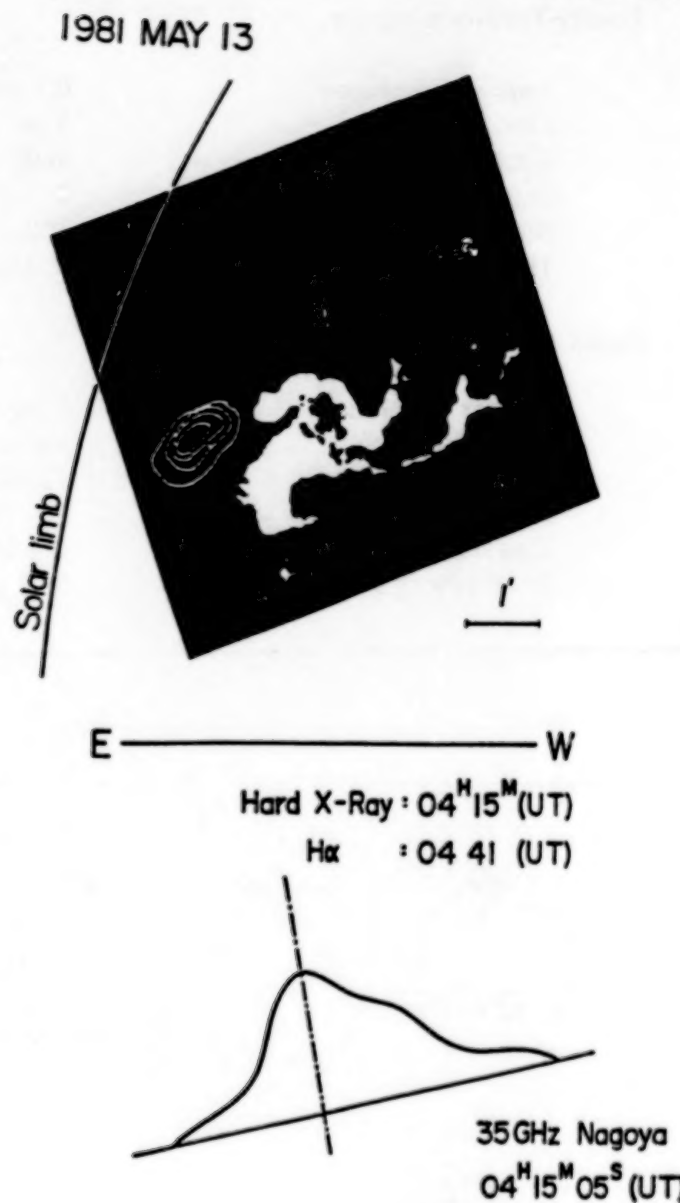
Figure 2. Hard X-ray coronal source during a flare on May 13, 1981 (Tsuneta et al., 1983). The lower part of the figure shows a one-dimensional image at 35 GHz. The observations show that stable trapping of a large population of non-thermal electrons can occur on extended magnetic loops.
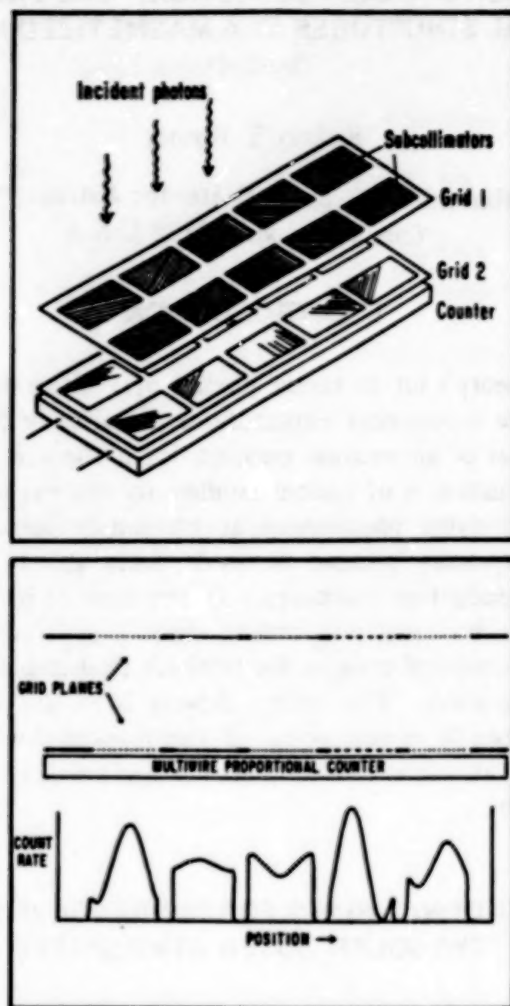
Figure 3. Principle of Fourier-transform imaging (Hurford and Hudson, 1985). Each subcollimator, or separate grid area, corresponds to one Fourier component of the source spatial distribution. A position-sensitive detector of moderate resolution (~10% of the subcollimator dimension) is necessary to read out the image.
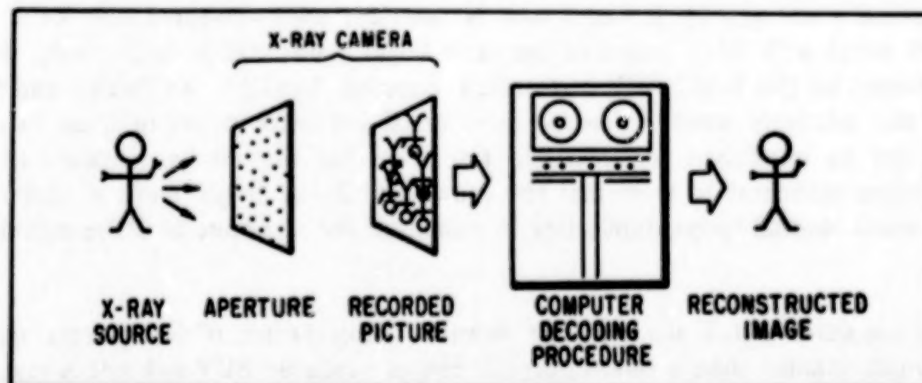
Figure 4. Example of a "uniformly redundant array" pattern for a coded-aperture imaging instrument (Fenimore and Cannon, 1978). Such mask patterns have the property that their autocorrelation function is flat, so that no spurious sidelobes appear in the resulting image.

THE SUN AT HIGH SPATIAL RESOLUTION: THE PHYSICS OF SMALL SPATIAL STRUCTURES IN A MAGNETIZED MEDIUM
(Invited)

Robert T. Rosner

Harvard-Smithsonian Center for Astrophysics
Cambridge, MA 02138 U.S.A.

I. INTRODUCTION

It is astrophysical theory's lot to rarely predict new phenomena, and far more commonly to be called upon to provide *a posteriori* explanations for already observed phenomena. I therefore find myself in somewhat of an unusual position for a theorist in discussing what has not as yet been observed. This situation is of course familiar to the experimenter, who wants to build new instrumentation for studying phenomena at previously unexplored scales or wavelength regimes, and is in a partial quandry because theory is rarely able to fully justify this step – that, after all, is the point of serendipitous discovery. In the case at hand, I am fortunately on surer grounds: although I will be discussing phenomena which may occur on as yet unobserved spatial scales, there *are* excellent theoretical reasons for thinking that important physical phenomena can be studied on these spatial scales. But before delving into the implications of such physical processes, I would like to briefly review some of the reasons for thinking that there do exist structures in the solar outer atmosphere with spatial scales smaller than those typically accessible to present-day instrumentation.

II. SOME OBSERVATIONAL HINTS FOR "UNRESOLVED" STRUCTURES IN THE SOLAR OUTER ATMOSPHERE

The current observational evidence for substantial spatial structuring of the outer solar atmosphere on a host of scales will be extensively and ably summarized by the other speakers, but I thought it might be useful to set the stage for my more theoretically-oriented talk by noting the most basic fact about the spatial structure of the solar chromosphere and corona: there is no evidence whatever that *any* part of the atmosphere has been fully resolved, no matter what the wavelength at which observations have been carried out. A rather typical example was provided several years ago by L. Golub and N. Sheeley, who compared soft X-ray images of an X-ray bright point with EUV images of the same bright point (taken, respectively, with the S-054 X-ray telescope and the S-082 EUV instrument onboard Skylab). As Sheeley and Golub (1979) point out, the relatively small difference in nominal resolving power of these two instruments, which was not an important constraint on resolution for the normal-incidence EUV telescope), was nevertheless sufficient to show that the unresolved X-ray bright point in fact consisted of a set of very small coronal loops, duplicating in miniature the structure of active region loop arcades (Figure 1).

This suggestion, that the effective volume filling factor of hot plasma above the solar surface is much smaller than a naive interpretation of available EUV and soft X-ray images would imply, has received strong support from a succession of differential emission measure studies of the transition region. For example, in a succession of models of this layer of the atmosphere, Feldman et al. (1979) and Feldman (1983) have shown that a plane parallel description is entirely inadequate to describe its structure, a conclusion also reached by Athay (1982: see also earlier references therein). In a recent summary of these observations, Rabin and Moore (1984)

presented a phenomenological model for the lower solar atmosphere in which appeal to highly localized heating (with < 1% filling factor) was made; whether or not the specific model proposed by Rabin and Moore really applies, the crucial point remains that unless appeal to highly localized energy release processes is made, it is difficult to understand the spatially *resolved* observations. Given this inconsistency with the most straightforward (i.e., plane-parallel) interpretation of the resolved observations, it behooves us to ask two questions: first (and most obvious), will higher spatial resolution observations resolve (in both senses of the word) the structure of the atmosphere; second, are there theoretical reasons for understanding why the atmosphere is structured on presently-unresolved scales, and can theory provide estimates of the likely spatial scales of this unresolved structure. In the following, I will give my personal perspective on these issues, based on recent studies of these sorts of problems I have been involved in.

III. THE THEORY OF SMALL SPATIAL SCALE STRUCTURES

The realization that important physical processes in the solar outer atmosphere *must* occur on very small spatial scales − certainly far smaller than the approximately 1 arcs (= 720 km) typically resolved by ground-based observations − goes back to the early work of Sweet (1958) and Parker (1963) on magnetic field dissipation and reconnection. The key points are, first, that we know that the solar surface magnetic fields change on time scales as short as minutes; and, second, that if one assumes the classical (Spitzer) magnetic diffusivity, then the diffusive time scale for structures of the size scale of solar active regions is of the order of years and longer. This basic difficulty first arose in the context of explaining the very short time scales associated with solar flares, but actually arises in understanding virtually any observed change in the *resolved* structure of the solar surface. The solution to this problem had to await Petschek's (1964) paper on neutral point reconnection, which showed that since the dissipative time scale varies with the square of the gradient scale length of the magnetic field, and only linearly with the inverse effective electron scattering frequency, it is essential to vastly reduce the spatial scale of magnetic field variations (even in the presence of other processes − such as scattering of electrons by electrostatic waves − which increase the effective electron collision frequency); one of Petschek's key contributions was to provide an explanation of how a sufficient reduction in spatial scales can come about. Thus, we can conclude that there *must* be processes which occur on spatial scales far below those which can be directly observed today (i.e., below roughly 1 arcs), and which have major consequences for the dynamics of *resolved* structures.

It remains to ask how small are these dissipative structures. Unfortunately, it is easy to show that their spatial scales very likely lie far beyond the resolution and sensitivity limits of planned experiments I am aware of (even if one imagines the effective electron scattering frequency to be vastly increased by, for example, scattering off ion-cyclotron waves). It is then appropriate to ask whether one expects to discover new phenomena in the spatial scale domain which we can realistically expect to reach within the next decade or so, that is, on scales of ~0.1 to 1.0 arcs (or ~ 70 to 700 km). I believe that the answer is a resounding "yes," and would like to illustrate the reasons for my optimism with two examples which arise in my own work. These examples focus on the possible geometric structure of a magnetized fluid from two rather distinct perspectives: I will first ask whether an initially uniform, magnetized, and current-carrying radiating plasma is stable; the answer turns out to depend sensitively on the precise nature of the initial state and, in particular, on what we believe might be the initial state of the

gas which becomes the observed structured solar chromosphere and corona. I will then turn to a problem first explored by H. Grad and E. N. Parker, namely, whether such an initially-uniform (magnetostatic) state can in general remain magnetostatic when subjected to arbitrary perturbations; and, more specifically, what geometric and topological properties such as perturbed equilibrium might have.

(a) The formation of small-scale structure in a radiating plasma

Although it is by now generally accepted that magnetic fields are largely responsible for the formation of the Sun's corona (and perhaps its chromosphere as well), it remains puzzling exactly how the "coronal" state (i.e., a highly spatially-structured, low density but high temperature plasma) is formed. That is to say, prior to asking how or why there is small-scale (e.g., sub-arcsecond) structuring, one should be concerned with how spatial structuring into the ubiquitous coronal "loops" occurs in the first place.

The basic reason why this puzzle arises at all is simply understood by considering the expansion of the photospheric magnetic fields (which are known to be highly spatially structured on scales ranging down to the sub-arcsecond level) *above* the photosphere. It is easy to show that because the overlying atmosphere is dominated by these magnetic fields, field lines should become space-filling within a few thousand kilometers of the level of optical depth unity in the continuum. Hence, if all emerging magnetic field lines were equally loaded with hot coronal matter ("coronal democracy"), then the corona should not show any major evidence for spatial structuring in the plasma emissivity (recall that the observed coronal inhomogeneity largely reflects variations in the local plasma density, rather than in the local plasma temperature). This is of course not observed to be the case: there does not seem to be coronal democracy, some (sets of) reentrant field lines being selected out by being relatively more loaded with hot coronal plasma than others — hence the loop structuring. This selection effect, together with the observation that any given loop structure is highly variable in its emission level (e.g., highly variable in the amount of matter loaded onto that set of magnetic field lines), suggests the operation of some sort of transient or instability which leads to the "filling" of only some flux tubes. As a momentary aside, I might note that it is of substantial interest to discover the plasma conditions along those field lines which are *not* loaded with substantial amounts of hot coronal matter: to answer this question will require imaging instrumentation sensitive to emission from a broad range of plasma temperatures, as well as high spatial resolution and extremely low sensitivity to scattering (the latter is essential in order to avoid overwhelming the likely weak emission contribution from the "unloaded" field lines with the copious emission from surrounding "loaded" field lines, a problem well known at X-ray wavelengths in studies of coronal holes; cf. Maxson and Vaiana, 1977).

As an example of the kind of theory which the considerations just discussed give rise to, I will describe recent work by Ferrari et al. (1982) and collaborators which suggests that this "loop filling" process is — at least during the initial stage of magnetic field emergence from the photosphere — the result of a heating instability driven by coronal currents. We know that the pre-coronal state of coronal plasma — the initial state — must be associated with the relatively cold gas entrained in magnetic fields as the latter are brought to the stellar surface by processes such as magnetic buoyancy. The question is then what happens. This plasma, which was initially entrained by the emerging fields, cools rapidly because it is no longer radiatively heated as it enters the small optical depth regime. However, because of (for example) accumulated stresses in the emerging "flux rope," one expects current flows, and hence associated Ohmic heating. This latter heating rate is not likely to be energetically significant until the plasma density in the cool emerging "flux rope" has dropped sufficiently that the radiative losses are of order of the

16

Ohmic heating rate (because cross-field thermal heat transport is strongly inhibited, the cool low-density "flux rope" emerges into the hot ambient medium – the chromosphere and above – energetically relatively insulated). The question is thus whether an equilibrium between Ohmic heating and radiative losses can be maintained; and if not, what the evolution of the unstable system leads to. In this view, the hot coronal envelope of a star such as the Sun is therefore thought of as a metastable configuration evolved from a cold initial equilibrium. To study this process, one considers a model magnetized atmosphere which is hydrostatically stratified (i.e., with gravity and non-vanishing pressure gradients), is in initial radiative equilibrium, and is initially uniform in temperature; and asks how such an atmosphere responds when subjected to perturbations in local heating rate due to current flows typically induced by photospheric motions (Heyvaerts, 1974a; Jockers, 1978). In the simplest case, in which gravitational stratification is ignored, the problem reduces to solution of a straightforward dispersion relation of the form (Heyvaerts, 1974b; Ferrari et al., 1982).

$$\omega = - i(\gamma - 1) \; [-(\kappa_\parallel \kappa_\parallel^2 + \kappa_\perp \kappa_\perp^2) \; (T_0/p_0) + (dh/dT)|_0 \; (T_0/p_0)$$
$$- (J_0^2/\sigma_0 p_0) \; (d \log \sigma/d \log T)|_0 \; (\sin^2 \theta - \cos^2 \theta)] \; ,$$

where $\kappa_\parallel$ and $\kappa_\perp$ are the parallel and perpendicular thermal conductivities, respectively, h is the effective radiative loss rate, θ is the angle between k and B, and the subscript "o" denotes parameters evaluated in the equilibrium state. Instability requires that the last term in the square brackets be positive and exceed the two preceding ones in absolute value: thus, the Ohmic heating term must overwhelm the (always-) stabilizing influence of thermal heat conduction and the influence of the net (radiative) losses. This mode of interest is the Joule mode, which is essentially transverse to the magnetic field, is connected with current filamentation, and operates only in the low-frequency limit in which the plasma can rapidly diffuse across the filaments (thus avoiding a pressure build-up that would stabilize the mode).

The Joule mode instability can be interpreted physically as follows. The initial spatially-uniform current density associated with the "non-potential" magnetic fields produced by photospheric motions becomes unstable, leading to the formation of current filaments inside which Joule dissipation is enhanced. The temperature thus increases within current filaments; and the local electrical conductivity therefore increases as well. Hence, the local current density within filaments further increases and, therefore, in order to maintain energy balance with radiative losses, yet further channelization is required (thermal runaway). This process can occur in the [total current I = constant] limit because we are in the low-frequency domain in which cross-field diffusion can occur (see detailed discussion in Ferrari et al., 1982; this constant current approximation is most appropriate because of the large self-inductance of the magnetized plasma). The ultimate mechanism for stopping the channelization is not established, but as noted by Ferrari et al. (1982), the instability may saturate in the nonlinear regime because of enhanced electron scattering by plasma turbulence (which increases the diffusion rates), or because the current sheets which form become unstable to the tearing mode (see discussion of this latter point in Bodo et al., 1985). For example, if the enhanced scattering is due to ion-cyclotron turbulence, then the effective heating rate will be a strong function of the drift speed, and will act to increase current diffusion precisely in the region of current concentration.

In order to proceed beyond these calculations, one must deal with the fact that analytical dispersion relations cannot be obtained for more realistic inhomogeneous (i.e., stratified)

configurations. Hence, it is necessary to resort to numerical means for solving for oscillatory perturbations as eigenfunctions of a boundary value problem (Bodo et al., 1985); one can then investigate the effects of atmospheric gradients and finite loop dimension on the scale of unstable perturbations. The equations used are the standard MHD conservation equations for mass, momentum, and energy, together with Maxwell's equations and Ohm's law. Only perturbations which are symmetric across the top of the loop turn out to be of interest, as antisymmetric perturbations can be shown to be stable. The basic features of the results obtained by Bodo et al. can be gleaned from Figure 2, in which is plotted the general dispersion relation of the Joule mode in the frequency-wave number plane. The physical parameters used in this example apply to a "classical" stellar atmosphere, without any chromosphere or corona (as may be the case for a buoyant magnetic loop, as it emerges from the solar interior at the solar surface); the results shown have greater generality than those obtained from the analytic dispersion relation written down above because they are obtained without imposing the low frequency limit. In the context of our discussion, the following features of the results are most noteworthy:

(1) There is a cut-off in the growth rate at small wavenumbers; this cut-off occurs because the plasma becomes frozen-in at these scales, so that pressure forces lead to stabilization.

(2) A second cut-off (at large wavenumbers) is also present; it is due to thermal conduction acting across sufficiently-thin filaments, which leads to suppression of local temperature contrasts, and hence to stability.

(3) For a large range of horizontal wavenumbers lying between these limits, the growth rate is roughly constant. Furthermore, this range of dominant spatial scales of the instability lies just below present limits on spatial resolution from the ground.

Thus, the thermal instability of the kind treated by Bodo et al. can actually affect loops, or portions of loops, as long as either their spatial extent or their apex densities are not too large; i.e., it will affect either the apexes of small loops in dense atmospheres, or entire small loops in rarified atmospheres. Of particular interest to the topic of this meeting is that the typical scale lengths of current filaments (= 10^3 - 10^6 cm for the cases considered) are too small to be detected by currently available direct observations, but are comparable to the dimensions of current inhomogeneities (and magnetic gradient scales) invoked in a number of in situ coronal heating models (Rosner et al., 1978; Hinata, 1980; Benford, 1983); in such models, the requirement for spatially-localized current flow is recognized, but the mechanism by which such current filamentation occurs is not detailed. The results for the thermal instability obtained by Bodo et al., and summarized here, are distinctly different from those obtained if one had started with an already existing chromosphere/transition region/corona atmospheric structure as the initial equilibrium state to be perturbed (e.g., Heyvaerts, 1974b). In this latter case, high temperature gradients along magnetic field lines are already present. Hence, a tight coupling between the low and high temperature portion of a loop is introduced by efficient thermal conduction and, unlike the case discussed here, the (cold) lower boundary can actively control the thermal evolution of the hotter overlying layers even in the linear regime (for example, see Peres et al., 1982). Because the observational evidence suggests that at least some of the coronal structures seen in soft X-rays (viz., X-ray bright points) arise as a direct consequence of the emergence of magnetic flux above the photosphere (cf. Golub et al., 1980), I believe that the assumption of a "cold" initial state for perturbed pre-coronal structures is far more appropriate than assuming an initially hot state (but note that the question of the stability properties of an already existing hot state is an important issue in its own right − and quite distinct from the problem treated here). The instability process I have briefly summarized here thus provides a natural explanation for the

18

sudden "turn-on" of coronal activity for emerging magnetic structures, though not of their subsequent thermal evolution.

As a final note to this section, I point out that the current-driven thermal instability discussed by Bodo et al. (1985) is complementary to the arguments of E. N. Parker presented in a recent series of papers (see Parker, 1983, and references therein), who has shown that most 2-D flows on a conducting surface penetrated by magnetic field lines (such as the photosphere) inevitably lead to sheared field/plasma geometries which cannot be in magnetostatic equilibrium, and are likely to be strongly dissipative (this point is discussed further below). The shear layers which result (where in fact currents of the type required by the calculations summarized here flow) are indeed also unstable to the Joule instability discussed above; thus, further filamentation similar to that encountered in tearing may occur, but now driven by thermal effects. In general, the results of Ferrari et al. (1982) and Bodo et al. (1985) I've just summarized, together with the arguments presented by Parker (1983) and in the discussion given in the next section, suggest that magnetized plasma emerging from the solar convection zone becomes highly structured in its thermodynamic properties transverse to the magnetic field very soon after its emergence. The observations of arcsecond coronal structuring, such as those reported by Sheeley and Golub (1979) and discussed above, and the recent observations suggesting transient coronal heating within volumes having very small filling factors (Martens, Van den Oord, and Hoyng, 1985), may well be a reflection of just such structuring processes.

(b) The "ordered" versus the "chaotic" magnetized corona

A rather different perspective on the question of sub-resolution structure in the solar outer atmosphere emerges from a long-standing problem in magnetohydrodynamics: can one always construct stable magnetostatic (or magnetohydrodynamic) equilibria for specified normal components of the field on the boundaries. That is, it is unknown whether such constrained equilibria (other than the relatively trivial force or current-free configurations) can always be devised without having some high degree of (coordinate) symmetry (see, for example, Manheimer and Lashmore-Davies, 1984, for a review of plasma equilibria and their stability properties; also Parker, 1979). This has led to the conjecture that the known difficulty of finding equilibria without coordinate symmetries is not just a computational problem, but rather that it is fundamental in the sense that the absence of equilibrium states for geometries that have no simple spatial symmetry is a fundamental property of magnetofluids (Grad, 1967; Parker, 1972, 1979).

This conjecture has recently received theoretical support from several studies. For example, Parker (1985) has shown for the magnetostatic (force-free) problem that arbitrary displacements of field line footpoints on the boundaries of a volume lead to field evolution within the volume which can be described by two independent scalar functions; but that if continued equilibrium is insisted upon as the system evolves, then one of these scalar functions is overdetermined, and that as a consequence, discontinuities (in the force-free alpha parameter) must arise. Similarly, Moffatt (1985) has recently shown that for a simple, initially current-free, magnetostatic configuration, arbitrary displacements of field lines on the boundary lead to current sheet formation. Finally, of particular relevance to the present discussion is the recent demonstration that in the absence of rigid boundaries and gravity, symmetric magnetostatic equilibria are topologically unstable (Tsinganos, 1983; Rosner and Knobloch, 1983; Tsinganos, Distler, and Rosner, 1984). That is, such equilibria have the property that (except for a special class of perturbations of zero measure) when they are subjected to arbitrary perturbations, the perturbed system is in general not guaranteed to be in magnetostatic equilibrium – pressure surfaces may no longer coincide with magnetic flux surfaces – so that the system can become dynamic.

19

Typically, the symmetry of the original equilibrium can be broken because singular points arise within the configuration (as discussed by Parker, 1985, and Moffatt, 1985) and, as shown by Parker (1982, 1983; see also Vainshtein and Parker, 1985), static equilibrium is not possible in the vicinity of such new singular points. Thus, the imposition of external perturbations on an equilibrium MHD structure can lead to a situation in which the system locally departs from static conditions, and local reconnection occurs (cf. reviews by Freiberg, 1982, and Manheimer and Lashmore-Davies, 1984). In the context of laboratory plasma confinement, this process is related to the destruction of magnetic surfaces and the formation of magnetic islands; in the context of heating the solar corona, Parker (1983) has extended this argument to the case for which the normal component of the magnetic field does not vanish on the surface bounding the magnetized plasma (e.g., at the photospheric footpoints of coronal magnetic structures). In this latter case, he has argued that local deviation from magnetostatics and reconnection arise in the lower solar atmosphere because of the continual deformation of coronal magnetic fields by the horizontal cellular photospheric flow field. In summary, local nonequilibrium (i.e., lack of local static equilibrium) can lead naturally to formation of localized reconnection regions and initially isolated magnetic islands throughout the loop volume.

What are some of the observable consequences of such local destabilization of coronal plasmas? Recently, E. Antonucci, K. Tsinganos, and I examined one possibility in the context of observing flare loops. Spectroscopic observations from the Solar Maximum Mission (SMM), P78-1, and Hinotori satellites have led to a number of qualitatively new observations of solar flares, perhaps the most striking of which are the data on line broadening observed during the initial stages of flares (viz., Culhane et al., 1981; Tanaka et al., 1982; Doschek et al., 1985). Thus, the onset of solar flares is characterized by large non-thermal broadening of helium-like soft X-ray resonance lines emitted by highly ionized heavy ions, such as Ca XIX and Fe XXV. This effect is usually attributed to the presence of non-thermal plasma motions (estimated turbulent velocity amplitudes derived from the presumed Doppler temperature are between 100 to 200 km sec^{-1}), and may be observed one or two minutes before the impulsive increase in hard X-ray flux (which traditionally marks the onset of flaring), and before the appearance of high-speed upflows of chromospheric material heated to coronal temperatures (chromospheric "evaporation," identified with the appearance of distinct blue wings in the X-ray lines; Antonucci et al., 1982, 1984). The excess line widths persist as long as there is observational evidence for energy release in the flare site. In the decay phase of flares, non-thermal velocities either are not observed, or are present at very low levels. The turbulence level in the plasma appears to be independent of the position of the flare on the solar disk. Although a number of interpretations of these data are possible (the most commonly-accepted of which regard the overall line profile as a superposition of various Doppler-shifted components resulting from integration along the line-of-sight of various distinct, unresolved loop structures, or parts of loop structures), we have suggested an alternative picture (Antonucci, Rosner, and Tsinganos, 1985), in which the observed line broadening is due to a superposition of Doppler-shifted line profiles arising from distinct plasma flows originating within a *single* loop structure. This hypothesis gives a good account of the data, and turns out to be a natural theoretical consequence of the lack of topological stability of coronal magnetic structures just alluded to. Consider the following key features abstracted from analysis of a large number of flares observed with the Bent Crystal Spectrometer of the SMM Soft X-ray Polychromator (SXRP; Antonucci et al., 1984; see also the extensive summary of the relevant data in Doschek et al., 1985):

(a) The non-thermal excess in the line width is symmetric about the line center of the broadened line for on-disk flares, is larger at flare onset, decreases monotonically during the impulsive phase, and occurs systematically before the onset of line blue shifts.

(b) The degree of non-thermal excess appears to be uncorrelated with the position of flares on the solar disk; i.e., there is no apparent longitude dependence of the isotropic turbulent flow parameters.

(c) When significant soft X-ray emission is detected before the hard X-ray burst, the non-thermal line broadening is observed to increase one or two minutes before the hard X-ray burst.

In summary, observations of individual flares indicate the presence of fairly isotropic flows during the *early* part of flare onset; these flows exist in addition to the systematic upward flows (which are most likely related to the initial "evaporation" of chromospheric material). The lack of any longitude dependence of both the red and blue wings of the line broadening for different flares and its symmetry suggests that the broadening is indeed isotropic (and not simply due to a superposition of Doppler-shifted components which arise within distinct, but unresolved, loops); the timing of the onset of strong line broadening calls into question its association with the evaporation process; and the fact that broadening occurs (and is largest) at the very onset of the flare argues that it is *pre-existing* (not newly-evaporated) coronal material which is responsible for the line broadening. Antonucci et al. thus argue the proposition that the observed broadening appears isotropic not because of accidental superposition of various unresolved flaring loops (and associated interior convective flows) along the line-of-sight, but because the fluid which gives rise to the observed emission is indeed isotropically turbulent in any one given loop structure (i.e., the fluid is, on the dimensions of the loop, locally isotropically turbulent).

What then is the model? The basic conjecture put forth by Antonucci, Rosner, and Tsinganos (1985) is that a loop system subjected to continual deformations applied to the photospheric footpoints will continue to evolve quasi-steadily (consistent with the field line topology imposed by the perturbation), leading to island formation and, when regions of overlapping islands have formed, to the onset of field line stochasticity, strongly enhanced local reconnection and dissipation, and enhancement of plasma transport coefficients (cf. Freiberg, 1982; in a related process, proposed in the context of a specific MHD instability, e.g., island overlap of unstable tearing modes located in distinct unstable tearing layers, has been proposed by Finn, 1975, and applied to the flare onset problem by Spicer, 1976, 1977). Antonucci et al. (1985) caution that it is essential to distinguish this succession of events from the destabilizing process previously suggested by Low (1982a,b) and others, who have argued that solar flares represent the terminal point of an evolutionary sequence of "nearby" equilibria through which a system evolves as it is subjected to external perturbations; this terminal point is reached when the sequence of equilibria ends in the sense that there are no longer any nearby equilibria to which the system could evolve. The model proposed by Antonucci et al. is distinguished from these earlier studies in that (i) it does not identify the onset of flaring with the point of termination of a sequence of nearby equilibrium states, but rather views it as the point at which a topological unstable, quasi-steadily evolving state (which need not be force-free; compare with Heyvaerts and Priest, 1983) reaches the stochastic domain; and (ii) the instability does not manifest itself in a global MHD instability, but rather in a drastic departure from statics throughout the entire volume of the system, wherever singular field line behavior as a result of island overlap, and local reconnection, occurs. These localized reconnection events are then expected to occur at the very onset of the flare — indeed, in this picture, they mark the very beginning of flare onset.

It is of course necessary to demonstrate quantitative, and not only qualitative, agreement with the observations, and Antonucci et al., indeed show that one can provide a reasonable "back-of-the-envelope" fit to the data, e.g., reconciling observed temperatures, densities, and inputed turbulent velocities with the model. In the present connection, one of the most intriguing results of this comparison with the data is that reasonable agreement with the data only

follows if one assumes a rather small filling factor for the matter which actually contributes to the isotropic broadening component: the volume filled by this component must be approximately 5% of the total volume seen by the SXRP in emission. This implies (in the most naive intepretation) an upper bound on the linear dimensions of the emission volume of roughly 10^8 cm; in a physically more plausible picture, in which the emission arises within thin structures enlongated along the background ("guide") field, the dimensions of the emitting regions would be just below the arcsecond level.

The model proposed by Antonucci et al. to account for the turbulent line broadening thus has several features which make it interesting from the point of view of "sub-resolution" structure. First, it predicts rather small filling factors for the regions primarily responsible for the isotropic component of the line broadening. Second, it is likely that the reconnection sites invoked to account for the macroscopic plasma streaming will also be sites of localized particle acceleration. Observational support for this suggestion is provided by the fact that hard X-ray bursts are observed precisely during the period in which turbulent line broadening is observed. This timing coincidence is to be expected if the fast particles which give rise to the bursts have their origin in the many scattered reconnection sites invoked in the flare line broadening process itself. This would imply that particle acceleration does not occur at just a very few selected sites within a loop, but rather occurs throughout the loop volume. An especially interesting possibility is then that particles accelerated in any one such reconnection region continue to be accelerated in other reconnection regions they encounter as they traverse the loop; such multiple acceleration encounters can provide the Fermi process called for by the particle spectra deduced from the SMM hard X-ray and gamma ray observations (viz., Ramaty et al., 1985, and references therein). A third feature of this model is that it does not sharply distinguish between flare heating and the far more prevalent low-level "microflaring" (Lin et al., 1984) and other low-level transient brightening (cf. Porter, Toomre, and Gebbie, 1984) which seems to characterize the active solar corona and transition region. Indeed, as argued by Rosner and Vaiana (1978), a stochastic energy release process of this kind naturally gives rise to the observed power law dependence of the integral number of (hard X-ray) transients on peak flux (or total energy released; see also Datlowe, Elcan, and Hudson, 1974). Thus, it may be that the transient formation of dissipative structures in the solar corona is responsible for much of the overall coronal heating (cf. Parker, 1972, 1979), a process which can only be studied by looking at the Sun's outer atmosphere with instruments of high (i.e., sub-arcsecond) spatial resolution.

IV. SUMMARY

In this paper, I have attempted to provide a personal perspective on the problem of spatial structuring on scales smaller than can presently be directly and regularly observed from the ground or with current space-based instrumentation. I believe that there is abundant evidence from both observations and theory that such spatial structuring of the solar outer atmosphere is ubiquitous not only on the observed scales, but also on spatial scales down to (at least) the sub-arcsecond range. This is not to say that we can anticipate the results to be obtained from observations on these small scales: quite the opposite. What is clear instead is that many of the classic problems of coronal and chromospheric activity – involving the basic dissipative nature of magnetized plasmas – will be seen from a novel perspective at these scales, and that there are reasons for believing that dynamical processes of importance to activity on presently-resolved scales will themselves begin to be resolved on the sub-arcsecond level. Since the Sun is the only astrophysical laboratory for which there is any hope of studying these processes in any detail, this observational opportunity is an exciting prospect for any student of magnetic activity in astrophysics.

REFERENCES

Antonucci, E., and 8 co-authors, 1982, *Solar Phys.*, 78, 107.

Antonucci, E., Gabriel, A. H., and Dennis, B. R., 1984, *Astrophys. J.*, 287, 917.

Antonucci, E., Dennis, B. R., Gabriel, A. H., and Simnett, G. M., 1985, *Solar Phys.*, 96, 129.

Antonucci, E., Rosner, R., and Tsinganos, K., 1985, *Astrophys. J.*, in press.

Athay, G., 1982, *Astrophys. J.*, 263, 982.

Benford, G., 1983, *Astrophys. J.*, 269, 690.

Bodo, G., Ferrari, A., Massaglia, S., Rosner, R., and Vaiana, G. S., 1985, *Astrophys. J.*, 291, 798.

Culhane, J. L., and 17 co-authors, 1981, *Astrophys. J. (Letters)*, 244, L141.

Datlowe, D. W., Elcan, M. J., and Hudson, H. S., 1974, *Solar Phys.*, 39, 155.

Doschek, G. A., et al., 1985, in *SMM Workshop Proceedings*, "Chromospheric Explosions," in press.

Feldman, U., 1983, *Astrophys. J.*, 275, 367.

Feldman, U., Doschek, G. A., and Mariska, J. T., 1979, *Astrophys. J.*, 229, 369.

Ferrari, A., Rosner, R., and Vaiana, G. S., 1982, *Astrophys. J.*, 263, 944.

Finn, J. M., 1975, *Nucl. Fusion*, 15, 845.

Freiberg, J. P., 1982, *Rev. Mod. Phys.*, 54, 801.

Golub, L., Maxson, C. W., Rosner, R., Serio, S., and Vaiana, G. S., 1980, *Astrophys. J.*, 238, 343.

Grad, H., 1967, *Phys. Fluids*, 10(1), 137.

Heyvaerts, J., 1974a, *Solar Phys.*, 38, 419.

Heyvaerts, J., 1974b, *Astron. Astrophys.*, 37, 65.

Heyvaerts, J. and Priest, E. R., 1983, *Astron. Astrophys.*, 117, 220.

Hinata, S., 1980, *Astrophys. J.*, 235, 258.

Jockers, K., 1978, *Astrophys. J.*, 220, 1133.

Lin, R. P., Schwartz, R. A., Kane, S. R., Pelling, R. M., and Hurley, K. C., 1984, *Astrophys. J.*, 283, 421.

Low, B. C., 1982a, *Rev. Geophys. Space Phys.*, 20, 145.

Low, B. C., 1982b, *Solar Phys.*, 77, 43.

Manheimer, W. M. and Lashmore-Davies, C., 1984, *NRL Report.*

Martens, P. C. H., Van den Oord, G. H. J., and Hoyng, P., 1985, *Solar Phys.*, 96, 253.

Maxson, C. W. and Vaiana, G. S., 1977, *Astrophys. J.*, 215, 919.

Moffatt, K., 1985, to be submitted.

Parker, E. N., 1963, *Astrophys. J.*, 138, 552.

Parker, E. N., 1972, *Astrophys. J.*, 174, 499.

Parker, E. N., 1979, *Cosmical Magnetic Fields* (Oxford, Clarendon Press).

Parker, E. N., 1982, *Geophys. Astrophys. Fluid Dyn.*, 22, 195.

Parker, E. N., 1983, *Geophys. Astrophys. Fluid Dyn.*, 24, 79.

Parker, E. N., 1985, *Geophys. Astrophys. Fluid Dyn.*, in press.

Peres, G., Rosner, R., Serio, S., and Vaiana, G. S., 1982, *Astrophys. J.*, 252, 791.

Petschek, H. E., 1964, in *AAS-NASA Symp. on Solar Flares* (NASA SP-50), p. 425.

Porter, J. G., Toomre, J., and Gebbie, K. B., 1984, *Astrophys. J.*, 283, 879.

Rabin, D. and Moore, R., 1984, *Astrophys. J.*, 285, 359.

Ramaty, R., et al., 1985, in *SMM Workshop Proceedings,* "Chromospheric Explosions," in press.

Rosner, R. and Knobloch, E., 1983, *Astrophys. J.*, 262, 349.

Rosner, R. and Vaiana, G. S., 1978, *Astrophys. J.*, 222, 1104.

Rosner, R., Golub, L., Coppi, B., and Vaiana, G. S., 1978, *Astrophys. J.*, 222, 317.

Sheeley, N. R., Jr., and Golub, L., 1979, *Solar Phys.*, 63, 119.

Spicer, D. S., 1976, *Naval Research Lab. Report No. 8036.*

Spicer, D. S., 1977, *Solar Phys.*, 53, 305.

Sweet, P. A., 1958, *IAU Symp. 6,* 123.

Tanaka, K., Watabane, T., Nishi, K., and Akita, K., 1982, *Astrophys. J. (Letters),* 254, L59.

Tsinganos, K., 1983, *Astrophys. J.*, 259, 832.

Tsinganos, K., Distler, J., and Rosner, R., 1984, *Astrophys. J.*, 278, 409.

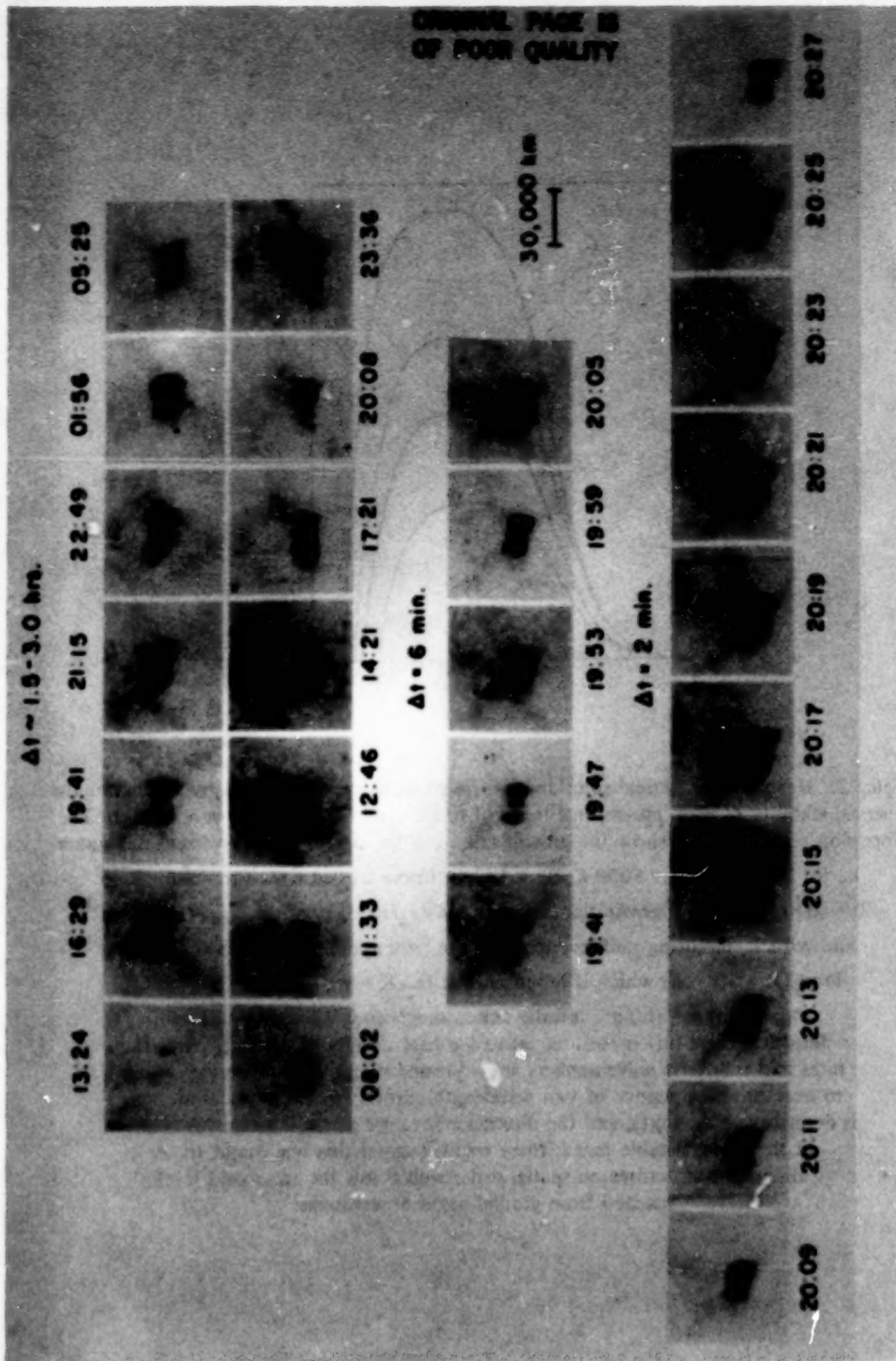Vainshtein, S. I. and Parker, E. N., 1985, preprint.

Figure 1. An example of structuring of the solar corona, seen at the very limits of spatial resolution attainable on Skylab over 10 years ago (from Sheeley and Golub, 1979). The images show a coronal bright point resolved into component "loops," much like the structure of the far larger active region complexes.
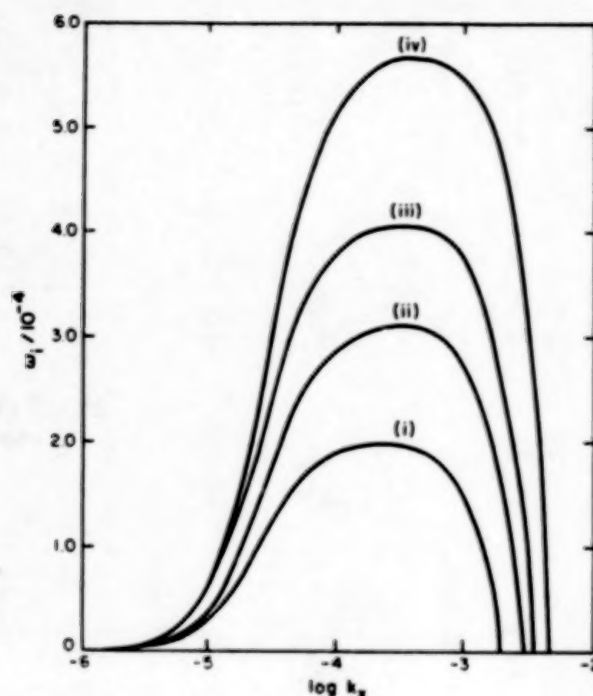
Figure 2: Results of numerical solution of the eigenvalue problem posed by solving for the thermal stability of cool, pre-coronal loops of finite extent (from Bodo et al., 1985). The dispersion relation curves show the growth rate $\omega_i(\equiv|\mathrm{Im}\ \omega|)$ versus transverse wavenumber k_x for loops with $T_0 = 5000$ K, $B_0 = 100$ G. Curve labeled (i) is for a finite loop ($R = 10^7$ cm) which is gravitationally stratified ($z_0/R = 1$), with $n_{apex} = 10^{12}$ cm^{-3} and with J_0 balancing radiative losses at the loop apex; curve (ii) is for a finite loop ($R = 10^7$ cm) which is homogeneous ($z_0/R = \infty$), with $n = 10^{12}$ cm^{-3}; curves (iii) and (iv) are infinite and homogeneous cases with different densities; curve (iii) is for n equal to the base density of case (i). Growth rates and transverse wavenumbers are expressed in cgs units. The key results to note are the presence of two wavelength cutoffs (whose physical meaning is described in the text), and the dimensional values of the inverse wavenumber in the most unstable range: these results suggest that one ought to see dissipative structures on spatial scales well below the arcsecond level reached from ground-based observations.

SOLAR X-RAY PHYSICS
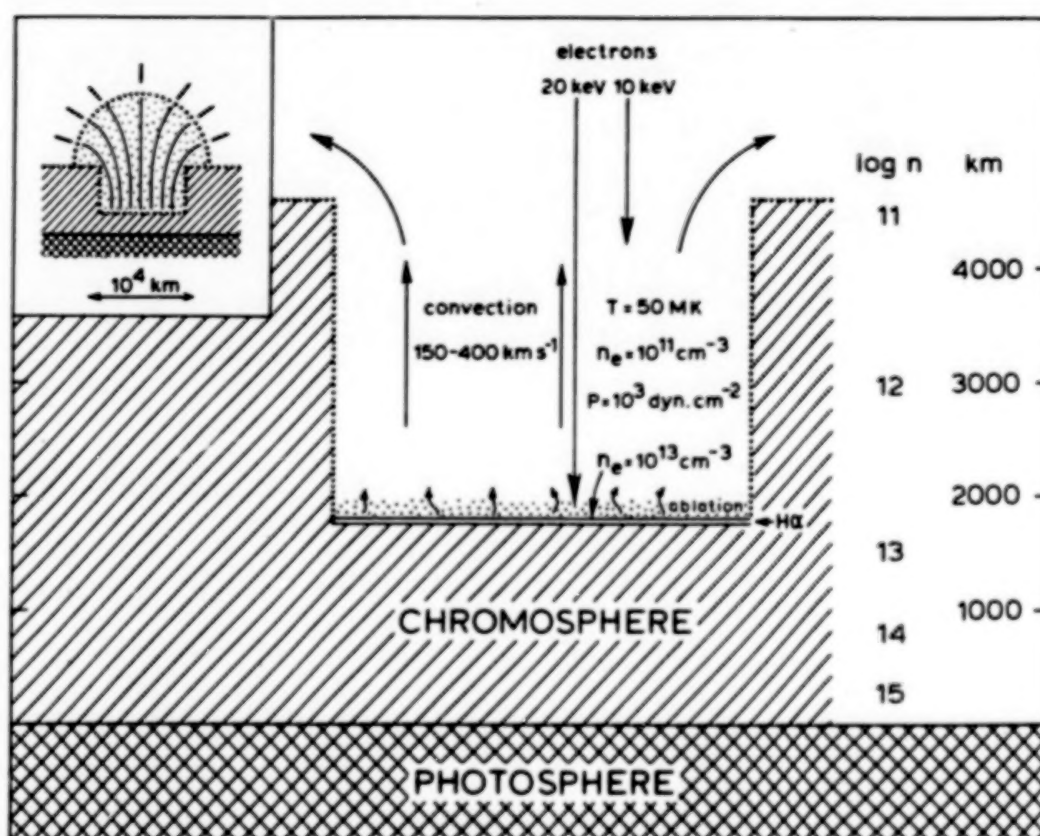
THE FLARE KERNEL IN THE IMPULSIVE PHASE
(Invited)

Cornelis de Jager

Laboratory for Space Research, Utrecht, the Netherlands

ABSTRACT

The impulsive phase of a flare is characterized by impulsive bursts of X-ray and microwave radiation, related to impulsive footpoint heating up to 50 or 60 MK, by upward gas velocities (150 to 400 km s^{-1}) and by a gradual increase of the flare's thermal energy content. These phenomena, as well as non-thermal effects, are all related to the impulsive energy injection into the flare. The available observations are, also quantitatively, consistent with a model in which energy is injected into the flare by beams of energetic electrons, causing ablation of chromospheric gas, followed by convective rise of gas. Thus, a hole is "burned" into the chromosphere; at the end of the impulsive phase of an average flare the lower part of that "hole" is situated about 1800 km above the photosphere. Hα and other optical and UV line emission is radiated by a thin layer ($\sim$ 20 km) at the bottom of the flare kernel. The upward rising and outward streaming gas cools down by conduction in about 45 s. The non-thermal effects in the initial phase are due to curtailing of the energy distribution function by escape of energetic electrons. The single flux tube model of a flare does not fit with these observations; instead we propose the spaghetti-bundle model. Microwave and gamma-ray observations suggest the occurrence of dense flare knots of $\sim$800 km diameter, and of high temperature. Future observations should concentrate on locating the microwave/gamma-ray sources, and on determining the kernel's fine structure and the related multi-loop structure of the flaring area.

I. MAIN CHARACTERISTICS OF THE IMPULSIVE PHASE

There are four main characteristics of the impulsive phase. The impulsive phase of a solar flare is primarily defined as the period of a few to ten minutes during which *impulsive bursts* of hard X rays ($\gtrsim$ 20 keV) and of microwave radiation are emitted. There is a hierarchy of impulsive bursts, starting with the *burst complexes*, each of which last for about one or two minutes (Figure 1). These consist each of a few to some ten shorter lasting bursts, the *elementary flare bursts* (De Jager and De Jonge, 1978) which lasts for about 5 to 15 seconds each. These, in turn, can consist of still shorter lived bursts, the *sub-second pulses* (Kaufmann et al., 1980; Orwig, Frost, and Dennis, 1981) which are observed both in hard X rays and in cm-mm radiowaves. If observed simultaneously in both wavelength regions they appear to be synchronous down to the accuracy of the measurements (Takakura et al., 1983).

Imaging observations in X rays by means of the Hard X-Ray Imaging Spectrometer aboard SMM (Van Beek et al., 1980) have shown that the hard X-ray bursts are emitted by small localized areas, the *footpoints* or *flare kernels* (Hoyng et al., 1981). These footpoints occur often in pairs, and are then localized at either side of the magnetic inversion line (the "neutral line"), an observation that supports the flux tube model of a flare. Although the footpoints are principally visible in hard ($\gtrsim$ 15 keV) X rays they can also be detected with about the same intensity in X rays of smaller photon energy ($\approx$ 5 keV) if sufficient care is taken to subtract the gradual X-ray background flux (De Jager and Boelee, 1984; De Jager, Boelee, and Rust, 1984); cf. Figure 2. Apparently, the footpoints, although not a specific characteristic of the hard X-ray component, are very significant for the impulsive phase, because they occur only during the emission of the burst complexes.

Very characteristic for the early part of the impulsive phase are the upward motions (Antonucci and Dennis, 1983; Antonucci, Gabriel, and Dennis, 1985) with observed velocity components of 150 to 400 km s^{-1}, values derived from X-ray spectral data. The upward motions start rather suddenly at the very onset of the impulsive phase and they decrease with time, quasi-exponentially, with a typical e-folding time of one to a few minutes; cf. Figures 3 and 4. These motions are ascribed to the upward convection of hot gas, originating by ablation of the chromosphere through heating by incident electron beams, or by a hot plasma front.

During the impulsive phase the *thermal energy content* of the X-ray emitting component of the flaring region *increases steadily* (De Jager and Boelee, 1984; Antonucci, Gabriel, and Dennis, 1985) until the last X-ray burst has terminated; cf. Figures 4 and 5. The burst signature is absent in the $E_{th}(t)$ relation which shows that the temporal behavior of the energy input, which occurs through the impulsive bursts, is smoothed out. We will see later that this is caused by the way gas is streaming convectively from the kernel into the surrounding area, the flare tongue, which is the region responsible for the emission of the gradual phase component.

The four aspects listed above: impulsive bursts, footpoints, convective motions, and energy input, are the main characteristics of the impulsive phase.

II. PHENOMENOLOGY AND SCENARIO OF FLARE KERNEL HEATING

An important aspect of the first part of the impulsive phase of flares with essentially one of at most two impulsive burst complexes is that the Doppler temperature derived from line broadenings of X-ray spectral lines becomes abruptly high at the onset of the impulsive phase (Antonucci, Gabriel, and Dennis, 1985; Figure 5). Within a minute it appears to rise to about 5×10^7 K or higher, to decrease slowly, and quasi-exponentially thereafter. With an e-folding time of 1.5 min it approaches the electron temperature derived from line intensity ratios. The temperature derived from the count-rate ratios in the medium-energy HXIS channels ($\approx$ 16 keV) shows the same behavior (Figure 6). The Doppler-temperature is an ionic temperature because it is derived from the thermal, or in any case, from the stochastic motion field of the ions. But it is at the same time an electron temperature, because the electron-ion exchange time in the kernel plasma is short, of the order of 0.1 s, so that a thermal energy distribution establishes rapidly. There is, however, one reserve. The average energy of electrons of 5×10^7 K is $\approx$5 keV, while the kernel area is transparent for electrons with $E \gtrsim 15$ keV, so that the tail of the electron energy distribution curve cannot form. The excitation and ionization of the gas ions is determined by the high-energy electrons, hence by the tail of the electron energy distribution function. This is the reason why the electron temperature derived from the line intensity ratios, and also the one derived from count-rates ratios in low-energy (3 to 10 keV) HXIS channels, is lower than the temperature derived from count-rate ratios around 16 keV, and also lower than the ionic Doppler temperature: the latter is defined by the main (average) part of the energy distribution curve.

The transparency of the kernel for particles with $E \gtrsim 15$ keV is also the reason why the high temperature in the early part of the impulsive phase must be due to heating of electrons with energies $\gtrsim 15$ keV: under standard kernel conditions only these can penetrate through the kernel and heat the underlying chromosphere.

From an analysis of the X-ray and XUV observations of two flares with essentially one burst-complex (8 April and 5 November, 1980) the present author (De Jager, 1985b) has derived a model of a flare kernel as shown in Figure 7. This model describes the flare kernel at the end

of the ablation process, hence at the end of the impulsive phase: heating of the chromosphere by bombardment with electron beams with $E \gtrsim 15$ keV causes ablation of the chromosphere. At the end of the impulsive phase the bottom of the kernal "hole" has decreased to a height of ≈ 1800 km above the chromosphere. There, the normal chromospheric particle density is $\approx 10^{13}$ cm^{-3}. At the transition between chromosphere and kernel a thin (≈ 20 km) layer of particles with $T_{el} \approx 10^4$ K forms, emitting Hα and other low energy lines. This layer is heated to 5×10^7K in about 10 s and is replaced by new material through continuous ablation. The ablated particles move upward convectively with velocities of ≈ 150 to 400 km s^{-1}. Since the kernel has a depth of ≈ 2500 km this heated gas takes 8 to 10 s to reach the "top" of the chromosphere. During the impulsive phase a "dome" of superhot gas is formed over the kernel. This dome contains about four times more particles than the kernel proper (see Figure 3), but its gas content has mainly a horizontal velocity component, with a possible structure as suggested in the insert to Figure 7. Guided by magnetic field lines, assumed vertical in the kernel, and fanning out into the "dome" and beyond (the "spaghetti-bundle model") it takes the plasma about 45 s to cool down conductively to the ~20 MK temperature, characteristic for the gradual phase component. The conduction time of 45 s is equal to the time gas needs with $v = 200$ km s^{-1} to move along the field lines through kernel and dome.

The kernel model, described here, consistently unites the XRP spectral observations of line intensity ratios, line broadening and displacement and the data on heating and temperature derived from HXIS and HXRBS data. As will be shown in Section IV this is also true quantitatively.

III. CORONAL EXPLOSIONS

Coronal explosions are a feature discovered by De Jager and Boelee (1984), and are further described by De Jager, Boelee, and Rust (1984), De Jager (1985a), and De Jager and Lemmens (1985). Figure 2, lower part, shows the explosion observed in the flare of 12 November 1980, 02:50 UT.

The coronal explosion is a density wave originating from a small area near to, or identical with, the flare's footpoints. The waves propagate with initial velocities of the order of a few hundred to more than a thousand km s^{-1}, a velocity which normally decelerates rapidly to values below 100 km s^{-1}. The explosion shown in Figure 2 has an initial lateral velocity component of 200 km s^{-1} which slowed down to 20 km s^{-1} in some two minutes. It started just after the last hard X-ray burst complex, cf. Figure 1.

The most probable explanation for these observations is that the explosion shows the lateral displacement of the plasma escaping from the kernel, guided by the magnetic field line pattern emanating from the kernel area, as suggested by the schematic drawing in the insert to Figure 7.

IV. NUMBERS AND ENERGIES

We summarize some typical values, derived from observations of the flares of 8 April and 5 November 1980.

Number of particles ablated (De Jager, 1985b):

> Per second for the whole kernel: 4×10^{36} s^{-1}
> During the whole impulsive phase for the whole kernel: 3.5×10^{38}
> During the whole impulsive phase, per cm^2: 3.2×10^{20} cm^{-2}.

Next we summarize values for the time integrated energies over the impulsive phase:

> Energy of incident electron beam > 25 keV (Dennis et al., 1985): 6×10^{30} erg
> Energy of incident electron beam > 16 keV (De Jager, 1985b): 13×10^{30} erg
> Energy of convective motions (Antonucci, Gabriel, and Dennis, 1985): 7×10^{30} erg
> Maximum thermal energy content of gradual phase component (Dennis et al., 1985):
> $\quad$ 2.6×10^{30} erg
> Energy needed to heat 20 km thick layer ($n_e = 10^{13}$ cm^{-3}) to 50 MK (De Jager, 1985b):
> $\quad$ 3.6×10^{30} erg.

These energy values are internally consistent and support the ablation-convection model.

V. MICROWAVE AND GAMMA-RAY OBSERVATIONS

These may yield important information on the − relatively − high density phenomena in flares. Microwave observations made at the highest frequencies (90 MHz) by Kaufmann et al. (1985a) demand an interpretation in terms of source densities of the order of $n_e \approx 10^{14}$ cm^{-3} (Kaufmann et al., 1985b) and source sizes of ≈ 800 km diameter. Their temperatures should be high, above 10^8 K. Also gamma-ray observations suggest source densities of that order (Chupp, 1984).

On the basis of the model shown in Figure 7 we therefore suggest that these sources are situated just below the flare kernel's base, in the dense parts of the chromosphere, at some 500 to 1500 km above the photosphere. The effects of flare heating by sources at that level need to be investigated and form an interesting challenge to theorists, as well as to observers who should locate these sources and determine their precise sizes.

VI. REQUIREMENTS FOR FUTURE RESEARCH: OBSERVATIONAL AND THEORETICAL

The model of the flare kernel described in Section II is a static model while a kernel is a dynamic feature. In its very beginning, when the hot ($n_e = 10^{11}$ cm^{-3}) gas has not yet formed, heating and ablation of the chromosphere is easier than later. In the course of the ablation process a high plasma pressure is built up ($\approx 10^3$ dynes cm^{-2}) which pushes the Hα emitting region downward; this explains the observed downwards velocities in Hα and other spectral lines. In addition, ablation "burns" a hole into the chromosphere, which, at the end of the impulsive phase, results in a structure outlined in Figure 7.

A first theoretical problem to tackle is the dynamic time development of the flare kernel. Another theoretical problem is that of the non-thermal character of the electron energy distribution in the kernel. Curtailing of the electron energy distribution curve by escaping electrons (as described in Section II) may lead to a significant difference between the ionic Doppler temperatures and the electron temperatures derived from low-energy count rate ratios or from line intensity ratios.

Observationally the solution of the following problems seems essential for further progress in the understanding of solar flares. The observation that the gradual component of flares is not confined to a single loop (as assumed in the classical flare picture) but to a large volume with a very small filling factor ($\approx 10^{-2}$) suggests the "spaghetti-bundle" model for the flare area. This model must also demand a considerable fine structure of the flare kernel seen from above. Hence it is worth investigating (a) if the kernel area ($\approx 10^8$ km^2) has a fine structure, and (b) if the gradual phase component consists of many loops, corresponding to the footpoints in the fine-structure of the kernel. In addition, it is of importance to examine if the propagation of the density waves related to the coronal explosions is associated with shock-wave phenomena such as the existence of a thin layer of temperature enhancement near the shocks.

One of the most important topics for future research seems the observation of the high temperature, high density, flare knots whose existence is suggested by extreme microwave and by gamma-ray observations. Are these knots really situated below the flare kernel and if so, at what level; what are their densities and sizes. Solution of this problem may be fundamental for further progress in our understanding of solar flares.

REFERENCES

Antonucci, E. and Dennis, B. R., 1983, *Solar Phys.*, *86*, 67.

Antonucci, E., Gabriel, A., and Dennis, B. R., 1985, in press.

Chupp, E. L., 1984, *Ann. Rev. Astron. Astrophys.*, *22*, 359.

De Jager, C., 1985a, *Solar Phys.*, *96*, 143.

De Jager, C., 1985b, *Solar Phys.*, accepted.

De Jager, C. and Boelee, A., 1984, *Solar Phys.*, *92*, 227.

De Jager, C. and De Jonge, G., 1978, *Solar Phys.*, *58*, 127.

De Jager, C. and Lemmens, A., 1985, *Solar Phys.*, in preparation.

De Jager, C., Boelee, A., and Rust, D. M., 1984, *Solar Phys.*, *92*, 245.

Dennis, B. R., Kiplinger, A. L., Orwig, L. E., and Frost, K. J., 1985, NASA Technical Memorandum 86187.

Hoyng, P., and 11 co-authors, 1981, *Astrophys. J. (Letters)*, *246*, L155.

Kaufmann, P., Strauss, F. M., Opher, R., and Laporte, C., 1980, *Astron. Astrophys.*, *87*, 58.

Kaurmann, P., Correia, E., Costa, J. E. R., Zodi Vaz, A. M., and Dennis, B. R., 1985a, *Nature*, *313*, 380.

Kaufmann, P., Correia, E., Costa, J. E. R., and Zodi Vaz, A. M., 1985b, *Astron. Astrophys.*, in preparation.

Orwig, L. E., Frost, K. J., and Dennis, B. R., 1981, *Astrophys. J. (Letters)*, *244*, L163.

Takakura, T., Kaufmann, P., Costa, J. E. R., Degaonkar, S. S., Ohki, K., and Nitta, N., 1983, *Nature*, *302*, 317.

Van Beek, H. F., Hoyng, P., Lafleur, B., and Simnett, G. M., 1980, *Solar Phys.*, *65*, 39.
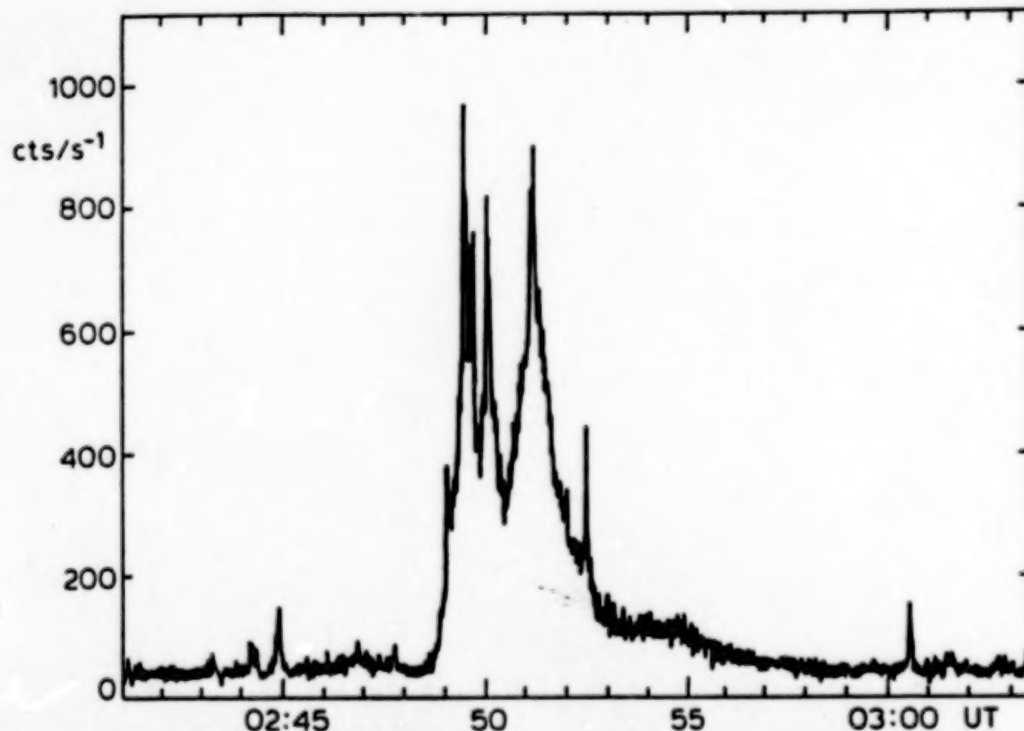
Figure 1. Impulsive bursts of the flare of 12 November 1980; 02:50 UT. The main burst complex is at 02:49-:51 UT. There are earlier weaker bursts; those at 02:44 UT and 02:45 UT mark the start of the flare (HXRBS observations, by courtesy of B. R. Dennis; see De Jager and Boelee, 1984).
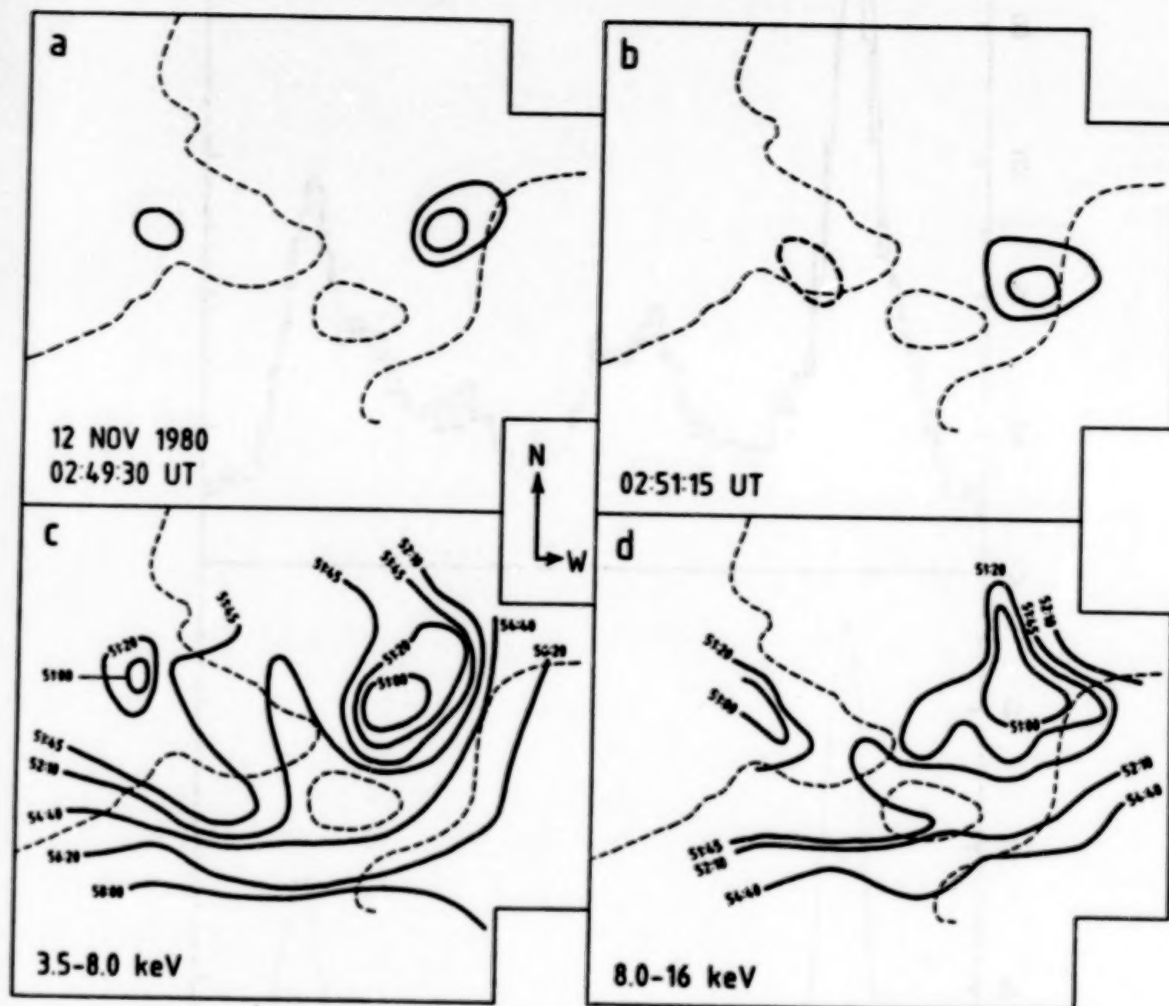
Figure 2. Upper part: even low-energy X-ray observations of flares show the footpoints, but only at the time of the hard X-ray bursts, and only after careful background subtraction (De Jager and Boelee, 1984; De Jager, Boelee, and Rust, 1984). The lower part shows the coronal explosion associated with this flare (see Section III) in two energy ranges. The lines are isochrones, labeled with the time in minutes and seconds after 12 November 1980, 02:00 UT. In all four figures the dashed line is the inversion line. For other data relevant to this flare see Figures 1 and 5.
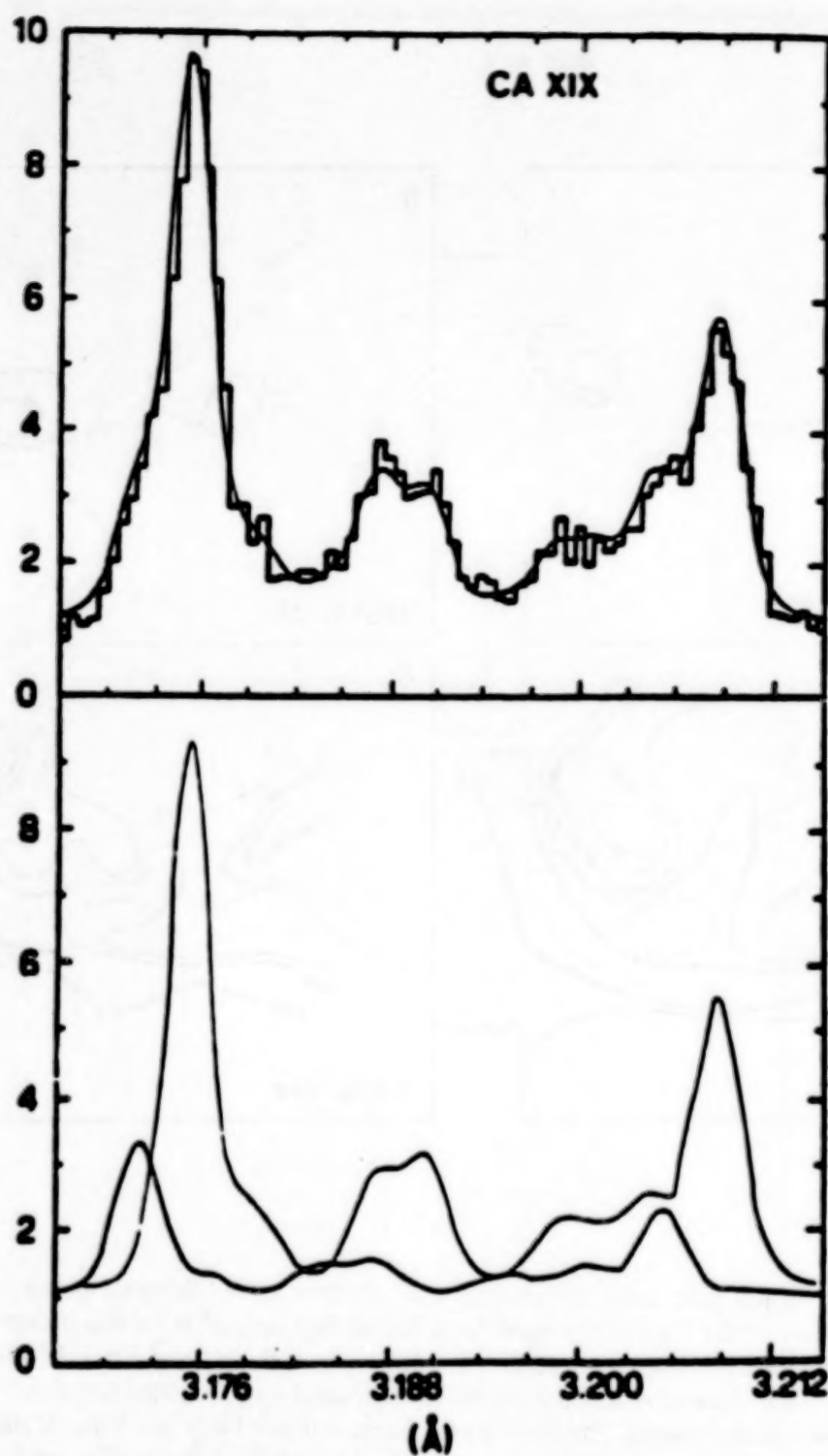
Figure 3. Convective velocities in flare kernels are derived from line displacements in
X-ray spectra. About one-fifth of the hot material shows upward displacement;
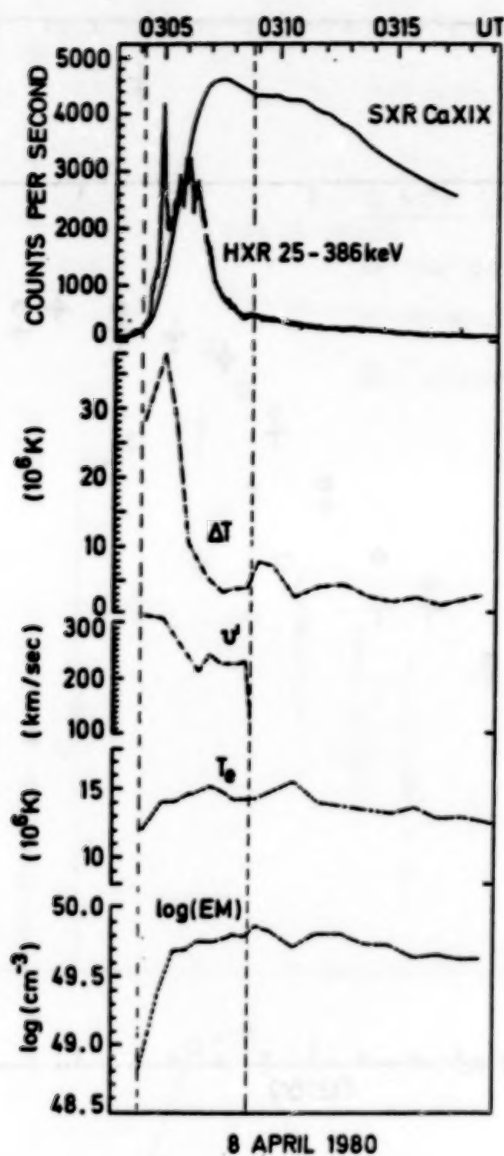the rest is stationary (Antonucci, Gabriel, and Dennis, 1985).

Figure 4. Phenomena in the impulsive phase of the flare of 8 April 1980; 03:50 UT.
The upward velocities (v') increase abruptly to high values at the start of the
impulsive phase, to gradually decrease afterwards. Note also the relation
with the impulsive hard X-ray burst complex, and with ΔT_D
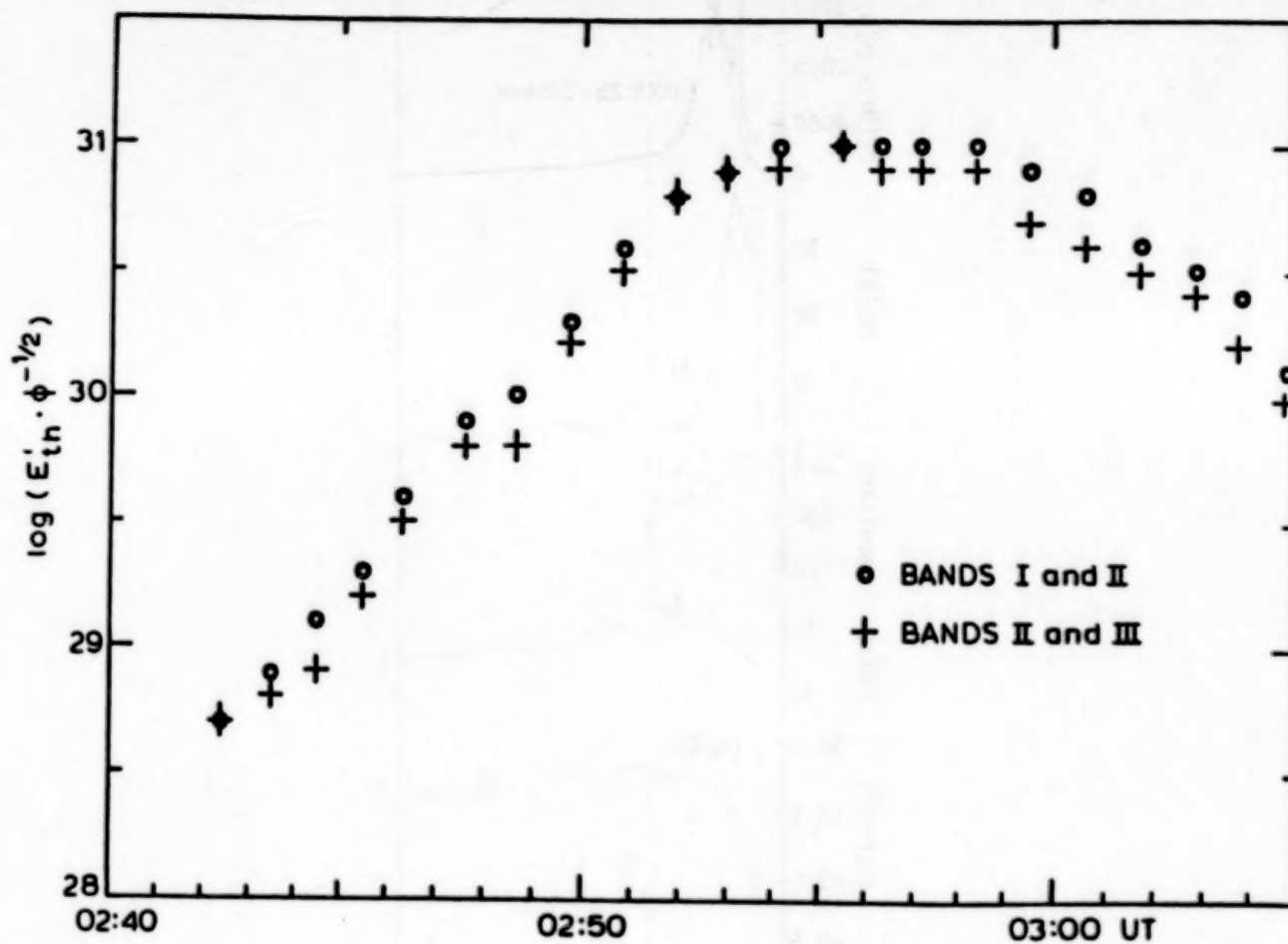(XRP observations; Antonucci, Gabriel, and Dennis, 1985).

Figure 5. Thermal energy content of a flare increases gradually and reaches a maximum at the end of the impulsive phase (De Jager and Boelee, 1984). Here, ϕ is the filling factor, $\approx 10^{-2}$.
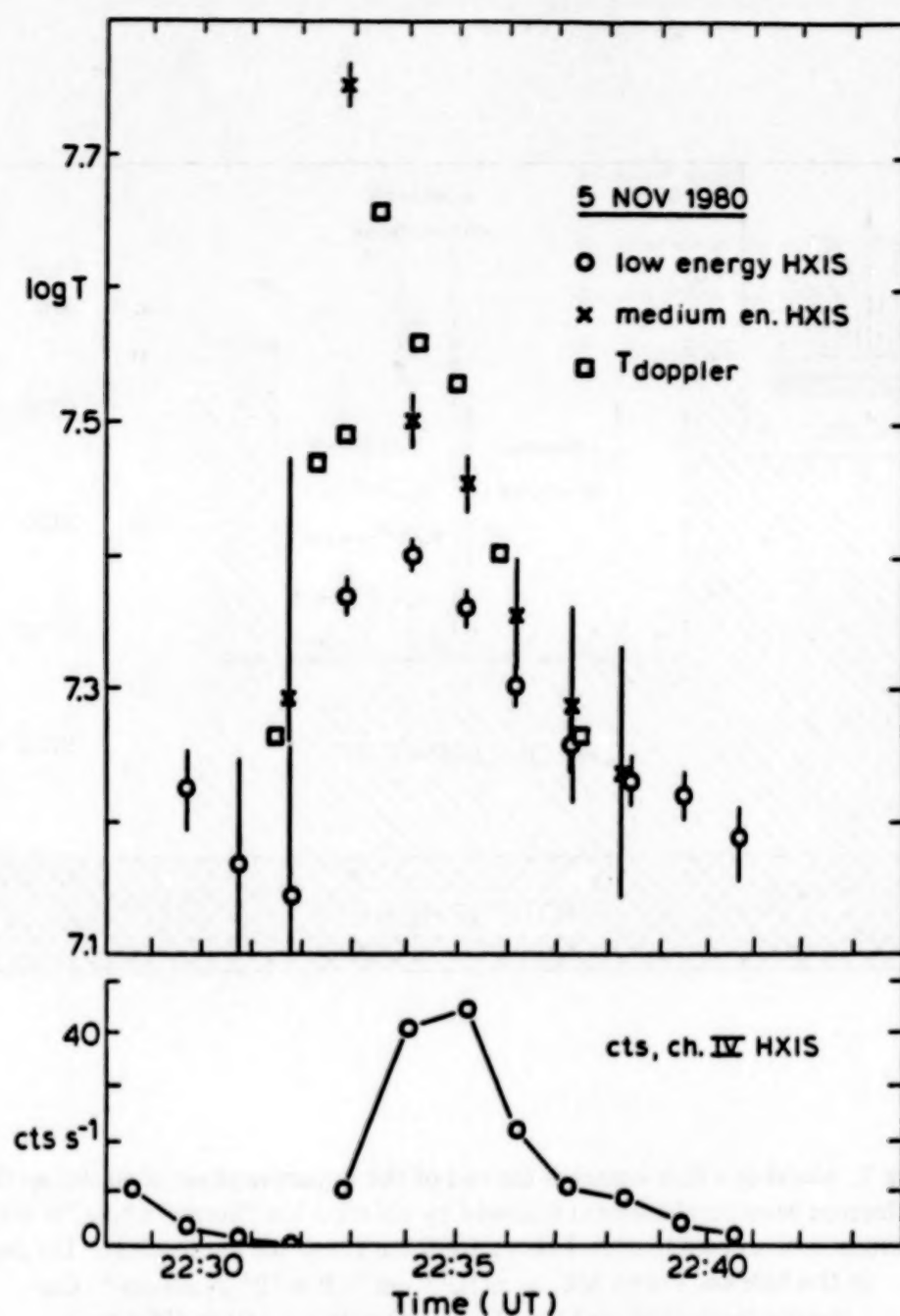
Figure 6. Non-thermal effects in the impulsive phase. At the flare's onset the temperature derived from line broadening, and the one derived from medium-energy HXIS count rates (≈ 16 keV) rise abruptly to ≈ 50 MK, to decrease quasi-exponentially thereafter, with an e-folding time of 1.5 min. The electron temperature, derived from line intensity ratios, and the temperature derived from low energy HXIS count-rate ratios increases too, but less. After a few minutes all temperatures are equal. The lower part of the figure shows the count rate in HXIS channel IV (11 to 16 keV), to give an impression of the time-development of the impulsive phase (De Jager, 1985b).

electrons
20 keV 10 keV

log n   km

11

4000

convection   T = 50 MK

150-400 km s⁻¹ $n_e = 10^{11}$ cm⁻³

12   3000

$P = 10^3$ dyn. cm⁻²

$n_e = 10^{13}$ cm⁻³

2000

ablation ← Hα

13

10^4 km
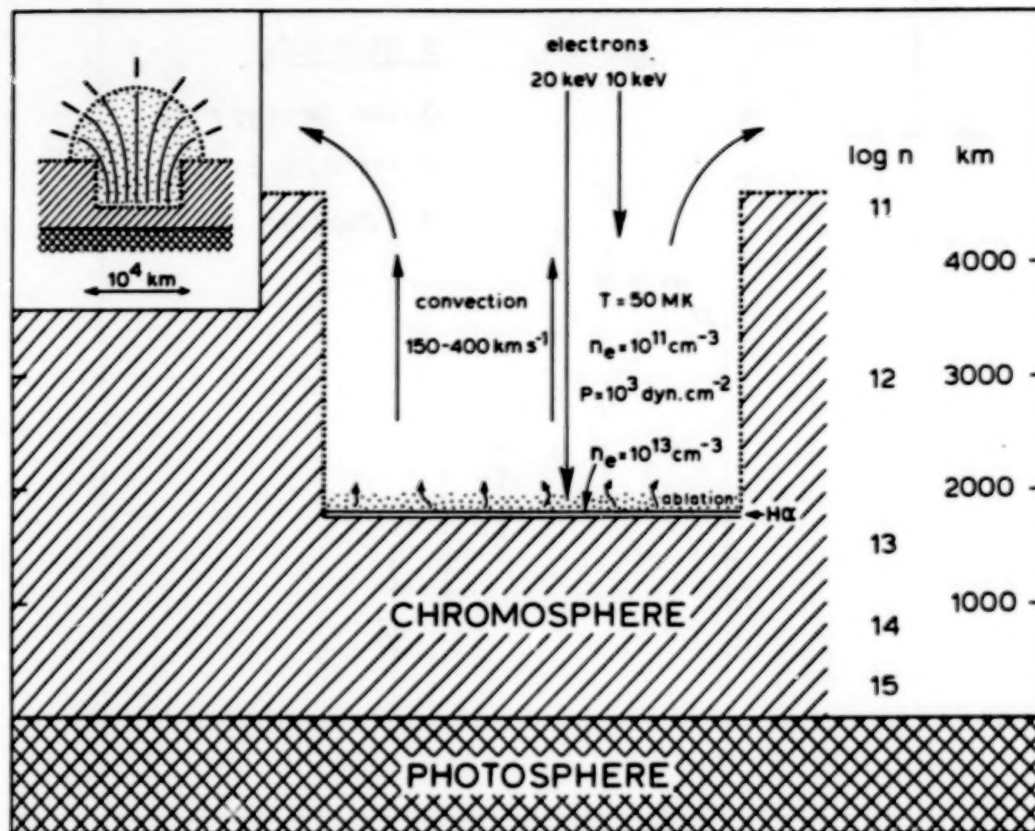
1000

CHROMOSPHERE

14

15

PHOTOSPHERE

Figure 7. Model of a flare kernel at the end of the impulsive phase of an average flare. Electron beam bombardment followed by ablation has "burned a hole" in the chromosphere down to a level about 1800 km above the photosphere. The gas in this hole has $T \approx 50$ MK, $n_e \approx 10^{11}$ cm⁻³, $P \approx 10^3$ dynes cm⁻². Gas streams up and outward (see the insert) with $v = 150$ to 400 km s⁻¹. Hα and other optical line radiation is emitted by a 20 km thick layer at the bottom of the kernel (De Jager, 1985b).

X-RAY IMAGING OF FLARE LOOPS AND CORONAL ARCHES

(Invited)

Zdenek Svestka

Laboratory for Space Research, Utrecht, The Netherlands

ABSTRACT

This paper summarizes HXIS results related to preflare, flare-decay, and post-flare phases in the solar corona. Particularly discussed are miniflares, long-lived X-ray enhancements along filament channels, flare precursors (some signifying the flare position, others possibly related to the onset of mass ejections), growth of post-flare loops, images of sites of field-line reconnections late in the flare development, giant post-flare coronal arches with energy contents comparable to coronal transients, and hot loops interconnecting active regions. The extremely low HXIS background, in particular, made it possible to discover many new, previously unknown features in the solar corona. Also emphasized are some problems that have appeared during the evaluation of HXIS data, for the benefit of those who plan future hard X-ray imaging experiments.

I. INTRODUCTION

The original aim of HXIS was an imaging of sources of hard X-ray bursts during the impulsive phase of flares. From the previous talk you could see and judge how well this task has been accomplished. During the eight months of its operations, however, HXIS was able to image many other phenomena of the active Sun in the energy range of 3.5 to 30 keV, and these additional results are the topic of my talk.

Only the two highest energy channels of HXIS, 5(16-22 keV) and 6(22-30 keV) really image hard X rays. The channels 3(8.0-11.5 keV) and 4(11.5-16 keV) represent intermediate energies, and the lowest two channels, 1(3.5-5.5 keV) and 2(5.5-8.0 keV), image soft X-ray emission from the Sun. However, it is important to realize that even the softest HXIS images are by almost one order of magnitude harder than the soft X-ray images of the Sun made on-board the Skylab. Thus, even in soft X rays, HXIS has been able to yield essentially new information about many active phenomena on the Sun.

One of the great advantages of HXIS has been its extremely low background which made it possible to integrate X-ray fluxes for tens of minutes and eventually during the whole (up to 60 min-lasting, sun-lit) orbit if necessary. Table I (Schadee et al., 1983) demonstrates how extremely weak X-ray fluxes can be imaged with statistical significance better than 3σ in the HXIS band 1 for different integration times.

Since the background is the same for every pixel, and the area of one pixel of the coarse field of view of HXIS equals the areas of 16 pixels in the fine field of view, this advantage could be used particularly well in the coarse field. It led to discoveries of completely new structures in the solar corona, undetectable in the high-background Skylab pictures at lower energies. These discoveries were not at all expected when HXIS was launched and are an extra product of the excellent performance of this instrument (for its description cf. Van Beek et al., 1980).

There are many more excellent characteristics of HXIS; for example, its relatively high spatial resolution of 8 arc s in the fine field of view which, after deconvolution (J. Schrijver in Svestka et al., 1984) could be still greatly improved for point-like sources; the capability of HXIS to record X-ray flux variations within each individual pixel, which made it possible to study velocity fields in flares (De Jager, 1985) and in post-flare corona (Svestka, 1984b), among others; the possibility to construct temperature maps of the solar corona which, for example, have led to the detection of rising thermal waves after two-ribbon flares (Svestka, 1984a; Svestka and Hick, 1985).

Nevertheless, and quite naturally, HXIS also had deficiencies. Since this Workshop aims at the preparation of future X-ray-imaging instruments, I consider it particularly important to mention all these deficiencies carefully and in full detail, since one can learn a lot from them. Therefore, while presenting the HXIS results, I will also emphasize all the difficulties and problems we have met when evaluating the data. While doing it, however, I ask the reader to kindly keep in mind that HXIS was an excellent instrument, one of the best flown onboard the SMM; let me, on behalf of all those who have benefitted (and will still benefit) from its data, congratulate Frank van Beek and his co-workers on the invention and construction of HXIS, and the Principal Investigator, Kees de Jager, on its performance and on the fruitful evaluation of HXIS data.

II. POST-FLARE LOOPS

The most important class of flares (since essentially all major flares belong to it) is the two-ribbon flare: two bright ribbons in the chromosphere as the site of footpoints of an arcade of loops which extend high into the corona. New higher loops are sequentially excited, or formed, in the corona, and at the same time their footpoints (the chromospheric ribbons) gradually separate.

This class of flares has been known for about three decades, from Hα observations. However, the "post-flare loops" seen in Hα are only the cooled remnants of the hot coronal loops, formed (or excited) minutes or tens of minutes before. The enormous advantage of X-ray observations is that we image here the new hot loops close to the time of their excitation or formation and can thus directly study the process of the heating of the loops (energy release) in the corona.

Figure 1 shows in its upper part HXIS images of the system of growing flare loops on 21 May 1980 – this is the flare where Hoyng et al. (1981) first gave the evidence of two hard X-ray footpoints during the impulsive phase (cf. the preceding talk by De Jager). The flare location was in the SW sector of the Sun so that the gradual extension of the X-ray emission to the south means a growth of the flare loops (brightest at the top) upwards in the corona (Svestka et al., 1982a).

At the bottom of Figure 1 we show the growth of the distance d of the brightest portion of the loops from the $H_I = 0$ line (Svestka and Poletto, 1985). For radial loops the real altitude would be 3.0 d. One can see that the growth of the flare loops in altitude was not continuous: the tops of the loops stay for minutes at a given altitude before, quite abruptly, other loop tops begin to appear above them. A similar observation was made by Hinotori on 13 May 1981, when the tops of flare loops stayed at the same altitude for 12 min (Tsuneta et al., 1983). No Hinotori data are available before, or after, this period so that no abrupt jump could be verified; but it is clear from Figure 1 that, quite analogically, 12 min of stationary altitude could have been seen by Hinotori if it had observed the 21 May 1980 flare.

A similar phenomenon, a growth of loops through abrupt jumps, was seen before in some Hα movies of post-flare loops. Whereas, however, the jumps seen in Hα might have been due to effects of differences in the cooling of plasmas at different initial densities, the X-ray jumps are clearly related to the loops excitation or formation. It is of interest that Forbes and Priest (1983) theoretically predicted the existence of multiple X-type neutral lines at different altitudes above two-ribbon flares, where distended field lines may subsequently reconnect and thus produce new sets of loops at different altitudes.

Figure 2 shows an enlargement of the abrupt rise in altitude that is seen in 21:12 UT in Figure 1. If the loops were radial, the rise would represent a jump from 26 000 to 43 000 km altitude. Figure 2 demonstrates that the rise was first seen in the highest energy channel (22 to 30 keV) with a later follow up at lower energies. This can be interpreted as a new release of energy in a very small volume of plasma at extremely high temperature (Svestka and Poletto, 1985). For an illustration, let us enhance the temperature of a small volume in the corona from 20×10^6 K to 50×10^6 K. Then the X-ray flux from this volume rises by a factor 2200 in the hardest HXIS band 6, but only by a factor of 3 in the softest band 1. Therefore, we can see the source in band 6 in spite of its small dimensions, whereas in lower-energy bands we must wait until its emission measure substantially increases. An obvious candidate for the process we observe here is the reconnection of field lines, in apparent agreement with the Kopp and Pneuman (1976) model of the formation of post-flare loops (in the basic configuration suggested by Sturrock (1968), and with the multiple neutral lines deduced by Forbes and Priest (1983)).

One has to be aware of the fact that the collimating techniques of HXIS may be partly responsible for the observed jumps in altitude: if the loops were thin, we would see them emitting in one HXIS pixel as long as they travel through this pixel, and "jump" in another pixel when leaving it. Broader loops will smear this "pixel-effect." On the other hand, it is of interest to note that the spatial resolution of Hinotori deteriorates with the growing size of the imaged source: thus moving loops must be quite extensive to be seen by Hinotori at a "constant" altitude for 12 min. Thus moving loops would be seen by HXIS at a fictitiously constant altitude if their real thickness was $\ll 8$ arc s, and by Hinotori if their thickness was $\gg 8$ arc s. This difference in imaging tends to support the supposition that the observed jumps in altitude were real.

In any case, new loops appeared at ∼21:12 UT at a higher altitude and were first seen in the highest energy band of HXIS. A unique set of parameters of the new source of energy release cannot be deduced from the available data. However, a reasonable agreement with the observation is found for a source with temperature of 50×10^6 K between 21:08 through 21:13 UT, growing in size (supposedly as an arcade of loops was formed) and reaching emission measure of 3×10^{45} cm^{-3} at the end of its development. Then the source cooled, and its emission measure was fast increasing (possibly through evaporation of chromospheric material into the new loops) to 3×10^{47} cm^{-3} at 21:17 UT, i.e., by two orders of magnitude during 4 min. Table 2 gives the estimated size of the new source of energy release at 21:13 UT for various (unknown) electron densities.

Figure 3 shows images of the flare from 21:09:17 UT onwards, in the six energy bands of HXIS. The image in band 4 at 21:09:17 presents the typical situation seen in all bands at earlier times: a maximum of brightness at a distance $d \cong 9000$ km from the $H_\parallel = 0$ line, marked here

approximately by the active region filament. In band 6, at that time, we see already an extension of the flux-contours to the south. This extension is more pronounced at 21:10:38, and finally a new maximum is formed, more to the SW, i.e., at a higher altitude, at 21.12:00 UT (marked by A in Figure 3). This is the site we begin to see at d ≅ 15,000 km in Figures 1 and 2. At lower energies this new brightening occurs successively later, as we have indicated by arrows in Figure 3.

The new brightening at A occurred 23 min after the flare onset and 17 min after the maximum in the hard X-ray burst. Thus it represents an energy release late in the post-maximum phase of the flare, which gives direct evidence that, in two-ribbon flares, energy is still being released after the impulsive phase is over.

(a) Pixel gain

Figure 3 can also be used for a demonstration of one of HXIS deficiencies: inhomogeneities in the gain of HXIS pixels; the gain G of a pixel is defined as the ratio between the outgoing signal and the energy of an incoming photon.

Most pixels do not deviate by more than 3% from the nominal gain $G = 1.00$. However, there are 20 pixels in the HXIS fields of view (out of 400) for which either $G \geq 1.05$ or $G \leq 0.95$. A difference in gain changes the effective energy band boundaries from E to E/G. How serious this effect can be is apparent from the pixel marked B in Figure 3. With $G = 1.05$ it images in HXIS band 6 X rays between 20.9 Å and 28.6 Å (instead of 22.0 Å and 30.0 Å) and thus creates a fictitious maximum in the brightness contours. As Figure 3 shows, the effect is most serious in the high-energy channels, but it has to be considered at the low energies as well when temperature maps are made (cf. Section III).

III. POST-FLARE ARCHES

The very low background of HXIS made it possible to detect large arch-like structures in the solar corona, which are formed, or become enhanced, after two-ribbon flares. Flares of other kinds do not affect them. These arches are seen in >3.5 keV X-rays for 10 hours or more, and temperature in them may exceed 20×10^6 K. Some appear to be stationary, while others show moving maxima of brightness associated with thermal disturbances propagating upwards with speeds of ~10 km/s. It appears that essentially every arch forms the base of a type I radio noise storm which developed from a stationary radio type IV burst initiated by the flare. Machado et al. (1983) imaged a similar structure in 3.5 to 5.5 keV X-rays above a type I noise storm source during its whole transit across the solar disc.

(a) Stationary arch of 21/22 May 1980

Figure 4 shows 3.5 to 5.5 keV images of the coronal arch seen after the two-ribbon flare of 21 May 1980, 20:52 UT (Svestka et al., 1982a; Svestka, 1983). These are half-an-hour integrations of an extremely weak coronal structure: the count rate of the peak in the last image, at 06:36 UT, only slightly exceeds 1 count/min; yet, this is still four-times more than the average background.

One can see that the brightest part (apparently the top) of the arch stayed in the same position since 03:20 UT (6.5 hours after the flare) until the end of the HXIS imaging. Unfortunately, SMM did not look at this active region for two orbits preceding 03:20 UT. Last images

prior to that are from 23:07 UT on 21 May when the post-flare loops still fully dominated the field so that it was extremely difficult to distinguish the much weaker coronal arch. Nevertheless, a careful analysis succeeded to separate the arch from the loops and the results are shown in Figure 5 (Hick and Svestka, 1985): since 23:02 UT the top of the arch was in the same position as in the much later images of Figure 4. Prior to that, from the beginning of the orbit at 22:28 UT, the maximum was in a neighboring pixel, but still at about the same altitude above the flare. If one follows the time development of the X-ray flux in these two pixels (and that is another great advantage of HXIS that it allows such local (8 x 8 arc s) photometry) one finds that the flux in the first pixel peaked at ~22:56 UT, whereas the other pixel peaked some 10 min later and since then stayed to be the brightest pixel in the field (Figure 6).

(1) Spatial resolution

These extensive coronal structures could be seen in the coarse field of view only, because of its lower effective background and much larger covered area on the Sun. For these advantages of the coarse field, however, we pay with very low spatial resolution of 32 arc s (FWHM). It is clear from Figure 4 that very little can be said about the real structure of the detected coronal arch. But sometimes indirect information gives some insight into the unresolved formations, like in Figures 5 and 6; e.g., one can tentatively conclude that the arch consisted of (at least) two separate arch-like structures, since they peaked in brightness at slightly different times.

Another restriction, caused by the low spatial resolution, applies to observations of any motions. A "stationary" source, seen for one hour in the coarse field of view, still could move by up to 0.53 arc s per minute (~6.5 km/s in projection on the disk) without its motion possibly being recognized. In our case, we saw the top of the arch in stationary position for 8 hr 20 min, which allows for a maximum motion of 0.78 km/s in projection. Thus, in this case we may really safely conclude that the arch was a stationary structure.

(2) Flare mode

A great obstacle in the study of these coronal structures near the time of their origin was the flare mode of HXIS operations: as soon as there was a flare (or the X-ray flux exceeding a certain limit), HXIS changed its normal observing interval of 7.5 s to 1.5 s and compensated for the lost time by omitting the imaging of weaker pixels. The aim of this special mode was to enhance the time resolution during flares and, of course, the main part of the flare was always imaged. However, any weaker features, including the coronal arches and potential X-ray counterparts of flare-associated radio bursts, disappeared from the images. This contributed to our difficulty to obtain the arch images in Figure 5 (when HXIS was in flare-mode 2 with time resolution of 4.5 s) and made it completely impossible to see anything from the arch in the orbit before, when the flare began (when HXIS was in flare-mode 1, with time resolution of 1.5 s). It is very regrettable that HXIS was suppressing data since we are unable to get any information whatever about the origin of this kind of post-flare coronal structures.

(b) Reviving arches of 6/7 November 1980

Another example of a post-flare coronal arch was recorded on 6 November 1980, after a major two-ribbon flare at 03:04 UT (imp. X9), which had not been seen by the SMM, but the spacecraft pointed to the flaring active region since 06:20 UT. This arch (or post-flare coronal cloud, since we have no direct evidence in this case, projected over the solar limb, that it was an arch structure) had many features common with the event of 21/22 May (Svestka et al., 1982b).

However, there was a very significant difference: the maximum of brightness was not in a stationary position, like in 21/22 May, but it was rising in the corona, as Figure 7 clearly demonstrates. Before this arch completely disappeared, it was revived, at 14:40 UT, after the occurrence of another two-ribbon flare in the same active region, and we saw again the same rise of the maxima in brightness as at the flare before (Figure 7). The two events were quite homologous (Svestka, 1984b).

This rise of a coronal disturbance after the flare can also be demonstrated in another way. Figure 8 shows a series of temperature maps, constructed from the flux ratio of HXIS bands 1 and 2, in the fine field of view of HXIS (Svestka, 1984a). One can see that shortly after the flare (the upper times in each frame) an extended region of high temperature was formed (with $T > 20 \times 10^6$K) which moved upwards across the solar limb and eventually disappeared from the fine field of view of HXIS some 2 hr 15 min after the flare. The continuation of this rise, in brightness of the arch, can then be further followed in the coarse field, as shown in Figure 7.

The arch revived once again at ~04:40 on 7 November, and it is very likely that already the first appearance of the arch (the upper row in Figure 7) was a revival, since a major two-ribbon flare at 13:41 UT on 5 November (not seen by the SMM) was probably the source of the first arch formation. Our present interpretation is (cf. Svestka et al., 1982a) that the post-flare arch is the upper product of the reconnection process which forms the post-flare loops below. The first arch is formed fast near the onset of the flare (Hick and Svestka, 1985) and the maximum stays in a constant position since its formation. When an arch revives, however, the new arch meets an obstacle at its formation – the pre-existing arch – and this leads to the gradual rise of the arch excitation seen in Figures 7 and 8 (Svestka, 1984b).

We have studied in detail the second arch on 6 November (following the flare at 14.40 UT), since this is the only arch we could observe during its whole development. Figure 9 shows the results: the arch began to brighten, and its temperature began to rise, from the very onset of the two-ribbon flare. The temperature reached its maximum about 1 hr later, the brightness in 3.5 to 5.5 keV X-rays peaked about 2.3 hr, and the emission measures more than 3 hr after the flare onset. It looks like a flare, with both the size- and time-scale enlarged by an order of magnitude. The physical characteristics deduced for this revived arch are summarized in Table III. One can see that the energy contents and mass are comparable to an average coronal transient (cf. the paper by N. R. Sheeley in these proceedings).

(1) Temperature measurements

When determining temperature from HXIS data (Mewe et al., 1985), we have encountered serious difficulties in the calibration of the energy band 2 which contains the helium-like complex of iron (Svestka and Poletto, 1985). As soon as temperature exceeds 20×10^6K (or during the impulsive phase, whichever statement is correct), the emission in band 2 is clearly overestimated, since T(2/1) results higher than T (3/2). The reason for this may be an incomplete knowledge of satellite iron lines which begin to become important for $T > 20 \times 10^6$ K, or perhaps an excitation by particle streams, whereas the calibration assumes Maxwellian distribution of velocities. In any case, one should avoid band 2 in temperature measurements if T exceeds 20×10^6 K. That is the reason, for example, why we have determined T from the bands 1 and 3 and not 1 and 2 (with better statistics) in Figure 1.

(2) Temperature maps

This uncertainty in the calibration of HXIS band 2 does not have much influence on the studies of coronal arches, since temperature in them is generally lower. However, other disturbing effects appear when constructing the temperature maps of the corona, and one has to be particularly cautious when preparing them.

First, there are ghost images produced by the collimator which appear towards the NS and WE directions from a bright source. They are extremely weak and usually do not play any disturbing role in the X-ray images. However, the ghosts are more intense at high energies; since temperature is determined from the flux ratios, irrespective of the flux intensity involved (provided there are enough counts to make the ratio statistically significant), these ghosts clearly appear as fictitious maxima in the temperature maps.

This effect of ghosts had been known before the launch and can be corrected if necessary. However, there is another effect which had not been expected, and which puzzled us for quite some time: if there is a bright flare source, we can see not only the ghosts in the temperature maps, but also temperature maxima elsewhere around the flare, sometimes producing almost a circle, or a semi-circle with the flare close to its center. First we thought, and Harrison and Simnett (1985) still believe that it is at least partly true, that we saw here the X-ray light from the source backscattered on the photosphere. However, Fárník (private communication) has found cases when such temperature maxima were seen also above the limb. Therefore, we are now convinced that the effect is mostly, and possibly completely, due to an instrumental effect: the FWHM of the HXIS pixels increases with increasing energy. Thus wherever the gradient of X-ray flux is high (like at a certain distance around the flare), the outlying pixels have a larger contribution from the high energy bands, which leads to a fictitious enhancement of temperature along the high-gradient boundary around the flare. A weak example of it can be seen in the first image in Figure 8, at 3 min 46 s before the peak of the impulsive phase of the flare (compare it with the flare position in the lower central frame of Figure 8). The effect is slightly visible in the other upper-row maps as well.

Therefore, we must always carefully check whether there is any instrumental effect (ghost, high gradients of flux) potentially responsible for maxima detected in temperature maps. Note that the accumulated isophotes at the left-hand side of the upper images in Figure 8 do not mean a high gradient of flux; they only mark the boundary where the flux ratio exceeds the statistical significance of 3σ. So the maxima in Figure 8 are real temperature enhancements traveling across the limb.

Also the inhomogeneous gain of HXIS pixels (cf. Section II) can produce false maxima in temperature maps similar to that one in flux demonstrated in Figure 3, even at lower energies (Svestka and Hick, 1985). Since, however, the gain for different pixels is known, this effect can be easily recognized and to a great extent eliminated.

IV. INTERCONNECTING LOOPS

After the discovery of the reviving postflare arches on 6 November 1980, Fárník et al. (1985) became interested in the further behaviour of this active region which was followed by the SMM up to its disappearance behind the western limb on 20 November. First they found another revival of the arch, late on 7 November and on 8 November (Figure 10), but the situation completely changed on 9 November. On that day another coronal structure appeared (Figure 10,

right-hand picture) which extended towards the SE, instead of SW. Since this structure first appeared after a major flare in another active region 17 251 (cf. Figure 10), Fárník et al. have assumed that HXIS imaged here a big loop interconnecting the observed region 17 255 with the (invisible for HXIS) region 17 251.

The two structures shown in Figure 10 definitely differ in their nature. The arch (to the SW) always revived after a two-ribbon flare in the region below it. The structure towards the SE behaved in relation to flares in a way very similar to that found for interconnecting loops during Skylab (Svestka and Howard, 1979): some flares (in both active regions) seem to enhance it; these definitely need not be two-ribbon flares; other flares have no impact upon the structure, and sometimes the structure brightens without any obvious flare association.

A very similar coronal structure, with the same loose association with flares, was also detected by Harrison et al. (1984) on 29 June 1980. Images of this interconnecting loop on the limb are shown in Figure 11 (left). The interconnecting loops could not be seen on the disk, but simultaneous X-ray brightenings in both the regions, like in the right-hand image of Figure 11, on 24 June, had suggested the existence of a coronal interconnection already on that day (Simnett et al., 1984).

Another difference between the SW arch and the SE structure in Figure 10 was the cooling time of the X-ray brightenings. The life time of the enhancements of the SW arch was 14 hr or more, whereas all enhancements of the SE structure were relatively short-lived; the SW arch shown in Figure 7 cooled for ~6 hr from $T = 14 \times 10^6$ K to $T = 8 \times 10^6$ K, whereas in the strongest brightening of the SW structure on 11 November the same temperature decrease was accomplished within 80 minutes. With the densities deduced (of the order of 10^9 cm^{-3}) this indicates that the heat conduction was inhibited in the SW arches, but active in the SE structure. This is to be expected with the complex magnetic structure of the arch, originating through a long-lasting sequence of reconnections and possibly even detached from the surface, in comparison to a simple-structured loop that interconnected two active regions.

(a) The field of view

Though there are strong arguments supporting the suggestion that the structure seen on 9 November and later on was an interconnecting loop, one can never be sure of it, since the other interconnected region was out of the field of view. This is only one demonstration of the disadvantages of the restricted field of view used by HXIS and other SMM instruments. In Figure 1 we could not study the thermal wave (analogic to Figure 8), because it was out of the fine field of view. The western footpoint of the arch of 21/22 May 1980 was out of the coarse field of view (Figure 4). The thermal wave disappeared from the fine field of view in Figure 8 and both the arches in the morning and afternoon of 6 November extended out of the coarse field of view (Figure 7). Besides, lots of interesting events (e.g., all γ-ray flares) were missed by the SMM and HXIS in 1980, because the spacecraft was pointed to another region on the Sun.

V. PRE-FLARE ENHANCEMENTS

Another unexpected discovery made by HXIS were X rays emitted by hot plasma in absence of flares. Schadee et al. (1983) have found that some active regions are characterized by long-lived X-ray enhancements above 3.5 keV along the filament channels. These sources are ~10^4 times weaker than a flare, can last for several hours, and some possibly mark the sites

where a major flare will occur many hours later. The temperature deduced for them from the HXIS bands 1 and 2 exceeds 10×10^6 K.

The low resolving power of the coarse field of view of HXIS makes it impossible to decide whether there is really an exact coincidence in position between these pre-flare enhancements and the coming flare. Only in the "Queens' " limb flare of 30 April, 1980 (De Jager et al., 1983), these pre-flare enhancements could also be seen in the fine field of view; most of them were then not in exact coincidence with the position of the flare; however, for 26 min prior to the flare an enhancement, faint but distinct, coincided exactly (within the resolution of 8 arc s) with the flare position. Also its shape was similar to the shape of the coming flare event.

Other active regions show a high number of short-lived X-ray variations, about 10^{-3} times weaker than a flare, which probably are X-ray mini-flares. Galzauskas, Schadee and Martin (private communication) succeeded to associate a few of them with tiny Hα brightenings.

An extremely interesting observation has been reported by Simnett and Harrison (1984) and Harrison et al. (1985): They claim that at a time consistent with a coronal mass ejection onset at the very early phase of a flare there is a small, soft X-ray burst (a precursor) which may signify the origin of the coronal transient. Figure 12 shows an example of such an event. The images of the preflare brightening at times marked a, b, c in Figure 12 are shown in Figure 13. The preflare structure really seems to rise near the time when an accelerating mass ejection might have started.

VI. CONCLUSIONS

We have tried to demonstrate that the hard X-ray imaging can yield data on many more coronal phenomena than just the impulsive (hard X-ray burst) phase of flares. There are X-ray enhancements in non-flaring active regions corresponding to mini-flares, long-lived high-temperature disturbances along filament channels, and flare precursors. Some of them may signify the origin of mass ejections prior to flares. Others perhaps indicate the site where the coming flare may occur. After the impulsive phase of a flare, X-ray images show post-flare loops in the shape close to their formation and may reveal new sites of field-line reconnections. After two-ribbon flares, giant post-flare coronal arches are imaged in X-rays, and their energy contents are comparable to the energy contents of coronal transients. They appear to be an important component of the post-flare corona and represent X-ray counterparts of stationary type IV bursts and type I noise storms. Also a few loops interconnecting active regions could be imaged by HXIS.

In the future hard X-ray experiments one should try to image the whole Sun (or at least, large fields of view on the Sun), since the limited fields of view used onboard the SMM caused lots of problems in the evaluation of the data, and many important data were missed. One should not omit lower energies (~3 keV), since some important coronal features seem to be prominent at these wavelengths. High spatial resolution is essential, as one can see from many illustrations in this contribution. High time resolution did not prove to be of real significance for HXIS, but this will surely change if, at the same time, also the spatial resolution greatly improves. Nevertheless, the HXIS experience speaks strongly against the use of any suppression of data (flare modes): the gain of this suppression (of which the author admits to be one of the initiators) was essentially nil whereas the losses (no images of type IV, type II, type V radio bursts, no knowledge about the early phase of the post-flare coronal arches) had been very harmful.

In summary, HXIS has been an extremely successful experiment. Its unbelievably low background permitted many new discoveries which had not been expected before the launch. The used techniques had some deficiencies, but these actually became important only at the occasions when we tried to evaluate data very close to the extreme limits of HXIS sensitivity. The present review has tried to summarize all the known pros and contras of the used collimating techniques, for the benefit of those who plan hard X-ray imaging experiments for the future.

REFERENCES

De Jager, C., 1985, *Solar Phys.*, *96*, 143.

De Jager, C., Machado, M. E., Schadee, A., Strong, K. T., Svestka, Z., Woodgate, B. E., and Van Tend, W., 1983, *Solar Phys.*, *84*, 205.

Fárník, F., Van Beek, H. F., and Svestka, Z., 1985, *Solar Phys.*, submitted.

Forbes, T. G. and Priest, E. R., 1983, *Solar Phys.*, *84*, 169.

Harrison, R. A. and Simnett, G. M., 1985, *Solar Phys.*, submitted.

Harrison, R. A., Simnett, G. M., Hoyng, P., Lafleur, H., and Van Beek, H. F., 1984, Proc. SCOSTEP-STIP Symp. on Interplanetary Intervals, p. 287.

Harrison, R. A., Wagget, P. W., Bentley, R. D., Phillips, K. J. H., Bruner, M., Dryer, M., and Simnett, G. M., 1985, *Solar Phys.*, 97, 387.

Hick, P. and Svestka, Z., 1985, *Solar Phys.*, submitted.

Hoyng, P., and 11 co-authors, 1981, *Astrophys. J. (Letters)*, *246*, L155.

Kopp, R. A. and Pneuman, G. W., 1976, *Solar Phys.*, *50*, 85.

Machado, M. E., Somov, B. V., Rovira, M. G., and De Jager, C., 1983, *Solar Phys.*, *85*, 157.

Mewe, R., Gronenschild, E. H. B. M., and Van Den Oord, G. H. J., 1985, *Astron. Astrophys. Suppl.*, in press.

Schadee, A., De Jager, C., and Svestka, Z., 1983, *Solar Phys.*, *89*, 287.

Simnett, G. M. and Harrison, R. A., 1984, *Adv. Space Res.*, *4*, No. 7, 279.

Simnett, G. M., Harrison, R. A., Hoyng, P., and Van Beek, H. F., 1984, Proc. SCOSTEP-STIP Symp. on Interplanetary Intervals, p. 273.

Sturrock, P. A., 1968, IAU Symp. 35, 471.

Svestka, Z., 1983, *Space Sci. Rev.*, *35*, 259.

Svestka, Z., 1984a, *Adv. Space Res.*, *4*, No. 7, 179.

Svestka, Z., 1984b, *Solar Phys.*, *94*, 171.

Svestka, Z. and Hick, P., 1985, *Solar Phys.*, to be submitted.

Svestka, Z. and Howard, R., 1979, *Solar Phys.*, *63*, 297.

Svestka, Z. and Poletto, G., 1985, *Solar Phys.*, *97*, 113.

Svestka, Z., and 14 co-authors, 1982a, *Solar Phys.*, *75*, 305.

Svestka, Z., Dennis, B. R., Pick, M., Raoult, A., Rapley, R. T., and Woodgate, B. E., 1982b, *Solar Phys.*, *80*, 143.

Svestka, Z., and 8 co-authors, 1983, *Solar Phys.*, *85*, 313.

Tsuneta, S., and 7 co-authors, 1983, *Solar Phys.*, *86*, 313.

Van Beek, H. F., Hoyng, P., Lafleur, H., and Simnett, G., 1980, *Solar Phys.*, *65*, 39.
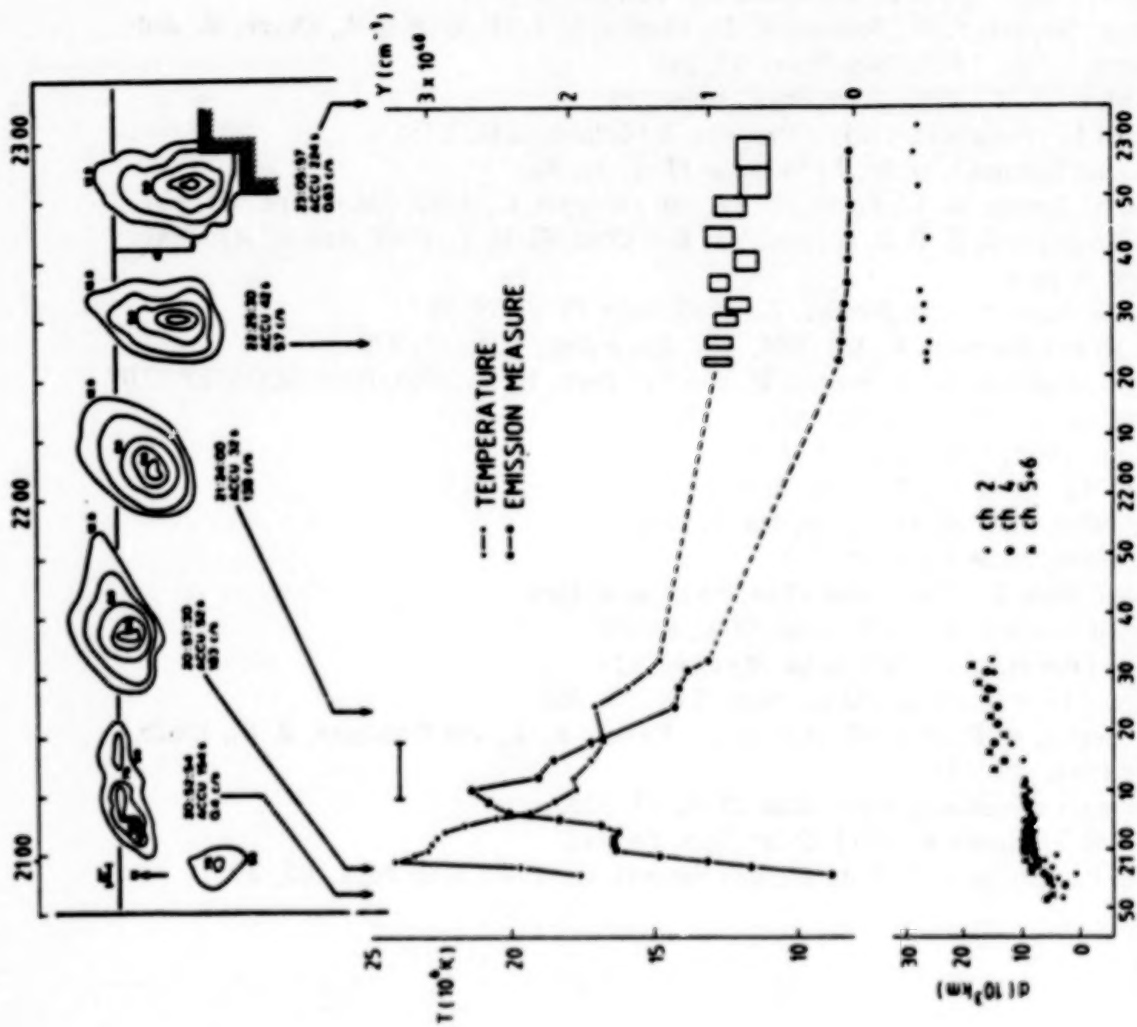
Figure 1. Top: Images of the flare of 21 May 1980 in 3.5 to 8.0 keV X rays. Center: Temperature and emission measure determined from the ratio of HXIS bands 3 and 1, for the four brightest pictures in band 1. (Emission measure Y pixel of fine field of view.) Bottom: The distance of the brightest part of the flare (tops of the loops) from the HI = 0 line, d, in projection on the disk, as determined from HXIS bands, 2, 4, and 5 + 6.
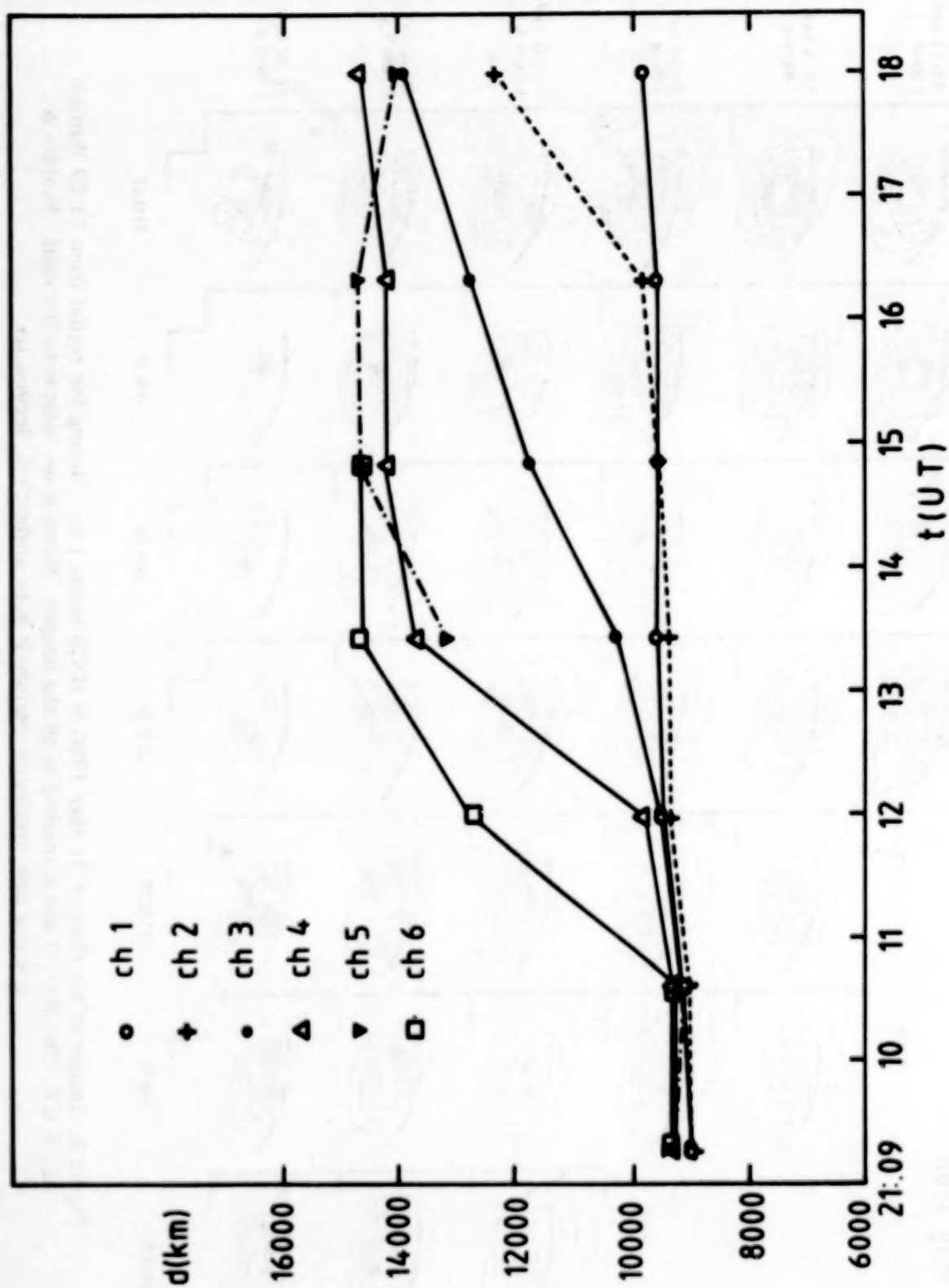
Figure 2. A detail of the variation of d in HXIS channels 1 to 6 during the jump in altitude which occurred at 21:12 UT (cf. the bottom part of Figure 1).
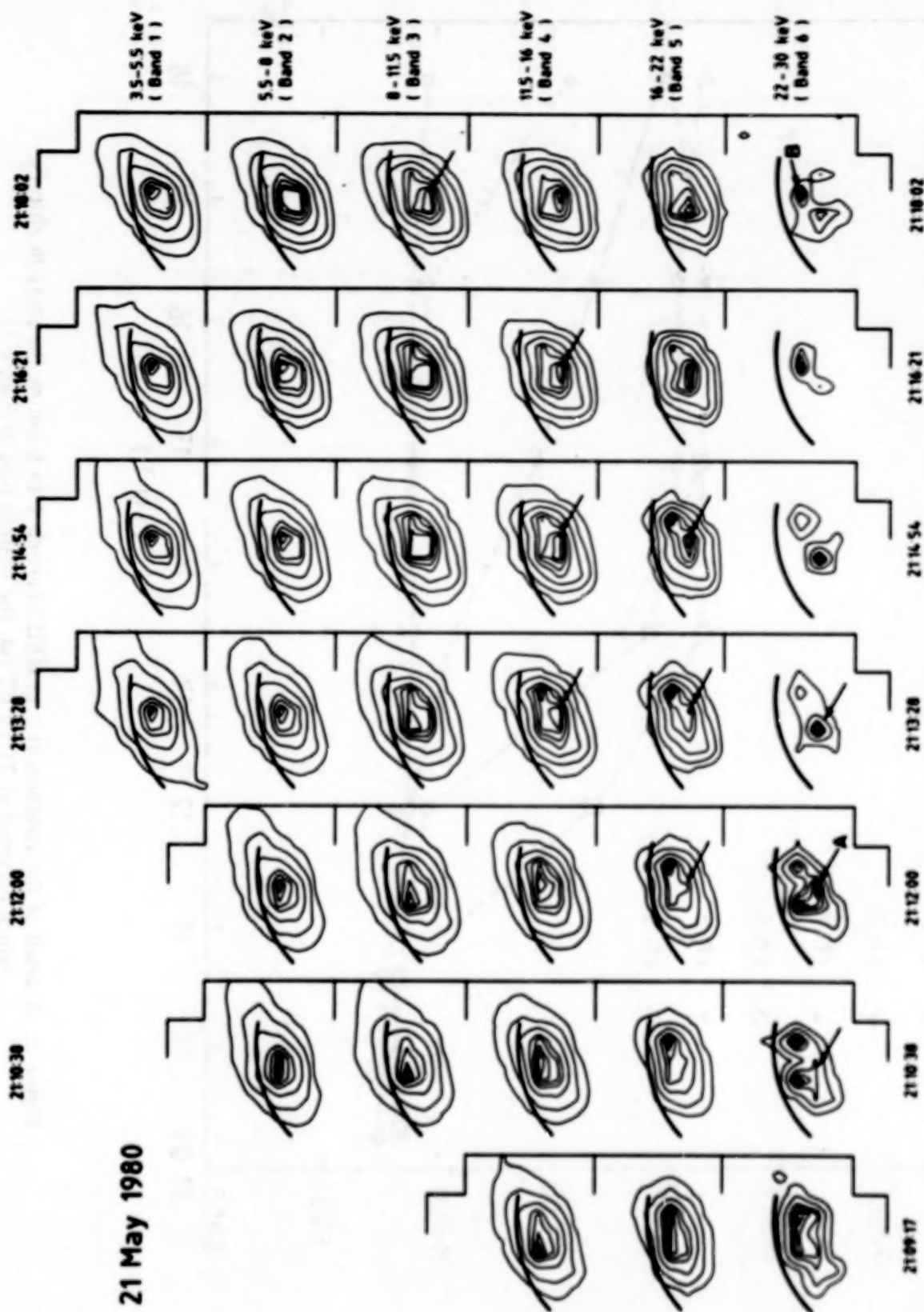
53

Figure 3. Images of the flare of 21 May 1980 in HXIS bands 1 to 6 during the period from 21:09 through 21:18 UT. The H$_1$ = 0 line is marked in all the images. North is up, west is to the right. Feature A is a real new maximum; feature B is an artifact (cf. Section II).
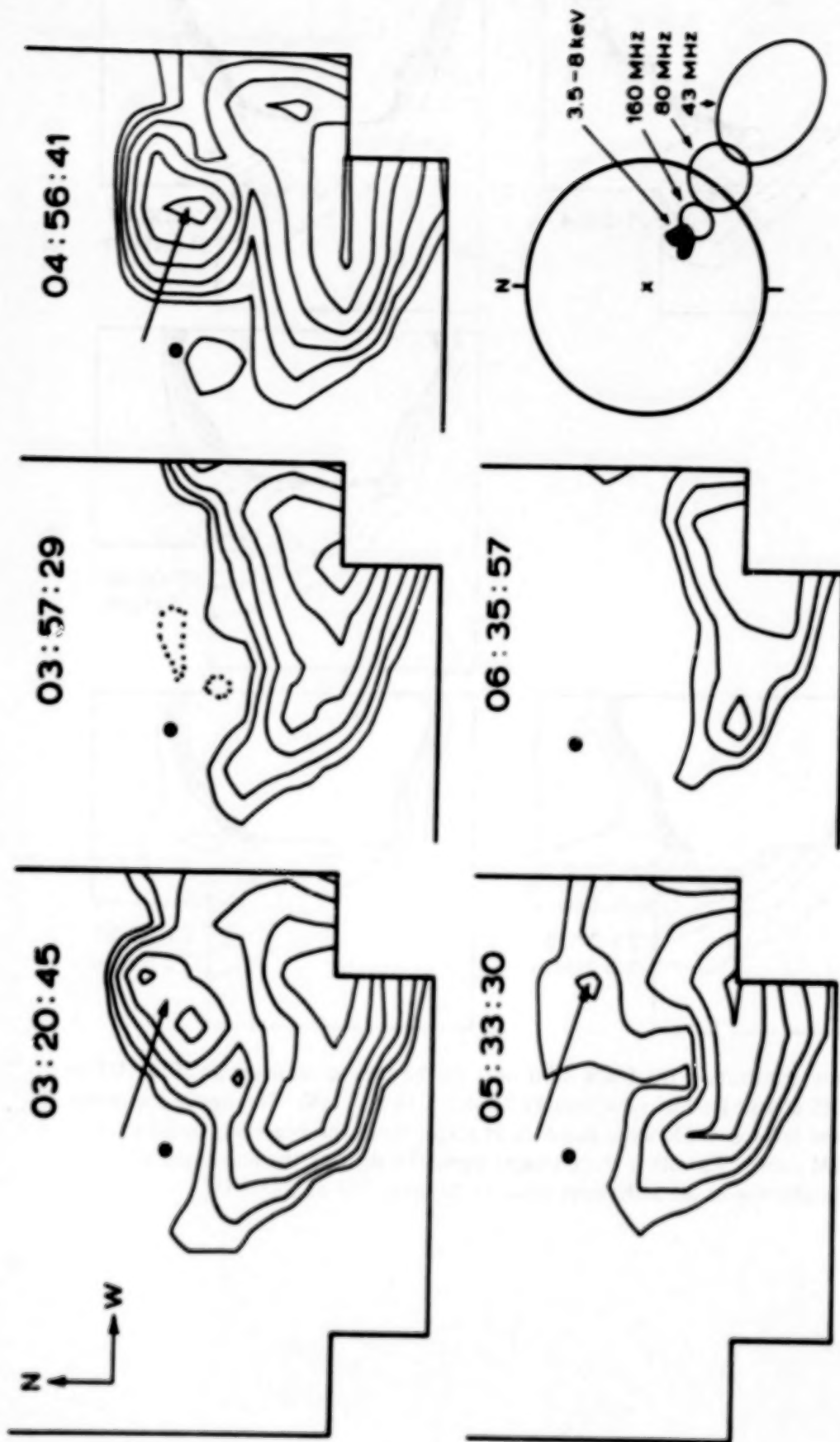
54

Figure 4. X-ray contours of integrated images of the post-flare coronal arch observed on 22 May 1980. Energy range: 3.5 to 5.5 keV. HXIS coarse field of view, resolution 32 arc s. The given times are mean times of 1525 s integrations. The position of the parent flare at 20:52 UT on 21 May is marked by dotted contours in the upper central image. The insert shows the relative position of the X-ray arch and three radio images of the stationary type I noise storm as seen at Culgoora at 03:20 UT on 22 May.
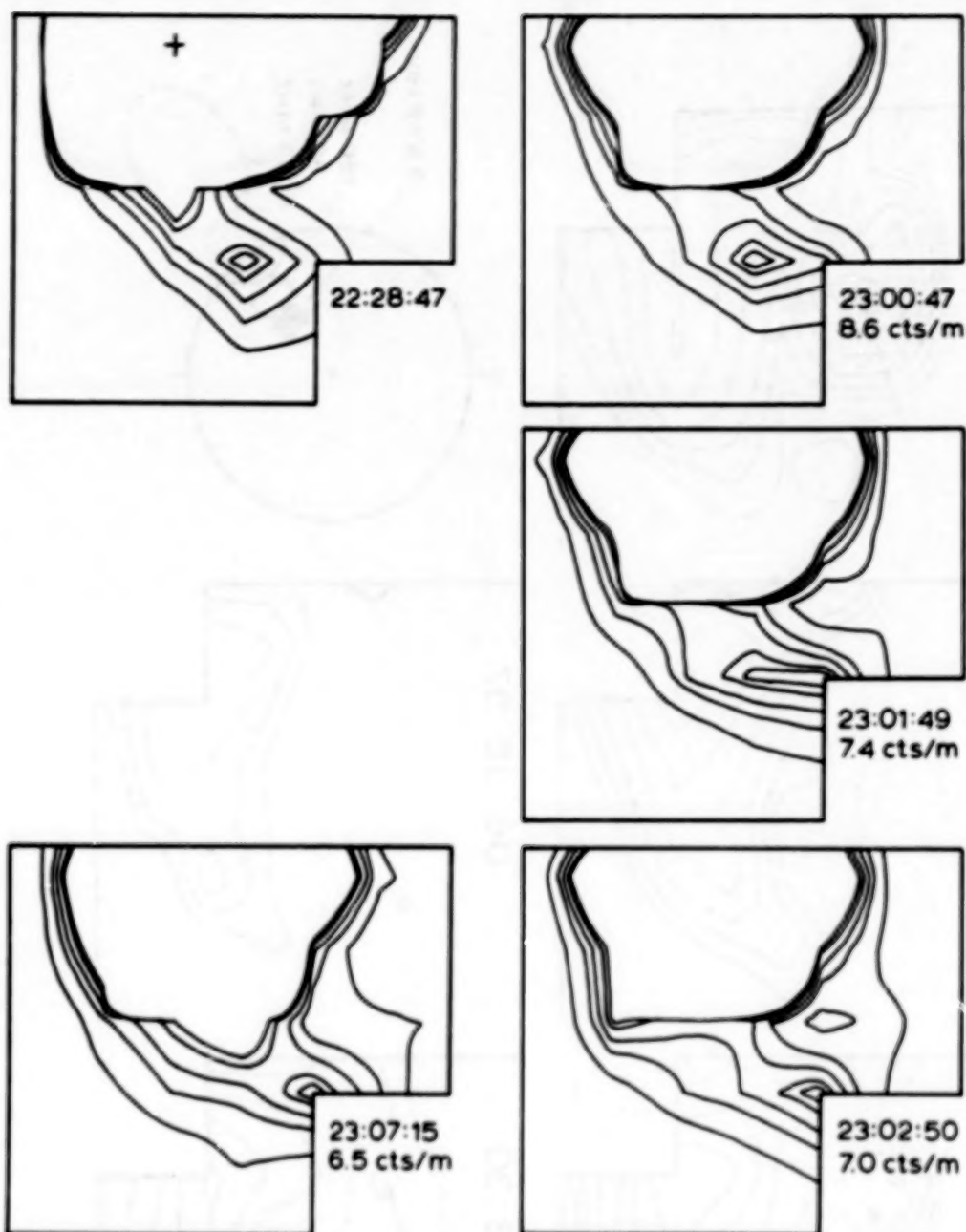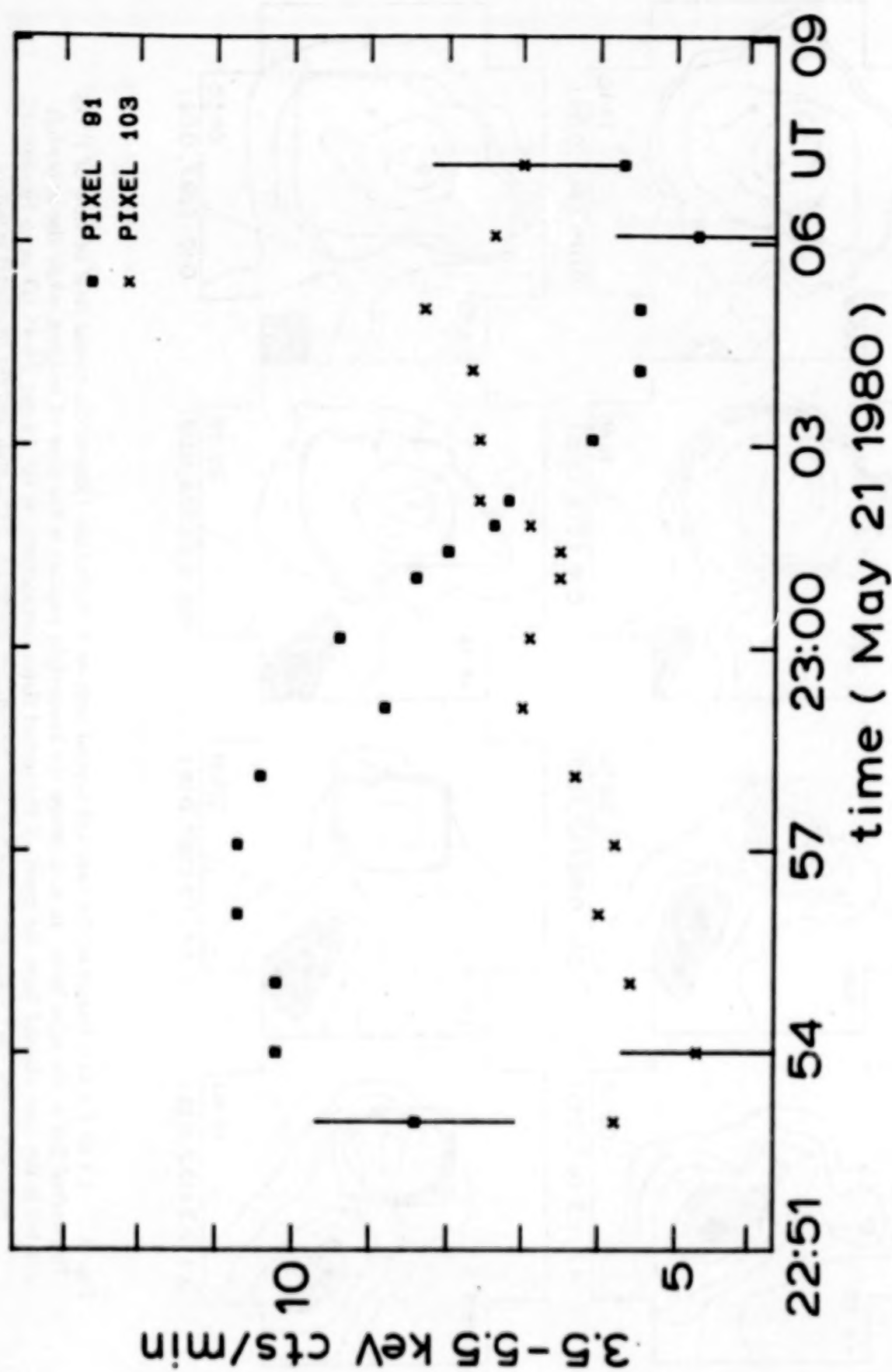
Figure 5.   X-ray contours in the SMM orbit next to the flare occurrence at 20:52 UT on
21 May.   HXIS coarse field of view, energy band 3.5 to 5.5 keV.   The upper and lower
images at the left-hand side were recorded at respectively the beginning and end of
the SMM orbit.   The other three images show the shift of the maximum of
brightness in the arch from pixel 91 to pixel 103 at 23:02 UT.

Figure 6. Count rates versus time for the two pixels 91 and 103 (maxima in Figure 5) around the time of their maximum brightness.
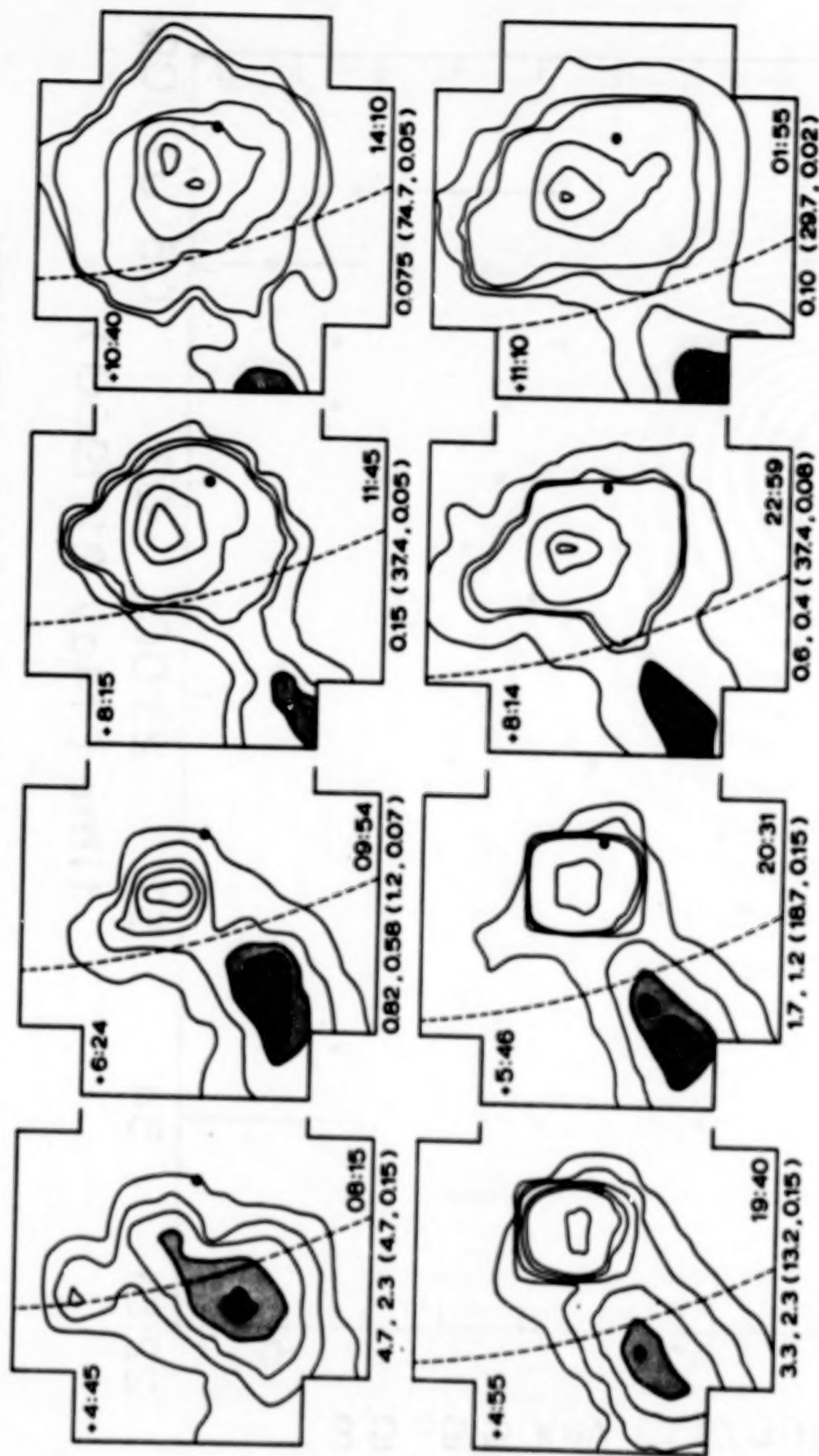
Figure 7. 3.5 to 5.5 keV images of the first and second arch on 6 November 1980 in the coarse field of view of HXIS. The dashed line is the solar limb. In each image the lower-right number is the time of imaging, while the upper-left number is the time elapsed from the onset of the parent flares (respectively at 03.30 and 14:45 UT on 6 November). Numbers below each image give counts/s for the hatched contours in the arch and (in brackets) counts/s for the brightest and least intense contour in each image.
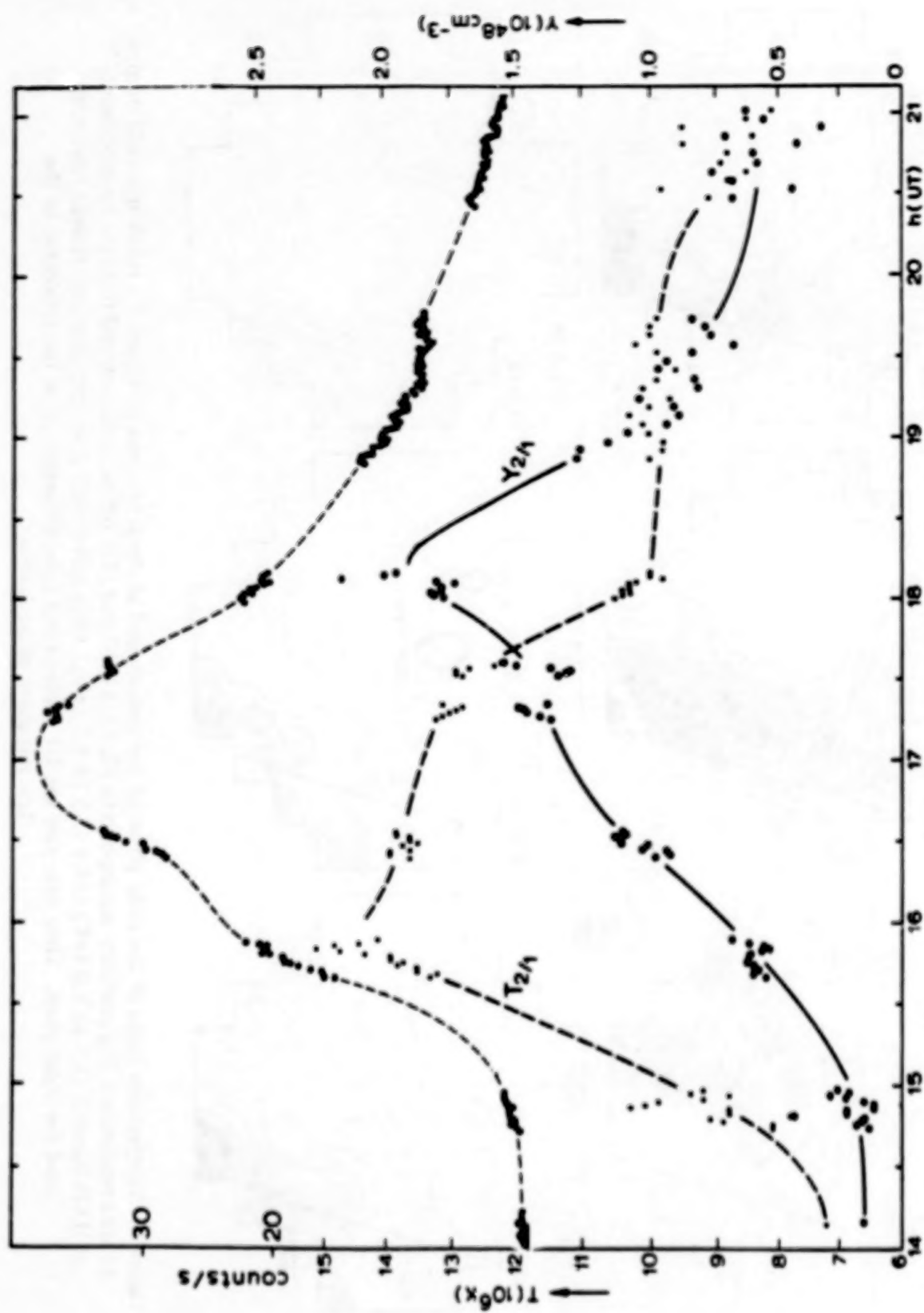
Figure 8. Temperature maps of the early phase of the arch imaged in the lower part of Figure 7. HXIS fine field of view (8 arc s resolution). The contours correspond to 10, 12, 14, 17 and 21 x 10⁶ K, as determined from the ratio of counts in HXIS bands 2 (5.5 to 8.0 keV) and 1 (3.5 to 5.5 keV). Only ratios with >3σ statistical significance have been used for these plots. Time data give the UT (below) and time difference from the maximum of the flare impulsive phase (above).

59

Figure 9. Time development of the arch brightening shown in the lower part of Figure 7. Above: counts/s in 3.5 to 5.5 keV X rays. Below: temperature, $T_{2/1}$, and emission measure per pixel, $Y_{2/1}$, from the ratio of counts in HXIS bands 1 and 2 (5.5 to 8.0 keV / 3.5 to 5.5 keV). These are mean characteristics of 6 pixels of HXIS coarse field of view at an average altitude of 100 000 km.

(c) NOV 8, 1980, 01:50 UT

(a) NOV 9, 1980, 04:38 UT

NOV 9, 1980
16:15 UT
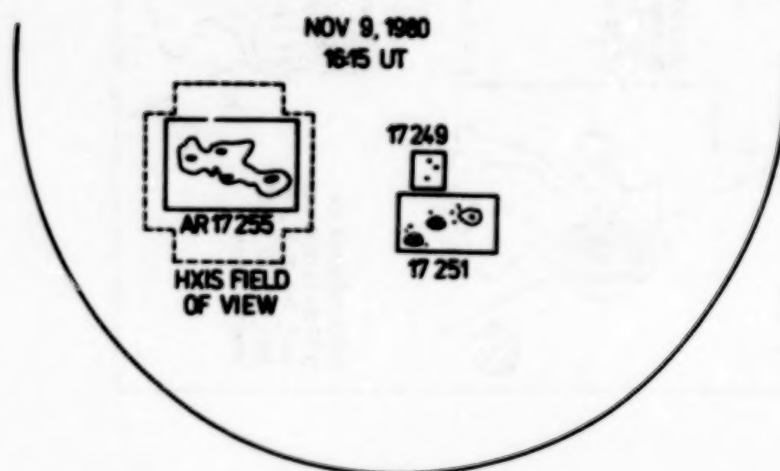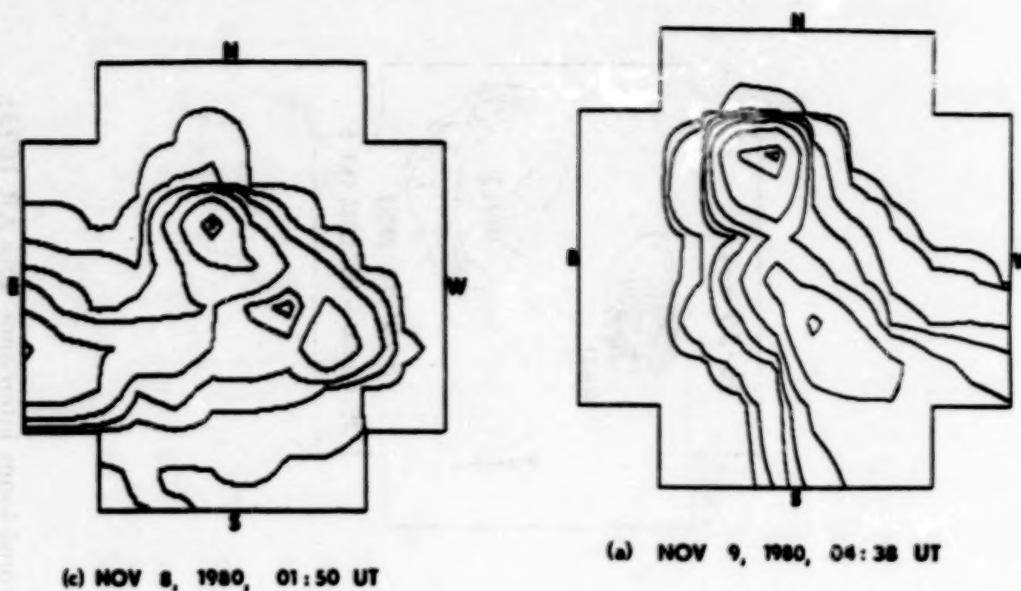
17249

AR 17 255

17 251

HXIS FIELD
OF VIEW

Figure 10. Top: 3.5 to 5.5 keV contours in the coarse field of view of HXIS. Left: the last
(probably fifth) revival of the arch shown in Figure 7, on 8 November, 01:50 UT (1008 s
integration, maximum count rate 0.7 counts/s). Right: a new structure seen on 9 November,
at 04:38 UT (383 s integration, maximum count rate 7.1 counts/s). This new structure
may be a loop interconnecting active regions 17255 and 17251, the position of
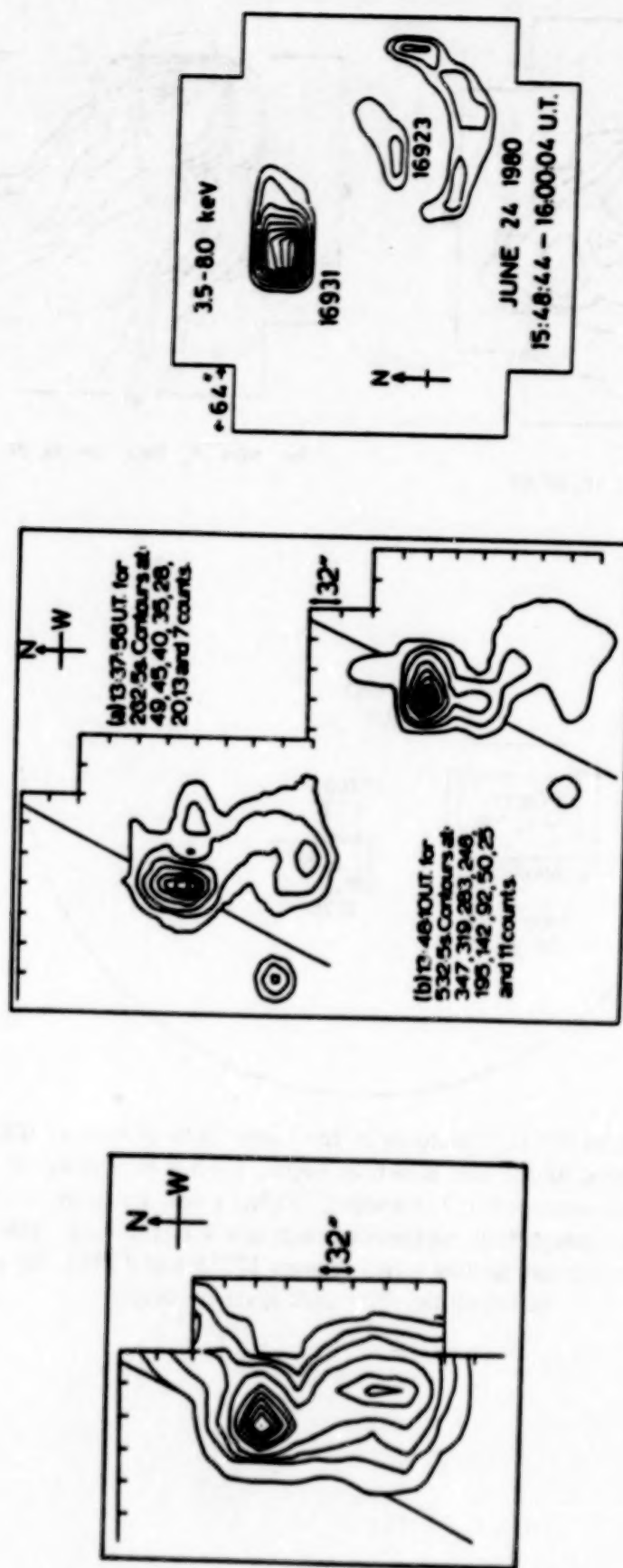which on the solar disk is shown below.

Figure 11. Left: Two X-ray contour plots (3.5 to 5.5 keV) showing the largest of the coronal loops interconnecting AR 16931 and AR 16923 on the western solar limb on 29 June 1980. Right: Five days earlier, on 24 June, simultaneous X-ray brightenings were seen in both these (supposedly interconnected) regions.
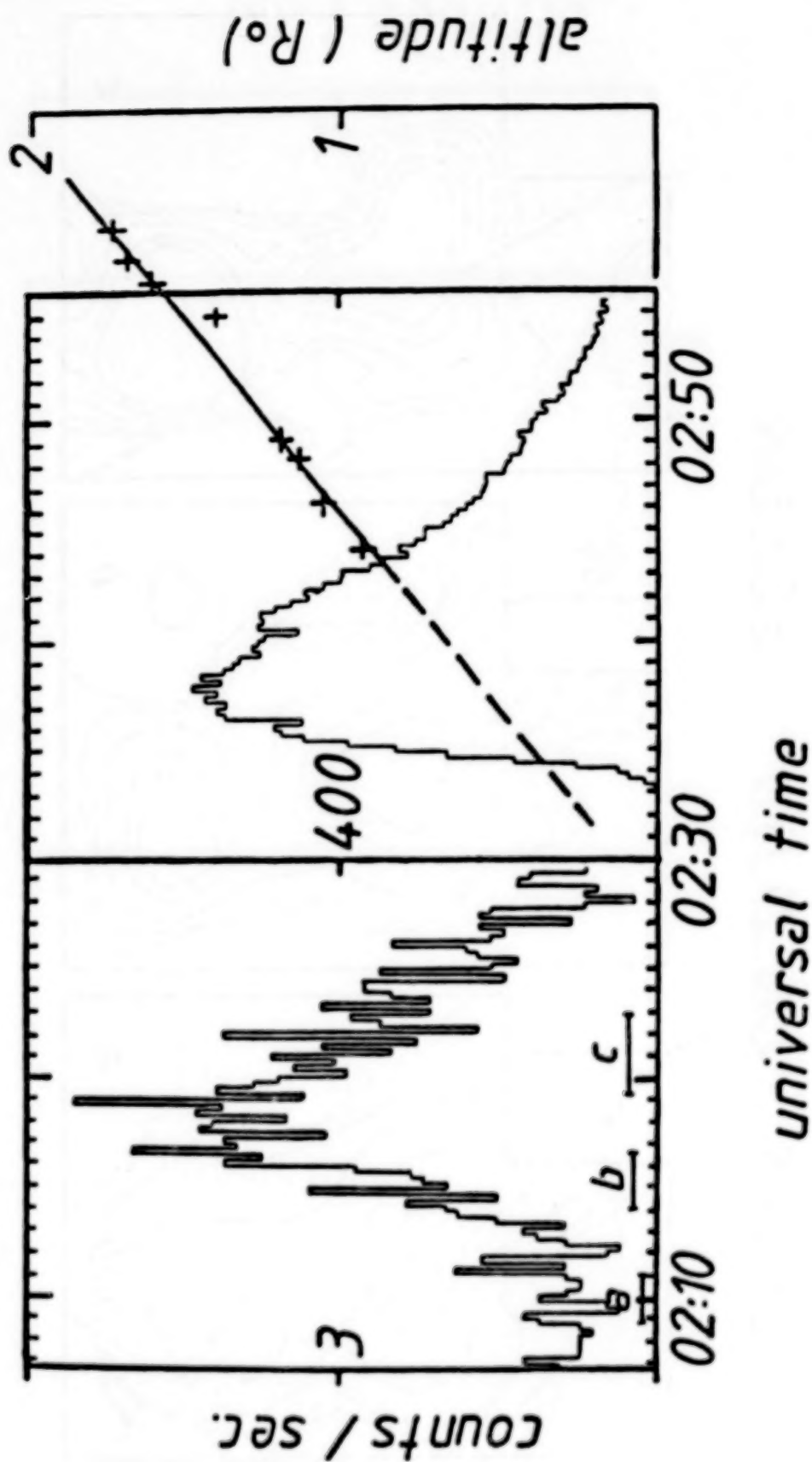
Figure 12. 3.5 to 5.5 keV intensity time profile for the flare at 02:33 UT on 29 June 1980, and its precursor (note the scale change at 02:30 UT). Superposed onto this are the altitude histories of the white-light coronal mass ejection (crosses) and an X-ray transient (a, b, c) which is shown in Figure 13.
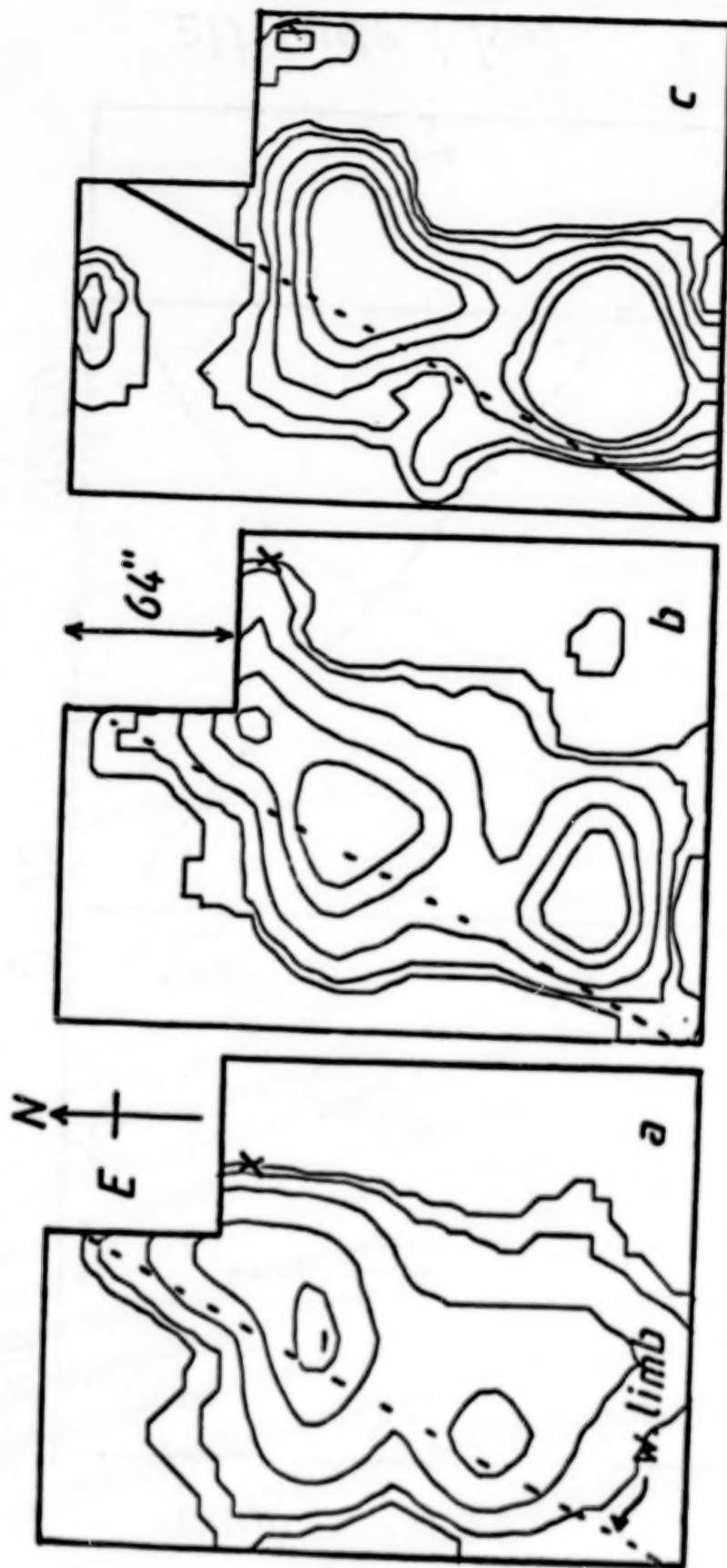
SMM-HXIS   JUNE 29, 1980   3.5-5.5 keV

Figure 13. The X-ray transient seen in the precursor phase of the flare of 29 June. Maximum intensity contour corresponds to 0.28 counts/s. The altitudes of the three crosses are plotted in Figure 12 (labeled a, b, c).

Table 1. Average count rate per pixel, F(k) in the 3.5 to 5.5 keV energy band for various exponents k in equation $F(k) = 2^{k/2} F_B$, where F_B is the average background flux, and the integration time (n seconds) needed for a 3σ statistical significance in nF(k).

k	F(k) (counts s^{-1})	n for S = 3.0 σ (s)	This corresponds in coarse FOV to
1	0.00645	3368	~limit of detection
2	0.00912	1974	
3	0.0129	1191	~10^{-4} a flare count
4	0.0182	740	
6	0.0365	308	
8	0.0730	139	
10	0.146	65.5	~10^{-3} a flare count
15	0.825	11.0	
20	4.67	1.93	
25	26.4		Subflare
30	149.4		Flare
35	845		Major flare

Table 2. Size of the new source at 21:13:19 UT for various electron densities

η_e	Volume	Radius (if source spherical)
10^9 cm^{-3}	3.4×10^{27} cm^3	9330 km
10^{10}	3.4×10^{25}	2010 km
10^{11}	3.4×10^{23}	430 km
10^{12}	3.4×10^{21}	90 km

Table 3. Physical parameters of the post-flare arch revived at 14:45 on 6 November 1980.

14:09 UT	PREFLARE:	$T_{2/1} = 7.2 \times 10^6$K
		$n_e = 6.8 \times 10^8$ cm^{-3}
14:44 UT	FLARE ONSET	
15:47 UT	MAX. TEMPERATURE	$T_{2/1} = 14.0 \times 10^6$ K
17:25 UT	MAX. ENERGY DENSITY	11.2 erg cm^{-3}
18:05 UT	MAX. DENSITY	$n_e = 2.4 \times 10^9$ cm^{-3}
	TOTAL VOLUME	1.1×10^{30} cm^3
	MAX. ENERGY CONTENT	1.2×10^{31} erg
	TOTAL MASS	4.4×10^{15}g

RESULTS FROM THE SOLAR MAXIMUM MISSION
(Invited)

Brian R. Dennis

Laboratory for Astronomy and Solar Physics
NASA Goddard Space Flight Center
Greenbelt, MD 20771 U.S.A.

ABSTRACT

The major results from SMM are presented as they relate to our understanding of the energy release and particle transportation processes that led to the high energy X-ray aspects of solar flares. Evidence is reviewed for a 152- to 158-day periodicity in various aspects of solar activity including the rate of occurrence of hard X-ray and gamma-ray flares. The statistical properties of over 7000 hard X-ray flares detected with the Hard X-Ray Burst Spectrometer are presented including the spectrum of peak rates and the distribution of the photon number spectrum. A flare classification scheme introduced by Tanaka is used to divide flares into three different types. Type A flares have purely thermal, compact sources with very steep hard X-ray spectra. Type B flares are impulsive bursts which show double footpoints in hard X-rays, and soft-hard-soft spectral evolution. Type C flares have gradually varying hard X-ray and microwave fluxes from high altitudes and show hardening of the X-ray spectrum through the peak and on the decay. SMM data are presented for examples of Type B and Type C events. New results are presented showing coincident hard X rays, O V, and UV continuum observations in Type B events with a time resolution of $\leq$ 128 ms. The subsecond variations in the hard X-ray flux during $\leq 10\%$ of the stronger events are discussed and the fastest observed variation in a time of 20 ms is presented. The properties of Type C flares are presented as determined primarily from the non-imaged hard X-ray and microwave spectral data. A model based on the association of Type C flares and coronal mass ejections is presented to explain many of the characteristics of these gradual flares.

I. INTRODUCTION

This paper is a personal review of some of the major results from the Solar Maximum Mission (SMM) with a strong emphasis on the hard X-ray observations, with which the author is most familiar from his role as Principal Investigator of the Hard X-Ray Burst Spectrometer (HXRBS). A much broader and deeper impression of the current state of solar flare physics can be obtained from the several chapters of the report from the three SMM workshops held in 1983 and 1984 at Goddard Space Flight Center (Kundu and Woodgate, 1985). No attempt has been made to ensure that this review is complete or comprehensive. In particular, the gamma-ray line and neutron observations are not discussed (see Chupp, 1984a), results from the Coronagraph/Polarimeter (C/P) and the Active Cavity Radiometer Irradiance Monitor (ACRIM) are not mentioned, and the major findings of the Hard X-Ray Imaging Spectrometer (HXIS) are left for the companion review papers by De Jager and Svestka.

SMM was launched in February 1980 and operated successfully until 22 November 1980, when the attitude control system failed. During those first nine months of operations, most of the new results, particularly those on the impulsive phase of flares, were obtained with the full complement of instruments. Some 1750 events were detected with HXRBS, 450 events with HXIS, and 700 with the Bent Crystal Spectrometer (BCS). After November 1980, the spacecraft

was maintained in a spinning mode with the instrument axes coning about the direction to the Sun with a typical offset angle of 10 to 15 deg. Consequently, only ACRIM intermittently and the wide-field instruments, the Gamma Ray Spectrometer (GRS) and HXRBS, could obtain useful data. By the time of the SMM repair in April 1984, HXRBS had detected over 7000 flares above 30 keV, GRS had detected over 140 flares above 300 keV, and a 152- to 158-day periodicity had been revealed in the rate of occurrence of these flares (Rieger et al., 1985; Kiplinger et al., 1985). After the replacement of the attitude control system and the C/P electronics, pointed observations were resumed and, almost immediately, on 24 April 1984 the biggest flare ever recorded by SMM occurred (Chupp, 1984b). The subsequent reduced level of solar activity has eased the problem of deciding where to point to catch the next flare and has allowed UVSP to make long-postponed, quiet-sun observations. Currently, all instruments are fully operational with the exception of HXIS, which failed in 1981 and could not be repaired, and UVSP, which has had intermittent wavelength drive problems since the repair. HXRBS has recorded its 7800th flare.

II. STATISTICAL ANALYSIS

One of the first things that can be done with the large number of events recorded with instruments on SMM is to determine the global properties of flares including the rate of occurrence, the spectrum of sizes, rise times, durations, spectral parameters, etc. Several catalogues of SMM events have already been prepared and distributed. These include the SMM Event Listing for 1980 (Pryor et al., 1981) and the HXRBS Event Listing for 1980-82 (Dennis et al., 1983). A comprehensive catalogue of data on all SMM events is available on the VAX computer at the SMM Data Analysis Center and plans exist to issue, in the near future, a revised version of the 1980 listing, a complete listing of all HXRBS events, and a new listing of all SMM events recorded since the repair.

(a) The 152- to 158-day periodicity

The most notable result from this statistical analysis is the discovery of a 152- to 158-day periodicity in the rate of flare occurrence during this solar cycle, cycle 21. This periodicity was first noticed by Rieger et al. (1985) in the tendency of 139 solar flares detected with GRS above 300 keV to occur in groups with a mean spacing of 154 days.

A much larger sample of 6775 hard X-ray flares detected with HXRBS above ~30 keV was used by Kiplinger et al. (1985) to reveal a similar periodicity illustrated in Figure 1. The number of flares detected per day by HXRBS is plotted versus time from launch in 1980 until the middle of 1984 with corrections made for the SMM duty cycle. A power spectrum analysis of the data plotted in Figure 1 was carried out using a Fourier transform routine that allows for the data gaps (Deeming, 1975) and this confirms the existence of a strong Fourier component having a period of 158 days and a semi-amplitude of approximately 40% of the mean flare rate. The sine wave superposed on the data in Figure 1 represents this Fourier component plus the first-order trend. Eight peaks can be seen in the flare rate at the expected times given by the sine wave up to June 1983. The expected peak in the fall of 1983 was not present but a ninth strong peak was observed in April/May 1984. Subsequently, no increase in flare rate was observed in the fall of 1984 but some weak activity was observed in January/February 1985.

A similar periodic component is present in an analysis of 6102 events with X-ray emission that does not exceed 140 keV. The power spectrum of this data set shown in Figure 2 also shows a strong peak at 0.0633 days^{-1} corresponding to a period of 158 days. Hence, the periodicity is present for a subset of flares that is independent of the 139 gamma-ray flares used

68

by Rieger et al. (1985). A periodicity of 152 days is also present in the rate of GOES events with a classification above M2.5 (Rieger et al., 1985), and Bogart and Bai (1985) report a 157-day periodicity of flare occurrence in the microwave data.

The interpretation of this 152- to 158-day periodicity in the solar flare rate during cycle 21 is still uncertain. The most complete theory has been developed by Wolff (1983) based on the rotational spectrum of g-modes in the Sun. He carried out a Fourier analysis of the variation of the mean monthly sunspot number in the years from 1749 to 1979 and found narrow but weak peaks in the power spectrum at a set of frequencies consistent with his model. The most prominent period found by Wolff below 200 days is 155.4 days, remarkably close to the period found for the flares in cycle 21. This period, according to Wolff's model, results from the beating between the rotation of an $\ell = 2$ mode and an $\ell = 3$ mode where ℓ is the spherical harmonic index. An attempt has been made to match the beat frequencies of other ℓ-modes to the other peaks in the power spectrum obtained from the HXRBS event rate but without success (Kiplinger, private communication).

In concluding this section, it is clear that there is compelling evidence for a periodicity in the rate of occurrence of solar flares during cycle 21 with a period of 152 to 158 days. It is impossible to say, at present, if this is a manifestation of the interacting g-modes as suggested by Wolff (1983). However, the possibility that this may be the case and the unique information concerning the solar interior that could then be determined lends great importance to this result and to the continued long-term accumulation of data.

(b) The spectrum of peak rates

A second result which has been obtained from the large number of flares recorded by SMM is an accurate spectrum of peak rates involving over 6000 flares recorded with HXRBS. This differential spectrum shown in Figure 3 was obtained from all complete events recorded with HXRBS above ~30 keV between launch and the beginning of 1985 and it can be well represented by an expression of the form

$$N(P) = 10^{-7} \, P^{-1.8} \text{ flares (counts s}^{-1} \text{ day)}^{-1}$$

where N(P) is the rate of flares detected with a peak rate P above background measured with HXRBS as the sum of the rate in all 15 channels. This expression fits the data over more than three orders of magnitude; the turnover below a peak rate of ~40 counts s^{-1} almost certainly results from the reduced efficiency of finding events in the HXRBS data that result in a less than doubling of the HXRBS background rate.

This differential spectrum of peak rates shown in Figure 3 is not directly comparable to the spectrum reported by Datlowe et al. (1974) and renormalized by Lin et al. (1984). Their integral spectrum is for the peak photon flux at 20 keV. It can be related to Figure 3 by noting that for a typical power-law photon spectrum with an index of 5, a peak HXRBS rate above background of 1000 counts s^{-1} corresponds to a photon flux at 20 keV of ~30 photons cm^{-2} s^{-1} keV^{-1}. This is the highest flux included in Datlowe et al.'s spectrum. Thus, Figure 3 extends the spectrum some two orders of magnitude to larger events. This is possible because the effects of pulse pile-up were less severe in HXRBS than in the OSO-7 detector (Datlowe, 1975) as a result of the ~0.06 cm thick aluminum window and the ~0.01 cm thick dead-layer on the HXRBS CsI(Na) crystal. In spite of these relatively thick absorbers, pulse pile-up is still a problem for HXRBS when the total counting rate greatly exceeds 10^4 counts s^{-1}, especially when the photon spectrum is steeper than ~E^{-5}.

There is no indication that the spectrum of peak rates changes shape as a function of time. When separate spectra are obtained for each of the 5 years from 1980 to 1984, all are consistent with the same slope as that shown in Figure 4. Furthermore, the power-law slope of -1.8 is consistent with the slope of -0.8 obtained for the integral spectrum in 1971/72 by Datlowe et al. (1974) and -0.9 obtained for the integral spectrum in 1969/71 using the detector very similar to HXRBS on OSO-5 (Dennis, unpublished).

(c) Distribution of spectral index

The HXRBS observations allow a counting rate spectrum to be obtained every 128 ms. From each such spectrum or from spectra accumulated over longer intervals, the spectrum of the incident photon flux can be determined as a function of time throughout the flares of interest. Unfortunately, as with all scintillation spectrometers such as HXRBS, the relatively poor energy resolution and the other factors contributing to the non-diagonal elements of the instrument response matrix, make it necessary to assume a form for the incident spectrum before the instrument deconvolution can be carried out. A power-law spectral form is commonly used and this can be expressed as follows:

$$N(E) = A\ E^{-\gamma}\ \text{photons cm}^{-2}\ \text{s}^{-1}\ \text{keV}^{-1}$$

where $N(E)$ is the photon flux (strictly flux density) in units of photons $\text{cm}^{-2}\ \text{s}^{-1}\ \text{keV}^{-1}$ at an energy E in keV that is incident on the detector. The parameters A and γ are determined from the observations using the technique described by Batchelor (1984).

The power-law spectral analysis has been carried out for many HXRBS events and the results have been used to determine the spectrum and energy content of the electrons producing the bremsstrahlung X rays (Wu et al., 1985). In Figure 4 we show the distribution in the value of γ determined at the time of peak HXRBS counting rate for all complete flares recorded in 1980 where that peak rate was greater than 1000 counts s^{-1}. The value of γ is seen to range from slightly less than 3 to as high as 10. It must be realized that, again because of the poor energy resolution of scintillation spectrometers, spectra steeper than E^{-7} cannot be accurately measured, and consequently, any value of γ greater than ~7 in Figure 4 should be considered as a lower limit at $\gamma = 7$. Corrections were applied for the effects of pulse pile up using the technique described by Datlowe (1975, 1977) so that we believe that the variation in the mean value of γ with the peak rate is real. This may be a further manifestation of the Big Flare Syndrome (Kahler, 1982) such that bigger flares tend to have harder spectra. Figure 4 also shows that flares that are relatively microwave rich and those that produce gamma-ray lines also have harder X-ray spectra (Bai et al., 1985).

Figure 4 can be compared to the distribution of γ given by Datlowe et al. (1974) with the understanding that they were looking at smaller flares with observations extending down to lower energies: 10 keV as compared to 25 keV for HXRBS. The values of γ obtained by Datlowe et al. (1974) extend from 2 to 7 with a median value of 4.0. This is clearly at least 1.0 lower than the median value of the smallest events in Figure 4. A median value of ~5.0 was obtained by Kane (1974) using OGO-5 data. Thus, it is possible that the generally steeper spectra found here is a result of the average spectrum being flatter from 10 to 25 keV and steeper at higher energies. This would agree with the sometimes better fit obtained at the peak of some flares to an exponential function expected for thermal bremsstrahlung (Dennis et al., 1981; Kiplinger et al., 1983b).

70

III. FLARE CLASSIFICATION SCHEMES

It has long been known that not all flares are alike, and various classification schemes have been proposed based on the appearance of different flares in certain wavelength or energy bands and different phases. These schemes have suffered from the difficulty of relating them to one another and in determining if the different classes were merely phenomenological or actually indicated the occurrence of different physical processes. It is vitally important to determine if different processes are occurring to produce the different types of flares. It has been one of the frustrations of solar flare physics that any generalization about flares that one tries to make is immediately met with many counter examples. If the counter examples can be shown to be different types of flares with a different process producing the particle acceleration, for example, then that would be an important step forward in understanding flares.

Pallavicini et al. (1977) developed a useful classification scheme based on soft X-ray images of limb flares made from Skylab. They identified three principal groupings: (A) flares characterized by compact loops, (B) flares with point-like appearance, and (C) flares characterized by large and diffuse systems of loops.

Considerable advances have been made in classifying flares as a result of more recent observations. This is best exemplified by the scheme introduced by Tanaka (1983) and used by Tsuneta (1983), Ohki et al. (1983), and Tanaka et al. (1983). This scheme is based on the hard X-ray imaging results from Hinotori but has found widespread value in coordinating other observations. Tanaka (1983) also divided flares into three classes referred to as Type A, B, and C, but it appears that the Pallavicini et al.'s A and B groups may correspond to Tanaka's Type B and A flares, respectively. Some flares, particularly the larger ones, can show characteristics of more than one type during their different phases. The three different flare types have the following distinct properties:

Type A Flares – hot thermal flares with $T \sim 3\text{-}5 \times 10^7$ K, compact, <5000 km, low altitude.

Type B Flares – typical impulsive bursts, double footpoints seen in hard X rays, highly sheared loop with lengths $\gtrsim 2 \times 10^4$ km, possible existence of electron beams producing hard X rays in thick-target interactions.

Type C Flares – high altitude X-ray sources, $\sim 5 \times 10^4$ km, gradually varying X-ray and microwave fluxes, X-ray spectral hardening and microwave delay suggesting trapped non-thermal electrons and/or continuous acceleration.

In this review I shall concentrate on discussions of SMM observations of Type B flares obtained mainly during 1980 and on Type C flares observed mainly after 1980. I will not discuss any observations of Type A flares since no good examples have been reported in the HXIS data set. The reader is referred to papers by Tsuneta (1983) and Tsuneta et al. (1984a) for discussions of Hinotori observations of this type of flare. There is some statistical evidence that Type C flares tend to occur preferentially during the decreasing phase of the solar cycle, and this may explain the difference between the 1980 results from the SMM Hard X-Ray Imaging Spectrometer (HXIS) in 1980 and the initial 1981 results from Hinotori. It appears that primarily Type B flares were detected with HXIS whereas the Hinotori team initially reported observations of Type C flares.

IV. PROPERTIES OF TYPE B FLARES OBSERVED WITH SMM

(a) The 5 November 1980 flare at 22:32 UT

The best example of a Type B flare in the SMM data set is the flare on 5 November 1980 starting at 22:32 UT. The soft and hard X-ray time profiles are shown in Figure 5, where the earlier flare at 22:26 UT can also be seen. Although the first flare was observed at 15 GHz with the Very Large Array (Hoyng et al., 1983), it was a factor of ten less intense in X rays than the second flare and the statistical significance of the HXIS images in the highest energy bands (16 to 30 keV) is poor. Hence, the second flare has been the subject of more extensive study than the first flare (Duijveman, Hoyng, and Machado, 1982; Duijveman and Hoyng, 1983; Rust, Simnett, and Smith, 1985; MacKinnon, Brown, and Hayward, 1984; Wu et al., 1985; and Dennis et al., 1985).

As shown in Figure 5, the hard X-ray time profile of this second flare was relatively simple, with a single, relatively smooth and intense spike lasting for 17 s (FWHM) followed some 90 s later by a second, less intense peak. The detailed spectral evolution of the first peak can be seen in Figure 6 where the HXRBS counting rates in three different energy ranges and the value of the power-law spectral index γ determined from the 34 to 405 keV HXRBS data are plotted on an expanded time scale. The value of γ decreases from 6 near the beginning of the event to 3.5 at the time of the peak rate and increases back to >6 on the decay. This soft-hard-soft spectral evolution was first reported by Kane and Anderson (1970) and is considered typical for impulsive flares. Some impulsive flares, however, show high energy tails on the spectrum above 50 to 100 keV that remain hard or become harder after the peak (Crannell et al., 1978; Dennis et al., 1981). Indeed this is also true for the 5 November peak above ~100 keV. It is not clear if this early indication of spectral hardening after an impulsive spike is the beginnings of a Type C flare as discussed below. It is possible that there is a continuous progression from purely impulsive Type B events with no spectral hardening after the peak to purely gradual Type C events with continuous spectral hardening through the peak. There are some events observed with HXRBS that clearly show Type B and Type C characteristics on different peaks within the same flare. Hence, events classified as Type B or Type C may just represent the extreme cases; impulsive and gradual phases may occur in all flares at some intensity and/or energy levels. It would seem, however, that the relative importances of these two phases must differ by several orders of magnitude for flares now classified as Type B and Type C.

The HXIS 16 to 30 keV images show three well resolved bright patches during the first impulsive peak in the second flare on 5 November 1980 at 22:33 UT (Fig. 7). Two patches labelled A and B following Duijveman, Hoyng, and Machado (1982) are separated by 1.6×10^4 km and a third patch labelled C is separated from B by 7×10^4 km. Comparisons with Hα images and magnetograms suggest that the bright patches were at the footpoints of two magnetic loops joining A and B, and B and C. Duijveman et al. (1982) claimed that the footpoints B and C started to brighten simultaneously to within ~5 s implying a velocity of $> 2 \times 10^9$ cm s^{-1} along the assumed semicircular loop. They showed that for this velocity to be interpreted as an Alfven velocity, the magnetic field in the loop must have been $\gtrsim 900$ G, implausibly high for such a large loop. They concluded that the most likely explanation for the simultaneous brightening was a beam of fast electrons traveling along the loop and producing X rays in thick-target interactions at the footpoints.

MacKinnon, Brown, and Hayward (1984) have shown that only a small fraction of the hard X rays in the HXIS 16 to 30 keV images come from the pixels that define the bright patches A, B, and C. They claim that the remainder come from a diffuse region around A and B although

the interpretation of the 2 or 3 images at the time of the first hard X-ray burst is complicated by the presence of a diffuse background resulting from the leakage of high energy photons through the walls of the instrument collimator. This conclusion that only a small fraction of the photons come from the footpoints is supported, however, by an extrapolation of the HXRBS spectrum above 30 keV down to the 16 to 30 keV HXIS energy range. Good agreement is found between this extrapolated spectrum and the total HXIS counting rate integrated over the whole fine field of view. When the counts in only the fine field of view pixels that define the three bright patches are summed, however, the resulting flux is an order of magnitude below the HXRBS extrapolation. If the spectrum of only the impulsive component is used; i.e., the more gradually varying component is subtracted from the fluxes in each energy band, then the spectrum becomes flatter at energies below 50 keV, E^{-3} compared to $E^{-3.9}$ for the spectrum of the total flux. This reduces the discrepancy and suggests that the impulsive component comes primarily from the footpoints whereas the more gradually varying component comes from a larger area.

Rust (1984) has also suggested that the total energy in electron beams in the 5 November flare was <10% of the total energy released and that the remainder appeared as a high temperature source. Evidence from HXIS images in bands 1 and 2 for a thermal conduction front traveling to point C is given in Rust, Simnett, and Smith (1985) but the interpretation of the moving contour lines is ambiguous. An equally valid interpretation would be one where the emission from loop BC increased uniformly along the loop as the plasma in the loop was heated by fast electrons traveling along the loop.

Later on in the same flare at 22:34:30 UT, a second hard X-ray peak occurred with an E^{-7} spectrum, much softer than the E^{-4} spectrum of the first peak. Furthermore, at the time of the second peak, the HXIS images show that the 16 to 30 keV X rays came predominantly from a location between the original bright patches A and B. The soft X-ray flux shows a second increase at about this time, as indicated in Figure 5, suggesting that almost the same amount of energy was released as during the first impulsive peak. The simplest explanation of these observations is that this second energy release served mainly to heat the plasma injected into the loop as a result of the first non-thermal energy release. Such a transition from an essentially non-thermal model to a thermal model during the impulsive phase of many flares has been proposed by Smith (1985) and by Tsuneta (1985). Smith (1985) proposes a dissipative thermal model, a term originally suggested by Emslie and Vlahos (1980), and he suggests that an increase in the ratio of plasma to magnetic pressure (the plasma β) at the energy release site later in the flare results in this transition from a non-thermal to a thermal model. It must be pointed out, however, that the blue shifts in the Ca XIX lines observed with the Bent Crystal Spectrometer (Acton et al., 1980) persist into the later stages of the impulsive phase of the 5 November 1980 flare indicating continuing chromospheric evaporation with upward velocities of ~200 km s⁻¹ even during the second hard X-ray peak (Antonucci, Gabriel,and Dennis, 1984).

(b) Simultaneous UV and hard X-ray emission

Another way to differentiate between the different flare models is to look at the timing relationship between UV and hard X-ray emission during impulsive flares. The simultaneity to within 1 s of UV and hard X-ray emission has been known since the observations of sudden ionospheric disturbances (SIDs) in conjunction with hard X-ray bursts (Donnelly and Kane, 1978; Kane et al., 1979). SIDs are caused by bursts of solar UV radiation between 10 and 1030 Å coming primarily from the transition region and low corona. The combined UVSP, HXIS, and HXRBS observations have now provided the required spatial information to allow the simultaneity of the UV and hard X-ray emissions to be used to significantly constrain the flare models.

Poland et al. (1982) and Cheng et al. (1981) have shown that the transition region line radiations – O V at 1371 Å, Si IV at 1402 Å, and O IV at 1401 Å – are strongly concentrated at the footpoints of magnetic loops. Woodgate et al. (1983) have shown that the simultaneity of the O V emission and the 25 to 300 keV X-ray flux to within 1 s for several impulsive flares observed on 8 November 1980. Here we show in Figure 6 the UV and hard X-ray observations for the 5 November 1980 flare at 22:33 UT from Dennis et al. (1985). The total O V emission summed over all nine UVSP pixels near footpoint B shown in Figure 7 is plotted in Figure 6 on the same time scale as the hard X-ray counting rate recorded by HXRBS in three energy ranges. This is a particularly clear example of the simultaneity to ≤ 1 s of a hard X-ray peak and the increase in the O V emission from a footpoint. It supports the conclusion reached by Woodgate et al. (1983) that the lack of any detectable time delay is inconsistent with flare models in which the hard X rays are initially produced at the loop top followed by the formation of thermal conduction fronts which travel to the footpoints where the UV burst is produced by heating. Models in which both X rays and UV radiation are both produced at the footpoints, or an electron beam transmits energy between the loop top and the footpoints in less than 1 s are allowed by these observations.

Attempts to quantify the expected O V flux for a given electron beam intensity have met with limited success. The theoretical problem is complicated by the fact that there are two competing effects of an electron beam incident from the corona. One is the depression of the transition zone to a lower altitude and higher density. This tends to increase the amount of material at the O V emitting temperature around 2.5×10^5 K suggesting that the O V flux should increase rapidly. The other effect suggests the opposite, however, and that is the steepening of the temperature gradient in the transition zone. This tends to reduce the amount of 2.5×10^5 K material and suggests that the O V flux should decrease. Thus, it is important to accurately model the transition zone in any theoretical calculation of the expected O V flux and this typically is difficult to do in the computer simulations because of its extremely small scale height. Poland et al. (1984), Emslie and Nagai (1984), and Mariska and Poland (1985) have carried out some exploratory model calculations to study the relationship between the energy emitted in hard X rays and in the O V line assuming that both result from an electron beam. Poland et al. (1984) find from the observations of individual flares that there is a definite relation between hard X-ray and O V emission throughout a given flare but that the flux ratio is different in different flares. They attribute these differences to the initial conditions in the flaring loops and their model calculations support this conclusion.

More recent observations made after the SMM repair have shown simultaneity of UV continuum and hard X-ray features in an impulsive flare to within 0.25 s (Woodgate, 1984). In a flare on 20 May 1984 at 02:59 UT, UVSP was recording at around 1600 Å with a time resolution of 75 ms in one pixel and HXRBS was recording the counting rate above 24 keV with 10 ms time resolution. (The UVSP wavelength drive was not working at this time so that the exact wavelength of the UV observations is not known nor is it known for certain if it was recording line or continuum emission. However, the two detectors separated by 17 Å recorded very similar rates and consequently it is believed that they were both in the continuum with little, if any, contribution from line emission.) The overall time profile of the impulsive phase of the event in UV and hard X rays is shown in Figure 8 and the first feature is shown on an expanded time scale in Figure 9. There are clearly significant differences between the overall UV and hard X-ray time profiles but the similarities are striking. In particular, the sharp feature at 02:59.23 UT shows up clearly in both time profiles with the start and peak times coincident to within 0.1 s.

If we assume that the detected UV emission for this event was continuum at ~1600 Å, then it was probably emitted low in the chromosphere at a temperature of ~5000 K according to Cook and Brueckner (1979). Thus, it is difficult to see how an electron beam incident on a footpoint from the corona could result in the measured 0.1 s simultaneity since electrons cannot reach deep in the chromosphere (Woodgate, private communi.ation). The possibility of the energy release itself occurring in the chromosphere would, of course, alleviate the problem.

Even more recent coincident UV and hard X-ray observations with 128 ms time resolution should ultimately help to differentiate between the different possible models. An impulsive flare on 24 April 1985 at 01:48 UT was recorded by both UVSP and HXRBS. UVSP was recording separately the emission in both the O V line and the continuum 17 Å from the line with a time resolution of 128 ms. Thus, the time profiles of the emission from the transition zone and from the lower chromosphere were obtained at the same time as the hard X-ray profile above 25 keV. The three time profiles are shown on the same time scale in Figure 10, where the rich detail is evident in this flare. It is too early in the analysis of these data to make any definitive statement about the relative timing, but it does appear as if the first peak in hard X rays and in the continuum emission are coincident to within 1 s. The O V emission, however, seems to reach its first peak a second or so later. This surprising result, if it can be verified, would support the idea that at least the initial energy release occurs in the chromosphere and not in the corona.

(c) Rapid fluctuations in the hard X-ray flux

The impulsive phase of solar flares is characterized by rapid variations in the hard X-ray and microwave flux. This must reflect the variations in the rate of energy release in the flare and the production of energetic electrons but the propagation of the electrons from the site of energy release to the location is also a factor in determining the observed variations. A detailed analysis of the most rapid variations that are observed has proved to be a useful tool to place limits on the models for the production and propagation of fast electrons.

Before 1980, observations of hard X rays had revealed variations on time scales as short as 1 s but as soon as better time resolutions become available, variations on time scales as short as a few tens of ms were observed (Orwig et al., 1981; Kiplinger et al., 1983a; Hurley et al., 1983).

One of the fastest variations observed with HXRBS is shown in Figure 12, where two seconds of the counting rate are plotted with a time resolution of 20 ms for an impulsive event that occurred on 6 June 1980. The most dramatic variation is the large, unresolved rise from 20 to 53 counts per 20 ms at 23:34:45.7 UT. Numerous other fast variations (not shown) occurring within 10 s of the plotted interval support the reality of this rapid fluctuation.

It must be remembered that only about 10% of all flares detected with HXRBS with a sufficiently high counting rate to see variations on a sub-second time scale, in fact, showed such rapid variations (Kiplinger et al., 1983a). Thus, sub-second variations are not a common phenomenon. Nevertheless, they can be used to constrain models for energy release and propagation. The short time scales involved are upper limits to the time scales of the acceleration process itself. Although both thermal and non-thermal interpretations of sub-second variations are viable, Kiplinger et al. (1983a) have shown that a thermal interpretation has no energetic advantage over a non-thermal interpretation for the production of hard X rays. Furthermore, Kiplinger et al. (1984) have shown for a particularly well resolved sub-second spike, that the observations allow constraints to be placed on the loop length and on the electron pitch-angle distribution assuming a non-thermal interpretation.

V. PROPERTIES OF TYPE C FLARES

The canonical Type C flare identified in the Hinotori data is the flare on 13 May 1981 (Tsuneta et al., 1984b). A part of the time profile of this event as determined with HXRBS is shown in Figure 12 together with the evolution of the power-law spectral index γ. We see immediately two differences between this event and the 5 November 1980 event shown in Figure 5 and 6. First of all, the 13 May 1981 flare is a much more gradually varying event with the hard X-ray peak lasting for ~8 min (FWHM) compared to 17 s for the major peak on 5 November. The beginning of the event was not seen with HXRBS since SMM did not emerge from spacecraft night until 04:08 UT, but Tsuneta et al. (1984b) report that this event showed no impulsive component in either hard X-rays or microwaves. The second difference is that for the 13 May event the hard X-ray spectrum gets progressively harder (γ decreases) through the peak in contrast to the soft-hard-soft spectral evolution of the 5 November event shown in Figure 6. The soft-hard-harder spectral evolution is also evident in Figure 13 where individual spectra are plotted for specific times on the rise and decay of the hard X-ray peak. The photon flux density was determined as a function of photon energy from the 15-channel HXRBS counting rate data using the technique described by Batchelor (1984) and a power-law fit was made to the points corresponding to channels 3 to 14. The lower two channels were excluded because there is a steep, low-energy component to the spectrum near the beginning of the rise and towards the end of the decay of the event as shown in Figure 13. Clearly, it is the spectrum above ~60 keV that participates in the spectral hardening with time. The steep spectrum at lower energies is most probably a high temperature thermal component similar to that reported by Lin et al. (1981).

The most striking result concerning the 13 May flare, however, is that the altitude of the X-ray and microwave source was ~4 x 10^4 km above the photosphere (Tsuneta et al., 1984b). This result was obtained from the 14 to 38 keV image in Figure 14, which shows that the X-ray source was displaced by ~1 arc min towards the limb from the two-ribbon Hα flare. Considering the location of the Hα source at N9-13 E54-58 (Solar Geophysical Data), this displacement corresponds to the altitude indicated above. This is again in marked contrast to the Type B flares, where at least a large fraction of the hard X rays are believed to come from low altitudes at the footpoints of magnetic loops.

Since hard X-ray imaging has not been available for many flares, attempts have been made to select Type C flares based on their more readily available properties. Cliver et al. (1985) have selected ten gradual hard X-ray bursts (GHBs) including the 13 May 1981 event that all show the following similar characteristics:

(1) The X-ray spectrum is harder than average (see Figure 4) with a typical value for γ of between 3 and 4.

(2) The hard X-ray spectrum systematically hardens (or at least does not soften) through the peaks and on the decay.

(3) The GHBs are often preceded, by as much as 60 min, by an impulsive phase although sometimes, as in the case of the 13 May 1981 event, no impulsive phase may be seen at all.

(4) The GHBs occur in the later, parallel-ribbon phase of major flares.

(5) A coronal mass ejection was observed, or inferred, in association with at least nine of the ten GHBs.

(6) The associated microwave bursts were also very gradual and peaked sometimes many minutes after the hard X-ray peak as shown for the 26 April 1981 flare in Figure 15.

(7) The GHBs were typically microwave rich in comparison with the hard X-ray flux as shown in Figure 16 and had relatively low peak frequencies suggesting a low density source and weak magnetic fields.

(8) The GHBs are associated with long duration soft X-ray events suggesting continuous energy release for up to several hours.

These properties of GHBs led Cliver et al. (1985) to propose that these events result from particle acceleration by magnetic reconnection following coronal mass ejection. This simplified picture of such an event shown in Figure 17 was first proposed by Cliver (1983). In this model, the magnetic field lines are envisioned as being stretched as the coronal mass ejection moves out. Magnetic reconnection takes place below the ejected material and it is at this point that the electrons are accelerated. Electrons moving upwards produce the associated radio Type IV emission; electrons moving downwards are trapped in the low density loops below the reconnection point and produce the hard X rays and microwaves.

It is not certain if the observed spectral hardening can be attributed to the decrease in energy loss rate with increasing electron energy in the trap or to the time dependence of the electron acceleration process itself. The density of the X-ray emitting source for the 13 May 1981 flare has been estimated by Tsuneta et al. (1984b) to be 3×10^{10} cm^3 from the soft X-ray observations. The decay time for 100 keV electrons in a trap with this density would be ~1 s assuming only Coulomb losses. Bai and Dennis (1985) give this argument and others in favor of the so-called second-step acceleration interpretation (Bai and Ramaty, 1979), in which protons are accelerated to >1 MeV and electrons to relativistic energies using particles accelerated by the primary (or first-step) mechanism as injection particles. For other flares where density information is not generally available, a combination of both continuous acceleration and energy losses may well be important.

VI. CONCLUSIONS

We have reviewed some of the more important results from SMM that have contributed greatly to our understanding of the processes that led to the high energy X-ray aspects of solar flares. The 152- to 158-day periodicity in the rate of occurrence of hard X-ray flares and other manifestations of solar activity may prove to be important in determining the dynamics of solar rotation as Wolff (1983) believes but only further analysis and more extensive data sets will resolve that issue. The classification of flares into three different types suggests that we are beginning to be able to distinguish between the three basic models for X-ray production: the purely thermal emission from Type A flares, the thick-target interactions at the footpoints in the impulsive Type B flares, and the coronal thin-target interactions in the gradual Type C flares. This interpretation is still controversial and many flares exhibit characteristics of all three types. Nevertheless, the fact that in certain flares we have begun to distinguish between the different models for X-ray production has allowed us to refine the constraints on the basic flare energy release mechanism or mechanisms.

Higher resolution hard X-ray images with better time resolution and extending to higher photon energies will allow us to improve the identification of the correct X-ray production models in any specific flare. The simultaneity of footpoint brightening on time scales of fractions of a

second is a very powerful indicator of the existence of electron beams. The detection of the thin-target emission from such beams in the loop would also give a clear picture of where the particles are accelerated in the loop and with what pitch-angle distributions. Imaging to energies above the 30 to 40 keV achieved with SMM and Hinotori is necessary to clearly separate the thermal emission of the $10 - 30 \times 10^6$ K plasma from the higher energy X-ray component. Furthermore, higher spectral resolution than is possible with scintillation spectrometers is required to resolve the very steep spectra of this thermal emission.

These requirements for future observations are well within the capabilities of new instruments being proposed for flights during the next solar maximum. Thus, the opportunity exists to build on our successes during this cycle 21 of solar activity and to achieve even more dramatic advances in our understanding of the fundamental flare processes during cycle 22.

REFERENCES

Acton, L. W., and 23 co-authors, 1980, *Solar Phys.*, *65*, 53.

Antonucci, E., Gabriel, A. H., and Dennis, B. R., 1984, *Astrophys. J.*, *287*, 179.

Bai, T. and Dennis, B. R., 1985, *Astrophys J.*, in press.

Bai, T. and Ramaty, R., 1979, *Astrophys. J.*, *227*, 1072.

Bai, T., Kiplinger, A. L., and Dennis, B. R., 1985, *Astrophys. J.*, submitted.

Batchelor, D. A., 1984, Ph.D.Thesis, Univ. of N. Carolina at Chapel Hill; also NASA Technical Memorandum 86102.

Bogart, R. S. and Bai, T., 1985, *Bull Am. Astron. Soc.*, *17*, 644.

Cheng, C.-C., Tandberg-Hanssen, E., Bruner, E. C., Orwig, L. E., Frost, K. J., Woodgate, B. E., and Shine, R. A., 1981, *Astrophys. J. (Letters)*, *248*, L39.

Chupp, E. L., 1984a, *Ann. Rev. Astron. Astrophys.*, *22*, 359.

Chupp, E. L., 1984b, *Nature*, *310*, 725.

Cliver, E. W., 1983, *Solar Phys.*, *84*, 347.

Cliver, E. W., Dennis, B. R., Kane, S. R., Neidig, D. F., Sheeley, N. R., Jr., and Koomen, M. J., 1985, *Astrophys J.*, in preparation.

Cook, J. W. and Brueckner, G. E., 1979, *Astrophys. J.*, *227*, 645.

Crannell, C. J., Frost, K. J., Matzler, C., Ohki, K., and Saba, J. L., 1978, *Astrophys. J.*, *223*, 620.

Datlowe, D. W., 1975, *Space Sci. Instru.*, *1*, 389.

Datlowe, D. W., 1977, *Nucl. Inst. Methods*, *145*, 365.

Datlowe, D. W., Elcan, M. J., and Hudson, H. S., 1974, *Solar Phys.*, *39*, 155.

Deeming, T. J., 1975, *Astrophys. Space Sci.*, *36*, 137.

Dennis, B. R., Frost, K. J., and Orwig, L. E., 1981, *Astrophys. J. (Letters)*, *244*, L167.

Dennis, B. R., Frost, K. J., Orwig, L. E., Kiplinger, A. L., Dennis, H. E., Gibson, B. R., Kennard, G. S., and Tolbert, A. K., 1983, NASA Technical Memorandum 84998.

Dennis, B. R., Kiplinger, A. L., Orwig, L. E., and Frost, K. J., 1985, Proc. 2nd India-US Workshop on Solar Terrestrial Physics, January 1984, New Delhi, India; also NASA Technical Memorandum 86187.

Donnelly, R. F. and Kane, S. R., 1978, *Astrophys. J.*, *222*, 1043.

Duijveman, A., Hoyng, P., and Machado, M. E., 1982, *Solar Phys.*, *81*, 137.

Duijveman, A. and Hoyng, P., 1983, *Solar Phys.*, *86*, 289.

Emslie, A. G. and Nagai, F., 1984, *Astrophys. J.*, *279*, 896.

Emslie, A. G. and Vlahos, L., 1980, *Astrophys. J.*, *242*, 359.

Hoyng, P., Marsh, K. A., Zirin, H., and Dennis, B. R., 1983, *Astrophys J.*, *268*, 865.

Kahler, S. W., 1982, *J. Geophys. Res.*, *87*, 3439.

Hurley, K., Niel, M., Talon, R., Estulin, I. V., and Dolidge, V. Ch., 1983, *Solar Phys.*, *86*, 367.

Kane, S. R., 1974, IAU Symp. 57 Coronal Disturbances, ed., G. Newkirk, Jr., p. 105.

Kane, S. R. and Anderson, K. A., 1970, *Astrophys. J.*, *162*, 1003.

Kane, S. R., Frost, K. J., and Donnelly, R. F., 1979, *Astrophys. J.*, *234*, 669.

Kawabata, K., Ogawa, H., and Suzuki, I., 1983, *Solar Phys.*, *86*, 247.

Kiplinger, A. L., Dennis, B. R., Emslie, A. G., Frost, K. J., and Orwig, L. E., 1983a, *Astrophys. J. (Letters)*, *265*, L99.

Kiplinger, A. L., Dennis, B. R., Frost, K. J., and Orwig, L. E., 1983b, *Astrophys. J.*, *273*, 783.

Kiplinger, A. L., Dennis, B. R., Frost, K. J., and Orwig, L. E., 1984, *Astrophys J. (Letters)*, *287*, L105.

Kiplinger, A. L., Dennis, B. R., and Orwig, L. E., 1985, *Bull. Am. Astron. Soc.*, *16*, 891.

Kundu, M. and Woodgate, B., 1985, NASA Special Publication from the SMM Workshops, in preparation.

Lin, R. P., Schwartz, R. A., Pelling, R. M., and Hurley, K. C., 1981, *Astrophys. J. (Letters)*, *251*, L109.

Lin, R. P., Schwartz, R. A., Kane, S. R., Pelling, R. M., and Hurley, K. C., 1984, *Astrophys. J.*, *283*, 421.

MacKinnon, A. L., Brown, J. C., and Hayward, J., 1984, preprint.

Mariska, J. T. and Poland, A. I., 1985, *Solar Phys.*, in press.

Ohki, K., Takakura, T., Tsuneta, S., and Nitta, N., 1983, *Solar Phys.*, *86*, 301.

Orwig, L. E., Frost, K. J., and Dennis, B. R., 1981, *Astrophys. J. (Letters)*, *244*, L163.

Pallavicini, R., Serio, S., and Vaiana, G. S., 1977, *Astrophys. J.*, *216*, 108.

Poland, A. I., and 10 co-authors, 1982, *Solar Phys.*, *78*, 201.

Poland, A. I., Orwig, L. E., Mariska, J. T., Nakatsuka, R., and Auer, L. H., 1984, *Astrophys. J.*, *280*, 457.

Pryor, H., Pierce, M. J., Speich, D. M., Fesq, L. M., Spear, K. A., Nelson, J. J., and McGovern, J. G., 1981, Solar Maximum Mission Event Listing, Internal Document of the SMM Data Analysis Center, NASA, GSFC.

Rieger, E., Share, G. H., Forrest, D. J., Kanback, G., Reppin, C., and Chupp, E. L., 1985, *Nature*, *312*, 623.

Rust, D. M., 1984, *Adv. Space Res.*, *4*, 191.

Rust, D. M., Simnett, G. M., and Smith, D. F., 1985, *Astrophys. J.*, *288*, 401.

Smith, D. F., 1985, *Astrophys. J.*, *288*, 801.

Svestka, Z., and 8 co-authors, 1983, *Solar Phys.*, *85*, 313.

Tanaka, K., 1983, IAU Coll. 71, Activity in Red-Dwarf Stars, eds. P. B. Byrne and M. Rodono, p. 307.

Tanaka, K., Nitta, N., Akita, K., and Watanabe, T., 1983, *Solar Phys.*, *86*, 91.

Tsuneta, S., 1983, Proc. Japan-France Seminar on Active Phenomena in the Outer Atmosphere of the Sun and Stars, 3-7 October 1983, eds. J.-C. Pecker and Y. Uchida, CNRS and Observatiore de Paris, p. 243.

Tsuneta, S., 1985, *Astrophys. J.*, *290*, 353.

Tsuneta, S., Nitta, N., Ohki, K., Takakura, T., Makishima, K., Murakami, T., Oda, M., and Ogawara, Y., 1984a, *Astrophys. J.*, *284*, 827.

Tsuneta, S., Takakura, T., Nitta, N. Ohki, K., Tanaka, K., Makishima, K., Murakami, T., Oda, M., Ogawara, Y., and Kondo, I., 1984b, *Astrophys. J.*, *280*, 887.

Wolff, C. L., 1983, *Astrophys. J.*, *264*, 667.

Woodgate, B. E., 1984, *Adv. Space Res.*, *4*, 393.

Woodgate, B. E., Shine, R. A., Poland, A. I., and Orwig, L. E., 1983, *Astrophys. J.*, *265*, 530.

Wu, S. T., et al., 1985, Proc. SMM Workshop on Solar Flares (M. R. Kundu and B. E. Woodgate, eds.), in preparation, ch. 5.
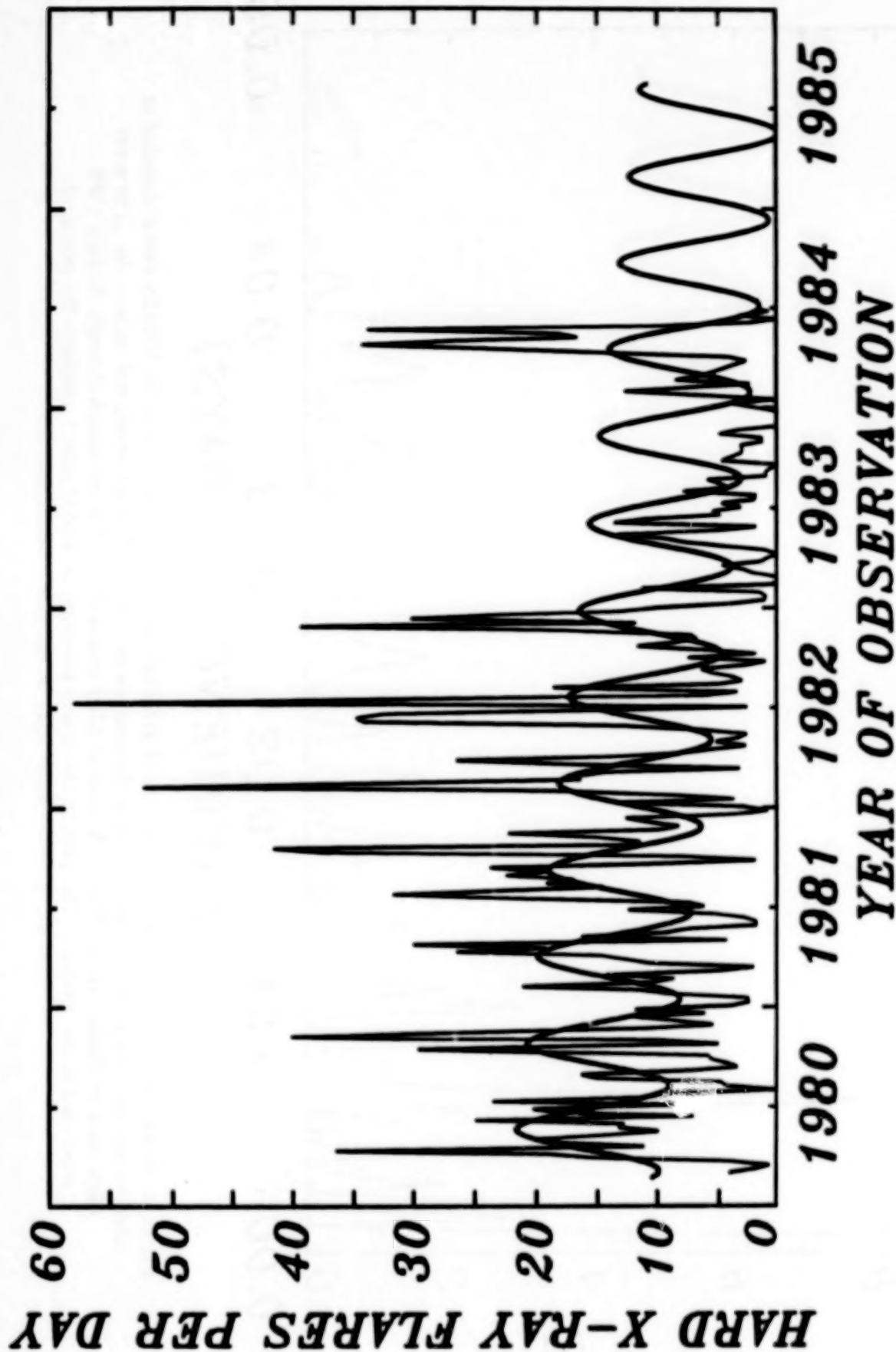
Figure 1. Plot of the weekly averaged rate of flares detected with HXRBS (corrected for the duty cycle) as a function of time from launch in February 1980 until after the repair in April 1984. The sine wave superimposed on the data is the Fourier component with a period of 158 days determined from the power spectrum analysis. A total of 6775 flares were included in the analysis. The energy threshold varied from 25 keV at launch to 33 keV in 1984.
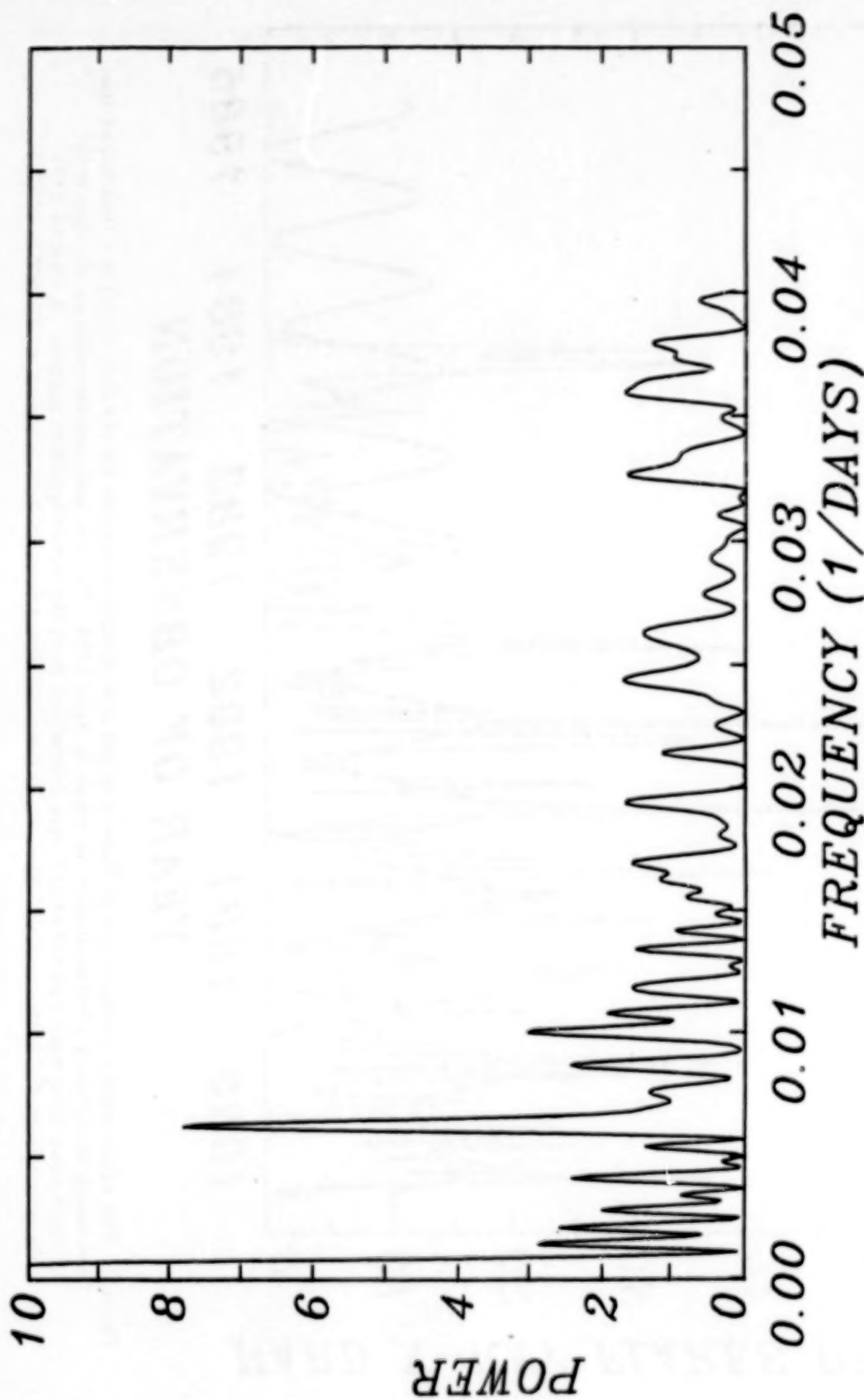
Figure 2. Power spectrum of the rate versus time of HXRBS low energy events. Only the HXRBS events detected at energies not exceeding 150 keV were used in the analysis so that the data set would not include the gamma-ray flares used by Rieger et al. (1985). A total of 6102 events detected from launch through 31 July 1985 were used in the analysis. The peak in the power spectrum at 0.0633 days^{-1} confirms the existence of the 158-day periodicity in this independent data set.
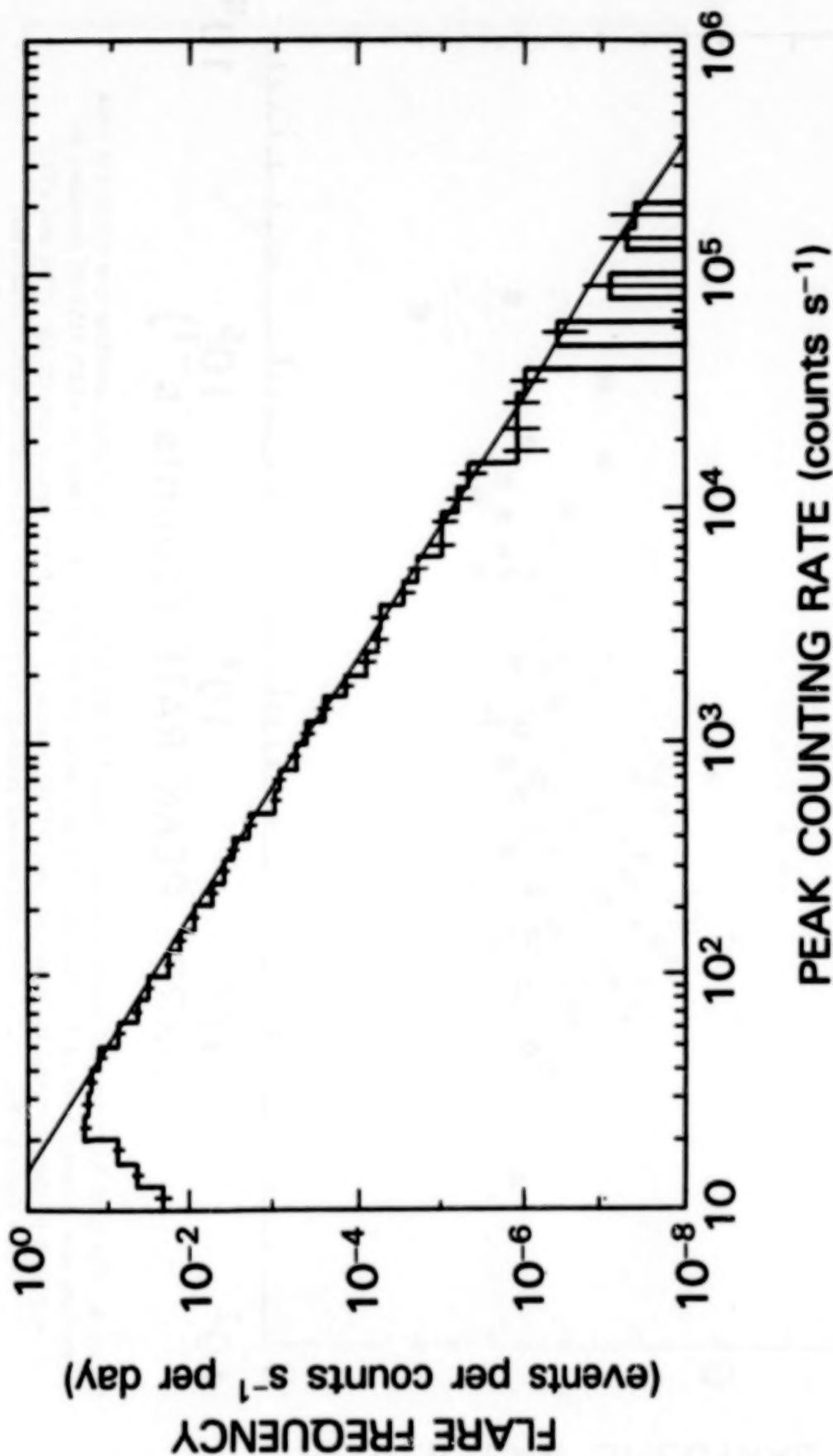
Figure 3. Peak rate spectrum of all complete events detected with HXRBS from launch to February 1985. The straight line through the data corresponds to the power-law expression given in the text with a spectral index of −1.8.
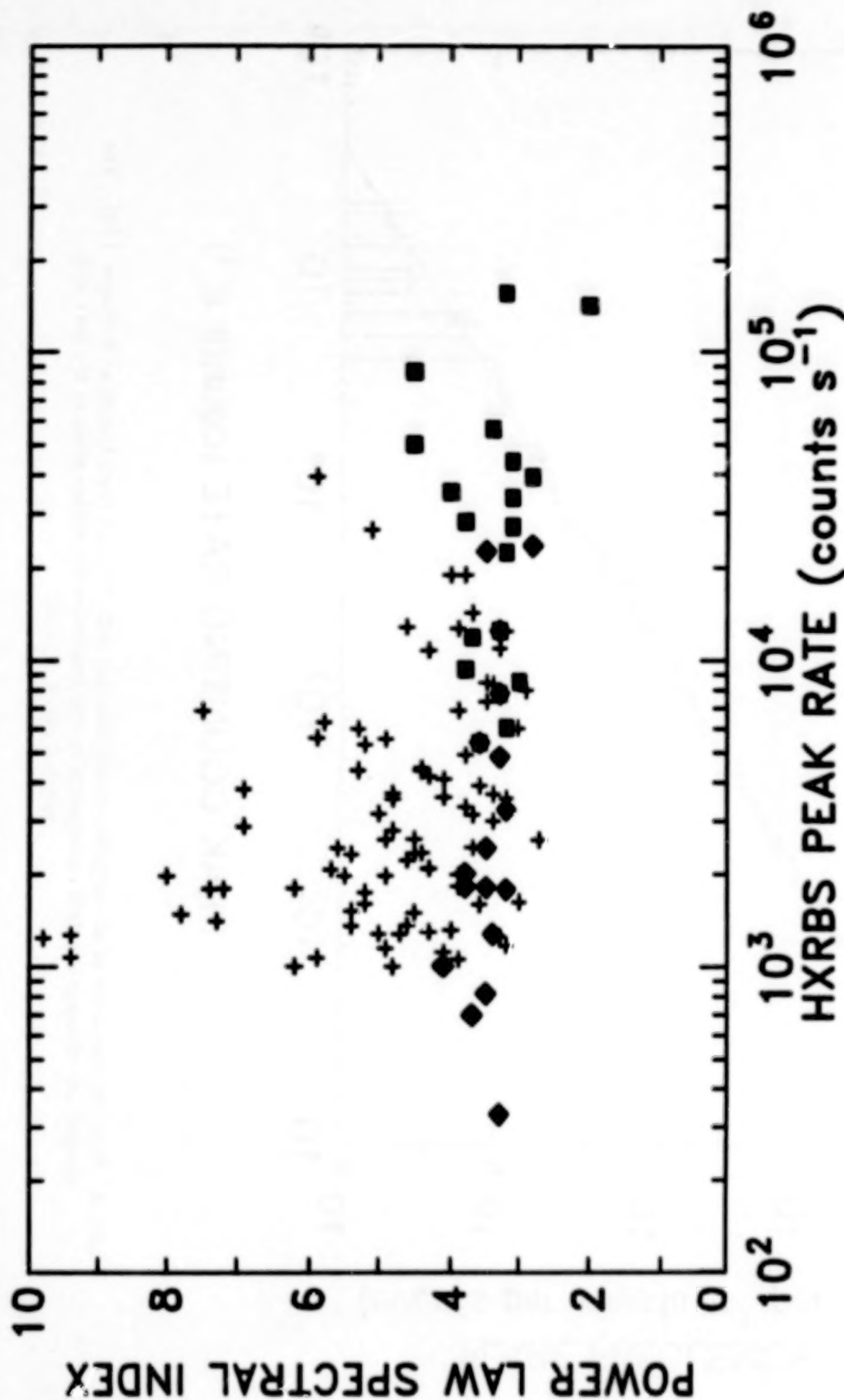
Figure 4. The hard X-ray spectral index γ obtained from HXRBS data at the time of peak counting rate versus the peak counting rate summed over all 15 channels. The plus signs are for all flares in 1980 for which HXRBS recorded the true peak of the event and the peak rate was >1000 counts s⁻¹. The filled squares are for the 1980 and 1981 flares listed by Bai et al. (1985) that showed evidence for gamma-ray line emission in the Gamma Ray Spectrometer (GRS) on SMM. The filled diamonds are for the gradual microwave-rich flares recorded in 1980, 1981, and 1982, and also listed in Bai et al. (1985).
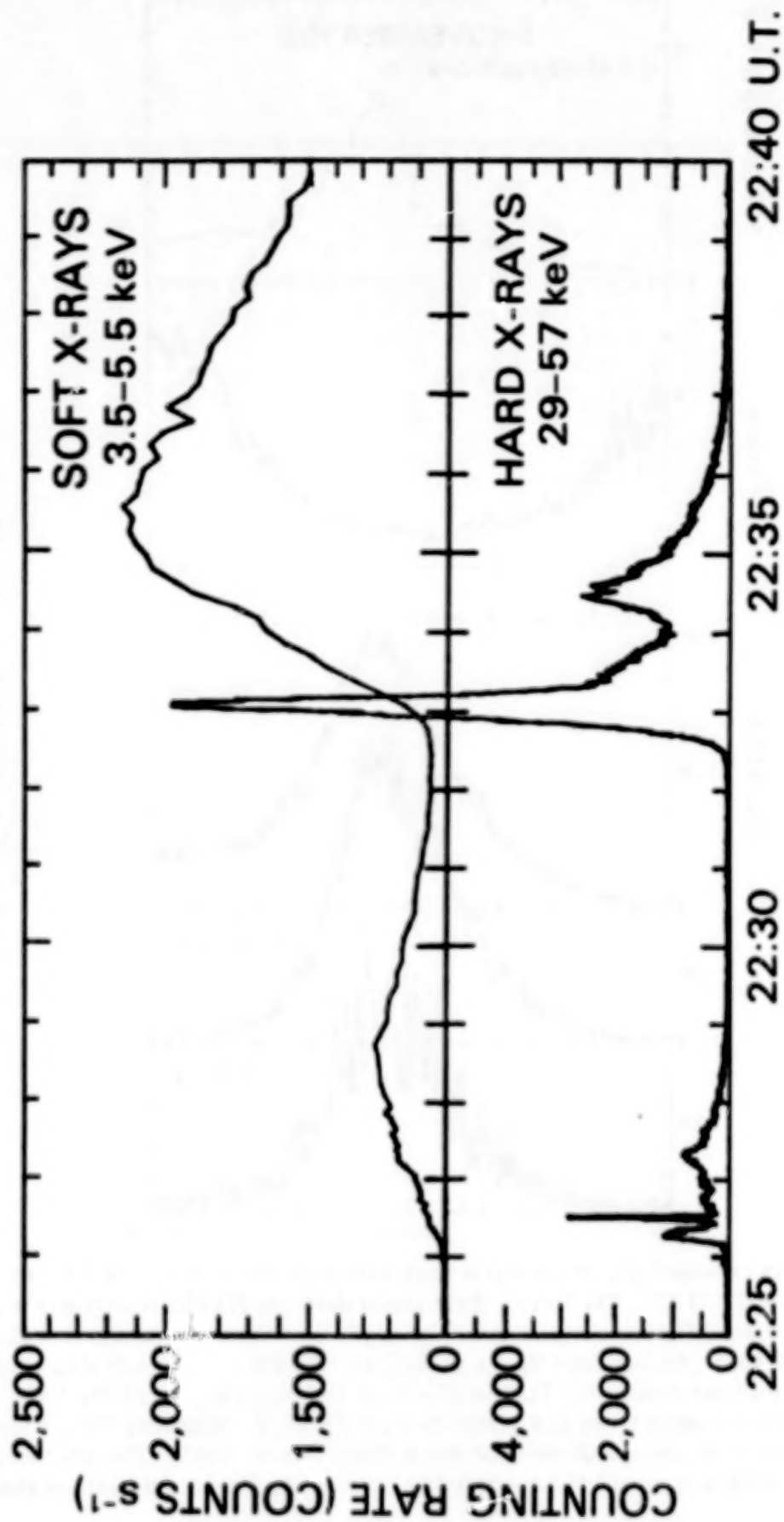
Figure 5. Soft and hard X-ray emissions as functions of time for the two flares on 5 November 1980. The soft X-ray counting rate is the sum of the counts in the HXIS band 1 in selected pixels of the coarse field of view. The hard X-ray rate is the sum of counts in HXRBS channels 1 and 2.

85
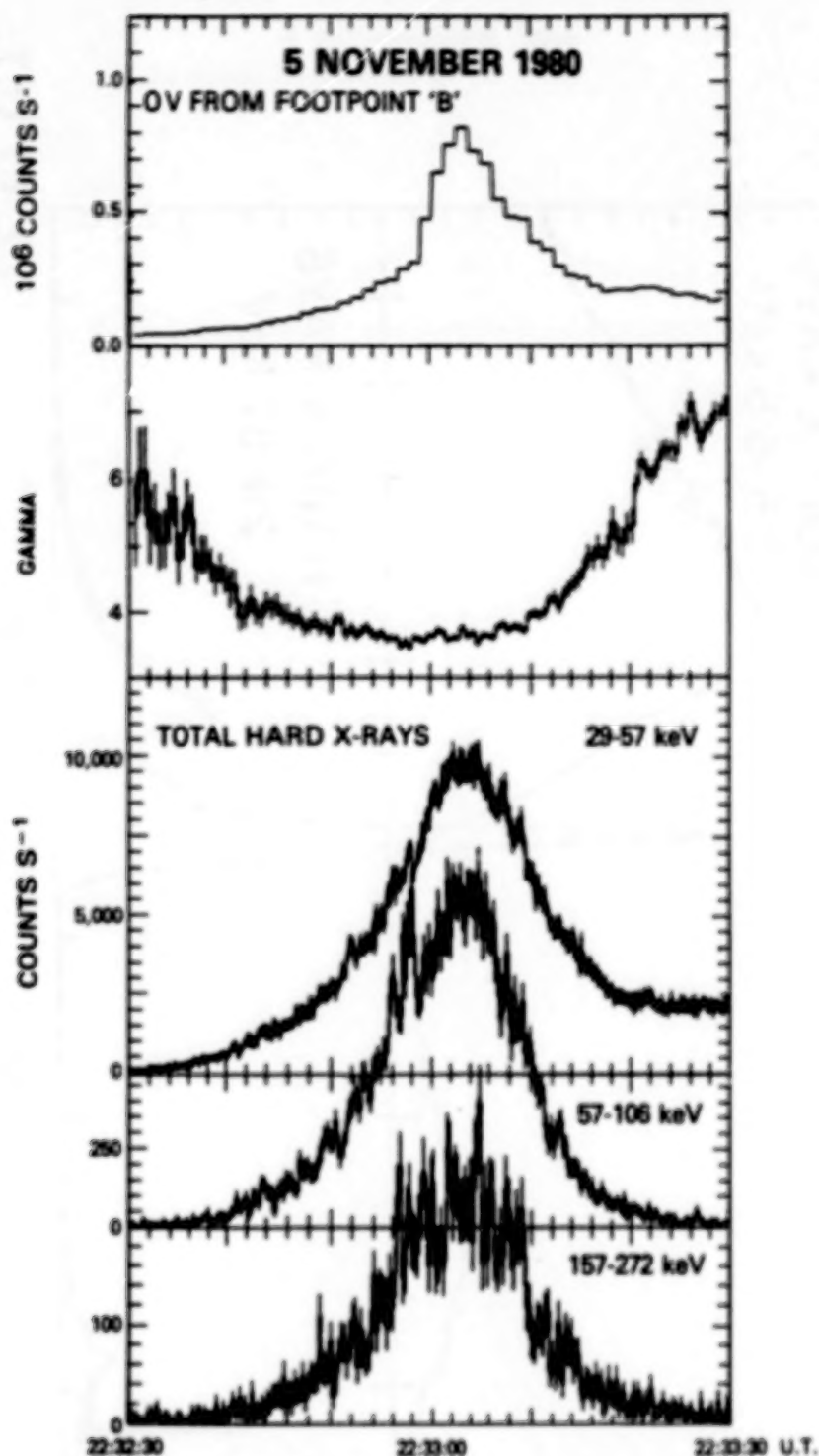
Figure 6. An expanded plot of the major hard X-ray peak shown in Figure 5 for the 5 November 1980 flare at 22:33 UT. The bottom three graphs show the HXRBS counting rates as functions of time in three different energy ranges. The middle plot shows the variation of the power-law spectral index γ obtained from the 34 to 405 keV HXRBS counting rate data (channels 2 to 14) on the same time scale. The top plot shows the time variation of the UVSP counting rate in O V summed over all 9 pixels shown in Figure 7. More than 90% of the counts came from the three southern-most pixels (Dennis et al., 1985). The error bars on all the plots represent ±1σ uncertainties based on the Poisson fluctuations alone.
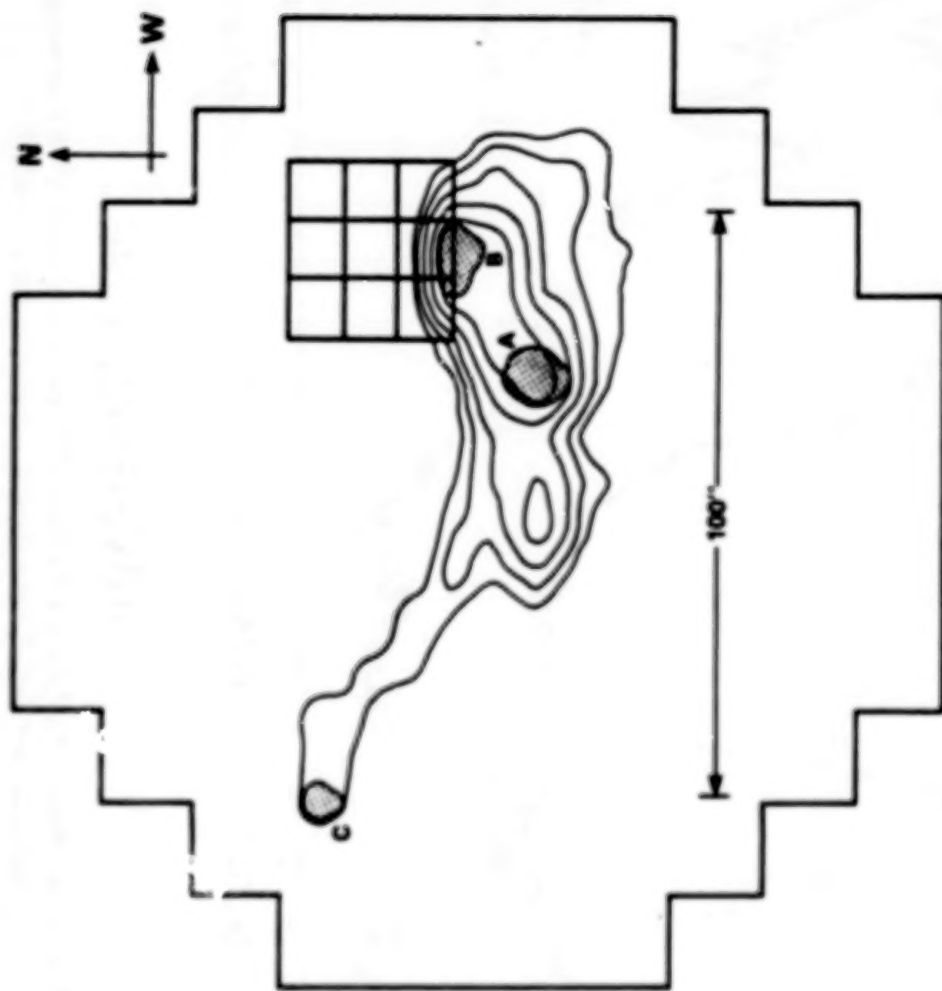
Figure 7. Contour plot obtained from the sum of three HXIS images showing the location of the soft and hard X-ray emission at the time of the most intense hard X-ray peak on 5 November 1980. Accumulation of the first image began at 22:32:53 UT. Each image had an accumulation time of 4.5 s with a 4.5 s gap between images. The contour lines were obtained from the 3.5 to 8 keV data with the collimator response deconvolved according to the method given by Svestka et al. (1983). The contour levels are at the following counts/pixel: 25, 50, 100, 200, and 400; the deconvolved peak rate was 902 counts/pixel. The cross-hatched areas labeled A, B, and C were obtained from the 16 to 30 keV data similarly deconvolved. The outer edge of these areas corresponds to a contour level of 40 counts/pixel for A and B and 20 counts/pixel for C with a deconvolved peak rate at 53 counts/pixel. The 3 x 3 array of 10 x 10 arc s squares represents the 9 UVSP pixels used for the OV observations shown in Figure 6.
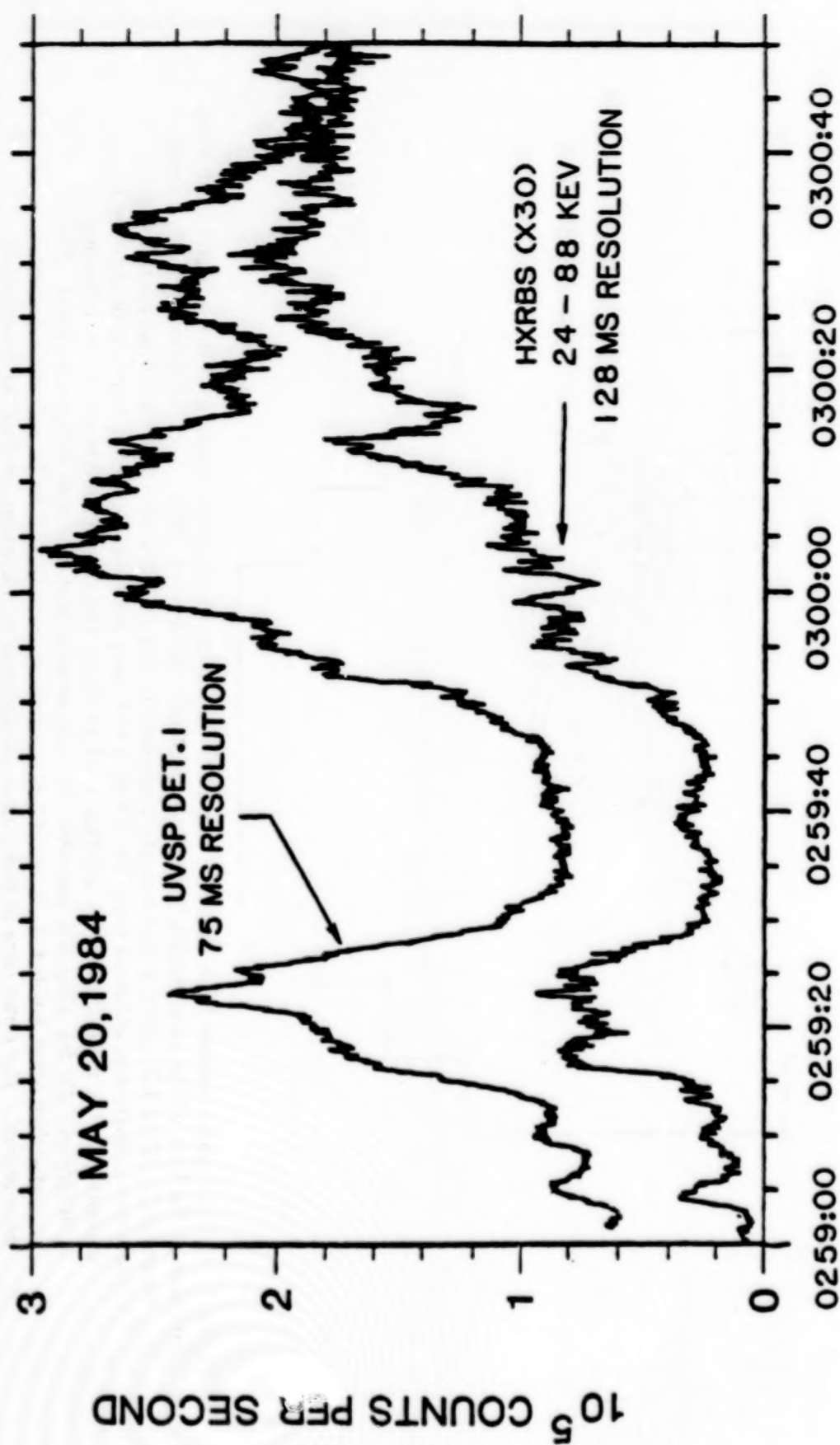
Figure 8. Impulsive bursts during the flare on 20 May 1984 beginning at 02:59 UT showing the similarity between the hard X-ray and UV continuum time profiles.
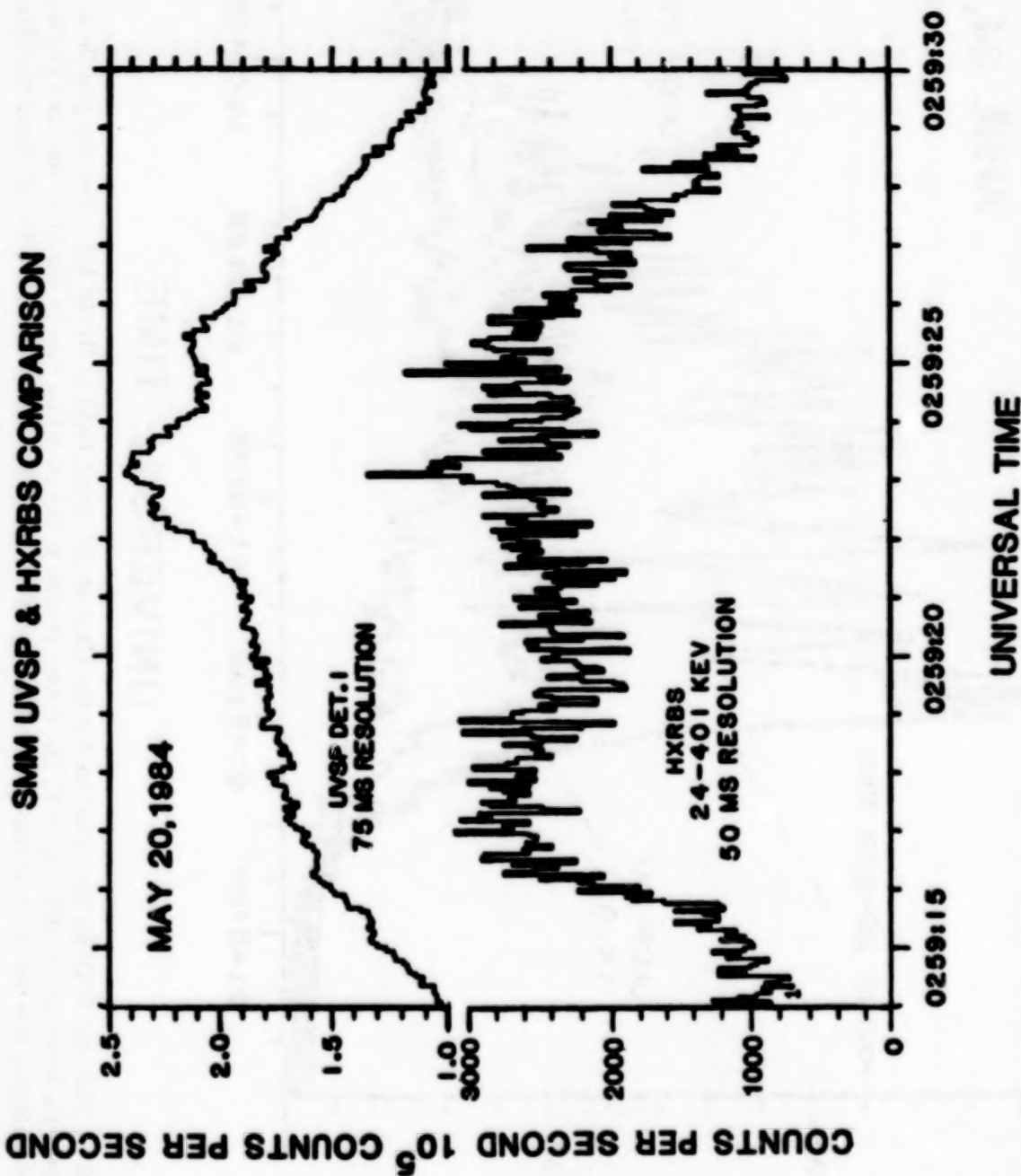
C-2

Figure 9. The first major feature of the flare on 20 May 1984 shown in Figure 8 plotted on an expanded time scale. The UVSP detector 1 time profile is believed to be for continuum emission at approximately 1600 Å and has a time resolution of 75 ms. The large scatter in the hard X-ray counting rate reflects the statistical uncertainty resulting from the mean rate at 02:59:20 UT of 115 counts per 50 ms interval. The feature at 02:59:23 UT is, however, clearly significant in both the hard X-ray and UV time profiles.
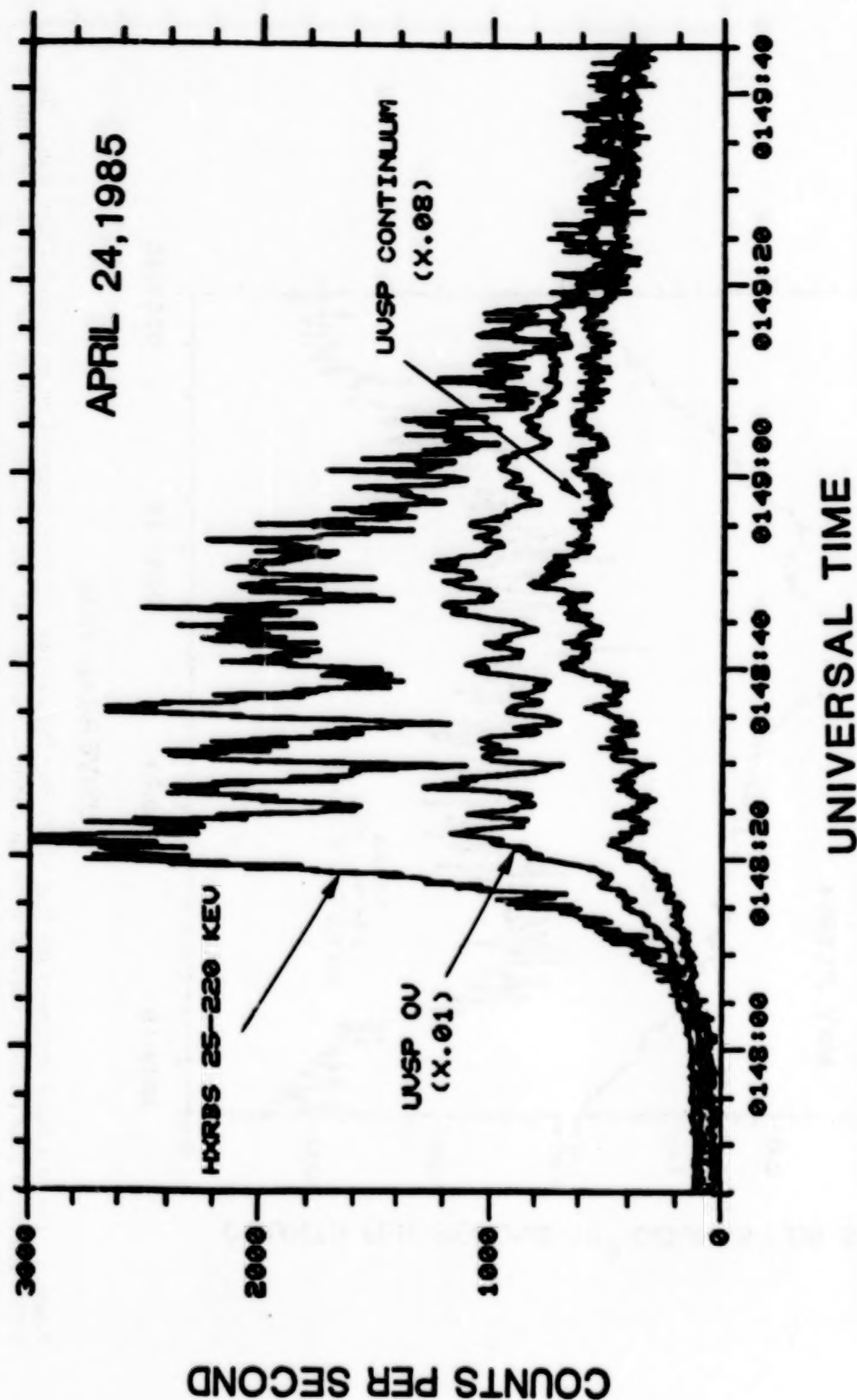
Figure 10. UVSP and HXRBS time profiles for the flare on 24 April 1985 at 01:48 UT. The top profile is the hard X-ray counting rate between 25 and 220 keV, the center profile is the counting rate in the O V line, and the bottom profile is the counting rate in the continuum 17 Å from the O V line. The time resolution for all three profiles is 128 ms.
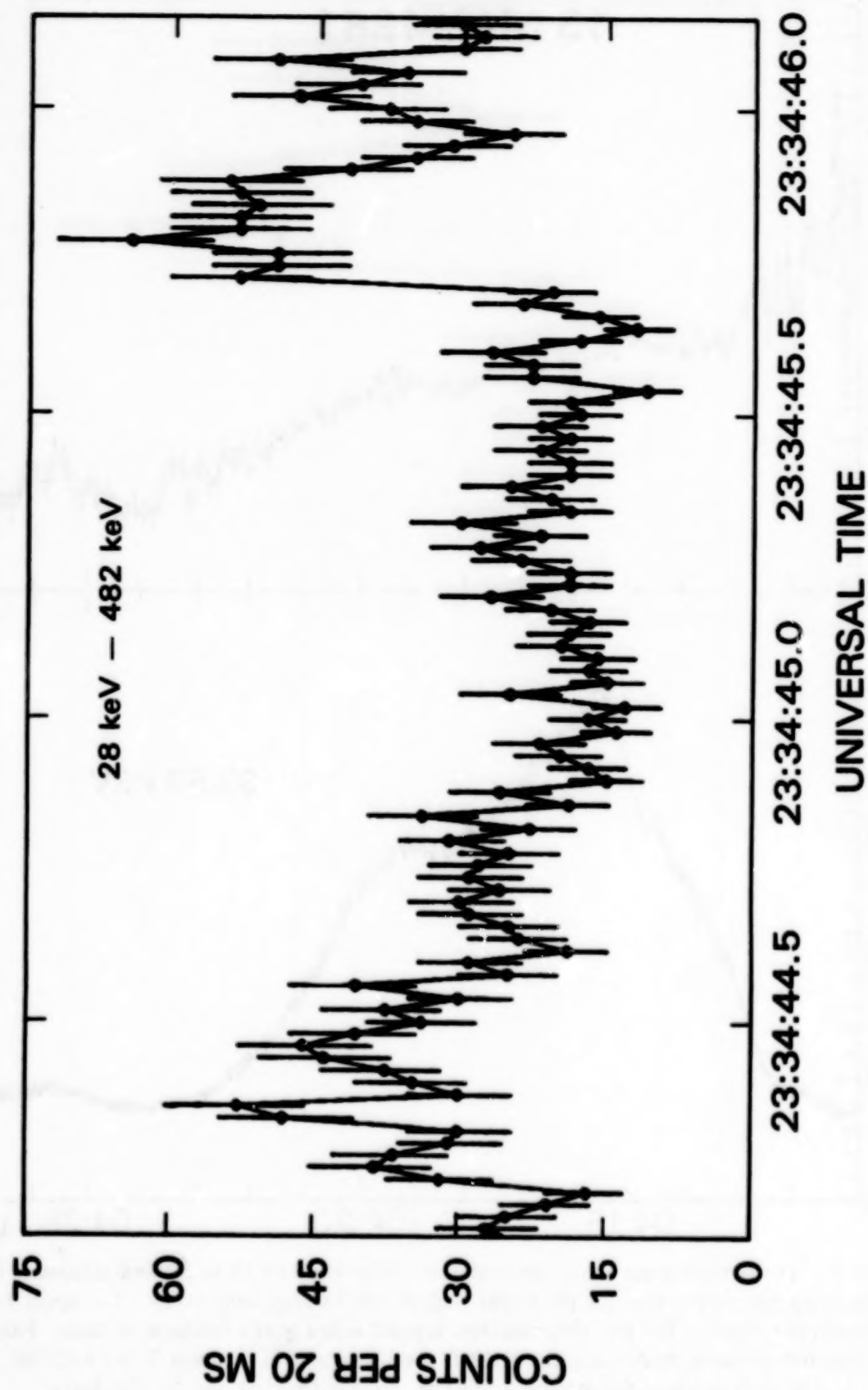
Figure 11. Two seconds of HXRBS memory data showing very rapid X-ray variations in a solar flare which occurred on 6 June 1980. The counting rate is plotted at a time resolution of 20 ms per point with ±1σ statistical error bars.
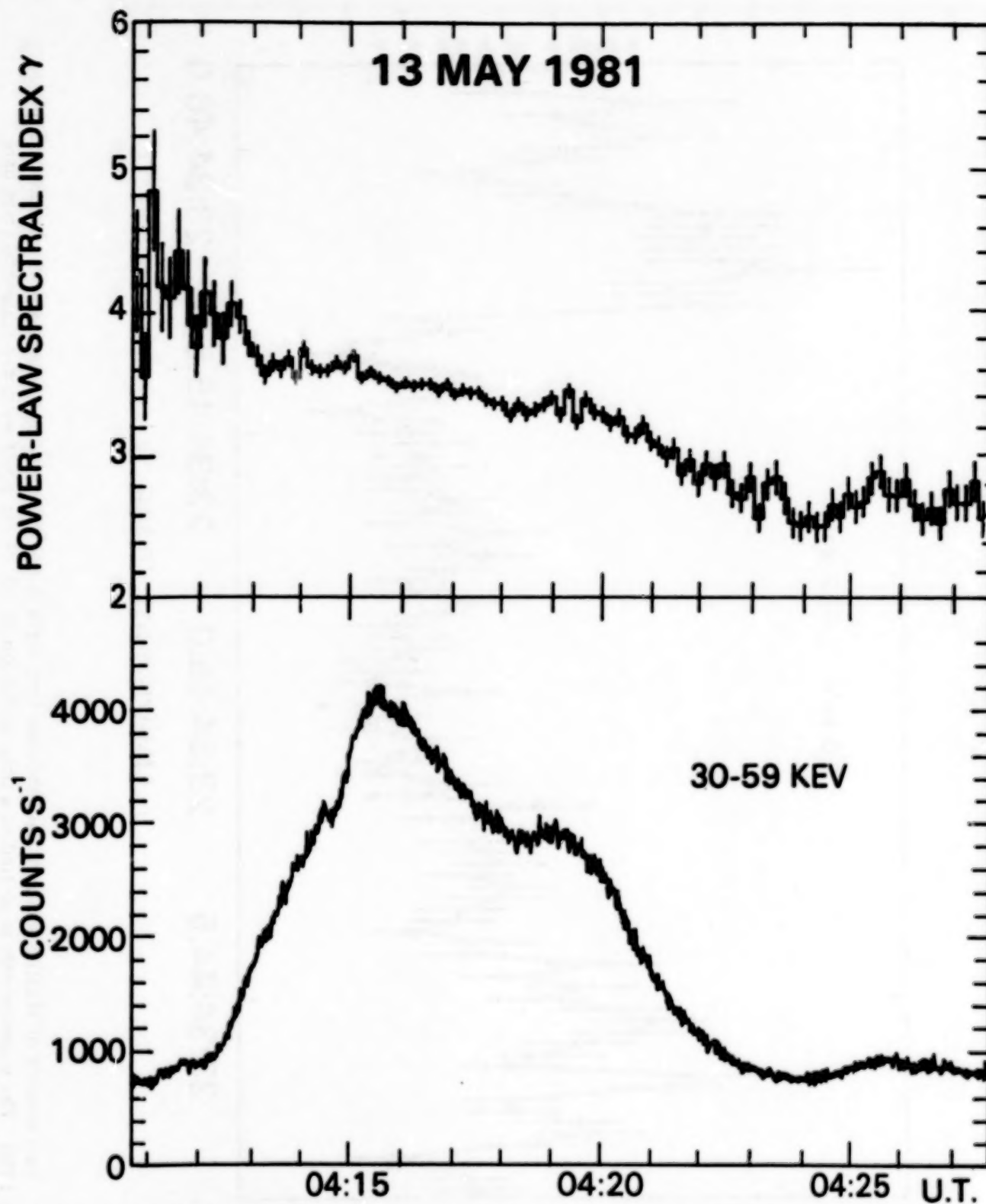
91

Figure 12. The bottom trace shows the variation of the HXRBS 30 to 59 keV (channels 1 and 2) counting rate versus time for the major peak of the 13 May 1980 event. The upper trace shows the value of the best fit power-law spectral index γ as a function of time. The spectral fits were made using the HXRBS counting rates in channels 3 to 14 (59 to 419 keV) to show the spectral hardening through the peak and on the decay. Individual spectra at different times during the event are shown in Figure 13.
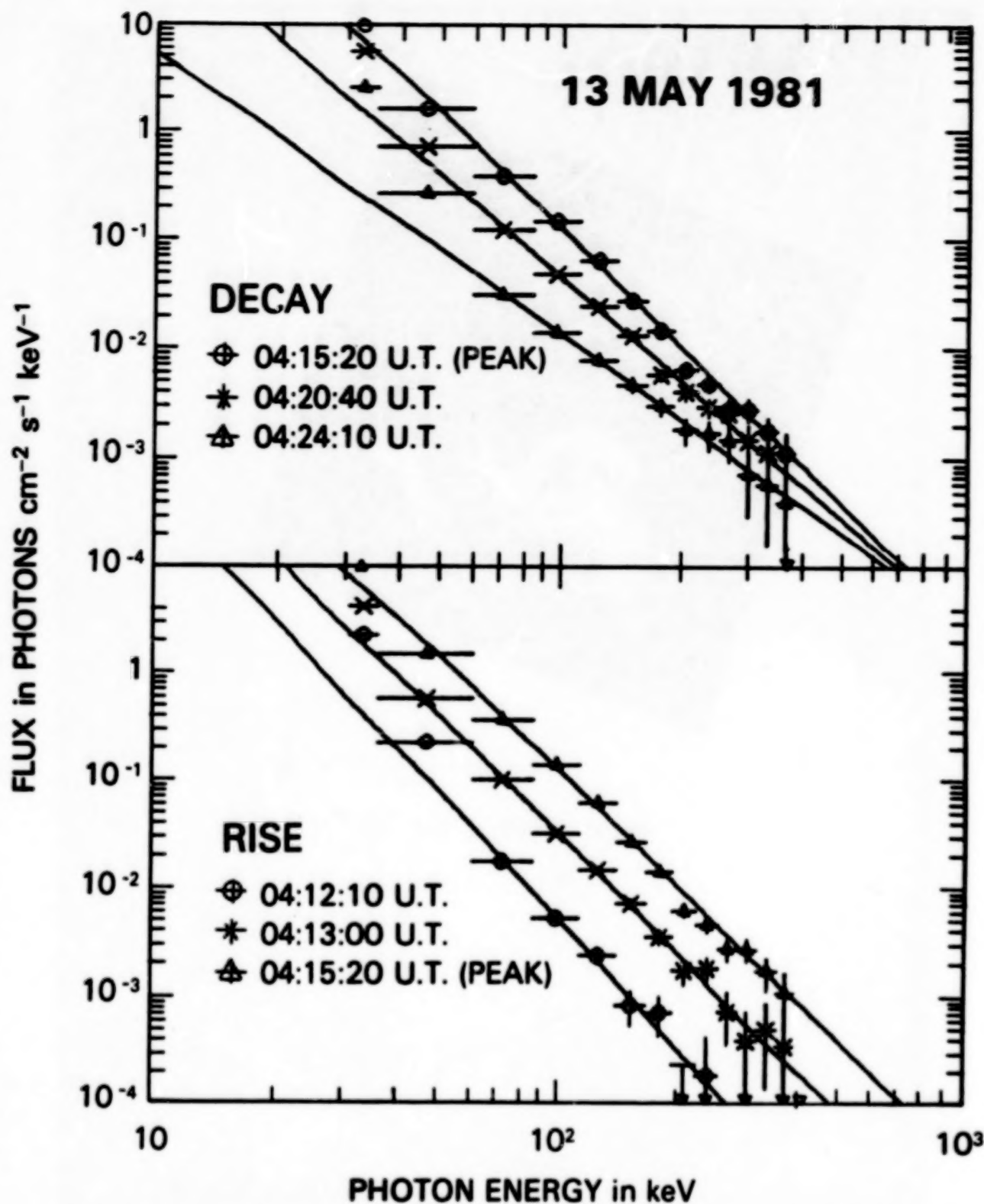
Figure 13. Hard X-ray spectra at five different times during the major feature of the 13 May 1981 event shown in Figure 12. The data points were derived from the HXRBS counting rates assuming the indicated least-squares power-law fit through the points for channels 3 to 14. The vertical lines through the data points are ±1σ error bars based on the statistical uncertainties alone. The horizontal lines through the points are not error bars but indicate the widths of the HXRBS channels.
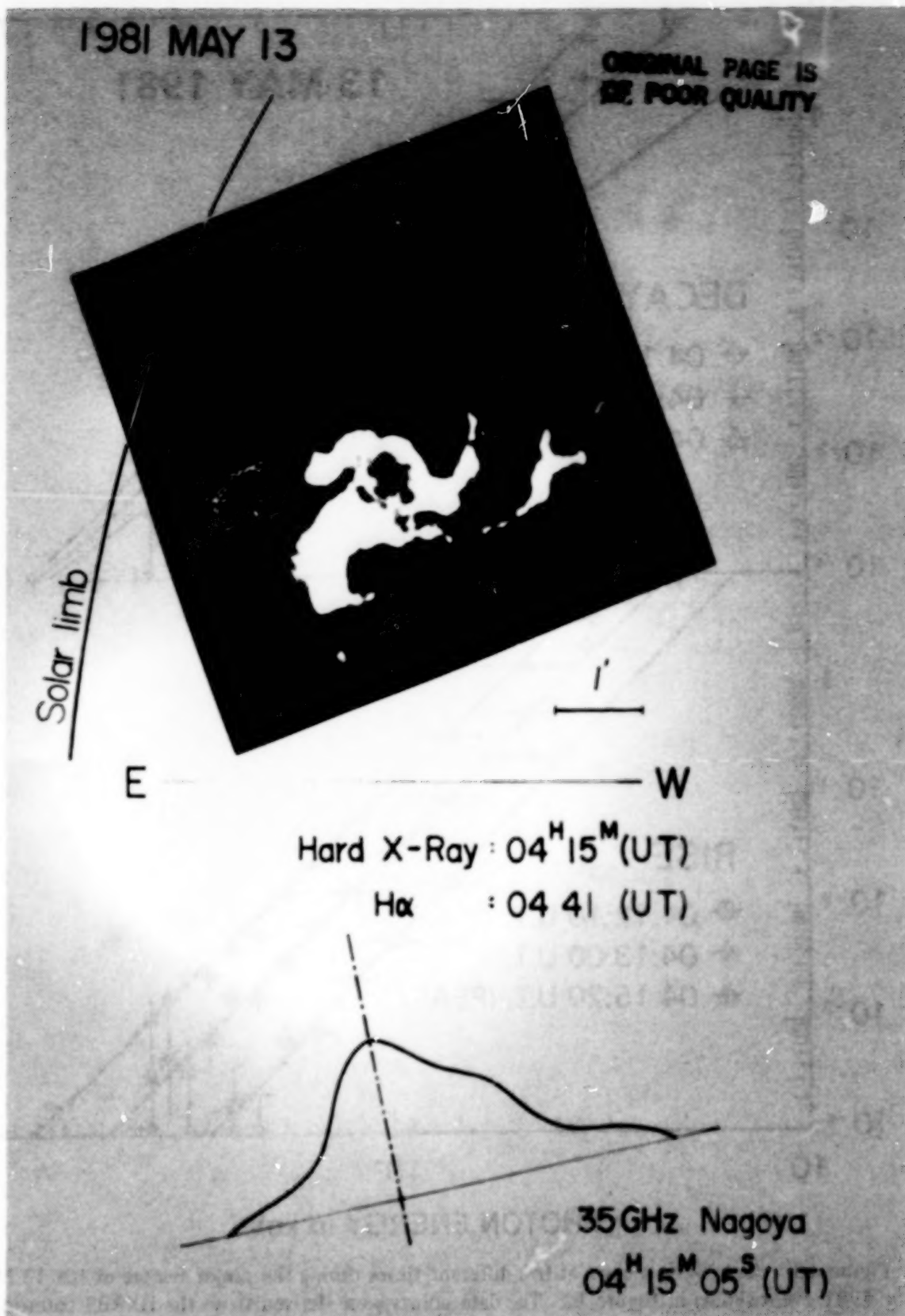
Figure 14. Overlay from Tsuneta (1983) of the Hinotori hard X-ray image of the 13 May 1981 Type C flare with an Hα photograph taken 26 min later. The one-dimensional microwave brightness distribution at 35 GHz is oriented to show that the bulk of this emission was from the same high altitude location as the X-ray source (Kawabata et al., 1983).
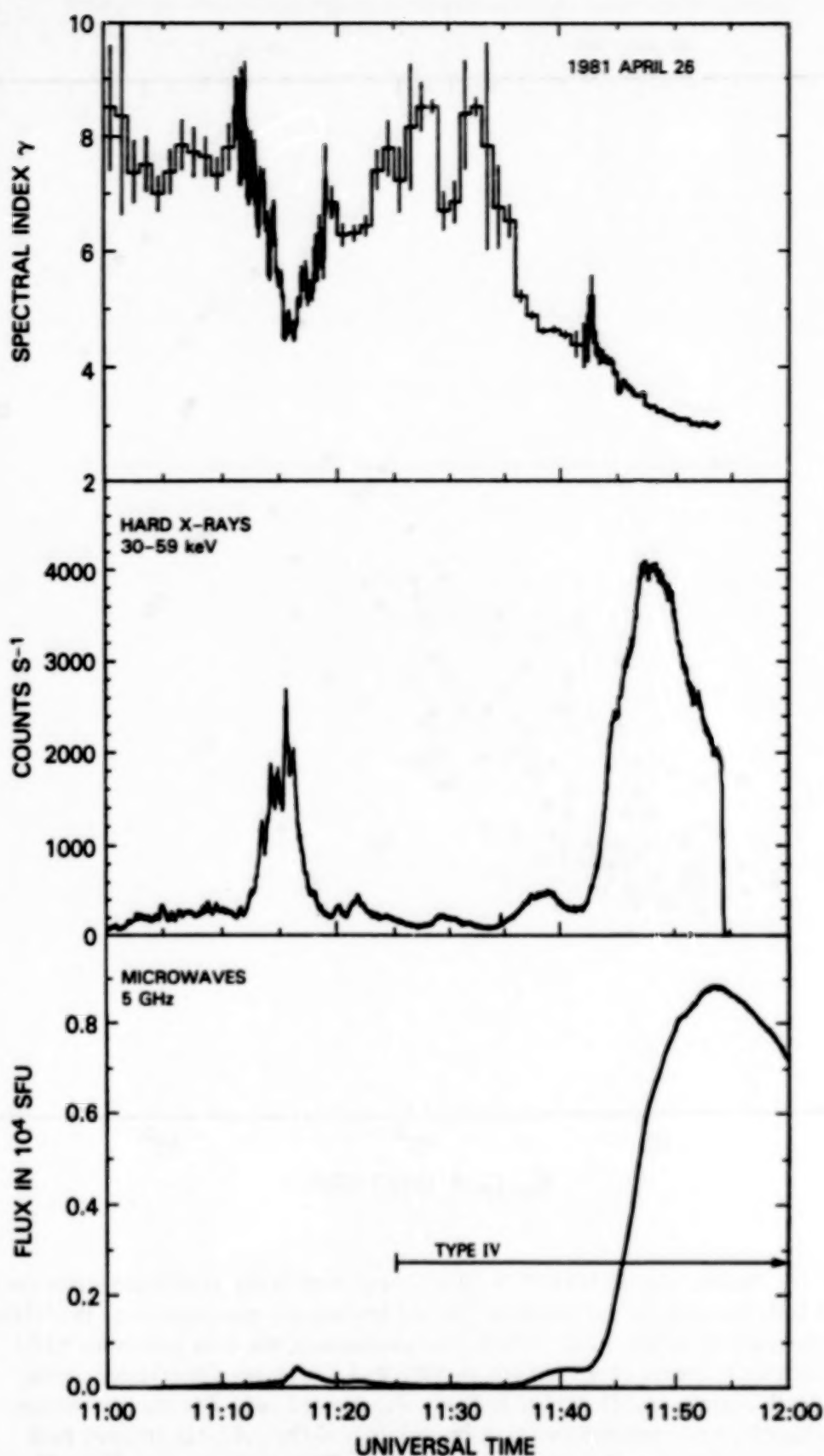
Figure 15. Hard X-ray and microwave time-intensity profiles of the 26 April 1981 solar flare. The upper panel shows the variation of the X-ray power-law spectral index γ with time.
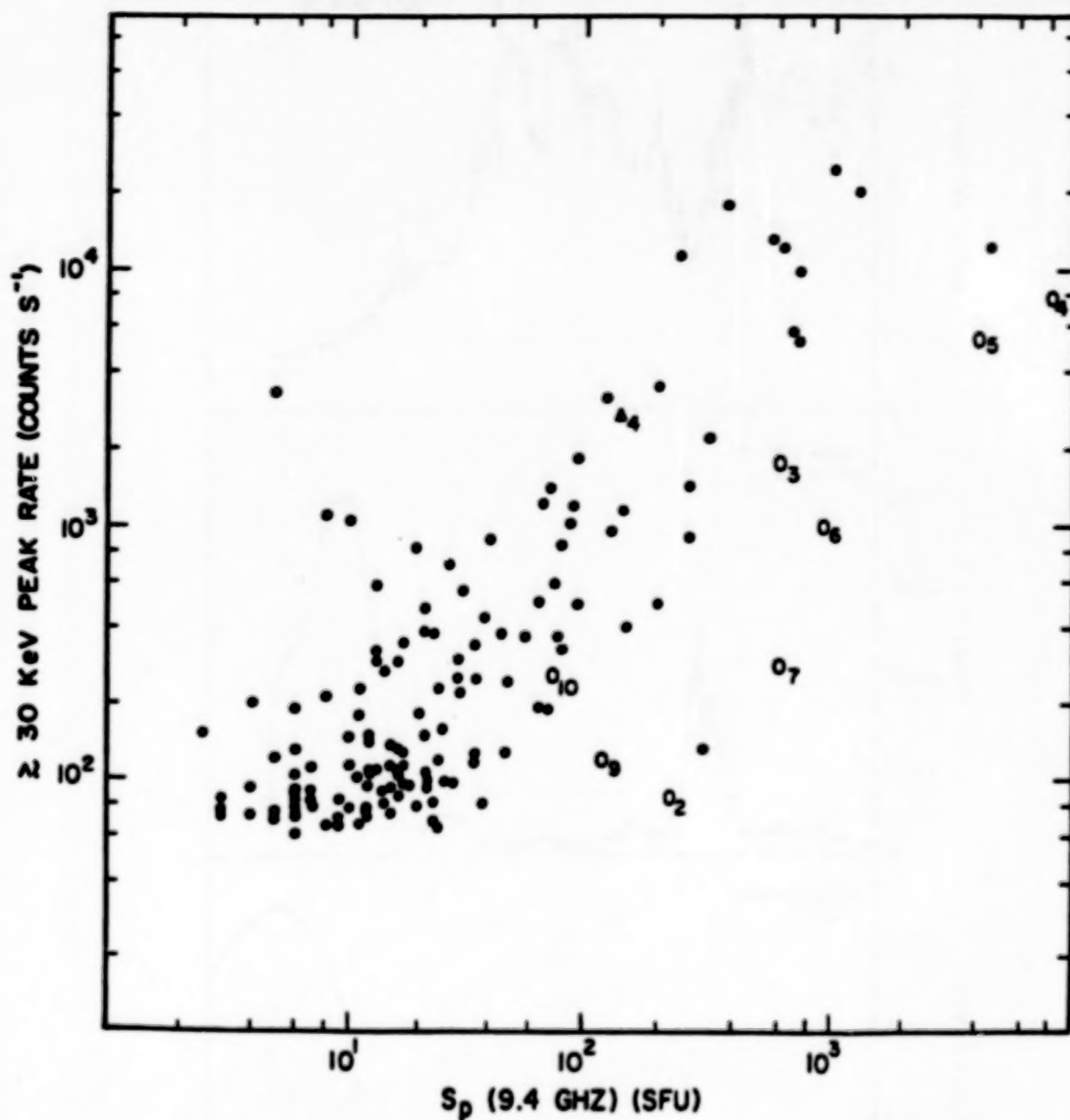
Figure 16. Scatter plot of HXRBS > 30 keV peak hard X-ray count-rate versus the peak
9.4 GHz flux-density for impulsive (Δ) and gradual (O) components of the GHBs
analyzed by Cliver et al. (1985). For comparison, the data points for ~130
impulsive events observed both by SMM and Toyokawa Observatory during
April, August, and December 1981 are also plotted (●). For the comparison
sample, we considered events to be impulsive if the 9.4 GHz emission peak
occurred within ±0.5 min of the HXRBS > 30 keV maximum. The ~40
counts s⁻¹ HXRBS background counting rate was not subtracted from
the >30 keV peak rates.
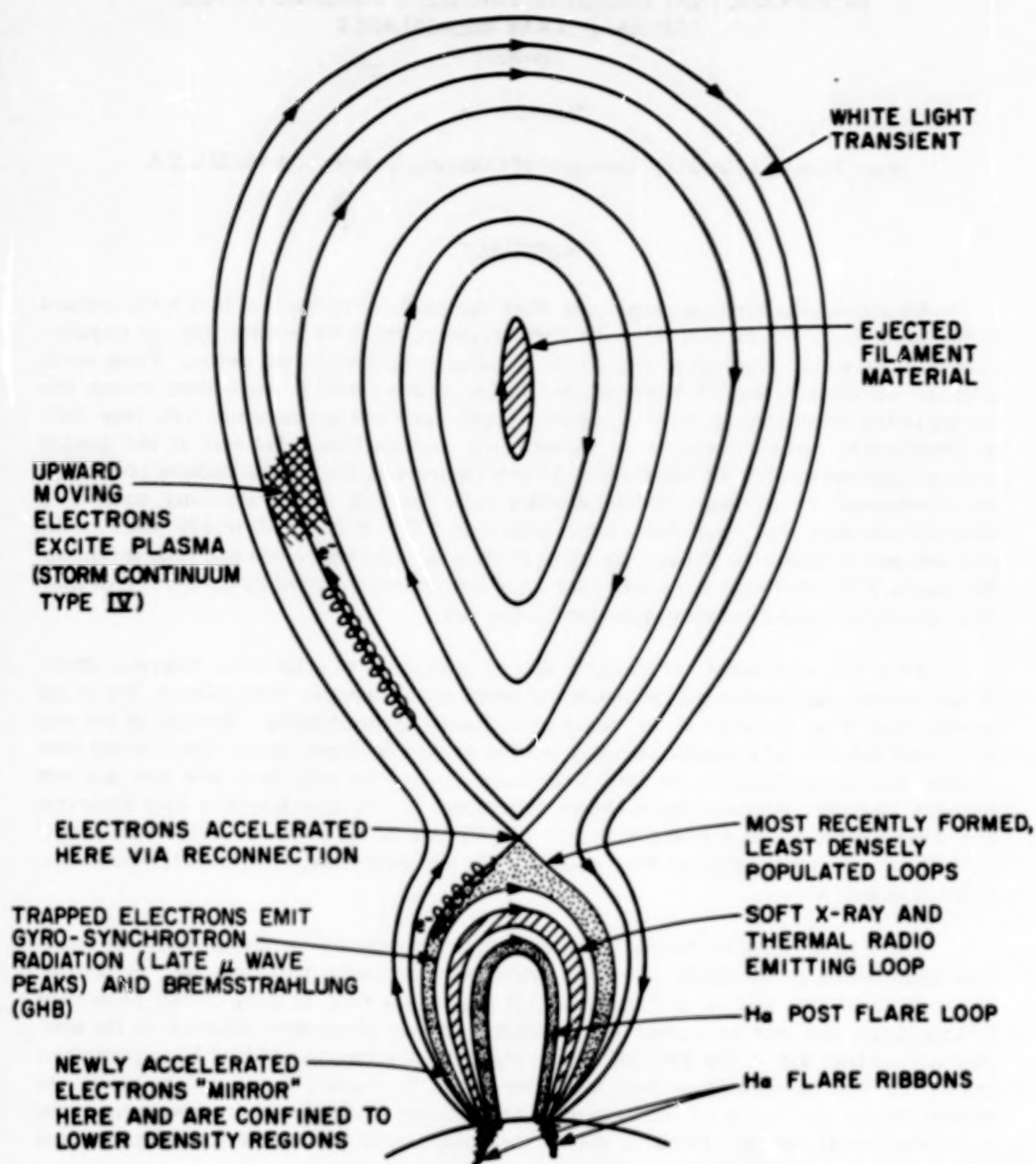
Figure 17. Proposed geometry in which electrons accelerated via neutral "point" reconnection are trapped and give rise to gradual hard X-ray bursts and secondary microwave peaks. The figure also indicates how concomitant Type IV storm continuum might occur. The drawing is not to scale. Characteristic heights of the soft X-ray loops and the leading edge of the transient at a time ~30 min after the flare flash phase are ~3 x 10⁴ km and >10⁶ km, respectively.

INTERPLANETARY ENERGETIC PARTICLES, CORONAL FLARES, AND HARD X-RAY MICROFLARES

(Invited)

Robert P. Lin

Space Sciences Laboratory, University of California, Berkeley, CA 94720 U.S.A.

ABSTRACT

We review solar electron phenomena which can produce low levels of hard X-ray emission at the Sun. Small ~2 to 100 keV solar electrons events, the most common type of impulsive solar particle emission, appear to originate in flare-like bursts high in the corona. These events often are accompanied by ~1 MeV/nucleon ^{3}He-rich particle events in which lower energy ions are apparently accelerated as well. Long-lived (many days) streams associated with large flares or interplanetary shocks dominate the interplanetary electron fluxes, but even at the quietest times a significant outflow of non-thermal ≥ 2 keV electrons occurs. These electron phenomena are accompanied by coronal and interplanetary radio emission. High sensitivity hard X-ray measurements show that microflares, bursts with peak >20 keV fluxes 10 to 100 times smaller than observed in small solar flares, may occur as often as once every 5 min near solar maximum. The proposed Pinhole/Occulter Facility hard X-ray instrumentation provides the increase in sensitivity required to image these phenomena for the first time.

There is a wide variety of energetic electron phenomena of solar origin, observed directly in the interplanetary medium or indirectly via metric and decametric radio emission, which will produce hard X-ray emission at the Sun via electron-ion bremsstrahlung. Because of the relatively small numbers of energetic electrons involved or the low density in the corona where some of these phenomena originate, the hard X-ray fluxes are very low and up to now have not been accessible to study. Recently balloon-borne observations of very high sensitivity have discovered hard X-ray microflares, bursts with peak >20 keV fluxes a factor of 10 to 100 less than normal small flares. The relationship of these microflares to the coronal and interplanetary phenomena, if any, is unknown.

The Pinhole/Occulter Facility X-ray instrumentation will provide several orders of magnitude improvement in sensitivity as well as vastly improved spatial resolution over present-day instrumentation. The leap in sensitivity makes it possible for P/OF to study coronal phenomena in hard X rays and thus to provide the connection between phenomena observed in the interplanetary medium and at the Sun, and also to study the characteristics of hard X-ray microflares and extend their distribution to even lower flux levels. In addition it may well be possible to observe directly the region of acceleration of the electrons in flares, which presumably occurs in the low density corona. Below we discuss the various interplanetary and coronal phenomena of interest, as well as microflares and flare-related phenomena.

I. INTERPLANETARY PHENOMENA

Impulsive 2 to 100 keV Electron Events

Observations show that energetic 2 to 100 keV electrons of solar origin are continuously present in the interplanetary medium in the years near solar maximum. Small non-relativistic

solar electron events appear to be the most common type of impulsive particle emission. Figure 1 shows an example of an impulsive solar electron event (Lin, 1974; Potter, Lin, and Anderson, 1980) observed by the University of California, Berkeley, particle experiment on the ISEE-3 (International Sun Earth Explorer) spacecraft. At the time of this event the spacecraft was located in a halo orbit about the L1 Lagrange point about 10^6 km upstream of the Earth. Several important characteristics are illustrated by this figure. There is clear velocity dispersion with the fastest electrons arriving earliest, consistent with the simultaneous injection of the electrons at the Sun and nearly scatter-free propagation along the interplanetary Archimedean spiral field line to 1 AU. The rapid rise and decay at all energies confirms the lack of significant scattering. The electron distributions are highly anisotropic and beamed along the magnetic field, especially at low energies, so dips in the electron fluxes (cf. ~1140 UT in Figure 1) are observed when the magnetic field swings out of the field of view of the detector. The electron energies extend up to ≥ 50 keV and down to 2 keV. Since electrons of low energies are easily lost by Coulomb scattering in the solar atmosphere, the presence of ~2 keV (the lowest energy measured) electrons indicates that most likely the coronal source of these particles is ≥ 0.5 to 1 $R_\odot$ high in the solar corona, although there is also the possibility that significant energy changes have occurred for the electrons in their propagation from the Sun to 1 AU.

A total of 326 impulsive electron events were observed by ISEE-3 in the ~15 month period from August 1978 to November 1979. These events appear to fill ~60 deg in solar longitude in the interplanetary medium, so ~130 events/month must occur over the full Sun. Because the interplanetary medium is often filled with long-lived intense fluxes of electrons at these energies, small impulsive events will often not be detected. Thus the rate of occurrence of these events is probably significantly greater than estimated here.

About half of all the electron events detected do not extend in energy above ~15 keV, but almost all are observed to extend smoothly down to 2 keV, the limit of the measurement. Almost all impulsive electron events are accompanied by a solar type III radio burst observed in the interplanetary medium, i.e., at frequencies of ~30 kHz to a few MHz. On the other hand, only ~50% are associated with metric/decametric type III bursts and a minority (40%) appear to have an associated Hα flare (Solar Geophysical Data) or microwave bursts at ~3000 MHz (18%). ISEE-3 solar hard X-ray observations show that only 29% were associated with a detectable hard X-ray burst. These associations also suggest that many of these impulsive electron events probably originate at heights of ~0.5 to 1 $R_\odot$. We estimate the total energy released in electrons above 2 keV is on the order of 10^{25} ergs and the release occurs on time scales of less than a few minutes.

^{3}He-Rich Events

Recently, Reames, von Rosenvinge, and Lin (1985) reported that virtually all solar ^{3}He-rich events are associated with impulsive 2 to 100 keV electron events. Solar ^{3}He-rich events (reviewed by Ramaty et al., 1980) represent one of the most striking composition anomalies among the observed populations of solar and interplanetary energetic particles, with ^{3}He/^{4}He ratios of order unity, while the typical ratios for the solar atmosphere or solar wind are a few times 10^{-4} (Geiss and Reeves, 1972). The solar wind ^{3}He/^{4}He ratio varies but always remains below 10^{-2}, and it is uncorrelated with the occurrence of solar ^{3}He-rich events (Coplan et al., 1983). Other properties of ^{3}He-rich events include reduced ^{1}H/^{4}He ratios and enhanced abundances of Fe and other heavy elements, and a tendency to larger ^{3}He enhancements in smaller events.

With the high sensitivity of the ISEE-3 energetic particle telescopes it is possible to obtain temporal profiles with good resolution ($\lesssim 1$ hr) of the ^{3}He fluxes at ~ 1 MeV/nucleon energy for the small ^{3}He-rich events. Figure 2 shows the 17 May 1979 events where velocity dispersion can be seen in the ^{3}He fluxes. In the lower panel the associated 2 to 100 keV impulsive electron event with its velocity dispersion can be seen. The timing of the particle onsets and maxima is shown in Figure 3, where we have plotted those times versus $1/\beta$ (the particle velocity $v = \beta c$). If particles of all velocities were released at the same time, t_0, and traveled the same distance, L, their arrival times would be related by $t = t_0 + L/\beta c$, which would be a straight line on Figure 3. The observed onset time depends upon the relative instrument sensitivity, the rise time, and the event amplitude. The ^{3}He onsets lag the time that would be expected from the electron measurements by no more than about 10 to 15 min. The traversal distance implied by the onset time of the lowest velocity ^{3}He is ~ 1.3 AU. This compares with ~ 1.25 AU for the electrons. The times of maximum of ^{3}He are also consistently later than those of electrons of the same velocity, implying a greater degree of scattering for ^{3}He in the interplanetary medium. The mean path lengths implied by the ^{3}He times of maximum are ~ 1.8 to 2.0 AU compared to ~ 1.45 AU for the electrons.

Energy spectra for the two species are shown in Figure 4. The spectral indices for the least-squares fits to a power law are 2.7 ± 0.1 and 2.7 ± 0.3 for electrons and ^{3}He, respectively. For electrons, only the region from 2.3 to 60 keV was fit because of apparent spectral changes at higher and lower energies. Note that ^{3}He and electrons have the same spectral slope over ranges of comparable particle velocities.

In the 15-month interval in 1978-79, about a dozen ^{3}He-rich events were observed with sufficient statistics to provide good temporal profiles. All of these events were accompanied by an impulsive 2 to 100 keV event with a temporal relationship similar to that shown in Figure 3. The solar associations for these ^{3}He electron events are essentially the same as for electron events in general: close association with kilometric wavelength type III bursts, small $H\alpha$ subflares or no reported $H\alpha$ association, very few hard X-ray bursts, and small or no soft X-ray bursts.

The close temporal associations and similar spectral slopes suggest that the same acceleration process is probably responsible for both electron and ^{3}He acceleration. The solar associations and the presence of low energy, 2 keV, electrons suggest that this acceleration probably takes place in the high corona.

A preliminary search indicates that ions of a few hundred keV total energy are accelerated at the same time as the ~ 1 MeV/nucleon ^{3}He and the electrons. These low energy ion fluxes are difficult to associate with an impulsive injection at the Sun because the travel time for the Sun to 1 AU is long, $\gtrsim 6$ hrs, and the flux increases for ^{3}He events are small. Furthermore, there are many variations in the low energy fluxes on these same time scales, due to local interplanetary effects. Even so, for many ^{3}He impulsive electron events there are increases in the few hundred keV ion fluxes at the right time for releases simultaneous with the electrons (Figure 5). At these energies we have no information on the composition of the ions.

Thus 2 to 100 keV electrons, ~ 1 MeV/nucleon ^{3}He, and even lower energy ions may be accelerated together in coronal flare or flare-like events which occur at heights of 0.5 to 1 $R_\odot$. This type of acceleration differs from large flare events, where ions are accelerated to >10 MeV energies and electrons to relativistic energies, with no ^{3}He enrichment.

Long-Lived 2 to 100 keV Electron Fluxes

The ISEE-3 spacecraft observes 2 to 100 keV electron fluxes to be present in the interplanetary medium at all times. Figure 6 shows the daily minimum flux in three energy intervals: 2 to 2.3 keV electrons, 19 to 45 keV electrons and protons (but primarily electrons), and >272 keV protons. This type of plot excludes the impulsive electron events discussed above since their time scales are typically less than a few hours. It can be seen that these particle fluxes are dominated by streams which last many days. Many of these streams arise from a large solar flare event or series of such events from a single active region (Anderson, Lin, and Potter, 1982). Others appear to be dominated by the passage of an interplanetary shock (Tsurutani and Lin, 1985). Still others, generally lower intensity ones, appear to be related to type III radio burst storms observed at hectometric and kilometric wavelengths (Bougeret et al., 1985). Even at the times of the lowest counting rates the fluxes are still well above detector background, and the electrons are still streaming outward away from the Sun along the interplanetary magnetic field. Thus the Sun must be a continual source of energetic ≥ 2 keV electrons. These flux levels are many orders of magnitude above the tail of the thermal 1 to 2×10^6 °K coronal electron distribution, so some non-thermal process must be the source. One exciting possibility is that these electrons might be a by-product of the processes which heat the solar corona.

II. OBSERVATIONS OF THE SOLAR CORONA

It is well known from radio observations that a wide variety of energetic, non-thermal phenomena occur in the solar corona. These phenomena include electron streams, both escaping (type III radio bursts) and trapped (type V and U bursts); shock wave electron acceleration (type II); acceleration and trapping of mildly relativistic electrons (type IV); and continual acceleration and storage of low energy electrons (type I bursts and continuum) (see reviews in Newkirk, 1974; Wild, Smerd, and Weiss, 1963; Kundu, 1965, 1982). Radioheliograph observations have shown that these phenomena may be highly complex, with source sizes ranging from a few arc minutes (about the resolution limit for the radio measurements) or less for type III or type I bursts to tens of arc minutes for large type II bursts. The energetic electrons that produce the radio emission will also produce hard X-ray emission via bremsstrahlung collisions with the solar coronal gas. Because the bremsstrahlung emission process is quantitatively well understood and the propagation of hard X rays through the corona is essentially unaffected by scattering and absorption, observations of coronal hard X rays can give quantitative information on the energetic electron populations in the solar corona, provided the ambient gas density in the X-ray source is known (see Brown, 1973; Lin, 1974).

Simultaneous spatially resolved hard X-ray and radio observations complement each other particularly well. Solar radio emission from the corona is believed to be generated primarily by two processes, synchrotron emission by electrons spiraling in a magnetic field and a two-step plasma wave emission process (Ginzburg and Zheleznyakov, 1958). The latter process appears to be responsible for the more common types of metric radio emission, types I, II, III, U, and possibly V. In the plasma process energetic electrons produce Langmuir plasma waves at the plasma frequency, $f_p = 9 \times 10^3 \, n^{1/2}$ Hz, where n is the plasma density in cm^{-3}. These waves then scatter off ion density fluctuations or low frequency waves, or off other Langmuir waves to produce electromagnetic radiation at the plasma frequency, f_p (fundamental), or twice the plasma frequency, $2f_p$ (2nd harmonic), respectively. The production of radio waves depends on the details of the energetic electron distribution function — whether it is unstable to the coherent generation of plasma waves — and also on the plasma wave to electromagnetic wave conversion process. The intensity of the radio emission, its apparent size, and its location in the corona will

be modified by scattering and absorption in the corona. It is difficult, therefore, to obtain quantitative information on the energetic electron population from the radio emission. On the other hand the ambient coronal density is closely related to the frequency of the observed radiation in the plasma wave emission process. Furthermore, radio waves, whatever the generation mechanism, cannot propagate through the coronal plasma unless their frequency is above the local plasma frequency. Thus, radio observations can provide the coronal density information needed for quantitative interpretation of the hard X-ray observations.

Hard, >20 keV, X-ray bursts are commonly observed during the impulsive phase of flares, but this emission most likely originates in the high density, $n \gtrsim 10^{10}$ cm^{-3}, chromosphere (see Kane, 1974, for review). A few hard X-ray events have been interpreted as X-ray emission from the corona because the associated flare was believed to be well behind the solar limb (Hudson, 1978; Hudson, Lin, and Stewart, 1982). Most coronal phenomena will produce a level of bremsstrahlung X-ray fluxes too low for detection by present-day solar hard X-ray instrumentation, because both the ambient densities in the solar corona and the number of energetic electrons involved are low. P/OF, with its coronagraph and hard X-ray imaging instruments, together with ground-based radioheliographs, would be ideal for quantitative studies of the coronal phenomena. Below we describe a few of the many scientific topics which can be investigated.

Type III Bursts

Type III radio bursts are the most common type of impulsive non-thermal phenomena at the Sun. They are characterized by a rapid frequency drift from high to low frequencies (Wild, Smerd, and Weiss, 1963). Simultaneous in situ particle and low-frequency radio observations from spacecraft at 1 AU have shown that type III bursts are excited by ~2 to 100 keV electrons which escape from the Sun following an impulsive acceleration (Lin, Evans, and Fainberg, 1973, 1981a). The observed starting frequencies for type III bursts extend down to ~100 to 500 MHz or greater, corresponding to initial ambient densities, n, of $\approx 10^8$ to 10^9 cm^{-3}. Most type III bursts are unaccompanied by flares or soft X-ray increases (based on OSO-7 soft X-ray observations). Hard X-ray emission has been observed for some flare-associated type III bursts, but these tend to occur for only ~25% of the most intense bursts with very high starting frequencies (i.e., high densities). In these the X-ray and radio emissions sometimes show coincident time structure (see Figure 7). The interplanetary measurements indicate the energetic electron spectrum for type III events extends down to $\lesssim 2$ keV (Figure 4). The total number of electrons escaping into the interplanetary medium is estimated to be $N(>5 \text{ keV}) \approx 5 \times 10^{34}$ in a typical type III event. At the Sun the radio event may comprise a number of individual bursts, quasi-periodically spaced.

As an example we calculate the X-ray emission for a type III burst under the model assumption of instantaneous acceleration of the electrons and escape from the Sun without significant losses. Suppose at t = 0, $N(>E_0)$ electrons were accelerated with a power-law energy spectrum, $dN/dE = AE^{-\delta}$, and released from a region of ambient density n_0. The ambient density $n(\text{cm}^{-3})$ of the region the electrons pass through is given by the frequency f(MHz) of the type III emission, if we know whether the emission is at the fundamental or the 2nd harmonic emission. The observed frequency drift rate then determines the change in ambient density as a function of time. Alvarez and Haddock (1973) find that between 550 MHz and 75 kHz the average $df/dt = 0.01 \, f^{1.84}$ MHz/s. Integrating, we obtain f(t) and therefore n(t):

$$n(t) = n_0(1 + atn_0^{0.42})^{-2.38}$$

where $a = 2.9 \times 10^{-4}$ for harmonic and 1.6×10^{-4} for fundamental emission. The X-ray emission is then given by

$$\frac{dJ}{d(h\nu)} = \frac{A \, n_i(h\nu)^{-\delta-\frac{1}{2}}}{1.2 \times 10^{42} \, (\delta + 1/2) \, (\delta - 1/2)^2 \, B(\delta, 3/2)} \,,$$

where B is the beta function. The computed temporal variation is given in Figure 8 for a variety of n_0 and fundamental and harmonic radio emission.

For typical type III events the detailed temporal and spatial structure can be resolved by P/OF. These observations will provide information on:

(i) The characteristics of the acceleration processes and the location of the acceleration region relative to other coronal structure. Comparison of type III and flare events should help determine whether two different acceleration processes are involved.

(ii) The characteristics of electron propagation in the solar corona. This is important because energetic electrons appear to fill an ~60 deg FWHM cone at 1 AU while type III burst sizes are much smaller near the Sun.

(iii) The magnetic field structure of the corona. The type III electrons are tracers of the magnetic field lines. For most type III bursts the radio location appears close to the flare or active region (Duncan, 1977) so these observations may show how magnetic fields from different areas of the Sun intermix in the corona.

(iv) The characteristics of the type III emission mechanism. Is the emission generated only in favored "core" regions (Smith and Nicholson, 1978)? Is the near-Sun emission at the fundamental or harmonic or both (Rosenberg, 1975)? Do the electrons begin generating radio emission immediately or must they travel some minimum distance to obtain an unstable distribution from velocity dispersion? Do the electrons lose energy rapidly through beam-plasma interactions near the Sun?

Other Coronal Radio Phenomena

Type I, V, and U bursts also occur very commonly. The origins of these phenomena are less well understood than type III bursts. Type I radio bursts are superimposed on noise storm continua. They often show frequency drifts in both senses with drift rates ~1/4 to 1/2 of type III's. Thus it is hypothesized that electrons of a few to 10 keV energy are the exciters of this radiation via the plasma mechanism. Type V and U's appear to be closely related to type III bursts, possibly just due to the electron stream traversing peculiar magnetic field configurations. Type V bursts follow type III bursts, and III-V bursts are closely correlated to observed flare hard X-ray impulsive bursts (Stewart, 1978).

Type II and IV bursts are rarer, occurring an average of several times per month. These phenomena are particularly interesting in that they appear to be associated with coronal acceleration of ions and relativistic electrons which occur for some large flares. The hard X-ray emission from type II bursts may have been observed for some flares beyond the solar limb (Frost and Dennis, 1971; Hudson, 1978; Hudson, Lin, and Stewart, 1982). Type IV bursts are apparently due to synchrotron radiation. Comparison of radio and X-ray spatial observations can be used to obtain information on the magnetic field in the corona. Type II radio bursts are associated with shock waves, but it is not clear how the emission is produced. One hypothesis is that electrons accelerated at the shock generate the radio emission via the plasma-wave process. Supporting this hypothesis is the observation of "herringbone" structure, fast drift bursts similar to type III's

which appear to originate at the shock. These III-like structures are observed to extend to low frequencies (Cane et al., 1981). Simultaneous coronal X-ray and radio observations would be useful for studying the acceleration processes in the shock.

Particle Storage and Continual Acceleration in the Corona

There exists substantial evidence for the continual acceleration and/or storage of energetic electrons in the corona. Radio continua at meter wavelengths, such as noise storms and stationary type IV events, last hours to days (see Kundu, 1965, for review). The interplanetary medium, even at the quietest times, contains a population of 2 to 100 keV electrons, presumably of solar origin. Much more intense fluxes of electrons appear in active region-associated particle streams which can last for several solar rotations (Anderson, 1969). Electron and proton fluxes from large solar flare events last for several weeks even though the time scale for the solar wind to sweep these particles out of the inner solar system is ~4 days (see McCracken and Rao, 1970, for review).

Coronal X-ray observations can answer several important questions:

(i) Are energetic electrons being stored in the corona? Where and for how long? What are the loss processes for these particles?

(ii) Is there acceleration of electrons in the absence of flares or other transient phenomena? Perhaps the same processes which heat the corona also continuously accelerate electrons.

(iii) Are energetic electrons stored in the corona a viable energy source for flares?

Using the electron energy loss rate in ionized hydrogen (Trubnikov, 1965) we find that the e-folding energy loss time is given by

$$t_e \approx 10^8 \; E^{3/2} \; n^{-1} \; .$$

Thus electrons of 5 and 20 keV energy must be stored at densities of $n = 10^4$ to 10^5 cm^{-3}, respectively, for 1-day e-folding loss times. Spatial and spectral observations of storage regions will give detailed information on the continual acceleration, storage, and loss processes. For example, if Coulomb collisions are the dominant loss process, the electron energy spectrum will harden between fresh accelerations. By utilizing interplanetary particle observations to estimate the electron escape term and solving the continuity equation for simple models, it may also be possible to obtain information on continuous acceleration processes in the absence of flares.

It is estimated that ~10^{35} to 10^{36} > 10 keV electrons are accelerated during flares. If the observed flare impulsive hard X-ray emission is produced by thin target processes, i.e., without significant losses for the electrons (Datlowe and Lin, 1973), then these electrons must be stored high in the corona since fewer than 1% are observed to escape. The stored electrons presumably produce X-ray emission at a level too low to be observed by present-day instrumentation, but this level of X-rays should be easily observed and imaged by P/OF. Since a small flare has a total energy output of ~10^{29} ergs, equivalent to ~10^{36} keV electrons, P/OF can provide conclusive evidence for or against the hypothesis that energetic particles slowly accelerated and stored in the corona are a viable energy source for flares (Elliott, 1969).

III. MICROFLARES

The Sun exhibits a broad spectrum of transient phenomena with total energy release substantially less than flares. Transient soft X-ray brightenings are observed in a continuum of intensities from flares down to tiny X-ray bright points. It is not known how similar these less energetic transient phenomena are to flares – whether they also involve significant particle acceleration or whether below some total energy released they are basically thermal in character.

High sensitivity hard X-ray observations of the Sun, made with balloon-borne instrumentation designed for detecting cosmic hard X-ray sources, provide an indication of what might be observed and imaged by P/OF. On 27 June 1980 the Sun was observed for ~141 min by a combination of a 300 cm^2 NaI/CsI phoswich scintillator and 50 cm^2 array of germanium detectors, both collimated and surrounded with active anticoincidence shields (Lin et al., 1981b; 1984). Figure 9 shows 16.384 s averages of the 22 to 23 keV count rate of the balloon phoswich scintillator for the solar observing periods. To provide a measure of the sensitivity of this detector, we note that the Crab nebula increases the 22 to 33 keV count rate by ~5 counts/s. The count rate of the 5 to 6 keV channel of the soft X-ray proportional counter detectors of ISEE-3 is shown above.

Besides the large flare (1614 to 1632 UT) there are at least four clearly recognizable bursts with count rate increases of ≥ 5 counts/s (1559, 1950, 1958, and 2032 UT). These tend to occur on the rising portion of their associated soft X-ray bursts, as is often observed for flares. On closer examination, many smaller bursts can be seen, for example, at 1532, 1545, 1605, 1939, 1953, and 2058 UT. We have made a detailed search for additional small bursts. In 141 min of solar observing, a total of 25 separate increases, including those listed above, were detected above the 3σ level. This compares with three to four events expected for this period of time from purely statistical fuctuations. Most of these hard X-ray microflares detected above the 3σ level in the solar observing periods appear to have an associated 5 to 6 keV soft X-ray burst and vice versa; however, the ratio of 22 to 23 keV flux to 5 to 6 keV flux varies by more than one order of magnitude.

The temporal structure of the four largest microflares is shown in Figure 10. There is some evidence that these small bursts are composed of smaller, more "elementary" bursts. The events at 1950 and 1958 consist of individual bursts of 1 to 2 s FWHM duration. The bursts at 1559 and 2032 UT could be deconvolved into groups of elementary bursts of the same 1 to 2 s FWHM duration.

Accurate energy spectra, as measured by the germanium detector array for the four largest microflares, are shown in Figure 11. The spectra are best fit by power laws,

$$dJ/dE = AE^\gamma ,$$

with slopes $\gamma \approx 4$ to 6. The spectra extend out to ~70 to 80 keV for the largest events. Preliminary comparisons with the ISEE-3 soft X-ray data indicate that the power-law spectrum often extends down into the energy range (5 to 14 keV) of the proportional counter detector.

Figure 12 shows the integral distribution of events versus the maximum 20 keV flux in the burst. For comparison, the distribution obtained in the previously published survey (Datlowe, Elcan, and Hudson, 1974) is also shown. We emphasize here that the balloon data on occurrence

rates are based on only ~2 hours of observation, at a time close to solar maximum, while the OSO-7 observations span an 8-month period several years after solar maximum. The slopes of the two distributions can be seen to be the same, about -1; however, the balloon data extend the flux range down by more than one order of magnitude. There is no evidence for flattening of the distribution down to flux levels of 10^{-2} (cm^2 s keV)$^{-1}$. The rate of occurrence during the balloon observations is about a factor of 3 greater than the OSO-7 average rate.

During this observation period solar hard X-ray bursts occurred at a rate far higher than that for reported Hα flares of radio bursts. Furthermore, the integral number of bursts continues to increase with decreasing flux, indicating that with a lower threshold even more bursts would be observed. Already at this threshold level the numbers of hard X-ray and soft (~5 keV) X-ray bursts are essentially comparable. These observations suggest that a common property of transient energy releases by the Sun is the acceleration of electrons to energies above ~20 keV.

The total energy combined in these electrons can be computed under the normal assumption of thick target, i.e., that the electrons lose their energy primarily through Coulomb collisions (Brown, 1973; Lin, 1974). The total energy in >20 keV electrons ranges from a few times 10^{26} to ~10^{28} ergs for the four largest events shown in Figure 2. The average rate of energy deposition by greater than 20 keV electrons from all the bursts above a flux threshold of 10^{-2} (cm^2 s keV)$^{-1}$ is ~10^{24} ergs/s. These energy figures will increase by about one order of magnitude for every factor of 2 lower in energy the power-law electron spectrum extends. Preliminary analysis of the ISEE-3 data suggests that the electron spectrum extends to at least ~10 keV, and perhaps 5 keV. Furthermore, the number of events continues to increase as the flux threshold decreases. Thus the total rate of energy released in electrons producing these small hard X-ray bursts may be substantial, perhaps even comparable to the 10^{27} ergs/s rate of heating of the active corona.

IV. P/OF HARD X-RAY OBSERVATIONS

We have used the estimates of the numbers of electrons (vertical scale of Figure 13) from the interplanetary observations as a basis for computing the hard X-ray emission from the corona for various phenomena. The numbers of electrons observed at 1 AU will constitute a lower limit to those at the Sun since electrons could be lost by various processes in propagating to 1 AU. The electrons will produce X rays via the electron-ion bremsstrahlung process in the solar corona. Since bremsstrahlung is a collisional process the X-ray flux will depend on the ambient ion density (horizontal scale of Figure 13).

For the long-lived streams the electron population in the corona are estimated assuming a steady-state outflow into a region whose cross section expands as r^2. The time scale for each phenomenon is also indicated. Those phenomena such as flares or microflares, which have been observed in hard X rays, are indicated by the diagonal regions. An estimate of the sensitivity of the proposed hard X-ray imaging instrumentation for P/OF is superimposed. It can be seen that essentially all the microflare and flare phenomena can be imaged by P/OF at appropriate time scales. P/OF will also provide a first look at coronal phenomena from long-lived streams to flare-related impulsive phenomena.

Finally it should be emphasized that P/OF may be able to locate and image the region of acceleration of electrons in flares, rather than the region where the electrons lose most of their energy. Presumably the acceleration occurs in a low density, $n_i \lesssim 10^9$ cm^{-3}, coronal region, perhaps at the top of the flare loop. If the loop length is a few x 10^4 km, then electrons will

travel to the footpoints in a few tenths of a second. With the sensitivity of P/OF it may be possible to image the acceleration region and follow the propagation of the energetic electrons in the flare loop in the few tenths of a second prior to the impact of the electrons in the footpoints. The identification of the acceleration region would then permit the determination of the physical parameters in the region by other instruments such as the coronagraphs and soft X-ray telescopes.

REFERENCES

Alvarez, H. and Haddock, F. T., 1973, *Solar Phys.*, *29*, 197.

Anderson, K. A., 1969, *Solar Phys.*, *6*, 111.

Anderson, K. A., Lin, R. P., and Potter, D. W., 1982, *Space Sci. Rev.*, *32*, 169.

Bougeret, J. L., Lin, R. P., Fainberg, J., and Stone, R. G., 1985, *Astron. Astrophys.*, in press.

Brown, J. C., 1973, *Solar Phys.*, *31*, 143.

Cane, H. V., Stone, R. G., Fainberg, J., Stewart, R. T., Steinberg, J. L., and Hoang, S., 1981, *Geophys. Res. Lett.*, *8*, 1285.

Coplan, M. A., Ogilvie, K. W., Boschler, P., and Geiss, J., 1983, *Solar Wind Five*, NASA Conference Publication 2280, Washington, D.C., p. 591.

Datlowe, D. W., Elcan, M. J., and Hudson, H. S., 1974, *Solar Phys.*, *39*, 155.

Datlowe, D. W. and Lin, R. P., 1973, *Solar Phys.*, *32*, 459.

Duncan, R. A., 1977, *Proc. Astron. Soc. Austral.*, *3*, 154.

Elliott, H., 1969, in *Solar Flares and Space Research*, eds. C. deJager and Z. Svestka, North-Holland Publ. Co., Amsterdam, p. 356.

Frost, K. J. and Dennis, B. R., 1971, *Astrophys. J.*, *165*, 655.

Geiss, J. and Reeves, H., 1972, *Astron. Astrophys.*, *18*, 126.

Ginzburg, V. L. and Zheleznyakov, V. V., 1958, *Soviet Astron.*, *AJ2*, 653.

Hudson, H. S., 1978, *Astrophys. J.*, *224*, 235.

Hudson, H. S., Lin, R. P., and Stewart, R. T., 1982, *Solar Phys.*, *75*, 245.

Kane, S. R., 1972, *Solar Phys.*, *27*, 174.

Kane, S. R., 1974, in *Coronal Disturbances*, ed. G. Newkirk, Jr., IAU Symp. 57, D. Reidel, Dordrecht-Holland, p. 105.

Kundu, M. R., 1965, *Solar Radio Astronomy*, John Wiley, New York.

Kundu, M. R., 1982, *Rep. Prog. Phys.*, *45*, 1435.

Lin, R. P., 1974, *Space Sci. Rev.*, *16*, 189.

Lin, R. P., Evans, L. G., and Fainberg, J., 1973, *Astrophysical Letters*, *14*, 191.

Lin, R. P., Potter, D. W., Gurnett, D. A., and Scarf, F. L., 1981a, *Astrophys J.*, *251*, 364.

Lin, R. P., Schwartz, R. A., Pelling, R. M., and Hurley, K. C., 1981b, *Astrophys. J. (Letters)*, *251*. L109.

Lin, R. P., Schwartz, R. A., Kane, S. R., Pelling, R. M., and Hurley, K. C., 1984, *Astrophys. J.*, *283*, 421.

McCracken, K. G. and Rao, U. R., 1970, *Space Sci. Rev.*, *4*, 155.

Newkirk, G., Jr. (ed.), 1974, *Coronal Disturbances*, D. Reidel, Dordrecht, Holland.

Potter, D. W., Lin, R. P., and Anderson, K. A., 1980, *Astrophys. J. (Letters)*, *236*, L97.

Ramaty, R., and 10 co-authors, 1980, in *Solar Flares, A. Monograph from the Skylab Solar Workshop II*, ed. P. A. Sturrock, Colorado Assoc. University Press, p. 117.

Reames, D. V., von Rosenvinge, T. T., and Lin, R. P., 1985, *Astrophys. J.*, in press.

Rosenberg, H., 1975, *Solar Phys.*, *42*, 247.

Smith, D. F. and Nicholson, D. R., 1978, preprint, Dept. of Astro-Geophysics, Univ. of Colorado.

Stewart, R. T., 1978, *Solar Phys.*, *58*, 121.

Trubnikov, B. A., 1965, *Rev. Plasma Phys.*, *1*, 105.

Tsurutani, B. and Lin, R. P., 1985, *J. Geophys. Res.*, *90*, 1.

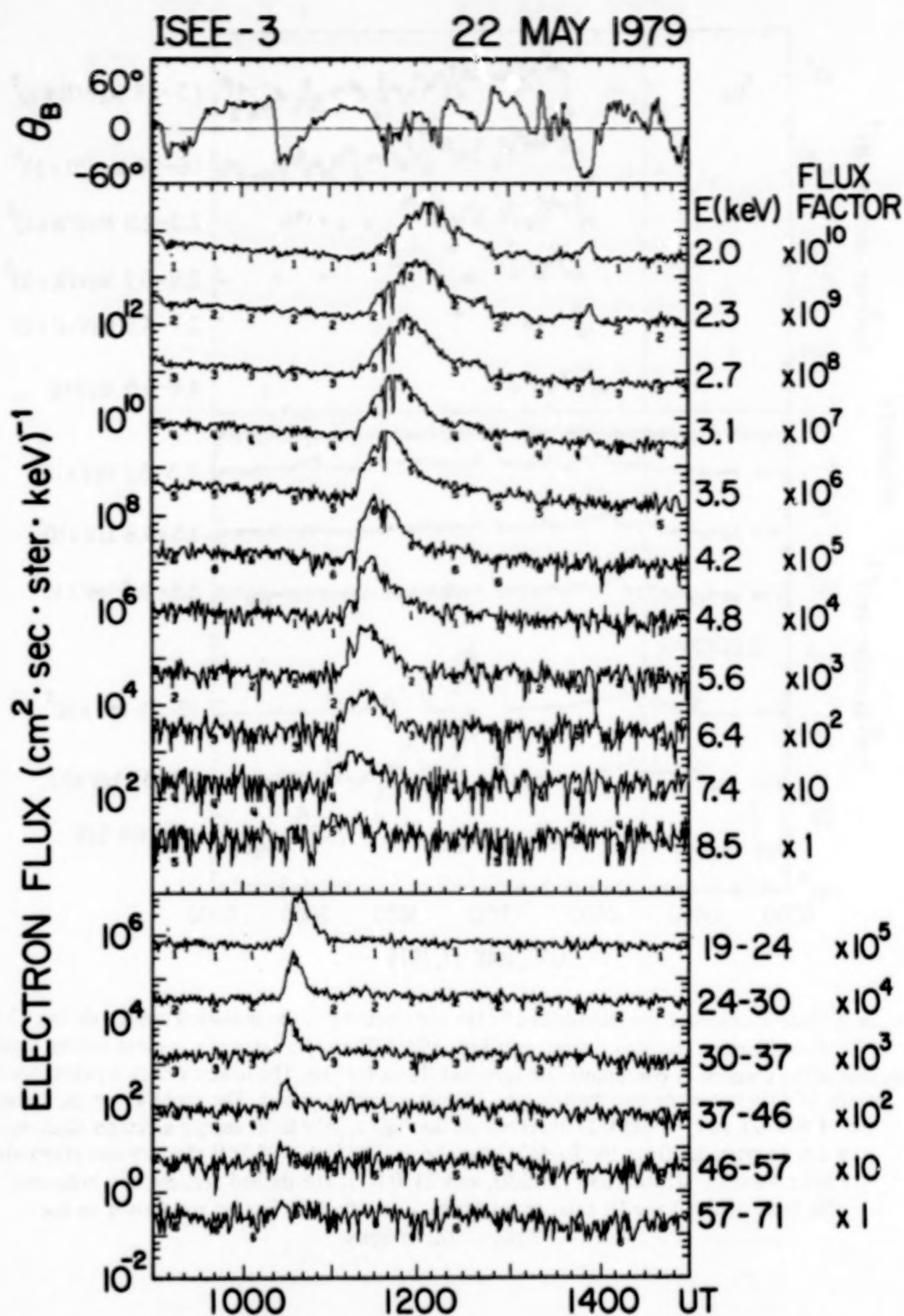Wild, J. P., Smerd, S. F., and Weiss, A. A., 1963, *Ann. Rev. Astron. Astrophys.*, *1*, 291.

Figure 1. An impulsive solar electron event observed by the ISEE-3 spacecraft. Note the rapid-rise rapid-fall profiles and the clear velocity dispersion. The top panel shows the angle of the interplanetary magnetic field direction to the ecliptic plane.
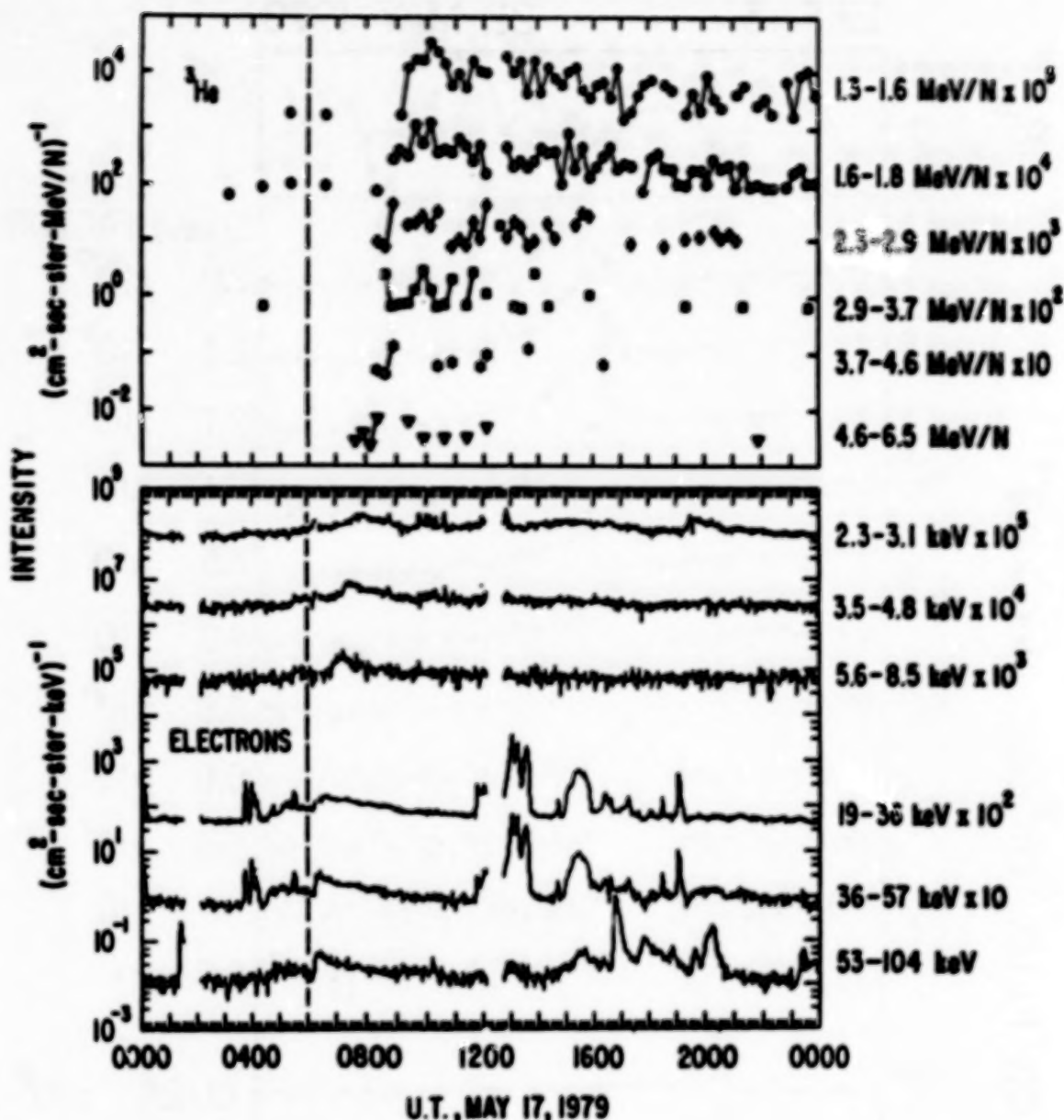
Figure 2. Time histories of the intensities of ^{3}He and electrons of the indicated energy during 17 May 1979 (from Reames, von Rosenvinge, and Lin, 1985). The appearance of the plots differs partly because of the absence of continuous background fluxes for ^{3}He. The lowest isolated points for each energy of ^{3}He represent one particle per 15-min averaging period. The rapidly varying bursts (at ~0400 UT and ~1200 UT) observed in the higher, >19 keV, energy electron channels are due to particles from the Earth's bow shock. The 53 to 104 keV channel also responds to solar X-rays (~0130, 1630 to 2030, and 2330 UT). The dashed vertical line indicates the time of the Type III solar radio burst. Intensity scale factors are shown to the right of the energies.
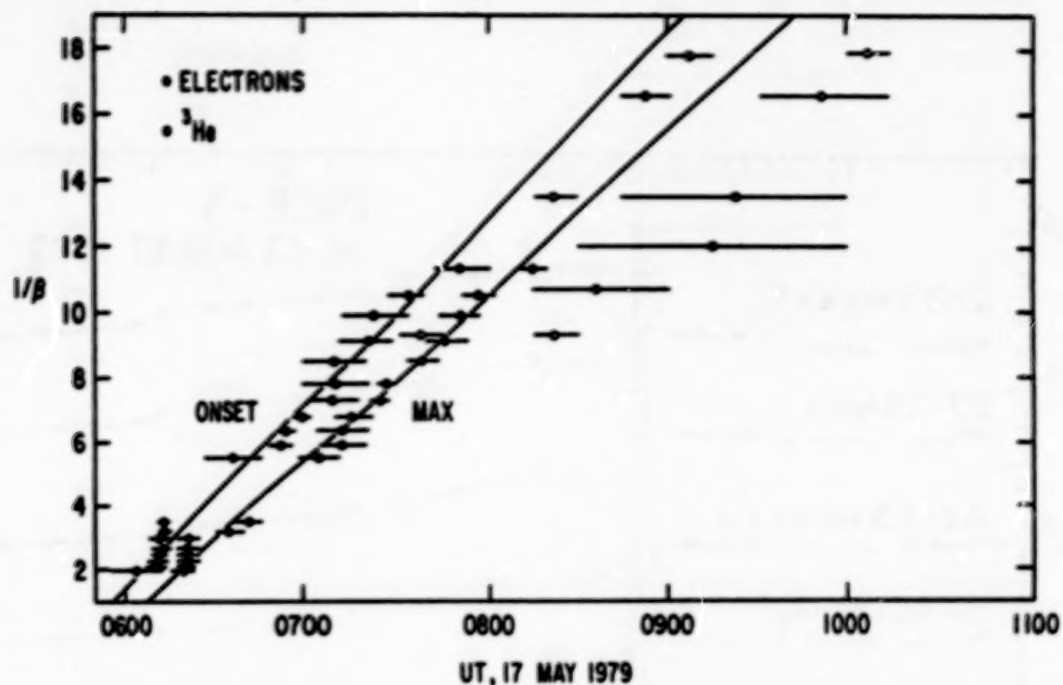
Figure 3. Time of onset and peak flux for particles plotted versus $1/\beta$ where $v = \beta c$ in the particle velocity (from Reames, von Rosenvinge, and Lin, 1985). The lines represent least-squares fits to the electron data only.
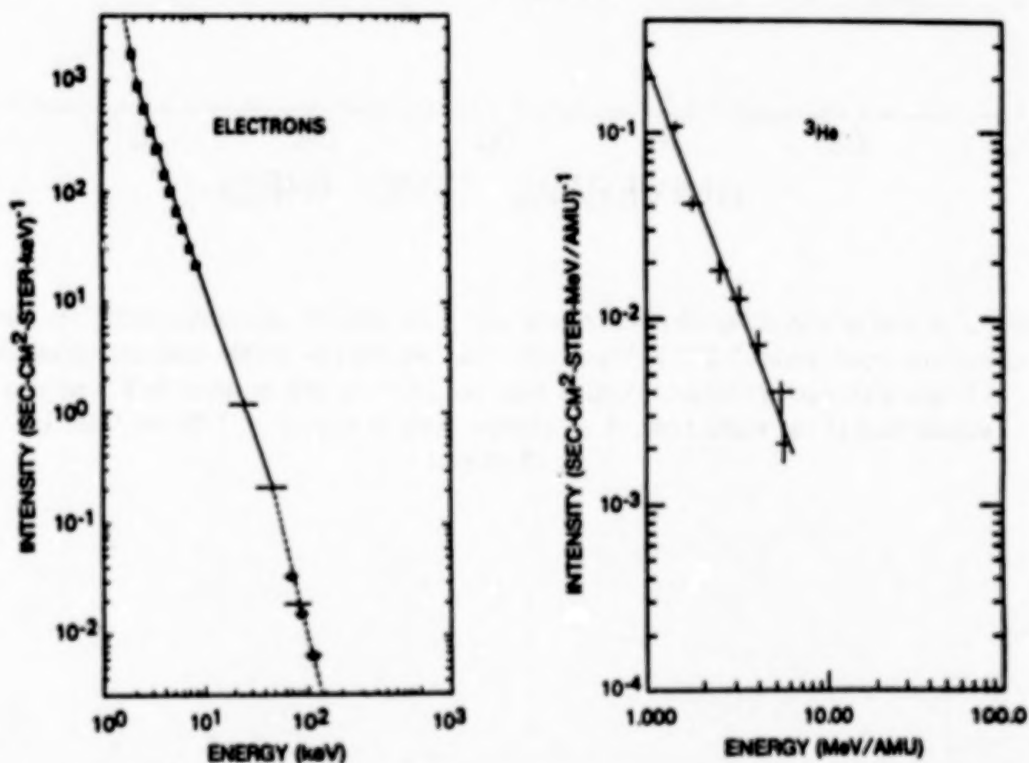
17 MAY 1979

Figure 4. Event-averaged energy spectra for electrons and ^{3}He in the 17 May 1979 event (from Reames, von Rosenvinge, and Lin, 1985). Lines through the data are least-squares fit lines to power-law spectra with resulting spectral indices 2.7 ± 0.1 for electrons and 2.7 ± 0.3 for ^{3}He. The electron fit was confined to the 2.5 to 60 keV region.
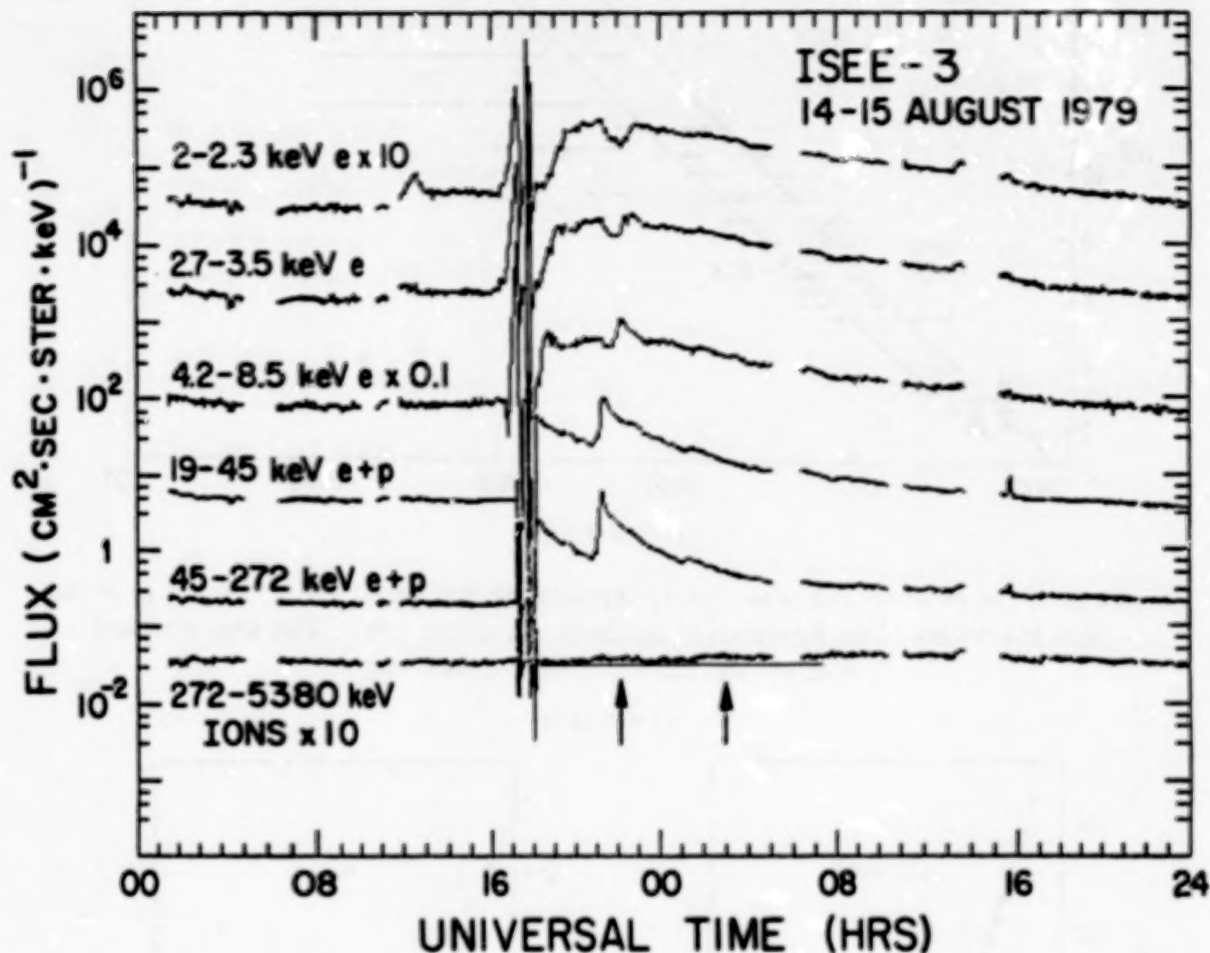
111

Figure 5. A pair of impulsive electron events which are closely associated with ^{3}He increases. The bottom trace shows >272 keV protons. The two barely visible small increases about 6 hours after each electron injection may be due to a few hundred keV ions also accelerated at the same time. A calibration cycle occurred at 1700 to 1800 UT on 14 August.
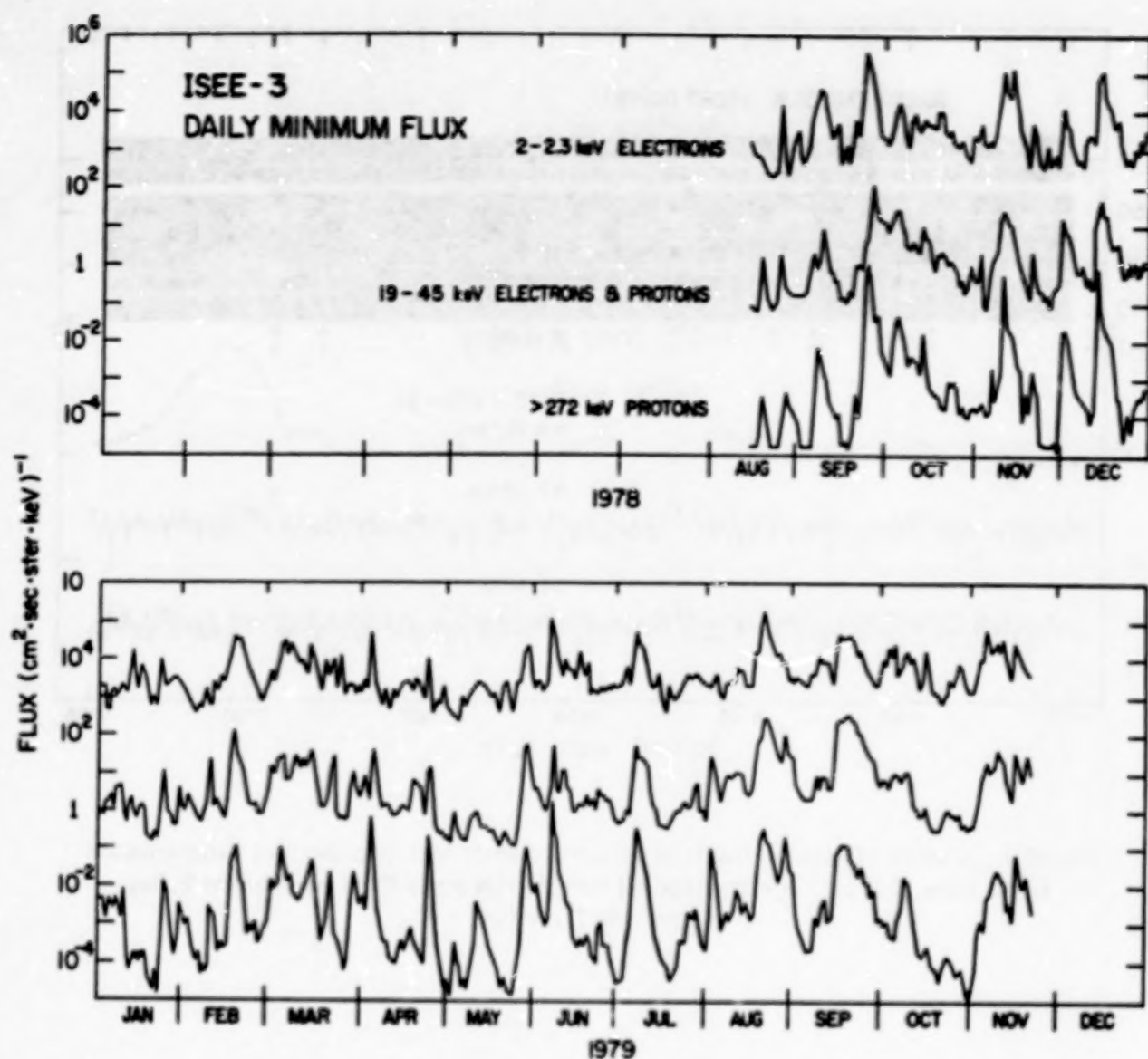
Figure 6. Plotted here are the minimum flux levels for each day of 2 to 2.3 keV electrons, 19 to 45 keV electrons and protons, and >272 keV protons, for August 1978 to November 1979. The fluxes are dominated by long-lived streams, but even at the quietest times there are significant fluxes of electrons.
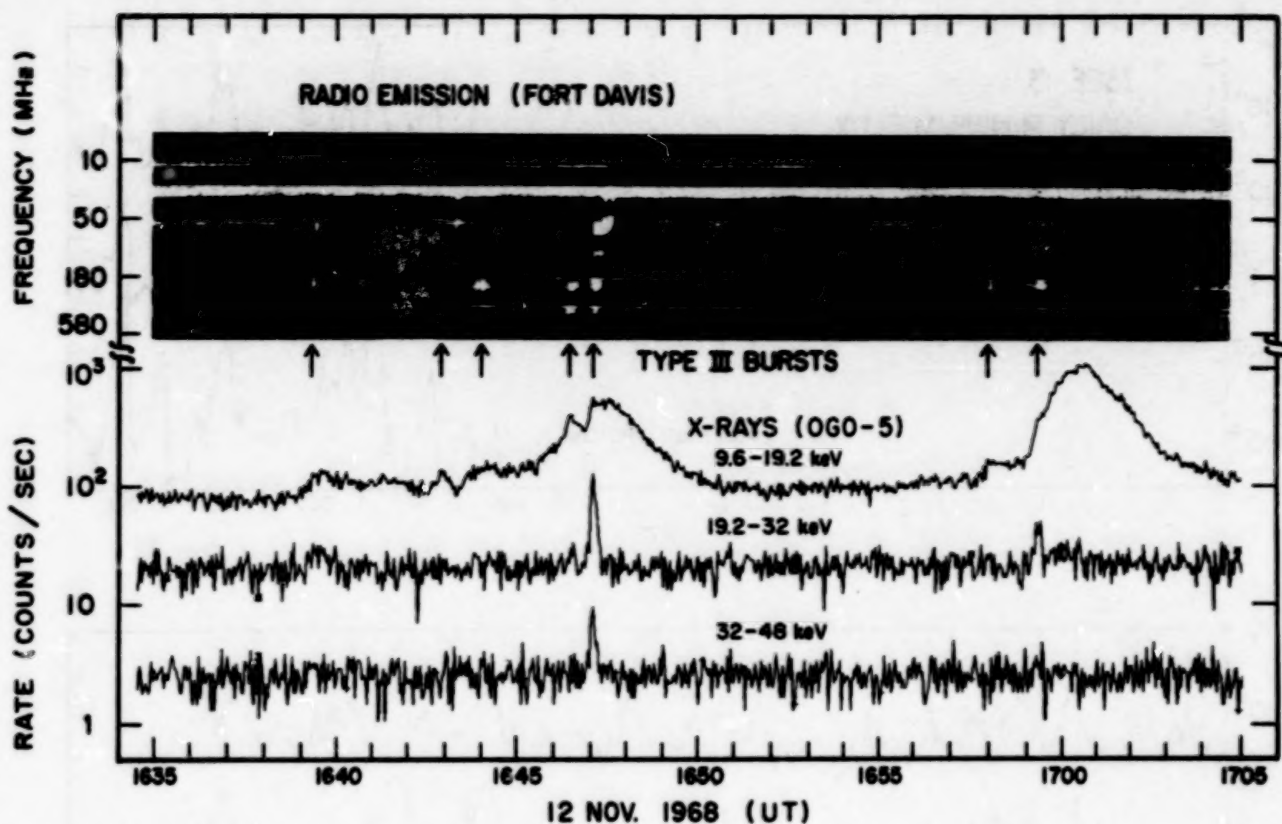
Figure 7. A series of type III bursts in time coincidence with non-thermal X-ray emission (from Kane, 1972). For every type III burst in this series there is a corresponding increase in X-ray flux.
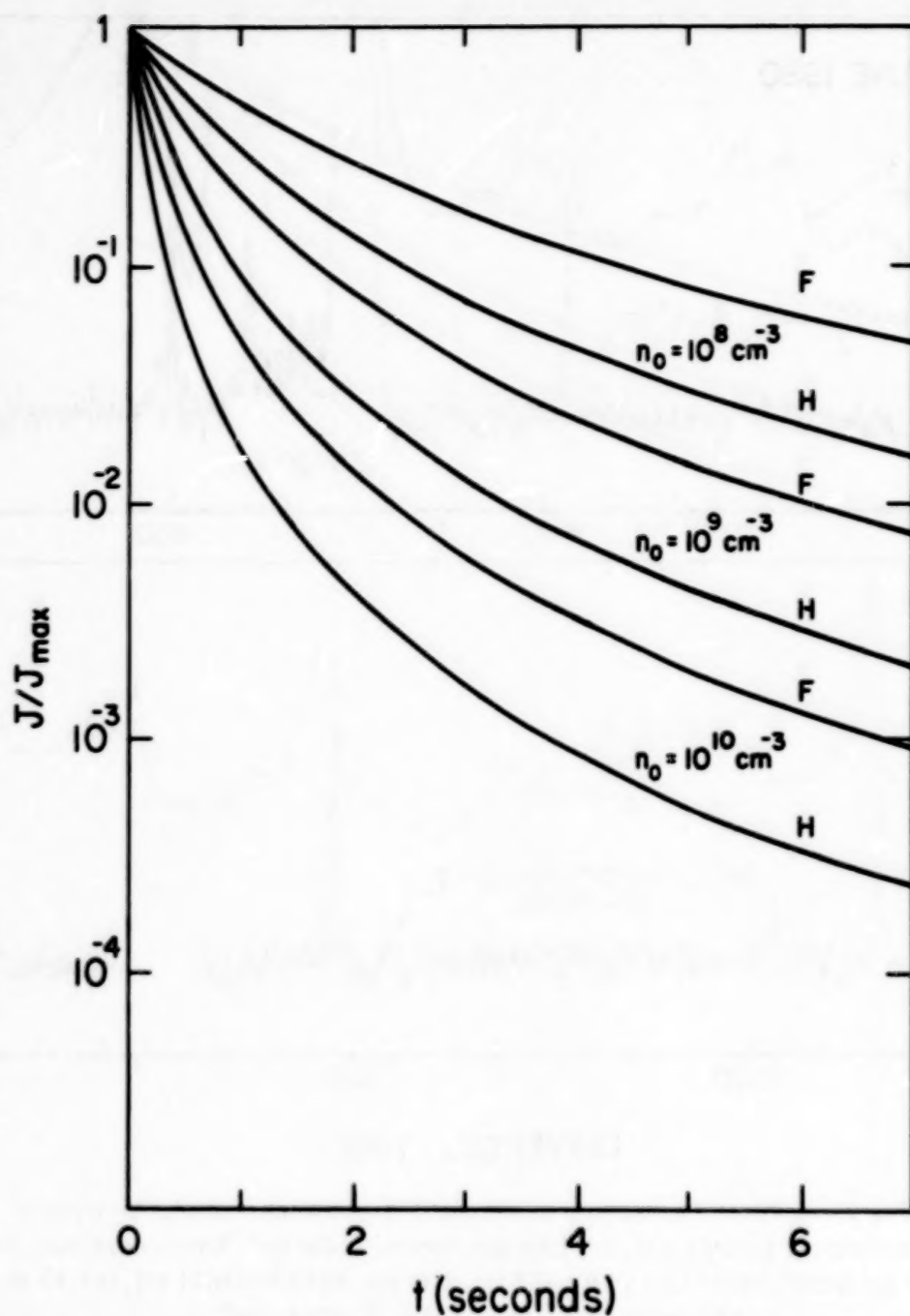
Figure 8. The time profiles for the coronal hard X-ray emission from a type III radio burst, computed under the assumption of instantaneous acceleration and escape of the electrons without significant energy loss. The curves are computed for different starting frequencies and normalized to the maximum flux. F and H denote interpretation of the radio emission as fundamental or harmonic.
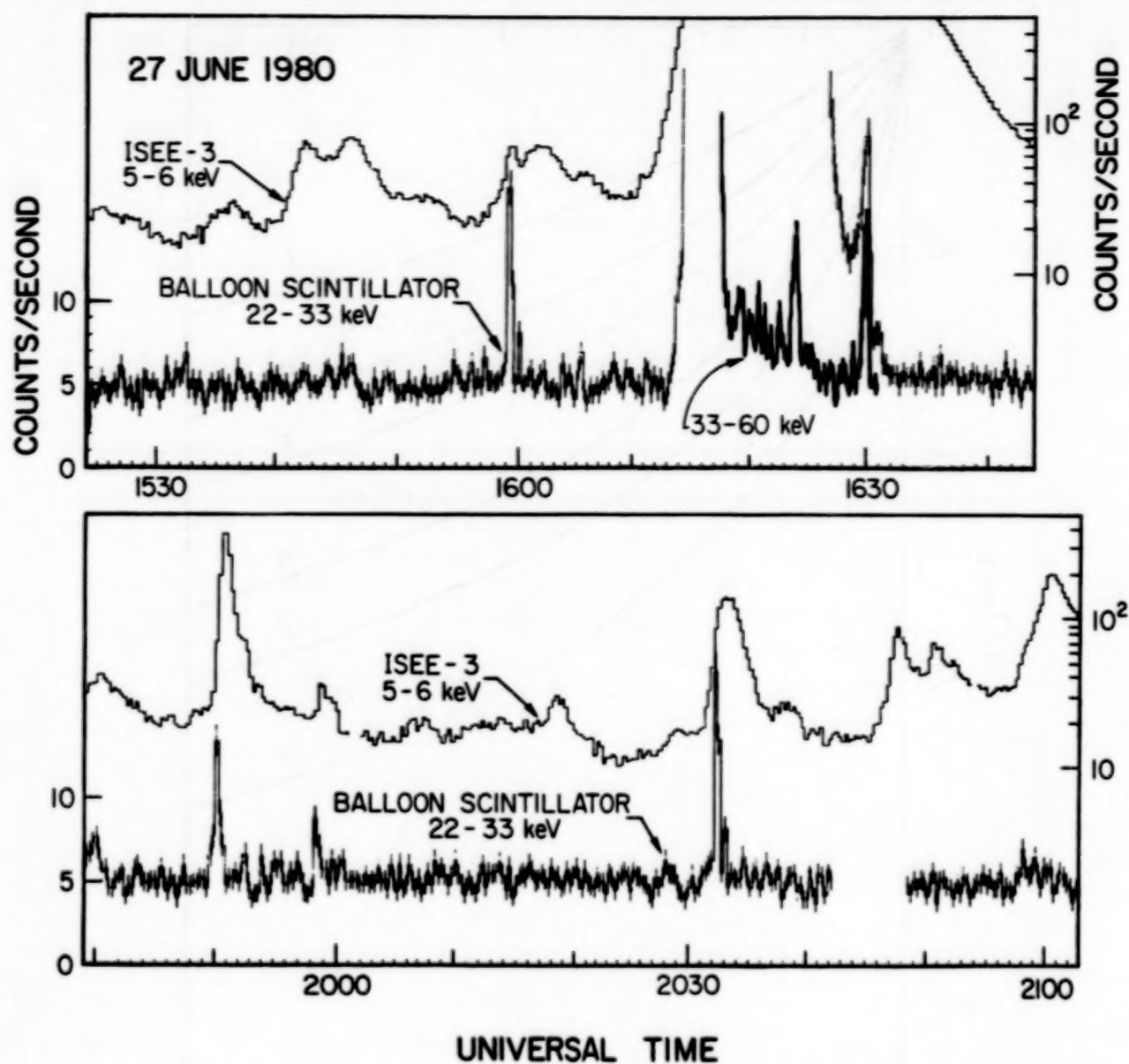
Figure 9. The 22 to 33 keV count rate of the NaI/CsI phoswich scintillation detector for the
two solar observing periods is shown here together with the soft X-ray count rate for the
ISEE-3 spacecraft (from Lin et al., 1984). Between 1618 and 1631 UT, the 33 to 60
keV count rate (thick line) is shown as well.

27 JUNE 1980
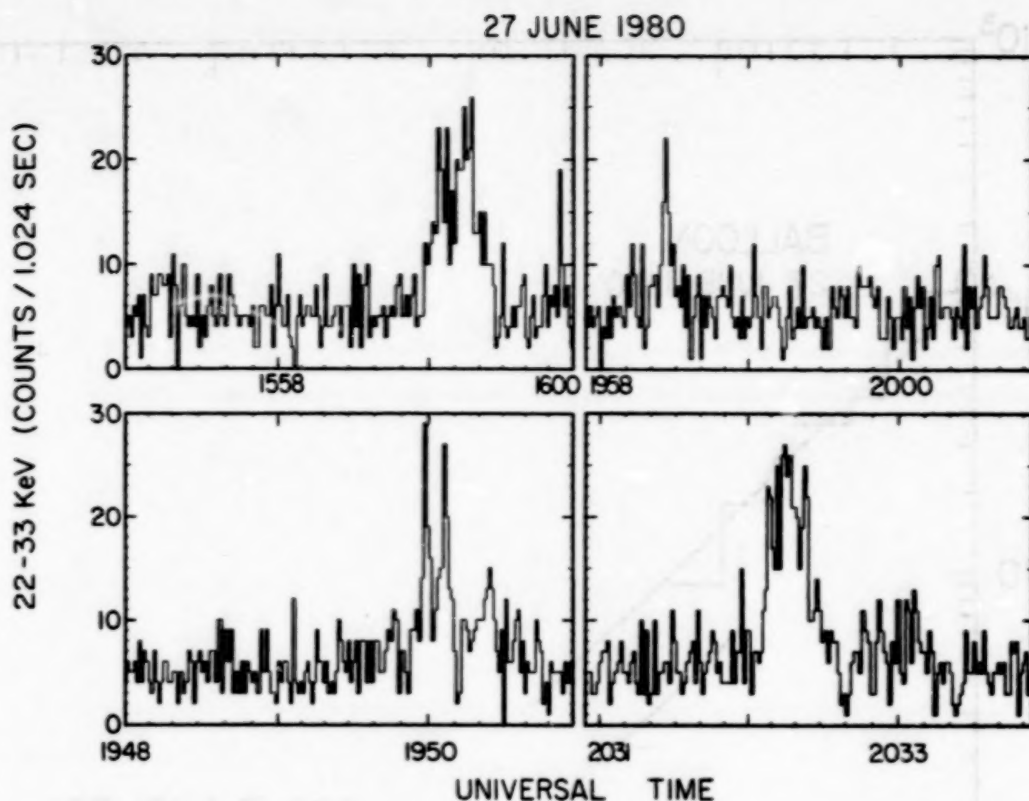
Figure 10.   The four largest hard X-ray microflares are shown here at 1.024 s
resolution (from Lin et al., 1984).

27 JUNE 1980
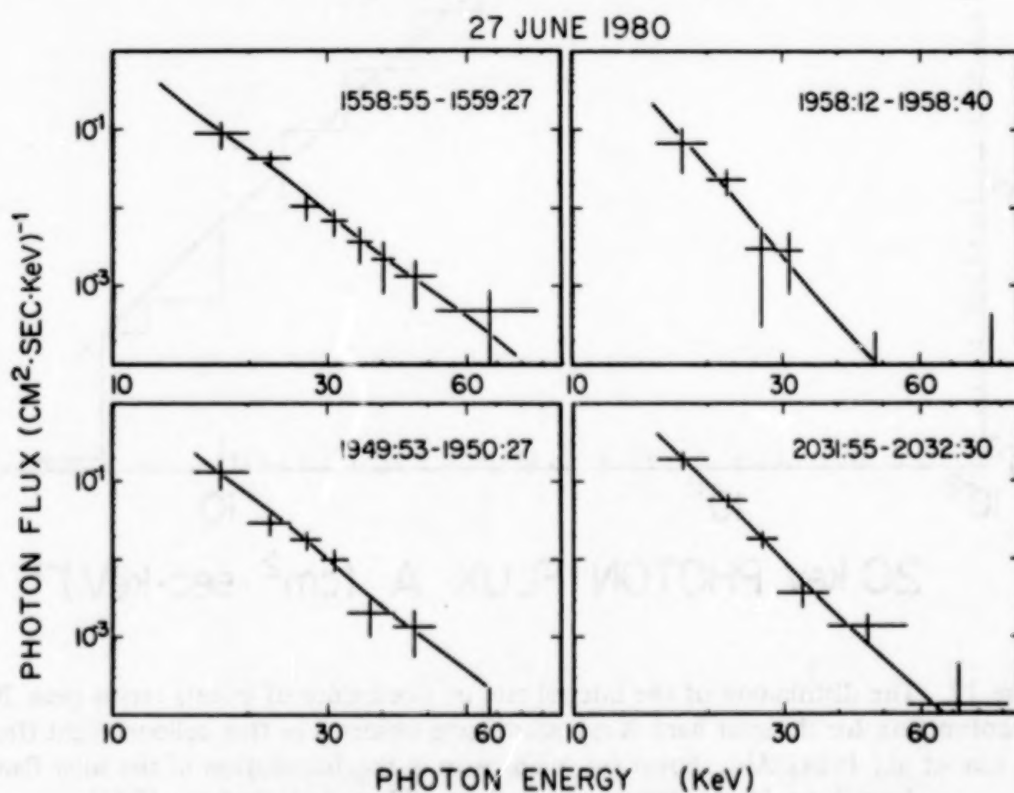
Figure 11.   Photon energy spectra from the planar germanium detectors, integrated over each
of the four bursts of Figure 10, are shown here (from Lin et al., 1984). The spectra
are well-fitted by power laws dJ/dE = AE$^{-\gamma}$ with $\gamma \approx$ 4 to 6.
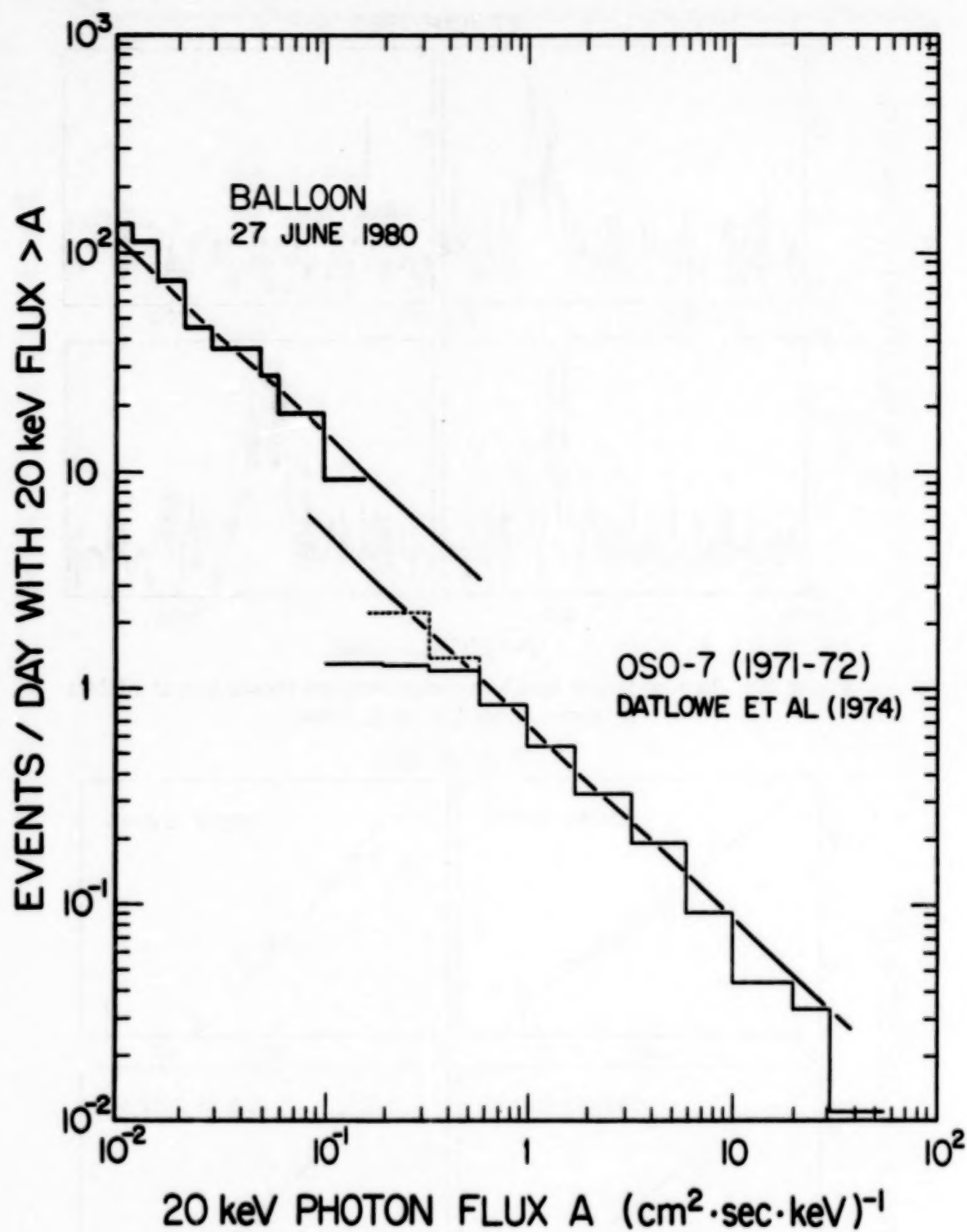
Figure 12. The distribution of the integral rate of occurrence of events versus peak 20 keV photon flux for the solar hard X-ray microflares observed in this balloon flight (from Lin et al., 1984). Also shown for comparison is the distribution of the solar flare hard X-ray bursts reported by Datlowe, Elcan, and Hudson (1974).
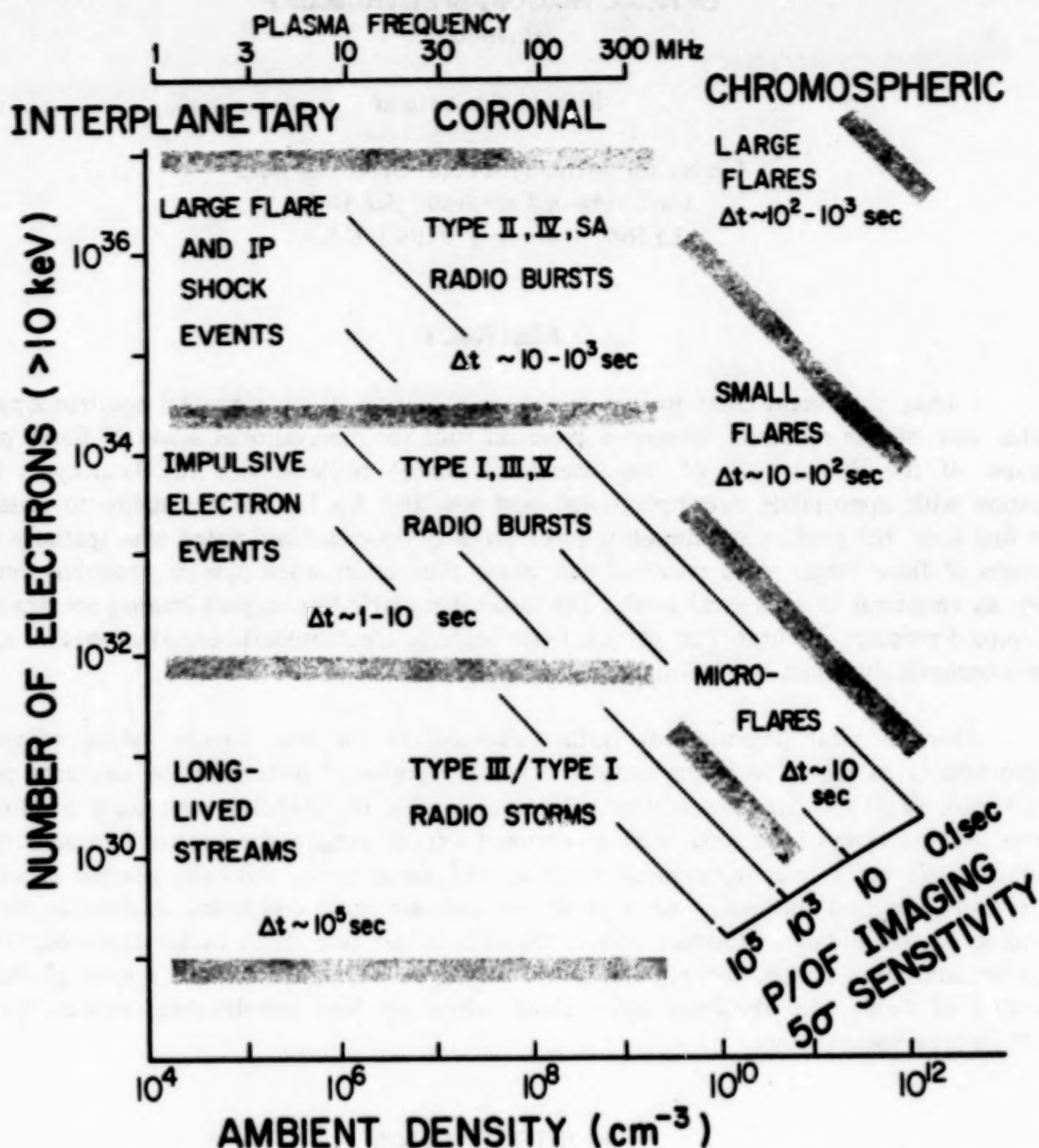
Figure 13. Various interplanetary, coronal, and chromospheric energetic electron phenomena
are shown here. The number of >10 keV electrons involved (vertical scale) has been
estimated from interplanetary observations at 1 AU except for the chromospheric
phenomena which are given by hard X-ray observations. The estimated 5σ
sensitivity for the planned P/OF hard X-ray instrumentation for different
integration times is indicated by the diagonal lines.

OPTICAL IMAGING SPECTROSCOPY
(Invited)

Richard C. Canfield

Center for Astrophysics and Space Sciences
University of California, San Diego
La Jolla, California 92093, U.S.A.

ABSTRACT

During the recent solar maximum the combination of imaging and spectroscopy in the visible part of the spectrum became a powerful tool for observational study of flares primarily because of the development of two-dimensional charge-coupled-device (CCD) arrays. In combination with appropriate new operational methods, this has led to the ability to observe, for the first time, the preflare and impulsive-phase physical processes associated with spatially resolved features of flare loops. As a result of concurrent theoretical developments, modeling progressed from an empirical to a physical level. This made it possible to interpret imaging spectra in terms of coronal pressure and heat flux, particle beam heating, chromospheric evaporation, and explosive chromospheric dynamics at the footpoints of flare loops.

There is clear potential for further advances in the near future, taking advantage of improvements in digital recording speed ($\sim$10-fold), number of photosensitive elements per array ($\sim$10-fold), real-time data pre-reduction (potentially 10- to 100-fold), and using multiple CCD arrays. By the time of the next solar maximum I expect imaging spectroscopy to achieve spatial resolution $\lesssim 1$ arc s, temporal resolution $\lesssim 5$ s, and simultaneous critically-sampled spectroscopy of several lines and continua. As a result, we can anticipate continued increase in our understanding of the physical processes and configurations of solar flares in the chromosphere, temperature minimum region, and photosphere. Even greater progress toward a more global understanding of flares will obviously come about when we have simultaneous optical, X-ray, and γ-ray imaging spectroscopy.

I. INTRODUCTION

Spectroscopy is much easier in the visible part of the spectrum than in other energy ranges. High photon flux and detector efficiency allow high spatial and temporal resolution. In addition, the optically thick nature of the visible solar atmosphere permits studies of the variation of physical conditions along a line of sight. Array detectors are presently leading to a quantum jump in our ability to utilize these advantages. We are seeing the merging of the morphological information contained in monochromatic Hα filtergrams and the physical information contained in spectra, in the form of what is called optical imaging spectroscopy. In this paper I will review the technological and operational advances that have enabled this advance, some of the physical understanding that has come about as a result, and the possibilities for the future. I will deliberately not describe some of the alternate uses of CCD arrays that are also attractive, such as their use with monochromatic filters to achieve high spatial or temporal resolution, at the sacrifice of spectroscopy.

II. OBSERVATIONAL METHODS

The observational methods of imaging spectroscopy are very simple. A two-dimensional array is placed at a focal plane of a slit spectrograph. One of the two dimensions of the array is oriented parallel to the spectrograph slit, so the pixels in this dimension sample a line of solar image elements, i.e., spatial variations. The other dimension of the array is then parallel to the spectral dispersion, and thus samples a line of spectral elements, i.e., the spectral line profile of a single spatial image element. The array is exposed, read, digitized, and recorded, producing an observation with one spatial and one spectral dimension; all samples from a single exposure of the array are simultaneous. A second spatial dimension is built up, in the manner of a traditional spectroheliogram, by scanning the solar image perpendicular to the spectrograph slit. Observations of the preflare and impulsive phases are ensured by taking data continuously in this manner, saving the data only if a flare occurs within the scan area.

Of course, reality forces various unsatisfying tradeoffs, which are well illustrated by the Hα imaging spectroscopy program Todd Gunkler and I carried out in 1980 at the Vacuum Tower Telescope at Sacramento Peak, in coordination with the Solar Maximum Mission (Acton et al., 1982; Gunkler et al., 1984). The worst bottleneck in our 1980 observing setup was real-time digital data recording on conventional 1/2 in. magnetic tape. To deal with this relatively slow data recording it was necessary to record only 50 x 100 elements of the array and to slow the observational cadence to four slit-position/read/write cycles per second. This, coupled with the need to cover a reasonable area to ensure preflare converage of the flare site, forced rather coarse spatial resolution, only ~2.5 arc s per pixel. A square 50 x 50 pixel spatial image, corresponding to 50 slit positions, required 12.5 s to record; slewing back to the starting point for the next scan brought the full cycle time to 15 s. Though this cycle time was much longer than desired, it at least permitted a few samples during the impulsive phase of a typical hard X-ray flare.

Our observational approach has placed strong emphasis on spectra, at the expense of imaging. All 100 spectral data points in each spatial pixel were sampled simultaneously. Also, though our spatial and temporal resolution were far less than optimal, our spectral resolution was quite sufficient; each spectral pixel was ~100 mÅ wide, which compares favorably with the 283 mÅ thermal Doppler width of Hα at 10^4 K. This emphasis on spectroscopy produced a unique new perspective on a variety of flare processes in the chromosphere, including the effects of coronal pressure, electron-beam heating, chromospheric evaporation, and flare dynamics.

III. USING CHROMOSPHERIC Hα PROFILES TO MEASURE CORONAL PRESSURE

Theoretical calculations have shown that the profile of the Hα line from hydrostatic model atmospheres is a useful diagnostic of coronal pressure (Canfield, Gunkler, and Ricchiazzi, 1984, henceforth CGR). The top panel of Figure 1 shows four different theoretical Hα profiles, computed from physical model atmospheres based on four different values of coronal pressure, P_0, in an idealized case in which the electron-beam heating, F_{20}, and transition-region conductive heat flux, F_5, are artificially held fixed. As pressure increases, both the total amount of Hα emission and its profile change. The total amount of emission increases with pressure both because there are more H atoms in the chromosphere and because the amount of Hα radiation per H atom increases. The line loses its central reversal because at high pressures, more frequent collisions of H atoms with free electrons tie the line emissivity more closely to temperature, which increases

monotonically outward in the chromosphere. CGR showed that although the total amount of emission is not a unique signature of coronal pressure, the relative strength of the central reversal is; only high coronal pressures ($\gtrsim 10^3$ dynes cm^{-2}) produce Hα profiles that are not centrally reversed.

A typical observed spectroscopic manifestation of the increase to high values of coronal pressure in the course of a flare is seen in Figure 2, which shows time sequences (15 s apart) of observed Hα profiles of two interesting pixels of one of the two 1980 flares that were well observed (i.e., imaging spectroscopy in Hα, soft X rays, and hard X rays) from both SMM and Sacramento Peak (the flare of ~1522 UT, 14 June 1980; Gunkler et al., 1984). The north pixel is typical of the impulsively-brightening north region of this flare, and the strand pixel typifies an Hα ribbon. The times of Hα observations during the period of impulsive hard X-ray emission are underlined; 28 to 54 keV X rays peaked at ~1523 UT. Comparison with the CGR theoretical Hα profiles suggests that, in the north pixel, the value of the pressure increased throughout the impulsive phase and remained at a high level, between 10^2 and 10^3 dynes cm^{-2}, immediately afterward. In the strand pixel, the comparison suggests that pressure was already at a high value by the time of hard X-ray peak, and also remained at such values (~10^3 dynes cm^{-2}) immediately thereafter.

Comparison of pressure values at the times of maximum thermal X-ray emission measure of both well-observed 1980 flares (1456 UT, 7 May and 1522 UT, 24 June) has demonstrated pressure equilibrium between the coronal parts of flares and their chromospheric footpoints, as one would expect from a loop flux-tube visualization of flare geometry (Gunkler et al., 1984; Canfield and Gunkler, 1985). Puzzling earlier indications of pressure imbalance between the chromosphere and corona (Acton et al., 1982) were shown by Canfield and Gunkler (1985) to be invalid, due to the use of physically incomplete empirical models rather than physical models for the theoretical interpretation of the observed Hα profiles.

IV. CHROMOSPHERIC FOOTPOINT PENETRATION OF NONTHERMAL ELECTRONS

Hα line profile calculations based on theoretical hydrostatic model atmospheres indicate that there is a unique signature of intense nonthermal electron heating by Coulomb collisions, in addition to the pressure signature discussed above. The lower panel of Figure 1 shows three different theoretical Hα profiles for physical model atmospheres based on three different values of F_{20}, the energy flux of nonthermal electrons above 20 keV. As F_{20} is increased, holding F_5 and P_0 constant, substantial wings of distinctly non-Gaussian form appear. This effect is due to linear Stark broadening of the upper and lower atomic levels of the Hα transition; Stark broadening has a much different spectral form in the wings than the Gaussian form appropriate to thermal broadening. This Stark-broadened wing emission arises relatively deep in hydrostatic chromospheres, where the density is large enough that Stark broadening becomes significant. CGR showed that such obvious Stark wings, having form much different from the more Gaussian form shown in the top panel, and extending >3 Å from line center, are a unique signature of intense electron beams ($F_{20} \gtrsim 10^{10}$ erg cm^{-2} s^{-1}).

Canfield, Gunkler, and Kiplinger (1984), studying the two well-observed 1980 flares, found direct spatial correspondence between Hα Stark-wing sites and the strongest $\gtrsim 16$ keV emission sites observed by the Hard X-Ray Imaging Spectrometer (HXIS). Hard X-ray and Hα Stark-wing sites from both flares were also well correlated in time with higher-energy X rays observed by the

Hard X-Ray Burst Spectrometer (HXRBS). Figure 3 shows hard X-ray counts for these two flares, and allows a comparison of their temporal variations with those of typical $H\alpha$ kernel (Stark-wing) pixels. Ignoring, for the moment, the $H\alpha$ asymmetry (red excess), there is a clear tendency for the $H\alpha$ line wings to broaden and narrow in close synchronism with the hard X-ray count rate while, for example, the $H\alpha$ line center intensity varies both more slowly and qualitatively differently. The obvious conclusion is that nonthermal particles not only stop at the footpoints of loops, as also indicated by hard X-ray imaging of impulsive flares, but actually penetrate into the chromosphere.

It is interesting that when observations of the extent of the $H\alpha$ wing broadening are used to estimate the value of F_{20}, one gets high values of F_{20} in the brightest kernels of both well-observed 1980 flares. These values, $F_{20} \sim 10^{11}$ erg cm^{-2} s^{-1}, are very close to what one would infer to be the limiting electron beam flux permitted by reverse current stability considerations. Moreover, F_{20} values of the same order are inferred for these events if F_{20} is calculated by a quite independent method, using the total flare power inferred from the spatially unresolved HXRBS data and the observed $H\alpha$ Stark-wing kernel area. This suggests that our 1980 $H\alpha$ spatial resolution, though only ~ 2.5 arc s, is probably within an order of magnitude of what is really necessary to properly resolve the true $H\alpha$ kernel image.

V. CHROMOSPHERIC EVAPORATION: BEAMS OR CONDUCTION?

A topic of considerable current interest is chromospheric evaporation, which is the process of heating chromsopheric material to typical flare coronal temperature ($T \gg 10^6$ K). Among the issues of debate (cf. Doschek et al, 1985) are: (1) Can chromospheric evaporation account for the amount of X-ray emitting material in flares; (2) What is the mechanism that drives chromospheric evaporation?

Various approaches have been taken to answering the first question, including the use of $H\alpha$ imaging spectroscopic observations. Acton et al. (1982) compared $H\alpha$ imaging spectra of the well-observed 7 May 1980 flare to theoretical $H\alpha$ profiles based on empirical model flare chromsopheres. On the basis of the relative strength of the central reversal, Acton et al. were able to assign to each pixel in the $H\alpha$ image an amount of material, per pixel, that had been evaporated. Integrating over the flare area, they compared this quantity to that implied by the soft X-ray observations, and found that the $H\alpha$ profiles implied the evaporation of more than enough material to account for the observed X-ray emission measure and image size. A less empirical approach, based on the physical models of CGR, was later taken by Canfield and Gunkler (1985), in the course of resolving the controversy over pressure imbalance alluded to in Section III above. However, because this approach treats coronal pressure and transition region conductive flux as independent parameters (although they are certainly not), it is capable of observationally confirming only the presence of high pressure, but not its physical cause. Hence, Canfield and Gunkler were able to show, on simple physical grounds based on coronal loop equilibrium scaling laws, only that conductively-driven evaporation could theoretically account for the inferred amount of X-ray emitting material.

The main contribution of $H\alpha$ imaging spectroscopy to the second question comes about because this method of observation gives information about both the spectrum and the image morphology. As discussed in Section IV above, this allows the observational determination of the electron beam energy flux F_{20}. In the two well-observed 1980 flares Gunkler et al. (1984) and Canfield and Gunkler (1985) determined F_{20} in order to estimate the amount of chromospheric evaporation that arose due to direct Coulomb heating by the beam electrons, which they found to be less than the amount of chromospheric evaporation due to classical thermal conduction, by the time of peak X-ray emission measure.

VI. CHROMSOPHERIC RADIATING SHOCKS AND CONDENSATIONS

Our theoretical understanding of the dynamics of the atmosphere contained in flare loops has progressed dramatically during this solar maximum. The most novel physics lies in the understanding of chromospheric aspects of explosive evaporation driven by intense impulsive electron beams, which initiate downward-propagating radiating shocks (Fisher, 1985) at the leading edge of dense chromospheric condensations (Fisher, Canfield, and McClymont, 1985). These chromospheric phenomena may have the same origin as the impulsive-phase X-ray blue-shifts seen from SMM, P78-1, and Hinotori (Doschek et al., 1985), though they certainly involve much different physics. Physical understanding of chromospheric condensations is so recent that there do not yet exist theoretical Hα line profiles with which to compare the observations. However, physical conditions in strong condensations are known, as shown in Figure 4, which focuses on the upper chromospheric part of a flare loop during the first few seconds of heating by an intense impulsive electron beam. To the left of the dashed vertical line, in all panels of the figure, is the high-temperature plasma that is thought to be the source of the blue-shifted X-ray emission. Between the dashed and solid vertical lines is the condensation itself, which is somewhat cooler and much denser than its surroundings, and is moving downward at velocities (initially approaching 100 km s^{-1}) that far exceed the sound speed in the underlying electron-beam-heated upper chromosphere. Fisher (1985) has recently developed a simple model of a radiating shock and condensation propagating into an isothermal chromosphere, which predicts that the timescale for disappearance of the downward motions should be ~1 min, independent of the strength of the condensation. Straightforward physical arguments, supported by the numerical simulations, indicate that explosive evaporation should take place only for $F_{20} \gtrsim 10^{10}$ erg cm^{-2} s^{-1} (Fisher, Canfield, and McClymont, 1985); since the observations discussed above imply such large values of F_{20} in flare kernels, we should expect to see spectroscopic evidence of chromospheric condensations.

The five 1980 flares for which we have both imaging spectroscopy in Hα and non-imaging spectroscopy in hard X-rays (from HXRBS on SMM) show properties that are very suggestive of chromospheric condensations driven by explosive chromospheric evaporation and electron beam heating (Canfield, Gunkler, and Kiplinger, 1985). One or more pixels of all five flares show the Hα Stark-wing signature. These pixels have several interesting properties in difference spectra, which are formed by subtracting their pre-impulsive spectrum, as shown in Figure 5. First, during the impulsive phase redshifts are ubiquitous; peak-observed Doppler velocities for all five events are typically 40 to 60 km s^{-1} downward. Multiple redshift episodes in the Hα spectrum can often be identified with major impulsive spikes in the hard X-ray count rate, as indicated in the figure. It is not uncommon for redshift episodes to decay to essentially zero in 30 to 60 s, though more long-lived redshifts (probably multiple episodes) are also often seen. It is often observed that in the wings of Hα the Doppler shift becomes independent of intensity, indicating either that the moving material becomes optically thin or that it is optically thick, but moving at the same velocity over a broad range of column depth. Often the excess spectrum is either weakly centrally reversed or not reversed at all, indicating high pressure.

During the time of the balloon flight that discovered hard X-ray microflares (Lin et al., 1984), we were making Hα imaging spectroscopic observations at Sacramento Peak. Canfield and Metcalf (1984) have found that the Hα counterparts of the larger observed hard X-ray microflares have bright kernels that show impulsive-phase Hα wing broadening that rises and falls in synchronism with hard X-rays, indicative of chromospheric electron-beam heating. The flare-excess emission of these larger microflares is clearly redshifted, with Doppler velocities that are typically ~50 km s^{-1}. Both the impulsive-phase wing broadening and the redshifts indicate that although these microflares are small in area, they still have intense electron beams with $F_{20} \gtrsim 10^{10}$ erg cm^{-2} s^{-1}. Metcalf and Canfield (1985) have examined the Hα counterparts of the smallest

microflares observed in hard X rays. They find that in them there is little or no Hα redshift. It is interesting that they still show evidence of electron beams, however, although with $F_{20} \lesssim 10^{10}$ erg cm^{-2} s^{-1}. In particular, they show weak Hα wing enhancements temporally correlated with hard X rays, and line profiles much like the theoretical profiles for low-pressure atmospheres heated by weak electron beams shown in Figure 1 (upper panel, $P_0 = 1$-10 dynes cm^{-2}, $F_{20} = 10^8$ erg cm^{-2} s^{-1}). Finally, there is evidence for Hα events much like the Hα counterpart of the smallest hard X-ray microflares, but without detected hard X-ray counterparts, supporting the suggestion of Lin et al. (1984) that the distribution of non-thermal events extends to very small events indeed.

VII. FUTURE PROSPECTS FOR THEORY AND OBSERVATION

One of the delights of working on impulsive-phase chromospheric flare physics at this time is that both theory and observation are advancing at a rapid pace.

On the theoretical side, it is clear that more work needs to be done to complete our physical understanding of the relationship between the properties of the mechanism that leads to explosive evaporation and the properties of the dynamic phenomena that ensue. For example, to what extent will a coronal conduction front lead to explosive evaporation, creating a chromospheric condensation? How is the velocity (or temperature density) of a condensation related to F_{20}? What effects will return currents or beam instabilities have? Second, we need to predict specific observable spectral parameters of dynamic atmospheres, much as has already been done for Hα from static atmospheres. How does the Hα profile reflect the presence of radiating shocks and condensations? How about transition-region lines, or lines formed deeper in the chromosphere? How much emission comes from the radiating shock and condensation, as compared with the underlying atmosphere that has not yet been shocked? How can simultaneous observations of more than one line, formed at different temperatures, discriminate between various transport processes?

On the observational side, it is obvious that during the next solar maximum we will be able to do dramatically better than what we did during the past one. We can estimate the quantitative improvements by assuming that we will use devices that are available right now. A major advance can certainly come from using analog-to-digital conversion and video recording hardware that has been developed for the home hi-fi market, rather than conventional 1/2 in. computer tape as we did at Sacramento Peak in 1980. Presently available video-digital interfaces for home hi-fi run at 1.6 megabits per second for each (stereo) channel, and retail for about $1000. Add a video recorder, and you can record on-line an order of magnitude faster than what we had in 1980. The number of photosites per array has also gone up about an order of magnitude over what we used in 1980. Data preprocessing, i.e., pre-reduction to reduce the number of bits actually written to tape, is now in daily use with the Multiple Diode Array (MDA) at Sacramento Peak. In principle, this will allow speed enhancements that might easily be 1 to 2 orders of magnitude. Conservatively, I estimate the potential benefit at a factor of 3, based on setups we have developed wiht the MDA in the last year, which simply reduce the effective spectral resolution in the wings of the Hα line to compensate for the effectively slower spectral variation of the absorption coefficient there. Finally, multiple arrays, each with its own recorder, can potentially enable one to make imaging spectroscopic observations of perhaps 10 different spectral features simultaneously, using an echelle spectrograph like the one at Sacramento Peak.

Combining all these improvements, by the time of the next maximum, I expect to be able to carry out imaging spectroscopic observations, critically resolved spectroscopically, that achieve both spatial resolution $\lesssim 1$ arc s and temporal resolution $\lesssim 5$ s, simultaneously, for many

spectral lines and continua formed at different temperatures or depths within the chromosphere, temperature minimum, and photosphere. However, only through imaging spectroscopy of higher-energy radiation such as microwaves, X rays, and γ-rays can we hope to build a compelling physical picture of the whole flare process, throughout the solar atmosphere. I look forward to the advances and challenges these new capabilities will provide for our physical understanding of acceleration and transport processes in solar flares.

REFERENCES

Acton, L. W., Canfield, R. C., Gunkler, T. A., Hudson, H. S., Kiplinger, A. L., and Leibacher, J. W., 1982, *Astrophys. J., 263*, 409.

Canfield, R. C. and Gunkler, T. A., 1985, *Astrophys. J., 288*, 353.

Canfield, R. C. and Metcalf, T. R., 1984, *Bull. Amer. Astron. Soc., 16*, 891.

Canfield, R. C., Gunkler, T. A., and Kiplinger, A. L., 1984, *Adv. Space Res., 4*, No. 7, 255.

Canfield, R. C., Gunkler, T. A., and Kiplinger, A. L., 1985, *Bull. Amer. Astron. Soc., 17*, 628.

Canfield, R. C., Gunkler, T. A., and Ricchiazzi, P. J., 1984, *Astrophys. J., 282*, 296.

Doschek, G. A., et al., 1985, in *Solar Flares: Proceedings of the SMM Workshop*, eds. M. Kundu and B. Woodgate, in press.

Gunkler, T. A., Canfield, R. C., Acton, L. W., and Kiplinger, A. L., 1984, *Astrophys. J., 285*, 835.

Fisher, G. H., 1985, *Bull. Amer. Astron. Soc., 17*, 634.

Fisher, G. H., Canfield, R. C., and McClymont, A. N., 1985, *Astrophys. J., 289*, 434.

Lin, R. P., Schwartz, R. A., Kane, S. R., Pelling, R. M., and Hurley, K. C., 1984, *Astrophys. J., 283*, 421.

Metcalf, T. R. and Canfield, R. C., 1985, *Bull. Amer. Astron. Soc., 17*, 644.
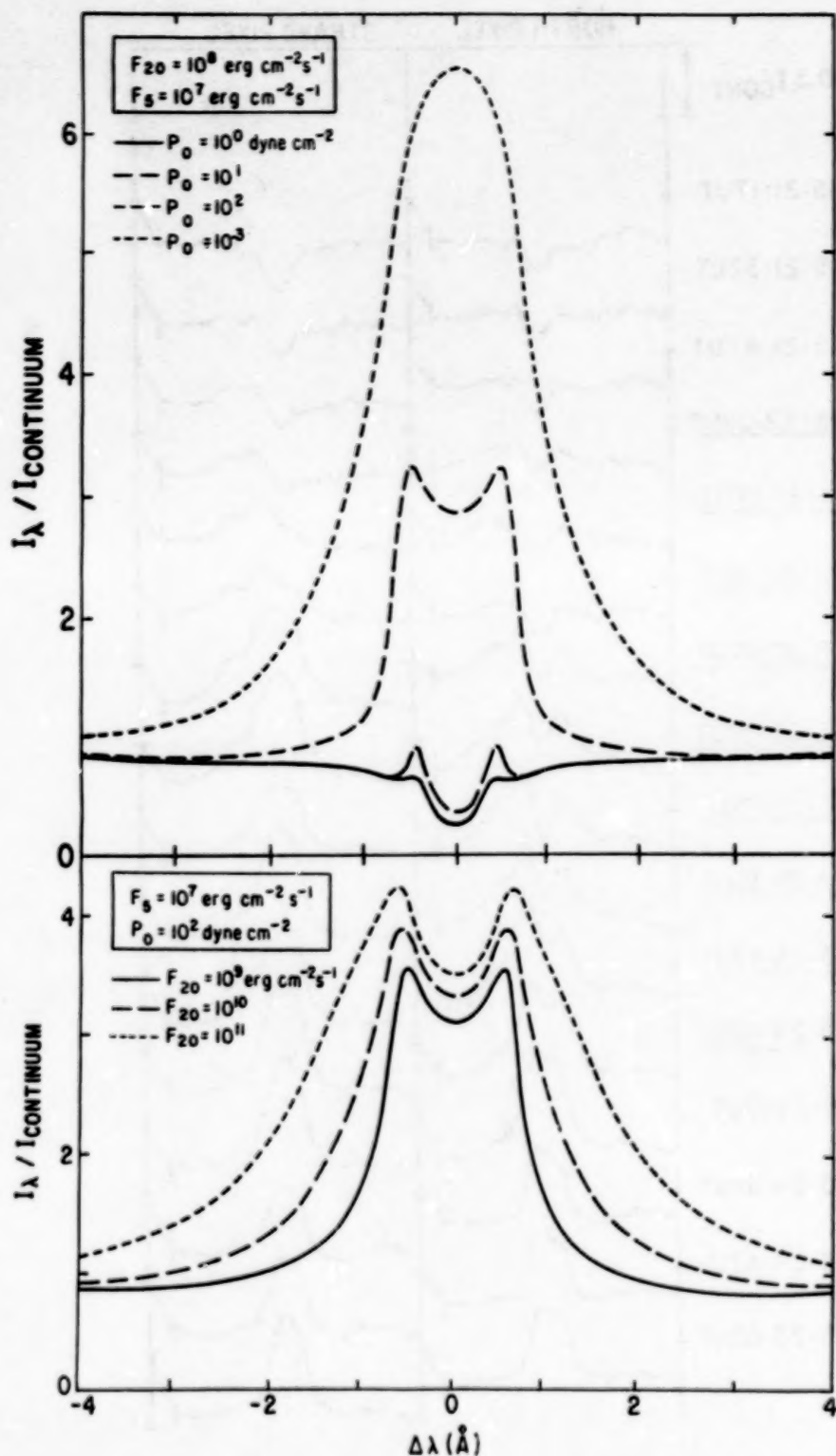
Figure 1. The effect of various physical processes on theoretical Hα profiles from hydrostatic model atmospheres. Upper panel: the effect of varying only coronal pressure P_0, holding the energy flux of nonthermal electrons F_{20} and the transition-region conductive flux F_5 fixed, showing the disappearance of the central reversal in the highest-pressure model. Lower panel: the effect of varying only F_{20}, holding P_0 and F_5 fixed, showing the appearance of Stark wings at high F_{20}. From Canfield, Gunkler, and Ricchiazzi (1984).
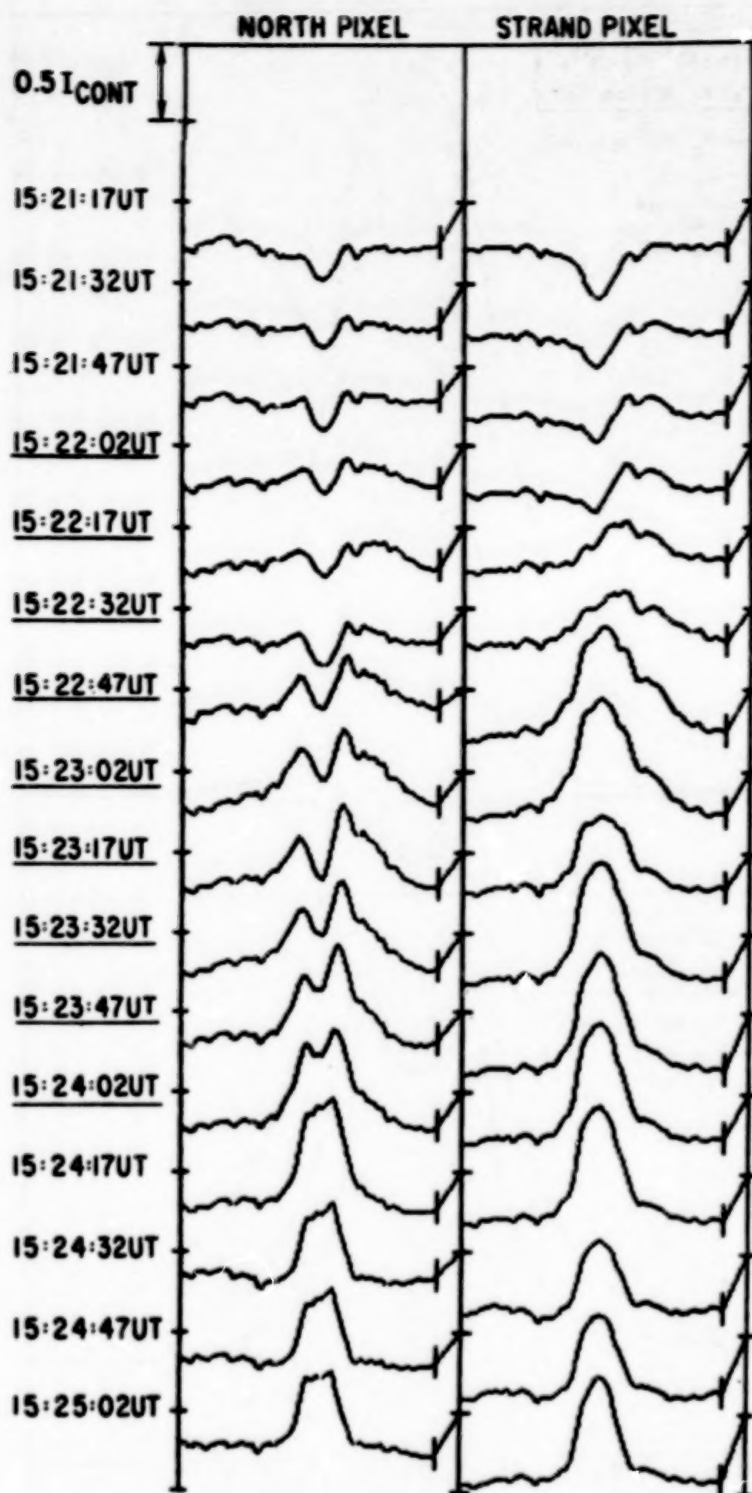
Figure 2. Observed Hα line profiles from two pixels of the flare of 1522 UT, 24 June 1980. Each column is a time sequence of profiles of a single pixel; the times given are those at which the spectrograph slit crossed the pixels shown. The spectral range of the profiles is Hα ± 4.8 Å, and the distance between tick marks on the vertical scale is half the quiet Sun continuum intensity. To correctly identify the time associated with each Hα spectrum, note the line segment to its right linking it to its quiet Sun continuum point. From Gunkler et al. (1984).
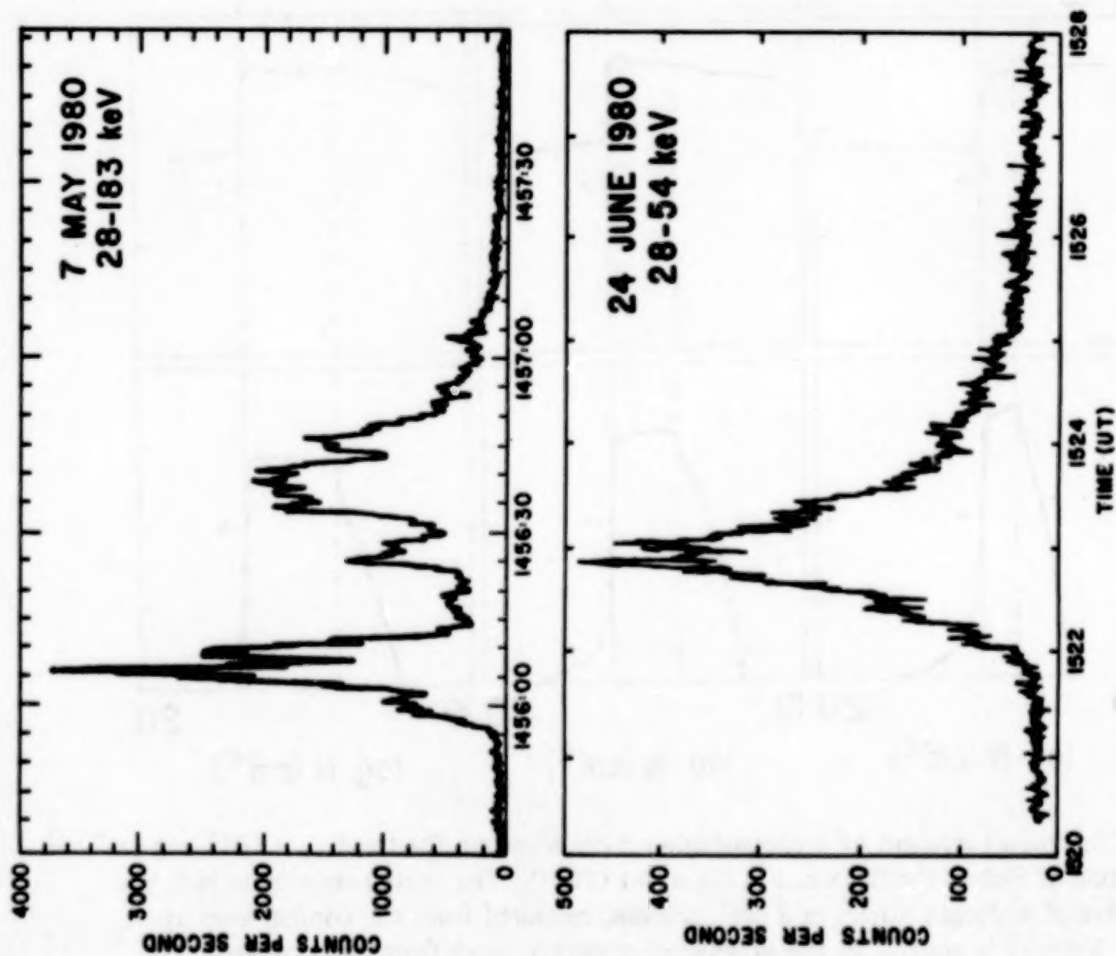
Figure 3. Hard X-ray count rates of the two 1980 flares observed well by Hα and X-ray imaging spectroscopy and times series of Hα profiles of a typical kernel pixel in each flare. The Hα spectral scales are the same as in Figure 2. From Canfield, Gunkler, and Kiplinger (1984).
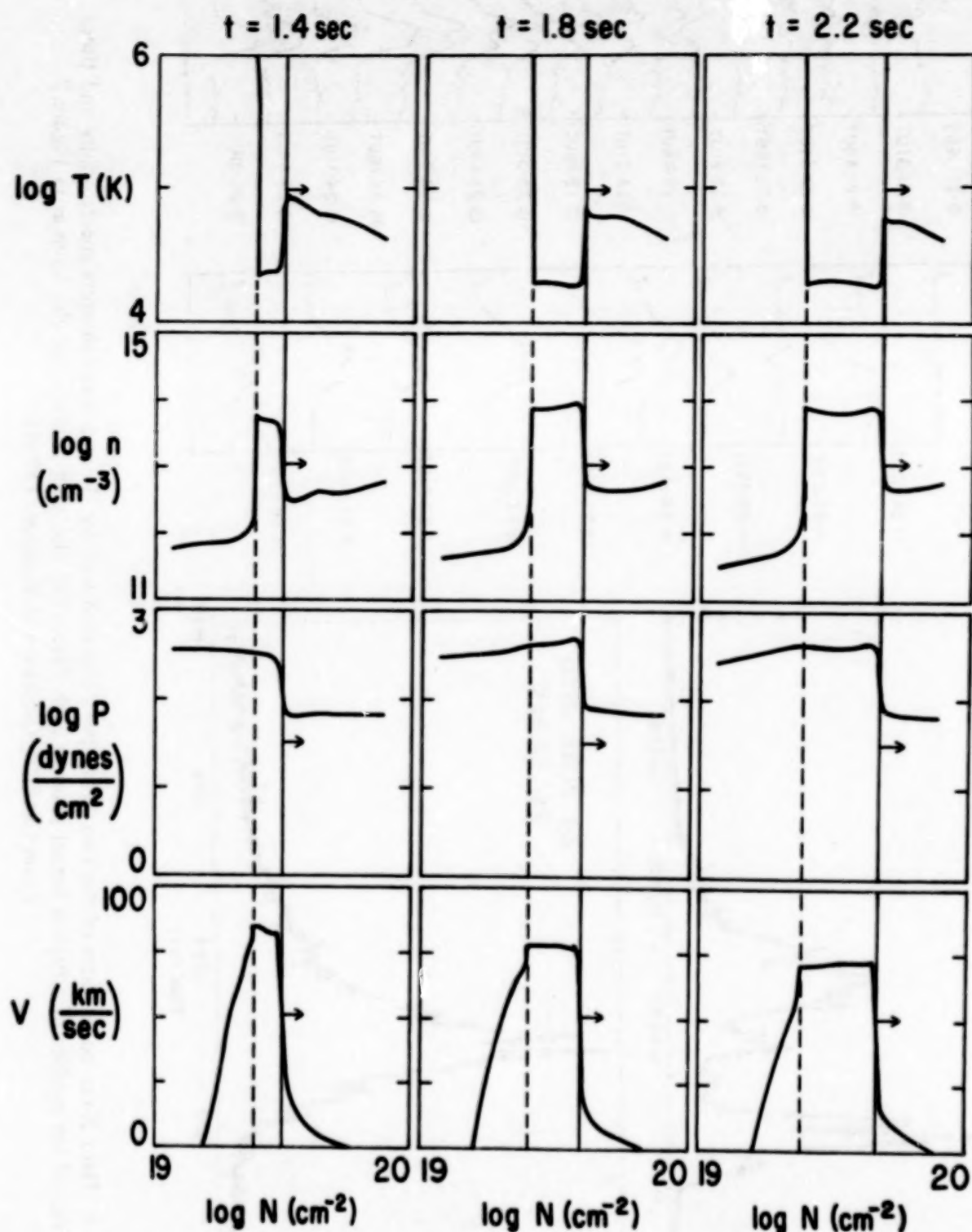
Figure 4. Computed evolution of a chromospheric condensation for the $F_{20} = 10^{11}$ erg cm^{-2} s^{-1} flare simulation of Fisher, Canfield, and McClymont (1985). The spatial coordinate N is the number of hydrogen nuclei in a cm^2 column, measured from the coronal loop apex. Velocity is positive in the downward direction, away from the loop apex.

130
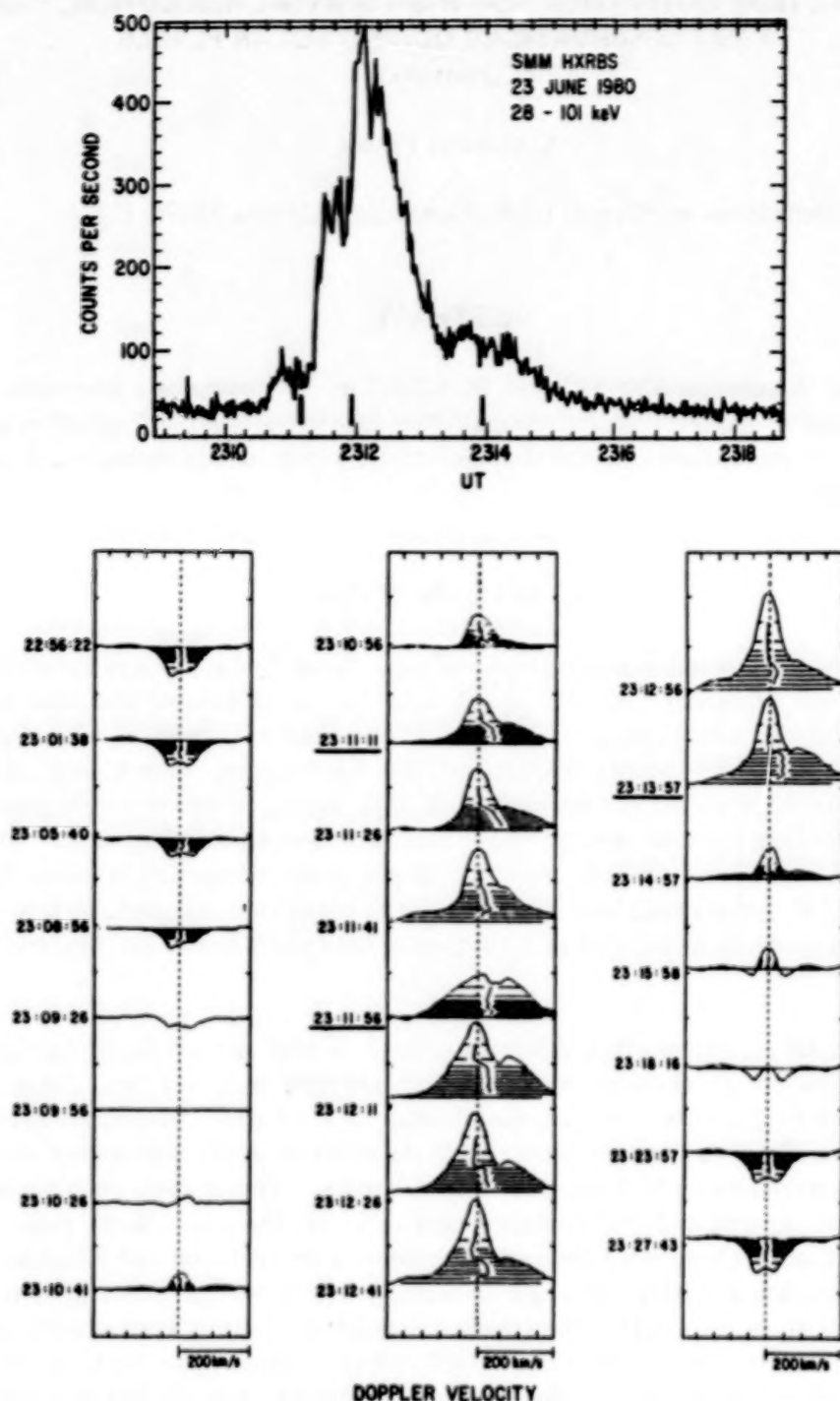
Figure 5. The relationship between (top) the hard X-ray count rate measured by the SMM Hard X-Ray Burst Spectrometer and (bottom) the Hα spectral excess (relative to its pre-impulsive Hα spectrum) and Doppler shift of one of the Hα kernel pixels of the flare of 2312,UT 23 June 1980. In difference spectra of sufficient amplitude a bisector is drawn at various intensity levels indicated by horizontal striations, centered within the most intense spectral feature. Both the hard X-ray count rate and the Hα Doppler shift show several episodes, whose occurrence is indicated by vertical bars (top panel) and underlined times of observation (bottom panel). From Canfield, Gunkler, and Kiplinger (1985).

THEORETICAL MOTIVATION FOR HIGH SPATIAL RESOLUTION, HARD X-RAY OBSERVATIONS DURING SOLAR FLARES
(Invited)

A. Gordon Emslie

Department of Physics, UAH, Huntsville, Alabana 35899, U.S.A.

ABSTRACT

We review the important role played by hard X-ray radiation as a diagnostic of impulsive phase energy transport mechanisms. It is argued that the sub-arc second resolution offered by an instrument such as the Pinhole/Occulter Facility (P/OF) can greatly increase our understanding of such mechanisms.

I. INTRODUCTION

For nearly three decades, observations of solar flares in hard X rays (photon energy $\epsilon \gtrsim$ 10 keV) have been vigorously pursued, in an attempt to understand the true nature of the impulsive phase of this astrophysical enigma. Although the total amount of energy emitted in hard X rays is a negligible ($\lesssim 10^{-5}$) fraction of the flare energy budget, this radiation is an extremely valuable diagnostic of the population of high energy electrons which produce the hard X rays, and, according to some models, these electrons constitute a dominant fraction of the energy released in the flare. Indeed, since the upper solar atmosphere is optically thin to all short-wavelength ($<$ optical) radiation, electrons must constitute the dominant form of energy transport there, and so the importance of high quality diagnostic hard X-ray observations becomes obvious.

It is generally accepted that solar flare hard X rays are produced by bremsstrahlung interaction of high energy electrons with ambient protons (see, however, Emslie and Brown, 1985). To investigate this farther, toward the ultimate goal of understanding the mechanisms that give rise to a solar flare, we must evaluate the characteristics of the high energy electron population through interpretation of its bremsstrahlung signature. This involves an investigation of the temporal, spectral, spatial, and polarization signatures of the hard X-ray radiation. Spectral information has been available since the earliest observations (Peterson and Winckler, 1959), with ever-increasing precision as higher resolution detectors with larger and larger detecting areas have been developed (Lin et al., 1981). The excellent statistics available from recent large detectors such as the Hard X-Ray Burst Spectrometer (HXRBS) onboard the Solar Maximum Mission (SMM) satellite have allowed studies of fine temporal structure ($\tau \approx 10$ ms) in flares to be made (Kiplinger et al., 1983). Polarization measurements are relatively sparse, yet have provided definite results (see Tramiel et al., 1984, and references therein) to be compared with model predictions.

One of the major problems of interpreting the above mentioned data has been the lack of spatial information on the source. This means that data represent a convolution over a wide extent of possible physical regimes, and it is extremely difficult, if not impossible, to deconvolve this spatial information. By way of an example, consider a model in which the (nonthermal) electrons responsible for the bremsstrahlung radiation are injected at the apex of a magnetic loop

and spiral about guiding magnetic field lines. The degree of curvature and torsion in the field line geometry will affect the predicted hard X-ray polarization from the entire source. Indeed, for a suitably inhomogeneous magnetic field, one expects the target-averaged electron velocity distribution to be nearly isotropic, leading to a near-zero observed polarization; however, over sufficiently localized regions of the source quite high polarization can result (see Leach et al., 1985). Similar problems exist in the interpretation of bremsstrahlung spectra in terms of a continuous injection thick target model (Brown, 1971): the physical processes operating on the electrons within the source volume can have as much of an effect on the emitted bremsstrahlung spectrum as does the electron spectrum at injection (Brown and MacKinnon, 1985). With spatial resolution these effects can be decoupled and the injected spectrum (with its associated constraints on the primary energy release process) better determined. It is thus clear that spatial resolution of hard X rays is essential for a better understanding of conditions in the impulsive phase of flares.

Imaging of solar flare hard X rays has so far been accomplished in three distinct ways. The Hard X-Ray Imaging Spectrometer (HXIS) on SMM observed solar hard X rays through multiple layers of collimator holes, with a large number of proportional counters (one per collimator channel) to record the data. This instrument yielded images of regions on the Sun in six energy bands spanning the range of 3.5 to 30 keV, with spatial resolution down to 8 arc s. The Solar X-Ray Telescope (SXT) onboard the Japanese Hinotori satellite used a rotating double-grid modulation collimator (see Makishima, 1982) to image the entire solar disk with a spatial resolution of order 10 arc s. Finally, use of stereoscopic views of behind-the-limb flaring regions (from different spacecraft) has yielded crude imaging in the form of a measure of the fraction of X-ray photons emitted above the occulting photospheric limb (Kane et al., 1979).

These data have traditionally been interpreted (see Hoyng et al., 1981; Brown et al., 1981) in terms of two distinct hard X-ray production models: the so-called "thermal" and "nonthermal" models. We refer the reader to numerous articles (e.g., Emslie and Rust, 1980; Brown and Smith, 1980; Emslie, 1983) for a description of these two canonical models and the physical differences between them. However, it is becoming increasingly obvious to modelers that neither of these simple models is really appropriate to actual flare conditions, with a suitable hybrid being employed frequently (e.g., Emslie and Vlahos, 1980). We therefore see that what is really required is a knowledge of the relative proportions of electrons with velocities much greater than the ambient thermal velocity ("nonthermal" electrons) to those with velocities of order of the thermal velocity. In fact, this article seems to be an appropriate place to lay this historical "thermal versus nonthermal" distinction to rest, and to turn our attention to the real unknown of the energetic electron problem – the electron phase-space distribution function $f^*(\underset{\sim}{r}, \underset{\sim}{v})$ and its evolution with time. Knowledge of $f^*(\underset{\sim}{r}, \underset{\sim}{v}, t)$ (electrons cm^{-3} (cm s^{-1})$^{-3}$) gives us not only the requirements on the acceleration region ($\underset{\sim}{r} = \underset{\sim}{0}$), but also the physics of the interaction of the energetic electrons with the ambient solar atmosphere. In the next section we will show how spatially resolved hard X-ray images can give us *direct* information on $f^*(\underset{\sim}{r}, \underset{\sim}{v}, t)$ and its derivatives, and so address both of these two areas of investigation. We will also discuss (Section III) theoretical and observational evidence that the behavior of $f^*(\underset{\sim}{r}, \underset{\sim}{v}, t)$ is at present poorly understood. In Section IV we summarize these results and look toward the P/OF as the logical next step in solar flare hard X-ray studies.

II. DETERMINATION OF THE ELECTRON PHASE SPACE DISTRIBUTION FUNCTION THROUGH SPATIALLY RESOLVED MEASUREMENTS OF HARD X-RAYS

Consider the observation of hard X rays from a "pixel" of a bremsstrahlung source. Let the volume of this pixel be V, the distribution of target protons within the source be $n_p(\underset{\sim}{r})$,

and the phase-space density of the bremsstahlung-emitting electrons be $f^*(\underset{\sim}{r}, \underset{\sim}{v}, t)$. For simplicity, we will here consider only the total X-ray yield from the pixel, and not its direction-ality or polarization properties. It is thus sufficient to work with the four-dimensional phase-space function $f(\underset{\sim}{r}, E, t)$ (electrons cm^{-3} erg^{-1}, where $E = 1/2\, m\, |\underset{\sim}{v}|^2$) and the isotropic non-relativistic Bethe-Heitler cross-section $Q_B(\epsilon, E)$ for calculations of the bremsstrahlung yield. With these simplifying assumptions, the flux of hard X-rays observed at the Earth will be

$$I(\epsilon, t + \Delta t) = \frac{1}{4\pi R^2} \int_{E=\epsilon}^{\infty} \left(\int_V f(\underset{\sim}{r}, E, t) n_p(\underset{\sim}{r}) d^3 \underset{\sim}{r} \right) v(E)\, Q_B(\epsilon, E)\, dE \text{ photons } cm^{-2}\, s^{-1}\, erg^{-1} \ , \quad (1)$$

where Δt is the light travel time from Sun to Earth and $R = 1$ AU. Following Brown (1971) we write

$$n_0 = \frac{1}{V} \int_V n_p(\underset{\sim}{r})\, d^3 \underset{\sim}{r} \tag{2}$$

and

$$\overline{f}(E, t) = \frac{1}{n_0 V} \int_V f(\underset{\sim}{r}, E, t) n_p(\underset{\sim}{r}) d^3 \underset{\sim}{r} \tag{3}$$

(the average value of f in the pixel, weighted with respect to n_p). Equation (1) then becomes

$$I(\epsilon, t + \Delta t) = \frac{n_0 V}{4\pi R^2} \int_{E=\epsilon}^{\infty} \overline{f}(E, t) v(E) Q_B(\epsilon, E) dE \ . \tag{4}$$

The formula may be straightforwardly inverted, as in Brown (1971), to give f(E,t) in terms of $I(\epsilon, t + \Delta t)$; we refer the reader to Equation (7) of Brown (1971) for the essential result. Here we wish to emphasize that *no assumptions regarding the origin of evolution of the electron distribution function* $f(\underset{\sim}{r}, E, t)$ have been made and that, if the pixel size is made sufficiently small that the averaging processes given by Equations (2) and (3) are redundant, then $f(\underset{\sim}{r}, E, t)$ can be *explicitly determined* from hard X-ray observations alone (with the proviso that the number of protons $n_0 V$ in the pixel must also be known). Thus hard X-ray observations of sufficiently good angular resolution allow us to trace the evolution of $f(\underset{\sim}{r}, E, t)$ throughout the source, fulfilling the dual scientific objectives of (a) determining the "injected" electron distribution $f(\underset{\sim}{0}, E, t)$, and (b) providing an evolutionary scenario for f throughout the target, against which to test theoretical transport models.

By way of illustration, let us calculate the predicted evolution of $f^*(\underset{\sim}{r}, \underset{\sim}{v}, t)$ in a model in which nonthermal electrons $(E \gg kT_e$, where k is Boltzmann's constant and T_e the ambient electron temperature) interact with a background plasma of uniform density n_0 by purely colli-sional processes. Let us further adopt a vertical geometry, so that $f^*(\underset{\sim}{r}, \underset{\sim}{v}, t)$ may be replaced by $g(z, E, t)$, where z is height in the source, and let us also assume a steady-state over timescales of interest, so that the t-dependence of g need not be considered explicitly. The bremsstrahlung yield from a pixel of height Δz centered on z then becomes

$$I(z,\epsilon) = \frac{n_0 A \Delta z}{4\pi R^2} \int_\epsilon^\infty g(z,E) \nu(E) Q_B(\epsilon,E) dE \ , \tag{5}$$

where A is the area of the vertical column imaged. Equation (5) can easily be inverted to give $g(z,E)$ in the manner of Brown (1971). By continuity of electron flux, however, we know that

$$g(z_1,E_1) \nu_1(E_1) \mu_1(E_1) = g(z_2,E_2) \nu_2(E_2) \mu_2(E_2) \ , \tag{6}$$

where z_1 and z_2 are different heights in the source and μ_1, μ_2 are the cosines of the pitch angles to the (vertical) guiding field lines, taken here to be single-valued functions of the respective energies E_1, E_2 (see below). In a purely collisional analysis, we have (Brown, 1972; Emslie, 1978)

$$\left. \begin{array}{l} E_1 = E_2 \left(1 + \dfrac{3K\Delta N}{\mu_2 E_2^2} \right)^{1/3} \\[4mm] \mu_1 = \mu_2 \left(1 + \dfrac{3K\Delta N}{\mu_2 E_2^2} \right)^{1/3} \end{array} \right\} \tag{7}$$

where $K = 2\pi e^4 \Lambda$, e being the electronic charge (e.s.u) and Λ the Coulomb logarithm, and $\Delta N = n_0(z_2 - z_1)$ is the intervening particle column density between the two levels. Substituting formula (7) into Equation (6) gives

$$g(z_2,E_2) = \left(1 + \frac{3K\Delta N}{\mu_2 E_2^2} \right)^{1/2} g \left[z_1, E_2 \left(1 + \frac{3K\Delta N}{\mu_2 E_2^2} \right)^{1/3} \right] \ . \tag{8}$$

The value of μ_2 appropriate to E_2 follows from the global equivalents of (7), viz. (Brown, 1972; Emslie, 1978)

$$\left. \begin{array}{l} E_2 = E_0 \left(1 - \dfrac{3KN}{\mu_0 E_0^2} \right)^{1/3} \\[4mm] \mu_2 = \mu_0 \left(1 - \dfrac{3KN}{\mu_0 E_0^2} \right)^{1/3} \end{array} \right\} \tag{7a}$$

where N is the total column density between the injection point ($E = E_0$) and the pixel in question. For a given injection pitch angle cosine μ_0 and prescribed pixel and energy E_2, the first relation of Equation (7a) gives implicitly the value of E_0; the second relation then gives $\mu_2 (\mu_0, E_2, N)$ for substitution in Equation (8).

Equation (8) is a theoretical prediction for the behavior of g, given the ambient density $n_0(z)$ and the injection pitch angle μ_0 of the electron beam. A corresponding, more complicated, result follows if the electrons are injected over a range of pitch angles μ_0. Either of these results can be compared with the forms of $g(z_2,E_2)$ and $g(z_1,E_1)$, deduced from inversion of Equation (5), in order to test whether a simple treatment of the beam dynamics in terms of collisional

135

scattering in the presence of a uniform magnetic field and suitable $n_0(z)$ is indeed appropriate. Other effects, such as collective processes and a non-uniform magnetic field, will modify Equation (8) in a way that can in principle be determined empirically through spatially resolved X-ray observations and Equations (4) and (6). In the next section we will briefly outline the existing evidence, both theoretical and observational, which suggests that Equation (8) is indeed an over-simplification, and that new input from high spatial resolution hard X-ray observations is required to better define the true relationship between the forms of $g(z,E)$ in different locations of the flare, and so the physics of electron transport in solar flare atmospheres.

III. EVIDENCE FOR NON-COLLISIONAL PROCESS AFFECTING ELECTRON TRANSPORT IN FLARES

In the additional presence of non-collisional processes the first of Equations (7) assumes the formal structure

$$E_1 = E_1(E_2, \Delta N; p_i) \quad , \tag{9}$$

where the p_i's are parameters of the electron distribution function and the ambient medium (e.g., temperature, electron/ion temperature ratio, magnetic field geometry, etc.). As pointed out in Section II, this relationship can in principle be determined through hard X-ray observations of sufficient quality at sufficiently high spatial resolution. However, there is already evidence to suggest that the collisional analysis leading to Equations (7) is inadequate and/or invalid. This evidence is both theoretical and observational.

Dealing first with the theoretical side, a purely collisional analysis assumes that (a) the magnetic field structure is uniform and that (b) collective effects can be ignored. Leach and Petrosian (1981) have analyzed the effect of a non-uniform magnetic field on the evolution of $g(z,E)$ and we refer the reader to that paper for details. Collective effects can be subdivided into two classes: coordinate-space and velocity-space. The former (coordinate-space) collective effect is that of the beam-neutralizing reverse current, which causes the beam electrons to lose energy sufficient to drive this reverse current through the finite resistivity of the ambient plasma. The electrical potential difference which each electron must overcome is given by $V = \int \eta j dz$, where η is the resistivity and j the beam current; the corresponding energy loss is $\Delta E = e \int \eta j dz$. Thus, the energy loss rate required to drive the reverse current is $\dot{E} = e \eta j \mu v = e \eta_0 j T_e^{-3/2} \mu v$. This loss rate differs from the collisional rate of $\dot{E} = K n_0 v/E$ (Emslie, 1978) in three basic ways: (1) dependence on the properties of the electron: $\dot{E} \propto E^{1/2}$ for reverse current ohmic heating, but $\dot{E} \propto E^{-1/2}$ for collisional heating, (2) dependence on the properties of the background atmosphere: there is a *temperature* dependence of $\dot{E}$ in the reverse current case, replacing a *density* dependence in the collisional case, (3) dependence on the parameters of the overall beam: $\dot{E}$ depends on the total beam current j in the reverse current case, a dependence which is totally absent in the collisional case. We therefore expect that, for high beam fluxes for which reverse current ohmic heating can become an appreciable contributor to the energetics of the beam electrons (Emslie, 1980, 1985), Equation (7) will be substantially modified to the form

$$E_1 = E_1(E_2, \Delta N; j, T_e) \quad , \tag{9a}$$

and this new form should be evidenced by the evolution of hard X-ray spectrum from pixel to pixel in the source.

Collective effects in velocity-space, as they apply to hard X-ray producing electron beams in flares, have only recently received attention. Emslie and Smith (1984) pointed out that, due to the inverse energy dependence of the collisional energy loss rate (see above), an injected flux of suprathermal electrons will develop a "hump" in velocity-space which moves to increasing energies with depth in the collisional target. For a sufficiently dense beam the hump eventually rises above the level of the background Maxwellian velocity distribution, creating an electron-electron two-stream unstable situation. Due to the great rapidity of microscopic collective plasma processes compared to the collisional lifetime of energetic electrons in plasmas of relevant densities, quasi-linear processes will effectively prevent this hump forming, so that instead a plateau of ever-increasing extent is formed as the electrons penetrate deeper into the target. The formula for the rate of change of the electron distribution function g is now a complicated function of g itself, and we must replace Equation (7) by

$$E_1 = E_1(E_2, \Delta N g(z_2, E_2)) \quad , \tag{9t}$$

the form of which has yet to be determined and represents work currently in progress (Emslie and McClements, 1985). It is possible that empirical determination of this form through spatially resolved hard X-ray measurements, as discussed in Section II, could increase our understanding of this collective process and how it operates.

We turn now briefly to the observational evidence for non-collisional processes affecting electron transport in flares. In an attempt to explain the stereoscopic data of Kane et al. (1979) in terms of a collisional model such as discussed above, Brown et al. (1983) found that the values of ΔN inferred from the "top pixel" (the unocculted part of the behind-the-limb flare, i.e., that part observed by both spacecraft — see Kane et al., 1979, for details) depended on the photon energy being observed — clearly an unphysical result pointing to the invalidity of the model (unless a suitably contrived energy-dependent pitch angle distribution of injected electrons was involved). Further, in an event discussed by Kane (1983; his Figure 7), the inferred value of the unocculted ΔN *rises* when determined using observations at one photon energy and *falls* when using observations at another. This is strongly indicative that a simple collisional model is inadequate.

IV. DISCUSSION AND CONCLUSIONS

We have seen in the previous two sections that our knowledge of electron energy transport in solar flares is at present quite possibly poorly understood, both from theoretical and observational standpoints, and how, in principle, hard X-ray observations with sufficiently fine spatial resolution can help to increase our understanding in this area.

Present hard X-ray imaging data, from both HXIS (SMM) and SXT (Hinotori), is not of a high enough quality to be of great aid in such an investigation. Indeed, there is great controversy over the basic interpretation of the images hitherto obtained. For example, Duijveman et al. (1982) claim to have observed the "footpoint" signature of precipitating nonthermal electrons in a flare on 5 November 1980. However, MacKinnon et al. (1985) claim that these "footpoints," although definitely representing real enhancements of emission in localized areas, may be simply due to the line of sight volume along a vertical column through the ends of a loop being greater than that along a similar column at the apex of the loop (see also Fennelly and Emslie, 1985). In addition, the "footpoint" spectra observed by HXIS are inconsistent with (lower than) the

extrapolated Hard X-Ray Burst Spectrometer (HXRBS) spec⁺ ₁ for the flare as a whole, implying that the "footpoint" emission is not the dominant component at HXIS energies. The need for statistically sound hard X-ray measurements at fine spatial evolution is therefore apparent, if only to unambiguously interpret the images obtained. For the ana.ysis of Section II we need hard X-ray spectra spanning as wide a range of photon energies as possible, with spatial resolution of order 1 arc second or better. (The reason for a wide energy survey is because of the possibly different nature of energy loss processes operating in different electron energy ranges — see Section III.) As discussed elsewhere in this volume, the Pinhole/Occulter Facility (P/OF) is indeed capable of such measurements and therefore represents the logical next step in solar hard X-ray observation.

REFERENCES

Brown, J. C., 1971, *Solar Phys.*, *18*, 489.

Brown, J. C., 1972, *Solar Phys.*, *26*, 441.

Brown, J. C., Carlaw, V. A., Cromwell, D., and Kane, S. R., 1983, *Solar Phys.*, *88*, 281.

Brown, J. C., Hayward, J., and Spicer, D. S., 1981, *Astrophys. J. (Letters)*, *245*, L91.

Brown, J. C. and MacKinnon, A. L., 1985, *Astrophys. J. (Letters)*, *292*, L31.

Brown, J. C. and Smith, D. F., 1980, *Rep. Prog. Phys.*, *43*, 125.

Duijveman, A., Hoyng, P., and Machado, M. E., 1982, *Solar Phys.*, *81*, 1_1.

Emslie, A. G., 1978, *Astrophys. J.*, *224*, 241.

Emslie, A. G., 1980, *Astrophys. J.*, *235*, 1055.

Emslie, A. G., 1983, *Solar Phys.*, *86*, 133.

Emslie, A. G., 1985, *Solar Phys.*, in press.

Emslie, A. G. and Brown, J. C., 1985, *Astrophys. J.*, *295*, 648.

Emslie, A. G. and McClements, K. G., 1985, in preparation.

Emslie, A. G. and Rust, D. M., 1980, *Solar Phys.*, *65*, 271.

Emslie, A. G. and Smith, D. F., 1984, *Astrophys. J.*, *279*, 882.

Emslie, A. G. and Vlahos, L., 1980, *Astrophys. J.*, *242*, 359.

Fennelly, J. A. and Emslie, A. G., 1985, in preparation.

Hoyng, P., and 11 co-authors, 1981, *Astrophys. J. (Letters)*, *246*, L155.

Kane, S. R., 1983, *Solar Phys.*, *86*, 355.

Kane, S. R., Anderson, K. A., Evans, ᵛ ⌐., Klebesadel, R. W., and Laros, J., 1979, *Astrophys. J. (Letters)*, *233*, L151.

Kiplinger, A. L., Dennis, B. R., Emslie, A. G., Frost, K. J., and Orwig, L. E., 1983, *Astrophys. J. (Letters)*, *265*, L99.

Leach, J., Emslie, A. G., and Petrosian, V., 1985, *Solar Phys.*, *96*, 331.

Leach, J. and Petrosian, V., 1981, *Astrophys. J.*, *251*, 781.

Lin, R. P., Schwartz, R. A., Pelling, R. M., and Hurley, K. C., 1981, *Astrophys. J. (Letters)*, *251*, L109.

MacKinnon, A. L., Brown, J. C., and Hayward, J., 1985, *Solar Phys.*, in press.

Makishima, K., 1982, *Hinotori Symposium on Solar Flares*, p. 120.

Peterson, L. E. and Winckler, J. R., 1959, *J. Geophys. Res.*, *64*, 697.

Tramiel, L. J., Chanan, G. A., and Novick, R., 1984, *Astrophys. J.*, *280*, 440.

THE ROLE OF HIGH RESOLUTION OBSERVATIONS IN DETERMINING ENERGY RELEASE AND TRANSPORT PROCESSES

Dean F. Smith

Berkeley Research Associates, Berkeley, CA 94701
and
Department of Astrophysical, Planetary and Atmospheric Sciences,
University of Colorado, Boulder, CO 80302

With present observations from the Solar Maximum Mission and Hinotori, we are seeing a very selective sample of spatially large flares in the soft part (10 to 50 keV) of the hard X-ray spectrum. The spatial resolution is at best 5600 km with a corresponding time resolution of 4.5 s for adequate count statistics. This resolution gives rise to the following problems: We cannot resolve the minor radii of the loops involved or tell where and how the energy release occurs. The manner in which loops interact and the relationship between the soft and hard ($\gtrsim 100$ keV) parts of hard X-rays remains elusive. We cannot see how energy propagates in most cases.

Thus it is desirable to determine the minimum increase in spatial and temporal resolution required to solve these problems. Spatially we need to resolve the minor radius of a small loop which is about 800 km or 1 arc s. Upper limits to observed speeds of conduction fronts and shocks are ~ 2000 km s^{-1} with theoretical limits running about a factor of 2 higher. Thus, a compatible minimum time resolution is in the range of 0.2 to 0.4 s. With these spatial and temporal resolutions, sufficient count statistics are required to go up to ~ 120 keV with a sufficient number of energy bands to obtain spectra.

Before noting some of the results to be expected with these resolutions, we briefly consider some recent results on energy transport which are described in detail in Smith (1985a). For the past several years starting with Brown, Melrose, and Spicer (1979) and Smith and Lilliequist (1979) there has been some question as to what extent a thermal hard X-ray source could be more efficient than a nonthermal thick-target source. The laser fusion community has devoted a considerable amount of effort to the problem of heat transport in steep temperature gradients (e.g., Campbell, 1984). The results of these studies have shown that the Spitzer-Harm conductivity has a very narrow range of applicability. In terms of the mean free path of the bulk thermal electrons

$$\lambda_s = \frac{K^2 T_e^2}{Z \pi e^4 n_e \ln\Lambda} \quad , \tag{1}$$

and the temperature scale height L, the condition for the applicability of Spitzer-Harm conductivity, is

$$\lambda_s/L < 10^{-3} \quad . \tag{2}$$

Here T_e and n_e are the electron temperature and density, respectively, Z is the ionic charge and $\ln\Lambda$ is the Coulomb logarithm. When condition (2) is violated, which can be determined using

$$\lambda_s/L = 6.31 \times 10^9 \ |q_{SH}| \ T_e^{-3/2} \ n_e^{-1} \quad , \tag{3}$$

where q_{SH} is the Spitzer-Harm conductivity, the actual conductivity q should be calculated from the following table for hydrogen (Z = 1):

TABLE 1. HEAT FLUXES FOR DIFFERENT λ_s/L

λ_s/L	q/q_{SH}	q/q_{FS}
0.0010	0.9998	0.0030
0.0032	0.9706	0.0094
0.010	0.8351	0.0251
0.032	0.5849	0.0564
0.10	0.3792	0.1142
0.32	0.2251	0.2169
1.00	0.1235	0.3718

Here $q_{FS} = n_e m_e v_e^3$ (v_e = electron thermal velocity) is the free streaming heat flux.

The physics in the reductions to q_{SH} in Table 1 is the following: Spitzer-Harm conductivity neglects the presence of fast tail electrons with mean free paths $\lambda_f \gg L$. Thus it overestimates the heat flux because it does not take into account the fact that these electrons cannot contribute to the local transport of heat. They do contribute to the global heat transport by depositing heat far beyond the temperature gradient. For most astrophysical applications where local values of the transport coefficients are important, it is sufficient to use Equation (3) and Table 1.

The effect of employing these results in thermal models for hard X-ray sources is the following (Smith, 1985a): The conduction fronts formed now travel at $\sim 5c_s$, where c_s is the ion-acoustic speed and for energy inputs up to 6.4×10^3 erg cm^{-3} s^{-1} (equivalent to the conversion of a 400 G field every second into heat) the maximum T_e reached is 10^8 K. Thus a thermal hard X-ray source can only be effective in the soft part of the hard X-ray spectrum. The hard part of the spectrum must be due to accelerated electrons. A possible acceleration scenario is given in Smith (1985b). By separately following the hard and soft parts of the hard X-ray spectrum we shall be able to test these theoretical results and thus determine the mode of energy propagation. This exercise will probably be most unambiguous for limb flares and theoretical support of this nature will be useful.

With the above desired resolutions we shall be able to determine where the energy release occurs and, with comparable optical and UV data to ascertain the preflare energy storage, to determine whether coronal storage is sufficient or energy must be transported from the photosphere. The role of the interaction of loops in this release and in particular acceleration should also become clear.

REFERENCES

Brown, J. C., Melrose, D. B., and Spicer, D. S., 1979, *Astrophys. J.*, *228*, 592.
Campbell, P. M., 1984, *Phys. Rev. A.*, *30*, 365.
Smith, D. F., 1985a, *Astrophys. J.*, submitted.
Smith, D. F., 1985b, *Astrophys. J.*, *288*, 801.
Smith, D. F. and Lilliequist, C. G., 1979, *Astrophys. J.*, *232*, 582.

WHY P/OF SHOULD LOOK FOR EVIDENCES OF OVER-DENSE STRUCTURES IN SOLAR FLARE HARD X-RAY SOURCES

Donald F. Neidig
Air Force Geophysics Laboratory, National Solar Observatory

Sharad R. Kane and J. J. Love
Space Sciences Laboratory, University of California, Berkeley

E. W. Cliver
Air Force Geophysics Laboratory, Hanscom Air Force Base

ABSTRACT

White-light and hard X-ray (HXR) observations of two white-light flares (WLFs) show that *if* the radiative losses in the optical continuum are powered by fast electrons directly heating the WLF source, then the column density constraints imposed by the finite range of the electrons requires that the WLF consist of an *over-dense region* in the chromosphere, with density exceeding 10^{14} cm^{-3}. Thus, we recommend that P/OF search for evidences of over-dense structures in HXR images obtained simultaneously with optical observations of flares.

I. SUMMARY OF CALCULATIONS

As a working hypothesis, we adopt a classical thick-target model, whereby nonthermal electrons are accelerated in a low-density coronal region and subsequently thermalized in the denser layers of the chromosphere. In the following steps we use optical and HXR data for two well-observed flares, 1 July 1980 and 24 April 1981; the calculated results are shown in Table 1.

a. The observed power (P_{WL}) in the optical continuum at the peak of the WLF was derived from measurements made with the Multiple-Band Polarimeter at Sacramento Peak (Neidig and Cliver, 1983; Kane et al., 1985).

b. The fast electron power loss spectrum (of the form $P(E) = AE^{-\delta}$, where E is the electron energy) was calculated from the associated HXR burst, assuming a thick-target model, at the time of the WLF peak power (Batchelor, 1984; Kane et al., 1985), and the electron energy E_0 above which the power in thick-target loss is equal to white-light power was then derived for both flares. Note that the values for E_0 obtained in this way are upper limits on the low-energy cut-off actually required under realistic conditions, as we assume (1) the electrons are depositing their energy only within the WLF area, and (2) all the energy in electrons with $E > E_0$ is converted into white-light emission.

c. The column density n_c that can be traversed by electrons of energy E_0 was calculated from the equations given by Bai (1982). Because the values for E_0 adopted in the previous step are upper limits, it follows that the column density n_c will be an upper limit on the range of the electrons that carry sufficient power to the WLF. If we take the electron trajectory to be normal to the sun's surface and with zero pitch angle, and denote the height (above $\tau_{5000} = 1$) of the acceleration site as z_1 and the height where the fast electrons are stopped as z_0, then

$$\int_{z_0}^{z_1} N(z)dz = n_c \quad ,$$

where $N(z)$ represents the vertical density distribution in the solar atmosphere. If we assume that the density at the acceleration site is $\leq 10^{12}$ cm^{-3} and $N(z)$ is similar to the density distribution in the quiet sun atmosphere, we can easily determine the electron stopping height z_0 (note that for the electron energies considered here, z_0 is not sensitive to the selection of z_1 as long as $N(z_1) \leq 10^{12}$ cm^{-3}).

d. Next, we considered the minimum amount of atmospheric material that could give rise to the WLF; i.e., we assumed H_{fb} emission at 10^4 K in an optically thin slab. In this way we obtained a lower limit on the linear emission measure, $N_e^2 \Delta z$, required to produce the observed WLF intensity. A more realistic lower limit on $N_e^2 \Delta z$ would actually be larger than the values listed in Table 1, as the observations of the peak WLF intensities were undoubtedly affected by seeing and finite spatial resolution of the telescope. Note that the adopted emission measures are considerably larger than the entire integrated atmospheric emission measures $\int_{z_0}^{\infty} N^2(z)dz$.

e. The minimum density, N_{WLF}, in the WLF source was then estimated from the quantities in steps (c) and (d), i.e., $N_{WLF} = N_e^2 \Delta z / n_c$.

II. CONCLUSIONS AND DISCUSSION

The calculations summarized above show that it is not possible to obtain the required WLF emission measures within the column densities allowed by the finite range of the energetic electrons. Thus, we conclude that *if* WLFs are powered by fast electrons, in the sense of a classic thick-target model, then the solar atmospheric structure must be modified in such a way as to produce a steeper density gradient than is found in the quiet sun. This could imply (1) the existence of an *over-dense* region formed in the flare atmosphere, or (2) the partial *removal* of the atmospheric mass overlying the denser regions of the deep chromosphere (but probably not via evaporation, as the mass might still remain in a column between the WLF and the electron acceleration site). Further, we find that the density in the WLF, if heated directly by fast electrons, must exceed 10^{14} cm^{-3}.

These conclusions are based on several assumptions, each of which was chosen to give the fast electron heating model every chance of success. Furthermore, the calculations were made at the time of the peak white-light emission; if, on the other hand, we consider the maximum E_0 able to satisfy the power requirements at all times during the 24 April flare, we find that E_0 must be decreased from 85 keV to 25 to 40 keV! The result is that the conclusion reached above is even more strongly reinforced.

WLF structures are sometimes quite small and short-lived (see Figure 1) and, therefore, if they are associated with electron bombardment, high-spatial resolution observations in HXR are required in order to study them. A major goal of P/OF science should be to obtain HXR images of WLFs, simultaneous with optical observations, and to look for evidences of over-dense structures.

REFERENCES

Bai, T., 1982, *Astrophys. J., 259,* 341.
Batchelor, D. A., 1984, Private Communication.
Kane, S. R., Love, J. J., Neidig, D. F., and Cliver, E. W., 1985, *Astrophys. J. (Letters), 290,* L45.
Neidig, D. F. and Cliver, E. W., 1983, AFGL-TR-83-0257, Hanscom AFB, MA.

TABLE 1. CALCULATED PARAMETERS FOR TWO WLFs

	1 July 1980	24 April 1981
Observed power, P_{WL}, in the optical continuum (erg s^{-1})	4.5×10^{27}	7.0×10^{27}
Electron energy cut-off E_0 (keV)	37	85
Electron range $n_c(E_0)$ (cm^{-2})	2.7×10^{20}	1.4×10^{21}
Electron stopping height z_0 (km)	1100	875
Emission measure, $N_e^2 \Delta z$, in the white-light source (cm^{-5})	5.3×10^{34}	1.6×10^{35}
Integrated atmospheric emission measure above z_0 (cm^{-5})	1.1×10^{33}	3.5×10^{34}
Minimum density in the white-light source (cm^{-3})	2.0×10^{14}	1.1×10^{14}

Figure 1. White-light flare of 4 June 1982, 1332 UT, photographed at 3610 Å. Small kernels show significant intensity variations in timescales of a few tens of seconds. (Photograph from National Solar Observatory, Association of Universities for Research in Astronomy, Inc.)

THE HEATING OF THE THERMAL PLASMA WITH ENERGETIC ELECTRONS IN SMALL SOLAR FLARES

Hua-An Lin and Robert P. Lin

Space Sciences Laboratory, University of California, Berkeley

The energetic electrons deduced from hard X-rays in the thick target model may be responsible for heating of soft X-ray plasma in solar flares. Datlowe (1975) has shown from OSO-7 studies that if a cutoff of 10 keV is assumed, the total electron energy is comparable to the thermal plasma energy. However, (1) the soft X-ray emission often appears to begin before the hard X-ray burst, (2) in about one-third of flares there is no detectable hard X-ray emission, and (3) for most events the energy content (assuming constant density) of soft X-ray plasma continues to rise after the end of the hard X-ray burst. To understand these problems we have analyzed the temporal relationship between soft X-rays and hard X-rays for 20 small events observed by ISEE-3 during 1980. One example is shown in Figure 1. The start of soft X-ray and hard X-ray bursts is defined as the time when the counting rates of the 4.8 to 5.8 keV and 25.8 to 43.2 keV channels, respectively, exceed the background by one standard deviation.

Problem (1) mentioned above may be due to the low sensitivity and high background of the solar hard X-ray detector. We find that Δt_{SH}, the difference in start times between the soft X-ray and hard X-ray burst, and $\Delta F_H/\Delta t_{HM}$, the rate of increase of the hard X-ray flux, are anti-correlated with a linear correlation coefficient of 0.70 (Figure 2). This result suggests that the hard X-ray burst may start simultaneously with the soft X rays, and the faster F_H grows, the shorter the time till F_H exceeds the hard X-ray detector background. In some flares the peak flux of hard X rays may not exceed the detector background rate, leading to an apparent absence of hard X-ray emission.

The thermal energy ϵ is proportional to $\epsilon \cdot n_e = 3KT \cdot EM$ for n_e = constant and to $\epsilon \cdot V^{\frac{1}{2}} = 3KT \cdot EM^{\frac{1}{2}}$ for V = constant. Figure 1 shows that t_N, the time of maximum thermal energy for n_e = constant, is later than t_V, the time for V = constant. We have obtained Δt_N, Δt_V and τ_H (Figure 1) from each event. Figure 3 shows that the thermal energy reached maximum before the end of hard X rays for about 30% of the analyzed events for n_e = constant, and for about 65% for V = constant. On average, the Δt_N is larger by 20 to 30 s than Δt_V. Thus, the temporal agreement [problem (3)] may be greatly improved if the volume rather than the density of the thermal plasma region is assumed constant in the flare process. In fact, the observations show that the volume of soft X-ray region varies relatively little compared with the density for compact flares (Moore et al., 1980).

Energetic electrons may provide energy to the soft X-ray plasma region in two ways: (1) chromospheric evaporation by the energy deposition of the higher energy electrons, which mainly increases the emission measure of the thermal plasma; and (2) energy deposition of lower energy electrons directly into the thermal plasma region, which mainly increases the temperature. The increase of the thermal energy for V = constant can be split into two components $\Delta\epsilon(\sqrt{EM})$ and $\Delta\epsilon(T)$, due to the increase in emission measure and in temperature, respectively. Since $\epsilon = 3KV^{\frac{1}{2}} \cdot T\sqrt{EM}$, we obtain $\Delta\epsilon \approx 3KV^{\frac{1}{2}} \cdot T \cdot \Delta\sqrt{EM} + 3KV^{\frac{1}{2}} \cdot \sqrt{EM} \cdot \Delta T$, where the first term is $\Delta\epsilon(\sqrt{EM})$ and the second $\Delta\epsilon(T)$, and $\overline{T}$ and $\sqrt{EM}$ are average values. We compute the ratio $\Delta\epsilon(\sqrt{EM})/\Delta\epsilon(T)$ during the phase of increasing temperature when the energy loss of thermal plasma by heat conduction and radiation may be ignored. This ratio and γ_{MIN}, the lower hard

X-ray spectral index, are anti-correlated (Figure 4). The correlation coefficient between $\ln(\Delta e(\sqrt{EM})/\Delta e(T))$ and γ_{MIN} is 0.62. This result indicates that as the proportion of higher energy electrons increases, the fraction of the thermal energy contributed by the emission measure correspondingly rises, and vice versa.

From an analysis of 20 small events, we conclude that if the volume rather than the density of the thermal plasma region is assumed constant in the flare process, energetic electrons could heat the soft X-ray plasma.

REFERENCES

Datlowe, D. W., 1975, in *Solar Gamma-, X-, and EUV Radiation* (ed. by S. R. Kane), IAU Symposium No. 68, p. 191.
Moore, R., McKenzie, D. L., and 14 co-authors, 1980, in *Solar Flares* (ed. by Peter A. Sturrock), Colorado University Press, Boulder, p. 341.
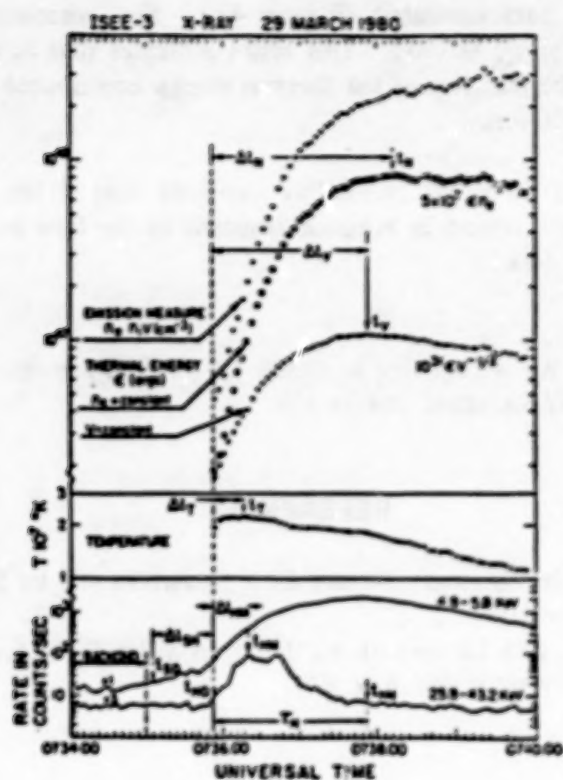
Figure 1. The temporal evolution of the solar flare of 29 March 1980
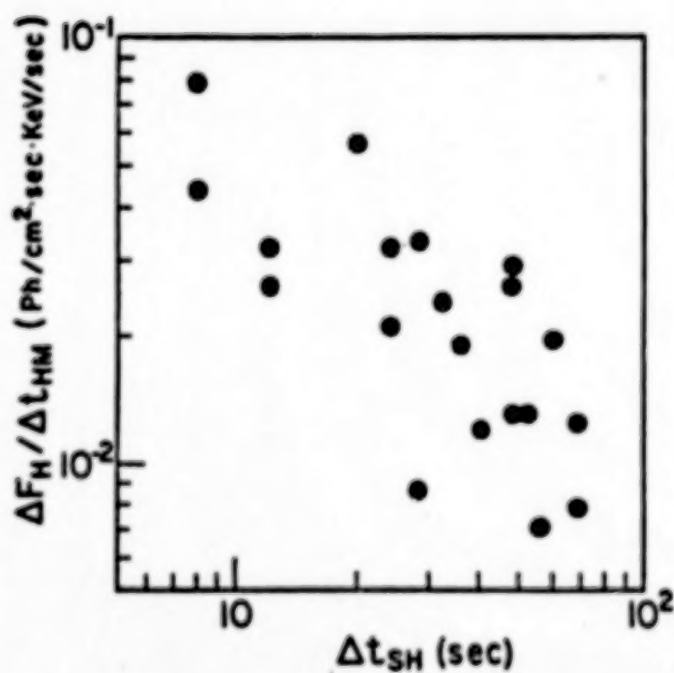and the definitions of various times.

Figure 2. Rate of increase of hard X-ray flux versus the difference in
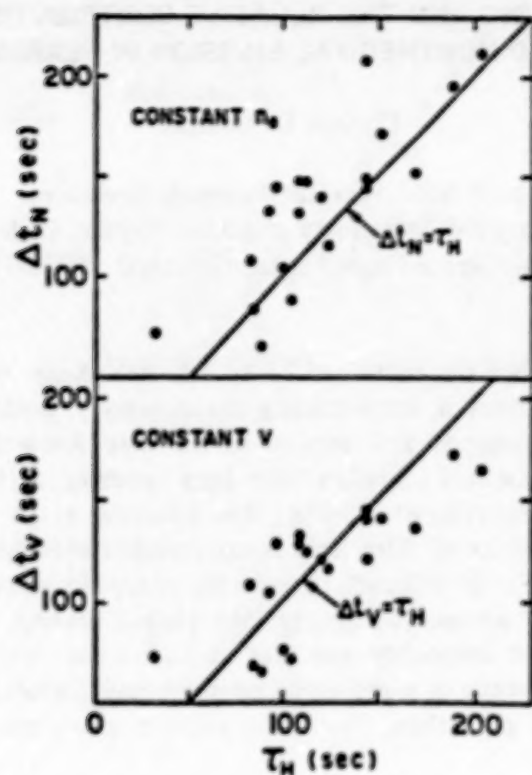start times between soft and hard X-ray bursts.

148

Figure 3. The relationship between the time when the thermal energy reached maximum and the duration of hard X-rays. Top panel: for constant density; bottom panel: for constant volume.
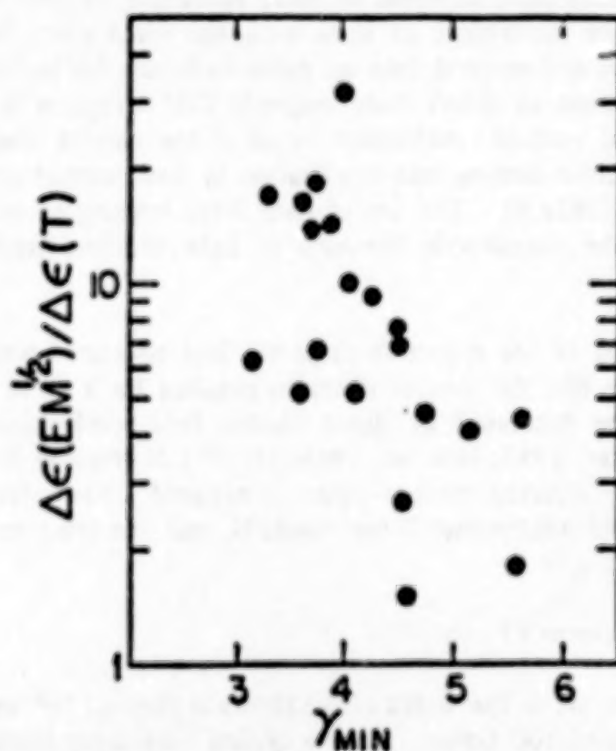

Figure 4. The ratio of the increase in thermal energy caused by increasing emission measure and by increasing temperature, versus the lowest hard X-ray spectral index.

HARD X-RAY IMAGING AND THE RELATIVE CONTRIBUTION OF THERMAL AND NONTHERMAL EMISSION IN FLARES

Gordon D. Holman

NAS/NRC Resident Research Associate
Laboratory for Astronomy and Solar Physics, Code 682,
NASA Goddard Space Flight Center, Greenbelt, MD 20771, U.S.A.

The question of whether the impulsive 25 to 100 keV X-ray emission from solar flares is thermal or nonthermal has been a long-standing controversy. Both thermal and nonthermal (beam) models have been developed and applied to the hard X-ray data. It now seems likely that both thermal and nonthermal emission have been observed at hard X-ray energies. The Hinotori classification scheme (Tsuneta, 1984), for example, is an attempt to associate the thermal/nonthermal characteristics of flare hard X-ray emission with other flare properties. From a theoretical point of view, it is difficult to generate energetic, nonthermal electrons without dumping an equal or greater amount of energy into plasma heating. On the other hand, any impulsive heating process will invariably generate at least some nonthermal particles. Hence, strictly speaking, although thermal or nonthermal emission may dominate the hard X-ray emission in a given energy range for a given flare, there is no such thing as a purely thermal or nonthermal flare mechanism.

For a hard X-ray instrument covering a wide range of photon energies, such as the HXRBS on SMM, it would not be surprising to find both thermal and nonthermal processes contributing to the X-ray emission from a given flare. Hence, instead of simply applying a specific thermal or beam model to the hard X-ray data, it would be more instructive to use combined flare data to try to determine the relative importance of these emissions for a given flare. Combined hard X-ray and microwave images and spectral data are particularly valuable for this. Since the energy released in flares is understood to derive from magnetic field energy, it is most likely that the impulsive phase heating and particle acceleration occur in the current channels associated with these magnetic fields. Electron heating and acceleration in these current channels have recently been studied by Holman (1985a,b). The use of hard X-ray imaging to determine the thermal/nonthermal character of the emission is discussed in light of these results in the following paragraphs.

Simple considerations of the induction magnetic field associated with a current of accelerated electrons have shown that the flux of electrons required for a 25 to 100 keV nonthermal hard X-ray burst cannot be generated by direct electric field acceleration in a single current channel (Hoyng, 1977; Spicer, 1983; Holman, 1985a,b). If this emission is to be nonthermal, a large number of oppositely directed current sheets is required. The relationship between the electron flux needed for the nonthermal X-ray burst, N, and the minimum number of current sheets required for the burst, s, is

$$N = 10^{30} \, s w_9 B_2 \text{ electrons s}^{-1}$$

(see Holman, 1985b), where w_9 is the width of the sheets in units of 10^9 cm and B_2 is the magnetic field strength in units of 100 Gauss. Since a typical hard X-ray burst requires 10^{35} electrons s^{-1} for $B = 300$ G and $w = 3 \times 10^9$ cm, a minimum of 10^4 current sheets is required. The thickness of each sheet is generally less than 1 km. Imaged hard X rays can be used to better determine N and estimate an upper limit for w.

Although a large number of current sheets makes the generation of the nonthermal X-ray emission possible, the heating of the thermal plasma in the acceleration region is also increased. Hard X-ray imaging in different energy bands can be used to determine the relative importance of the thermal and nonthermal emissions at different photon energies, and how the emission is distributed within the flaring region. Simultaneous second-of-arc resolution soft X-ray images would also be useful for determining how thermal energy (both from direct Joule heating in the acceleration region and the evaporation of chromospheric material by the nonthermal beam) is distributed within the flaring region. Hard X-ray images and spectra will also be valuable for determining if the transition from impulsive to gradual emission observed in many flares represents a transition from nonthermal to thermal emission, as is widely believed.

An interesting test for multiple current sheets with an X-ray imager would be to search for small-scale spatial structure in the emission region. Although the individual sheets would not be resolvable, spatial variations in the X-ray emission due to variations in the physical properties of the individual sheets may be detectable. This may be detectable in the thick-target, nonthermal emission region if the accelerated electrons from the individual sheets remain well separated, but is more likely to be detected in the thermal emission from the acceleration region.

A large number of current sheets is not required when the 25 to 100 keV X-ray emission is thermal. Holman (1985b) has shown that a thermal hard X-ray burst can be generated by a single current sheet within a flaring region. The energetic electrons required for a nonthermal microwave burst can also be accelerated within the single current sheet. Although the 25 to 100 keV X rays from the single sheet cannot be nonthermal, a transition to nonthermal emission is expected at energies above 100 keV. Hence, X-ray imaging (and spectra) in the 100 to 500 keV range is particularly valuable for testing for bursts generated within a single sheet. Simultaneous microwave images and spectra are, of course, also valuable for comparison with the X-ray data.

An interesting result of the single current sheet analysis was that a thermal hard X-ray burst can be generated without requiring anomalous resistivity in the sheet if the density in the X-ray emitting region is 10^{11} cm^{-3} or greater. Since the emission measure and estimated source volume obtained from hard X-ray imaging data can be used to estimate the density in the source region, the observations can yield information about the resistivity in the current sheet. The resistivity in the sheet must be anomalous if the average density in the X-ray emitting volume is less than 10^{11} cm^{-3}.

It is shown in the previously cited paper (Holman, 1985b) how a comparison of hard X-ray and microwave rise times (or, more specifically, the Joule heating and electron acceleration time scales) can be used to obtain more detailed information about the flaring region (see Shevgaonkar and Kundu, 1985, for a recent application). In particular, the electric field strength and resistivity in the current sheet can be deduced from such a comparison. The maximum energy to which electrons are accelerated in turn depends upon the electric field strength and the length of the current sheet. This maximum energy can be estimated from the hard X-ray or gamma-ray continuum data for a given flare. For complex, multiple-spike bursts, hard X-ray and microwave imaging will help in properly identifying the Joule heating and acceleration timescales.

An additional important task for X-ray imaging (both hard and soft) is to determine how thermal energy, once deposited, is transported within the flaring region. The observed properties of the thermal X-ray emission will be quite different if the thermal energy is readily transported to large volumes rather than primarily confined to the energy deposition region. High spatial and temporal resolution X-ray observations will provide a tracer for the transport of this energy during a flare.

REFERENCES

Holman, G. D., 1985a, in IAU Symposium 107, *Unstable Current Systems and Plasma Instabilities in Astrophysics,* eds., M. R. Kundu and G. D. Holman (Dordrecht: Reidel), p. 191.

Holman, G. D., 1985b, *Astrophys. J., 293,* 584.

Hoyng, P., 1977, *Astron. Astrophys., 55,* 23.

Shevgaonkar, R. K. and Kundu, M. R., 1985, *Astrophys. J., 292,* 733.

Spicer, D. S., 1983, *Adv. Space Res., Vol. 2,* No. 11, p. 135.

Tsuneta, S., 1984, in Proc. Japan-France Seminar on Active Phenomena in the Outer Atmospheres of Stars and the Sun, eds., J.-C. Pecker and Y. Uchida, p. 243.

SUPER ACTIVE REGIONS AND PRODUCTION OF MAJOR SOLAR FLARES

Taeil Bai

Center for Space Science and Astrophysics, Stanford University
Stanford, CA 94305

The success of imaging detectors with small fields of view such as HXIS or P/OF (Pinhole/ Occulter Facility) depends heavily on pointing to the right place at the right time. During the solar maximum years many active regions coexist on the solar disk. Therefore, in order to point the imaging detector to the right place, it is important to know which active region is most likely to produce major flares. This knowledge is also important for flare prediction.

As a first step toward this goal, I have identified active regions which produced major flares observed by HXRBS (Hard X-Ray Burst Spectrometer) on SMM during February 1980 through December 1983. For this study I have used the HXRBS Event List (Dennis et al., 1983), an updated flare list compiled by the HXRBS group, and the Comprehensive Reports of the Solar Geophysical Data. During this period, HXRBS detected hard X rays from ~7000 solar flares, out of which only 441 flares produced X rays with peak count rates exceeding 1000 counts/s. I call flares with such high peak count rates major flares. During the same time period about 2100 active regions passed across the solar disk, out of which only 153 active regions were observed to produce major flares. (Some active regions are known to persist for several solar rotations, but at each passage new active region numbers are assigned and my estimate is based on active region numbers.) Out of these 153 active regions, 25 were observed to produce 5 or more major flares. Considering their high productivity of major flares, we may call these active regions "super active regions." These 25 super active regions produced 209 major flares, accounting for 51% of all the major flares with identified active regions.

In Table 1 I have listed number of active regions as a function of observed major flares. One finds that 82 active regions produced only one major flare each during SMM observation periods, and several active regions were found to produce more than 10 major flares. Because SMM is in the Earth's shadow ~50% of time, the actual rates should be regarded about double the rate in this table. In Table 2 super active regions are listed chronologically, with some pertinent information. Active region 18405 (NOAA region number 3763) produced the largest number (18) of major flares, making June 1982 the most active month in terms of major flare production. During the same month active region 18422 (NOAA region number 3776) produced 15 major flares, and it was still very active during its next passage across the disk (active region number 18474; NOAA region number 3804), producing 13 major flares. One could learn a great deal about solar flares by studying such super active regions in detail with use of magnetograms and optical observations. If we can find some common properties of the super active regions in Table 2, it would also help understand flare production.

TABLE 1. NUMBER OF MAJOR FLARES PER ACTIVE REGIONS

Number of Major Flares from Single Active Region	1	2	3	4	5	6	7	8	9	10	11	12	13	14	15	16	17	18
Number of Active Regions	82	29	11	6	7	3	3	3	1	1	1	1	1	1	1	1	0	1

TABLE 2. CHARACTERISTICS OF SUPER ACTIVE REGIONS

ORDER	HALE (NOAA) REGION NUMBER	NO. OF MAJOR FLARES*	NORTH OR SOUTH	CMP DATE	CMP DAYS AFTER 00 UT 80.1.1	ROTATION	CARRINGTON LONGITUDE
1	16747 (2372)	8 (0)	N	80 APR 7.3	97.3	New	103
2	16923 (2522)	5 (0)	S	JUN 23.3	174.3	1,2; 16864	166
3	16978 (2562)	6 (1)	S	JUL 17.3	198.3	New	207
4	17244 (2776)	11 (3)	N	NOV 6.6	310.6	2nd: 17181	165
5	17255 (2779)	16 (2)	S	NOV 11.6	315.6	2nd; 17188	100
6	17491 (2958)	6 (2)	S	81 MAR 2.8	426.8	New at 17436 & 17438	74
7	17590 (3049)	7 (2)	N	APR 20.7	475.7	2nd; 17535	150
8	17751 (3221)	5 (1)	S	JUL 24.2	570.1	3rd; 17709 - 17667	340
9	17760 (3234)	9 (2)	S	JUL 28.3	574.3	2nd; 17713	290
10	17777 (3257)	7 (2)	S	AUG 10.0	587.0	1,2; 17737	118
11	17824 (3310)	5 (0)	S	SEP 4.9	612.9	2nd; 17777	133
12	17830 (3317)	10 (3)	N	SEP 10.6	618.6	New	59
13	17906 (3390)	12 (3)	S	OCT 14.3	652.3	New	334
14	17969 (3432)	5 (0)	S	NOV 4.9	673.9	New at 17890	50
15	18176 (3576)	5 (1)	S	82 FEB 1.4	762.4	New	323
16	18201 (3594)	5 (0)	S	FEB 10.7	771.7	2nd; 18142	202
17	18280 (3659)	8 (1)	N	MAR 29.0	818.0	New	309
18	18405 (3763)	18 (6)	S	JUN 8.5	889.5	New	85
19	18422 (3776)	14 (3)	N	JUN 18.8	899.8	New at 18382 & 18383	310
20	18430 (3781)	8 (1)	N	JUN 21.5	902.5	New	276
21	18474 (3804)	13 (4)	N	JUL 15.0	926.0	2nd; 18422	320
22	18473 (3814)	8 (0)	N	JUL 15.5	926.5	4,5; 18421	314
23	(3994)	7 (1)	S	NOV 20.0	1054.0		72
24	(4026)	5 (3)	S	DEC 16.9	1080.9	2nd; 3994	80
25	(4171)	6 (2)	S	83 MAY 13.0	1228.0		298

* Numbers in this column represent numbers of flares with HXRBS peak rates > 10,000 counts/s.

Inspecting Carrington longitudes of the super active regions in Table 2, one can find that the super active regions are clustered in the 60 to 120 degree and 300 to 360 degree intervals, and that no super active regions are found in the 0 to 30 degree and 210 to 270 degree intervals. It has been suggested that there exist active longitudes where the occurrence probability of active regions producing interplanetary protons is much higher than other areas (Svestka, 1970; for a review see Svestka, 1976). The present study confirms the existence of active longitudes. Recently Gaizauskas et al. (1983) have shown that many active regions frequently occur in "complexes of activity," which rotates near the Carrington rate. According to Svestka's (1970) study, there was only one sector of active longitudes during 1963 through 1967. However, in the present study we can find two sectors of active longitudes whose medians are separated by about 120 degrees. The existence of active longitudes may be due to giant convection cells (McIntosh and Wilson, 1985).

Because the Carrington rotation period is not *the* rotation period of the Sun, one can determine the mean rotation rate of the sectors of active longitudes by the following procedure: Adopt a system rotating rigidly at an assumed rate, count the number of major flares occurring in 20 degree longitude bins in this system, and calculate the rms flare numbers. Then by changing the rotation rate around the Carrington rate, find the rotation rate which maximizes the rms value. By this procedure I found that the rotation period 27.34 days (synodic) maximizes the rms value. The number of major flares in 20 degree longitude bins in the system rotating with the 27.34 day period is given in Table 3. Here I have adopted the Eastern limb at 00 UT on 1 January 1980 as 0 degree. We can see that a large number of major flares occurred in the 120 to 140 degree and 240 to 260 degree bins.

In the following I summarize the highlights of the present study which are pertinent to future P/OF observations of solar flares:

(1) All active regions are not created equal, but a small number of "super active regions" produce the majority of major flares. Therefore, it is very important to find out the properties of such super active regions. When we can recognize super active regions with the aid of such properties (yet to be found), we would have better chance of detecting major flares by pointing imaging detectors to such active regions.

(2) There exist sectors of active longitudes, where large fractions of major solar flares are produced. Active regions appearing in active longitudes are good candidates to point imaging detectors to.

TABLE 3. NUMBER OF MAJOR FLARES PER LONGITUDE BIN

| Longitude Bin	0 20	20 40	40 60	60 80	80 100	100 120	120 140	140 160	160 180	180 200	200 220	220 240	240 260	260 280	280 300	300 320	320 340	340 360
Number of Flares	20	10	5	9	34	17	77	18	12	7	5	39	60	20	19	19	22	9

REFERENCES

Dennis, B. R., et al., 1983, NASA Technical Memorandum 84998.

Gaizauskas, V., Harvey, J., Harvey, K., and Zwann, C., 1983, *Astrophys. J., 265,* 1056.

McIntosh, P. S. and Wilson, P. R., 1985, *Solar Phys., 97,* 59.

Solar Geophysical Data, 432-488 Part II, 1980-1984 (U.S. Dept. of Commerce: Boulder, Colorado).

Svestka, Z., 1970, *Space Res., 10,* 797.

Svestka, Z., 1976, *Solar Flares* (Reidel: Dordrecht-Holland), pp. 247-249.

SOLAR RADIO PHYSICS
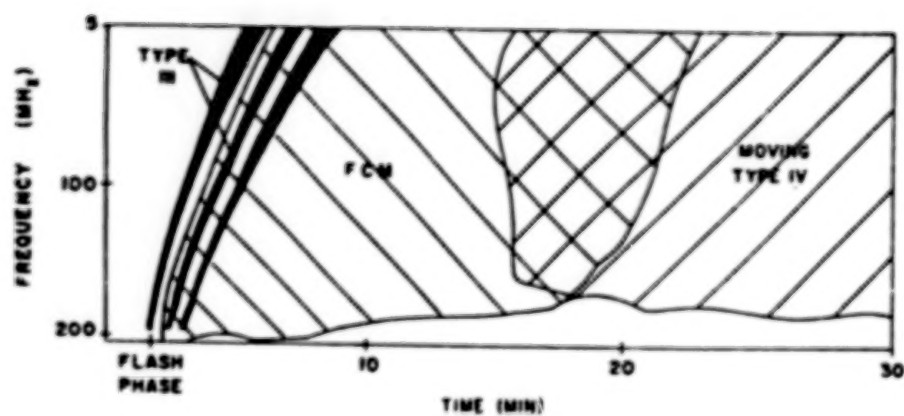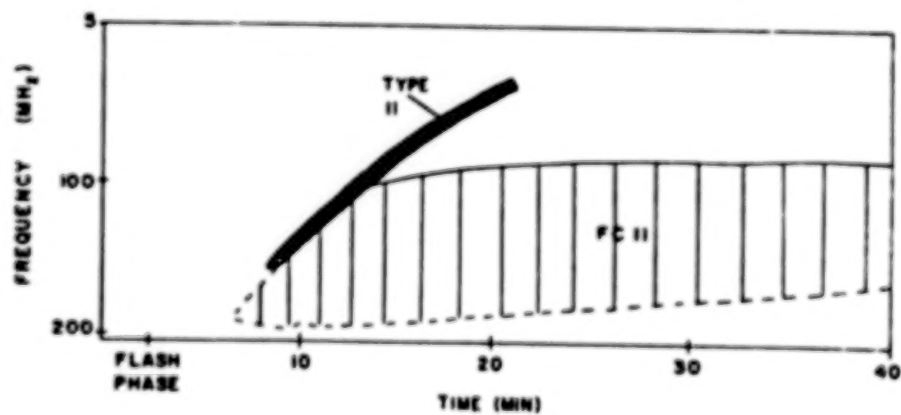
THE SOLAR RADIO CORONA: MANIFESTATIONS OF ENERGETIC ELECTRONS

(Invited)

Monique Pick

Observatoire de Paris-Meudon, DASOP, UA 324

I. INTRODUCTION

Most of the topics I am going to discuss in this talk concern the acceleration of particles during solar flares. The energy transferred to particles is in fact a great fraction of the energy released during a flare; hence, the problems related to the acceleration/injection process are of crucial importance for build-up and evolution of the flare.

The accelerated particles produce a wide variety of electromagnetic radiation including hard X-ray and radio bursts. The various kinds of emissions are generated in the corona through different mechanisms in sources with different physical parameters. Hence, any common feature in the temporal evolution of the fluxes can be attributed to the energetic particles. Furthermore, the different heights of emission enable us to deduce information on the three-dimensional structure of the source region from imaging observations in hard X rays, microwaves, and meter waves. One of the best prospects for understanding the electron acceleration has recently emerged from observations of X-ray and radio emission with a time resolution of <1 s. A detailed comparison of source locations and temporal evolution at different wavelengths is an important means to investigate crucial problems of the flare development such as:

— The temporal evolution of the electron population in the sources under the influence of acceleration/injection and interaction with the ambient medium.

— The magnetic structure involved in the acceleration/injection site.

— The alternative between long-term particle storage in the corona and continuous or repetitive injection.

My talk will be divided into two chapters: The first one deals with the solar flare development: pre-impulsive and impulsive phases, gradual and post gradual phases. A few points related to electron acceleration outside of flares will be also briefly discussed. The second chapter concerns a few problems related to the radio emission processes.

II. THE SOLAR FLARE DEVELOPMENT: PARTICLE ACCELERATION DURING AND OUTSIDE OF FLARES

(a) Impulsive phase

It is well accepted that electrons responsible for type III bursts and hard X-ray emission have a common origin. This idea is based on the temporal association between these emissions, when they are both produced. In fact, Raoult et al. (1985) have shown that the hard X-ray bursts associated with metric type III (or U) groups are of moderately small importance. They have a peak flux <1 ph cm^{-2} s^{-1} keV^{-1} at about 30 keV. On the opposite, X-ray bursts associated with type III/V emission lasting more than 30 s are considerably more intense with peak

fluxes around 30 keV exceeding 1 ph cm^{-2} s^{-1} keV^{-1} and spectra extending to $\geqslant$100 keV. The study of the spatial and temporal characteristics of type III/V events as well as their temporal association with X-ray emission came out with new information on the development of the impulsive phase. The observations (see Figures 1a and 1b) can be summarized as follows:

– There is an overall temporal correlation between X-ray and radio emissions. As X rays are produced in dense regions, this correlation implies a quasi-continuous input of accelerated electrons in the corona.

– In the early stage of the event, during the pre-impulsive phase which is shorter than 1 min, radio emission is primarily type III or U bursts, the type III bursts arising from several locations. The X-ray flux ($\leqslant$1 ph cm^{-2} s^{-1} keV^{-1} at 30 keV, similar to pure type III flare events) grows as the type III frequency increases. This effect is frequently observed. As the radiation of the type III bursts is emitted at the local plasma frequency or its harmonic, the starting frequency corresponds to the density at the point where the electron beams become unstable. Thus, the fast variation of the starting frequency may be explained by a real variation of the electronic density in the source (downward shift or compression of the injection/acceleration site) (Kane and Raoult, 1981). Alternatively, this effect may be linked to a variation in the distance traveled by the electron beam from the acceleration site before it becomes unstable to plasma waves (Kane et al. 1982).

– During the fast increase of the X-ray flux, one of the type III sources labeled A′ in Figure 1 becomes predominant and a new different source B appears. These two sources fluctuate together with short time delays of often less than 1 s. Both sources contribute together to the spiky (burst) and smooth continuum part of the radio emission. The simplest interpretation of the behavior of these two sources is that fast electrons are injected simultaneously into two magnetic structures as illustrated in Figure 2. This can happen if two magnetic structures suddenly interact at the acceleration/injection site. Several other observations give complementary information.

Microwave observations show effectively the electron propagation inside an arch. Indeed, they have revealed the existence of secondary bursts occurring at distances of 10^5 to 10^6 km from the primary site (Nakajima et al., 1985). The secondary burst has a time profile similar to the primary burst with a delay of 2 to 25 s. Some of these events occur simultaneously with meter-wave type III/V bursts. These observations strongly suggest that the distant microwave burst is produced by 10 to 100 keV electrons channeled along a coronal loop from the flare site to the distant footpoint of the loop.

Analysis of soft and hard X-ray imaging observations obtained with HXIS aboard SMM or with Hinotori also support the evidence of two systems of loops interacting. As an example, for one event, on 29 June 1980 associated with type III/V emission, different components of the X-ray source have been resolved. These features are labeled A, B, C, and D in Figure 2d (Hernandez et al., 1985). Feature A is a small loop (length <20 000 km). Features B and C are located in a large loop system, C corresponding to the footpoint, and B to a coronal source. The spatial configuration strongly suggests that the radio source B is the counterpart of the coronal X-ray source B. Furthermore, feature D which looks like a surge-like structure is located in the interaction volume of the 2 loops and its temporal behavior (Figure 3) reveals that the maximum of *thermal* energy release occurs in this region. Similar surges have been observed in Hα, and a systematic study has proved the close association between the appearance of these surges and type III burst occurrence (Mein and Avignon, 1985; Chiuderi-Drago et al., 1985):

there is a relationship between the evolution of the velocities of the Hα dark material and the occurrence of the type III bursts; the radio emission occurs in coincidence, within 1 min, with the blueshift maxima. The production of these surges may be due to the interaction volume which induces compression and thermal instability (Poland et al., 1982).

In conclusion, major progress has been achieved in the understanding of the impulsive development. Nevertheless, with the instruments presently available, it is difficult to achieve properly a quantitative interpretation. X-ray instruments with improved sensitivity and spatial resolution are necessary. Indeed, during the pre-impulsive phase, the comparative study between the temporal evolution of the X-ray spectrum and the radio emission cannot be carried out presently. Similarly, the time resolution of the X-ray image is too poor to obtain the exact evolution of the different features and their temporal association. In particular, we do not know if the bright points at the foot of the flaring loop appear simultaneously. Finally, the spatial resolution is insufficient to understand the exact topology of the accelerating site, and how, for example, electrons can be injected along several discrete diverging magnetic paths. The mechanism of electron acceleration that takes place is not yet understood. For this purpose, I would like to mention now the potential interest of radio decimeter observations.

Spikes of duration less than 100 ms are frequently observed above the starting frequency of type III bursts. An example is shown in Figure 4 together with a hard X-ray time profile for comparison (Benz, 1985). The spikes tend to occur in the early phase of the type III groups and predominantly in the rising phase of hard X rays. The most plausible interpretation is emission at the electron cyclotron frequency or harmonic (upper hybrid wave emission or cyclotron maser) (Benz, 1985). Figure 5 displays the temporal evolutions of average spike flux, metric type III flux, and hard X-ray counting rate. The observed correlation clearly demonstrates the close connection between spikes and the injection of energetic electrons. Following Benz, the spikes originate close to, or in the energy release region. "The observed fragmentation of the decimetric radiation into spikes might be a secondary effect of one global energy release or it could reflect that the energy of flares is released in thousands of 'microflares' (typical energy ≅ 10^{26} ergs)." The latter interpretation suggests that type III bursts may be related to integrated effects of elementary acceleration events during the solar flares (Benz, 1985).

All the observations shown here have pointed out the quasi-continuous and nearly simultaneous injection of electrons into distinct magnetic structures (type III/V emission) and precipitating, at least partially, electrons associated with hard X-rays bursts. The accelerating region must share different diverging field lines (Kane et al., 1980). Another possibility, proposed by Sprangle and Vlahos (1983), is the acceleration of secondary electrons generating type III bursts by intense radio waves. The signature of these radio waves is given by the presence of decimetric bursts. In this model, the "flaring loop model," the primary accelerated electrons are produced in the flaring loop, and excite the e.m. radio waves which can easily escape from the flaring region.

It must be indicated that joint observations obtained with a multifrequency radioheliograph and the hard X-ray imaging instrument of the Pinhole/Occulter Facility will provide in principle an answer to this problem. Indeed, the respective location of the spike and type III bursts will be obtained as well as the hard X-ray source structure.

(b) Gradual and late phases of large solar flares

It is now widely accepted that during the gradual phases of large solar flares, the electrons are continuously or repetitively injected into different coronal structures where they emit hard X rays and broadband continua from centimeter to meter radio waves (Kai et al., 1983; Hudson et al., 1982; Klein et al., 1983). The strongest argument supporting this conclusion is the similarity of time profiles between hard X rays, microwaves, and meter emissions.

Despite this general agreement several problems still remain confused. First of all, it seems to me that a great deal of ambiguity arises from the inhomogeneous terminology adopted by different authors to describe the successive stages of type IV events. This led some authors to suggest an association between hard X-ray emission and, indifferently, "flare continuum" or late "stationary type IV burst" without any clear distinction between these two components. The consequence has been a confusion in the electron energy responsible for the different components of a type IV burst. Secondly, type II bursts which are produced by shock waves are often observed at the onset of type IV bursts. The exact role of shocks in the acceleration of electrons responsible for type IV emission is not yet understood.

A typical radio observation of a big solar flare is shown in Figure 6. Let me recall that:

(1) The gradual phase comprises a broadband emission from centimeter to meter waves that often starts during the impulsive phase. This part, very well-observed at single frequencies called "flare continuum" (Wild, 1970), has in general a duration of a few tens of minutes, exceeding sometimes one hour for large events (Pick, 1961; the "phase A" in this paper is identical to the term "flare continuum"). Sometimes this emission is accompanied by a "moving type IV burst" at meter waves. This is in contradiction with what was reported later on by Cliver (1983). This author had in mind that the flare continua are of short duration, and he designated as stationary type IV burst events that were in fact typical flare continua extending to microwave frequencies.

(2) The post gradual phase, "stationary type IV burst," corresponds to a long lasting emission up to many hours at meter decameter wavelengths and occurs in some flares during the fading of the flare continuum or sometimes without any proceeding impulsive or gradual phase.

Figures 7 and 8 compare the temporal evolution of hard X-ray and radio emissions between two flares containing a flare continuum which starts at the time of the impulsive phase emission. Flare continuum and hard X-ray emissions start and finish together, presenting an overall similar temporal behavior. The observed nearly simultaneous end of the burst and of some of its fine structure features, in both spectral ranges, indicates that the electrons are not efficiently trapped. The electrons must be quasi-continuously injected.

Furthermore, one can notice that for the 13 August 1980 event (Figure 8), the onset of the flare continuum at meter wavelengths clearly occurs during the flash phase, *before* the type II burst occurrence. Thus, it is not classified as FCII continua which are initiated by the passage of the shock wave accelerating *locally* the electrons (Robinson and Smerd, 1975) (see also Figure 9). On the other hand, Hudson et al. (1982) associated a hard X-ray event with an FCII flare continuum. They suggested that the timings of the FCII, the X-ray, and microwave emissions were all consistent with the shock wave as the accelerating agent. Then, it is not understandable that the onset of the hard X-ray event lagged significantly behind the appearance of the type II burst and the 80 MHz continuum (Figure 10). Hudson et al. (1982) suggested that the particle acceleration site is largely remote from the impulsive first-stage energy release, contrary to other major flares. As the corresponding flare occurs behind the limb, I suggest that a large part of the gradual X-ray event may be occulted as well as the impulsive phase. Indeed, Kane (1983) has shown that, for impulsive and gradual bursts, the bulk of hard X rays is below 3000 km.

Occasionally, for disk events a delay between X-ray and radio emissions has been observed. The onset of X-ray bursts precedes the onset of the meter-radio emission.

In conclusion and for discussion:

(a) Flare continua are produced by energetic electrons.

(b) The temporal relationship between X-ray emission and flare continuum has still to be clarified. It is indeed not clear enough whether two physically distinct accelerating mechanisms exist; one corresponding to an injection/accelerating site located relatively low in the corona and producing electrons continuously or repetitively during the whole development of the event; another one corresponding to an in situ accelerating process linked for a given altitude to the passage of the shock wave. Robinson himself, who introduced the distinction between FCM and FCII flare continua, notices that "the type FCII activity is accompanied by an unclassified continuum burst sometimes having the properties of the type III/V" (Figure 11) (Robinson, 1977). I suggest that the energetic electrons responsible for FCII events may be also produced in the lower levels of the solar atmosphere, close to the site of flare energy release. Kundu and Stone concluded similarly for the kilometric solar radio bursts detected by Cane et al. (1981) and referred to them as shock-accelerated (SA) events (Kundu and Stone, 1984).

(c) The source topology during both impulsive and gradual phases looks roughly similar. Both phases require a quasi-continuous acceleration mechanism. Despite this analogy, we do not yet understand why some large flares are only associated with relatively short type III/V events (plausibly "flare of class B" in the Hinotori classification) and others with "flare continua" of longer duration (plausibly "flares of class C" in the Hinotori classification). The mechanism maintaining a continuous input of energy from the interaction region is still unknown.

(d) One of the important results coming out from the SMM mission is that protons and heavy ions are rapidly accelerated during the impulsive phase (Forrest et al., 1981; Chupp, 1982). It was suggested that all flares might produce γ-ray lines and that only the threshold sensitivity distinguishes the gamma-ray line flares from the others. On the opposite, Bai and Dennis argued that γ-ray line events exhibit distinct characteristics from other flares. They concluded that these events belong to a distinct class of flares (Bai and Dennis, 1985). One of the characteristics is the close association between type II/IV bursts and γ-ray line events. Let me emphasize the fact that an *association* between two features has not the same meaning as a "temporal correlation." In that way, it must be noticed that the 3 June 1982 flare, one of the most important γ-ray line events observed by SMM, showed 3 successive blobs of activity, comparable to 3 type V events (Figure 12) followed by a type IV event. The onset and the development of the γ-ray emission occurs during the first type V burst. On the other hand, Raoult et al. (1985) notice that γ-ray events may occur in association with type III/V events and in the absence of any type IV burst.

The Post Gradual Phase

When the gradual meter emission is followed by a storm continuum (stationary type IV burst), the latter is not associated with detectable hard X rays, but only with soft ones (Stewart, Wolfson, and Lemen, 1979; Svestka et al., 1982; Klein et al., 1983). An isolated storm continuum has been observed by Lantos et al. (1981), with spatial resolution in the meter and soft X-ray range. Although the sources are widely separated, their fluxes evolve in the same manner. Lantos et al. proposed that electrons of about 10 keV in the tail of the thermal distribution emitting soft X rays escape from the X-ray source and generate the radio emission inside a large expanding loop transient.

(c) Electron acceleration outside of flares

(1) Micro-activity at meter decameter wavelengths

Using a balloon-borne instrumentation of very high sensitivity, Lin et al. (1984) have detected many hard X-ray microbursts, 25 in 141 min, with peak fluxes exceeding 7×10^{-3} ph cm^{-2} s^{-1} keV^{-1} at 20 keV and with a power-law energy spectrum. Hα flares were only reported for a few of the strongest bursts. The integral number of events varies approximately as the inverse of the peak flux (Figure 13). Lin et al. concluded that the energy contained in accelerated electrons might contribute significantly to the heating of the active corona. Kundu and Stone (1984) proposed that these microbursts could be of the same nonthermal nature as the frequent microbursts observed at meter and decameter wavelengths. The CLRO radioheliograph recorded many micro-type-III-like bursts lasting from a few seconds to several tens of seconds with flux densities ranging from a few tens to hundreds of milli sfu. As shown by Kundu and Stone, the integral number of events also varies inversely to the peak flux (Figure 13). The Clark Lake Radioheliograph images show that the radio source persists for many hours. These type-III-like burst storms are also frequently observed at higher frequencies as weak meter type I noise storms. The exact origin of the electrons responsible for these emissions is not yet understood.

(2) Noise storm onsets or enhancements related to transient coronal modifications

The most rapid variations of the K corona, coronal transients, have been extensively studied, and some of them are known to be associated with type II-IV bursts (for a review, see the chapter on "coronal mass ejections and coronal structures" by Hildner et al. in the SMM workshop proceedings, 1985). I am not going to discuss these large events here.

Combining SMM - C/P observations and Nançay Radioheliograph measurements, Kerdraon et al. (1983) found that noise storm onsets or enhancements are systematically associated with the appearance of additional material in the corona. These coronal brightenings are not necessarily transient mass ejections. Most often, they appear as a stepwise increase on a timescale of one hour and remain stable for several hours. In all cases, the radio source is cospatial with the region of increased white light brightness. Whatever may be the process causing the mass increase, it is a necessary condition for the noise storm emission to change intensity or to appear. This result represents the first systematic association between visible features and noise storm production. Indeed, attempts to associate this activity with chromospheric flares (Elgaroy, 1977) or with surges (Garczynska et al., 1982) did not reveal any systematic relationship.

In conclusion, electrons can be accelerated quasi-continuously in the absence of any detectable chromospheric activity. The observations summarized in this section may suggest that these electrons may have a purely coronal origin. In order to progress, joint observations between radioheliographs, white-light and UV coronographs, especially observing below 1.5 solar radii from disk center, are necessary to establish more clearly this coronal origin.

III. RADIO EMISSION PROCESSES AND ELECTRON BEAM OBSERVATION

(a) Type III radio bursts

In the last years, both theory and observational techniques of solar type III bursts have been developed up to a level where it became possible to investigate the fine structure of type III radio emission and to use it as a test of the theory. At kilometric wavelengths, pioneering work in this direction has been done by Lin et al. (1973), Gurnett and Anderson (1976), and

Fitzenreiter et al. (1976) from an observational point of view, and by Goldstein et al. (1979) from a theoretical point of view. For example, it was possible to confirm that the radio emission is produced by streaming electrons. In the higher frequency band, in situ verification of the theory is not possible. Indirect investigation by means of the radio emission has been the appropriate way to get information about the early development of the electron beams. The conclusions diverge significantly. On the other hand, many authors have invoked propagation effects of electromagnetic waves, such as coronal scattering or wave ducting to explain observed size, position, directivity, and characteristics of fundamental-harmonic pairs (F-H) (Steinberg et al., 1971; Stewart, 1976; Duncan, 1980; Dulk and Suzuki, 1980). On the other hand, other authors have noted that type III bursts may be resolved into elementary sources which can be explained by the discrete diverging structures in the corona (Axisa et al., 1972; Mercier, 1975; Raoult and Pick, 1980). This was recently confirmed by direct combined white-light and radio observations obtained with the SMM coronograph/polarimeter and the Nançay Radioheliograph. It was shown that type III sources are located in the vicinity of thin ray-like structures which are over-dense, short-lived (1 day or less), and sometimes diverging (Trottet et al., 1982). More generally, the type III source structure tends to follow that of the corona. Even if propagation effects are not excluded, they must be estimated in the context of a corona composed of small discrete structures. This has direct implication on the type III burst modeling. For example, type III pairs are often observed; most of the observed type III pairs have been widely interpreted as fundamental and harmonic emission (F-H). However, this interpretation may sometimes encounter serious difficulties as the observations fit occasionally better with the assumption of 2 electron beams propagating along different diverging magnetic paths (Benz et al., 1982).

In situ measurements of electron beams in connection with coronal observations will yield powerful diagnostics of the radio emitting mechanisms. Indeed, electron beam propagation characteristics will be clearly identifiable and distinguishable from propagation effects of electromagnetic waves. Finally, it must be emphasized that results which have been obtained from in situ measurements at low frequencies in the interplanetary medium cannot be automatically extrapolated to higher radio frequencies emitted at coronal levels.

(b) Pulsating structure

Flux variations with quasi-periods of the order of 1 s are frequently observed in type IV continua (McLean et al., 1971). They are referred to as "pulsating structure." Theories involving incoherent or coherent gyrosynchrotron radiation from energetic electrons trapped in a magnetic arch and periodic oscillations of this arch have been often invoked for the interpretation of pulsating structure (Rosenberg, 1970).

Combined imaging and spectral observations have made a detailed study possible of both the spatial structure of the source and its emission spectrum. This led to the discovery of new properties of these modulations as high temperatures $\sim 10^{11}$ K, limited frequency spectrum, spatial and spectral drift of the peak frequency within one pulse (Trottet et al., 1981). It has been shown that these characteristics exclude gyrosynchrotron radiation as the emission mechanism. As an alternative, processes where the plasma emission of trapped particles is inhibited by perturbations of the loss cone distribution have been proposed. These perturbations can correspond to repetitive injections of fast electrons as suggested by Benz and Kuijpers (1976) for the interpretation of "sudden reductions" in continua. As mentioned by Trottet et al., "simultaneous X-ray and radio observations of similar pulsating structure events will furnish clues concerning the changes in distribution function and the correctness of the model."

IV. CONCLUSIONS

Radio observations are powerful tools which are complementary to the space missions devoted to the physics of the flares, of the corona, or of the interplanetary medium. I would like to take this opportunity to stress the fact that two multifrequency radioheliographs presently exist: the Nançay instrument (the multifrequency facility will be in operation by the end of 1985) observes the middle corona at decimeter-meter wavelengths, and the Clark Lake radioheliograph, operating at decameter wavelengths, is the only one in the world to have the ability of observing the outer corona above the disk.

REFERENCES

Axisa, F., Martres, M. J., Pick, M., and Soru-Escaut, I., 1972, Goddard, NASA Symposium.

Bai, T. and Dennis, B. R., 1985, *Astrophys. J.*, in press.

Benz, A., 1985, *Solar Phys, 96*, 357.

Benz, A. O. and Kuijpers, J., 1976, *Solar Phys., 46*, 275.

Benz, A. O. Treumann, R., Vilmer, N., Mangeney, A., Pick, M., and Raoult, A., 1982, *Astron. Astrophys. 108*, 161.

Cane, H. V., Stone, R. G., Fainberg, J., Stewart, R. T., Steinberg, J. L., and Hoang, S., 1981, *Geophys. Res. Lett., 8*, 1285.

Chiuderi-Drago, F., Mein, N., et al., 1985, in preparation.

Chupp, E. L., 1982, in *Gamma Ray Transients and Related Astrophysical Phenomena*, ed., R. A. Lingenfelter, New York, p. 409.

Cliver, E. W., 1983, *Solar Phys., 84*, 347.

Datlowe, D. W., Elcan, M. J., and Hudson, H. S., 1974, *Solar Phys., 39*, 155.

Dulk, G. A. and Suzuki, S., 1980, *Astron. Astrophys., 80*, 203.

Duncan, R. A., 1980, *Solar Phys., 63*, 389.

Elgaroy, O., 1977, *Solar Noise Storms*, ed., D. Ter Haar, New York, Pergamon Press.

Fitzenreiter, R. J., Evans, L. G., and Lin, R. P., 1976, *Solar Phys., 46*, 437.

Forrest, D. J., et al., 1981, in *Proc. 17th Intl. Cosmic Ray Conf. (Paris), 10*, 5.

Garczynska, I., Rompolt, B., Benz, A., Slottje, C., Tlamicha, A., and Zanelli, C., 1982, *Solar Phys., 77*, 277.

Goldstein, M. L., Smith, R. A., and Papadopoulos, K., 1979, *Astrophys. J., 234*, 683.

Gurnett, O. A. and Anderson, R. R., 1976, *Science, 194*, 1159.

Hernandez, A. M., Machado, M. E., Sneibrun, C. V., Trottet, G., and Vilmer, N., 1985, to be submitted.

Hildner, E., et al., 1985, in Proceedings of the SMM Workshop.

Hudson, H. S., Lin, R. P., and Stewart, R. T., 1982, *Solar Phys., 75*, 245.

Kai, K., Nakajima, H., Kosugi, T., and Kane, S. R., 1983, *Solar Phys., 86*, 231.

Kane, S. R., 1983, *Solar Phys., 86*, 355.

Kane, S. R., Pick, M., and Raoult, A., 1980, *Astrophys. J. (Letters), 241*, L113.

Kane S. R. and Raoult, A., 1981, *Astrophys. J. (Letters), 248*, L77.

Kane, S. R., Benz, A. O., and Treumann, R. A., 1982, *Astrophys. J., 263*, 423.

Kerdraon, A., Pick, M., Torttet, G., Sawyer, C., Illing, R., Wagner, W., and House, L., 1983, *Astrophys. J. (Letters), 265*, L19.

Klein, L., Anderson, K., Pick, M., Torttet, G., and Vilmer, N., 1983, *Solar Phys., 84*, 295.

Kundu, M. R. and Stone, R. G., 1984, *Advances in Space Research*, ed., P. A. Simon, *4*, 261.

Lantos, P., Kerdraon, A., Rapley, C. G., and Bentley, R. D., 1981, *Astron. Astrophys., 101*, 33.

Lin, R. P., Evans, L. G., and Fainberg, J., 1973, *Astrophys. Letters, 14*, 191.

Lin, R. P., Schwartz, R. A., Kane, S. R., Pelling, R. M., and Hurley, K. C., 1984, *Astrophys. J., 283*, 421.

McLean, D. J., Sheridan, K. V., Stewart, R. T., and Wild, J. P., 1971, *Nature, 234*, 140.

Mein, N. and Avignon, Y., 1985, *Solar Phys., 95*, 2, 331.

Mercier, D., 1975, *Solar Phys., 45*, 169.

Nakajima, H., Dennis, B. R., Hoyng, P., Nelson, G., Kosugi, T., and Kai, K., 1985, *Astrophys. J., 288*, 806.

Newkirk, G., 1961, *Astrophys. J., 133*, 983.

Pick, M., 1961, *Ann. Astrophys., 24*, 183.

Poland, A. I., Machado, M. E., Wolfson, C. J., Frost, K. J., Woodgate, B. E., Shine, R. A., Keny, P. J., Cheng, C. C., Tandberg-Hanssen, E. A., Bruner, E. C., and Henze, W., 1982, *Solar Phys., 78*, 201.

Raoult, A. and Pick, M., 1980, *Astron. Astrophys.*, *87*, 63.

Raoult, A., Pick, M., Dennis, B. R., and Kane, S. R., 1985, *Astrophys. J.*, submitted.

Robinson, R. D. and Smerd, S. F., 1975, *Proc. A.S.A.*, *2*, 374.

Robinson, R. D., 1977, Thesis.

Rosenberg, H., 1970, *Astron. Astrophys.*, *9*, 159.

Sprangle, P. and Vlahos, L., 1983, *Astrophys. J. (Letters)*, *273*, L95.

Steinberg, J. L., Aubier-Giraud, M., Leblanc, Y., and Boischot, A., 1971, *Astron. Astrophys.*, *10*, 362.

Stewart, R., 1976, *Solar Phys.*, *50*, 437.

Stewart, R., Wolfson, C. J., and Lemen, J. R., 1979, *NZJS*, *22*, 567.

Svestka, Z., Dennis, B. R., Pick, M., Raoult, A., Rapley, C. G., Stewart, R. T., and Woodgate, B. E., 1982, *Solar Phys.*, *80*, 143.

Trottet, G., Kerdraon, A., Benz, A. O., and Treumann, R., 1981, *Astron. Astrophys.*, *93*, 129.

Trottet, G., Pick, M., House, L., Illing, R., Sawyer, C., and Wagner, W., 1982, *Astron. Astrophys.*, *111*, 306.

Wild, J. P., 1970, *Proc. A.S.A.*, *1*, 365.
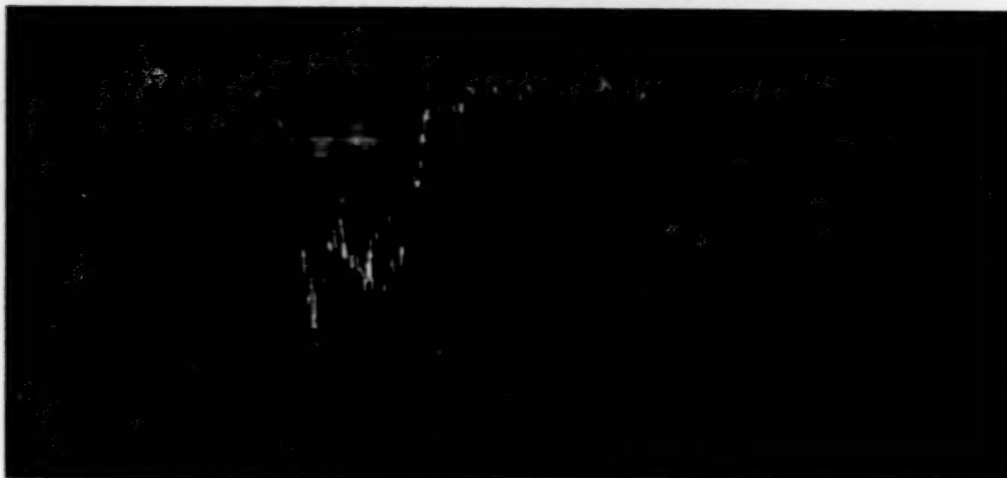
Figure 1a. Type III/V bursts on 29 July 1981 observed with the Nançay Radiospectrograph and the associated hard X-ray burst observed with HXRBS on SMM. Evolution of the X-ray emission compared to the evolution of the radio event. Note the inverted scale for the X-ray data. (From Raoult et al., 1985.)
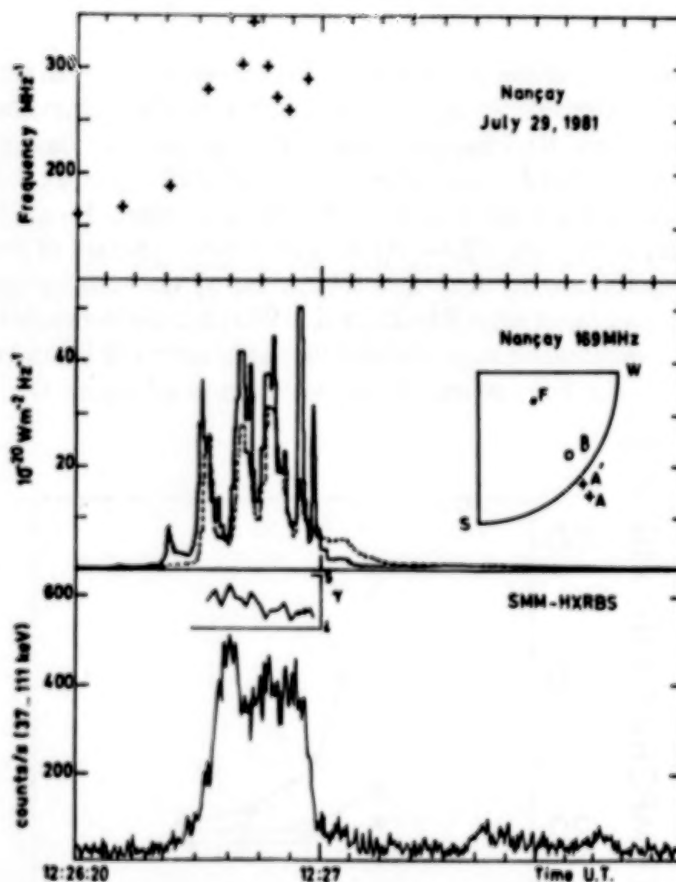

Figure 1b. 29 July 1981 event. Top: starting frequency of the radio emission measured on the Nançay digital spectrograph. Middle: evolution of the radio flux from source A' (solid line) and B (broken line) as observed by the Nançay Radioheliograph. Location of radio sources A-A' and B (see text) observed during the development of the event. Bottom: evolution of the X-ray power-law spectral index observed with the HXRBS on SMM and of the hard X-ray emission. (From Raoult et al., 1985.)
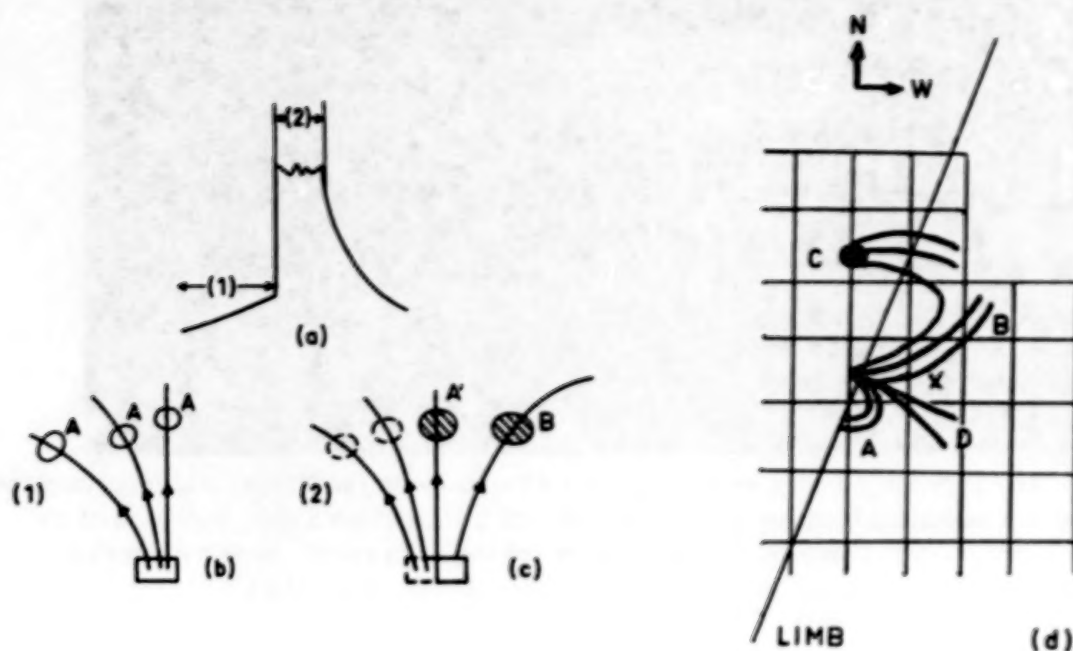
Figure 2. (a) Schematic evolution of an X-ray burst showing (1) "preflash phase," (2) impulsive phase. (b) Suggested geometry of the flare during the preflash phase showing the presumed magnetic field lines from the electron acceleration/injection site through the metric radio sources labeled A. (c) Similar geometry of the flare during the impulsive phase showing the location of the metric radio source A′ and the new source B (see text). (d) 29 June event, HXIS soft X-ray data, 10.40 UT (3.5-11.5 keV). Sketch of the field geometry assumed by the authors, overlaid on a HXIS field of view display (size of individual pixels, 32 arc s). (a,b,c from Raoult et al., 1985; d from Hernandez et al., 1985) The spatial configuration suggests that the radio source B is the counterpart of the X-ray source B. (X: see caption of Figure 3).
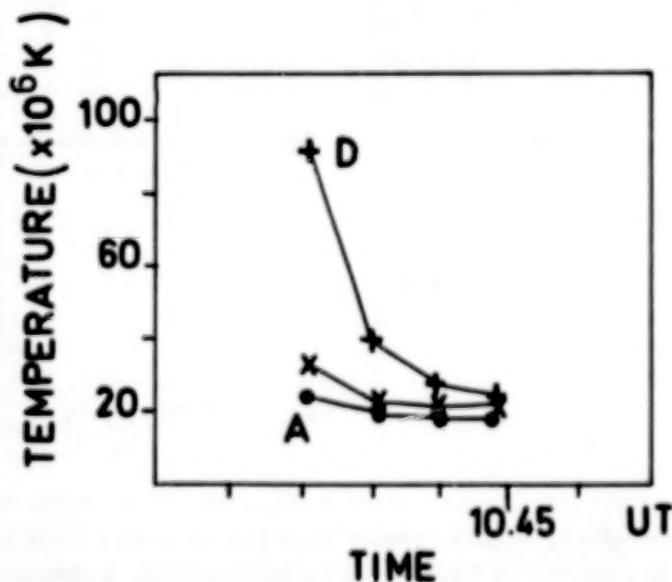
Figure 3. 29 June event 10.40 UT. Temperature versus time plots for features A, D, and its neighbor (pixel indicated by an x in Figure 2d). (From Hernandez et al., 1985.)
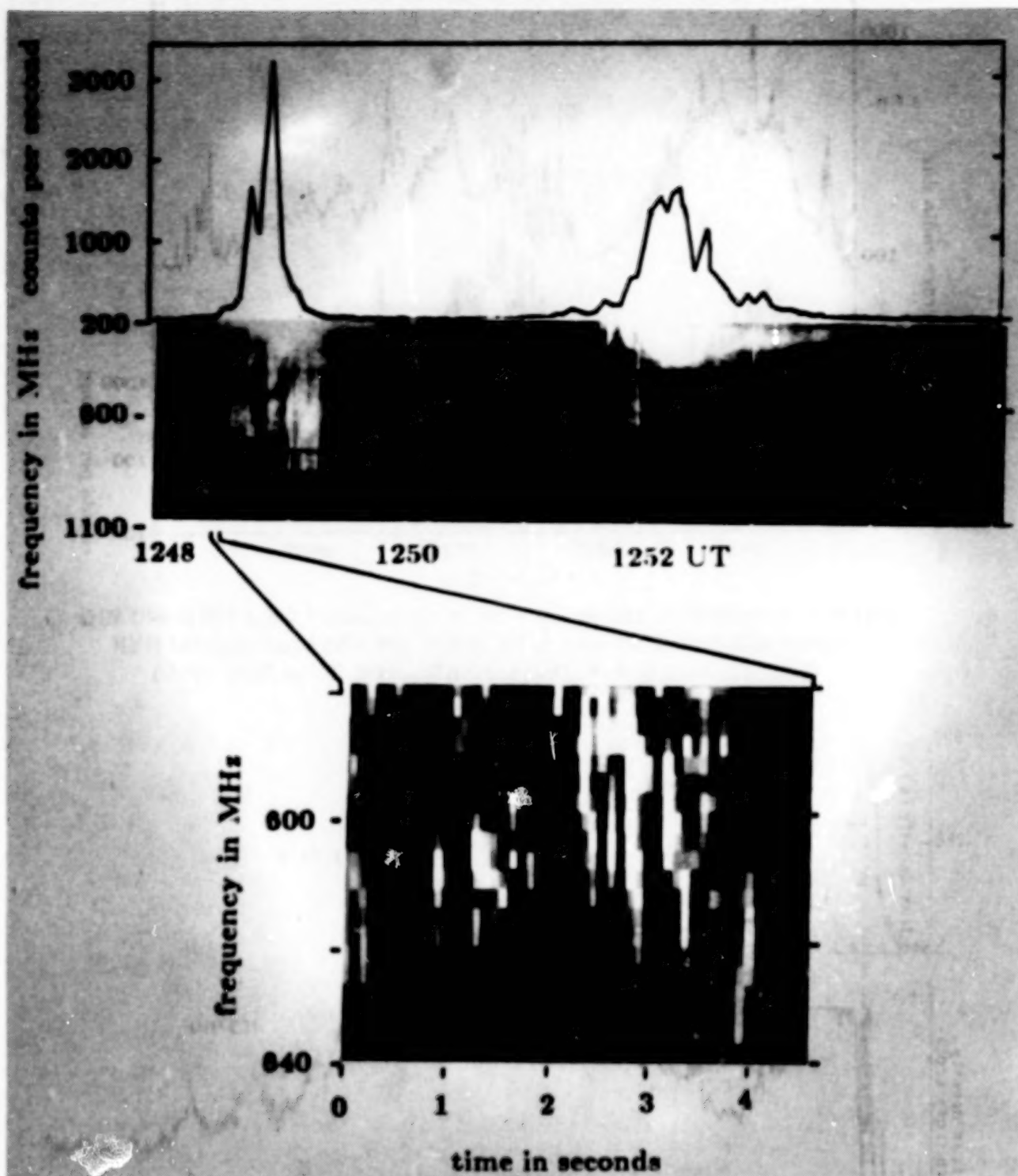
170

Figure 4. Decimetric spikes on 31 August 1980. Top: Composed figure showing HXR counts versus time (>30 keV, observed by HXRBS onboard SMM) (courtesy B. R. Dennis) and radio spectrogram registered by the analog spectrograph (Dacedalus). The spectrogram shows type III bursts at metric wavelengths and spike activity above about 350 MHz. Bottom: Blow-up of a small fraction of the spectrogram produced from data of the digital spectrometer (Ikarus) presenting single spikes. (From Benz, 1985.)
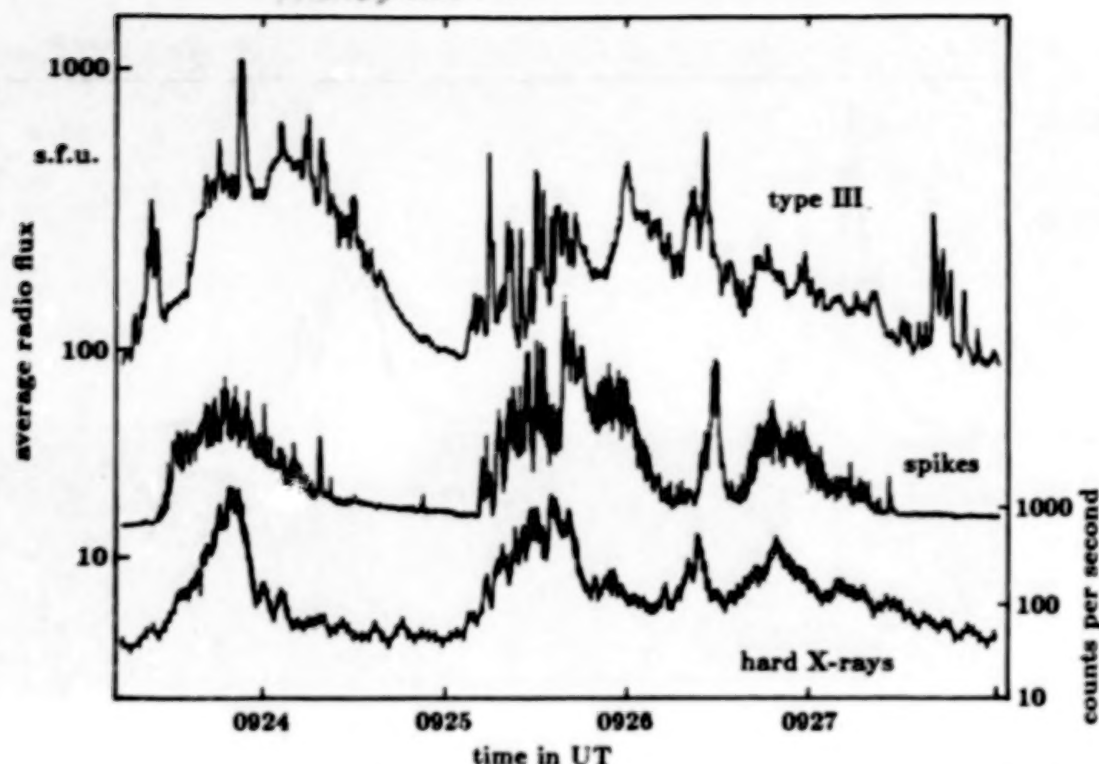
Figure 5. Correlation of average spike flux in the frequency band 580 to 640 MHz (middle) with type III emission in the 250 to 310 MHz band (top) and HXR (bottom), courtesy B. R. Dennis, HXRBS/SMM. (From Benz, 1985.)
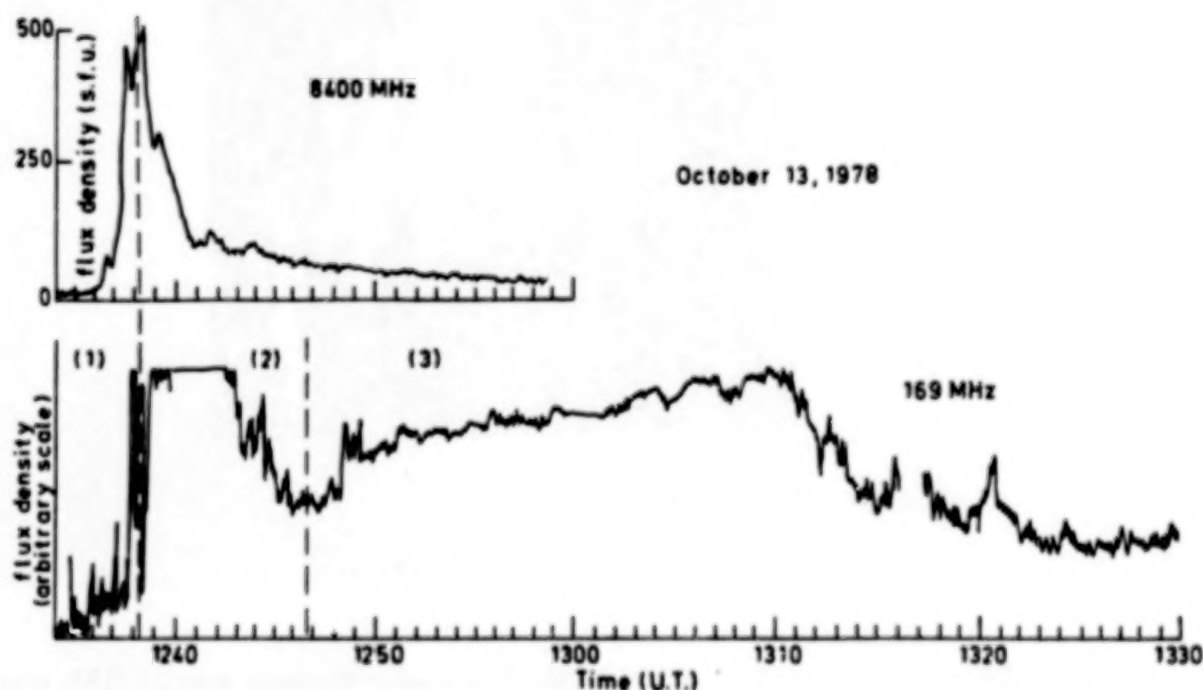

Figure 6. Time evolution of a typical event at meter wavelengths (169 MHz, Nançay) compared with the corresponding microwave event (8400 MHz, Bern). The numbers (1), (2), and (3) correspond to the impulsive phase, the flare continuum and moving type IV burst, the stationary type IV burst, respectively. (From Klein et al., 1983.)
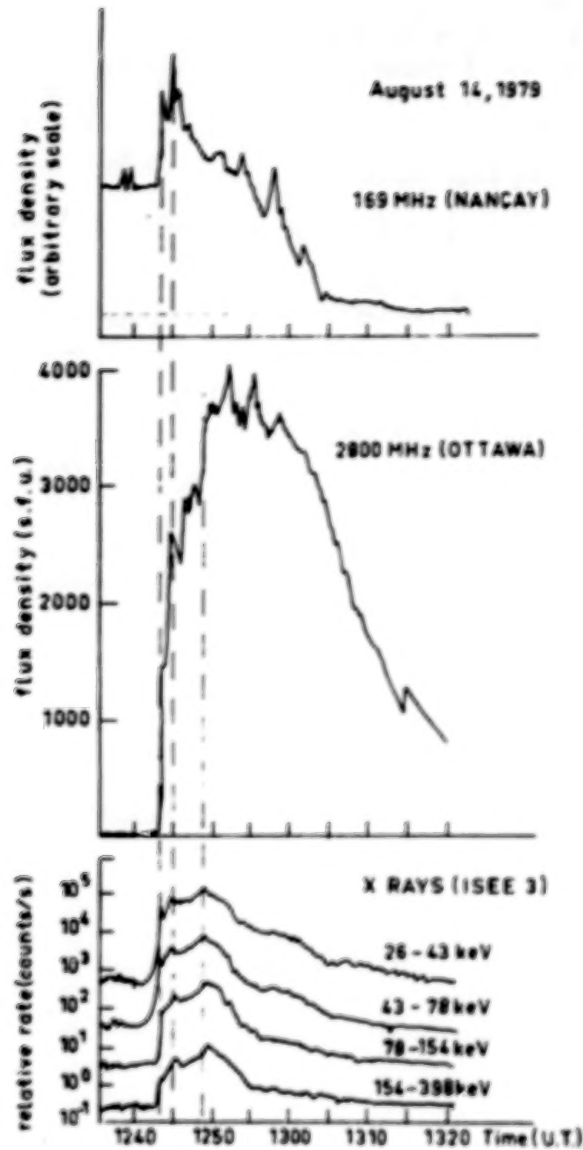
Figure 7. Time evolution of the flux densities at 169 MHz and at 2800 MHz compared with that of the hard X-ray flux (maximum fluxes: 12.0, 4.0, 2.04 and 0.46 photons cm^{-2} s^{-1} keV^{-1}) during the 14 August event. The background level at 169 MHz is shown by the dotted line. The excess flux before the onset of the type IV burst is due to a noise storm which rose slowly from about 11:43 UT and peaked around 12:30 UT. (From Klein et al., 1983.)
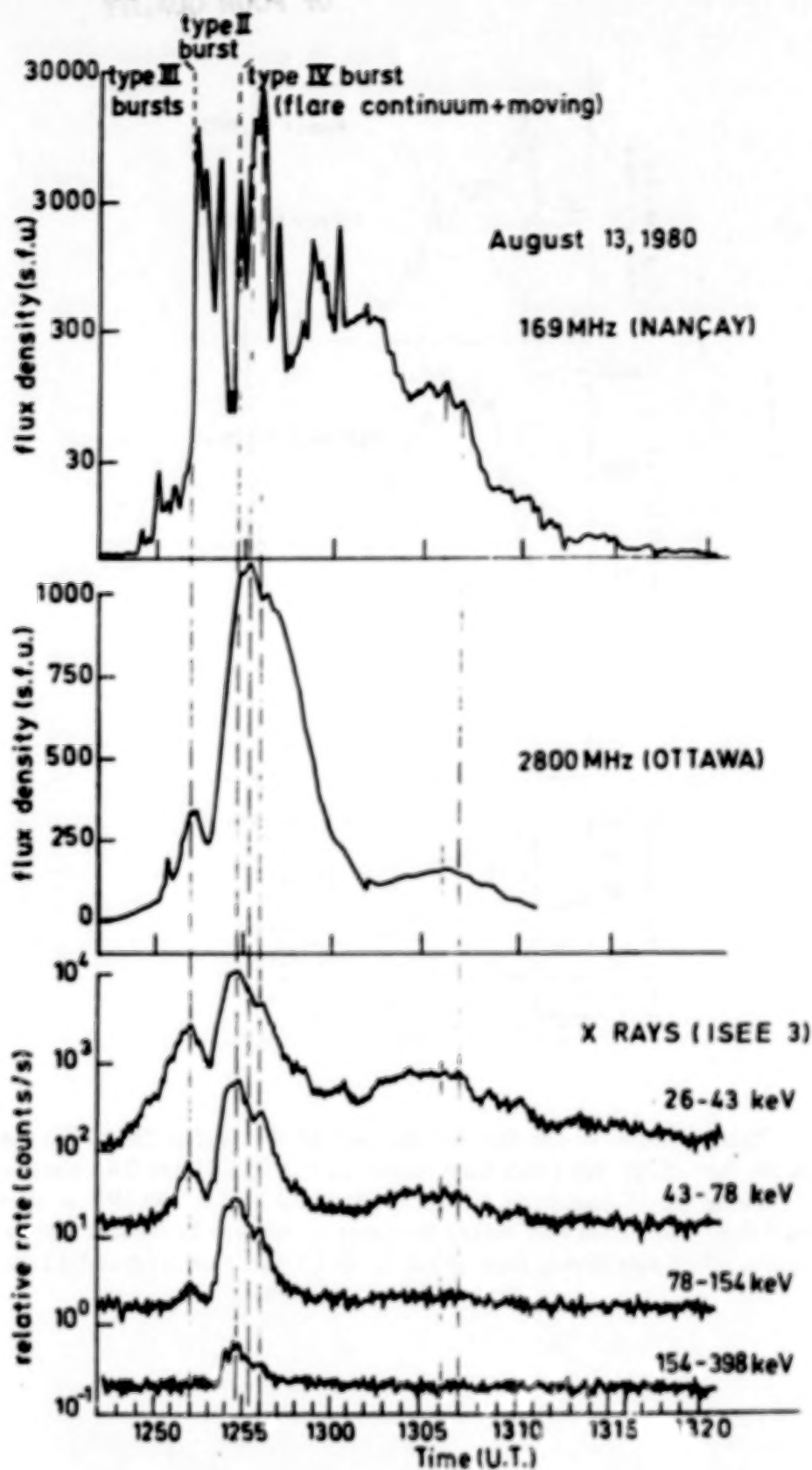
Figure 8. Same as Figure 7 for 12 August 1980 event (maximum X-ray fluxes: 6.9, 1.3, 0.33, and 0.03 ph cm^{-2} s^{-1} keV^{-1}). (From Klein et al., 1983.)
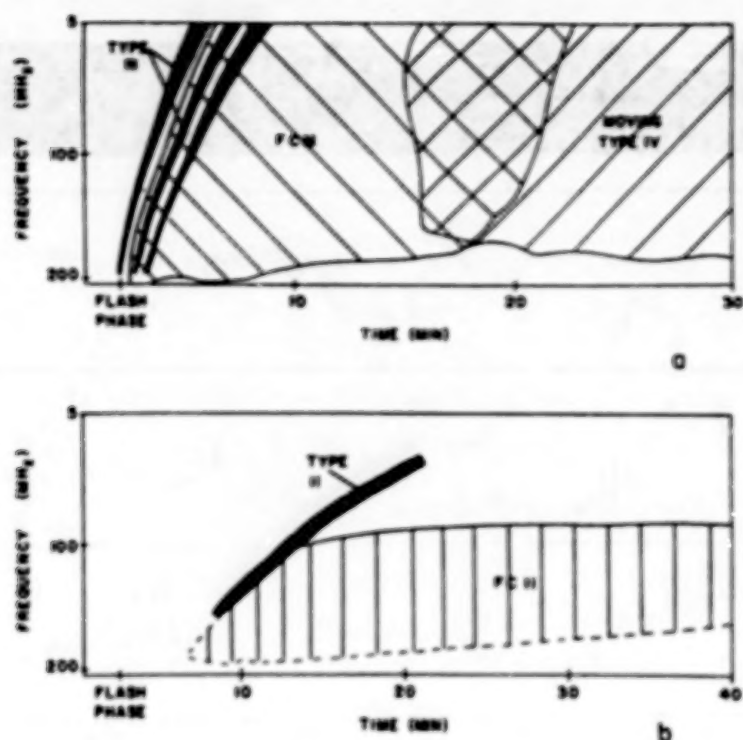
Figure 9. Schematic representation of (a) an FCM and (b) an FCII. (From Robinson, 1977.)
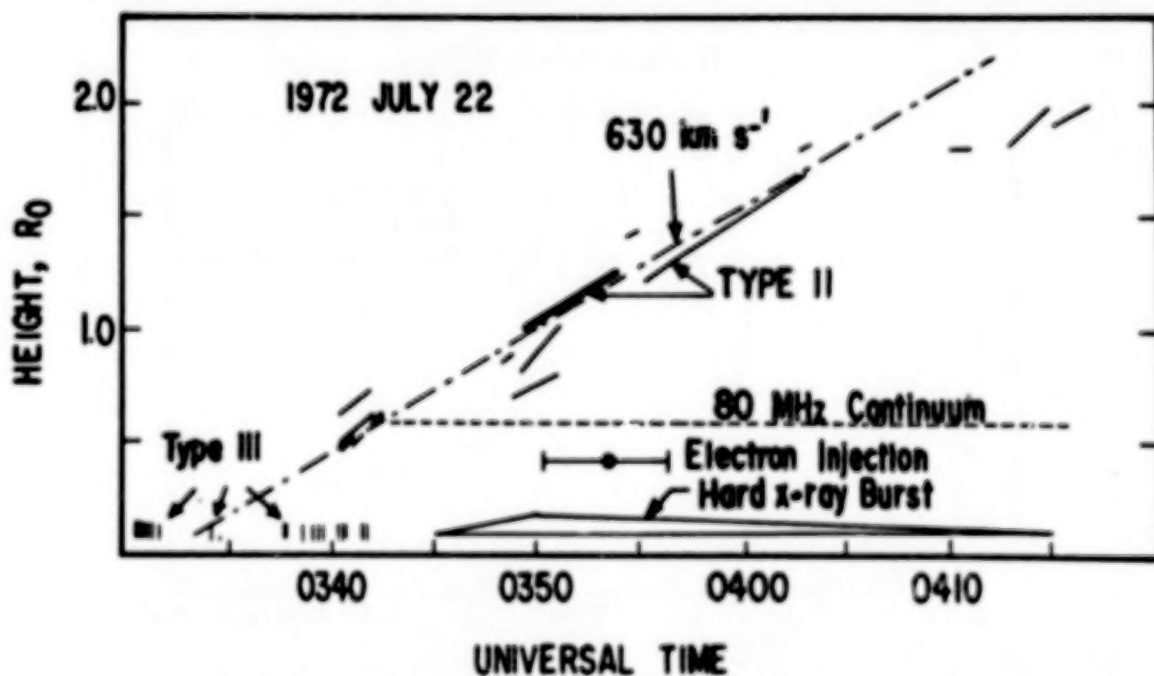

Figure 10. Height-time plot of the type II burst of 22 June 1972. Heavy sloping lines indicate (assumed fundamental) type II bands; medium sloping lines represent (assumed second harmonic) bands. The light broken line indicates a shock speed ~630 km s⁻¹. Type II frequencies were converted to heights using the Newkirk (1961) coronal streamer density model. Also shown are the times of type III bursts (vertical bars), the flare continuum source at 80 MHz at an observed height ~0.6 solar radii, and the time profile of the hard X-ray burst. Error bar indicates the injection time inferred from interplanetary observations. (From Hudson et al., 1982.)
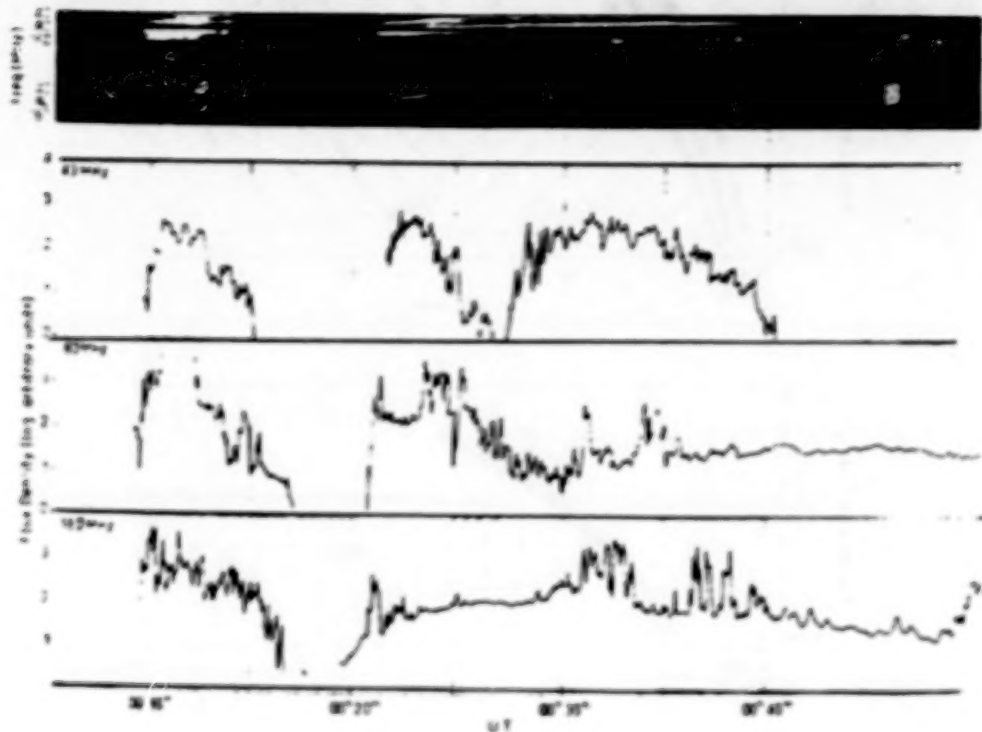
Figure 11. An FCII event which includes flash phase activity. A swept frequency spectrum
and single frequency flux observations at 43, 80, and 160 MHz are given.
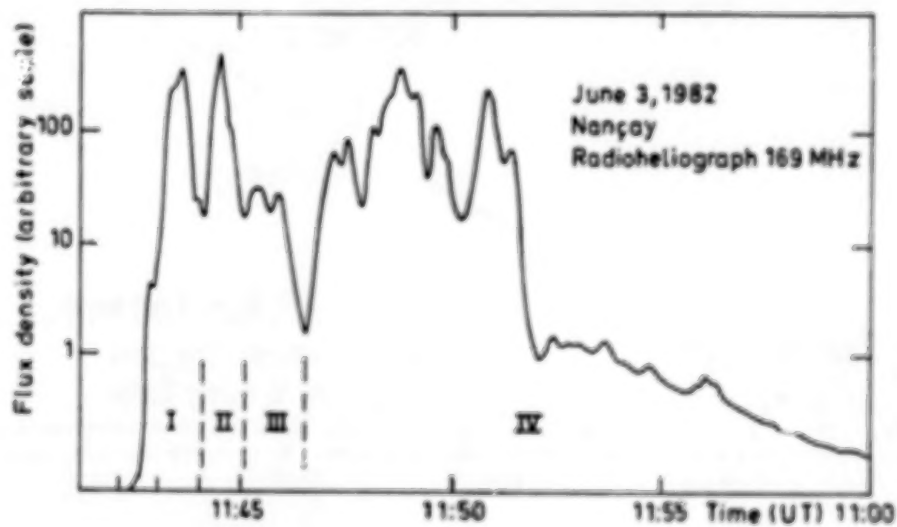(From Robinson, 1977.)

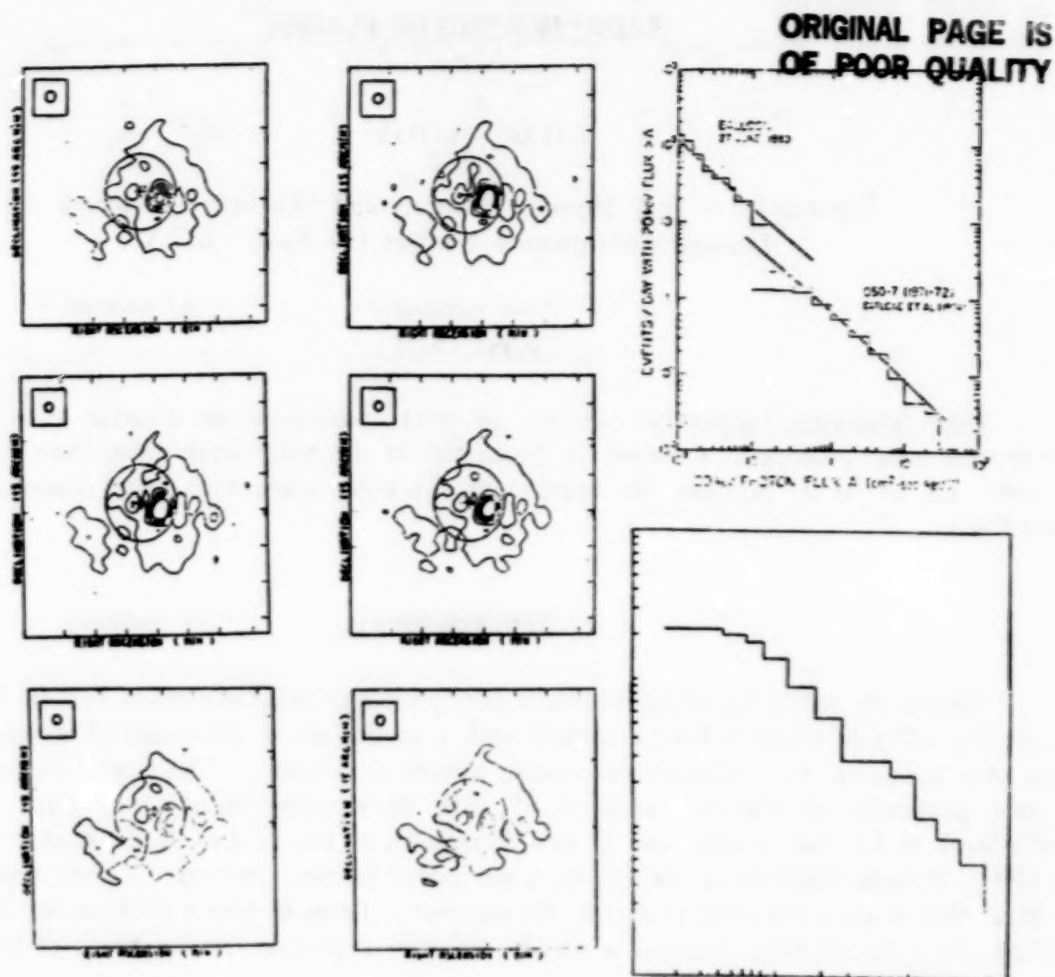Figure 12. 3 June 1982 event. Radio observations.

176

Figure 13. (left) A sequence of radioheliograms at 150 MHz showing the positions of type III-like bursts. Successive images were taken every 1 to 2 seconds. (Right top) Distribution of hard X-ray microbursts observed by Lin et al. (1984) as a function of peak keV photon flux. Also shown for comparison is the distribution of hard X-ray bursts reported by Datlowe et al. (1974). (Right bottom) Distribution of meter-decameter microbursts at 50 MHz as a function of intensity in arbitrary units. The lowest intensity is a small fraction of 1 sfu. (From Kundu and Stone, 1984.)

C - 3

RADIO IMAGING OF FLARES
(Invited)

George A. Dulk

Department of Astrophysical, Planetary and Atmospheric Sciences
University of Colorado, Boulder, CO 80309, U.S.A.

ABSTRACT

High resolution (arcseconds to tens of arcseconds) mapping of solar microwave bursts has recently been achieved. I review the properties of the radio images that have been reported to now and, so far as possible, the relation of the radio sources to X-ray observations of the same flares.

I. INTRODUCTION

One of the most important advances during the past solar maximum was the development of the capability of imaging flare emissions with a resolution of some tens of arcseconds to less than one arcsecond, i.e., adequate to resolve almost all sources. This capability was achieved in one dimension in Nagoya, Japan at 35 GHz, Nobeyama, Japan at 17 GHz, Westerbork, Netherlands at 1.4 and 5 GHz, and in two dimensions at the VLA in the USA at 1.4, 5, 15, and 22 GHz. Because Westerbork and the VLA are general purpose instruments, only a small fraction of their time is used for solar studies so the number of flares observed by them has been severely limited; nevertheless they obtained a number of very important results, some of which will be described here.

Of particular relevance to this workshop is the fact that radio waves in the decimetric-centimetric band emanate from the same populations of energetic electrons that produce soft and/or hard X rays. Time profiles ("light curves") of radio bursts are nearly identical to those of X-ray bursts even on time scales of 1 s or less. In general the form and duration of the light curves vary with radio frequency and X-ray energy, with the curves of the higher frequency radio waves corresponding better with those of the higher energy X rays; some aspects of the correlations and spectral properties will be discussed by G. Hurford at this meeting. Because of this high temporal correlation, one would expect that images made at radio and X-ray wavelengths would also be similar, with source structure at some tens of GHz resembling that at hundreds of keV, structure at a few GHz resembling that at tens of keV, and structure near 1 GHz resembling that at a few keV. However, verification of the expectation has not been possible because (1) no X-ray images have been obtained at energies $\gtrsim 30$ keV, (2) the number of flares imaged in radio waves has been small and those with simultaneous X-ray imaging even smaller, and (3) in almost all cases of joint coverage the frequency of the radio image has not matched the energy of the X-ray image. Only in the event described by Kundu et al. (1984) was there near compatibility — 5 GHz radio and 16 to 30 keV X rays, and then the images were indeed very similar.

In addition to mapping the intensity of radiation, it is possible at radio frequencies to make maps in both right-hand (RH) and left-hand (LH) polarization, or equivalently, in Stokes parameter $V = RH - LH$ or degree of circular polarization $r_c = V/I = (RH - LH)/(RH + LH)$. At the higher frequencies where the source is optically thin, the sense of circular polarization

immediately gives the direction of the magnetic field in the source region, with RH and LH polarizations implying that the longitudinal component of field is directed toward and away from the observer respectively. Here it is assumed that gyrosynchrotron radiation is the radio emission mechanism of the relevant bursts, an assumption that is well substantiated by both theory and observations. With additional information on electron energies, sometimes available from hard X-ray observations, it is also possible to infer the magnetic field strength in the source region. Typical values are in the range of 100 to 500 Gauss.

In the remainder of this paper I will describe the main results achieved from radio imaging of flares by showing some examples of the better-observed flares or ones illustrating the points most clearly. Two cautions are necessary: the first is the usual one that flares differ so much in their temporal, morphological, and spectral characteristics that it is difficult to make deductions that apply to more than a subclass of flares, and second is the point that I can illustrate only a handful of cases, so the selection is both incomplete and biased towards flares observed in two dimensions, i.e., with the VLA. The reader can find more illustrations and implications in reviews by Marsh and Hurford (1982), Kundu and Vlahos (1982), Kundu (1982), and Canfield et al. (1985), and in detailed reports by Allisandrakis and Kundu (1978), Kattenberg (1981), Kundu, Bobrowsky, and Velusamy (1981), Marsh et al. (1981), Kundu et al. (1982), Ohki et al. (1982), Velusamy and Kundu (1982), Duijveman and Hoyng (1983), Dulk, Bastian, and Hurford (1983), Hoyng et al. (1983), Kai et al. (1983), Kawabata, Ogawa, and Suzuki (1983), Lang and Willson (1983), Tsuneta et al. (1983), Willson (1983), Kundu et al. (1984), Lang and Willson (1984), Dulk, Bastian, and Kane (1985), and Nakajima et al. (1985).

II. DISCUSSION OF INDIVIDUAL EVENTS AND THEIR IMPLICATIONS

Event of 5 November 1980, 2226 UT

Hoyng et al. (1983) and Duijveman and Hoyng (1983) described the hard X-ray and radio imaging of this flare, a relatively weak one that preceded by about 7 min a more intense flare much described in the literature but for which no radio images are available. As seen in Figure 1 the flare lasted only a few minutes and had three peaks, the last was visible mainly in softer X rays and was not evident at 9.4 or 15 GHz; the first two peaks were not properly resolved with 10 s time resolution of the VLA. The upper-right part of Figure 1 shows the flaring region at the times of the first two peaks with the magnetic neutral line, the 15 GHz radio sources, and the HXIS pixels in which there were significant numbers of counts (shaded) in the 16 to 30 keV range. The 15 GHz sources are seen to straddle the neutral line of the magnetic field; this is a general rule to which there are only a few exceptions. The sources are very small, less than about 5 $''$ in extent; this also is common, with sizes averaging about 3 $''$ at 15 GHz, 10 $''$ at 5 GHz, and 30 $''$ at 1.4 GHz. Because of the weakness of the flare, few counts were recorded in the HXIS 16 to 30 keV channel. During the first peak (top right), two separated pixels had a significant number of counts, probably near footpoints of loops arching over the neutral line. During peak 2 one of the two pixels with significant counts was the central one coinciding with the radio source, but its X-ray spectrum was probably softer than that of the outer pixel. Peak 3 was also largely from the central pixel, and its spectrum was softer yet.

The bottom part of Figure 1 shows the location of the RH and LH radio sources of peak 2 relative to the neutral line and the Hα bright features. The neutral line as drawn may be misplaced by a few arcseconds, and its probable location is between the two ribbons of the flare. In any case the RH and LH radio sources are predominantly on the sides of + and − polarity, respectively. In addition, the radio source straddles the region of the brightest Hα kernels. These also are common, nearly ubiquitous features of radio images of flares.

179

The 15 GHz brightness temperature in RH polarization during peak 2 was 9.4 x 10⁸ K, and the source was optically thick or nearly so. From this it follows that the average energy of the emitting electrons was $\geq$100 keV; in fact, the HXRBS experiment observed X rays to about 300 keV. From the degree of circular polarization and the radio spectrum, the magnetic field strength in the 15 GHz source was estimated to be about 500 Gauss. With the density estimated from X-ray data to be about 3×10^{10} cm^{-3}, the plasma beta was $\beta \approx 10^{-2}$, showing a dominance of magnetic energy density in the source region.

Event of 24 June 1980, 1522 UT

Kundu et al. (1984) described the hard X-ray and VLA imaging at 5 GHz of this flare. It was located within 30 deg of disk center and was of importance SB in Hα and M1 in soft X rays. Figure 2 shows light curves in soft and hard X rays; the duration of the latter was only about 3 min. Figure 2 also shows the relationship of the 5 GHz radio source to the soft and hard X-ray sources and the off-band Hα features. Several points are notable: (1) The 5 GHz source size, about 10 $''$ x 20 $''$, was only slightly smaller than the hard X-ray source. (2) The radio and hard X-ray sources overlapped but seemed to be slightly displaced from each other; however, this might not be significant in view of possible alignment errors. (3) The radio source lay near the extremity of the off-band Hα brightening and it is not clear what its relation was to the magnetic field. However, on polarization maps (not shown) the northern and southern parts of the radio source were polarized in the LH and RH sense, respectively. (4) The soft X-ray source was considerably larger ($>$60 $''$) than either the hard X-ray or radio source and its center was displaced from them. (5) After the radio and hard X-radiation had ceased, the soft X-radiation covered a huge area that generally coincided with but even exceeded the extent of the Hα brightenings.

Event of 12 June 1980, 1340 UT

Willson (1983) described this impulsive event which was observed with the VLA at its lowest frequency of 1.4 GHz. While the overall flare lasted several minutes, we describe only the first of three peaks, one which lasted only about 10 to 20 s. Figure 3 shows the VLA images at three times, 10 s apart. The left panel shows the region just before the burst or possibly at its leading edge, with the radiation being slightly RH polarized. The middle panel is for the next 10 s interval, the one containing the burst. The source size was about 30 $''$, considerably larger than is typical of 5 or 15 GHz sources. The brightness temperature was only moderate, 1.5 x 10⁸ K. The polarization had changed dramatically from the previous 10 s map, being RH polarized only on the eastern edge while the brightest part was nearly 100% LH polarized. The right panel shows the region 10 s later yet, during burst decay, when the polarization had returned nearly to its pre-burst state.

In the absence of further information it is not possible to decide with confidence the origin of this burst. At decimetric wavelengths not all bursts are due to the same gyrosynchrotron mechanism responsible for the 15 and 5 GHz radiation of the events described previously. Plasma radiation and cyclotron maser radiation are also known to occur near 1.4 GHz.

Event of 22 November 1981, 1743 UT

The events described above involved flares on the disk. This allows the positions of sources to be related to magnetic and Hα features but prevents any direct measurements of source altitudes. From stereo observations from two spacecraft of X-ray bursts, Kane et al. (1979, 1982) have established that impulsive hard X-ray sources are located at very low altitudes,

<2500 km, which is consistent with the belief that they are at the footpoints of magnetic loops. If images are made of flares near the limb, it is possible, at least in principle, to measure directly the source altitudes.

To date only one such flare has been reported. Dulk, Bastian, and Kane (1985) made simultaneous observations at 4.9 and 15 GHz of a flare at 85 deg longitude. The results are summarized in Figure 4. The light curves at the upper left show a weak, impulsive flare with two peaks. For the first peak, the profiles at the two radio frequencies are similar to each other and to that of the 12 to 20 keV X rays (for this burst the highest energy range with enough counts to give a reliable profile). The three middle panels show the radio sources at three times: early in the rise, the first peak, and the second peak. As usual the 15 GHz source is smaller than the 4.9 GHz source, but surprisingly the sources are not cospatial, a fact that would not have been suspected from the light curves alone. There is little or no 4.9 GHz radiation from the main part of the 15 GHz source and vice versa. The upper right panel shows, for the two frequencies, the brightness temperatures near the centers of the two sources. The considerable differences suggest that the emission mechanisms may not be the same in the two sources, and this is borne out in detailed study. On the basis of the combined X-ray and radio data, the northern, 15 GHz source was found to be due to gyrosynchrotron radiation from a small number of ~300 keV electrons, with the 4.9 GHz emission from those electrons being gyroresonantly re-absorbed as it passed over a large sunspot enroute to Earth. The southern, mainly 4.9 GHz source was found to be due to thermal bremsstrahlung from a hot plasma with a temperature ranging from about 5×10^6 K at the periphery to about 20×10^6 K at the center.

The bottom panel of Figure 4 shows the two sources at the time of the burst maximum in relation to the Hα limb and the Hα flare brightenings. In projection the radio sources were at the same height or below the Hα features, probably at an altitude of 3000 km or less. This is rather similar to the height of hard X-ray sources derived by Kane et al. (1979, 1982). Hence, it seems that the fast electrons that emit both the microwaves and hard X-rays in impulsive flares are confined to very low-lying loops or their footpoints.

Event of 8 May 1981, 2200 UT

The events described above were concerned with short-lived impulsive flares, with the evidence indicating that hard X rays come largely from footpoints of low-lying loops and radio waves largely from their central positions. A distinctly different type of flare is typified by a long duration and a large source at a high altitude. An example of this kind of flare occurred on 8 May 1981 and was imaged in soft and hard X-rays by Hinotori, and at 4.9 and 15 GHz by the VLA; it has been described by Ohki et al. (1982) and by Dulk, Bastian, and Hurford (1983). Figure 5 shows two light curves of 15 GHz radiation and one of the 25 to 400 keV X-radiation. Taking into account the linear versus log scales, the 15 GHz profile from Owens Valley is very similar to the hard X-ray profile, but the VLA profile is similar only at the earliest times, before 2220 UT. The VLA profile represents the flux as seen by an interferometer with a fringe spacing of 15.4 arcsecond, the lowest resolution of any antenna pair on that occasion. The decrease in VLA flux after 2220 UT (while it was increasing on the Owens Valley antenna with its 3 ″ resolution) demonstrates that the source increased its size to well above 15 ″. The 4.9 GHz flux recorded by a VLA interferometer with 40 ″ resolution behaved in a similar way, showing that the 4.9 GHz source too was exceptionally large. The lower panel of Figure 5 shows the hard X-ray sources near the time of burst peak and their relation to magnetic and Hα features. Two X-ray sources were present, the main one's size was nearly 1 ″. Also shown in the figure are three small sources that were imaged by the VLA, but they contained only a tiny fraction of the total 15 GHz flux, and their relation to magnetic, hard X-ray, or Hα features is unclear.

A lesson to be learned from this flare is that the VLA is most useful when in a compact configuration, especially if dual frequency observations are desired. When in a widespread configuration there is danger that large-scale structures become invisible and that ambiguities may not allow the positions of small-scale features to be determined.

Event of 29 January 1984, 1825 UT

As reported by Lang and Willson (1984), this flare was imaged at the VLA at several frequencies in the range 1.4 to 1.7 GHz. Figure 6 shows light curves at two frequencies spaced about 0.03 GHz apart, and in the two senses of circular polarization. The burst was weak and the spiky components appeared almost exclusively in RH polarization. There are significant differences in the intensity of a few of the spikes at the two closely spaced frequencies, notably spike 7; this implies that the bandwidth of the spiky radiation was very small, only about 2%.

The upper two panels of Figure 6 shows RH (solid) and LH (dashed) images at the two closely spaced frequencies at the times of peaks 1 to 7. While the structures are seen to be quite similar at the two frequencies, the intensities are not always similar. Further, the LH and RH radiation occurred at distinctly different spatial locations. (It is possible that the polarization of the southern source may have been low, with the corresponding RH contours not visible because of the limited dynamic range of the maps.)

The temporal, spectral, and polarization characteristics of this event suggest that two emission mechanisms were involved, the normal gyrosynchrotron process for the weak, southern source, and the cyclotron maser process for the strong, RH-polarized northern source. The former process is not capable of producing bursts of nearly 100% polarization and narrow bandwidth, but these are typical characteristics of a maser (e.g., Melrose and Dulk, 1982). It would be of great interest to know how hard X rays behaved in the spatial, spectral, and temporal domains at times of microwave spike bursts of the kind illustrated by this event.

III. CONCLUSIONS

In summary, I list some of the general properties derived from radio imaging of flares.

(1) The most common, observed characteristic is that impulsive radio burst sources lie over neutral lines of magnetic fields, and that the source is near the top of one magnetic loop or an arcade, but extending over much of the loop lengths. Radio sources are seldom found only at footpoints.

(2) Radio sources are larger at the lower frequencies; for impulsive flares they are typically 3 ″ at 15 GHz, 10 ″ at 5 GHz, and 30 ″ at 1.4 GHz. However, they are sometimes much larger, especially for extended flares, reaching 1 ′ or more.

(3) The heights of the impulsive radio sources are quite low, perhaps not much higher than the 2500-km limit found for several hard X-ray bursts. However, this conclusion rests mainly on one limb flare observed with the VLA and requires verification.

(4) The field strengths in the source regions are usually in the range of 100 to 500 Gauss and the plasma beta is usually much less than unity.

(5) Most radio emission at frequencies higher than a few GHz is due to gyrosynchrotron radiation from electrons of energy >100 keV, with the higher frequencies being produced by the more energetic electrons. For γ-ray flares the frequency of peak radio flux extends to 50 GHz or more, with the highest frequency radiation produced by relativistic electrons. Extrapolating the source size versus frequency relation, one would expect the relativistic electrons to occupy a very small volume, $\lesssim 1$ $''$.

(6) Following the impulsive phases of flares, it is likely that thermal bremsstrahlung from the soft X-ray plasma plays a role in producing the slowly decaying tail of radio emission that is especially evident at the lower frequencies.

(7) At frequencies $\lesssim 3$ GHz cyclotron maser and plasma radiation become increasingly more important. Cyclotron maser emission probably produces the microwave spike bursts observed mostly at $\lesssim 1$ GHz, but occasionally to 3 GHz. In impulsive flares it may also play a major role in the transport of energy from the energy release/hard X-ray/cm burst region into the larger, soft X-ray region (Melrose and Dulk, 1984).

(8) Simultaneous imaging observations in radio and hard X rays have revealed several important phenomena in flares, but their potential has hardly been tapped because X-ray imaging has so far achieved relatively poor spatial resolution compared with radio imaging, and because images have so far been made only at relatively low X-ray energies.

REFERENCES

Allissandrakis, C. E. and Kundu, M. R., 1978, *Astrophys. J.*, *222*, 342.

Canfield, R. C., and 15 co-authors, 1985, Chapter 3 of *Solar Flares: Proc. SMM Workshop*, eds., B. E. Woodgate and M. R. Kundu, in press.

Duijveman, A. and Hoyng, P., 1983, *Solar Phys.*, *86*, 279.

Dulk, G. A., Bastian, T. S., and Hurford, G. J., 1983, *Solar Phys.*, *86*, 451.

Dulk, G. A., Bastian, T. S., and Kane, S. R., 1985, *Astrophys. J.*, submitted.

Hoyng, P., Marsh, K. A., Zirin, H., and Dennis, B. R., 1983, *Astrophys. J.*, *268*, 865.

Kawabata, K., Ogawa, H., and Suzuki, I., 1983, *Solar Phys.*, *86*, 247.

Kai, K., Nakajima, H., Kosugi, T., and Kane, S. R., 1983, *Solar Phys.*, *86*, 231.

Kane, S. R., Anderson, K. A. Evans, W. D., Klebesadel, R. W., and Laros, J. G., 1979, *Astrophys. J. (Letters)*, *233*, L151.

Kane, S. R., Fenimore, E. E., Klebesadel, R. W., and Laros, J. G., 1982, *Astrophys. J. (Letters)*, *254*, L53.

Kattenberg, A., 1981, Ph.D. Thesis, Univ. of Utrecht.

Kundu, M. R., 1982, *Rep. Prog. Phys.*, *45*, 1435.

Kundu, M. R. and Vlahos, L., 1982, *Space Sci. Rev.*, *32*, 405.

Kundu, M. R., Bobrowsky, M., and Velusamy, T., 1981, *Astrophys. J.*, *251*, 352.

Kundu, M. R., Schmahl, E. J., Velusamy, T., and Vlahos, L., 1982, *Astron. Astrophys.*, *108*, 188.

Kundu, M. R., Machado, M. E., Erskine, F. T., Rovira, M. G., and Schmahl, E. J., 1984, *Astron. Astrophys.*, *132*, 241.

Lang, K. R. and Willson, R. F., 1983, *Adv. Space Res.*, *2*, No. 11, 91.

Lang, K. R. and Willson, R. F., 1984, *Adv. Space Res.*, *4*, No. 7, 105.

Marsh, K. A., and 6 co-authors, 1981, *Astrophys. J.*, *251*, 797.

Marsh, K. A. and Hurford, G. J., 1982, *Ann. Rev. Astron. Astrophys.*, *20*, 497.

Melrose, D. B. and Dulk, G. A., 1982, *Astrophys. J.*, *259*, 844.

Melrose, D. B. and Dulk, G. A., 1984, *Astrophys. J.*, *282*, 308.

Nakajima, H., Dennis, B. R., Hoyng, P., Nelson, G., Kosugi, T., and Kai, K., 1985, *Astrophys. J.*, *288*, 806.

Ohki, K., and 8 co-authors, 1982, *Proc. Hinotori Symp. Solar Flares*, Tokyo: Inst. of Space and Astronaut. Sci., p. 102.

Tsuneta, S., and 7 co-authors, 1983, *Solar Phys.*, *86*, 313.

Velusamy, T. and Kundu, M. R., 1982, *Astrophys. J.*, *258*, 388.

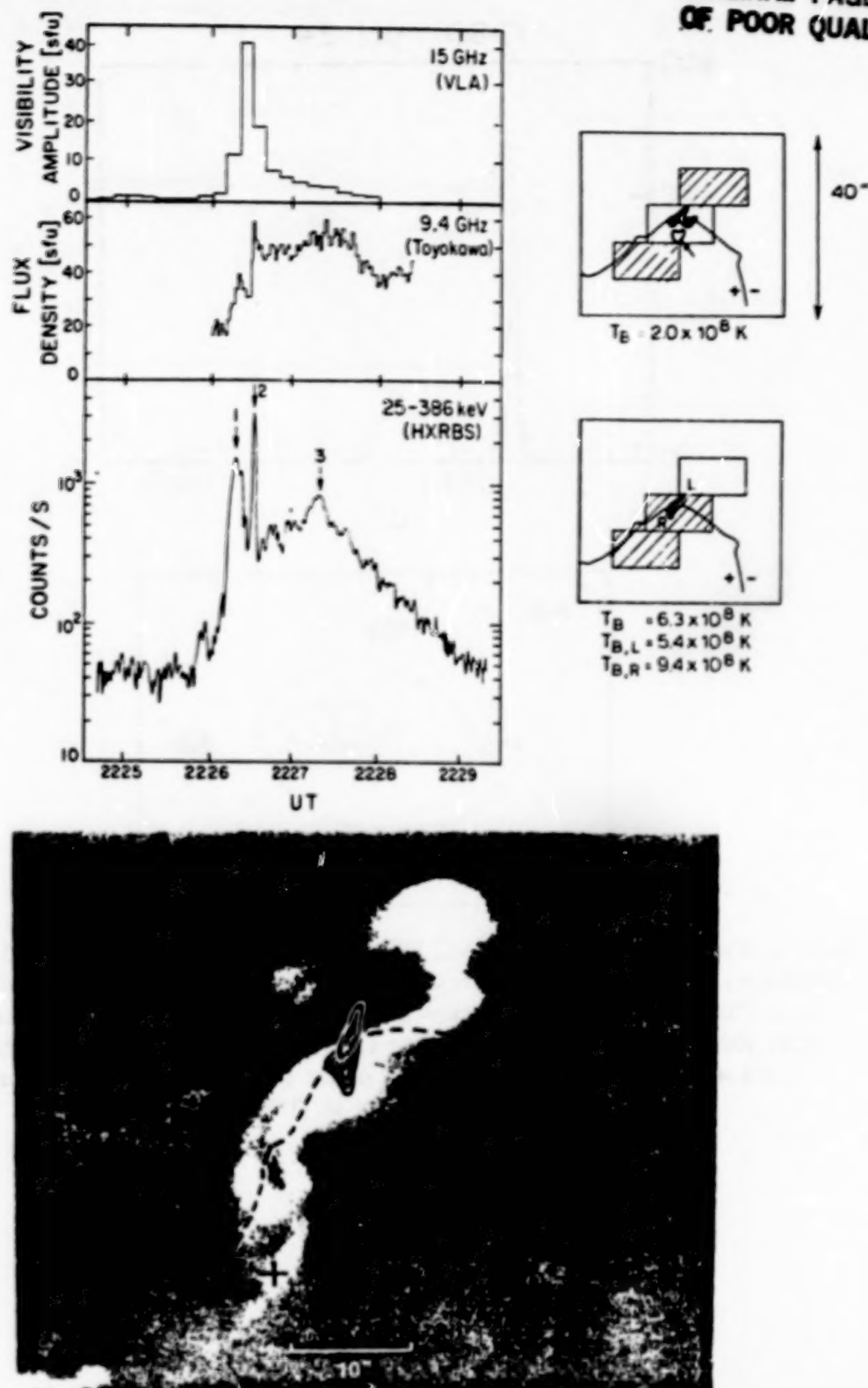Willson, R. F., 1983, *Solar Phys.*, *83*, 285.

Figure 1. Event of 5 November 1980, 2226 UT. Upper left: light curves at 15 GHz, 9.4 GHz, and 25 - 386 keV X rays. Upper right: images at the times of peaks 1 and 2 of the burst. The solid line represents the magnetic neutral line, the black areas are the 15 GHz sources, and the hatched areas represent HXIS pixels with significant counts in the 16 to 30 keV range. Bottom: superposition of VLA sources in RH (black contours) and LH (white contours) radiation on the Hα picture of the two ribbon flare. From Duijveman and Hoyng (1983) and Hoyng et al. (1983).
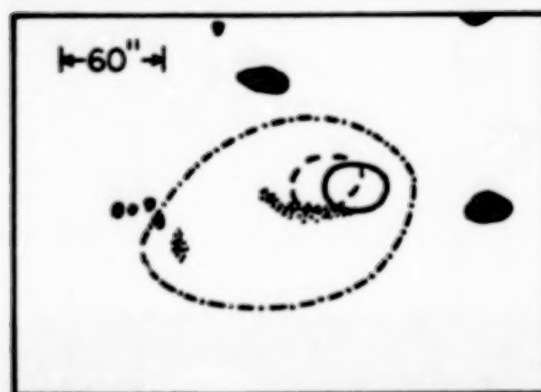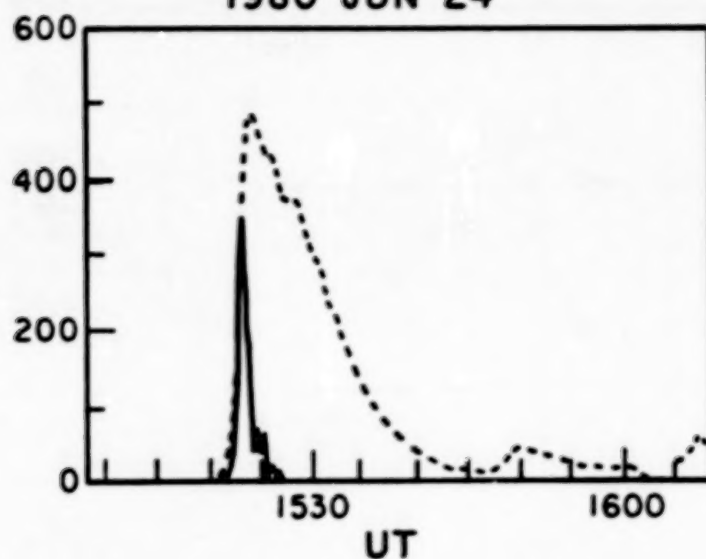
185

1980 JUN 24

Figure 2. Event of 24 June 1980, 1522 UT. Top: light curves of the soft (3.5 to 8 keV; dotted line) and hard (22 to 30 keV; solid line) X-ray emission. Bottom: positions and sizes of the 5 GHz source (solid curve), hard X-ray source (dashed curve), and soft X-ray source (dot-dash curve) in relation to bright, off-band Hα features (stippled) and sunspots (dark areas) at the time of the peak of the hard X-ray burst. From Kundu et al. (1984).
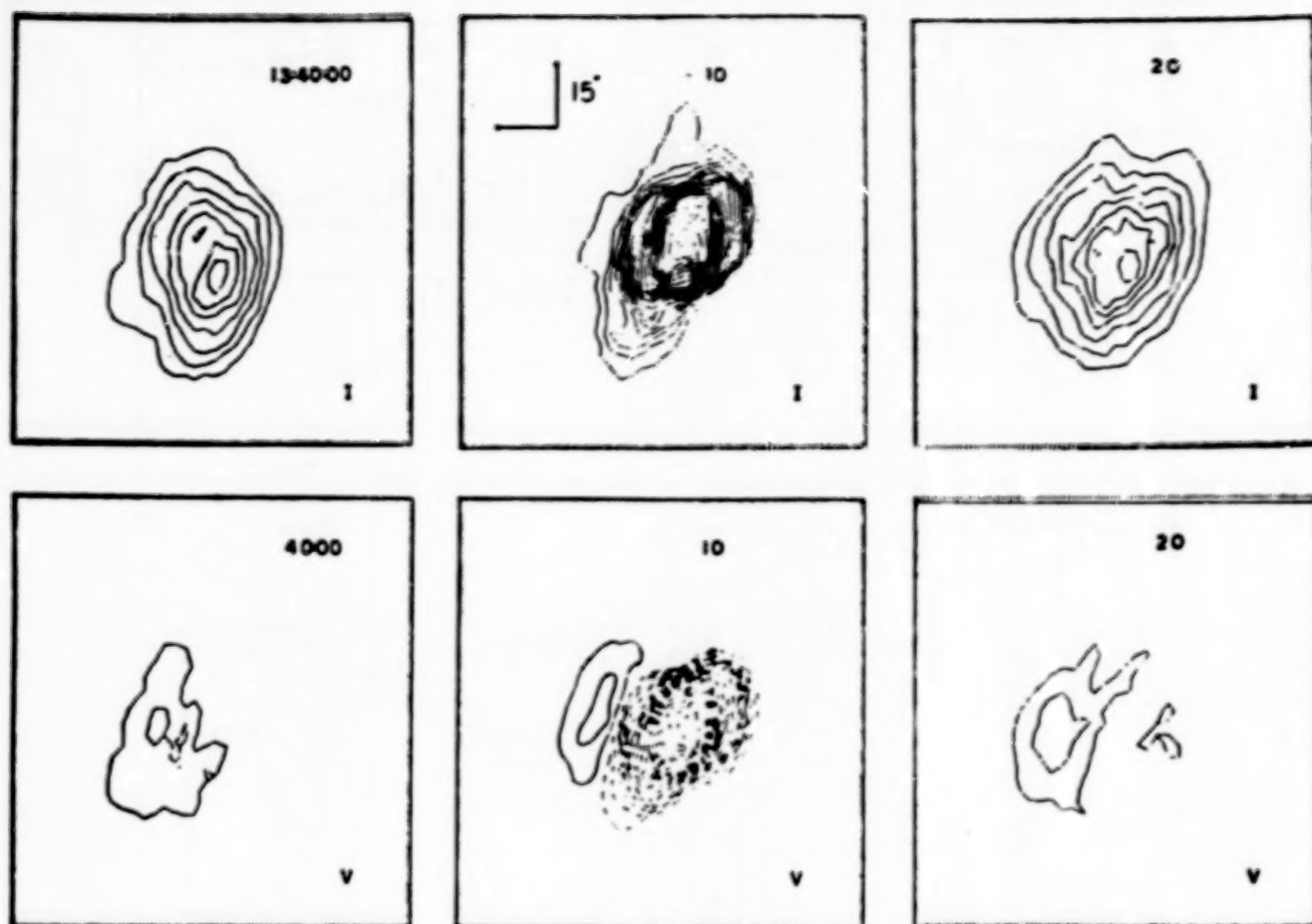
Figure 3. Event of 12 June 1980, 1340 UT. Three successive 10 s VLA maps of intensity
(top) and circularly polarized intensity (bottom). Solid and dashed contours represent
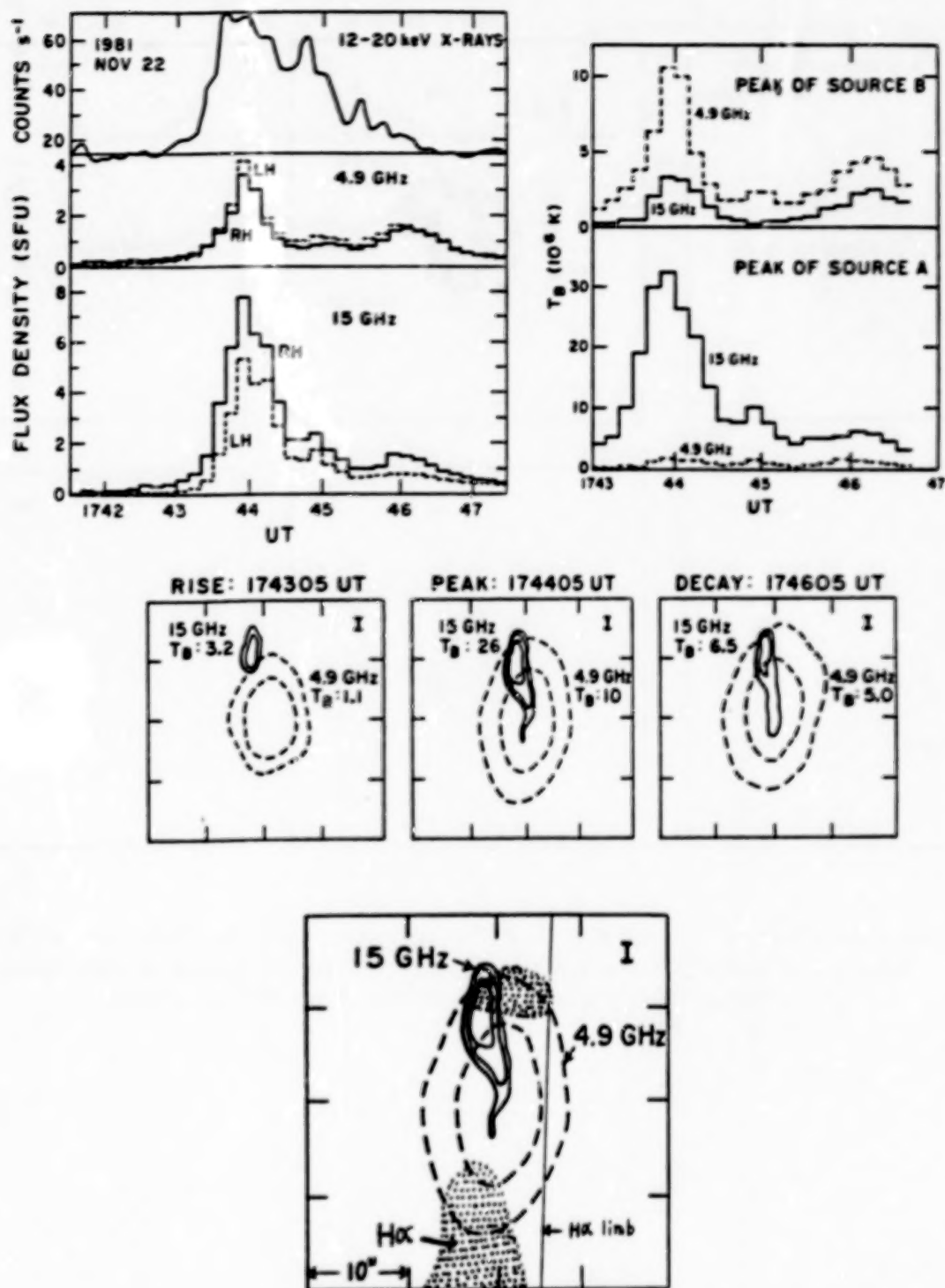RH and LH polarization, respectively. From Willson (1983).

Figure 4. Event of 22 November 1981, 1743 UT. Upper left: light curves of hard X rays and 4.9 and 15 GHz radio waves. Middle: VLA maps of the 4.9 and 15 GHz radio sources at three stages of the flare: rise, first peak, and second peak. Upper right: time variation of the brightness temperature of the RH polarized radiation at the centers of the two sources evident in the middle panel. Bottom: enlarged view of the 4.9 and 15 GHz sources at the time of the first peak, showing their relation with the Hα limb and the bright, flaring Hα features. From Dulk, Bastian, and Kane (1985).
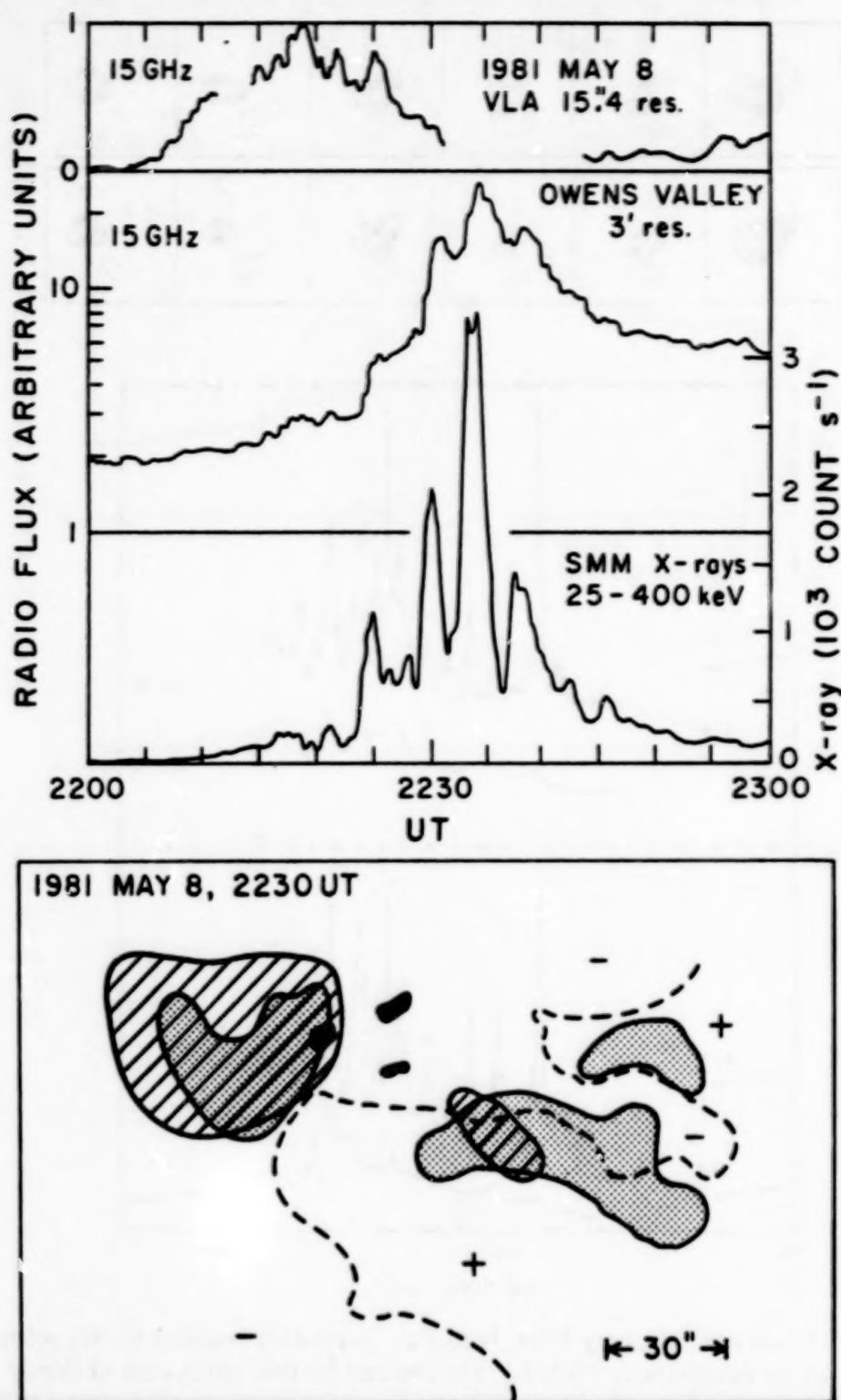
Figure 5. Event of 8 May 1981, 2200 UT. Top: light curves of 15 GHz radiation recorded with a VLA antenna pair with 15.4 arcsecond resolution, 15 GHz radiation recorded with an Owens Valley antenna with 3 ⌢ resolution, and 25 to 500 keV X rays recorded on SMM. Bottom: map of the 17 to 40 keV source structure (shaded areas), its relation to the magnetic neutral line (dashed line), the bright, off-band Hα features (strippled), and three 15 GHz hot spots (dark areas). From Ohki et al. (1982) and Dulk, Bastian, and Hurford (1983).
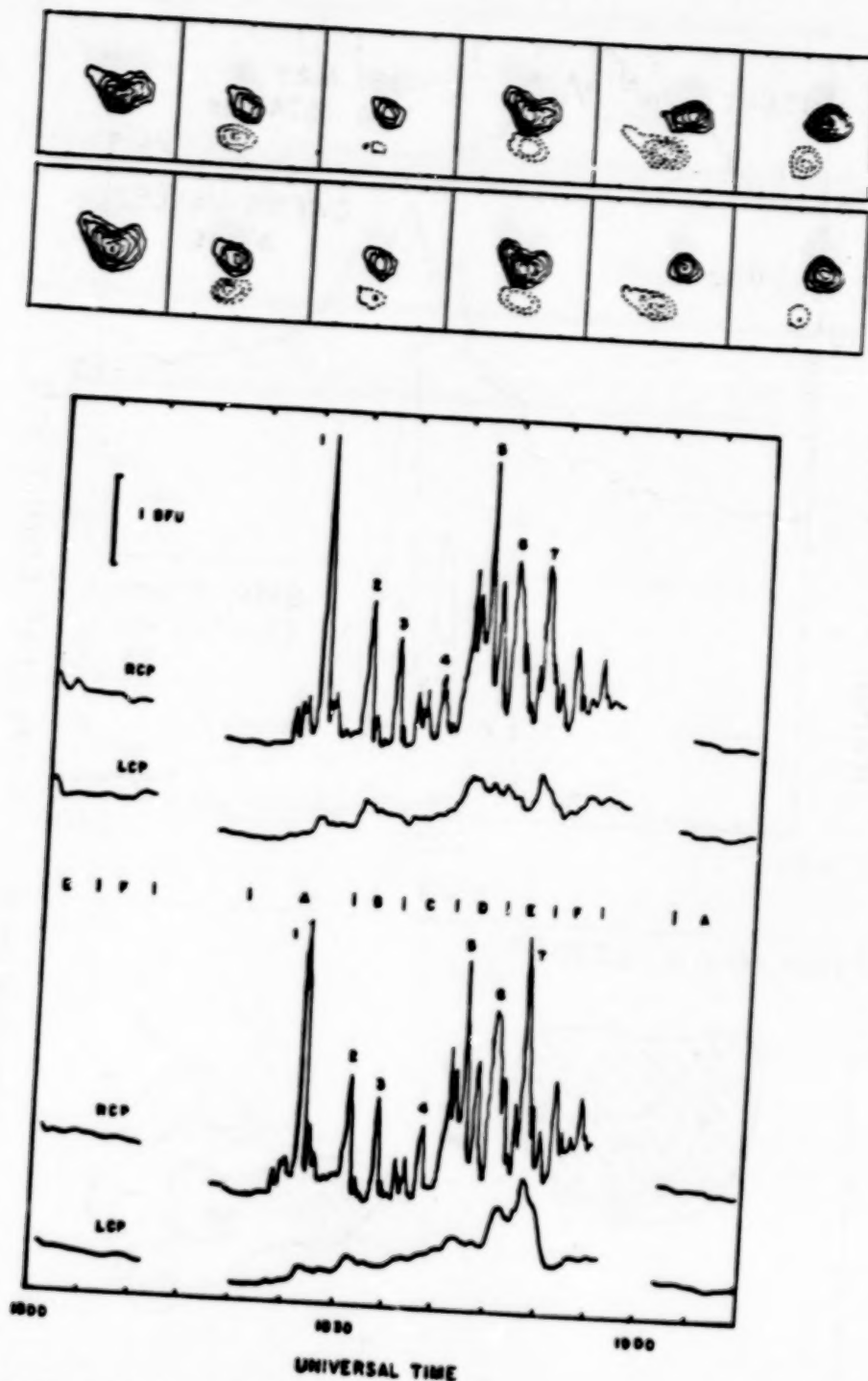
Figure 6. Event of 29 January 1984, 1830 UT. Bottom: a sequence of RH polarized spiky bursts at frequencies near 1.4 GHz. The top and bottom profiles are at closely spaced frequencies, about 30 MHz apart. Both frequencies were changed every 5 min or so, but staying in the range of 1.4 to 1.7 GHz. Top: VLA maps at the times of the seven spikes numbered in the bottom panel. The upper and lower series are for the higher and lower of the closely spaced frequencies, respectively. Solid and dashed contours designate RH and LH polarization, respectively. Peak 7 (far right) has a large difference in brightness temperature at the two frequencies: 1.1×10^8 and 6.0×10^7K, respectively. The angular scale is shown by the size of the boxes: 16 arcminute square.

HIGH-SPECTRAL RESOLUTION SOLAR MICROWAVE OBSERVATIONS

Gordon J. Hurford

Caltech, Pasadena, CA 91125

ABSTRACT

The application of high-spectral resolution microwave observations to the study of solar activity is discussed with particular emphasis on the frequency dependence of microwave emission from solar active regions. A "shell model" of gyroresonance emission from active regions is described which suggests that high-spectral resolution, spatially-resolved observations can provide quantitative information about the magnetic field distribution at the base of the corona. Corresponding observations of a single sunspot with the Owens Valley frequency-agile interferometer at 56 frequencies between 1.2 and 14 GHz are presented. The overall form of the observed size and brightness temperature spectra was consistent with expectations based on the shell model, although there were differences of potential physical significance. The merits and weaknesses of microwave spectroscopy as a technique for measuring magnetic fields in the solar corona are briefly discussed.

I. INTRODUCTION

During the past solar maximum, considerable insight into many aspects of solar activity has been gained through the use of high-spatial resolution microwave observations (e.g., Dulk, 1985; Kundu and Vlahos, 1982; Marsh and Hurford, 1982). The value of such observations has been not only to reveal the size, location, and morphology of the microwave sources but also to enable the brightness temperature of such sources to be determined. The brightness temperature, determined from the ratio of source flux to area, is the quantity which is related most directly to the physical conditions in the source or to the characteristics of the energetic particle population. For example, the brightness temperature of an optically thick, thermal plasma is equal to its electron temperature.

In this paper, we shall be concerned with the frequency dependence of microwave emission from active regions. Such emission can be divided into three frequency regimes depending on the location and physical mechanisms which dominate. In the first regime, at millimeter wavelengths, emission from the corona can be entirely neglected and the situation is dominated by thermal bremsstrahlung from the chromosphere. Active regions are relatively difficult to discern, except through absorption features associated with filaments (Figure 1).

At centimetric wavelengths, thermal bremsstrahlung from the corona begins to make a contribution to the observed surface brightness. The low density and high temperature of the corona can only provide a small optical depth, and so the resulting brightness temperatures fall well below coronal values. Gyroresonance opacity, however, can render the corona optically thick at locations where the magnetic field has the appropriate values. This is observed as small, localized areas in which the brightness temperature achieves coronal values.

At decimetric frequencies, the optical depth of thermal bremsstrahlung from the corona has increased to the point where coronal brightness temperatures can be approached so that the morphology of the corresponding microwave maps changes again (e.g., Dulk and Gary, 1983), almost to the point of being suggestive of soft X-ray maps.

For many active regions, observations at the VLA frequencies, 15, 5, and 1.4 GHz, would yield three different morphologies, corresponding to these three regimes.

This paper will be concerned with the frequency dependence of active region emission in the second regime where gyroresonance opacity is important. It will be suggested that the size and brightness temperature spectrum of the compact microwave sources can be used to directly measure the strength and distribution of coronal magnetic fields. This suggestion will be illustrated by preliminary results of high-spatial and high-spectral resolution, multifrequency observations of a solar active region.

II. A SHELL MODEL OF MICROWAVE EMISSION

Let us now consider in more detail some characteristics of the gyroresonance emission from active regions, with particular emphasis on what might be learned from the frequency dependence of such emission. To simplify the discussion, we consider the case of a single isolated sunspot. In the absence of gyroresonance opacity, thermal bremsstrahlung would yield emission with brightness temperatures of 10^4 to 10^5 K. Under the specific conditions where gyroresonance can be effective, however, the increased brightness temperature to $\sim 10^6$ K would be readily observable as a bright source against a relatively cool background. The corresponding sources have been observed by many workers with high-resolution, microwave imaging instruments such as the Very Large Array and the Westerbork Interferometer (e.g., McConnell and Kundu, 1984; Lang, Willson, and Gaizauskas, 1983).

Gyroresonance opacity is significant at frequencies which are low integral multiples of the local gyrofrequency, ν_g (GHz) = 2.8 B (kG). It is important to recall that the gyrofrequency depends only on the magnetic field, B, and is independent of electron temperature, density, or velocity. At temperatures and densities typical of coronal conditions, gyroresonance opacity usually provides significant optical depth at the 2nd and 3rd harmonics in the extraordinary propagation mode (left circular polarization for downward directed fields) and at the 2nd harmonic in the ordinary mode. The optical depth at higher harmonics is usually much less than 1 and so can be neglected.

These considerations lead to the schematic picture, illustrated in Figure 3, whereby at a fixed frequency, the coronal microwave emission above a sunspot is generated in magnetic shells, representing isogauss surfaces. At 5 GHz for example, the emission would come from shells where the magnetic fields are approximately 600 and 900 Gauss. (At 600 and 900 Gauss, the gyrofrequencies are 1.7 and 2.5 GHz, whose 2nd and 3rd harmonics are 5 GHz.) Thus, at 5 GHz, the ordinary mode emission comes from a surface where the magnetic field is 900 Gauss, whereas the extraordinary mode emission comes from a 600-Gauss shell. (In the extraordinary mode, the 900-Gauss shell also would emit at 5 GHz, but such emission normally would be hidden under the opaque 600-Gauss shell.)

To imaging observations, these shells appear as the localized areas with coronal brightness temperature. The diameter of the observed sources is determined by the intersection of the isogauss shells with the transition region. (Emission by the shell below the transition region is unimportant since even if it were optically thick, it could not have 10^6 K brightness temperature.) Thus, the outline of the resulting 10^6 K source represents a specific isogauss contour at the base of the corona.

In this picture, observations at a different frequency would correspond to a correspondingly different magnetic field contour. For example, at higher frequencies, the emission shells would correspond to stronger fields and a decreased source diameter would be expected. In fact, at a frequency corresponding to the shell which is tangent to the transition region, we would expect that the diameter would approach zero and that at frequencies above this cutoff, coronal brightness temperatures would not be achieved.

Note that the diameter of these shells as a function of frequency depends on the configuration of the magnetic field in the corona. Rapidly diverging fields would differ markedly from well constrained flux tubes in terms of the variation of the contour diameter with field at the base of the corona. Thus, measurement of the diameter and temperature of the corresponding microwave sources as a function of frequency could provide a direct, quantitative measurement of the magnetic field distribution at the base of the corona.

III. OBSERVATIONS

To explore the feasibility of such a technique for determining coronal fields, observations were conducted with the frequency-agile interferometer of the Owens Valley Radio Observatory (OVRO). This system (Hurford, Read, and Zirin, 1984) can observe at up to 86 frequencies between 1 and 18 GHz in both right and left circular polarization (RCP,LCP). With its capability of rapid switching among frequencies, detailed spectra can be obtained in a few seconds.

Early results (Hurford, Gary, and Garrett, 1985) used two antennas for measurements of active regions. With only a single baseline, it was not possible to directly measure the size of the sources. The resulting spectra were consistent, however, with the arguments advanced in Section I. Soviet workers (cf., Akhmedov et al., 1983) have conducted corresponding multifrequency measurements between 7.5 and 15 GHz using their RATAN-600 instrument.

The present results are based on the first such interferometric measurements using three antennas. At the time of these observations, the east-west separation of the antennas was 0.183, 1.067, and 1.250 km with the central antenna displaced 0.032 km north of the line joining the outer two. The resulting resolution (fringe spacing) was inversely proportional to frequency (5 arc s at 10 GHz), which was more than adequate to resolve the sources at each frequency. The limited field of view afforded by the use of large antennas (27 to 40 m diameter paraboloids) made it possible to restrict the field of view to a single active region (at all but the lowest frequencies).

Calibration of interferometer amplitudes as a function of polarization, baseline, and frequency was based on extended observations of 3C273 and 3C84. The resulting amplitudes are estimated to be known to about 10%, with a principal source of uncertainty being an imperfect knowledge of the calibrator spectra.

The preliminary results discussed below are based on data acquired in right and left circular polarization (RCP,LCP) at 56 frequencies between 1.2 and 14 GHz during ~20 min integrations on 3 successive mornings (26-28 July 1984).

Optical data showed that the target region (AR4549) was dominated by a progressively weakening, single sunspot. Therefore, we anticipated that only a single gyroresonance source

would be present. This hypothesis was tested by forming the closure phase* (Pearson and Read-head, 1984) at each frequency and polarization and rejecting data which were inconsistent with the single gyroresonance source. (Rejected data were primarily at the highest and lowest frequencies where emission by thermal bremsstrahlung was competitive.)

To determine the size of the source at each frequency/polarization, a Gaussian profile was assumed. In this case the dependence of amplitude, A [Jy], on projected baseline, L [km], for a Gaussian source of FWHM diameter, D [arc s], observed at frequency, ν [GHz] is given by:

$$A = A_0 \, e^{-9.3 \times 10^{-4} \, (LD\nu)^2}$$

where A_0 [Jy] is the limiting amplitude at L = 0, corresponding to an unresolved source. Thus, a plot of ln(A) versus L^2 should be a straight line whose slope yields the value of D, the source diameter. A typical plot of this type, shown in Figure 3, shows that the diameter can be measured to an accuracy of about 5%.

Having measured the diameter and A_0, the corresponding brightness temperature is given by the ratio of source flux to area, using the relation,

$$T_b = 3.5 \times 10^6 \, A_0 \, (D\nu)^{-2} \quad .$$

The resulting size and brightness temperature spectra for 26 July 1984 are illustrated in Figure 4. Figure 5 shows the evolution of these quantities over the three successive days as the sunspot decayed.

IV. RESULTS

In broad terms, the features of the spectra in Figure 4 are consistent with expectations based on the shell model discussed in Section II. For example, in LCP (extraordinary mode emission) the brightness temperature maintained coronal values up to ~12 GHz while below this frequency the source size increased as frequency decreased. The interpretation is that the isogauss contours at the base of the corona are larger at the weaker fields corresponding to the lower frequencies. Above 12 GHz, the brightness temperature is seen to drop rapidly to a few times 10^5 K. This is consistent with the expectation that the brightness temperature would fall at a transition frequency where the corresponding isogauss shell was tangent to the transition region. The relatively constant value of source size above ~10 GHz is not understood at present, but might be related to spatial fragmentation of high frequency sources such as observed by Lang, Willson, and Gaizauskas (1983) at 15 GHz. (A group of unresolved sources would be seen by a three-element interferometer to have a diameter corresponding to their spatial envelope and a correspondingly diluted brightness temperature.)

Comparing the RCP and LCP brightness temperature spectra, we note that the same qualitative behavior is observed in RCP as in LCP. Of particular interest, however, is the fact that shifting the RCP spectrum up in frequency by a factor of 3/2 provides a reasonable agree-

---

*Closure phase can be defined an appropriately signed sum of the interferometer phases observed on the three baselines. Its usefulness here is derived from the fact that the closure phase should be zero for the expected small, single, symmetrical source, and generally nonzero for more complex sources.

ment with the LCP brightness temperature spectrum. This is consistent with the expectation that the 2nd and 3rd harmonics are the highest ones that are optically thick in the ordinary and extraordinary modes, respectively.

Some aspects of the spectra in Figure 4 are not understood at present. A scaled comparison of the RCP and LCP size spectra might be expected to behave in the same manner as the scaled brightness temperature spectra. Although they are indeed consistent in terms of the size and scaled frequency at which the size levels off, the RCP results at lower frequencies seem significantly higher than expected on the basis of the LCP spectra. Another unexpected feature is the apparent systematic increase from 2 to 4 x 10^6 K as frequency increases. The significance of this in terms of the physics of the coronal fields is not clear.

The evolution of the coronal field as the sunspot disappeared is illustrated in Figure 5. Assuming that the 3rd harmonic is the relevant one in the extraordinary mode, from the brightness temperature spectra, it is apparent that the maximum field at coronal levels decreased from about 1300 to 1000 to 600 G over a 2-day period. The relatively modest change in the size spectra at the lower frequencies over this period is also significant. It may suggest that the weaker fields were not affected by the spot's disappearance to the same extent as were the stronger fields.

Another interesting facet to the field evolution was the systematic decline in brightness temperature associated with the strongest fields on each day, from 4 to 2 to 1 x 10^6 K.

V. DISCUSSION

The observations presented above represent preliminary analyses of the first interferometric size and brightness temperature spectra of an active region. The region selected for this analysis was deliberately chosen to be a simple one, a single isolated sunspot. In broad terms, we have seen that the spectra matched expectations based on straightforward application of gyroresonance effects, as exemplified by magnetic shells. We have also seen that there are some aspects of the spectra that are not yet understood.

At this stage, it is perhaps premature to consider detailed interpretation of the data in terms of the solar coronal fields. Nevertheless, it may be worthwhile to comment on the strengths and weaknesses of microwave spectroscopy (as now understood) for the measurement of such fields.

Unlike photospheric magnetograms which measure magnetic FLUX (averaged over the seeing-dependent instrumental resolution), microwave spectroscopy depends on the magnetic FIELD in the corona. (Thus, for example, the present data are inconsistent with a model in which much of the coronal field is concentrated in small bundles of intense field.) Through the gyrofrequency, the field measurements are inherently calibrated. Thus, long-term comparisons are quite feasible. More complete exploitation of the interferometer phase data will enable the location of the coronal fields to be accurately established. In such circumstances, limb observations would enable the field profile as a function of height to be directly determined. Finally, since measurements such as these can be made in a few seconds, insight into flare-related coronal fields can be expected as well.

The use of microwave spectroscopy for the measurement of coronal fields has some clear weaknesses. As our model suggests, the magnetic measurements represent emission coming from a

range of heights, characterized by temperature, not distance above the photosphere. Thus, although the measured isogauss contours refer to the base of the corona, the corresponding temperature values average over a range of heights. There can also be potential sources of ambiguity related to the specification of the appropriate harmonic, particularly for magnetic field directed close to the line of sight. This, however, can be overcome in a straightforward manner with more detailed calculation of the emission (e.g., Kruger, Hildebrandt, and Furstenberg, 1985; Hurford, Gary, and Garrett, 1985). Perhaps the most serious weakness, however, is that with a three-element interferometer, there are limitations as to the morphological complexity of active regions which can be effectively studied. This problem cannot be resolved without the addition of more antennas.

Despite these weaknesses, these preliminary results suggest that microwave spectroscopy has the potential to directly determine the magnetic field profile at the base of the corona. Given the importance of coronal fields to many aspects of solar activity, this may prove a useful adjunct to the next generation of coronal and hard X-ray imaging instrumentation.

REFERENCES

Akhmedov, Sh. B., Gelfreikh, G. B., Furstenberg, F., Hildebrandt, J., and Kruger, A., 1983, *Solar Phys.*, *88*, 103.

Dulk, G. A., 1985, these proceedings.

Dulk, G. A. and Gary, D. E., 1983, *Astron. Astrophys.*, *124*, 103.

Hurford, G. J., Read, R. B., and Zirin, H., 1984, *Solar Phys.*, *94*, 413.

Hurford, G. J., Gary, D. E., and Garrett, H. B., 1985, *Radio Stars* (R. M. Hjellming and D. M. Gibson, eds.), D. Reidel, p. 379.

Kruger, A., Hildebrandt, J., and Furstenberg, F., 1985, *Astron. Astrophys.*, *143*, 72.

Kundu, M. R. and Vlahos, L., 1982, *Space Sci. Rev.*, *32*, 405.

Lang, K. R., Willson, R. F., and Gaizauskas, V., 1983, *Astrophys. J.*, *267*, 455.

Marsh, K. A. and Hurford, G. J., 1982, *Ann. Rev. Astron. Astrophys.*, *20*, 497.

McConnell, D. and Kundu, M. R., 1984, *Astrophys. J.*, *279*, 421.

Pearson, T. J. and Readhead, A. C. S., 1984, *Ann. Rev. Astron. Astrophys.*, *22*, 97.
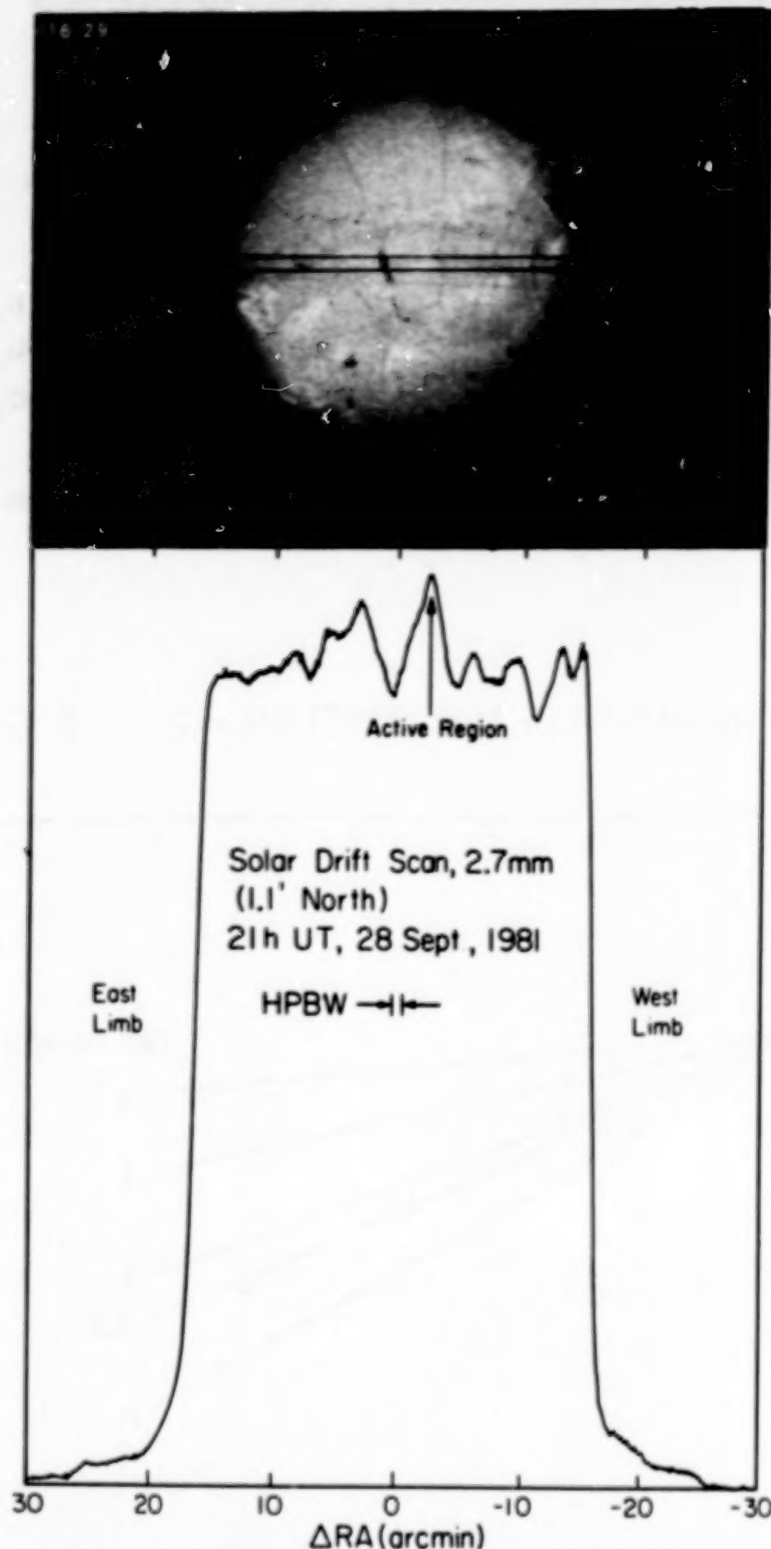
Figure 1. Comparison of a solar profile at 114 GHz with the corresponding Hα full-disk image. The two parallel lines on the optical image show the track of the half-power points of the radio beam as it scanned the Sun. Even when the beam crossed an active region, the brightness temperature did not significantly exceed its ~7000 K average value. The most striking correspondence is between the filaments in Hα and absorption features in the radio. (The data were acquired by a 10 m telescope at Owens Valley in collaboration with P. G. Wannier and G. A. Seielstad.)
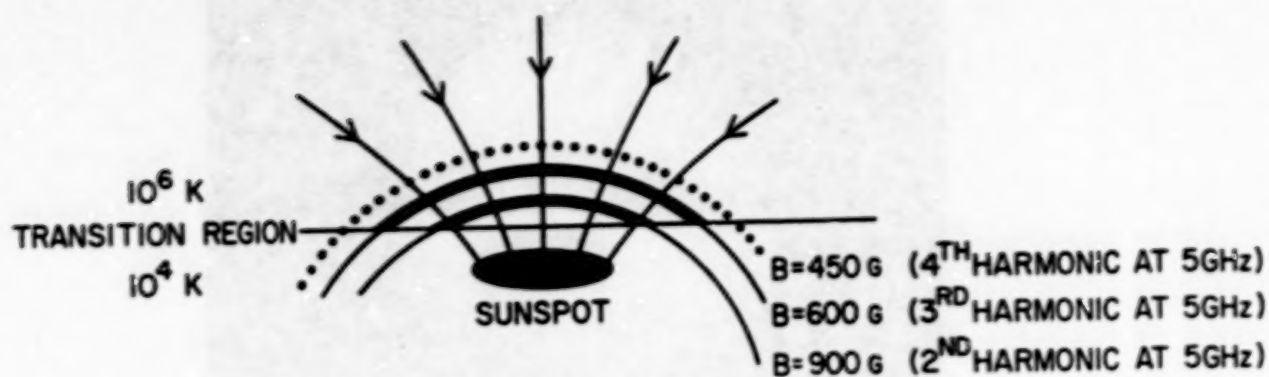
Figure 2. Schematic illustration of magnetic field lines above an isolated sunspot showing isogauss contours for 450, 600, and 900 Gauss.
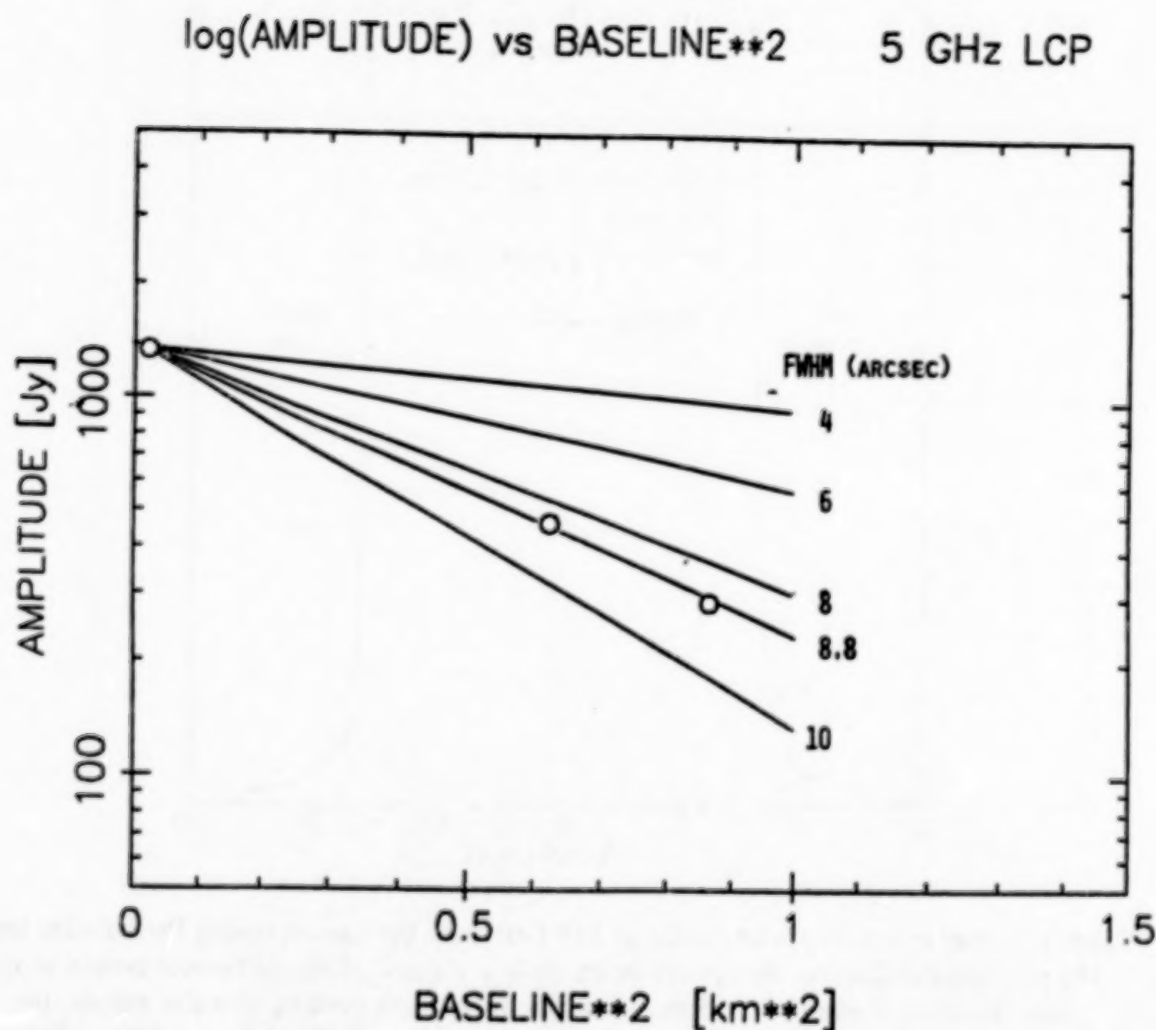

Figure 3. A typical plot showing the dependence of observed amplitude (circles) on projected baseline. Gaussian sources of different FWHM diameters would yield lines with the slopes as indicated. In this case the source FWHM diameter is 8.8 arc s.
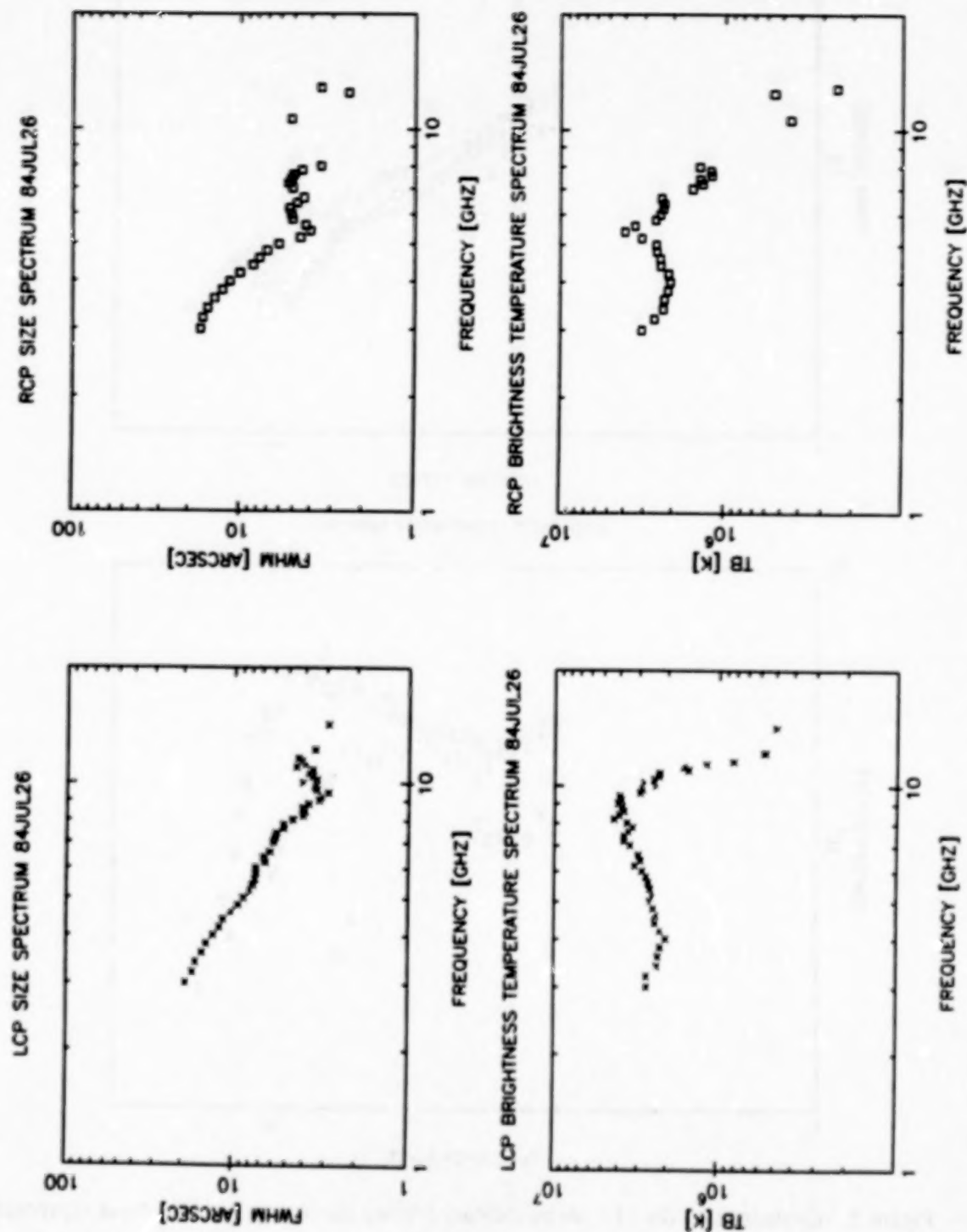
Figure 4. Size (top) and brightness temperature (bottom) spectra in LCP and RCP, respectively, as observed on 26 July 1984.

SIZE SPECTRA

BRIGHTNESS TEMPERATURE SPECTRA

Figure 5. Evolution of the LCP (extraordinary mode) size (top) and brightness temperature (bottom) spectra as the sunspot disappeared. Data acquired on 26, 27, and 28 July are represented by 0, 1, and 2, respectively. With the assumption that the 3rd is the highest optically thick harmonic, the frequency scale can be interpreted in terms of the magnetic field scale inserted at the top.

SINGLE-DISH HIGH SENSITIVITY DETERMINATION OF SOLAR LIMB EMISSION AT 22 AND 44 GHz

J. E. R. Costa, J. L. Homor, and P. Kaufmann

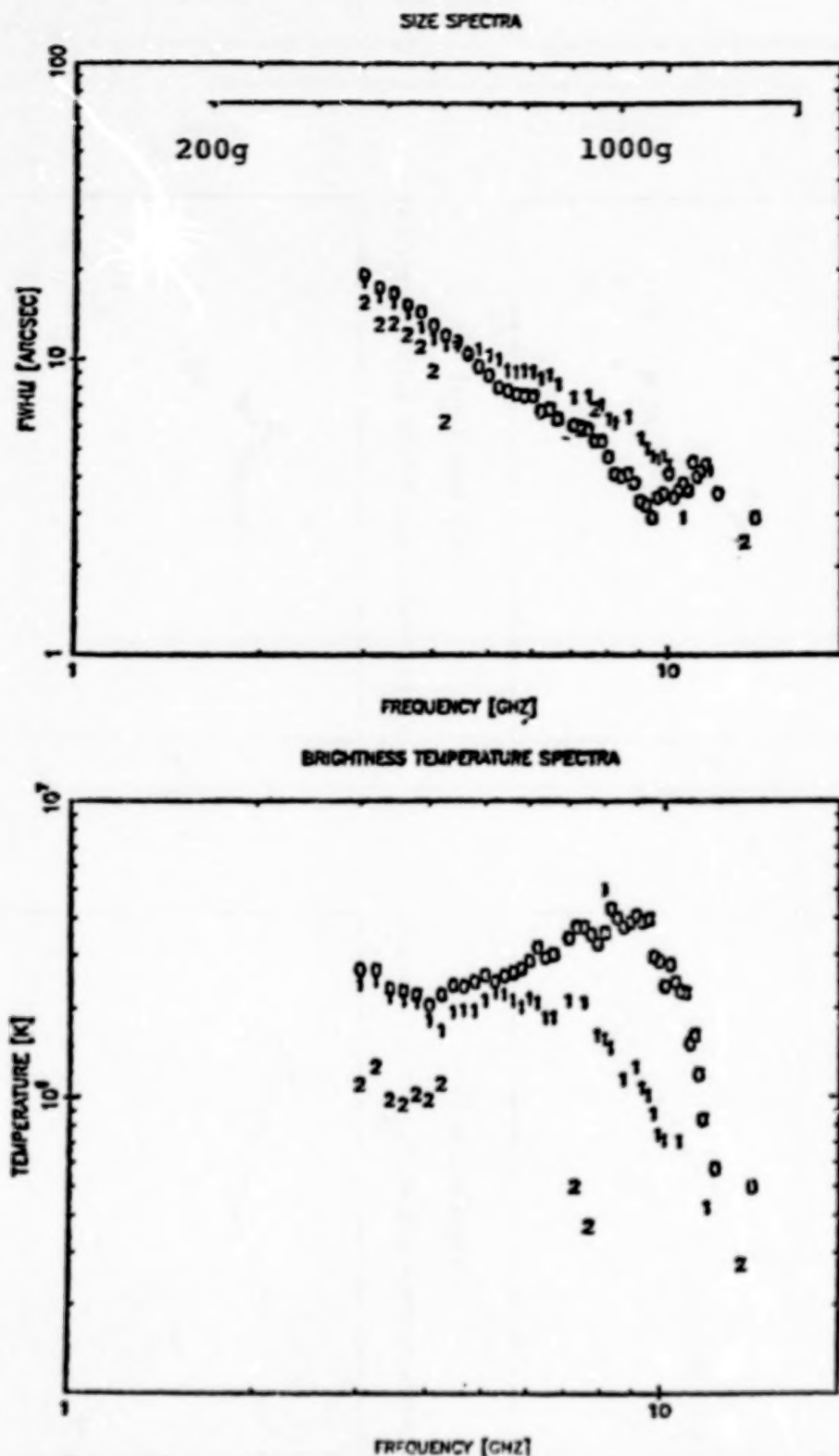INPE: Instituto de Pesquisas Espaciais, CNPq, C.P. 515, 12.200 São José
dos Campos, SP, Brazil

ABSTRACT

A large number of solar maps were obtained with the use of the Itapetinga 14-m (45-ft) antenna at 22 GHz and 44 GHz in the 1978-1982 period. A statistical study of these maps, reduced using original techniques, permitted the establishment of the solar radius with great accuracy (<1.5 arc s r.m.s.) at the two frequencies. It has been found that 22 GHz and 44 GHz radiation originates at 16 000 km and 12 500 km, respectively, above the photosphere. Excess emission due to active regions was clearly identified at lower solar latitudes above and below the equator, extending up to 26 000 km and 16 500 km above the photosphere at 22 GHz and 44 GHz, respectively.

DISCUSSION

During 1978-1982 the Itapetinga 14-m (45-ft) radome-enclosed antenna was intensively used in a large number of solar runs in connection with SMY and real-time operations with SMM satellite measurements and by other observatories. Each observing session (a few days up to two months) was carried on at 22 GHz and 44 GHz linear polarization, simultaneously, or at 22 GHz, right- and left-handed polarization. Only one run was carried on at 22 GHz, two orthogonal linear polarizations (May 1980). Details on the experimental setup are given elsewhere (Kaufmann et al., 1982). During each run, at least one full-Sun map was obtained per day. Every full-Sun map was obtained in a timescale relatively short (6 min) compared to timescales required by other large antennas (1 to 2 hr). The sensitivity attained was very high: 10 to 20 K in antenna tem-perature. The antenna half-power beamwidth was 4 arc min at 22 GHz and 2 arc min at 44 GHz, but the spatial definition of "hot spots" of more than 15 percent above the quiet Sun was better than 15 arc s.

The present study was based on 353 full-Sun maps obtained at 22 GHz, and 79 maps obtained at 44 GHz. Each map was obtained using the drift-scan technique, with scans in right-ascension separated by 2 arc min in declination. For the study of the solar limb, we determined one isotherm contour corresponding to the antenna temperature that was one-half of the value of the most probable antenna temperature found in the solar disc (assumed as representative of the quiet Sun). An arbitrary circle was adjusted by least-squares fit to the points that generated that contour, and the center of the radio-Sun was determined. With this technique we eliminate uncertainties due to any systematic pointing error. The radius was then determined as the mean distance from the center to the coordinates defining the isotherm contour previously established.

This method was found to be highly accurate. In terms of solar photospheric radius $R_\odot$, we obtained

- Solar radius at 22 GHz: (1.02305 ± 0.00082) $R_\odot$
- Solar radius at 44 GHz: (1.01922 ± 0.00135) $R_\odot$

or, correspondingly, the height above the photosphere of the 22 GHz emission was of 16 000 ± 600 km, and at 44 GHz it was of 12 500 ± 1000 km, determined from 353 maps and 79 maps, respectively. The corresponding accuracy was of less than 1.5 arc s r.m.s. These results have greater accuracy and are consistent with measurements obtained by various authors at frequencies above 10 GHz (Figure 1). It was possible to determine, for example, the apparent variation of the solar radio-radius with the variation of the distance of the Earth to the Sun (i.e., the variation of the apparent size of the optical solar disc), as shown in Figure 2.

The solar limb features were analyzed in terms of departures from the mean solar radio-radius, as it was described before. In Figure 3 we show the mean departures for 353 maps at 22 GHz, in solar heliocentric polar coordinates. It consists of one point every 0.5 deg (720 points over 360 deg). The principal findings were the following ones:

- The contribution from active regions clearly concentrate around 18 deg North and South, at both East and West limbs. A clear minimum occurs at the solar equator.

- The active regions' emissions at 22 GHz extend up to 26 000 km above the photosphere (or up to 10 000 km above the radio-radius at 22 GHz).

- A "darkening" was noticed to be more pronounced at the south solar pole. No physical interpretation has been attempted yet. It might be meaningful to point out that for the 353 maps used in this study, the southern pole was towards the Earth for most of them, with a mean inclination of -1.2 deg for all the collection.

In Figure 4 similar data are shown for 44 GHz, for the solar limb departures from the mean radio-radius. The plot is considerably noisier than the 22-GHz plot due to the smaller number of maps used in the statistics (79). The 44-GHz emission due to active regions are suggested at the East and West limbs, extending up to about 16 500 km above the photosphere (or up to 4000 km above the radio-radius at 44 GHz). A depression or "darkening" is indicated near the NE limb, for which no explanation has been found. The south pole limb seems to be slightly "darker" than the north pole limb (the mean inclination was +2.0 deg for the 79 maps).

Finally, from the data shown in Figures 3 and 4, we confirm that the best estimate of the solar radius can be obtained at limb coordinates corresponding to 45 deg West and East of the poles, when the reference solar radio-radius is not established in advance (Furst, Hirth, and Lantos, 1979).

REFERENCES

Coates, R. J., 1958, *Proc. IRE, 46*, 122.

Furst, E., Hirth, W., and Lantos, P., 1979, *Solar Phys., 63*, 257.

Horne, K., Hurford, G. J., Zirin, H., and de Graaw, Th., 1981, *Astrophys. J., 244*, 340.

Kaufmann, P., Strauss, F. M., Schaal, R. E., and Laporte, C., 1982, *Solar Phys., 78*, 389.

Kislyakov, A. G., Kuznetsov, I. V., Kuznetsova, N. A., Chernyshev, V. I., and Serov, N. V., 1975, *Sov. Astron., 18*, 612.

Labrun, N. R., Archer, J. W., and Smith, C. J., 1978, *Solar Phys., 59*, 331.

Pelyushenko, S. A. and Chernyshev, V. I., 1983, *Sov. Astron., 27*, 340.

Swanson, P. N., 1973, *Solar Phys., 32*, 77.

Wrixon, G. T., 1970, *Nature, 227*, 1231.
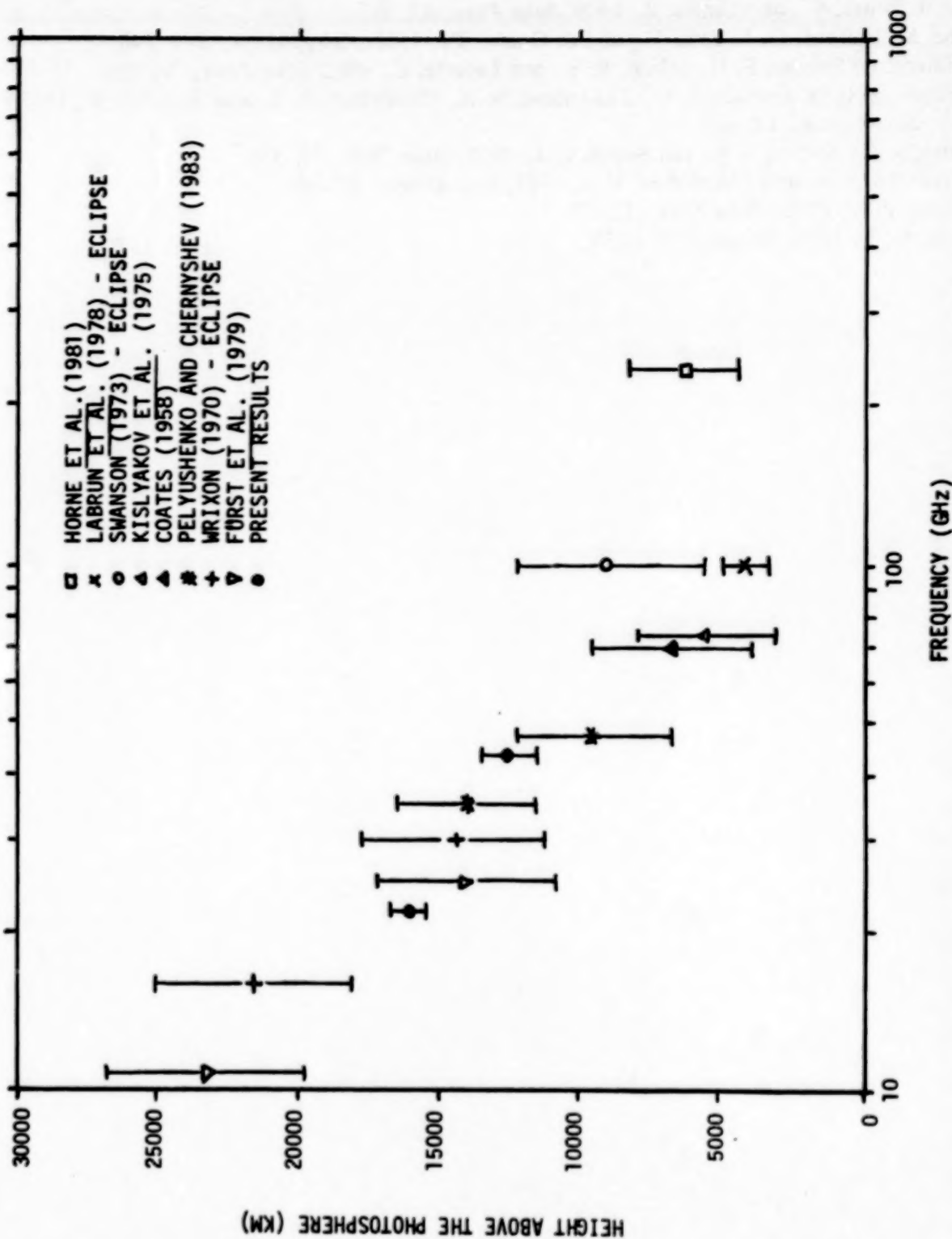
Figure 1. Some determinations of the height above the photosphere of radio emission at frequencies above 10 GHz, reported by various authors, indicated at the top-right corner, using different techniques. The present results are considerably improved in accuracy, and fit well to the general trend in the range 10 to 70 GHz.

Legend:
- ☐ HORNE ET AL. (1981)
- ✗ LABRUN ET AL. (1978) – ECLIPSE
- ○ SWANSON (1973) – ECLIPSE
- ◄ KISLYAKOV ET AL. (1975)
- ◄ COATES (1958)
- ✹ PELYUSHENKO AND CHERNYSHEV (1983)
- + WRIXON (1970) – ECLIPSE
- ▽ FÜRST ET AL. (1979)
- ● PRESENT RESULTS

FREQUENCY (GHz)

HEIGHT ABOVE THE PHOTOSPHERE (KM)
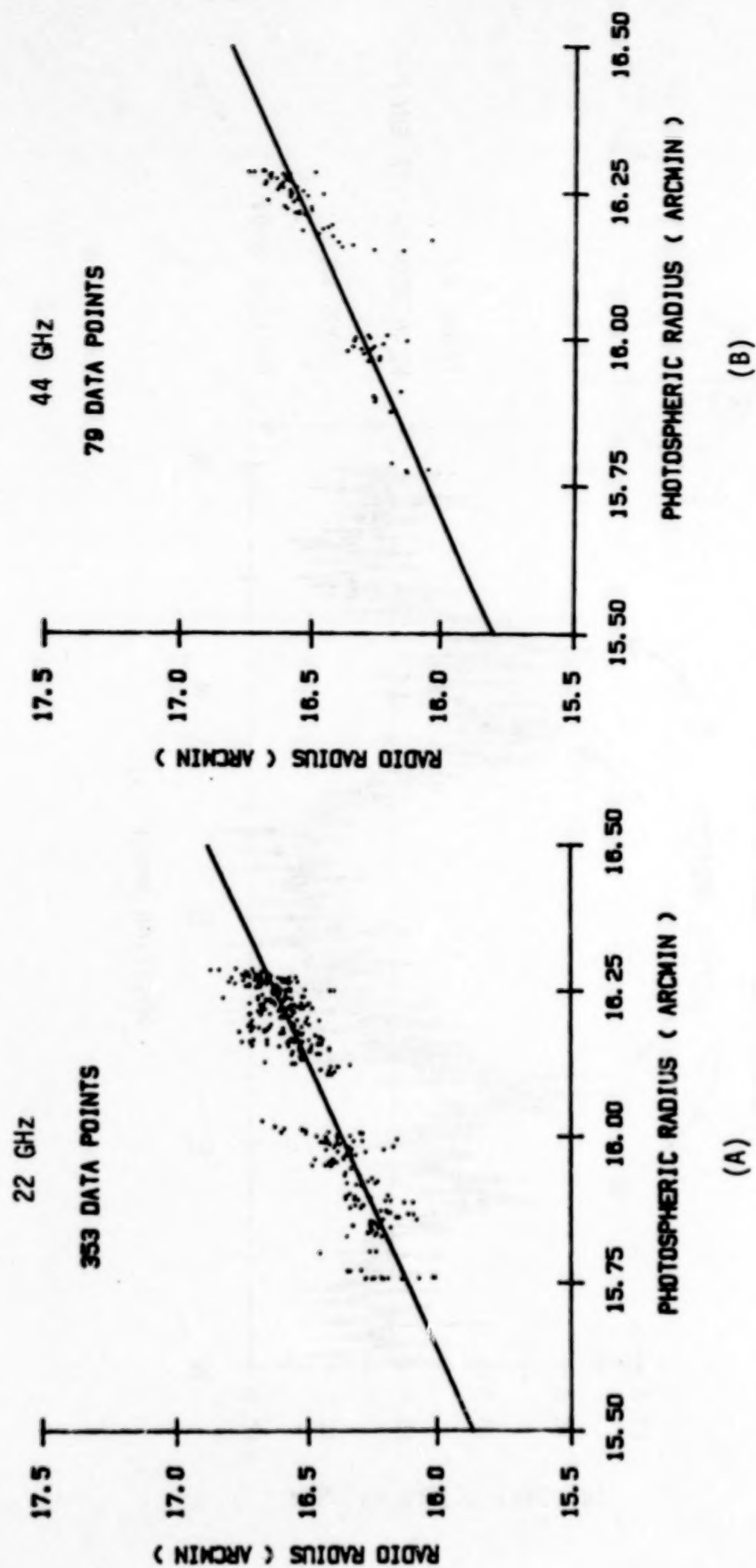
Figure 2. Plots of the measured solar radio-radius (ordinates) against the apparent optical disc radius (abcissae), for data obtained at 22 GHz (A) at 44 GHz (B).
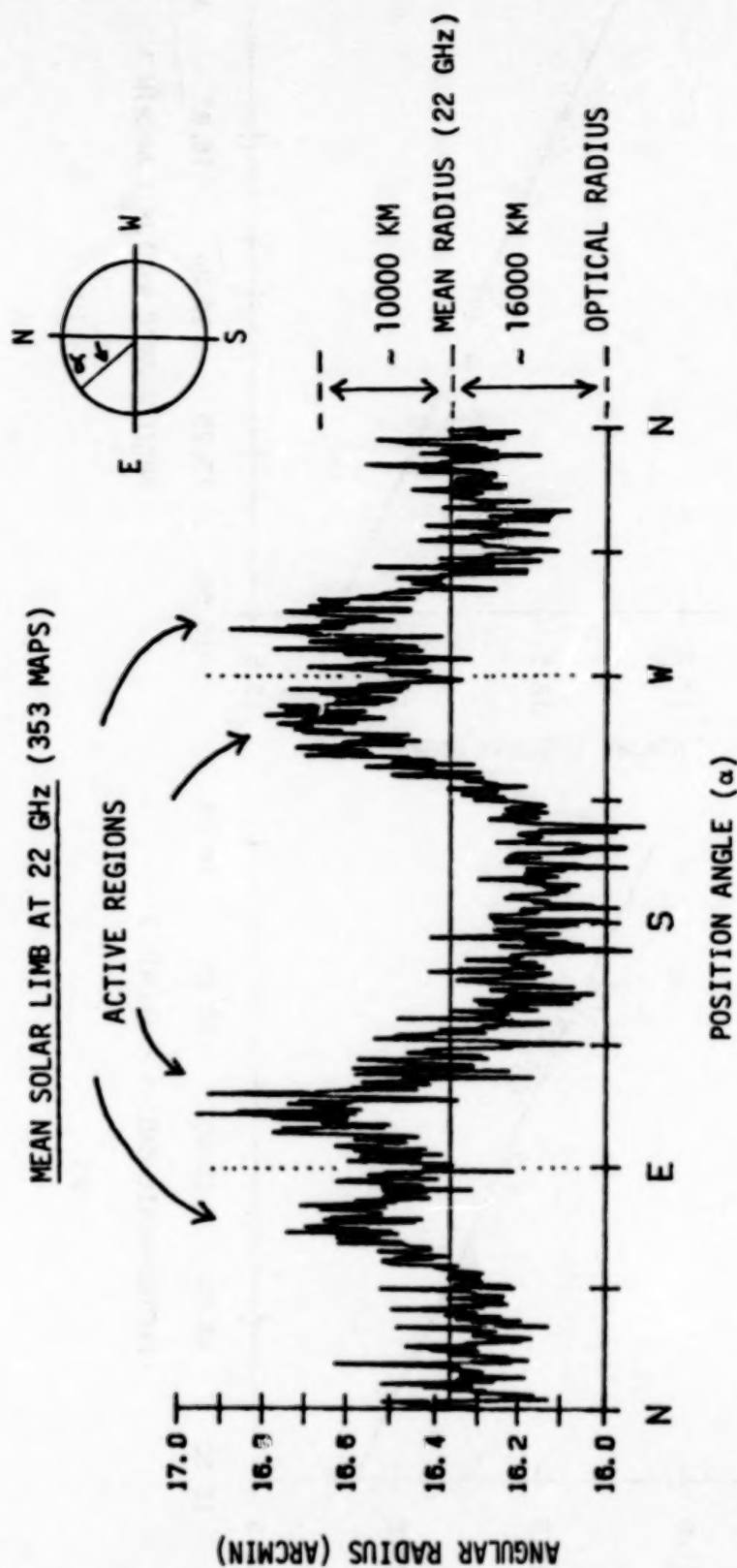
Figure 3. Mean departures from the mean solar radius at 22 GHz as a function of position angle referred to the optical disc set at 16 arc min. Active regions' contributions clearly concentrate at about 18 deg North and South of the equator, at both East and West limbs, extending up to 26 000 km above the photosphere. A "darkening" was evidenced on the southern polar limb, which might be attributed to a net negative inclination of the Sun for the 353 maps.

Figure 4. Mean departures, from the mean solar radius at 22 GHz, similarly to Figure 3. Data are "noisier" due to the smaller number of maps (79). Active regions are suggested to be concentrated at lower solar latitudes and extending up to about 16,500 km above the photosphere. A depression near the NE limb is of unknown origin.

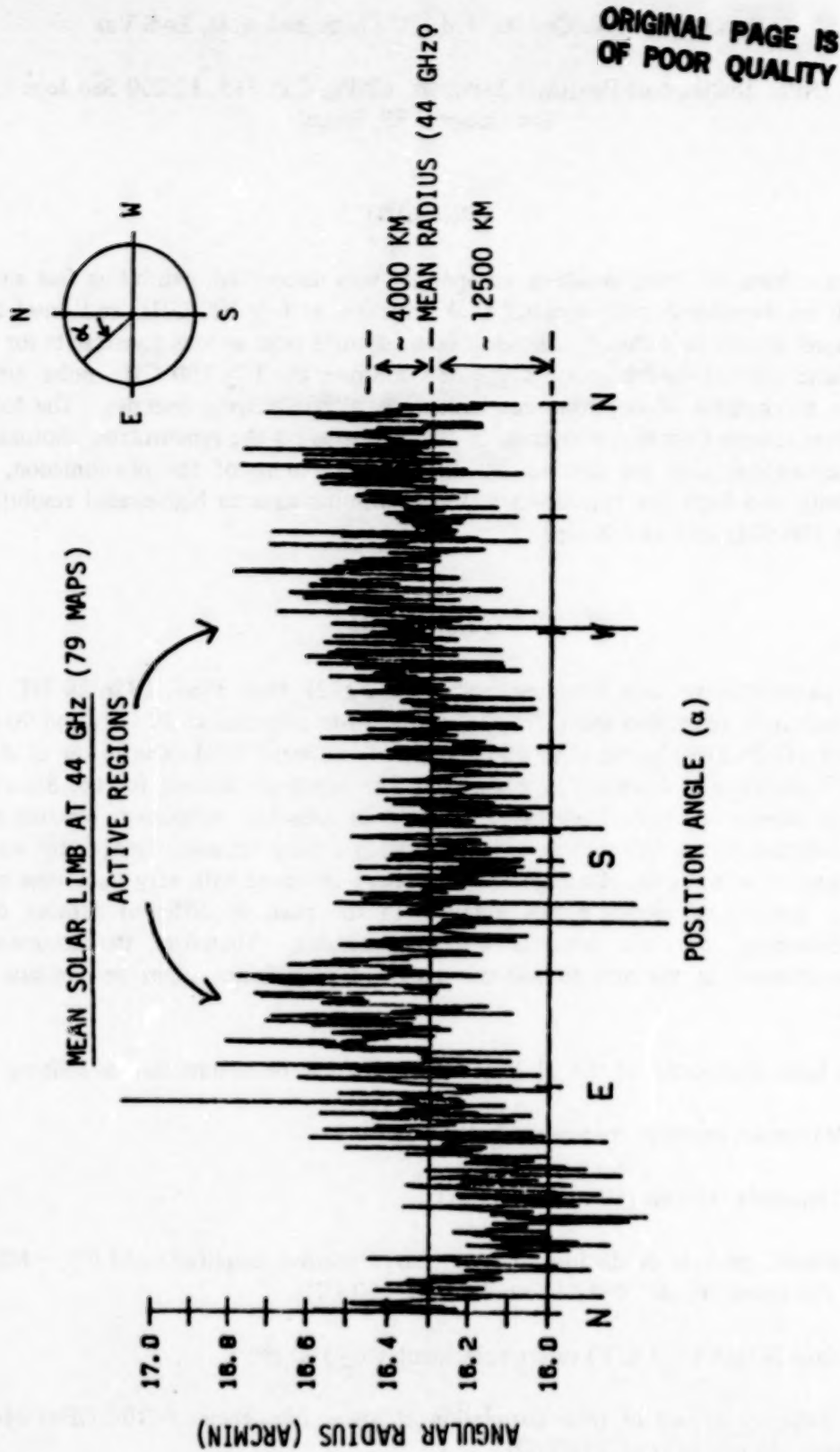# SHORT-LIVED SOLAR BURST SPECTRAL COMPONENT AT $f \gtrsim$ 100 GHz

P. Kaufmann, E. Correia, J. E. R. Costa, and A. M. Zodi Vaz

INPE: Instituto de Pesquisas Espaciais, CNPq, C.P. 515, 12.200 São José
dos Campos, SP, Brazil

ABSTRACT

A new kind of burst emission component was discovered, exhibiting fast and distinct pulses (~60 ms durations), with spectral peak emission at $f \gtrsim$ 100 GHz, and onset time coincident to hard X-rays to within ≤128 ms. These features pose serious constraints for the interpretation using current models. One suggestion assumes the $f \gtrsim$ 100 GHz pulse emission by synchrotron mechanism of electrons accelerated to ultrarelativistic energies. The hard X-rays originate from inverse-Compton scattering of the electrons on the synchrotron photons. Several crucial observational tests are needed for the understanding of the phenomenon, requiring high sensitivity and high-time resolution (~1 ms) simultaneous to high-spatial resolution (<0.1 arc s) at $f \gtrsim$ 100 GHz and hard X-rays.

DISCUSSION

An extraordinary solar burst was observed on 21 May 1984, 1326:20 UT, with high sensitivity and time resolution using the Itapetinga 14-m antenna, at 30 GHz and 90 GHz, and at hard X-rays (>25 keV) by the HXRBS experiment onboard SMM (Kaufmann et al., 1985a). The event is shown and described in Figure 1. The spectrum derived for the Structure A of this event is shown in Figure 2, clearly suggesting an emission component towards millimeter (or sub-millimeter) waves only. The existence of such a burst emission component was, in fact, already suggested in the past, although the data were obtained with very poor time resolution. In Figure 3, spectra of various bursts obtained in the past, by different authors, do suggest either a "flattening" or a rise towards higher frequencies. Therefore, the occurrence of an emission component in the mm to sub-mm range of frequencies might be common to many solar flares.

The basic diagnostics of the 21 May 1984 burst can be summarized as follows:

- Maximum emission frequency $\gtrsim 10^{11}$ Hz

- Timescale ~30 ms (60 ms durations)

- Several packets of distinct pulses. Large relative amplitude ($\Delta F/F$) ~ 60%. Much larger than the usual "ripple" (~1%) found at $f <$ 100 GHz.

- Hard X-rays (>25 keV) onset coincident to ≤100 ms.

- "Delays" or lack of time correlation at lower frequencies (<100 GHz) with respect to hard X-rays, do not exist at ≥100 GHz.

The 21 May 1984 burst-observed emission (for Structure A, Figure 1) in the radio and hard X-ray ranges is shown as thick solid lines in Figure 4, which also includes the typical fluxes reported for white-light flares (Neidig and Cliver, 1983). Several tentative spectral fits, based on different energy loss mechanisms, are indicated in the figure and described in its caption.

All the loss processes, spectra are shown in Figure 4, imply timescales considerably larger than the observed ones (60 ms). If hard X-rays are produced by bremsstrahlung, the short timescales observed require ambient plasma densities of the order of 10^{15} cm^{-3}, which are quite too high. Therefore, another loss process might be acting in order to account for the short lifetime of the pulses observed. One possibility is to assume the effectiveness of inverse-Compton (I.C.) scattering, reducing the electron energies in short timescales, and originating the observed hard X-rays. This possibility was already considered in the past (Shklovsky, 1964). One interpretation was recently suggested to explain the features of the 21 May 1984 event (Kaufmann et al., 1985b). The pulses are attributed to primary accelerators located somewhere in an unstable loop, producing "instantaneously" a population of ultrarelativistic electrons which constitute a self-absorbed synchrotron source inside which the I.C. quenching on the source photons originate the hard X-ray photons. Equating the synchrotron and I.C. conditions, the model predicts the observed fluxes at radio and at hard X-rays, and accounts for the small timescales observed, which are shown in Figure 4. The predicted Synchrotron 1 spectrum peaks in the infrared ($\sim 10^{13}$ Hz), and implies electrons accelerated to $\gtrsim 100$ MeV energies, in magnetic fields ranging from 100 to 1000 G. A similar mechanism spectrum has been proposed by Stein and Ney (1963) to explain white-light flare (WLF) continuum emission.

According to this interpretation (Kaufmann et al., 1985b), the pulse sources are very short-lived (~ 60 ms), very small ($\lesssim 10^7$ cm), and exhibiting high apparent brightness temperatures ($\gtrsim 10^{10}$ K). As these sources vanish, the electrons decay into lower energy levels and might still be able to produce the better-known longer-lasting emissions at microwaves and X-rays.

Alternative interpretations might be considered by placing the primary accelerator sources deep into the chromosphere, in a very high ambient plasma atmosphere. This new physical situation needs further investigations. One attempt is currently in progress reconciling it with the burst impulsive phase description recently proposed by de Jager (1985).

REFERENCES

Akabane, K., Nakajima, H., Ohki, K., Moriyama, F., and Miyaji, T., 1973, *Solar Phys.*, *33*, 431.

Cogdell, J. R., 1972, *Solar Phys.*, *22*, 147.

Croom, D. L., 1970, *Solar Phys.*, *15*, 414.

de Jager, C., 1985,   these proceedings.

Kaufmann, P., Correia, E., Costa, J. E. R., Zodi Vaz, A. M., and Dennis, B. R., 1985a, *Nature*, *313*, 380.

Kaufmann, P., Correia, E., Costa, J. E. R., and Zodi Vaz, A. M., 1985b, *Astron. Astrophys.* (submitted).

Neidig, D. F. and Cliver, E. W., 1983, "A Catalog of Solar White-Light Flares (1859-1982), Including Their Statistical Properties and Associated Emissions," Rept. AFGL-TR-83-0257.

Ohki, K. and Hudson, H. S., 1975, *Solar Phys.*, *43*, 405.

Shimabukuro, F. I., 1970, *Solar Phys.*, *15*, 424.

Shimabukuro, F. I., 1972, *Solar Phys.*, *23*, 169.

Shklovsky, J., 1964, *Nature* (Letter to Editor), *202*, 275.

Stein, W. A. and Ney, E. P., 1963, *J. Geophys. Res.*, *68*, 65.

Zirin, H. and Tanaka, K., 1973, *Solar Phys.*, *32*, 173.
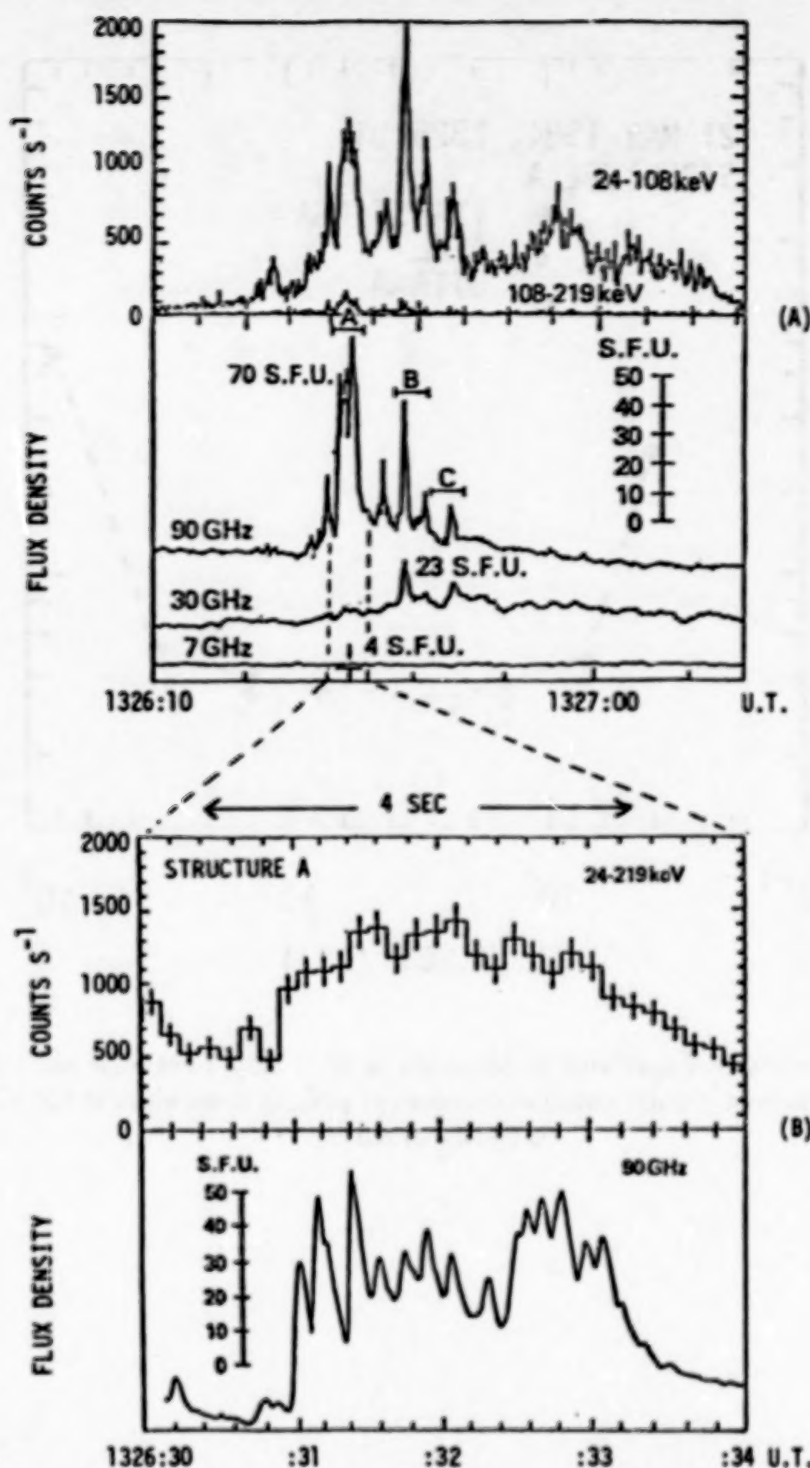
Figure 1. The solar burst of 21 May 1984 is shown in compressed timescale (A), with two hard X-ray energy ranges at the top, and 90 GHz, 30 GHz, and 7 GHz at the bottom. All hard X-ray burst structures correlate in time very well with the 90-GHz emission, but not well for lower frequencies emissions. The major Structure A is time expanded in (B), with hard X-ray (24 to 219 keV) data at the top, restricted to 128-ms time resolution, and 90-GHz data at the bottom, displayed with 10-ms time constant. The structure consists in a packet of distinct pulses, repeating at about 7 Hz. The e-folding rise time of a pulse is about 30 ms. The hard X-ray onset is coincident to the 90-GHz onset by less than 128 ms.

211
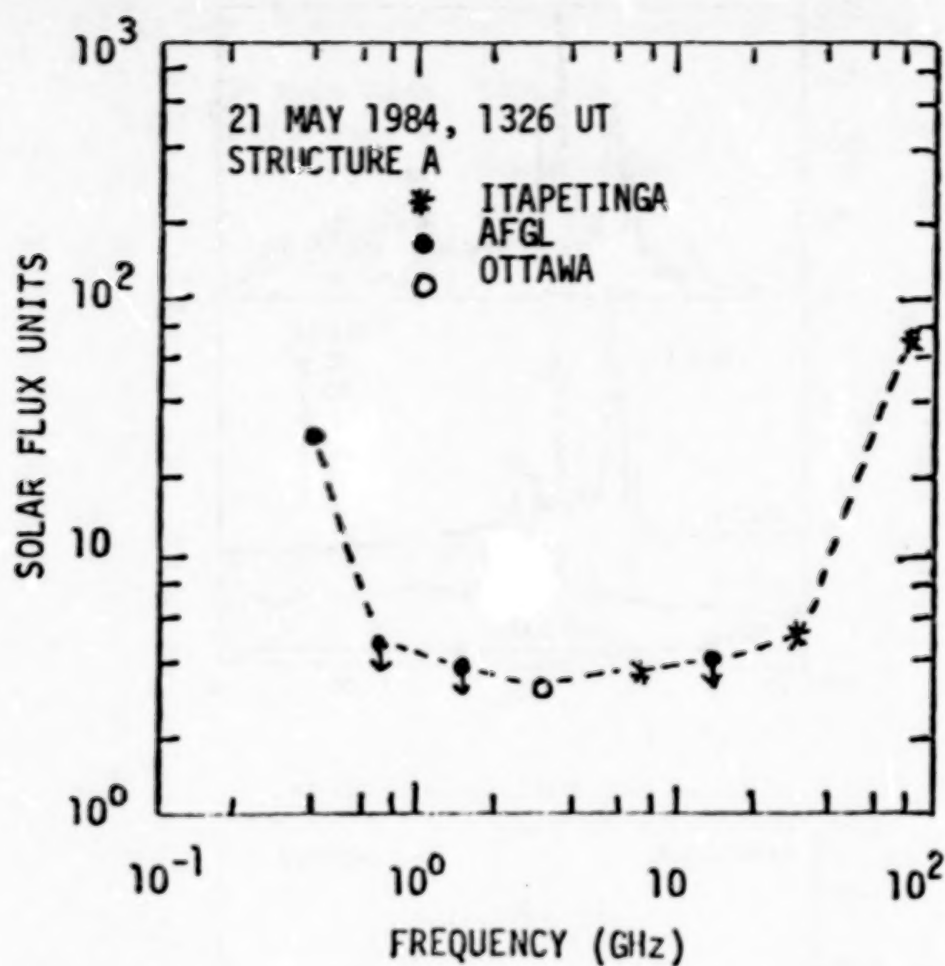
Figure 2. The observed spectrum of Structure A of 21 May 1984 solar burst (Figure 1). The existence of a burst emission component peaking somewhere at $f \gtrsim 100$ GHz is clearly evidenced.
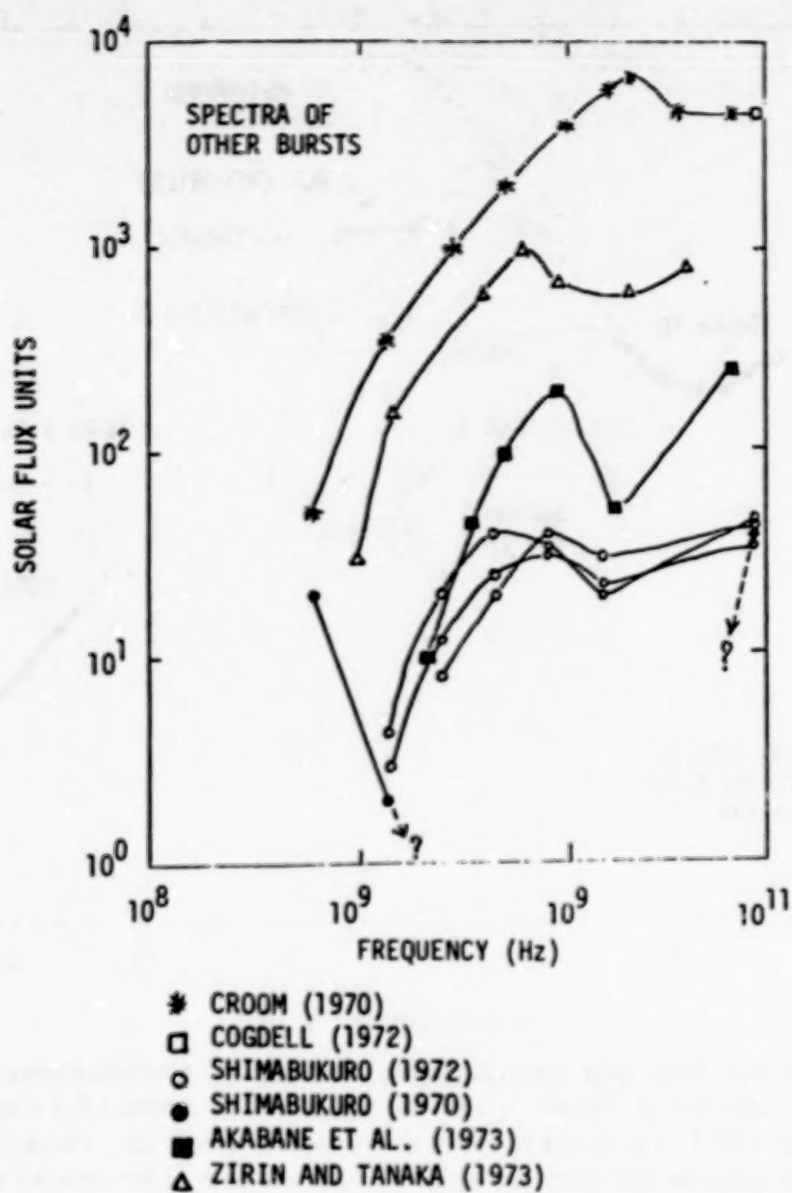
Figure 3. Spectra of various solar bursts obtained in the past by various authors, with symbols and names quoted at the bottom. They confirm that the occurrence of a burst emission component in the mm to sub-mm range of frequencies is common to many flares. One of these spectra (Shimabukuro, 1970) is possibly very similar to the spectrum of the event studied here (Figure 2).
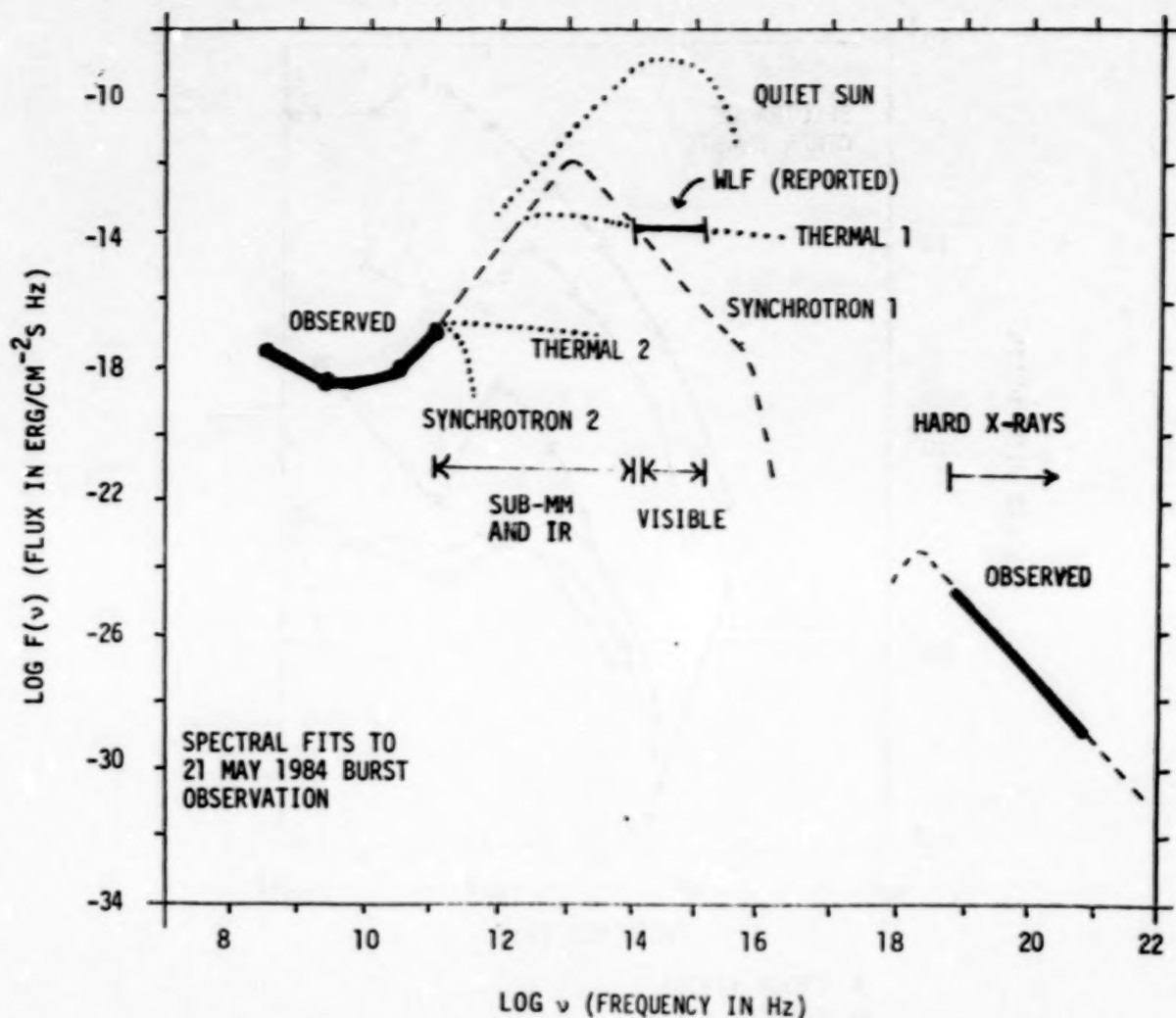
Figure 4. A radio-hard X-ray range spectral display, showing the observed emissions of 21 May 1984 solar burst (Structure A, Figure 1), and the typical fluxes reported for white-light flares (Neidig and Cliver, 1983). The tentative spectral fits (points' lines) are: Thermal 1: a thermal component with turnover frequency somewhere in the sub-mm or far infrared range of frequencies, fitting white-light flare reported fluxes (Ohki and Hudson, 1975); Thermal 2: a thermal component with turnover frequency at about 100 GHz (Shimabukuro, 1970); and Synchrotron 2: losses by electrons with relativistic energies, with emission spectrum peaking at about 100 GHz (implying in electrons energies 7 MeV in a 500 Gauss magnetic field). The Synchrotron 1 plot in dashed line, peaking in the infrared, is a model prediction for a synchrotron/inverse-Compton mechanism (implying electrons' energies ~100 MeV in a 500 Gauss field) (Kaufmann et al., 1985b). The quiet-Sun blackbody spectrum is shown at the top.

POLAR-CAP AND CORONAL-HOLE-ASSOCIATED BRIGHTENINGS OF THE SUN
AT MILLIMETER WAVELENGTHS
(Extended Abstract)*

T. Kosugi**
Laboratory for Astronomy and Solar Physics
NASA Goddard Space Flight Center, Greenbelt, MD

M. Ishiguro
Nobeyama Radio Observatory, Minamimaki, Minamisaku, Nagano 384-13, Japan

K. Shibasaki
Research Institute of Atmospherics, Nagoya University, Toyokawa, Aichi 442, Japan

Mapping observations of the Sun at millimeter wavelengths were made on 16 to 22 July 1984 with the 45-m telescope of the Nobeyama Radio Observatory. Seven 36-GHz (8.3-mm) maps and five 98-GHz (3.1-mm) maps were taken with half-power beam widths of 46 ʺ and 17 ʺ, respectively.

Instead of the conventional rastering technique, we adopted a radial-scan method in which every scan passes through the disk center. Accordingly, the variation of the atmosphere attenuation due to changes in the weather conditions can be easily estimated and removed by using the brightness values at the disk center as calibration data. Also, the pointing errors of the telescope due to the high-speed scans can be corrected by using the solar limbs as position references. The rms residual errors in relative brightness and position after the corrections were estimated to be ~2% and ~5 ʺ, respectively. To further reduce these errors, a smoothing technique was applied in making the two-dimensional maps. Thus, the radial-scan method, together with the beam of the telescope with a small error pattern, enabled us to make high-quality maps with $\leq$1% uncertainty in brightness. Here and in the following, brightness is expressed in terms of the average brightness of the solar disk as a unit. Note that the brightness temperature of the quiet Sun is ~8000 K and ~6000 K at 36 GHz and 98 GHz, respectively (e.g., see a review by Furst, 1980).

We perceived on the maps many local brightness enhancements and depressions, most of which are correlated well with active regions and optical filaments (e.g., Furst et al., 1973). However, we found that on the 36-GHz maps there are two types of brightness enhancements which are not associated with active regions.

One is what we call polar-cap brightnening (cf., Babin et al., 1976; Efanov et al., 1980a,b). It was an extended region around the poles with a brightness excess of ~5%. It can be seen in both polar regions in all the maps taken at 36 GHz between 16 and 22 July 1984. The boundary of the polar-cap brightenings was located at a latitude of ~65 deg in both hemispheres, which was very close to the boundary of the polar coronal holes observed in the 10830 Å helium line in this period. There is no doubt that the polar-cap brightening is a pole-related phenomenon but not a so-called limb brightening, because the apparent north-south asymmetry between two polar-cap brightenings is well explained by the orientation of the poles

---

*Full paper will appear in Publ. Astron. Soc. Japan (1985).
**NASA/NRC Research Associate, on leave from Tokyo Astronomical Observatory.

with respect to the line of sight, and also because no limb brightenings above 1% are observed in the equatorial region on the same maps.

The other type of brightness enhancement is found in one equatorial coronal hole region (cf., Papagiannis and Baker, 1982). Again the brightness excess was ~5%. However, the bright region occupied only half the area of the coronal hole region. Moreover, another equatorial coronal hole region was not associated with millimeter-wave brightenings, though two small areas in this region appeared to be slightly brighter than the surroundings. From the comparisons with optical and other observations, it seems that the presence of white-light faculae and/or an intense magnetic field are essential for the brightening to occur in a coronal hole region.

No corresponding brightenings are found at 98 GHz for either type of 36-GHz enhancements.

It is suggested that the two types of brightenings at 36 GHz are two aspects of one phenomenon, associated with polar and equatorial coronal holes, and that the temperature and density structure of the upper chromosphere in coronal holes differs from that outside holes.

REFERENCES

Babin, A. N., Gopasyuk, S. I., Efanov, V. A., Moiseev, N. S., and Tsap, T. T., 1976, *Izv. Krymsk. Astrofiz. Observ.*, *55*, 3 (in Russian).

Efanov, V. A., Labrum, N., Moiseev, I. G., Nesterov, N. S., and Stewart, R. T., 1980a, *Izv. Krymsk. Astrofiz. Observ.*, *61*, 52 (in Russian).

Efanov, V. A., Moiseev, I. G., Nesterov, N. S., and Stewart, R. T., 1980b, in M. R. Kundu and T. E. Gergely (eds.), *Radio Physics of the Sun*, IAU Symp., *86*, 141.

Furst, E., 1980, in M. R. Kundu and T. E. Gergely (eds.), *Radio Physics of the Sun*, IAU Symp., *86*, 25.

Furst, E., Hachenberg, O., Zinz, W., and Hirth, W., 1973, *Solar Phys.*, *32*, 445.

Papagiannis, M. D. and Baker, K. B., 1982, *Solar Phys.*, *79*, 365.

SOLAR CORONAL PHYSICS

PARTICLE ACCELERATION?

SHOCK? $\Delta n, \Delta v, \Delta T$ ACROSS SHOCK

WAVE or FLOW?

FATE of COOL LOW ION STATE MATTER?

FORERUNNER WAVES?

PLASMA HEATING?

MAGNETICALLY or THERMALLY DRIVEN?

ERUPTIVE PROMINENCE
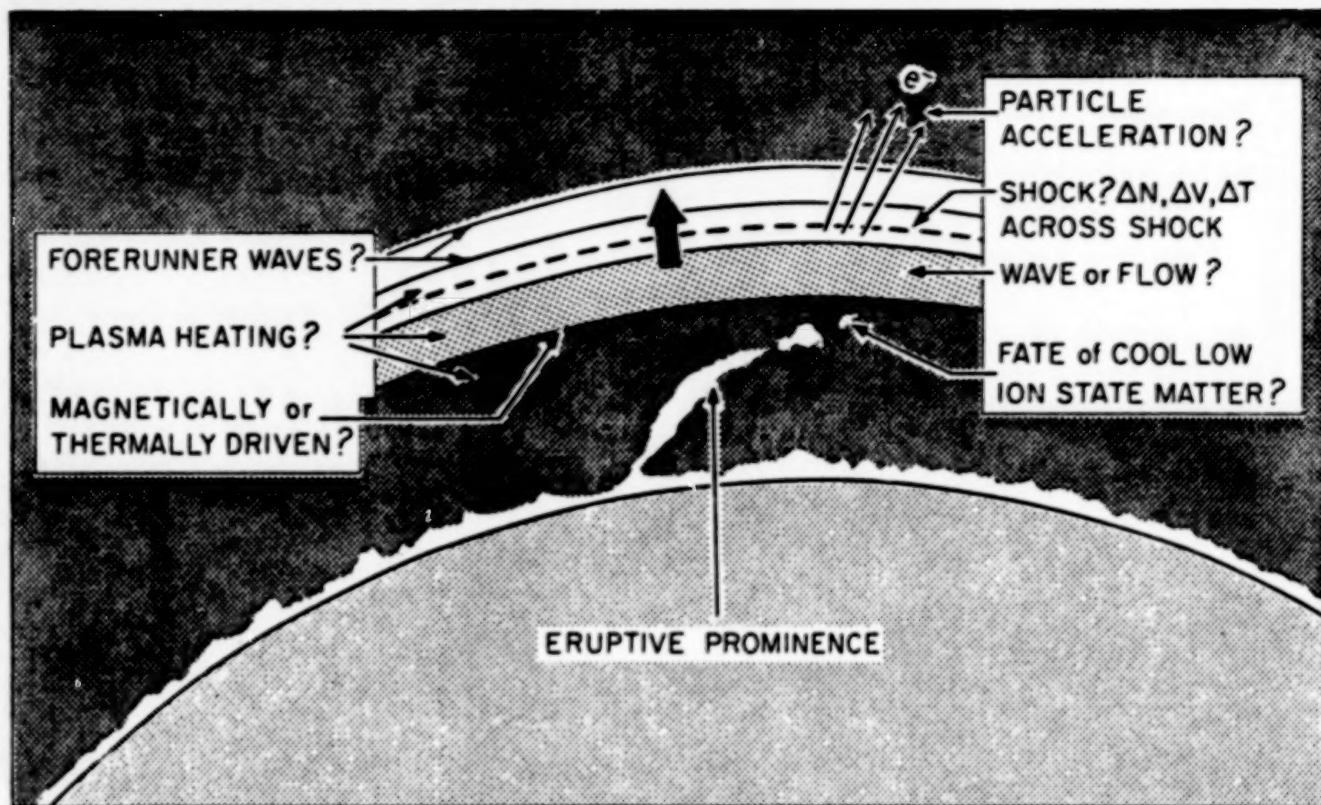
CORONA AND SOLAR WIND
(Invited)

George L. Withbroe

Harvard-Smithsonian Center for Astrophysics, Cambridge, MA 02138, U.S.A.

ABSTRACT

The Pinhole/Occulter Facility is a powerful tool for studying the physics of the extended corona and origins of the solar wind. Spectroscopic data acquired by the P/OF coronal instruments can greatly expand empirical information about temperatures, densities, flow velocities, magnetic fields, and chemical abundances in the corona out to $r \gtrsim 10\ R_\odot$. Such information is needed to provide tight empirical constraints on critical physical processes involved in the transport and dissipation of energy and momentum, the heating and acceleration of plasma, and the acceleration of energetic particles. Because of its high sensitivity, high spatial and temporal resolutions, and powerful capabilities for plasma diagnostics, P/OF can significantly increase our empirical knowledge about coronal streamers and transients and thereby advance the understanding of the physics of these phenomena. P/OF observations can be used to establish the role in solar wind generation, if any, of small-scale dynamical phenomena, such as spicules, macrospicules and coronal "bullets," and the role of the fine-scale structures, such as polar plumes. Finally, simultaneous measurements by the P/OF coronal and hard X-ray instruments can provide critical empirical information concerning nonthermal energy releases and acceleration of energetic particles in the corona.

I. INTRODUCTION

Improved knowledge of the physical conditions throughout the solar corona is critical to the development of an understanding of the physical state of the corona and the physical mechanisms responsible for plasma heating, solar wind acceleration, energetic particle acceleration and the transport of mass, momentum, and energy. The Pinhole/Occulter Facility (Hudson et al., 1981; Tandberg-Hanssen et al., 1983) can be a very powerful tool for acquiring this knowledge. Because the P/OF occulting disk is large and located much farther (~50 m) from the telescope than for any previous externally occulted coronagraphic instrument, it is possible to employ telescopes of large aperture (~0.5 m). This gives the P/OF coronal instruments sufficient collecting area to have several orders of magnitude more sensitivity than any coronagraphic instrument previously flown on sounding rockets or orbiting spacecraft. As a result the P/OF coronal instruments can provide measurements with high spatial resolution (~1 arc s, an order of magnitude or more better than more conventional instruments) and good time resolution for studying transient phenomena, as well as providing a capability for measuring weak coronal lines at large distances from the Sun (out to $r \gtrsim 10\ R_\odot$). The P/OF occulter also serves as a multi-pinhole array for high resolution ($\lesssim 1$ arc s) hard X-ray imaging. This gives P/OF a means of detecting signatures of nonthermal energy releases and energetic electrons. These capabilities yield an instrument package with unprecedented power for probing the extended corona, investigating the origins and physics of the solar wind, and studying energetic particle acceleration in the corona.

The purpose of this paper is to briefly discuss the role that P/OF can play in addressing a few scientific problems in the above areas. Section II discusses spectroscopic plasma diagnostics and coronal physical processes. Sections III and IV deal with the structure and physics of streamers and coronal holes, while Section V considers coronal transients and mass ejections.

221

II. SPECTROSCOPIC PLASMA DIAGNOSTICS AND CORONAL PHYSICAL PROCESSES

Plasma diagnostic information derived from spectroscopic measurements can provide critical empirical constraints on mechanisms for transport and dissipation of energy and momentum in the corona, acceleration of energetic particles, and production of differences in coronal chemical composition. For example, information on temperatures and flow velocities is important for studying mechanisms for plasma heating and solar wind acceleration and for separating mechanisms that depend upon driving the solar wind thermally and those driving it through wave-particle interactions. At the present time there are very few measurements of most basic plasma parameters (other than electron densities) beyond a few tenths of a solar radius above the solar surface. New spectroscopic techniques made possible by the use of coronagraphic instrumentation with reflecting optics are being developed and proven using instruments flown on sounding rockets and Spartan (cf., Kohl et al., 1980, 1983, 1985). These are small instruments with limited collecting area, spatial resolution, and wavelength coverage. The P/OF instruments with their large collecting areas, high spatial and spectral resolutions, and broad wavelength range, spanning the visible to the XUV, offer a means of implementing a wide variety of plasma diagnostic techniques that can provide information of a number of critical plasma parameters.

There have been a number of papers published recently which have discussed various spectroscopic plasma diagnostic techniques that can be used in the extended corona (cf., Beckers and Chipman, 1974; Kohl and Withbroe, 1982; Bommier and Sahal-Brechot, 1982; Withbroe et al., 1982a; Kohl, et al., 1983); hence, we will discuss them only briefly here. We consider first the measurement of temperatures. In the outer corona, $r \gtrsim 1.5 \, R_\odot$, the temperatures of particle species such as electrons, protons, and heavy ions can differ (because the collisional exchange of energy among particles of different masses is slow at low density). Coronal temperatures can be determined from measurements of the widths of spectral lines.   The line width $\Delta\lambda \sim T_w^{1/2}$, where the temperature T_w includes the effect of line broadening by thermal and nonthermal motions along the line of sight.   Nonthermal motions can be produced, for example, by MHD waves propagating through the corona. The temperature determined from the line width is related to the thermal temperature T_t by $T_w = (T_t + M\xi^2/2k)^{1/2}$, where M is the mass of the particles species producing the spectral line and ξ is the rms velocity component due to plasma motions along the line of sight that occur on a spatial scale much larger than the particle mean free path, but smaller than the path length over which the spectral line is formed. Additional information about the plasma in the line of sight can be obtained if the shape of the profile is measured as well as its width, since the shape depends upon the velocity distribution of the particles along the line of sight. By observing lines from ions of different masses one can obtain empirical constraints on the magnitude of mass-dependent and mass-independent motions.

An example of how widths of line profiles can be used to test theoretical models for the solar wind is shown in Figure 1. One of the problems with current solar wind models is satisfactorily accounting for the flow speeds in high speed solar wind streams originating from coronal holes. Additional energy over and above that calculated using models with thermally driven winds is needed to yield solar wind speeds of the magnitude measured. In addition, unless one invokes a mechanism for heating protons far from the Sun, the proton temperatures predicted by the theoretical models are too low.   Because signatures of MHD waves are detected with in situ measurements of the solar wind far from the Sun, there is speculation that Alfvén waves may play a significant role in driving the solar wind and heating the protons (see reviews by Hollweg, 1981, Leer et al., 1982). Since the velocity amplitude of Alfvén waves is expected to vary as $N^{-1/4}$ in the corona, the amplitude of these waves increases rapidly with increasing distance (and therefore decreasing density N) from the solar surface. By measuring spectral line profiles from atoms and

ions of different masses (and thus different thermal widths) one can obtain tight empirical constraints on the flux of Alfvén waves propagating outward from the Sun in coronal holes and other solar regions.

Figure 1 compares some existing measurements of Lyman alpha with widths calculated for a theoretical two fluid solar wind model which includes the effects of Alfvén waves on line broadening. (The resonantly scattered hydrogen Lyman alpha line is expected to be the strongest emission line in the extended corona; see Kohl and Withbroe, 1982.) The solid line gives the predicted behavior for a model with no Alfvén wave flux, the dashed line shows how the introduction of an appropriate amount of broadening by Alfvén waves yields a better fit to the Lyman alpha measurements (Esser et al., 1985). Although the fit is better, the evidence for the presence of Alfvén waves is not compelling because of the magnitude of the uncertainties in the measured widths. However, if measurements of a heavy ion such as Fe XII are available, one obtains a much tighter constraint on the Alfvén wave mechanism, as illustrated by the curves calculated for the Fe XII λ 1242 line. With P/OF one could not only observe profiles of Fe XII and other heavy ions, one could also obtain much better Lyman alpha profiles (hence smaller uncertainties in the line widths) for $r < 4$ R_Θ and observe them much farther out where the amplitude of the Alfvén waves is expected to become very large. One also obtains constraints on the energy spectrum of the waves from the shape of the spectral line profiles, particularly from profiles of heavy ions such as Fe XII λ 1242.

In order to place the maximum empirical constraints on theoretical mechanisms for plasma heating and for energy and momentum transport, it is desirable to measure profiles from a wide variety of particle species. P/OF is ideally suited for accomplishing this, because of the high sensitivity and wide wavelength coverage that can be achieved, spanning visible through XUV wavelengths. P/OF can measure profiles of numerous spectral lines, including very weak lines such as the electron-scattered component of hydrogen Lyman alpha, over a wide range of heights. With such data one can determine the electron temperature (electron-scattered component of Lyman alpha) and either determine or place upper limits (depending on the nature of the non-thermal broadening and plasma heating mechanisms present) on proton temperatures (from resonantly scattered Lyman alpha) and heavy ion temperatures (from ions such as O VI, Ne VII, Ne VIII, Na IX, Mg X, Al XI, Si XII, and ions of iron from Fe VIII to Fe XVI).

The second important class of plasma parameters are particle densities. The densities of the two most abundant particle species, the electrons and protons, can be measured using the electron-scattered component of the coronal white-light emission (for determining N_e) and resonantly scattered hydrogen Lyman alpha (for determining N_p). Densities of various heavy ions can be measured using the intensities of appropriate spectral lines. By measuring densities of several stages of ionization of an element and/or temperatures and densities of critical particle species (e.g., one or more stages of ionization of a given element and the electrons which are responsible for collisional excitation and ionization), one can either measure or place tight empirical constraints on chemical abundances of the heavier particles such as He, N, O, Ne, Na, Mg, Al, Si, S, Fe, and Ni (cf., Kohl and Withbroe, 1982,; Withbroe et al., 1982a). Such information is needed to obtain insights and empirical constraints on mechanisms for production of the variations in chemical composition of the solar wind which are measured in the solar wind far from the Sun (cf., Hirshberg, 1975).

The third critical plasma parameter is the flow velocity. P/OF can measure flow velocities through use of "Doppler-dimming" of the intensities of spectral lines. In the outer corona where the densities are low, many coronal lines have a strong resonantly scattered component. This component is produced by resonant scattering of the line radiation from the solar disc and low

corona. The intensity of the scattered radiation depends on the number of particles in the line of sight capable of scattering radiation in the line and on the intensity of the incoming radiation from the solar disk and lower levels of the corona. The number of scatterings is a function of the outflow velocity of the solar plasma. In a static atmosphere the central wavelength in the coronal scattering profile is identical to that of the disk profile. However, in a region with solar-wind flow the scattering profile is Doppler-shifted with respect to the disk profile and hence there is less efficient scattering, resulting in a reduction in intensity of the scattered radiation. Examples of this effect, known as Doppler-dimming, are illustrated in Figure 2 for hydrogen Lyman alpha λ 1216 and O VI λ 1032 (Kohl and Withbroe, 1982). The Lyman alpha line is sensitive to flow velocities greater than about 100 km/s, while the O VI line is sensitive to flow velocities above 30 km/s. By comparing the intensity of a spectral feature that is affected by Doppler-dimming with the intensity of a spectral feature that is not (e.g., electron-scattered white-light radiation), one can determine the amount of Doppler-dimming and hence the outflow velocity.

Measurements of Doppler-dimming acquired on several sounding rocket flights have been used to demonstrate that the outflows in some regions are subsonic for $r \lesssim 4\ R_\odot$ (cf., Withbroe et al., 1982a, 1985). The most recent data provide evidence for supersonic flow in a polar coronal hole at smaller radii, $r \approx 2\ R_\odot$ (Kohl et al., 1984). Much more extensive observations are needed, particularly measurements made with high sensitivity in a wide variety of spectral lines over a wide range of heights in order to place constraints on solar wind acceleration mechanisms for particles of different masses as well as to determine the role of different types of coronal structures, such as streamers and coronal holes of different sizes and geometrical configurations, in the generation of the solar wind.

Another critical parameter is the vector magnetic field. Current work suggests that measurements of the Hanle effect may provide a very useful tool for placing empirical constraints on coronal magnetic fields (Bommier and Sahal-Brechot, 1982; Kohl and Strachan, 1985). Measurements of magnetic fields via the Hanle effect make use of the influence of magnetic fields on the polarization of spectral lines. It has been used, for example, to measure magnetic fields in prominences (see references cited in Bommier and Sahal-Brechot, 1982). Because of the high sensitivity of the P/OF coronal instruments, it will be possible to measure polarization of a variety of spectral lines and thereby obtain constraints on coronal magnetic fields.

P/OF is a powerful tool for studying the acceleration of energetic particles in the corona, because of its unique capability for spectroscopically probing the coronal plasma with high spatial and temporal resolutions while simultaneously observing signatures of energetic electrons. The P/OF hard X-ray instruments can observe the location of the region where the electrons are accelerated and the number, energy spectrum, and trajectory of the accelerated electrons. The P/OF coronal instruments can observe the spatial and temporal variations of the coronal structure, density, and temperature of the thermal electrons, and provide empirical constraints on ion temperatures, magnetic field strengths, and flow and turbulent velocities at the acceleration site and in the surrounding medium. Clearly, P/OF offers rich prospects for the study of energetic particle acceleration in low density plasmas in an astrophysical source.

In summary, the P/OF coronal instrument can provide a wide variety of plasma diagnostics for determining the physical conditions in the corona and inner heliosphere where the solar wind originates and is accelerated. It can provide empirical information on electron, proton, and ion temperatures, densities, and flow velocities as well as information of chemical abundances and nonthermal velocities produced by wave motions. This information can be used, for example,

with the solar wind equations to determine and/or place limits on the magnitude of the non-radiative energy deposited as a function of distance from the solar surface — separately for electrons, protons, and heavy ions. This would provide critical insights concerning possible heating mechanisms which can have different characteristic dissipation lengths and may preferentially heat particles of a specific mass or charge-to-mass. For example, in coronal holes fast-mode MHD waves preferentially heat electrons (Habbal and Leer, 1982). Precise measurements of spectral line shapes made possible by the high sensitivity of the P/OF coronal instruments can provide additional constraints on processes for energy transport and dissipation. Measurements by the hard X-ray instruments can provide information on in situ energy releases, nonthermal energy deposition, and the acceleration of energetic electrons.

III. STRUCTURES AND PHYSICS OF STREAMERS

Streamers are the most prominent bright features observed in white-light photographs of the corona (see Figure 3). These large structures extend far out into the heliosphere from the Sun, often to distances greater than 10 solar radii. Because streamers extend beyond the heights readily accessible with traditional spectroscopic instruments operating at visible, EUV, and X-ray wavelengths, relatively little is known about the physical conditions in these features other than information about geometry and electron densities derived from white-light observations. There is little or no information about critical parameters such as temperatures, chemical composition, magnetic field strengths, and outflow velocities. For example, although streamers clearly contribute mass to the solar wind, it is not known how much. There is evidence from in situ measurements of the solar wind far from the Sun that streamers are sources of slow speed solar wind (cf., Gosling et al., 1981). However, until measurements of the outflows in streamers are acquired, there will be uncertainty as to the nature of their contribution to the outflow of coronal plasma into the heliosphere.

P/OF will have the capability to greatly expand our empirical knowledge about the physical conditions in streamers. It will have the high spatial resolution required to probe in detail the structure of these features and obtain the plasma diagnostic information required to investigate the physics of these prominent structures of the solar corona. P/OF can provide empirical information to address questions such as: What are the differences in the temperatures, densities, mass flows, and plasma heating in the magnetically open and closed regions of streamers and between streamers and the surrounding areas? What are the physical conditions in the outermost extensions of streamers where we expect there are current sheets separating regions of oppositely directly magnetic fields? What are the physical conditions in the region near the top of the "helmet" where the magnetic field lines make a transition from closed to open? Do magnetic reconnection, plasma heating, nonthermal energy releases, and/or particle acceleration occur here? Are MHD waves present in various regions of the streamer?

Streamers are also a laboratory for studying interactions between magnetic fields and plasmas in open and closed configurations and in the transition regions between these configurations. Skylab and SMM observations show that streamers are dynamic structures which can move about (Illing et al., 1981; Mun and Fisher, 1985), presumably in response to changes in the large scale magnetic field of the Sun. These observations also indicate that the amount of material contained in a given structure can vary with time. Because of their very high spatial resolution, the coronal instruments on P/OF are particularly well suited to studying temporal variations in streamers. With P/OF it will be possible to observe the structure of a streamer (on both large and small spatial scales) and monitor the physical conditions in the streamer and its surroundings as a function of time. It should be possible to obtain, for example, insights as to whether observed changes in the shape or orientation of a streamer are in response to magnetic forces or changes

in plasma heating. Streamers are an ideal place to search for signatures of magnetic reconnection with P/OF because of (1) the high spatial resolution of the P/OF instruments, (2) the capability for simultaneously monitoring plasma properties and detecting the release of nonthermal energy and the acceleration of energetic electrons, and (3) the large scale (compared to the P/OF resolution) structure of streamers.

In short, P/OF will provide the first opportunity to probe in detail the physical conditions in streamers and obtain empirical information needed to provide insights for developing realistic physical models for these features and for testing theories for various physical processes occurring in them. Figure 4 summarizes in "cartoon" or schematic fashion some of the questions discussed above.

IV. STRUCTURE AND PHYSICS OF CORONAL HOLES

The discovery that coronal holes are sources of recurrent, high-speed, solar wind streams has generated much interest in these low density regions of the outer solar atmophere. Coronal holes are the only unambiguously identified source of steady-state solar wind. Figure 3 shows a particularly large coronal hole observed during the 1973 solar eclipse. From white-light observations, such as illustrated in Figure 3, and He I λ 10830, XUV, and X-ray observations of coronal holes on the disk (e.g., Figure 5) we have been able to obtain information about the geometries and densities of coronal holes, their lifetimes (often many solar rotations), and mean temperatures ($\sim 10^6$ K) at their coronal bases (see Zirker, 1977, 1981). From limited spectroscopic observations acquired by a combined UV/white-light coronagraphic payload flown several times on a sounding rocket we have also obtained some empirical constraints on temperatures and flow velocities out to several solar radii in several polar regions where coronal holes were located (Kohl et al., 1980, 1984; Withbroe et al., 1985). These measurements suggest that the temperatures, densities, and coronal outflow velocities can be different for different coronal holes, possibly because of differences in size and geometry.

Existing instruments have insufficient sensitivity, spatial resolution, and spectroscopic diagnostic capabilities for addressing several fundamental questions concerning the physics of coronal holes. The high spatial resolution of P/OF ($\sim$1 arc s as compared to several arc min for existing UV coronal spectrometer and 8 to 10 arc s for white-light instruments) is of particular importance for determining the role of small-scale structures in the generation of the solar wind outflow from coronal holes. The high sensitivity of P/OF (several orders of magnitude beyond that of existing instruments) and access to spectral lines over a wide range of the spectrum (current instruments are limited to measuring intensities of a few spectral lines and profiles of only hydrogen Lyman alpha) is needed for performing extensive plasma diagnostics in the low density regions such as coronal holes. As summarized in Section II, these diagnostics are required for placing tight empirical constraints on processes for energy transport and dissipation and for solar wind acceleration.

The most prominent fine-scale structures observed in polar coronal holes are polar plumes, ray-like structures often visible in white-light eclipse photographs (e.g., lower pole in Figure 3). These features, which have widths of a few times 10^4 km, are believed, in many cases, to trace open magnetic field lines. Skylab observations in the EUV and XUV showed that coronal bright points are found at the bases of polar plumes (cf., Bohlin, 1977). This is illustrated in Figure 6, which contains several spectroheliograms acquired by the NRL Skylab spectroheliograph. The arrows point to several plumes which are best seen in the Mg IX λ 368 image. It appears that plumes can contain 10 to 20% of the coronal mass in polar coronal holes and may contribute a comparable fraction, perhaps more, of the solar wind mass flux originating in polar regions of the

Sun (Ahmad and Withbroe, 1977; Ahmad and Webb, 1978). A determination of whether or not this is the case requires new high resolution measurements of the type that can be acquired by the coronal instruments on P/OF.

The high sensitivity of the P/OF instruments will be important for studying the temporal behavior of polar plumes. There is evidence from Skylab data that there are short term variations (minutes to tens of minutes) in the EUV emission from these features, variations which could result from dynamical phenomena (Withbroe, 1983b). One possible source of the variations are flares in the coronal bright points which underlie plumes. Coronal bright points are often the site of flare-like phenomena (cf., Golub et al., 1974); hence, it is possible that they may also be the source of small-scale coronal transients or mass ejections. Often 50% or more of the energy in flares in active regions is carried away in the form of mass ejections. It would be interesting to determine whether or not similar phenomena occur for the smaller "flares" observed in coronal bright points. It would also be interesting to determine whether or not acceleration of energetic particles occurs during bright point flares and, if so, whether these particles escape into the helio-sphere, for example, along the open magnetic field lines in plumes overlying the bright points. Hence, observations of polar plumes and coronal bright points with the entire complement of P/OF instruments could lead to significant discoveries concerning the physics of solar wind flow, transient phenomena, and possibly particle acceleration in coronal holes.

Another prominent feature in polar coronal holes are the large spicules known as macro-spicules (cf., Bohlin, 1977). These features are most clearly seen in the He II λ 304 image in Figure 6 as narrow ($\lesssim 10^4$ km) jets of emission extending above the solar limb. Macrospicules have lifetimes of 10 to 20 min and appear to be jets of cool ($\lesssim 10^5$ K) material ejected from the chromosphere with velocities up to 150 km/s, velocities comparable to the sound speed in the corona. Skylab EUV observations indicate that most, perhaps all, of the mass appears to fall back into the chromosphere (Withbroe et al., 1976; Withbroe, 1983a). It is possible that macro-spicules, and the more numerous, less energetic spicules found in the quiet chromosphere, are associated with upward-propagating waves or shocks (cf., Hollweg et al., 1982; Shibata, 1982).

A less frequent, but much more energetic phenomena that may or may not be related to spicules and/or macrospicules are the high-energy jets, sometimes called coronal "bullets," observed by the NRL HRTS rocket experiment (Brueckner and Bartoe, 1983), especially in the C IV spectral lines formed at temperatures ~2 x 10^5 K. The velocities associated with these energetic events are typically of the order of 400 km/s. Their role in the acceleration of the solar wind is unknown. It is interesting to note that the upward flux of mass and energy flows asso-ciated with these features is comparable to that in the solar wind. New high resolution spectro-scopic measurements at chromospheric and coronal heights are required to determine the effects of these phenomena (spicules, macrospicules, and high-energy jets) on mass and energy flows in the overlying corona. It would also be interesting to determine whether or not significant numbers of energetic particles are accelerated in conjunction with these small-scale dynamical phenomena. This requires simultaneous observations by the P/OF coronal and hard X-ray instru-ments and the Solar Optical Telescope and/or the NRL HRTS instrument. The latter instru-ments could provide the chromospheric and transition region observations needed to complement the P/OF coronal and hard X-ray measurements. Figure 7 summarizes schematically some of the questions concerning the physics of small-scale phenomena which can be addressed with P/OF.

Another type of structure that may be found in coronal holes are standing shocks. Theo-retical investigations of the solar wind indicate that standing shocks can develop in coronal holes under appropriate conditions depending on the geometry and momentum deposition (cf., Habbal

227

and Rosner, 1984). The P/OF coronal instruments have the sensitivity, spatial resolution, and spectroscopic diagnostic capabilities to detect standing shocks and establishing whether such phenomena actually occur in solar coronal holes as predicted.

V. CORONAL TRANSIENTS AND MASS EJECTIONS

One of the most spectacular forms of solar activity is the coronal mass ejection, the most common type of coronal transient disturbance (see reviews by MacQueen, 1980; Sheeley et al., 1982; Wagner, 1984; Michels et al., 1984). Figure 8 shows a coronal transient photographed by the Skylab white-light coronagraph. Although we have learned a great deal about coronal transients from the extensive series of observations obtained by white-light coronagraphs on space-craft such as Skylab, SMM, and P-78, there is much we do not know. White-light observations have provided a wealth of information about the forms, frequencies, masses, and apparent velocities of these phenomena. The rate of production of coronal transients appears to be about one to two per day (MacQueen, 1980; Sheeley et al., 1982, 1985). From measurements of the rate of outward propagation of regions of enhanced brightness, assumed to be caused by the outward flow of coronal material associated with the transient, it appears that coronal transients often exhibit acceleration out to five or six solar radii and reach velocities of 200 to 1000 km/s. Because of the presence of accelerating forces over large distances above the solar surface and frequent association of coronal transients with loop structures, proposed models for these phenomena often invoke magnetic forces (MacQueen, 1980). The amount of mass involved generally falls between 10^{15} and 10^{16} g and the total energy associated with these events is typically of the order of 10^{31} erg. For flare-associated coronal transients the amount of energy represented by the transient is comparable to or greater than that released by the flare in other forms (e.g., radiation and energetic particles).

In spite of the great progress made in the past decade, much remains unknown about the physics of coronal transients. As for other phenomena observed in the corona beyond heights where measurements by traditional spectroscopic instruments are very limited, there is insufficient empirical information about critical plasma parameters to determine, for example, the spatial and temporal variations of the temperature of the plasma in the transient and in the ambient medium. P/OF does not have these limitations. Because of its capability for acquiring much more detailed plasma diagnostic information and detecting signatures of energetic electrons and nonthermal energy releases, P/OF will provide a quantum leap in capability for addressing a wide variety of questions concerning the physics of coronal transients. With P/OF it will be possible to obtain spectroscopic signatures of shocks associated with transients (measuring, for example, temperature, density, and velocity jumps across a shock front) while simultaneously probing for energetic electrons accelerated in conjunction with the shocks. (Existing observations indicate that coronal transients are often associated with acceleration of energetic particles.) Through use of Doppler-dimming techniques it will be possible to distinguish between brightenings caused by waves and those caused by flows. It will also be possible (1) to determine the fate of cool, low-ionization state matter from eruptive prominences associated with transients, (2) to determine when and where plasma heating occurs, and (3) to obtain insights as to whether the transient is magnetically or thermally driven (see Figure 9).

There are a variety of radio transient phenomena produced by energetic electrons accelerated in or passing through the corona (see review by Pick, 1985). Through simultaneous observations with the P/OF coronal and X-ray instruments and ground-based radio telescopes, it should be possible to learn much about the acceleration of energetic electrons in the corona and their interaction with the coronal plasma. As indicated in Section II, the P/OF coronal instruments

can observe the spatial and temporal variations of the coronal structure, density, and temperature of thermal electrons, and provide constraints on ion temperatures, magnetic fields, and turbulent velocities at the coronal sites of electron acceleration and along the paths where the electrons propagate. The P/OF hard X-ray instruments and ground-based radio telescopes can provide simultaneous information of the location of the acceleration site and the number, energy spectrum, and trajectory of the accelerated electrons. With such observations one can investigate, for example, the acceleration of energetic electrons in shocks associated with coronal transients and the physics of Type III bursts. Clearly, such observations offer great promise for improving our knowledge about physical processes governing the production, transport, and energy-dissipation of nonthermal electrons in low-density astrophysical plasmas.

VI. SUMMARY

The Pinhole/Occulter Facility is a powerful tool for studying the physics of the extended corona and origins of the solar wind. It offers unique, unprecedented capabilities for probing the source region of the solar wind, coronal transients, and the acceleration of energetic particles. Spectroscopic data acquired by the P/OF coronal instruments can greatly expand empirically derived information about the temperatures, densities, flow velocities, magnetic fields, and chemical abundances in the extended corona, the region where the solar wind is generated. Empirically derived knowledge of the physical conditions throughout most of this region has been limited and, hence, the processes for energy and momentum transport (other than radiation and thermal conduction) and for energy and momentum deposition have not been identified. Identification of these mechanisms in the Sun will help make possible development of realistic physical models for stellar wind acceleration in late type stars.

Improved knowledge of the physical conditions in the extended corona are required to determine the role of coronal streamers in the generation of the solar wind. Observations made with high spatial resolution are required to establish the role, if any, of the dynamical phenomena such as spicules, macrospicules, coronal "bullets," and fine-scale structures, such as polar plumes, in the generation of the solar wind. Although we have numerous white light photographs of coronal transients and mass ejections, we have little information about the physical conditions in these dynamic phenomena other than densities and velocities. The P/OF coronal instruments can greatly expand the amount and quality of the available information and thereby significantly advance our understanding of these spectacular phenomena which account for a substantial fraction, typically greater than 50%, of the energy released in energetic transient phenomena such as solar flares.

A fundamental problem in astrophysics is the development of knowledge of the processes by which energetic particles are accelerated in nature. Simultaneous solar observations of the signatures of accelerated energetic electrons and of the physical conditions and the structures of coronal sites where acceleration occurs offer exciting prospects for studying particle acceleration in an astrophysical plasma.

In short, coronal observations by the Pinhole/Occulter Facility can lead to major advances in our understanding of the physics of the only stellar corona and source of stellar wind which can be probed in detail to provide tight empirical constraints on critical physical processes involved in (1) the transport and dissipation of energy and momentum, (2) the heating and acceleration of plasma, and (3) the acceleration of energetic particles.

REFERENCES

Ahmad, I. A. and Webb, D., 1978, *Solar Phys.*, *58*, 323.

Ahmad, I. A. and Withbrow, G. L., 1977, *Solar Phys.*, *53*, 397.

Beckers, J. M. and Chipman, E., 1974, *Solar Phys.*, *34*, 151.

Bohlin, J. D., 1977, in J. B. Zirker (ed.), *Coronal Holes and High Speed Solar Wind Streams*, Colorado Assoc. Univ. Press, Boulder, CO, p. 27.

Bommier, V. and Sahal-Brechot, S., 1982, *Solar Phys.*, *78*, 157.

Brueckner, G. E. and Bartoe, D. F., 1983, *Astrophys. J.*, *272*, 329.

Cheng, C. C., Doschek, G. A., and Feldman, U., 1981, *Astrophys. J.*, *227*, 1037.

Esser, R., Habbal, S. R., Leer, E., and Withbroe, G. L., 1985, to be sumitted to *J. Geophys. Res.*

Golub, L., Krieger, A. S., Silk, J. K., Timothy, A. F., and Vaiana, G. S., 1974, *Astrophys. J. (Letters)*, *189*, L93.

Gosling, J. T., Borrini, G., Asbridge, J. R., Bame, S. J., Feldman, W. C., and Hansen, R. T., 1981, *J. Geophys. Res.*, *86*, 5438.

Habbal, S. R. and Leer, E., 1982, *Astrophys. J.*, *253*, 318.

Habbal, S. R. and Rosner, R., 1984, *J. Geophys. Res.*, *89*, 10645.

Hirshberg, J., 1975, *Rev. Geophys. Space Phys.*, *13*, 1059.

Hollweg, J. V., 1981, in S. Jordan (ed.), *The Sun as a Star*, NASA Special Publication 450, NASA, Washington, D. C., p. 355.

Hollweg, J. V., Jackson, S., and Galloway, D., 1982, *Solar Phys.*, *75*, 35.

Hudson, H. S., Kohl, J. L., Lin, R. P., MacQueen, R. M., Tandberg-Hanssen, E., and Dabbs, J. R., 1981, *The Pinhole/Occulter Facility*, NASA Technical Memorandum 82413, Marshall Space Flight Center, Alabama.

Illing, R. M. E., Wagner, W. J., House, L. L., and Sawyer, C., 1981, *Bull. Amer. Astron. Soc.*, *13*, 911.

Kohl, J. L., Munro, R. H., Weiser, H., Withbroe, G. L., and Zapata, C. A., 1984, *Bull Amer. Astron. Soc.*, *16*, 531.

Kohl, J. L. and Strachan, L., 1985, private communication.

Kohl, J. L., Weiser, H., Withbroe, G. L., and Munro, R. H., 1985, in G. Doschek (ed.), *Proceedings of the Eighth International Colloquium on Ultraviolet and X-Ray Spectroscopy and Laboratory Plasmas*, NRL, Washington, D.C.

Kohl, J. L., Weiser, H., Withbroe, G. L., Noyes, R. W., Parkinson, W. H., Reeves, E. M., Munro, R. H., and MacQueen, R. M., 1980, *Astrophys. J. (Letters)*, *241*, L117.

Kohl, J. L. and Withbroe, G. L., 1982, *Astrophys. J.*, *256*, 263.

Kohl, J. L., Withbroe, G. L., Zapata, C. A., and Noci, G., 1983, in M. Neugebauer (ed.), *Solar Wind Five*, NASA, Conference Publication 2280, Washington, D. C., p. 47.

Leer, E., Holzer, T. E., and Fla, T., 1982, *Space Sci. Rev.*, *33*, 161.

Macqueen, R. M., 1980, *Phil. Trans. Roy. Soc.*, *33*, 219.

Michels, D. J., Sheeley, N. R., Howard, R. A., Koomen, M. J., Schwenn, K., Mulhauser, K. H., and Rosenbauer, H., 1984, *Adv. Space Res.*, *4*, Proceedings XXV COSPAR Meeting, Graz, Austria.

Munro, R. H. and Fisher, R. R., 1985, these proceedings.

Pick, M., 1985, these proceedings.

Sheeley, N. R., Jr., Howard, R. A., Koomen, M. J., Michels, D. J., Harvey, K. L., and Harvey, J. L., 1982, *Space Sci. Rev.*, *33*, 219.

Sheeley, N. R., Jr., Howard, R. A., Koomen, M. J., and Michels, D. J., 1985, these proceedings.

Shibata, K., 1982, *Solar Phys.*, *81*, 99.

Tandberg-Hanssen, E. A., Hudson, H. S., Dabbs, J. R., and Baity, W. A. (eds.), 1983, *The Pinhole/Occulter Facility*, NASA Technical Paper 2168, NASA, Washington, D.C.

Wagner, W. J., 1984, *Ann. Rev. Astron. Astrophys.*, *22*, 267.

Withbroe, G. L., 1983a, *Astrophys. J.*, *267*, 825.

Withbroe, G. L., 1983b, *Solar Phys.*, *89*, 77.

Withbroe, G. L., and 8 co-authors, 1976, *Astrophys. J.*, *203*, 528.

Withbroe, G. L., Kohl, J. L., Weiser, H., and Munro, R. H., 1982a, *Space Sci. Rev.*, *33*, 17.

Withbroe, G. L., Kohl, J. L., Weiser, H., and Munro, R. H., 1985, *Astrophys. J.*, in press.

Withbroe, G. L., Kohl, J. L., Weiser, H., Noci, G., and Munro, R. H., 1982b, *Astrophys. J.*, *254*, 361.

Zirker, J. B. (ed.), 1977, *Coronal Holes and High Speed Solar Wind Streams*, Colorado Assoc. Univ. Press, Boulder, CO.

Zirker, J. B., 1981, in S. Jordan (ed.), *The Sun as a Star*, NASA Special Publication 450, NASA, Washington, D. C., p. 135.
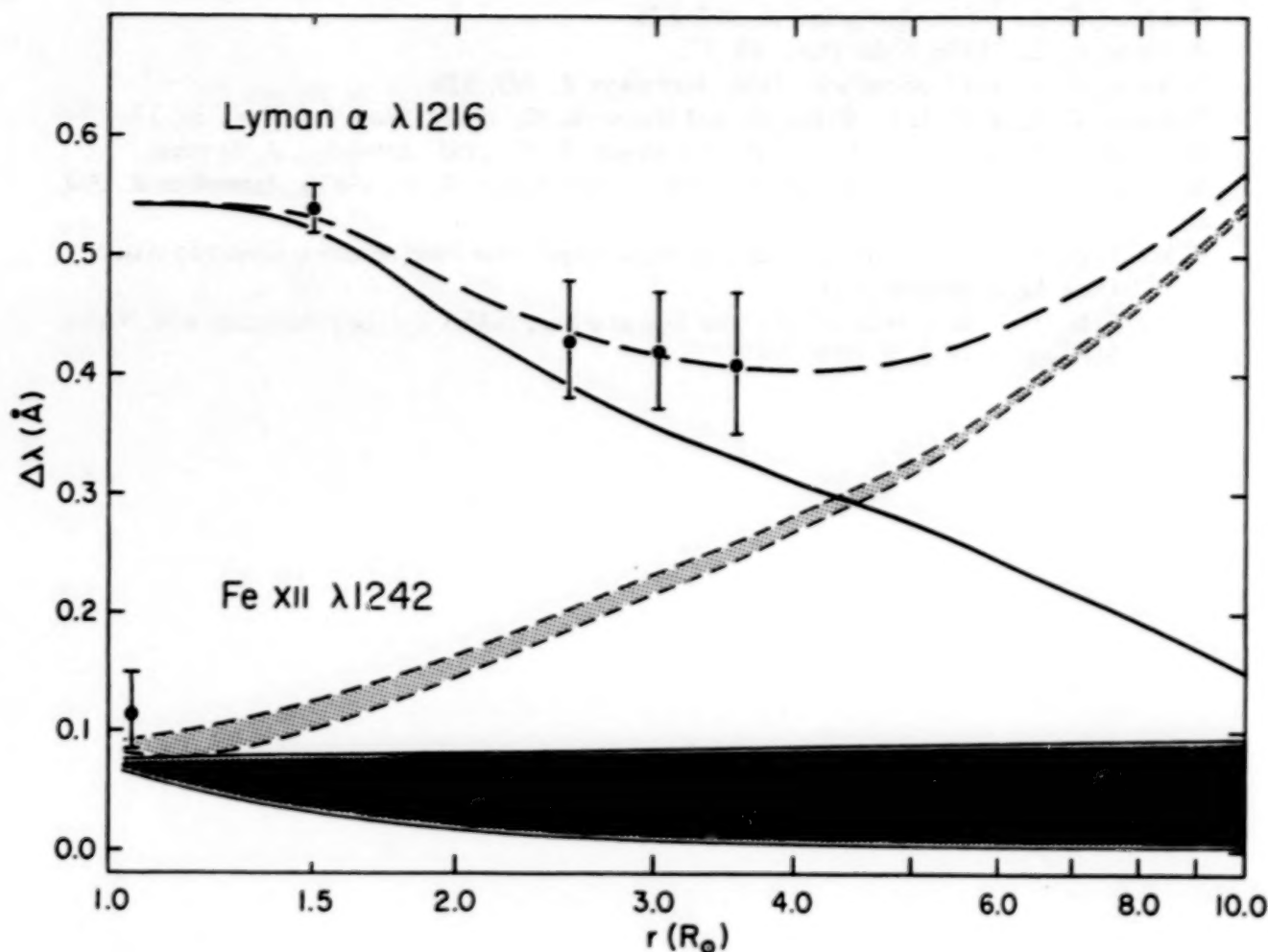
Figure 1. Spectral line widths plotted as a function of distance from Sun-center. The solid curve is for Lyman alpha widths calculated for a simple two-fluid model without any Alfvén wave flux; the dashed line is for a model with an Alfvén wave flux added to account more satisfactorily for the empirical Lyman alpha widths measured (points) in a polar region where a coronal hole was located (see Esser et al., 1985; Withbroe et al., 1985). From the results of the two-fluid model calculations one can estimate the behavior of a line from a heavy ion (e.g., Fe XII λ 1242). The figure shows how the width of this line would vary in a model with Alfvén waves present (narrow cross-hatched region) and without Alfvén waves (nearly horizontal cross-hatched area). (Because of uncertainties of the amount of electron/Fe XII and proton/Fe XII coupling, we can only calculate limits in the Fe XII widths without carrying out a detailed, multi-fluid model calculation.) The empirical Fe XII width (point) near r = 1 $R_\odot$ is typical of measurements made in quiet coronal regions (cf., Cheng et al., 1981).
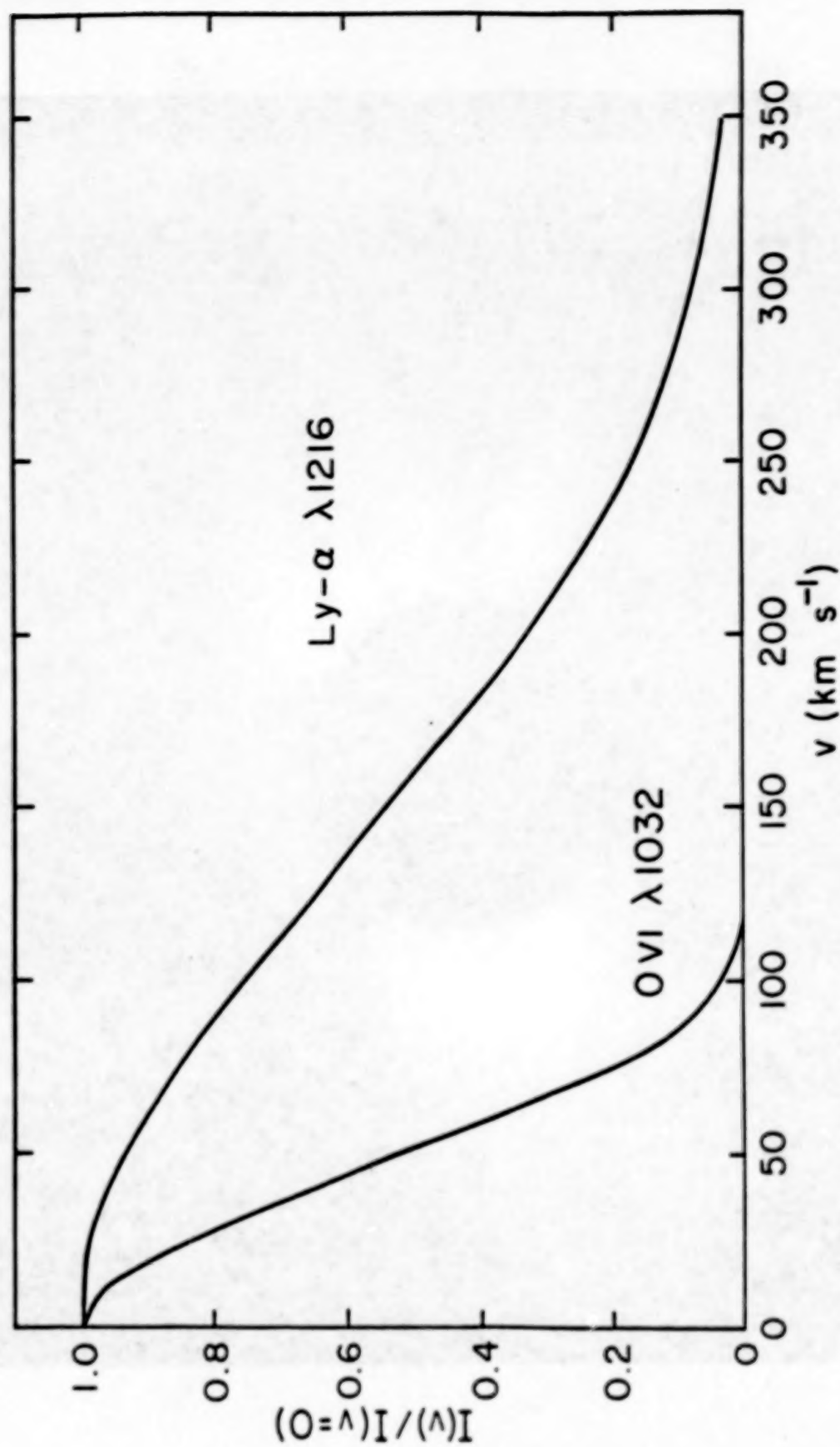
Figure 2. Doppler-dimming calculated for an isothermal corona with $T = 1.5 \times 10^6$ K.
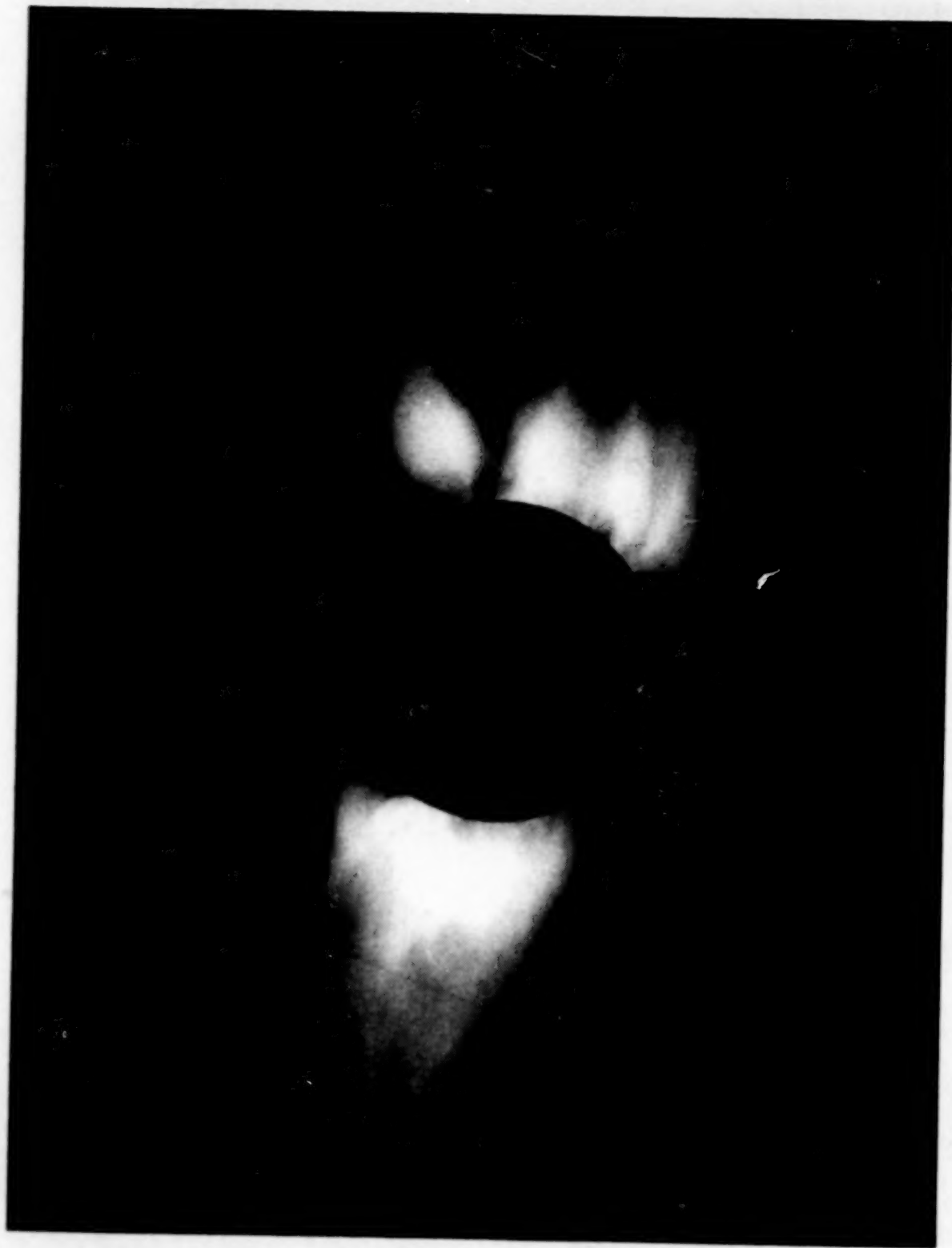
Figure 3. White-light eclipse photograph of the corona obtained at a total eclipse in 1973 (courtesy of High Altitude Observatory). A large polar coronal hole is located at the north (upper) pole.
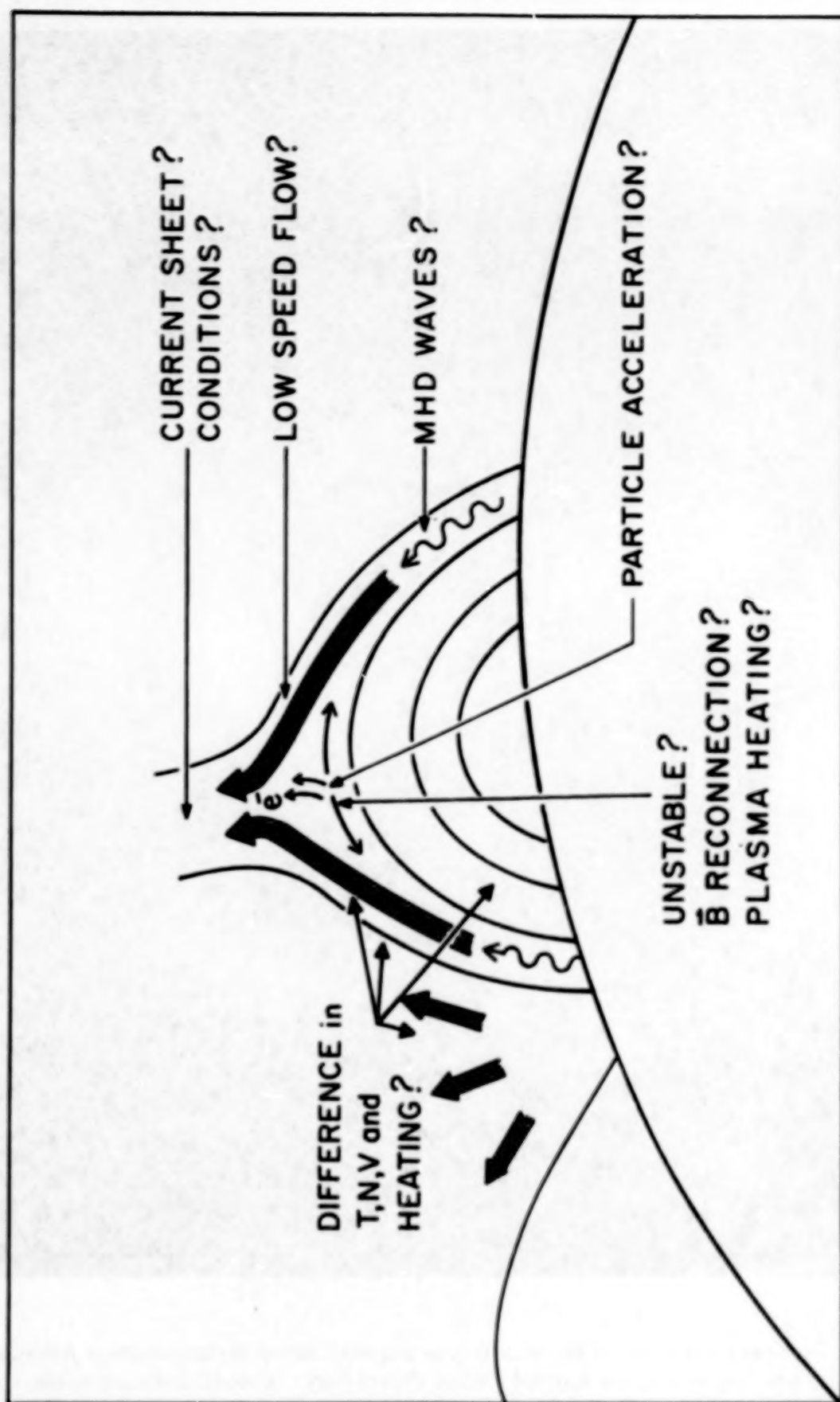
Figure 4. Schematic summarizing some questions concerning the structure and physics of streamers.

CURRENT SHEET ?
CONDITIONS ?

LOW SPEED FLOW ?

MHD WAVES ?

PARTICLE ACCELERATION ?

DIFFERENCE in
T, N, V and
HEATING ?

UNSTABLE ?
B̄ RECONNECTION ?
PLASMA HEATING ?

235

Figure 5. X-ray photograph of the solar corona acquired during Skylab (courtesy American Science and Engineering and Harvard College Observatory). Coronal holes are visible as dark areas at the north (upper) pole and near the east (left) limb.
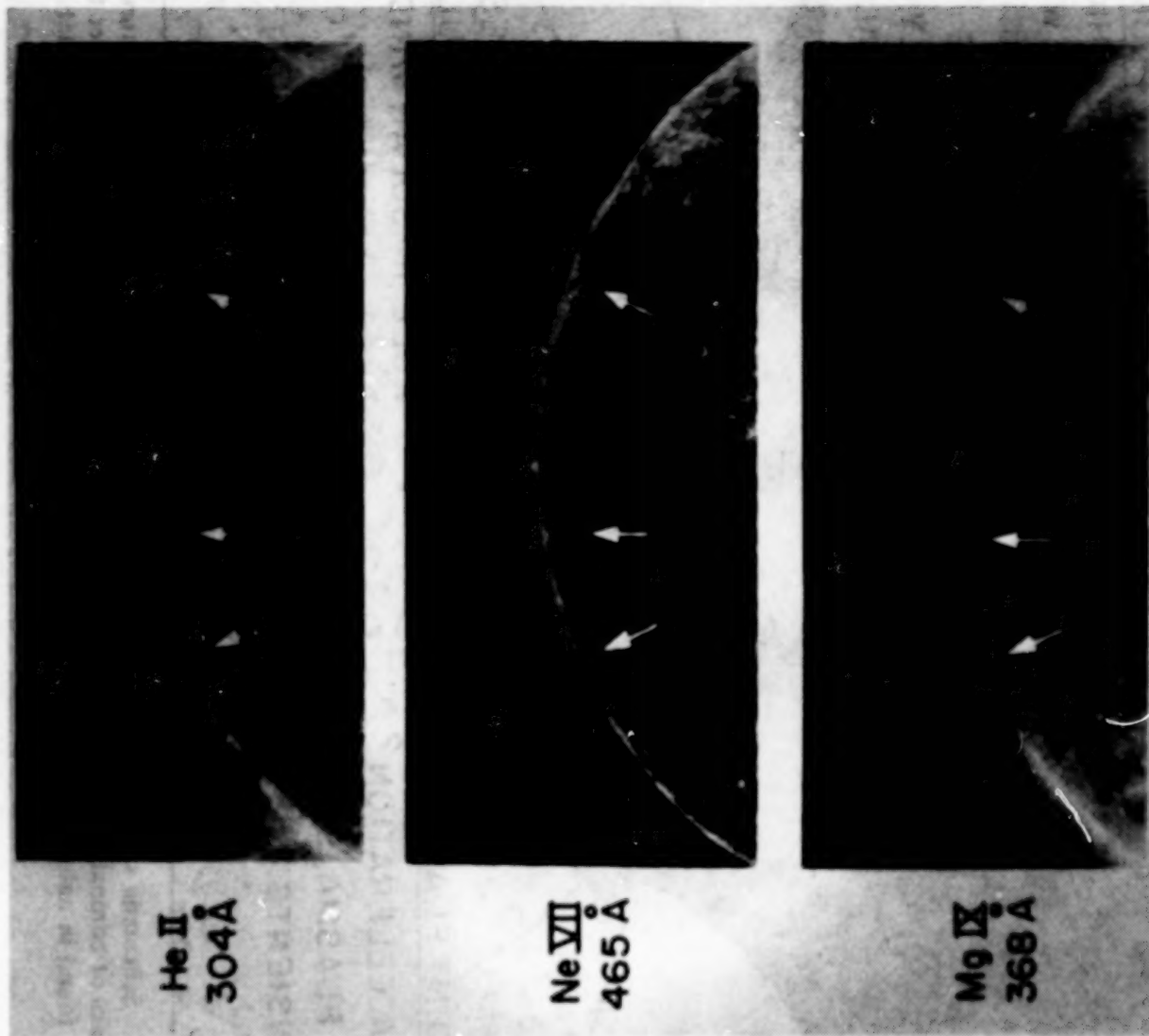
Figure 6. Spectroheliograms obtained by the NRL experiment on Skylab showing coronal bright points and overlying polar plumes (arrows) and macrospicules at the limb in a polar coronal hole.

He II
304Å

Ne VII
465 Å

Mg IX
368 Å

POLAR PLUMES:

SOURCE of HIGH SPEED
SOLAR WIND ?

STEADY ?
IMPULSIVE ?
THERMALLY DRIVEN ?
MAGNETICALLY DRIVEN?

MACROSPICULES,
SPICULES and CORONAL "BULLETS":

ROLE IN SOLAR WIND ?

BRIGHT POINT FLARES:

PARTICLE ACCELERATION ?
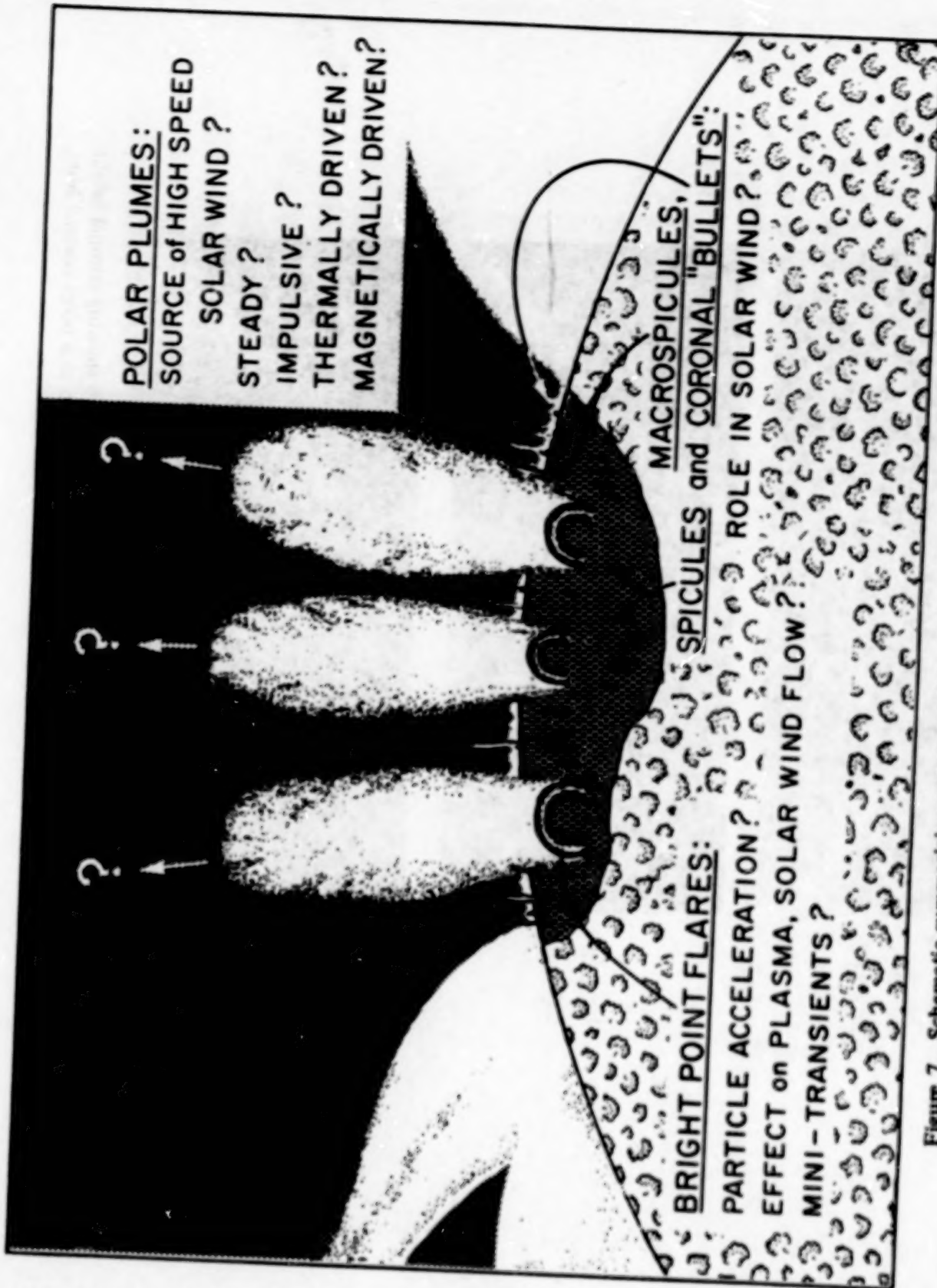EFFECT on PLASMA, SOLAR WIND FLOW ?
MINI-TRANSIENTS ?

Figure 7. Schematic summarizing some questions concerning the role of small-scale structures in the physics of coronal holes. (In this illustration the plumes are drawn several times wider than usually found in nature in order to show the loop structure of the underlying bright points — compare with plumes visible in Figures 3 and 6.)
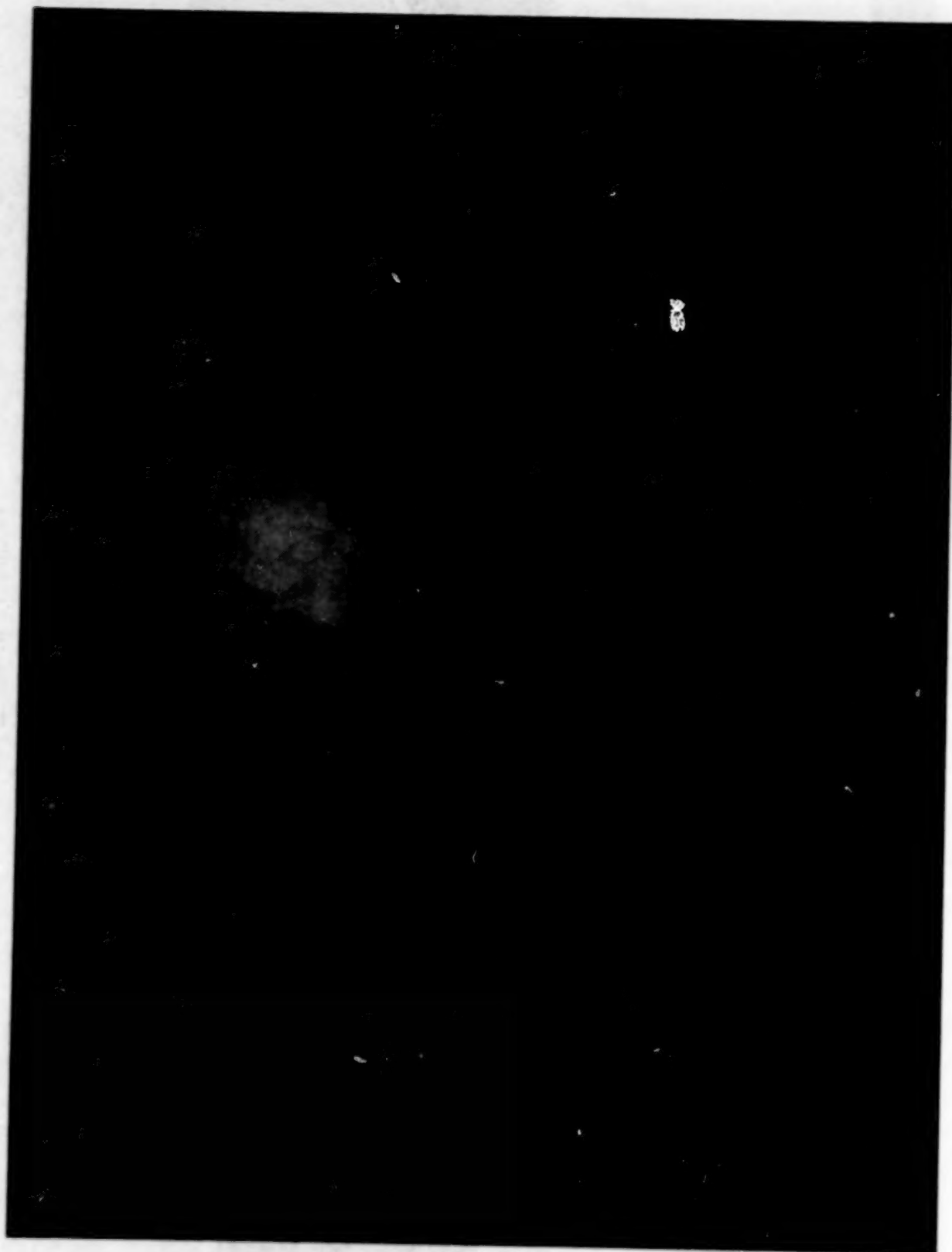
238

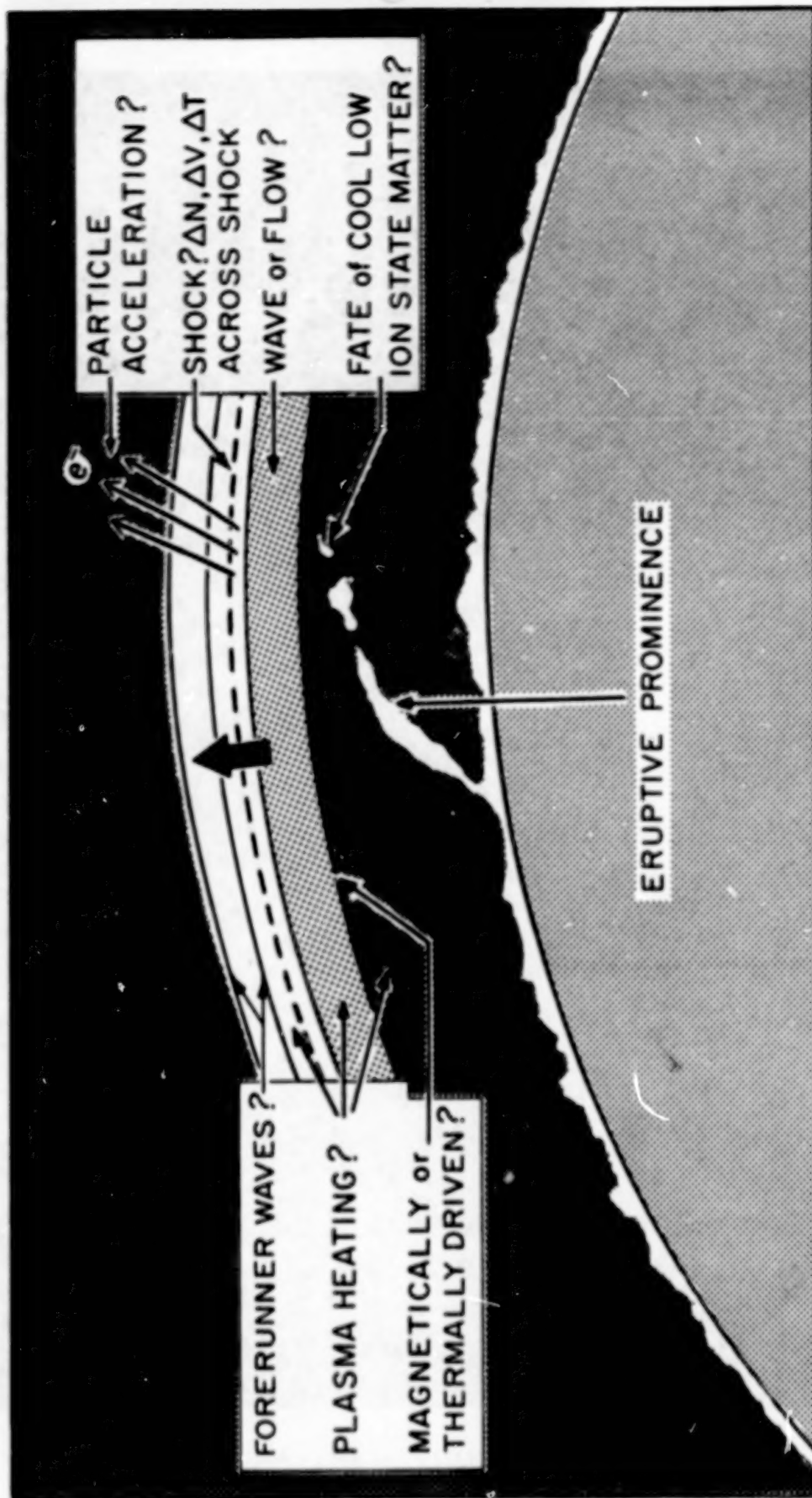Figure 8. Coronal transient observed by HAO white-light coronagraph on Skylab.

Figure 9. Schematic illustrating some problems concerning the physics of coronal transients and associated phenomena.

SOLWIND OBSERVATIONS OF CORONAL MASS EJECTIONS DURING 1979-1985
(Invited)

N. R. Sheeley, Jr., R. A. Howard, M. J. Koomen,* and D. J. Michels

E.O. Hulburt Center for Space Research, Naval Research Laboratory
Washington, D.C. 20375-5000, U.S.A.

ABSTRACT

Coronal observations have been processed for parts of each year during the interval 1979-1985. Around sunspot maximum, coronal mass ejections (CMEs) occurred at the rate of approximately 2 per day, and had a wide range of physical and morphological properties. During the recent years of relatively low sunspot number, CMEs occurred at the rate of only 0.2 per day, and were dominated by the class of so-called "streamer blowouts." These special CMEs maintained a nearly constant occurrence rate of roughly 0.1 per day during the entire interval.

I. INTRODUCTION

All but a few months of the Solwind coronal observations have been processed for the interval March 1979 to December 1981 around the maximum phase of sunspot cycle 21. During this interval more than 1000 coronal mass ejections (CMEs) were identified. Their properties have been measured and studied statistically by Howard et al. (1985), and summaries of this work have been published elsewhere (cf., Howard et al., 1984; Michels et al., 1984). In addition, several investigators have studied the associations between these CMEs and a variety of other solar and interplanetary phenomena including soft X-ray events (Sheeley et al., 1983a), metric Type II radio bursts (Sheeley et al., 1984; Kahler et al., 1984b), interplanetary shocks (Schwenn, 1983; Sheeley et al., 1983b, 1985; Woo et al., 1985), energetic proton events (Kahler et al., 1984a), and magnetic clouds (Burlaga et al., 1982).

The Solwind instrument has continued to obtain coronal images routinely since December 1981, and is still doing so at the time of this writing (May 1985). However, our processing of these data was interrupted for about one year while we were converting to a new computer. During the past few months, we have resumed the processing, and are rapidly reducing the observations during 1982-1985. The most striking characteristic of the recent observations is the persistent streamer structure and the substantial reduction in the occurrence rate of coronal mass ejections. The resulting correlation between the occurrence rate of CMEs and the level of sunspot activity (the sunspot number) is similar to that deduced by Hildner et al. (1976) from their study of mass ejections during the Skylab mission in 1973-1974. It is substantially different from the nearly constant CME rate that Hundhausen et al. (1984) derived by combining their SMM observations in 1980 with their reanalysis of the Skylab data. We suppose that the discrepancy results from assumptions about the "dead time" of the Skylab and SMM coronagraphs.

Perhaps even more interesting is the fact that the recent CMEs have consisted primarily of the so-called "streamer blowout" class (cf., Sheeley et al., 1982; Howard et al., 1985). During 1979-1981 we found that this class of CME constituted only 5% of all mass ejections and only 8% of all "major" mass ejections. During the four months of 1984-1985 for which we have

---

*Sachs/Freeman Associates, Bowie, MD 20715.

processed continuous data, these special CMEs have constituted 36% of all CMEs and 67% of all major CMEs. Furthermore, it appears that the occurrence rate of "streamer blowout" CMEs has been approximately constant during the interval 1979-1985 at a value of nearly 0.1 per day.

In this paper, we shall present a brief summary of these recent results, and refer the reader to the published studies and review papers for more detailed properties of Solwind mass ejections and their associations.

II. THE RESULTS

(a) The CME Occurrence Rate

From their study of 998 CMEs during 1979-1981, Howard et al. (1985) found that CMEs could be conveniently classified by morphological structure and importance. They identified nine more or less distinct classes, examples of which are shown in Figure 1. The importance of a CME is a somewhat subjective quantity, but in effect it is a measure of the CME's projected size and brightness. In practice, the classification was performed by two observers, and the assignment was either major (Y) or minor (N) when both observers agreed on this assignment. The assignment was questionable (Q) when the observers could not agree or when data gaps made the assignment indeterminate. Figure 2 illustrates the importance categories for five different morphological classes of mass ejection.

Howard et al. (1985) found that during the entire interval 1979-1981 the occurrence rate for all CMEs (regardless of structural class or importance category) was 1.8 per day. This determination was based on their choice of 4.5 hrs as the minimum "dead time" required to constitute a data gap. This gave a 66.5% duty cycle. When the minor (N) CMEs were excluded, the occurrence rate was 0.9 per day, which is essentially the same as Hundhausen et al. (1984) obtained from their analysis of CMEs observed by the SMM satellite during 1980.

Figures 3, 4, and 5 illustrate the variation of the occurrence rate on a variety of time scales during 1979-1981. Although there was considerable variation on the shorter scale of 7 days, this variation does not seem to be strongly or consistently related to fluctuations in the sunspot number. However, when we began to process observations during 1984-1985, we found intervals of several weeks at a time when there were no CMEs. We never found such intervals during 1979-1981. After processing completely the observations during June 1984, October and November 1984, and March 1985, we found only 22 CMEs (of all classes and importance categorys), for an average rate of only 0.2 per day. If one corrects this rate using the 4.5-hr dead time correction that was used for the CMEs during sunspot maximum, then the rate increases to 0.4 per day. However, we think this correction is not necessary during sunspot minimum because our difference images show long intervals of 12 hrs or more during which there is no appreciable change at all. Thus, if a CME had occurred in a 12-hr data gap during this phase of the sunspot cycle, we would have seen indications of it.

Figure 6 summarizes our measurements to date. The recent observations have been assigned to the date 1984, and for consistency both the uncorrected value of 0.2 per day and the "overcorrected" value of 0.4 per day have been plotted. For reference, the dashed line indicates the rate that Hildner et al. (1976) deduced from their analysis of the Skylab observations. Although it is probably premature to emphasize the detailed agreement between the Solwind and Skylab results, the comparable trend with sunspot number is both obvious and significant.

242

If we adopt the value of 0.2 per day for CMEs (of all classes and importances) during 1984-1985, then we find a value of only 0.1 per day when the minor CMEs are excluded. Of these, 67% or 0.07 per day consisted of streamer blowouts. This is comparable to the rate of 0.09 per day for streamer blowouts during 1979-81 when this class constituted only 8% of all major CMEs. Figure 7 shows the occurrence rate for these special CMEs during the interval 1979-1985. Although the statistics are poor, especially for the recent time, the resulting variation is in sharp contrast to that obtained for all classes of CME shown in Figure 6.

(b) The Properties

Figure 8 shows the evolution of a typical "curved front" CME on 18-19 November 1981. Mass ejections like this one constituted at least 15% of the CMEs that occurred in the years around sunspot maximum. Howard et al. (1985) found that such CMEs had average speeds of 584 km/s, spans of 62 degrees in the sky plane, mass of 8.4×10^{15} gm, and kinetic energy of 6.4×10^{30} ergs. Characteristically, they were associated with long-duration X-ray events (Sheeley et al., 1983a), interplanetary shocks (Sheeley et al., 1985), and energetic protons (Kahler et al., 1984a).

Notice in Figure 8 that a coronal streamer moved southward as the CME transited the field of view. Figure 9 shows the subsequent eruption or "blowout" of this streamer during a 19 hr interval on 19-20 November 1981. Howard et al. (1985) found that the average properties of such streamer blowouts included a relatively low speed of 200 km/s, a span of 44 degrees, a moderately high mass of 5.4×10^{15} g, but a relatively low kinetic energy of 0.56×10^{30} ergs. One of these streamer eruptions (cf., Figure 10a) was associated with a large shock (cf., Figure 10b) at the Helios 1 spacecraft (Sheeley et al., 1983b, 1985). However, during 1979-1981 most of these streamers and their eruptions occurred at relatively high latitudes and thus did not affect the near ecliptic spacecraft conditions. However, like the streamers with which they originate, the streamer blowout CMEs have tended to occur at relatively lower latitudes during 1984-1985 than they did during 1979-1981. Figure 11 shows a sample of these more recent events, and Figure 12 shows the evolution of a particularly well observed one.

It is interesting to compare some average properties of CMEs observed in the two intervals 1979-1981 and 1984-1985. Whereas the average projected latitude was 45 degrees near sunspot maximum, it was 22 degrees toward minimum. Similarly, the average span in position angle dropped from 44 degrees to 22 degrees. The average CME speed dropped from 472 km/s to roughly 130 km/s, which is consistent with the fact that most of the recent CMEs were the characteristically slow streamer blowouts.

III. DISCUSSION

In view of the preliminary state of our recent results, we can only speculate on their significance. The order-of-magnitude drop in the CME rate between sunspot maximum and the present time is surely significant. It points to a strong connection between the occurrence of CMEs and the level of solar magnetic activity. This seems consistent with the idea that CMEs are tracers of the ejection of flux from the Sun. It is also consistent with the fact that a large fraction of fast CMEs are associated with major X-ray flares, metric Type II bursts, interplanetary shocks, and energetic protons.

On the other hand, the nearly constant occurrence rate of the streamer blowout CMEs points to their possible identification as a normal state of the evolution of coronal streamers.

Such structures are present at all phases of the sunspot cycle. Only their heliographic location evolves with time. Thus, one might speculate that the streamer blowouts are simply phases in the evolution of streamers just as disappearing filaments (eruptive prominences) are phases in the evolution of filaments (prominences). Indeed, it is tempting to suppose that streamer blowouts and eruptive prominences are two aspects of the same process. However, further study is certainly required before we can take this speculation seriously.

Finally, we note the similarity between the helmet-like magnetic structure of coronal streamers and the teardrop structure of planetary magnetotails and comet tails. Thus, it is possible that an understanding of the physics of streamer blowouts will have a broad application to other astrophysical objects.

REFERENCES

Burlaga, L. F., Klein, L., Sheeley, N. R., Jr., Michels, D. J., Howard, R. A., Koomen, M. J., Schwenn, R., and Rosenbauer, H., 1982, *Geophys. Res. Lett., 9*, 1317.

Hildner, E., Gosling, J. T., MacQueen, R. M., Munro, R. H., Poland, A. I., and Ross, C. L., 1976, *Solar Phys., 48*, 127.

Howard, R. A., Sheeley, N. R., Jr., Koomen, M. J., and Michels, D. J., 1984, *Adv. Space Res., 4*, 307.

Howard, R. A., Sheeley, N. R., Jr., Koomen, M. J., and Michels, D. J., 1985, *J. Geophys. Res.* (submitted).

Hundhausen, A. J., Sawyer, C. B., House, L., Illing, R. M. E., and Wagner, W. J., 1984, *J. Geophys. Res., 89*, 2639.

Kahler, S. W., Sheeley, N. R., Jr., Howard, R. A., Koomen, M. J., Michels, D. J., McGuire, R. E., von Rosenvinge, T. T., and Reames, D. V., 1984a, *J. Geophys. Res., 89*, 9683.

Kahler, S. W., Sheeley, N. R., Jr., Howard, R. A., Koomen, M. J., and Michels, D. J., 1984b, *Solar Phys., 93*, 133.

Michels, D. J., Sheeley, N. R., Jr., Howard, R. A., Koomen, M. J., Schwenn, R., Muhlhauser, K. H., and Rosenbauer, H., 1984, *Adv. Space Res., 4*, 311.

Schwenn, R., 1983, *Space Sci. Rev., 34*, 85.

Sheeley, N. R., Jr., Howard, R. A., Koomen, M. J., Michels, D. J., Harvey, K., and Harvey, J., 1982, *Space Sci. Rev., 33*, 219.

Sheeley, N. R., Jr., Howard, R. A., Koomen, M. J., Michels, D. J., 1983a, *Astrophys. J., 272*, 349.

Sheeley, N. R., Jr., Howard, R. A., Koomen, M. J., Michels, D. J., Schwenn, R., Muhlhauser, K. H., and Rosenbauer, H., 1983b, in M. Neugebauer (ed.), *Solar Wind Five*, NASA Conference Publication 2280, Washington, D.C., p. 693.

Sheeley, N. R., Jr., Steward, R. T., Robinson, R. D., Howard, R. A., Koomen, M. J., and Michels, D. J., 1984, *Astrophys. J., 279*, 839.

Sheeley, N. R., Jr., Howard, R. A., Koomen, M. J., Michels, D. J., Schwenn, R., Muhlhauser, K. W., Rosenbauer, H., 1985, *J. Geophys. Res., 90*, 163.

Woo, R., Armstrong, J. W., Sheeley, N. R., Jr., Howard, R. A., Koomen, M. J., Michels, D. J., and Schwenn, R., 1985, *J. Geophys. Res., 90*, 154.
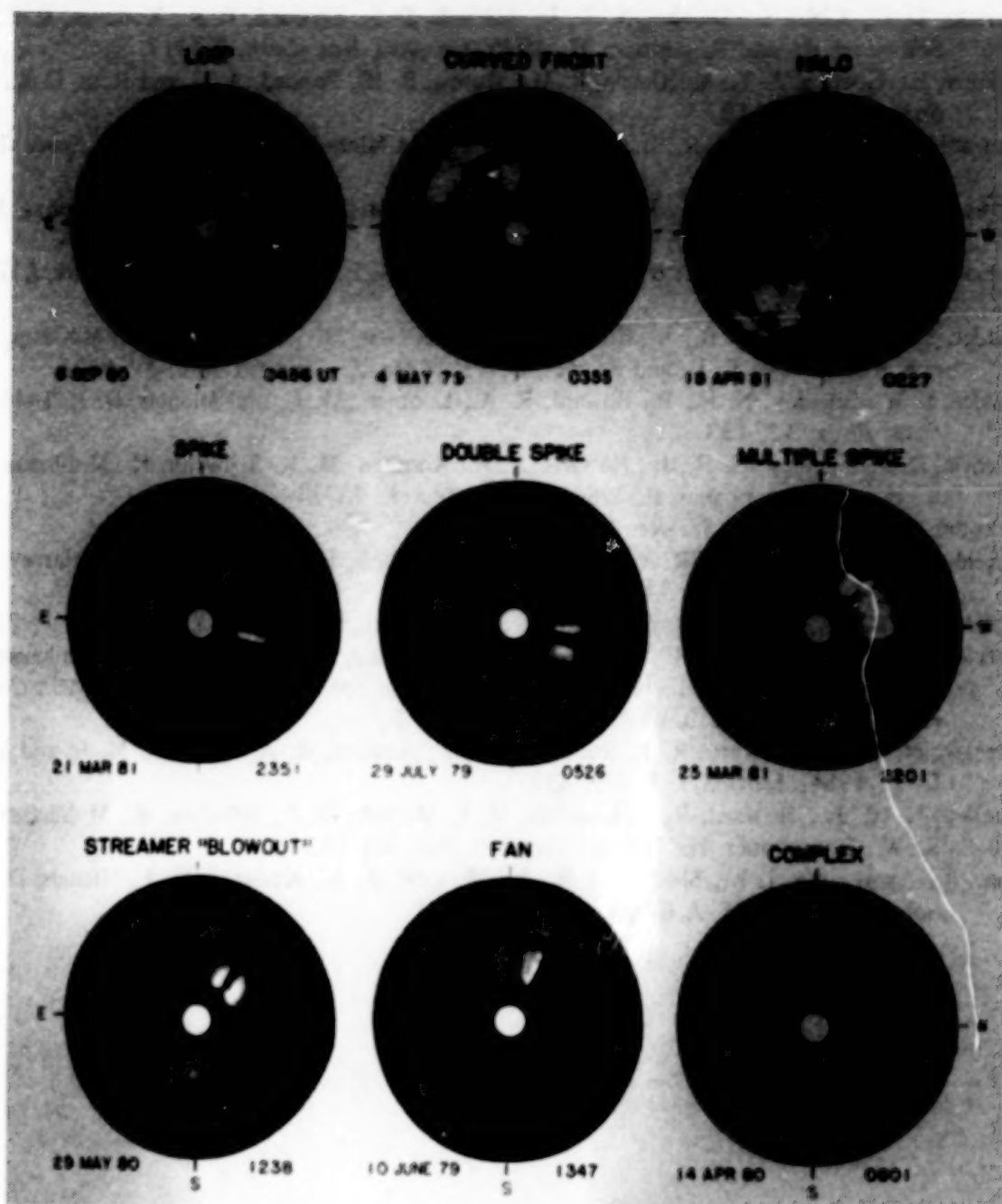
Figure 1. A sample of Solwind coronal mass ejections during 1979-1981 illustrating the variety of morphological classes as defined by Howard et al. (1985). The small white disk indicates the size of the solar disk.
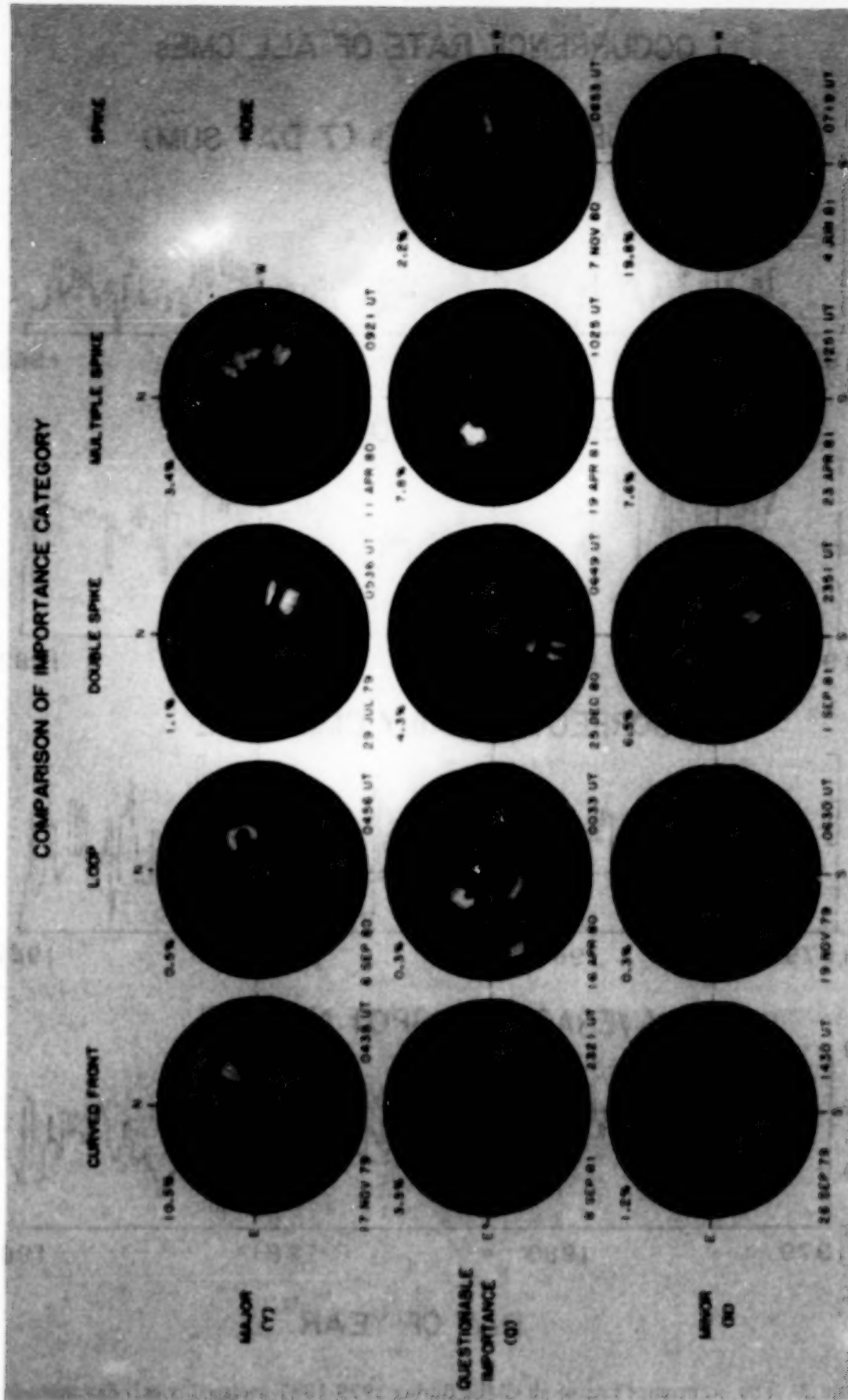
Figure 2. A sample of Solwind CMEs during 1979-1981 illustrating major (Y), questionable (Q), and minor (N) importance categories according to Howard et al. (1985).
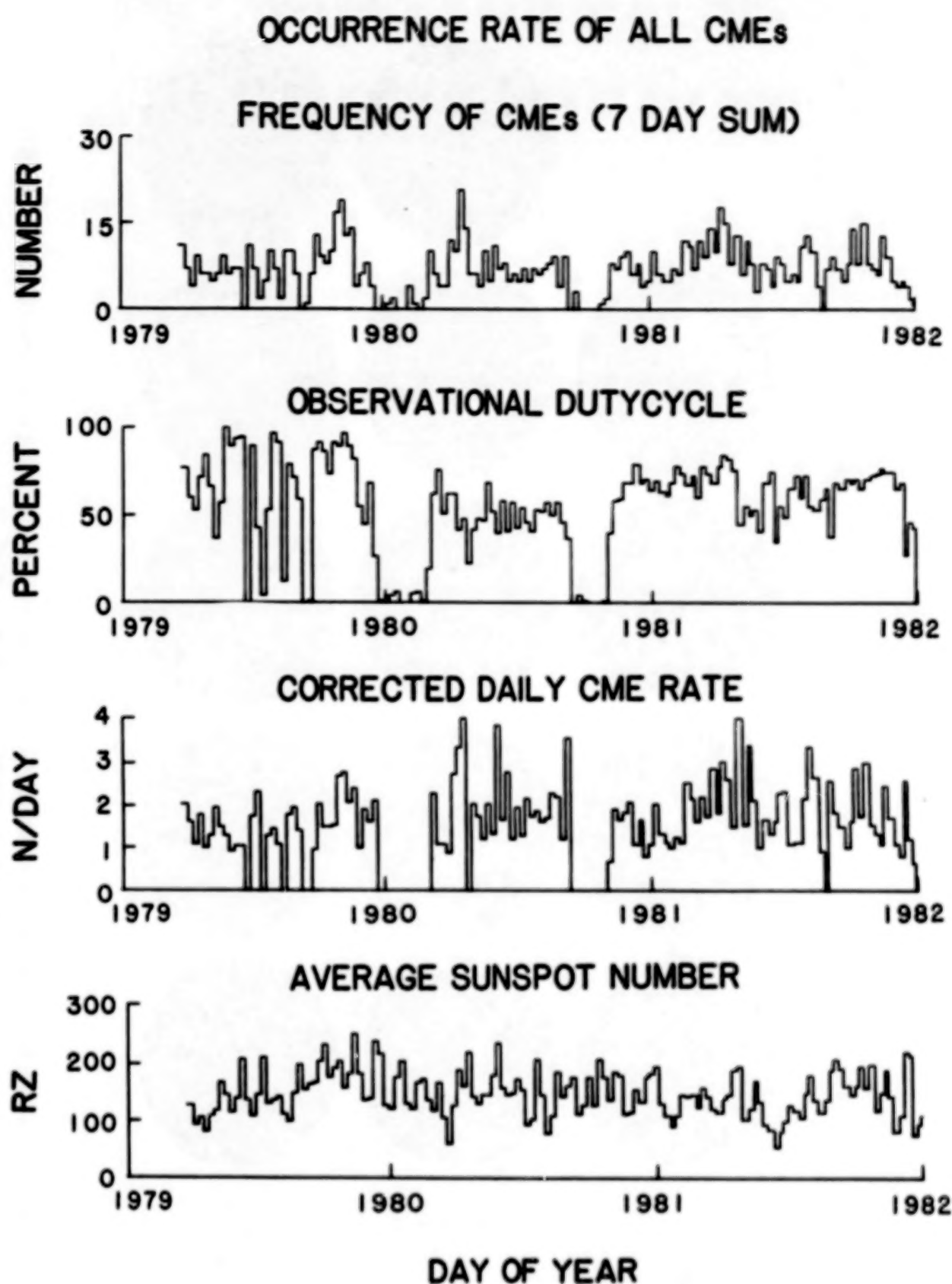
OCCURRENCE RATE OF ALL CMEs

FREQUENCY OF CMEs (7 DAY SUM)

OBSERVATIONAL DUTYCYCLE

CORRECTED DAILY CME RATE

AVERAGE SUNSPOT NUMBER

DAY OF YEAR

Figure 3. The occurrence rate of all CMEs during 1979-1981 averaged over 7-day intervals.

248

OCCURRENCE RATE OF ALL CMEs

FREQUENCY OF CMEs (27 DAY SUM)

OBSERVATIONAL DUTYCYCLE

CORRECTED DAILY CME RATE
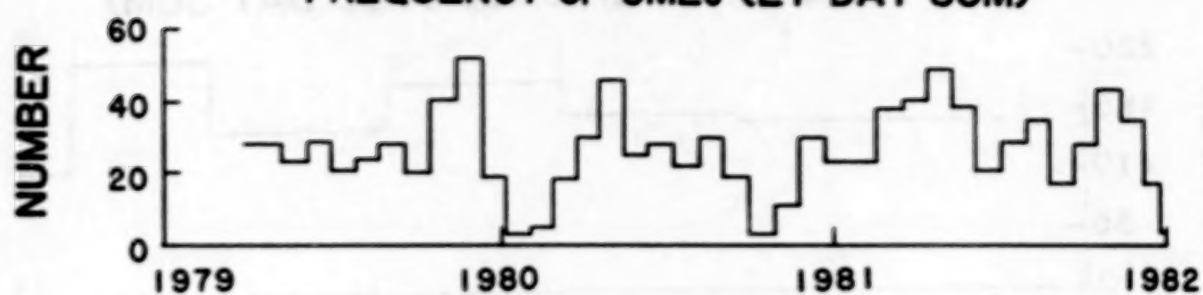
AVERAGE SUNSPOT NUMBER

DAY OF YEAR

Figure 4. The occurrence rate of all CMEs during 1979-1981 averaged over 27-day intervals.
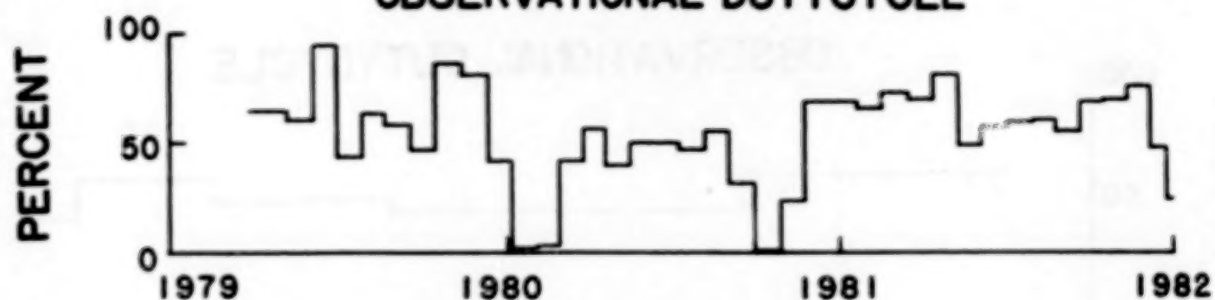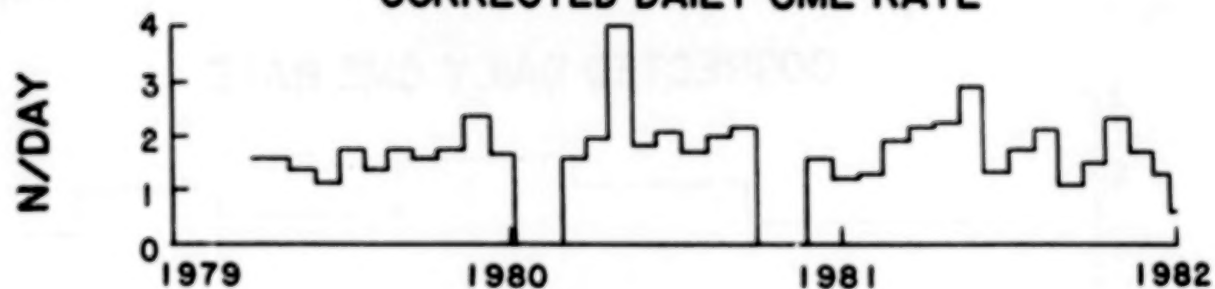
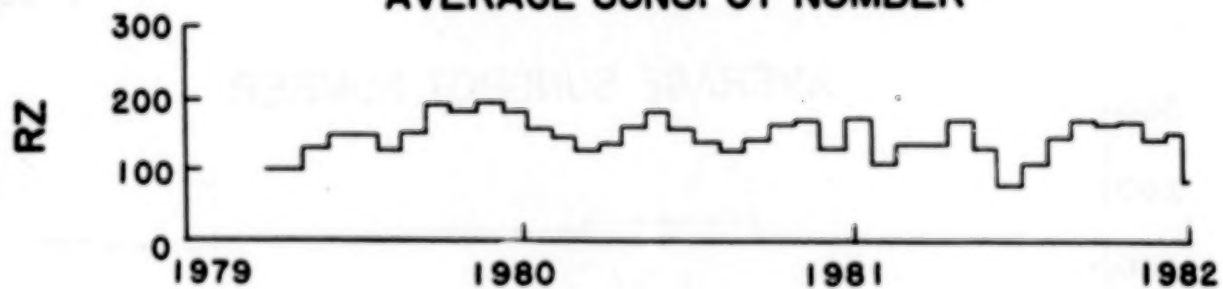# OCCURRENCE RATE OF ALL CMEs

FREQUENCY OF CMEs (180 DAY SUM)

OBSERVATIONAL DUTYCYCLE

CORRECTED DAILY CME RATE

AVERAGE SUNSPOT NUMBER

DAY OF YEAR

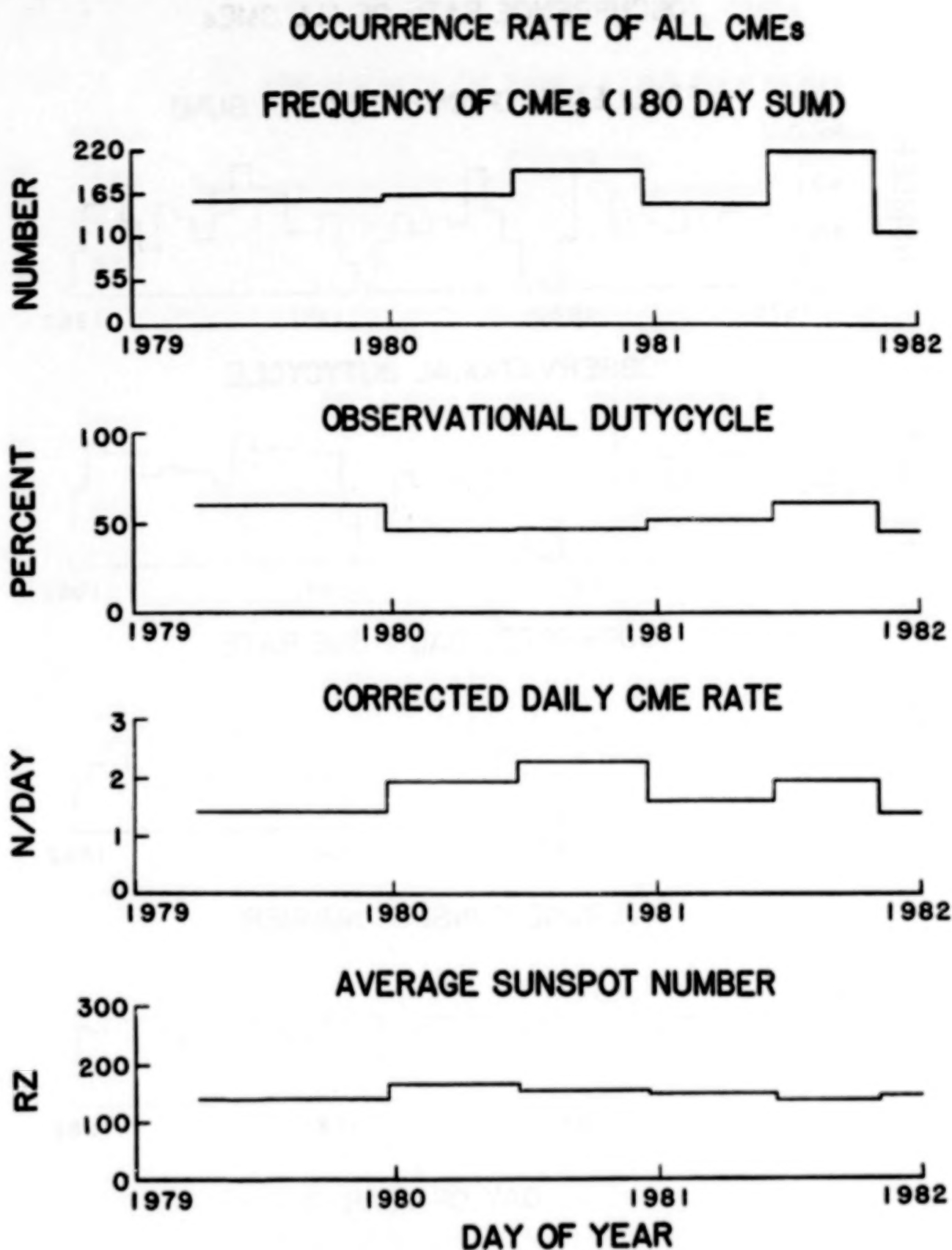Figure 5. The occurrence rate of all CMEs during 1979-1981 averaged over 180-day intervals.
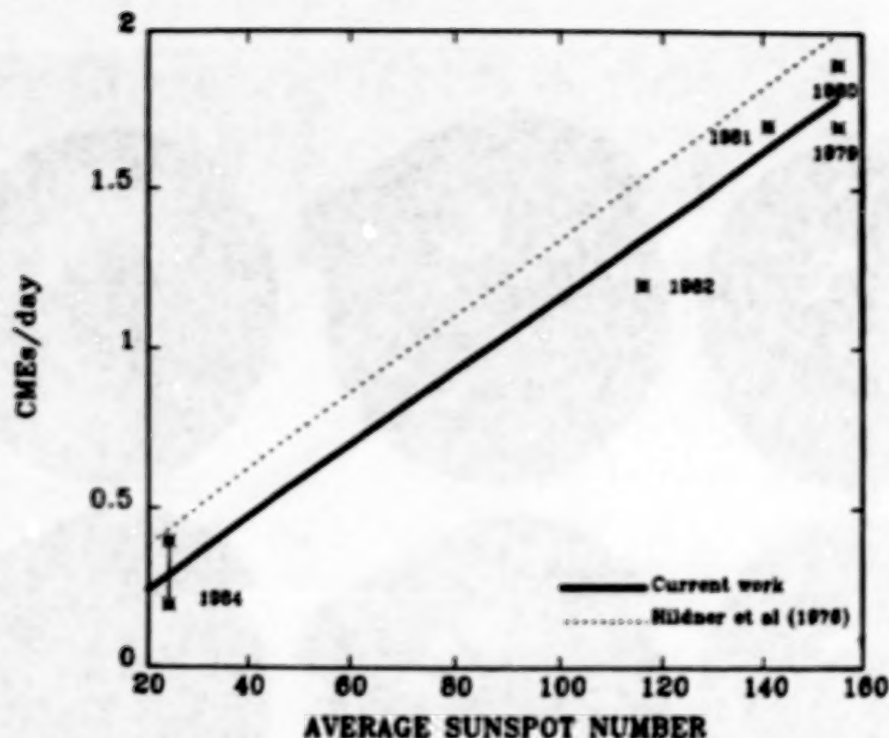
Figure 6. The Solwind CME occurrence rate plotted as a function of the average sunspot number during 1979-1984. The solid line is a least-squares fit to the data with the two points in 1984 treated equally.
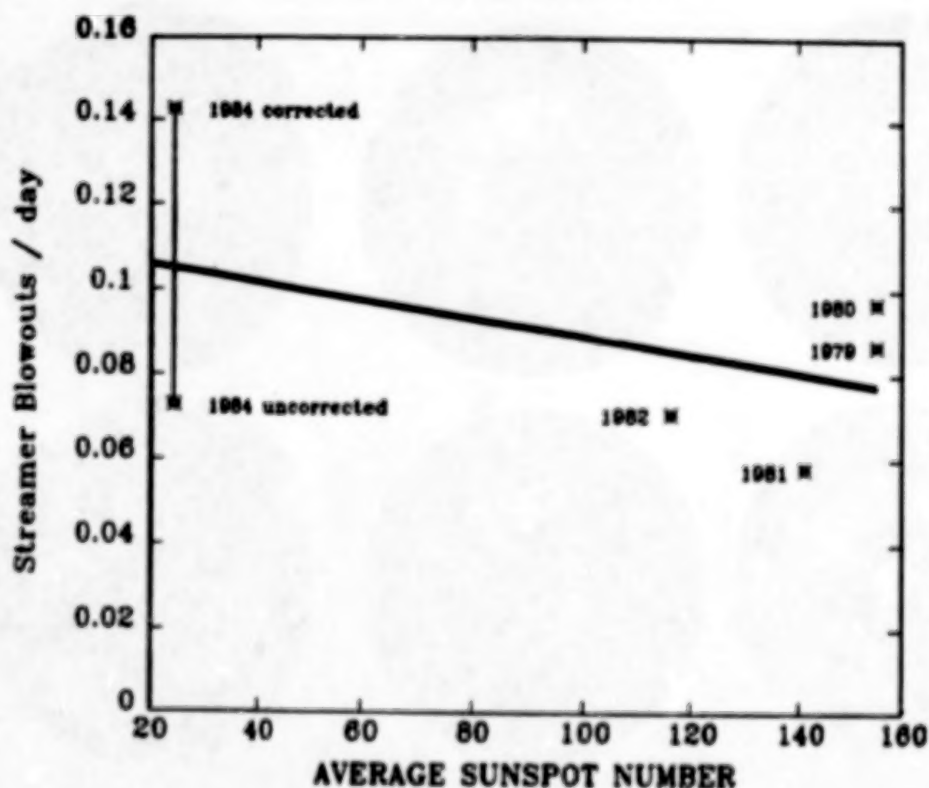
Figure 7. The Solwind occurrence rate for streamer blowout mass ejections illustrating the nearly constant rate during 1979-1984.

251
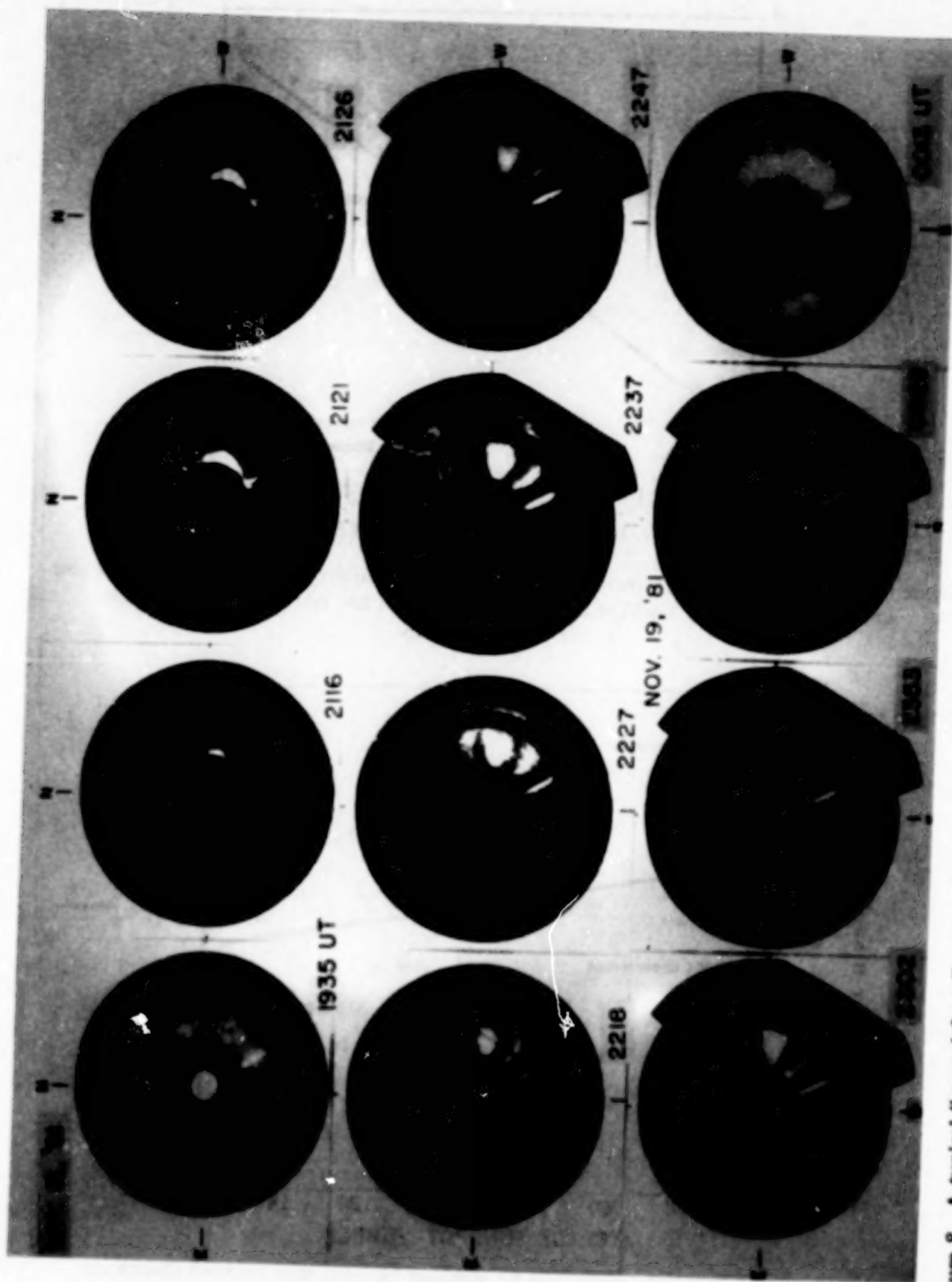
Figure 8. A typical "curved front" mass ejection according to Howard et al. (1985). Such CMEs have become rare in 1984-1985. Note the streamer that was deflected as the CME transited the coronagraph's field of view on 18 November 1981 (cf., Fig. 9).
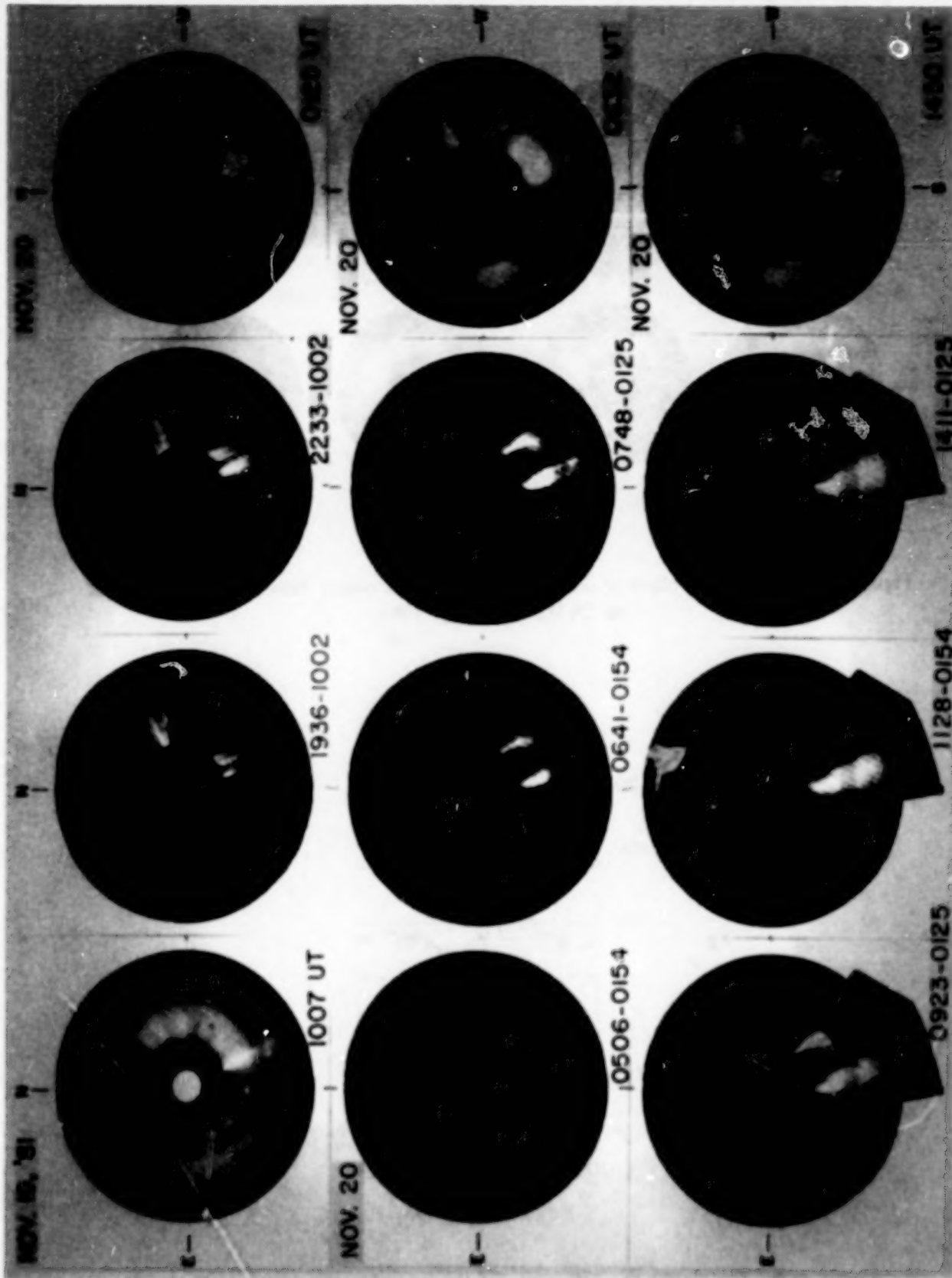
Figure 9. The eruption of the 18 November streamer during a 19-hr interval on 19-20 November 1981 (cf., Fig. 8). This illustrates a typical high-latitude "streamer blowout" CME near sunspot maximum.
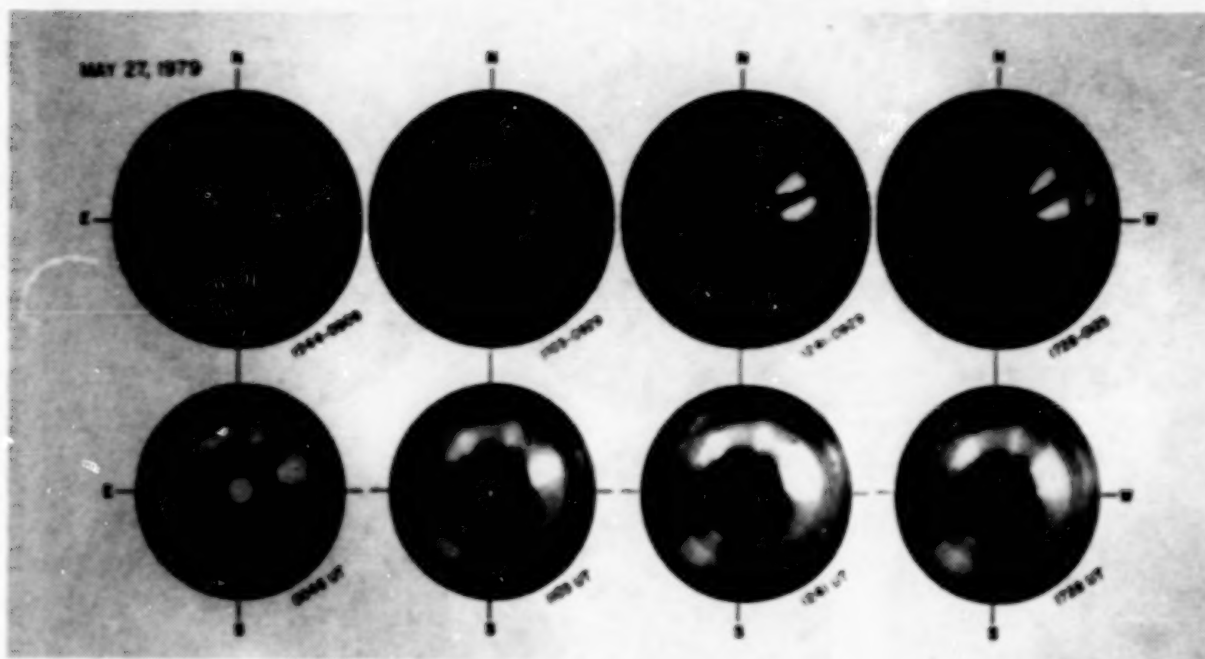
Figure 10a. A streamer blowout on 27 May 1979 , associated with the Helios 1 shock
on 28 May (cf., Fig. 10b).
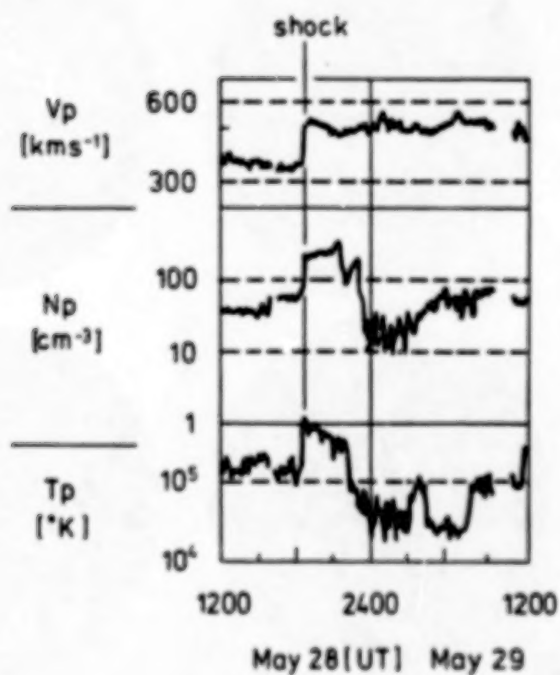
Figure 10b. The plasma measurements of the interplanetary shock at Helios 1
located at 0.43 AU, W90 degrees on 28 May 1979.
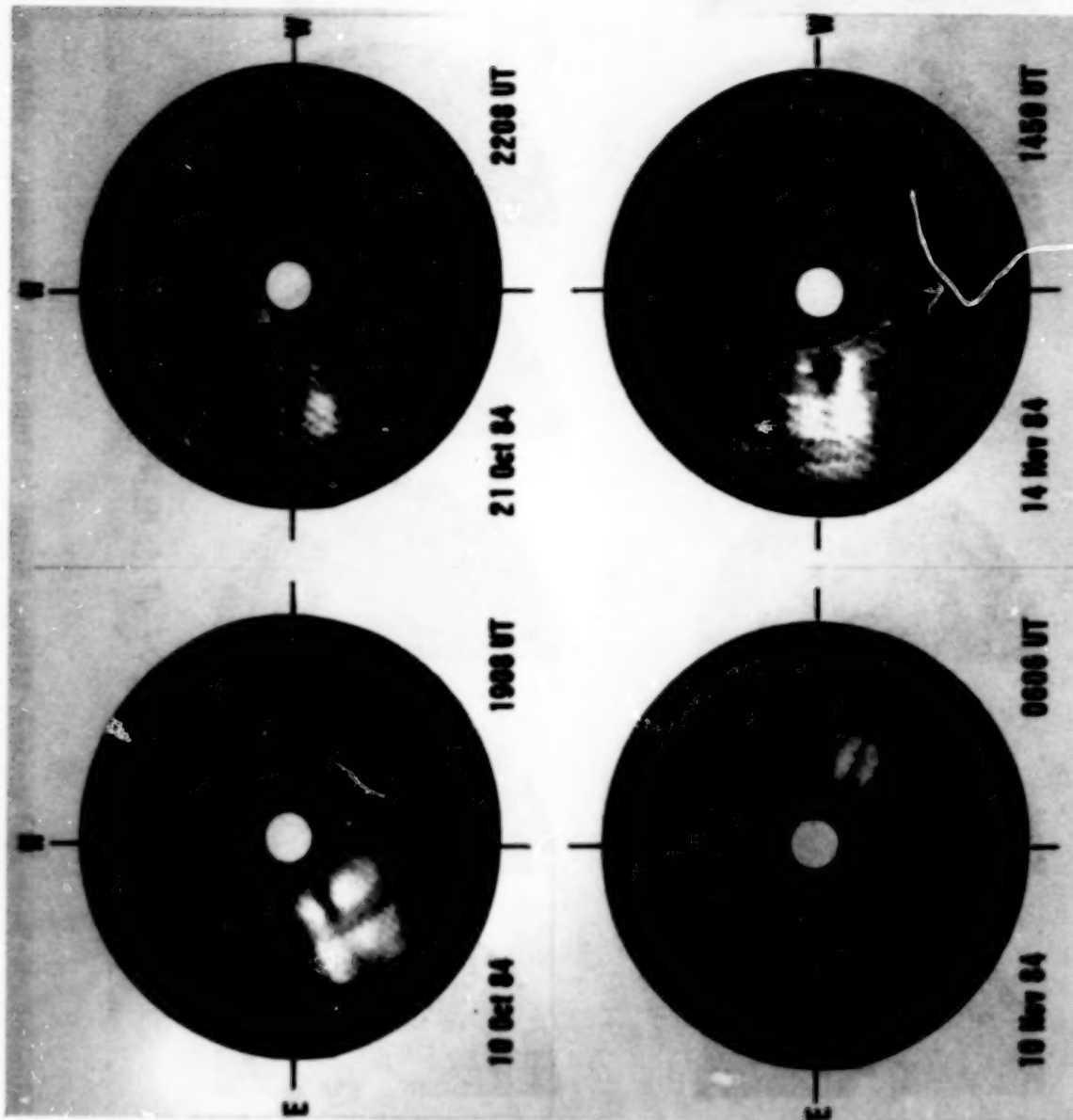
Figure 11. A sample of recently observed streamer blowout CMEs during October-November 1984. Note the relatively low latitudes of the events on 21 October and 14 November.
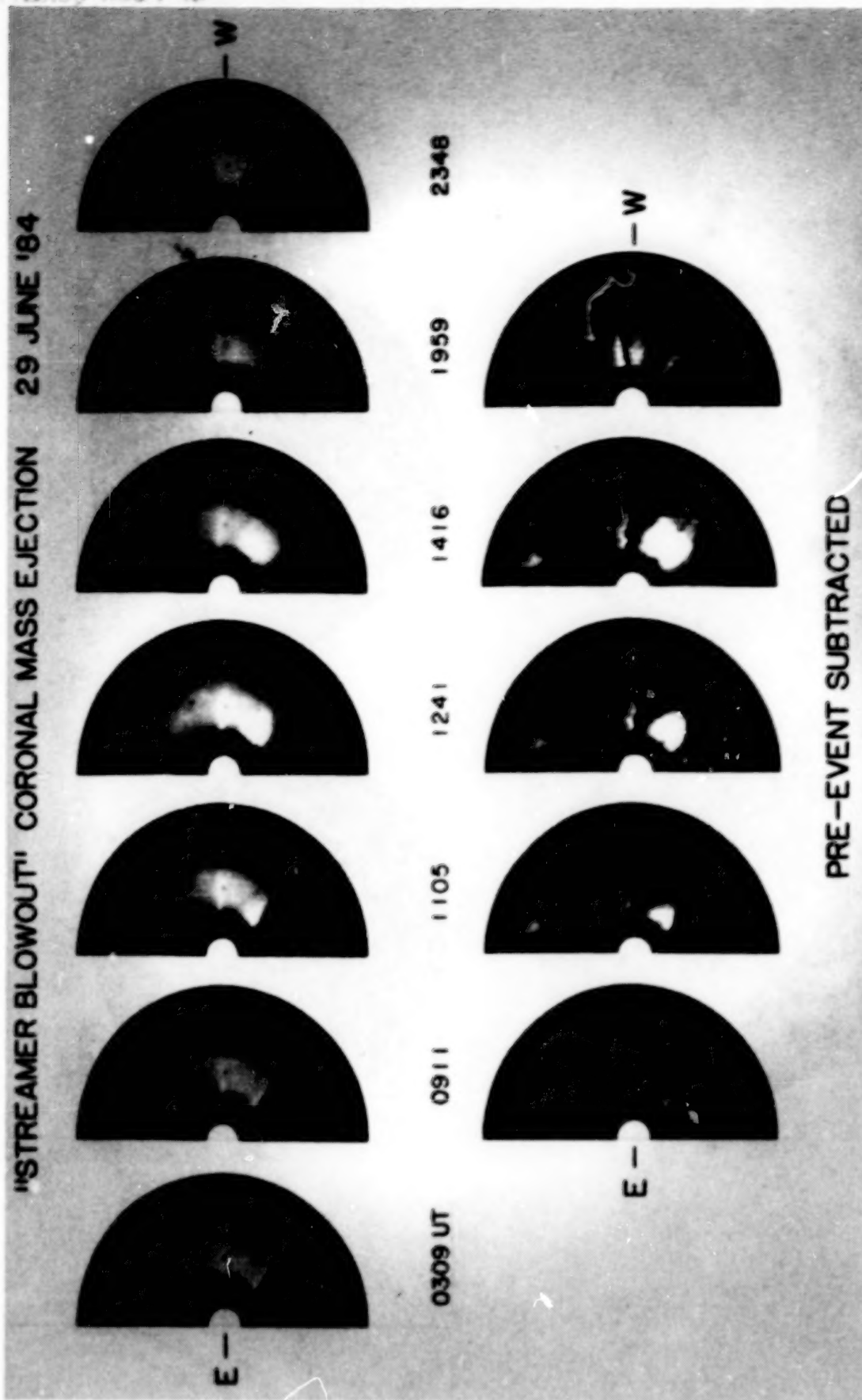
Figure 12. The evolution of a well-observed streamer blowout during 29 June 1984. The moon is visible on the difference images at 1105, 1241, and 1416 UT. The white disks also indicate the size of the solar disk.

INTERPRETATION OF CORONAL SYNOPTIC OBSERVATIONS

Richard H. Munro and Richard R. Fisher

High Altitude Observatory, National Center for Atmospheric Research, Boulder, CO

I. INTRODUCTION

Three-dimensional reconstruction techniques used to determine coronal density distributions from synoptic data are complicated and time consuming to employ. Current techniques also assume time invariant structures and thus mix both temporal and spatial variations present in the coronal data. The observed distribution of polarized brightness, pB, and brightness, B, of coronal features observed either at eclipses or with coronagraphs depends upon both the three-dimensional distribution of electron density within the structure and the location of the feature with respect to the plane-of-the-sky. By theoretically studying the signature of various coronal structures as they would appear during a limb transit, it is possible to recognize these patterns in real synoptic data as well as estimate temporal evolutionary effects.

## II. TIME INDEPENDENT MODELS

Coronal streamers, large-scale white-light structures found in the solar corona, are the most impressive and easily observed features of the extended solar atmosphere. In the summer of 1984, a period in which there were few structures associated with solar active regions, the corona was dominated by streamers associated with the large-scale solar magnetic field. Rotating more rigidly than the photospheric material, several streamers were observed near the solar limbs on DOY 222 with both the spacecraft and ground based instruments. For this investigation, only the distribution of polarized brightness (pB), at a reference height of 1.3 R_Θ, over latitude and longitude has been used to estimate a model-dependent electron density at the base of these streamers. Portions of the K-coronameter synoptic record are shown in Figure 1.

The investigation of the gross brightness properties of the solar corona does not require a detailed model of the density structure. Thus we have chosen to represent coronal features using simple "ad hoc" mathematical descriptions. Coronal streamers are assumed to be radial features with circular cross sections that depend on radius. The bottom portion of "helmet-like" shape (increasing then decreasing cross-sectional projection) was obtained from eclipse measurements. The cross-sectional area is set to a constant above a given height ($\sim$2.5 R_Θ). At 1.3 R_Θ, the angular width of the streamer measured from Sun center is 15 degrees. For these calculations, the density structure within the streamer has the identical radial logarithmic gradient as the surrounding background, but with a constant enhancement over the background (corresponding to an increased base pressure). Model streamers were placed in solar longitude and latitude at the corresponding brightness maxima of the observations.

Note that during the period of these observations, the large-scale corona contained six bright regions or streamers. On DOY 222, two of these were located in the southern hemisphere on the east limb, two were located near the plane-of-the-sky on the west limb in the northern hemisphere, and the remaining two streamers, somewhat fainter than the others, spanned the equator near the center of the disk.

An equatorial symmetric background corona was initially used to determine a multiplier to the Allen (1963) Minimum Model to replicate the observed polarized brightness between the streamers at 1.3 $R_\odot$. The streamer enhancements required to match the observed maximum polarized brightnesses for each structure averaged 3.1 times the equatorial background. This enhancement in streamer density required is, of course, dependent upon the specific model geometry given above, and is only a sufficient model. Taken at face value, a mean density of 5.6 x 10^7 electrons cm^{-3} in the streamer is obtained at the reference height. The ratio of streamer pB to the background corona is roughly the same as that found by Wilson (1977). On the other hand, the absolute density for the entire corona is about a factor of 2 lower than the extrapolated value obtained from Wilson's study. Estimates of the expected polarized brightness distribution (Fig. 2), obtained by using the model density distribution, replicate the observed distribution of polarized brightness with reasonable fidelity.

III. SIGNATURES OF STREAMERS IN K-CORONAMETER DATA

The major features found in the observed synoptic chart (Fig. 1) from the east and west limb data are reproduced (Fig. 2), providing insight into the effects of the long integration path through the corona and the variation of the apparent location of the streamer as a function of solar rotation. Thus, it is clear that this relatively simple modeling technique allows the rapid interpretation of K-coronameter and coronagraph results, at least in the case of the largest features found in the solar corona. However, some of the characteristic signatures displayed in the model are absent in the data. The dashed lines on the observed synoptic chart mark the theoretical track of the two streamers closest to the solar poles. While the southern streamer matches the model calculations, a glaring discrepancy exists for the northern-most high-latitude streamer. In this case, the data do not display a symmetric feature, but rather a strange trailing extension from the maximum polarization brightness region (time runs right to left in coronal synoptic maps). To gain insight into this problem, synoptic observations from the three HAO K-coronameters covering the years 1965-1984 were used to classify the signature of streamers as they appeared during limb passage. The shape categories included round, trailing extensions, leading extensions, symmetric extensions, and other complex features. The results are summarized in Table 1. Although it is possible to construct static models of coronal density distributions that produce the observed shape of the extensions, round coronal signatures cannot be produced by a static structure.

Emerging from an examination of a long-term synoptic record is the perception that while the underlying organization of the large-scale photospheric magnetic field tends to be quite persistent, at least one-third of the streamers identified in K-coronameter synoptic charts must evolve with a timescale approximately equal to the length of time such a structure is visible using coronagraphic techniques. Taking this argument further, the overwhelming number of trailing extensions over leading extensions implies that the temporal scales for injecting material into a streamer are shorter than for removing the material.

IV. TIME DEPENDENT MODELS

To investigate how time-dependent density enhancements and reductions might appear in synoptic observations, the model streamers described above were subjected to linear rates of formation and destruction. Figure 3 depicts sample signatures for streamers at a latitude of 45 degrees North where the maximum density for the streamers occurs one day after, at, and one day

before limb passage for the top, middle and bottom panels, respectively. With each panel, the model streamers form in one day, but decay in one, two, three, and four days. The signatures for slow formation and rapid decay are mirror images of these forms about the central time of the individual panels (or 90 degrees longitude).

These calculations show that:

(1) The absence of an extension implies rapid density variations and "round" signatures require both rapid injection and removal of material.

(2) The location of the observed maximum brightness depends on the time when the streamer attained its maximum density, and only weakly on the spatial location of the streamer. The physical location of the streamer remained constant in the models displayed in Figure 3; only the time of maximum density was allowed to vary. As a rule of thumb, the observed maximum brightness signals the time of maximum density within 8 hours as long as the peak density was attained within 2 days of the streamer's limb passage. Thus, caution must be used when associating the physical location of streamers as determined by synoptic observations with underlying photospheric features.

(3) The shape of the brightness distribution of an observed streamer can provide clues as to the nature of the temporal evolution of streamer material. This variation can be seen by selecting a particular injection and removal rate (e.g., 1:4, the lower right of each panel), and comparing the signatures as the time of peak density varies from after (top) to before (bottom) limb passage.

REFERENCES

Allen, C. W., 1963, in *Astrophysical Quantities*, University of London, London, p. 176.
Wilson, D. C., 1977, *The Three Dimensional Solar Corona — A Coronal Streamer*, NCAR Cooperative Thesis No. 40, National Center for Atmospheric Research, Boulder, Colorado.
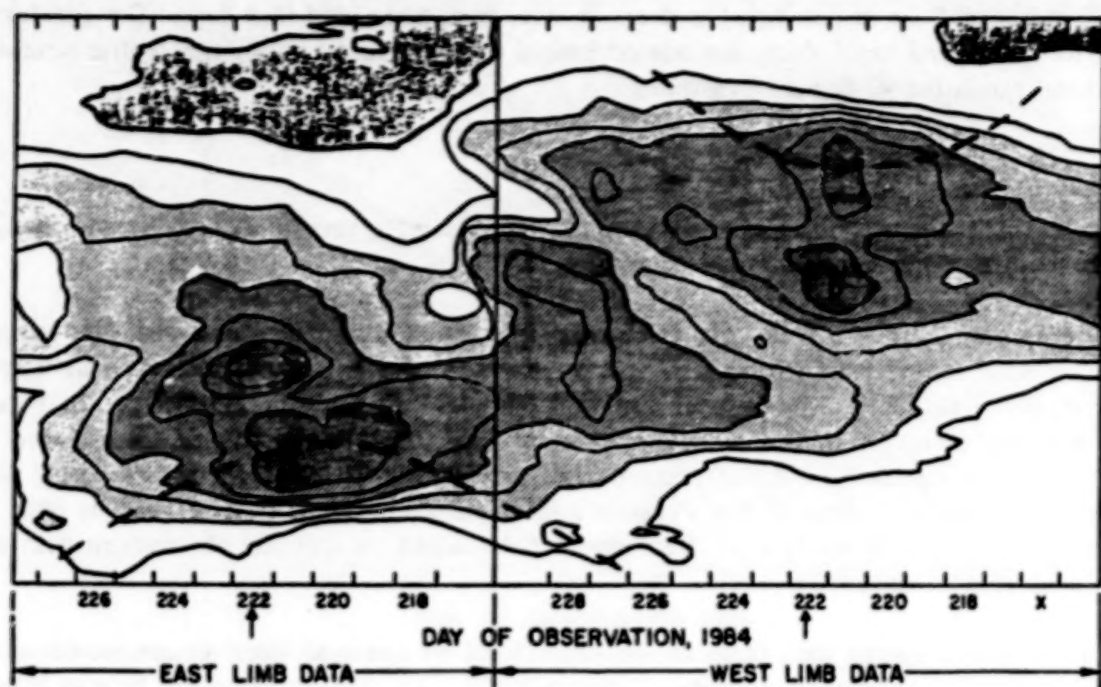
Figure 1. Portions of the K-coronameter synoptic record, from both the east and west limbs, centered on DOY 222 1984. Amplitude of the polarized brightness of the corona is plotted as a function of solar latitude and day of observation. Dashed lines mark the theoretical track of the northern-most and southern-most streamers.
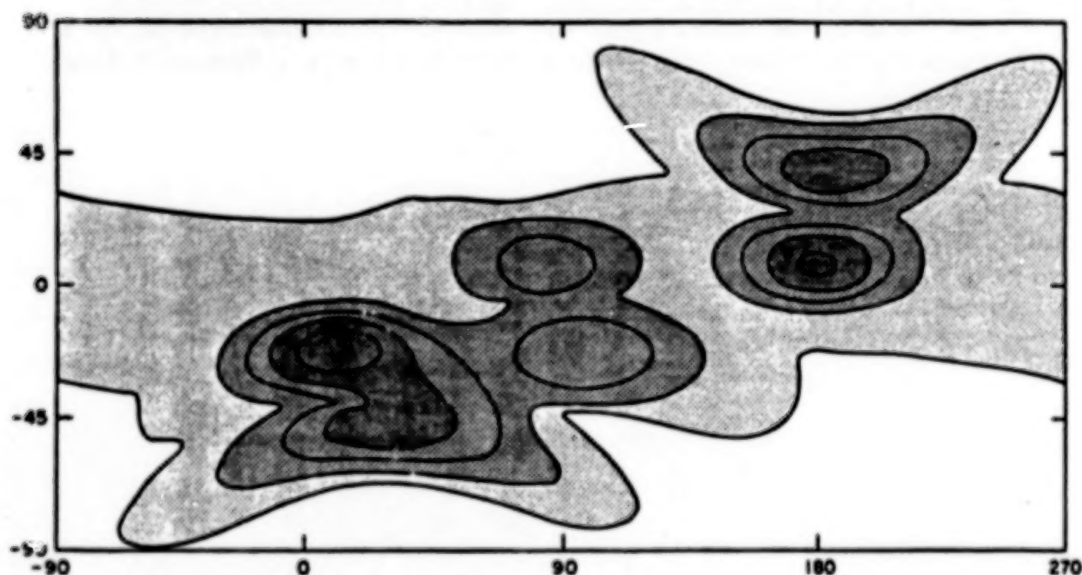
Figure 2. The estimated polarized brightness that would be observed from the earth if material were distributed over the volume of the corona in accordance with a model that has (1) a quiet background contribution, the axis of symmetry which is tilted with respect to the solar rotation axis, and (2) six embedded streamers with the geometrical properties given in the model (see text). The streamer densities have been adjusted so as to achieve the observed peak polarized brightness.
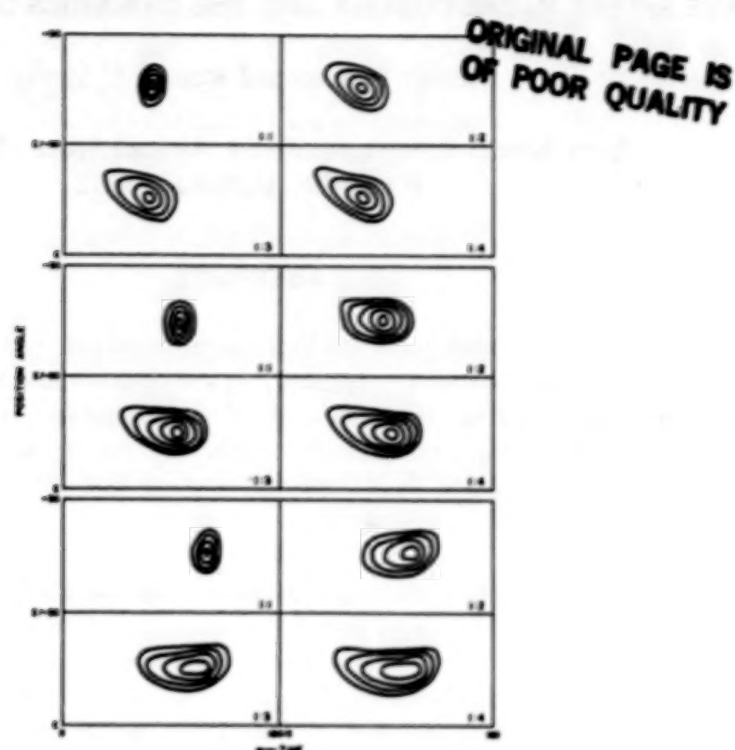
Figure 3. Synoptic observational signatures of time-dependent model streamers with varying
rates of material removal and time of maximum density enhancement.
(See text for additional information.)

TABLE 1. OBSERVED STREAMER SIGNATURES IN THE HAO
K-CORONAMETERS 1965–1984

	Stationary	Obvious Temporal Evolution			Sum	Other, Complex Features	Total
		Round	Trailing Extension	Leading Extension			
Number	77	250	412	57	796	1131	1927
Fraction	4%	13%	21%	3%	41%	59%	100%
Fraction	10%	31%	52%	7%	100%		

WAVE SPEEDS IN THE CORONA AND THE DYNAMICS OF MASS EJECTIONS

Steven T. Suess and Ronald L. Moore

Space Science Laboratory, NASA Marshall Space Flight Center
Huntsville, Alabama 35812

ABSTRACT

A disturbance or coronal mass ejection being advected by the solar wind will expand at the fastest local characteristic speed — typically approximately the fast-mode speed. To estimate this characteristic wave speed and the velocity field in the ambient corona, it is necessary to know the magnetic field, temperature, and density. Only the density is known from coronal observations. The temperature, magnetic field, and velocity are not yet directly measured in the outer corona and must be estimated from a model.

In this study, we estimate the magnetic field, solar wind velocity, and characteristic speeds using an MHD model of coronal expansion between 1 and 5 solar radii ($R_\odot$) with a dipole magnetic field at the base. This model, for a field strength of about 2 gauss at the base, gives flow speeds at low latitudes (near the heliospheric current sheet) of <250 km/s at 5 $R_\odot$ and, <50 km/s at 2 $R_\odot$, and fast-mode speeds to 400 to 500 km/s everywhere between 2 and 5 $R_\odot$. This suggests that the outer edge of a mass ejection will appear to move at a nearly constant rate of 400 to 500 km/s between 2 and 5 $R_\odot$. This result is in agreement with the observed velocity of mass ejections reported by MacQueen and Fisher (1983) and implies that the acceleration mechanism for coronal mass ejections is other than simple entrainment in the solar wind.

INTRODUCTION

The kinematics of coronal transients have been well described elsewhere. It is not our intent to review this research or to put forth a new or original hypothesis for the origin of coronal mass ejections. Rather, what we propose is to offer a deeper physical insight into the dynamics of coronal transients in a way that relates to physical parameters of the corona. The motivation for our study comes from the velocity data reported by MacQueen and Fisher (1983). They examined the kinematic properties of several "loop-like" coronal transients over the range 1.2 to 2.4 $R_\odot$ from Sun center. Their results are partially summarized in Figure 1(a). In this figure, velocity profiles for all of the transients analyzed are reproduced. In Figures 1(c) and 1(d), the results are split into transients observed in the inner corona with the Mauna Loa K-coronameter system and transients observed in the outer corona with the coronagraphs on Skylab and the SMM. Radial expansion speeds are seen to range from 60 to 900 km/s — except for the anomalous 6 September 1973 event. Flare-associated events were found to exhibit high speeds and little acceleration with height. Eruptive-associated events exhibited large accelerations. MacQueen and Fisher conjectured that the pressure gradient forces responsible for the generation of the solar wind may play an important role in accelerating the eruptive-associated events.

Here, we examine the behavior of an isolated blob of gas riding upon the background solar wind and suggest that this behavior is very much like the behavior of coronal mass ejections. The distinction between the hypothesis made by MacQueen and Fisher and what we are describing is that rather than riding passively on the solar wind, the expansion of the mass ejection into the ambient medium is the main cause of the observed motion of the leading edge of the mass ejection.

RESULTS

The model that we use for our computation of characteristic wave speeds in and near streamers is that published by Steinolfson, Suess, and Wu (1982) (hereafter referred to as SSW). In that calculation, a model was developed for the formation of a steady coronal streamer through numerical solution for the time-dependent, dissipationless MHD equations of motion in a meridional phase, for axisymmetric flow. The flow is polytropic and the atmosphere is stationary in magnetically closed regions and flowing outward in open regions. The solution is found through a relaxation in time in a domain extending from 1 to 5 $R_\odot$ and from pole to pole. The flow and magnetic fields, density, and temperature are thus known everywhere in the corona.

CMEs never occur in coronal holes. Therefore, in using the results of SSW, we limit ourselves to results in the neighborhood of the global streamer – polar angles of 90 degrees to 140 degrees (the equator lies at 90 degrees and the polar hole is centered at 180 degrees). The region of interest is shown in Figure 2, modified from SSW. The closed field lines near 90 degrees are in magnetostatic equilibrium – the flow speed there is effectively zero. In Figure 2, the shaded portion is coronal hole-like and therefore excluded from consideration; three radial cuts through the topology are indicated at 100, 120, and 140 degrees. Figure 3 shows the flow speed, sound speed, and Alfvén speed along these radii. A profile is not given for 90 degrees because that is the magnetic neutral sheet, the field strength is zero there, and hence the Alfvén speed is also zero.

Also shown in Figure 3 is the flow + fast-mode speed, where we have used the term "fast-mode" for the sum of the sound speed and the Alfvén speed – strictly only a correct terminology for propagation perpendicular to the magnetic field. We will ignore this distinction because the propagation of a transient through the corona seems to strongly deform the ambient field and hence almost certainly have its motion dominated by the Alfvén speed.

Figure 3 shows that the flow speed is never very large in the vicinity of the streamer, that the Alfvén speed is quite large near the Sun, and – most striking of all – the sum of fast mode and flow speed is both nearly constant in radius and on the order of 400 km/s. The sound speed between 1 and 5 $R_\odot$ is so small as to be unimportant in this sum.

These results apply only to the streamer vicinity. The Alfvén speed is quite different in coronal holes and will be the subject of a separate study. However, near streamers, we feel the tendency shown in Figure 3, for the flow speed + Alfvén speed sum to be nearly constant in radius, is representative of the corona in the vicinity of real streamers. The difference between individual streamers will be dominated by field strength and density – the sum will be larger for higher field strength streamers because the density does not rise as fast as the field strength (SSW). For geometrically more compact streamers, there should be no qualitative difference – the characteristic speeds will still be of the same order of magnitude.

DISCUSSION

The results shown in Figure 3 are relevant to mass ejections because the front edge of a disturbance moving through the corona will always move at the fastest local characteristic speed (Steinolfson, 1985). Thus, if we imagine a blob of plasma injected into the corona and having a finite overpressure, then its center of mass will move upwards with the solar wind expansion speed. In addition, its front edge (and back edge as well) will expand outwards away from the center of mass with the fastest local characteristic speed in the solar wind moving frame of reference.

263

An obvious question is why should the front edge necessarily be the same as the visible front edge of a transient. It is true that it does not necessarily have to be the visible front edge. However, if the front edge is initially visible at the beginning of the transient, then under normal circumstances, we believe it will only get more visible. This is because a compressive disturbance in the corona always steepens (Steinolfson, 1985; Zel'dovich and Razier, 1966; Montgomery, 1959; Cohen and Kulsrud, 1974; Steinolfson, 1981; Kantrowitz and Petschek, 1966).

It is also obvious that the sum of speeds shown in Figure 3(d) is a lower bound. After a shock is formed, the front edge of the disturbance moves at the shock speed. Thus, no freely expanding CME can move less rapidly through the corona than with the sum of speeds shown here – about 400 km/s. This is the reason for the result quoted in a study of the numerical simulation transients by Steinolfson (1982) There, he used the steamer model shown in Figure 2 and introduced a perturbation in pressure at the base. He found that, depending on the magnitude and character of the perturbation, he could generate a variety of propagating disturbances, but that these disturbances never traveled outward more slowly than about 400 km/s in the neighborhood of the streamer.

By the time a CME reaches a height of 2.0 solar radii, it should be almost free of whatever initiated the transient or restrained it from freely moving outwards. Thus, on the order of the time it would take for information to propagate across the transient with the local characteristic speed, the front edge of CME will appear to be moving at the sum of the solar wind flow speed + fast-mode speed.

Returning to the data shown in Figure 1, we also offer a hypothesis for why some CMEs are moving slowly at heights of 2.0 $R_\odot$ and accelerating rapidly. Since the time for information to propagate across the CME is short with respect to the time it takes the CME to reach these heights, the CME cannot be moving outwards freely. Apparently the CMEs are being restrained from moving outwards and the rapid acceleration reflects the release of this restraint. These considerations suggest that the restraint is due to the linkage of the magnetic field in a CME back to the surface and that this connection is not completely broken at distances below about 2 $R_\odot$. These events may therefore more accurately be called "coronal mass releases" rather than mass ejections.

REFERENCES

Cohen, R. H. and Kulsrud, R. M., 1974, *Phys. Fluids, 17*, 2215.

Kantrowitz, A. R. and Petschek, H. E., 1966, in *Plasma Physics in Theory and Application* (W. B. Kunkel, ed.), McGraw-Hill, New York.

MacQueen, R. M. and Fisher, R. R., 1983, *Solar Phys., 89*, 89.

Montgomery, D., 1959, *Phys. Rev. Letters, 2*, 36.

Steinolfson, R. S., 1981, *J. Geophys. Res., 86*, 535.

Steinolfson, R. A., 1982, *Astron. Astrophys., 115*, 39.

Steinolfson, R. S., 1985, in the proceedings of the AGU Chapman Conference on Collisionless Shock Waves in the Heliosphere, Napa Valley, California, 20-24 February 1984, in press.

Steinolfson, R. S. Suess, S. T., and Wu, S. T., 1982, *Astrophys. J., 255*, 730.

Zel'dovich, Ya. B. and Razier, Yu. P., 1966, *Physics of Shock Waves and High Temperature Hydrodynamic Phenomena*, Academic Press, New York.
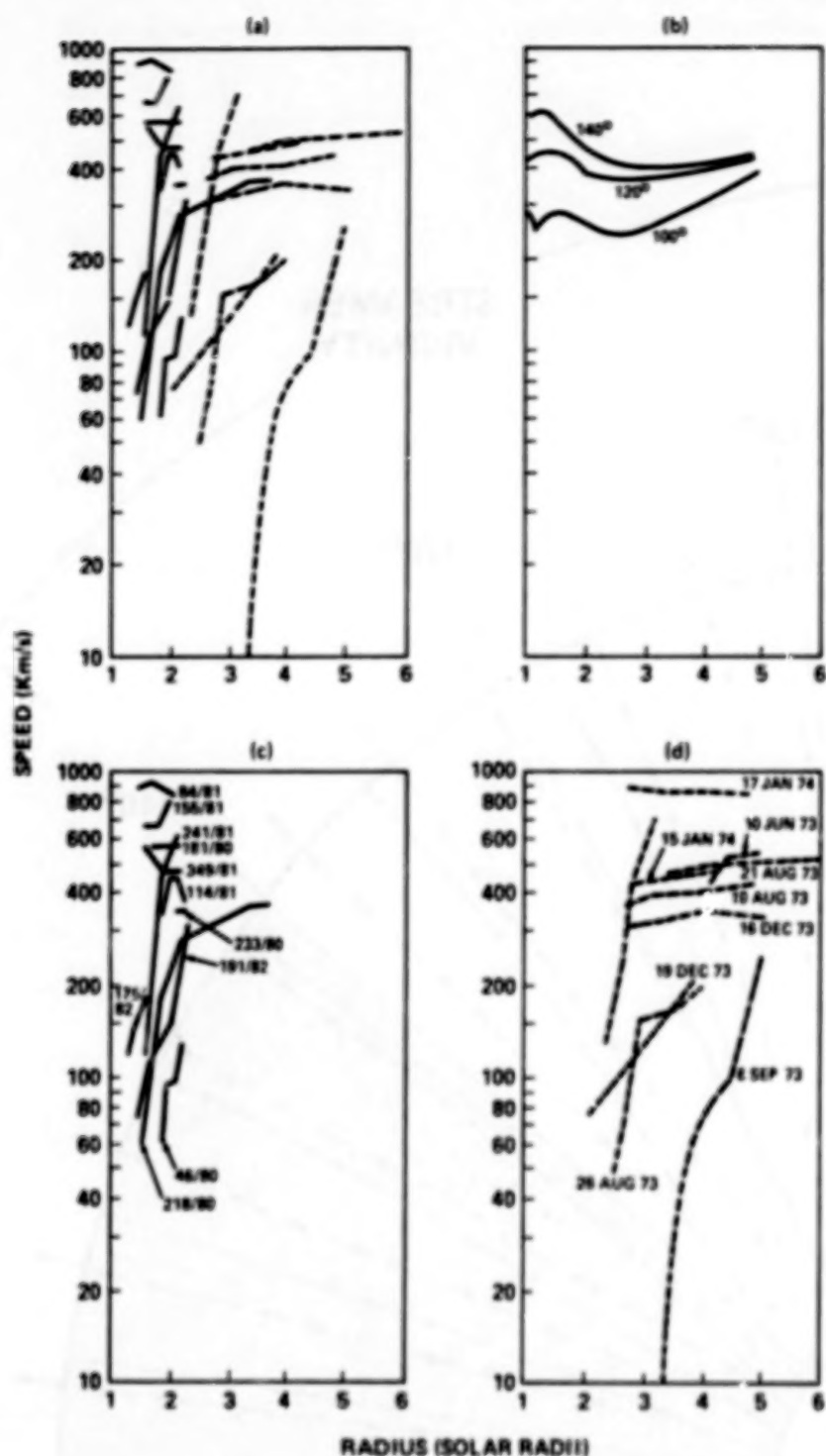
Figure 1. (a) Radial speed of transients, including measurements from the Mauna Loa
K-coronameter, Skylab coronagraph, and the SMM coronagraph/polarimeter. (From
MacQueen and Fisher, 1983.) (b) Sum of flow speed and fast-mode speed for three positions
in and near an MHD model coronal streamer. (From Steinolfson, Suess, and Wu, 1982.)
(c) Data from panel (a) that were taken only with the Mauna Loa K-coronameter, with the
date the observations were made. (d) Data from panel (a) that were taken only from the
Skylab coronagraph and SMM coronagraph/polarimeter, with the date the observations
were made.
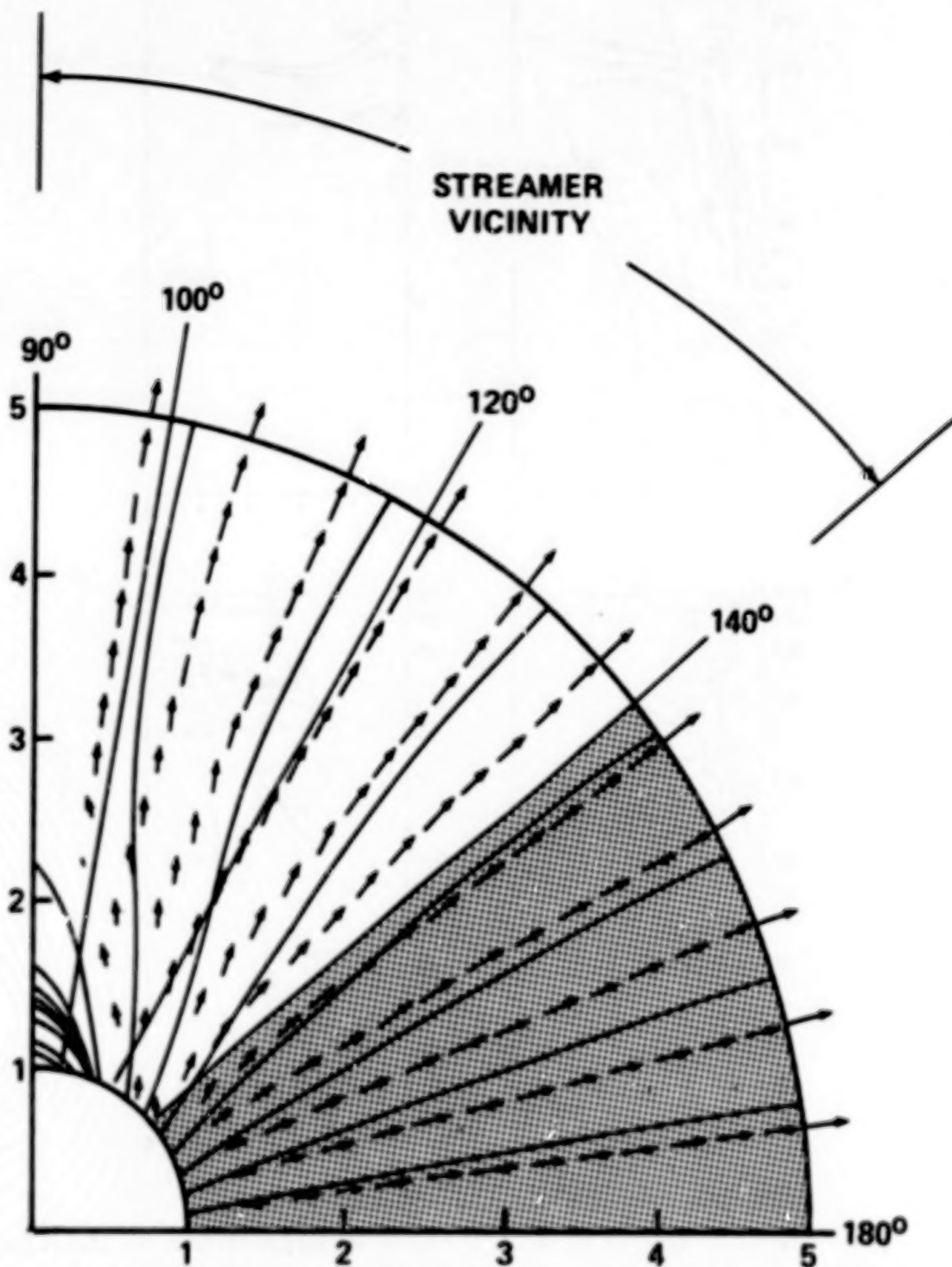
Figure 2. Magnetic field lines and flow speed vectors for the MHD streamer model of Steinolfson, Suess, and Wu (1982). The three radial cuts marked at 100, 120, and 140 degrees are where the data shown in Figure 1(b) and Figure 3 were taken from.

N86-24635
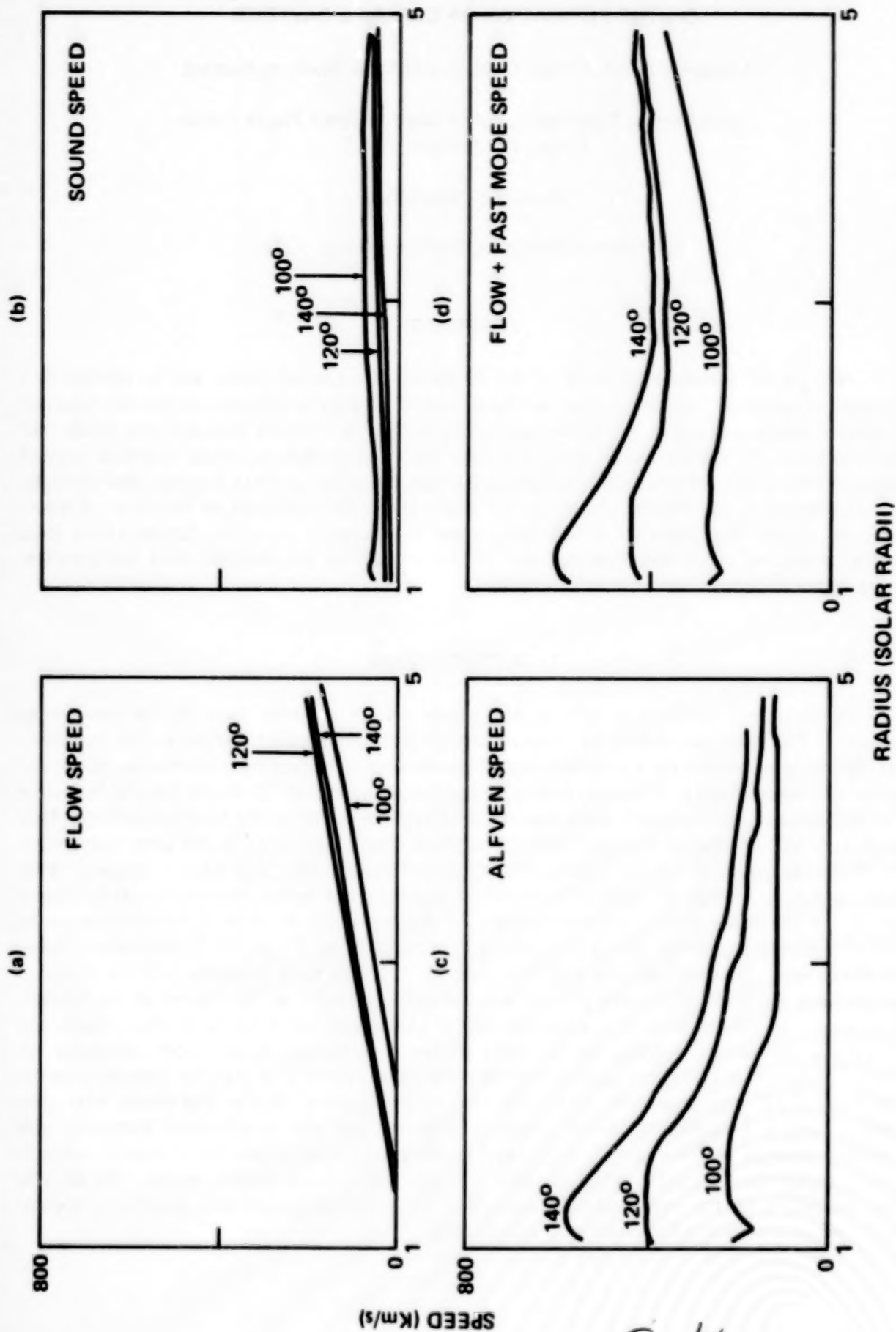
Figure 3. (a) Flow speed, (b) sound speed, (c) Alfvén speed, and (d) sum of the flow speed, Alfvén ("fast-mode") speed, and sound speed along the three radial cuts through the streamer model shown in Figure 2.

267

ON THE FORMATION OF CORONAL CAVITIES

Chang-Hyuk An, Steven T. Suess, and Einar Tandberg-Hanssen

Space Science Laboratory, NASA Marshall Space Flight Center
Huntsville, Alabama 35812

Richard S. Steinolfson

University of California, Irvine, California 92717

ABSTRACT

We present a theoretical study of the formation of a coronal cavity and its relation to a quiescent prominence. We argue that the formation of a cavity is initiated by the condensation of plasma which is trapped by the coronal magnetic field in a closed streamer and which then flows down to the chromosphere along the field lines due to lack of stable magnetic support against gravity. The existence of a coronal cavity depends on the coronal magnetic field strength; with low strength, the plasma density is not high enough for condensation to occur. Furthermore, we suggest that prominence and cavity material is supplied from the chromospheric level. Whether a coronal cavity and a prominence coexist depends on the magnetic field configuration; a prominence requires stable magnetic support.

I. INTRODUCTION

The coronal cavity is a dark region whose density is lower than in the surrounding streamer. The close association of coronal cavities with prominences has led to the suggestion that the coronal cavities are a manifestation of prominence formation by condensation of coronal plasma (Pneuman, 1983). However, Saito and Tandberg-Hanssen (1973) found that the formation of a prominence requires much more material than available in the cavity before depletion. They concluded that prominence material must be supplied from below (e.g., in the form of spicules), not from the adjacent corona. Here, we investigate further how and when a coronal cavity forms, and suggest what the relation is between a coronal cavity and a prominence. It is believed that the global steady corona is a consequence of the interaction between outward flowing solar wind plasma and the cornal global magnetic field (Pneuman and Kopp, 1971; Steinolfson, Suess, and Wu, 1982). When interacting with the magnetic field, the plasma adjusts itself for energy as well as force balance. We believe that the coronal cavity is formed in the process of the dynamic adjustment. In this paper we study the stability of the streamer model of Steinolfson, Suess, and Wu (1982) (henceforth referred to as SSW) to the condensation mode. SSW calculated the dynamic interaction between outward flowing solar wind plasma and a global coronal magnetic field using a 2-D, time-dependent, ideal MHD computer simulation. In the final steady state, they found a density enhancement in the closed field region with the enhancement increasing with increasing strength of the magnetic field. Our stability calculation shows that if density enhancement is higher than a critical value, the plasma is unstable to condensation modes. We describe how, depending on the magnetic field configuration, the condensation may produce a coronal cavity and/or initiate the formation of a prominence.

II. CONDENSATION AS A CAUSE OF CORONAL CAVITIES

The initial plasma density from the steady hydrodynamic solar wind equations and the two final states with $\beta = 0.5$ and 4 are shown in Figure 1. For $\beta = 4$ the density is enhanced about 1.4 times the initial value, while for $\beta = 0.5$ the maximum enhancement is 4.3 times the initial value at $r = 1.3 R_\Theta$. Figure 2(a) shows the magnetic field configuration and plasma velocity in the nearly steady-state for $\beta = 0.5$. Note that velocity is zero in the closed region. An expanded view of the closed field region of the figure is shown in Figure 2(b), with the condensation mode growth rate ω for $\beta = 0.5$ and 4 shown on the right side of the vertical axis (s implies stability).

For evaluation of the stability, we neglect the temperature and density variation along field lines but consider the variation on each field line of different equatorial height. Heat conduction perpendicular to the magnetic field was neglected − only a parallel component was considered. The ambient heating rate was assumed to be constant in time and is balanced to the radiation in a steady-state. An (1985) found that the plasma is stable against condensation modes if the local growth rate $\omega = -\rho_0 \Phi / \gamma P_0$ is positive on all the field lines, but unstable if ω is negative on any field line. Here,

$$\Phi = \frac{(\gamma - 1) T_0}{\rho_0} \left[\left(\frac{\partial R}{\partial T} \right)_P + \frac{T_0^{5/2}}{B_0^2} \frac{t_r}{t_c} (\bar{k} \cdot \bar{B}_0)^2 \right]$$

and R, T_0, ρ_0, B_0, and P_0 are dimensionless radiative energy loss rate, temperature, density, magnetic field, and pressure, and $\bar{k}$ is a wave vector. The quantities t_r and t_c are radiative and heat conduction timescales defined as $t_r = 3P_0/2R$ and $t_c = L^2 P_0 / \kappa_0 T_0^{7/2}$. Because of the local nature of the stability we evaluate ω on each field line of the closed field region. Figure 2(b) shows that the stability of the final states for $\beta = 0.5$ and 4 is significantly different. For $\beta = 4$, all the field lines are stable − mainly because the density enhancement over the initial value is small as seen in Figure 1. For $\beta = 0.5$ all the field lines of equatorial height less than $r = 2.05 R_\Theta$ are unstable. The local growth rate ω is maximum at the field line nearest to $r = R_\Theta$ and decreases with height. If we include the gravity in the calculation, the height above which the plasma is stable is far less than $r = 2.05 R_\Theta$ due to the stabilizing effect of the gravity (Wragg and Priest, 1982; Antiochos and An, 1985).

Next, let us discuss how, depending on the magnetic field configuration, the thermal instability initiates a coronal cavity or prominence formation. As plasma density increases above a critical value the plasma becomes unstable to condensation modes. The condensed plasma accumulates on or falls along the field lines depending on whether or not the field lines provide stable support against gravity. If the condensed plasma accumulates, the radiative loss rate continues to increase until the plasma cools to $T = 10^5$ K (An et al., 1983). The plasma keeps cooling to T_C (~10^4 K) after the temperature reaches $T = 10^5$ K because the radiative energy loss rate exceeds heat conduction and ambient heating rate. As the temperature approaches T_C, the ambient heating rate is approximately equal to the radiative energy loss rate and heat conduction is negligible in the overall energy balance. The temperature T_C ($< 10^4$ K) and corresponding density N_C are typical of prominence temperature and density.

If the condensed plasma falls down along field lines, runaway condensation is not possible. During initial condensation, the temperature decreases, density increases, and the radiative energy loss rate increases. If condensed plasma slips down faster than the radiative energy loss rate

$(t_r = 2 \times 10^4$ s for the $\beta = 0.5$ streamer at $r = 0.1\ R_\odot)$ the radiative energy loss rate decreases until it reaches an energy balance and the condensation and slippage cease. However, because the plasma cools during the initial condensation and the temperature change is negligible during the slippage, energy balance can be reached only after the density is depleted below the initial value (assuming the ambient heating rate is constant in time). The density depletion causes the plasma to become stable to the thermal instability. Since SSW considered a simple dipole field which may not provide stable support, the thermal instability for $\beta = 0.5$ will lead to a cavity. On the other hand, for $\beta = 4$, the streamer is thermally stable and cannot have a cavity. Saito and Hyder (1968) argue that the difference between prominences with and without clearly defined coronal cavities could be explained by geometry. Our stability calculation suggests that the existence of the cavity also depends on the coronal field strength.

Saito and Tandberg-Hanssen (1973) and Saito and Hyder (1968) found that plasma mass in a cavity is not sufficient to account for the mass of the prominence. The other possibility is that the material comes from below (Saito and Tandberg-Hanssen, 1973), possibly in the form of spicules. For a newly formed prominence with height 10^4 km, it takes about one day for a spicule material of average flux density $F = 1.2 \times 10^{15}$ cm^{-2} s^{-1} (Athay and Holzer, 1982) to fill the prominence. The time is about equal to the timescale of a quiescent prominence formation (Zirin, 1978). The spicule plasma which is thermalized in the corona and flowing outward will be trapped by and accumulated on the closed field. If the accumulation is sufficiently high to initiate condensation and the magnetic field gives stable support at the base but no such support above, we will find a prominence at the base below a coronal cavity. In other words, a prominence below a coronal cavity is formed by the material supplied from below as Saito and Tandberg-Hanseen (1973) suggested and is a consequence of condensation of the plasmas. The main difference is that prominences require magnetic support and continuous consideration of coronal material supplied by spicules for fully developed prominences. We schematically summarize our results in Figure 3, showing four different regions; region 1 is an open field region and source of solar wind plasma. In region 2 the plasma has reached a steady-state with energy and force balance. In region 3 condensed plasma flows down along the field lines, leaving a cavity behind. Region 4 is the local field region in which the condensation initiates prominence formation. The local sheared magnetic field provides stable support against gravity.

REFERENCES

An, C.-H., 1985, submitted.

An, C.-H., Canfield, R. C., Fisher, G. H., and McClymont, A. N., 1983, *Astrophys. J.*, *267*, 421.

Antiochos, S. K. and An, C.-H., 1985, to be submitted.

Athay, R. G. and Holzer, T. E., 1982, *Astrophys. J.*, *255*, 743.

Pneuman, G. W., 1983, *Solar Phys.*, *88*, 219.

Pneuman, G. W. and Kopp, R. A., 1971, *Solar Phys.*, *18*, 258.

Saito, K. and Hyder, C., 1968, *Solar Phys.*, *5*, 61.

Saito, K. and Tandberg-Hanssen, E., 1973, *Solar Phys.*, *31*, 105.

Steinolfson, R. S., Suess, S. T., and Wu, S. T., 1982, *Astrophys. J.*, *255*, 730.

Wragg, M. A. and Priest, E. R., 1982, *Astron. Astrophys.*, *113*, 269.

Zirin, H., 1978, *Physics of Solar Prominences*, IAU Colloquium No. 44 (E. Jensen, P. Malthy, and F. Q. Orrall, eds.), Institute of Theoretical Astrophysics, Blidern, Oslo.
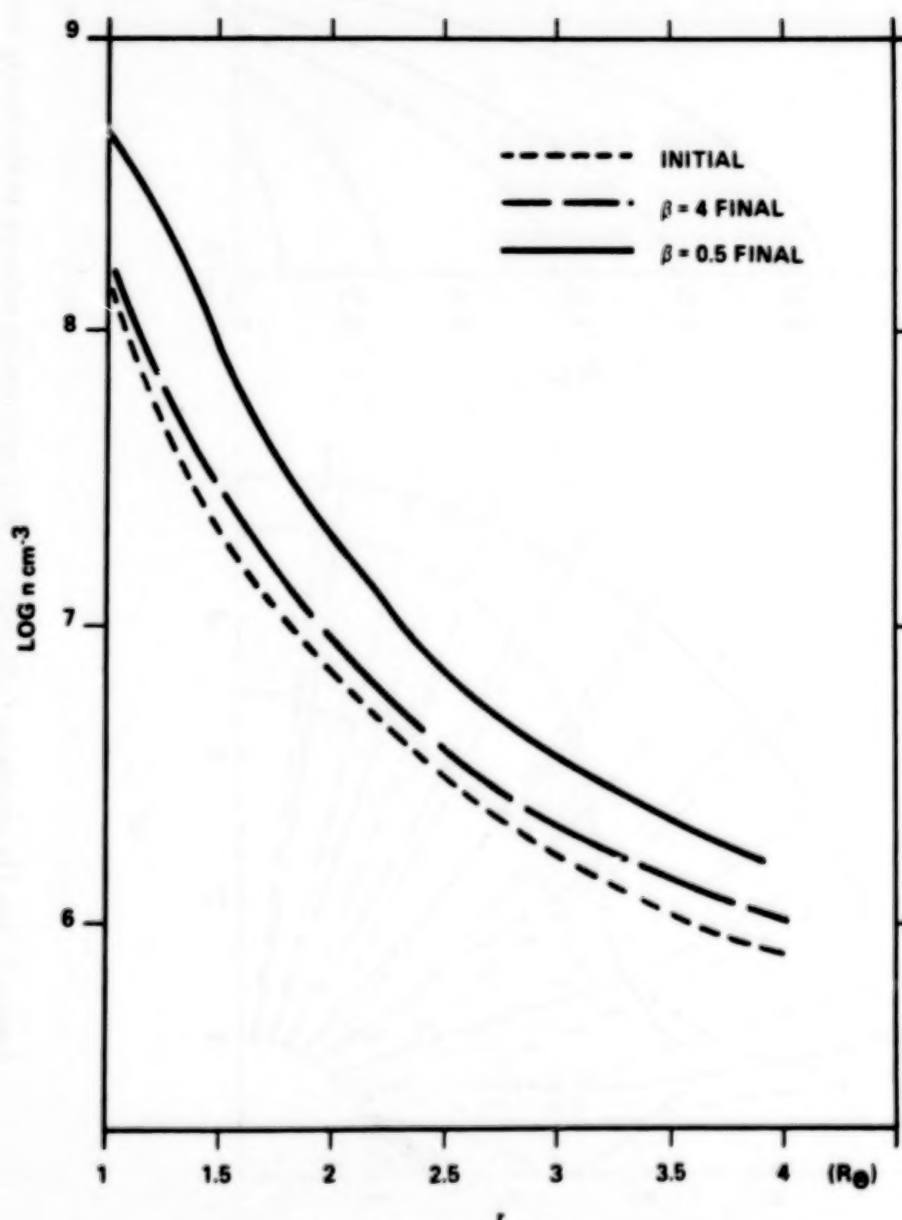
Figure 1. Density profiles in the initial and final states.
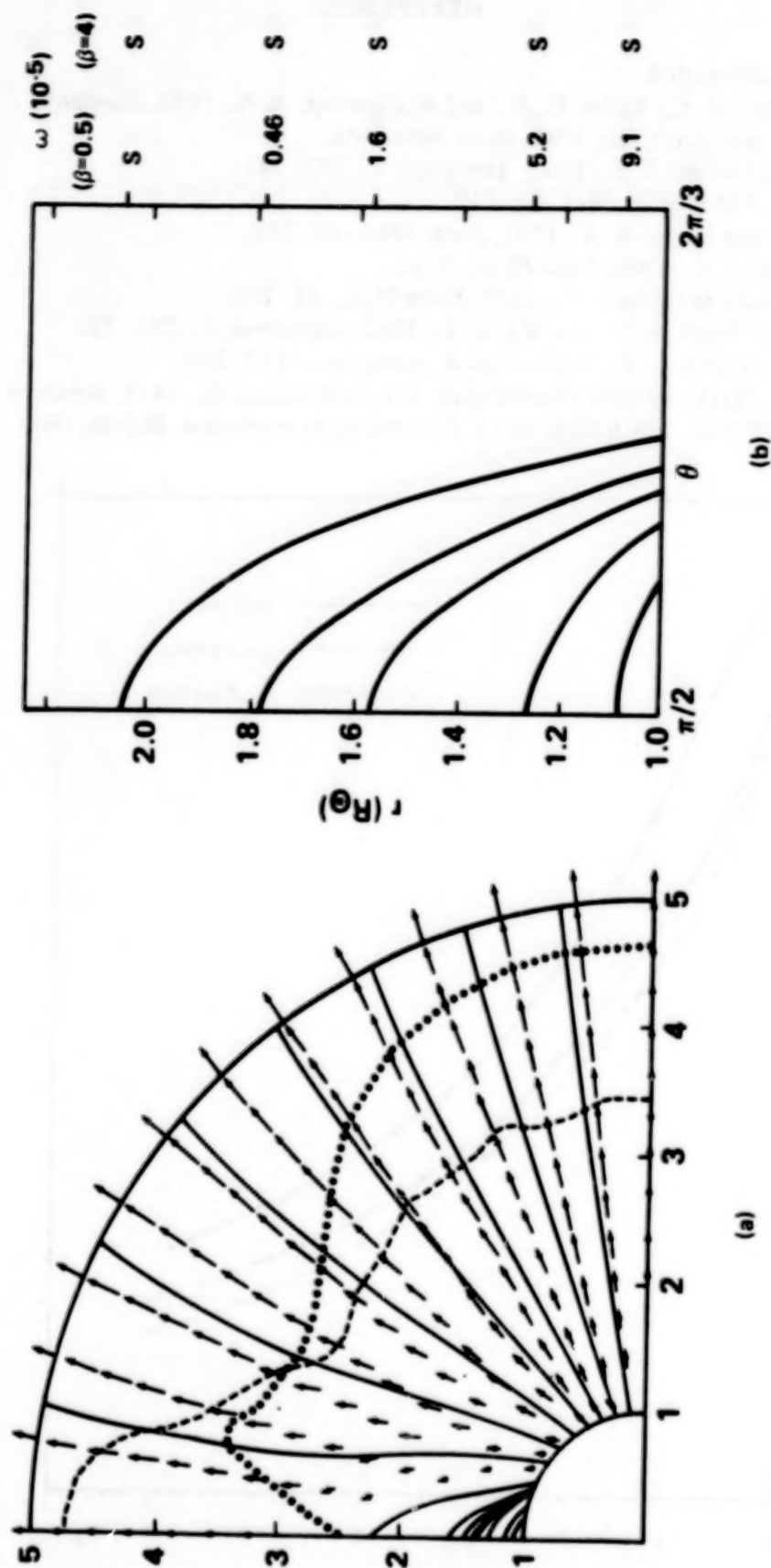
Figure 2. (a) The magnetic field configuration and plasma velocity in the nearly steady-state for $\beta = 0.5$ (from Steinolfson, Suess, and Wu, 1982). The dotted-line is the Alfvén and the dashed-line is the sonic curve. (b) The expanded closed field region of (a) with the instability growth rate ω for $\beta = 0.5$ and 4 on the right side of the vertical axis (s = stability).
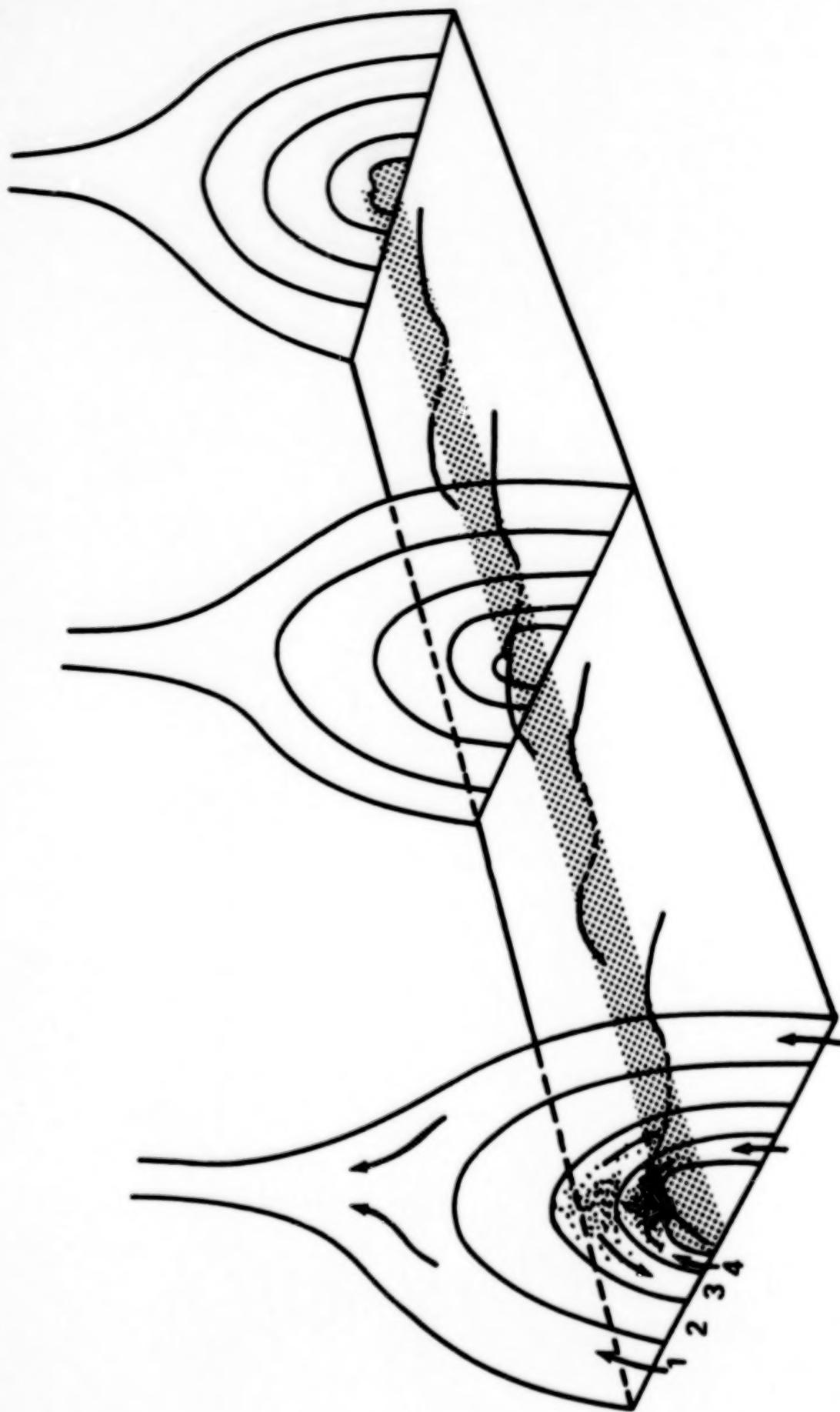
Figure 3. A three-dimensional sketch for a coronal streamer and its fine structures. The arrows represent the plasma flows.
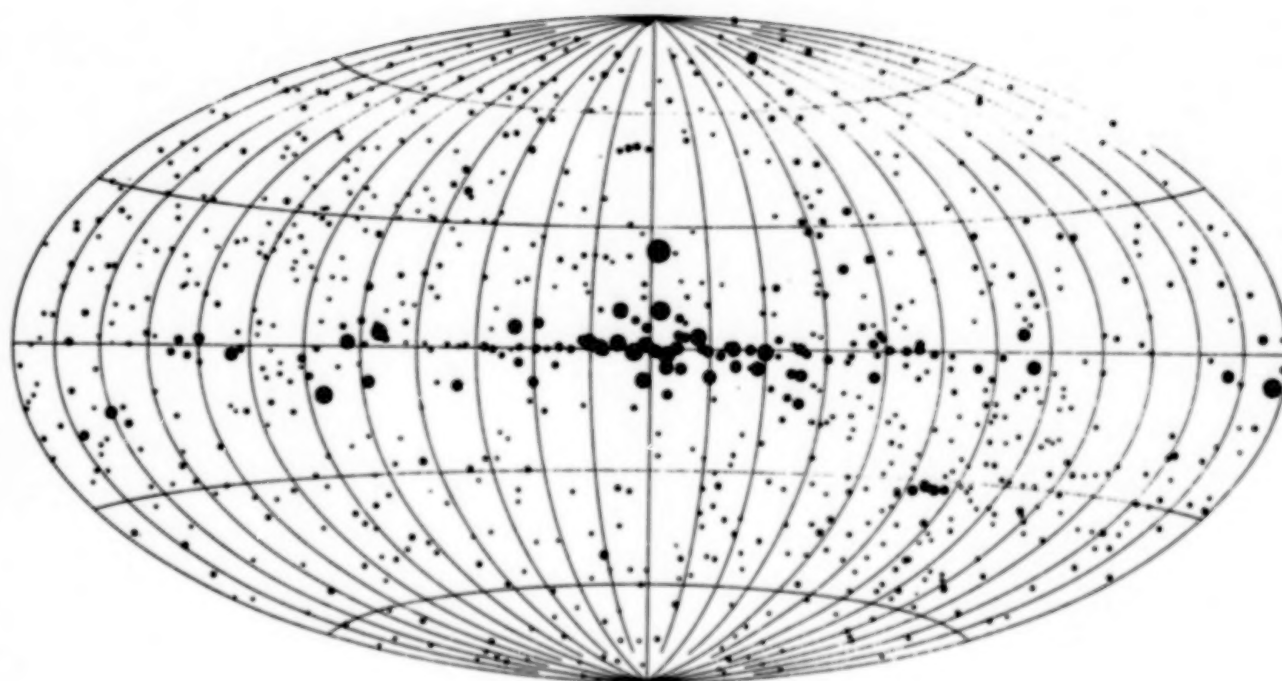
X-RAY ASTRONOMY

THE PINHOLE/OCCULTER AS A TOOL FOR X-RAY ASTRONOMY
(Invited)

Kent S. Wood

E. O. Hulburt Center for Space Research, Naval Research Laboratory
Washington, D.C. 20475-5000, U.S.A.

ABSTRACT

The two X-ray transform telescopes on the Pinhole/Occulter Facility (P/OF) will provide sub-arcsecond angular resolution, high sensitivity imaging in hard X-rays for the first time, as well as improved capabilities for timing studies and spectroscopy. Although the design was driven by solar observing requirements, the result is an instrument of major importance for astronomical as well as solar observations. Fundamental astrophysical measurements could be made on supernova remnants, clusters of galaxies, active galaxy cores, accreting binary systems, and active coronae of nearby stars. Ways in which astronomical observations will benefit solar research are discussed.

INTRODUCTION

The Pinhole/Occulter Facility (P/OF) is proposed to carry a complement of two hard X-ray imaging instruments and two coronagraphic instruments that together will provide new capabilities for solar observations. This discussion concerns itself solely with the X-ray instruments, and looks at them primarily from the standpoint of their suitability as tools for celestial, rather than solar, observations. Descriptions of the P/OF instrumentation may be found in Tandberg-Hanssen et al. (1983) and in Hurford and Hudson (1980). These references should be consulted for details, but a brief description is as follows: one of the X-ray instruments, the coded-aperture imaging (CAI) telescope, has a 50% transparent mask with a coded pattern of "pinholes," placed 50 m from a detector that records positions, times, and energies of X-rays transmitted by the mask. The other instrument is a Fourier-transform telescope (FTT) employing two sets of grids, an upper one on the mask platform and a lower one directly in front of a detector similar to that in the CAI. Upper and lower grids consist of ~100 "subcollimators"; each subcollimator consists of a set of fine, parallel slits. Slit spacing and orientation vary from one subcollimator to the next, so that each subcollimator measures a different Fourier component of the spatial image. In both the CAI and FTT designs, the pattern recorded in the detector is not the source image but rather a transform of that image that must be inverted to recover the source brightness distribution. Both designs belong to the class of transform telescopes.

Two main points will be stressed here. The major theme is that P/OF will be a powerful instrument for high energy astrophysics, in the first rank of X-ray astronomy facilities now foreseen. A second point is that inclusion of the astronomical observations in the P/OF program will benefit the solar program conducted with the facility, as well as solar physics generally.

Capabilities of the X-ray instruments on P/OF will be assessed from the astronomical perspective, in part through comparison with other major astronomical instruments now planned or under discussion. The estimated performance characteristics of P/OF will then be used as a basis for characterizing the expected scientific results. Applications will be described in several areas including source population studies, imaging of extended sources, photometry, and spectroscopy.

I. PERFORMANCE CHARACTERISTICS OF P/OF IN CELESTIAL OBSERVATIONS

In 1979, the Naval Research Laboratory, the University of Birmingham, and the Los Alamos Scientific Laboratory submitted a proposal to NASA for a large-area coded aperture instrument, to be used exclusively for astronomical observations in hard X-rays. It is interesting and instructive to note that this instrument as proposed was roughly similar to the coded aperture X-ray telescope on P/OF, in its energy range, size, and angular resolution, as well as in design. This coincidence in parameters means that a single basic instrument concept is able to serve as a frontier research tool in both solar physics and X-ray astronomy. How does this happen? Naively, the roughly 12 orders of magnitude difference in flux between bright solar flares and celestial sources at 1 keV would seem to raise serious questions about feasibility.

It turns out that there is no single answer, but rather a combination of several factors that disposes of these orders of magnitude. Comparison must be made not in units of flux but rather in terms of the fluence per pixel in a typical image. Several aspects of typical solar flare imaging in hard X-rays collectively create a requirement for extremely high sensitivity, which in turn makes celestial work possible. First, P/OF is not designed solely for the brightest flares, but rather for the ones that would be seen during a typical Shuttle mission at solar maximum. Hence, it must detect flares $\sim 10^3$ times fainter than the brightest ones. Second, the solar flares are to be imaged at $E > 20$ keV. The highest priority solar goals, such as imaging bright X-ray regions near loop footpoints, fall in this energy range. This means that the very steep solar spectrum (typically E^{-4}) in hard X-rays will drastically reduce the photons available in the band of greatest interest, relative to energies near 2 to 10 keV. In contrast, celestial observations will cover a range of 2 to 120 keV. The celestial spectra of interest are much harder than E^{-4} and sometimes harder than E^{-1}, so that the relative attrition of count rates with increasing energy is far less severe. In addition, integration times for solar applications are, very conservatively, less than 1 s, in contrast with celestial sources, wherein 10^4 or 10^5 s integrations are appropriate and longer ones are feasible if the task warrants it. Each of the factors just mentioned disposes of 3 to 5 orders of magnitude in the naive flux discrepancy. A fourth factor is image complexity. The solar flare flux, integrated over a typical observing integration time, must ultimately be assigned to a number of pixels, distributed in a complex way, whereas the faintest objects dealt with in celestial work are point sources. When all four factors are combined, there is great overlap in the expected range in fluence per pixel used in typical solar and cosmic observations made with the P/OF.

Granting that the celestial observations are feasible with P/OF, it is still necessary to understand how data from P/OF would compare with those from other X-ray astronomy instruments.

Sensitivity for a coded aperture instrument such as P/OF depends on detector area and background in a manner similar to other X-ray instruments, to within factors of 2. It improves as the square root of integration time for faint sources, because the dominant consideration is detection of a signal in the presence of Poisson noise. Typically, the detector background per unit area is much larger than the diffuse X-ray background, and also much larger than the flux from the source. In this case the minimum detectable flux, F_{lim}, is given by

$$F_{lim} = 2 \eta (B/\epsilon \ A \ \delta E \ \tau)^{\frac{1}{2}} , \tag{1}$$

where

δE = energy range, e.g., 2 to 10 keV

B = background, e. g., 3×10^{-4} cts cm^{-2} s^{-1} keV^{-1}

A = effective area, $\sim 10^4$ cm^2

τ = integration time, 10^4 – 10^5 s

η = detection significance = 5σ

ϵ = efficiency.

Typical values are, at 5 keV, F = 0.03 $(10^4$ s/$\tau)^{1/2}$ microjansky and, for δE = 15 to 30 keV, F = 1.3×10^{-5} $(10^4$ s/$\tau)$ cts cm^{-2} s^{-1}. These numbers compare favorably with most X-ray astronomical instruments that have flown or are now planned, with the single exception that AXAF will achieve substantially greater sensitivity at energies well below the cutoff energy of its X-ray mirror, ~ 10 keV. For many hard X-ray observations, P/OF has no equal in sensitivity.

Figure 1 is a spectral sensitivity curve comparing P/OF with instruments from the first two decades of X-ray astronomy as well as AXAF. The P/OF curve, taken for a 10^5 s integration, represents the CAI and Fourier-transform telescope instruments taken together. It is clearly more sensitive than the HEAO-1 instruments and aligns roughly with the upper end of the Einstein Observatory HRI spectral sensitivity curve. All curves, including P/OF, refer to point sources detected at 5σ.

In considering Figure 1, it should be recognized that the sensitivity advantage conferred by grazing incidence optics does not exist beyond ~ 10 keV. Hard X-ray instruments must rely on some nonfocussing technique in order to have imaging at all. The other hard X-ray instruments shown in Figure 1, UHURU and the HEAO-1 experiments, had coarse pencil beam angular responses (a few square degrees) achieved with mechanical collimators. Unlike these, P/OF enjoys true high-resolution imaging.

Table 1 summarizes parameters besides sensitivity that affect imaging and timing performance. The P/OF field of view is comparable to that of the Einstein Observatory IPC, while the angular resolution is substantially better than the HRI, 0.2 arc s. The timing resolution is 1 ms. The total collecting area excellently supports fast timing observations even in the millisecond domain, as does the large telemetry allocation.

Table 2 gives key parameters of several major X-ray astronomy missions expected over the next few years. Comparing areas, P/OF is seen to be larger than these future payloads, two of which have grazing incidence optics (ROSAT, AXAF) and two of which (ASTRO-C, XTE) do not. The sensitivity advantage of focussing optics pertains to sources at very low flux levels. For sources whose flux exceeds the background per unit area in the detector, the sensitivity advantage lies with the instrument having greater collecting area, whether or not it has optics. For P/OF this crossover would fall near UHURU flux unit (1 UFU = 2.4×10^{-11} erg cm^{-2} s^{-1}, 2^{-10} keV, or roughly 1.1 microjansky at 5 keV, for a Crab-like spectrum) so that the area advantage of P/OF would be an unqualified performance asset over the focussing instruments above that flux level. P/OF's area would be (within a factor of 2) the same as ASTRO-C and XTE, but it would gain in performance by virtue of its imaging and higher bit rate. On fainter sources, ROSAT and AXAF would perform far better than P/OF, but only up to the cutoff of their X-ray optics. At higher energies, where P/OF's most novel capabilities lie, it is simultaneously superior in collecting area, sensitivity, and angular resolution.

It would thus be reasonable to characterize P/OF as being roughly the hard X-ray counterpart to AXAF, with angular resolution comparable to that instrument and with superior capabilities for timing and low-resolution spectral work on bright sources. Its sensitivity for faint sources would be roughly like that of the Einstein HRI, the detector that has reached the lowest flux levels of any X-ray astronomical instrument to the present time.

II. THE X-RAY SKY: SOURCE COUNTS AND CLASSES

P/OF will have the power of a general purpose X-ray astronomy facility; hence, complete discussion of all observations it could perform would entail a prohibitively vast survey of X-ray astronomy. The most important thing is to assess where its unique features − hard X-ray imaging and high sensitivity in hard X-rays − will be effective. This will be undertaken in a brief survey emphasizing bright X-ray sources. The survey will analyze X-ray astrophysics from several standpoints: by source populations, by type of observation (imaging, photometric, etc.), and by the astrophysical problems addressed.

A convenient way to begin is with the full-sky surveys from HEAO-1. The lower portion of Figure 2 shows the HEAO A-1 full-sky survey (Wood et al., 1984), which covers energies from 0.5 to 25 keV. Although the flux limit varies in a systematic way with position on the sky because of variations in sky exposure, it is typically at least 1 UFU, and ~450 sources are seen above this level. The display is in galactic coordinates, with the size of the dot representing a source proportional to the logarithm of its intensity in counts cm^{-2} s^{-1}. Five major source populations are encountered among the identified objects: clusters of galaxies, active galactic nuclei, accreting binaries, supernova remnants, and stellar coronae.

The upper portion of Figure 2 shows the HEAO A-4 catalog (Levine et al., 1984) displayed in the same mode. The energy range is now higher, 13 to 120 keV. The epoch observation over which this high-energy map was accumulated includes that of the other map, but is roughly three times as long. The sources seen here are a subset of the previous sample, mainly the brighter objects. None is unidentified, and most of the major classes are again represented. All sources have lower flux at this higher energy, but they do not all scale the same way because of differences in spectral hardness. Improving the flux limit tenfold would reveal many more objects in all classes, particularly the extragalactic ones. It is noteworthy that despite the lower full-sky source count at higher energies, the regions that were crowded at low energies remain crowded. Since collimators used in most high-energy designs other than P/OF are comparatively coarse, this crowding becomes a very serious problem. Ultimately, some imaging is needed as limiting flux decreases, from source confusion considerations alone.

The most fundamental sense in which confusion provides a limitation is in the fluctuations from pixel to pixel in the number of unresolved sources. The problem is exemplified by Figure 3, which shows source counts obtained with HEAO A-1 using two different collimators. The points at higher flux levels are obtained with 1 deg x 4 deg collimators, and reach a level of roughly 1 UFU. The lowest point is obtainable only by using a collimator eight times finer, 1/2 deg x 1 deg, on a small field of sky where a long integration time was obtained. Instrumental source confusion has been analyzed formally in several studies, many of them prompted by the early sky surveys done with radio pencil beams. It can be shown that in work with a particular point source response function ("beam width"), it is not possible to isolate more than one source in every few tens of beam widths. The collimator that obtained the lowest point in Figure 3 had the smallest field of view of any pencil beam design that has yet flown. To go below this limit requires imaging or modulation collimator designs to achieve smaller effective beam sizes.

The Pinhole/Occulter Facility would never encounter source confusion within practical integration times, even up to a few weeks. This is essentially because the very fine resolution places its confusion limit at a flux level too low to be reached in practical integrations. Accessibility of sources would depend mainly on integration time and energy. Table 3 estimates the number of sources that would be accessible at various energies. These are extrapolated from surveys, particularly those shown in Figures 2 and 3, according to expected number-flux relations.

It is clear that all major source classes would be available. There would not be time to observe all accessible sources, because it would require at least 10^4 seconds on each of about 40 000 fields, i.e., well over 10 years. A feasible observing program would be to look at bright targets of special interest, sampling each class, and to conduct statistical studies based on random sampling with long integrations. This tactic was used with the Einstein Observatory and could be extremely effective with P/OF.

With overall source accessibility thus characterized, it is appropriate to survey particular classes and objects. In appreciating P/OF's role, it may help to recall that, in contrast to the optical sky, virtually every source known to X-ray astronomy has proven to be either extended or variable, so that the combination of high-resolution imaging, high sensitivity, and fast timing available with P/OF necessarily finds wide application. As X-ray astronomy matures, measurements needed to advance understanding become more subtle and difficult, creating demand for advanced instrumental capabilities.

III. IMAGING APPLICATIONS

Supernova remnants, active galactic nuclei, and clusters of galaxies are the major X-ray source classes having extended X-ray components in which surface brightness mapping with P/OF would be of great value.

Supernova Remnants (SNR)

The Crab Nebula was the first X-ray source discovered to be extended, a fact determined originally using lunar occultations (Bowyer et al., 1964; Wolff et al., 1975). This nebula and the pulsar within it present a wealth of astrophysical phenomena, over radio to gamma-ray wavelengths. The pulsar is thought to be the energy supply for the entire nebula, but details of energy transport remain a challenge to high-energy astrophysics. Insights gained here, for example concerning particle acceleration and transport, may well transfer to other astrophysical situations.

The angular structure as a function of energy can be used to discriminate between diffusion and bulk transport models of the energy flow. Diffusion predicts a specific relation for shrinkage of the nebula as energy increases into hard X-rays. P/OF can precisely determine the nebular size to high energies. It can also tell whether there are localized fine features in X-rays, corresponding perhaps to optical wisps that move appreciably over the course of time.

The combination of high angular resolution and high timing resolution available on P/OF makes possible a very basic measurement, namely determination of the continuum flux from the Crab Pulsar (PSR 0532+21). The observation is difficult because the pulsar must be seen against the nebular background, and must be imaged using data strobed at the pulse period, accepting only portions of the cycle when the pulsar is at its minimum. Such an image shows whether there is excess steady flux at the pulsar position. No excess has been detectable with previous instruments (Harnden and Seward, 1984), but feasibility of the measurement is strongly

dependent on the angular resolution available. P/OF, with resolution roughly 25 times finer than the Einstein Observatory's HRI, should provide a definitive measurement. The intent behind this measurement is determination of the neutron star cooling timescale. Since it is known that the supernova that produced the Crab Pulsar occurred in AD 1054, determination of the surface temperature at the present epoch fixes the cooling time; an upper limit on current temperature sets a limit on the cooling time. The cooling time is sensitive to the constituents of the neutron star interior and the processes whereby they contribute to heat loss.

P/OF is also suited to mapping other bright, young SNR such as Cas A, that contain regions of high temperature and high surface brightness. Angular size scales are such that arcsecond or better imaging is required. From Einstein observations (Murray et al., 1979) one estimates that Cas A would give a flux/pixel ratio of 4×10^{-12} erg cm^{-2} s^{-1} pixel^{-1}, for pixels 10 arcseconds on a side, so that imaging should be possible up to 10 to 15 keV. The Tycho and Kepler supernova remnants should also be detectable and possibly some SNR in the large Magellanic Cloud. Hard X-ray imaging will supplement data from lower energy instruments, such as AXAF, providing improved knowledge of temperature gradients or of how kinetic energy in the expanding remnant is thermalized.

Active Galactic Nuclei: Jets and Extended Features

Active galactic nuclei (AGN) are a broad class that includes a number of distinct kinds of bright, compact, variable galaxy cores, including highly luminous (10^{43} to 10^{47} erg s^{-1}) quasars and BL Lacertae objects, as well as less luminous (10^{42} to 10^{45} erg s^{-1}) Seyfert I galaxies and emission line galaxies. Much of the total power in these sources is radiated at high energies. The central power source may be a supermassive black hole, of mass 10^6 to 10^8 solar masses. Many of these sources have outer radio lobes, powered by jets of material ejected from the central object.

In NGC 5128 (Cen A) an X-ray jet has been detected using the Einstein Observatory (Schreier et al., 1979; Feigelson et al., 1981). This jet includes small knots, interpreted as regions of synchrotron emission. Jets are also seen in radio wavelengths, and are evidence for transfer of energy from the nucleus to outer radio lobes. Much of the lifetime energy output of the source may be in such ejecta, and imaging at high energies is crucial to developing physical models. Known X-ray jets range in size from a few arc seconds to several arc minutes, but the total number detected remains small: only in 3C273, M87, and Cen A have jets been seen (Schreier, Gorenstein, and Feigelson, 1982). The jet in Cen A has an intensity of 3×10^{-12} erg cm^{-2} s^{-1}, or about 0.1 microjansky; hence, P/OF could detect it. The X-ray spectrum of the jet would be determined from, for the first time, P/OF observations. A jet like that in Cen A should be observable with P/OF at greater distances because of its high angular resolution. If it were ten times farther away, its surface brightness would be unchanged, and it would still be resolvable. P/OF will thus be able to range over a larger volume of space in searching for jets, and should enlarge the list of X-ray jets.

Clusters of Galaxies: Imaging the Hot Intercluster Medium

Previous work has shown that most clusters of galaxies contain X-ray-emitting gas, usually at temperatures exceeding 8 keV. The surface brightness has been mapped using the Einstein Observatory for at least 30 clusters, revealing a variety of structures rather than a single recurrent morphology. In addition, spectral measurements indicate that there is in some clusters a nonthermal component extending to hard X-ray energies (Lea et al., 1981), although the relative

location of this component is unknown. Locating such features is one example of a task that P/OF could perform on clusters of galaxies. Another would be imaging of clusters in iron lines near 6.7 keV. Iron line images need to be combined with temperature maps determined from continuum observations to be maximally useful in modeling the gas distribution and its dynamics. In combination with a hydrostatic model, mapping of the gas temperature provides a way to measure the total mass enclosed within a particular radius; this has been used to demonstrate that there is considerable "missing mass" in M87 (Fabricant, Lecar, and Gorenstein, 1980), that is, nonluminous matter that contributes to the gravitational mass.

Resolving Multiple Point Sources in Crowded Fields

In several parts of the sky, bright X-ray sources become so crowded that resolving confusion becomes a major aspect of any observation. Below ~1 UFU, serious confusion exists everywhere in the sky for most conventional collimators and imaging becomes essential, but confusion is encountered at much higher flux levels in the central part of our galaxy, in the Magellanic Clouds, and elsewhere. The role of imaging in these situations is to resolve point sources from one another, rather than to map surface brightness.

The galactic center contains 6 X-ray sources within 1 square degree (Watson et al., 1982) and interstellar absorption restricts observations to energies above about 3 keV. There may be unusually frequent bursting in this region (Proctor, Skinner, and Willmore, 1978). This is also the region where 511-keV line emission has been seen (Leventhal, MacCallum, and Stang, 1978), and P/OF could well play a role in positioning the source of that emission through simultaneous observations with gamma-ray instruments. P/OF can survey the galactic center region carefully, going 2 to 3 orders of magnitude fainter than previous surveys above 4 keV.

Crowded field regions also exist in other galaxies of the Local Group. The Large Magellanic Cloud has several sources at small angular separations, and some of them so close to one another that hard X-ray spectral determinations without P/OF are impossible. Point sources in M31 that were imaged with the HRI on Einstein (van Speybroeck et al., 1979) should be accessible to P/OF in long integrations. The spectral characteristics of an ensemble of binary sources could be determined in this way.

The number-flux relationships for source populations were used earlier to characterize source accessibility, but they have a deeper significance in that the departures from $N(S) \sim S^{-3/2}$ (the Euclidean, isotropic case) reflect population evolution and cosmological corrections to the Euclidean volume element. A main ambition of high-energy astrophysics has been to determine whether and how the diffuse background resolves into discrete sources. The $S^{-3/2}$ relation cannot continue to arbitrarily low fluxes without truncation because it will diverge; hence, a turnover is expected. At the lower end of the P/OF's energy range it should be possible to observe this turnover in very long integrations, perhaps one or two weeks. This might be accomplished by summing images from several shorter integrations. Faint sources seen in these long integrations would be positioned to very high accuracy, so that their counterparts could be identified in optical and radio wavelengths. While the turnover flux level could be reached at energies >10 keV only with unacceptable long integration time, shorter integrations would greatly advance the statistical knowledge concerning source populations at those energies. The hard X-ray continuation of the diffuse background problem could be addressed by modeling and extrapolations but with unprecedented rigor, in much the same way as the same problem at energies <3 keV is now treated using source counts from the Einstein Observatory.

IV. TIMING AND SPECTROSCOPY

Let us now consider cases where timing and low-resolution spectroscopy are vital to advancing physical understanding. These come chiefly from the accreting binary sources and active galactic nuclei (AGN). It is natural to regard P/OF as primarily an imaging instrument, but its design is also ideal for point-source spectroscopy and photometry, being superior for these purposes to mirror instruments (for the bright sources where most work is done) by reason of greater area and energy bandwidth, and superior to non-imaging detector arrays of comparable area because its imaging permits clean target isolation from other sources and background variations. These assets give P/OF a data quality advantage in many practical situations.

Accreting Binary Sources

The brightest objects in the X-ray sky are compact objects accreting in binary systems. These divide into three subclasses, according to whether the accreting component is a black hole, neutron star, or white dwarf. Further subdivision may be made: e.g., when an accreting neutron star has a strong magnetic field it will be a pulsar, but a weak field will give either an X-ray burst source or one of the so-called "bulge sources," found mainly but not exclusively in the region of the galactic bulge and which neither pulse nor burst.

Black holes are predicted by General Relativity and other gravitation theories as well. They become luminous X-ray sources if they accrete matter from their surroundings. Several candidates are known in our galaxy and the LMC, the best studied being Cygnus X-1. In these objects, accreted material is provided by a binary companion. Determination of binary orbit parameters has provided mass estimates, one type of evidence for the black hole interpretation. (Stable neutron star configurations do not exist above ~ 3 $M_\odot$.)

Much literature has been devoted to rapid intensity variations in black hole candidates. These bursts have a noisy, aperiodic character, with timescales as short as a few milliseconds now established. (See Meekins et al., 1984, which describes techniques for analyzing rapid aperiodic variability that occurs over a wide range of timescales.) Study of these fluctuations is a good task for P/OF in virtue of its collecting aperture and timing resolution. P/OF's broad energy range will allow spectra of the rapid outbursts to be established for the first time.

There can be few problems in astrophysics more important than understanding black holes and the plasma processes taking place in their vicinity; quasars and other active galactic nuclei may represent the same phenomenon on large scales (see Rees, 1984, for a recent review of models). It can be argued on general grounds that the rapid fluctuations must originate near the innermost part of the accretion disk around the black hole; hence, they are the best probe of the most extreme non-Euclidean space accessible to astronomical observation.

Generally speaking, the millisecond domain is accessible only to collecting areas > 1000 cm^2, and calls for telemetry rates of at least a few kbps and preferably more. These considerations have to date limited the information gathered on fast processes, but new results from HEAO-1 and EXOSAT plus anticipated results from ASTRO-C and XTE will make millisecond X-ray astronomy a rich field by the time P/OF flies.

Fast processes have been in neutron stars as well as in black hole candidates. Figure 3 shows X-ray bursts from the source MXB 1728-34, with risetimes resolved using HEAO A-1. The total collecting area, 2000 cm^2, was far smaller than the P/OF collecting area. P/OF should

obtain much better statistics and be able to determine how the spectrum evolves during the rise of the burst. This should test hydrodynamic calculations of burst evolution. Using EXOSAT data, van der Klis et al. (1985) have recently reported detection of quasiperiodic oscillations at high frequencies (several to a few tens of Hz) in GX 5-1. This new phenomenon presents observational goals again well matched to P/OF's capabilities, for essentially the same reasons as in the black hole fluctuations and X-ray bursts.

Magnetized accreting neutron stars (binary pulsars) have had a large role in X-ray astronomy beginning with UHURU. About 20 systems are now known, with spin periods ranging over 4 orders of magnitude, 69 ms to 13 minutes. In most systems the spin period decreases over time, but this spin-up is irregular, being driven by accretion torques and possibly other processes. Variations in period and luminosity can be used to determine neutron star parameters such as the moment of inertia or the magnetic moment. A detailed model of the accretion flow and of the dynamic response of the neutron star to the associated torque is one goal of current work.

The source A0538-66, located in the Large Magellanic Cloud, exemplifies several points about the demanding nature of binary X-ray pulsar observations. This source is unusual because (1) it has the shortest spin period (69 ms) of any binary pulsar, (2) it is a "recurrent transient," sometimes unobservable but turning-on at periodic intervals, (3) it is not always pulsing when it is active, and (4) by straightforward arguments, it must have the weakest magnetic field of any binary pulsar. These facts show it has a most atypical accretion environment that will make it the target for many future observations, surely including hard X-ray pulse phase spectroscopy. Yet it is separated by only ~30 arc min from another bright LMC source, LMC X-4; hence, gathering the needed data will simultaneously exercise P/OF's imaging (to achieve isolation from LMC X-4), time resolution (to handle the short spin period), and hard X-ray sensitivity.

The effects of 10^{12} to 10^{13} G magnetic fields on radiation processes have been studied to date solely by means of hard X-ray spectral and timing measurements, i.e., by means of cyclotron features seen in binary pulsars and possibly in gamma-ray bursts as well. This is likely to remain a phenomenon uniquely accessible in hard X-rays, partly because the canonical magnetic fields of binary pulsars place the cyclotron resonance in hard X-rays. Furthermore, if the resonance were to occur below 10 keV in some sources, then it would be more difficult to isolate from other spectral features such as atomic lines and absorption edges that strongly affect spectra at lower energies. Cyclotron features have sometimes been isolated by subtracting the spectrum obtained at one phase of the pulse cycle from that obtained at another phase (e.g., Trümper et al., 1977). P/OF could employ imaging for background removal and provide high-quality source spectra in all pulse phases over 2 to 120 keV. It is difficult to overstress the importance to physics of systematics-free data on hard X-ray cyclotron resonances. These effects result from electron transitions between energy states that are not dominated by a nuclear Coulomb field but rather by a magnetic field 5 to 6 orders of magnitude beyond anything produced in terrestrial laboratories. Pulsar observations should remain the principal source of data.

Active Galactic Nuclei (AGN)

Active galactic nuclei have been discussed in connection with imaging extended jets. However, most of the X-ray flux from these objects comes from compact components having unresolved X-ray angular diameters. These cores will probably remain unresolved with P/OF, although this is not completely certain. The compact components undergo variations that can be as slow as months to years but which can also occur on timescales less than days (Snyder et al., 1980; Tennant et al., 1981). P/OF can make a unique contribution to the study of such variations. The AGN are comparatively faint sources, but spectrally they are comparatively hard.

It is important to ascertain the spectral character of these temporal variations, determining for example how spectral indices evolve during outbursts. Obtaining several hard X-ray spectra, at intervals of minutes to months, on relatively faint sources that sometimes must be isolated from other nearby sources and that always must be isolated by careful removal of background variations, is a straightforward task for P/OF but one that is difficult by other means.

Such spectral/temporal data can be used to determine radiation mechanisms and ultimately to study particle acceleration. A deep gravitational potential well, quite possibly containing a black hole, is required to power the process. As with stellar black hole candidates, the most rapid variations at high modulation will necessarily come from the central regions and therefore assist in probing the nature of the core and its energy release.

V. RELATION TO SOLAR PHYSICS AND SOLAR OBSERVATIONS

The examples from preceding sections show P/OF to be a facility of major significance for X-ray astronomy. Limiting fluxes will be at least a factor of ten below other hard X-ray instruments, and the imaging will be of unprecedented angular resolution (0.2 arc s) for high–energy astrophysics. Spectroscopic and photometric capabilities of P/OF will also provide major contributions.

P/OF's first role, however, is as a facility for solar physics. Its use for astronomical observations carries several benefits for the solar program that should be explicitly noted.

The clearest benefit is through the X-ray observations of other stellar coronae, the only major X-ray source class not discussed above. Such coronae are bright enough to show up among the bright X-ray sources (Figure 2, bottom) and become quite conspicuous during stellar flares, with peak fluxes exceeding 50 UFU in some instances (Heise et al., 1975). P/OF would be able to observe these stellar flares to higher energies than any other instrument now planned. Detection of flares can be accomplished by an independent X-ray sky monitor such as the one planned for XTE. P/OF will either need operational capability to respond promptly to such events or else must conduct prolonged monitoring of a flaring source while it is active. Data would be obtained on flares of greatly intrinsic different size scales from solar flares: emission measures for stellar flares reach 10^{55} cm^{-3}, and luminosities reach 10^{32-33} erg s^{-1}.

The brightest flares are seen from RS Canum Venaticorum binary systems and dMe flare stars (see Ambruster et al., 1983, for examples of each type). Fainter flares have been seen from associations of T Tauri stars. Quiescent fluxes from some of these objects will also be detectable, including W Ursae Majoris systems (Carroll et al., 1980). It may even be that the imaging capability will come into play, with detection of a measurable extent to the nearest of the RS CVn binaries. Models for the spectra of these systems require the hardest component to have dimensions comparable to those of the binary separation. Since the binary separation of Capella, the nearest RS CVn system, is 0.2 arc s, it is possible that a finite extent to its X-ray component will barely be measurable, establishing the size of the corona directly.

Another benefit is that astronomical observations provide checks and calibrations on the P/OF instrument itself. Point sources will test imaging systems, providing the best confirmation of theoretical point-source response functions. Point response functions obtained from stellar observations may prove important in fitting the shapes of flare emitting regions on the Sun. Because most point sources are variable, there will be a shortage of standard candles, but the

time-average of the Crab pulsar will represent a reasonable calibration source. Many astronomical situations such as mapping supernova remnants or crowded source fields will exercise image reconstruction techniques to be used on solar flares, and will give high confidence in solar results obtained by those same methods.

Possibly the most significant benefit will be the transfer of scientific information and the exchange of ideas that the use of one facility for solar and cosmic observations will encourage. Certainly there is overlap between the physical problems studied in the two contexts. Particle acceleration is a case in point, with examples coming from stellar coronae, supernova remnants, and AGN, as well as the Sun.

Finally, one should realize that P/OF could be an intermediate engineering step toward yet more advanced 21st century facilities that would push angular resolution down to tens of milliarcseconds. Achievement of X-ray angular resolution in that range is not presently foreseen for focussing X-ray instruments; hence, transform telescopes should have an ever-growing role in X-ray imaging. The commonality of interest between astronomers and solar physicists that begins with P/OF will extend to these subsequent facilities.

REFERENCES

Ambruster, C., and 7 co-authors, 1983, *Astrophys. J.*, *269*, 779

Bowyer, S., Byram, E., Chubb, T., and Friedman, H., 1964, *Science*, *146*, 912.

Carroll, R., and 8 co-authors, 1980, *Astrophys. J. (Letters)*, *235*, L77.

Fabricant, D., Lecar, M., and Gorenstein, P., 1980, *Astrophys. J.*, *241*, 552.

Feigelson, E., Schreier, E., Delvaille, J., Giacconi, R., Grindlay, J., and Lightman, A., 1981, *Astrophys. J.*, *251*, 31.

Harnden, F. and Seward, F., 1984, *Astrophys. J.*, *283*, 279.

Heise, A., Brinkman, J., Schrijver, J., Mewe, R., Gronenschild, E., and den Boggende, A., 1975, *Astrophys. J. (Letters)*, *202*, L73.

Hurford, G. and Hudson, H., 1980, preprint UCSD-SP-79-27.

Leventhal, M., MacCallum, G., and Stang, P., 1978, *Astrophys. J. (Letters)*, *225*, L11.

Levine, A., and 17 co-authors, 1984, *Astrophys. J. Suppl.*, *54*, 581.

Lea, S., Reichert, G., Mushotzky, R., Baity, W., Gruber, D., Rothschild, R., and Primimi, F., 1981, *Astrophys. J.*, *246*, 369.

Meekins, J., Wood, K., Hedler, R., Byram, E., Chubb, T., and Friedman, H., 1984, *Astrophys. J.*, *278*, 288.

Murray, S., Fabbiano, G., Fabian, A., Epstein, A., and Giacconi, R., 1979, *Astrophys. J. (Letters)*, *234*, L69.

Proctor, R., Skinner, G., and Willmore, A., 1978, *M.N.R.A.S.*, *185*, 745.

Rees, M., 1984, *Ann. Rev. Astron. Astrophys.*, *22*, 471.

Schreier, E., Feigelson, E., Delvaille, J., Giacconi, R., Grindlay, J., Schwartz, D., and Fabian, A., 1979, *Astrophys. J. (Letters)*, *234*, L39.

Schreier, E., Gorenstein, P., and Feigelson, E., 1982, *Astrophys. J.*, *261*, 42.

Snyder, W., and 12 co-authors, 1980, *Astrophys. J. (Letters)*, *237*, L11.

Tandberg-Hanssen, E., Hudson, H. S., Dabbs, J. R., and Baity, W. A., 1983, NASA Technical Paper 2168, Marshall Space Flight Center, Alabama.

Tennant, A., Mushotzky, R., Boldt, E., and Serlemitsos, P., 1981, *Astrophys. J.*, *251*, 15.

Trümper, J., Pietsch, W., Reppin, C., Sacco, B., Kendziorra, E., and Staubert, R., 1977, *Ann. N.Y. Acad. Sci.*, *302*, 538.

van der Klis, M., Jansen, F., van Paradijs, J., Lewin, W., Trümper, J., and Sztajno, M., 1985, IAU Circular No. 4043.

van Speybroeck, L., Epstein, A., Forman, W., Giacconi, R., Jones, C., Liller, W., and Smarr, L., 1979, *Astrophys. J. (Letters)*, *234*, L45.

Watson, M., Willingale, R., Grindlay, J., and Hertz, P., 1982, *Astrophys. J.*, *250*, 142.

Wolff, R., Kestenbaum, H., Ku, W., and Novick, R., 1975, *Astrophys. J. (Letters)*, *202*, L15.

Wood, K., and 9 co-authors, 1984, *Astrophys. J. Suppl.*, *56*, 507.
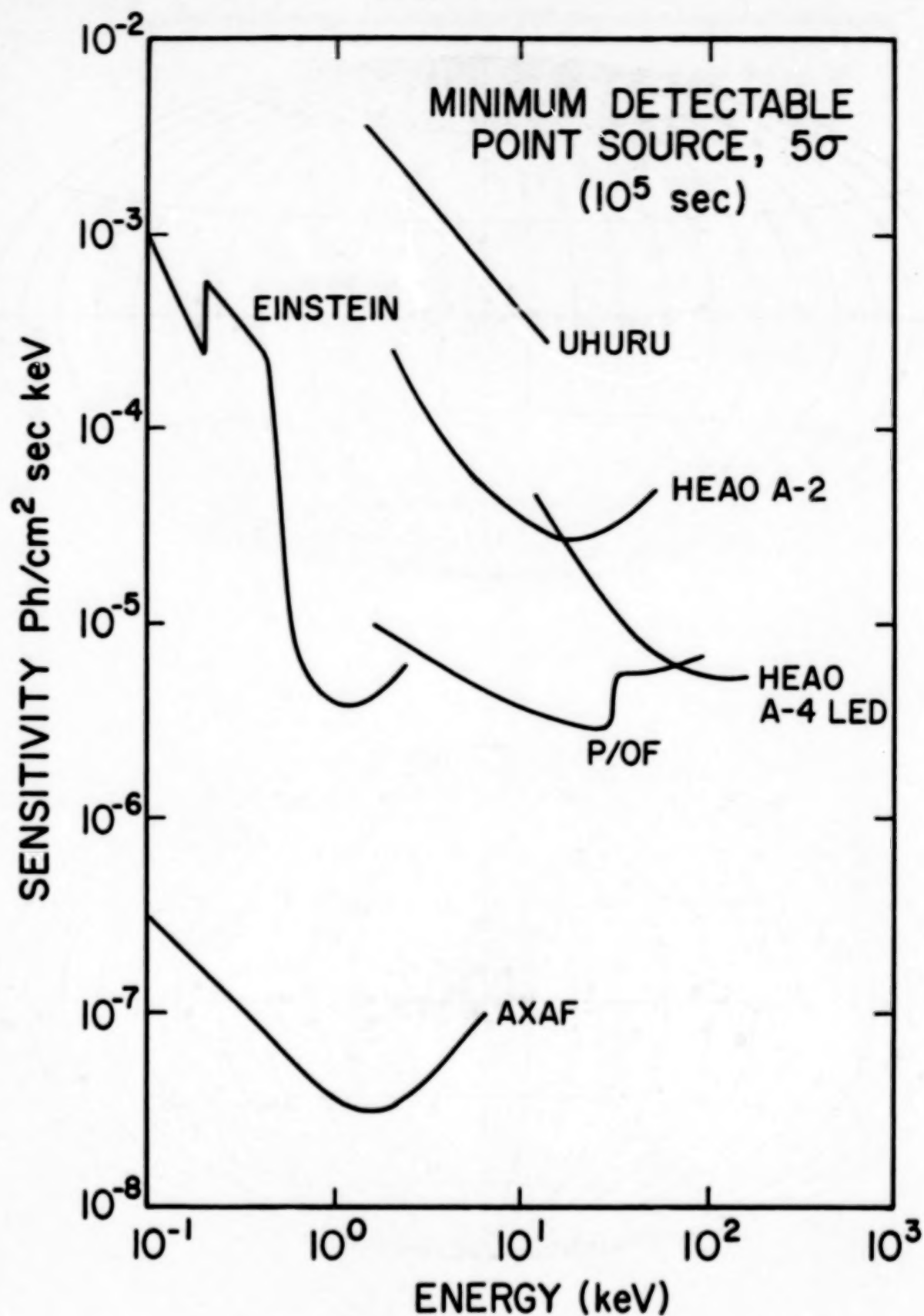
Figure 1. Spectral sensitivity of P/OF compared with other X-ray astronomy instruments.
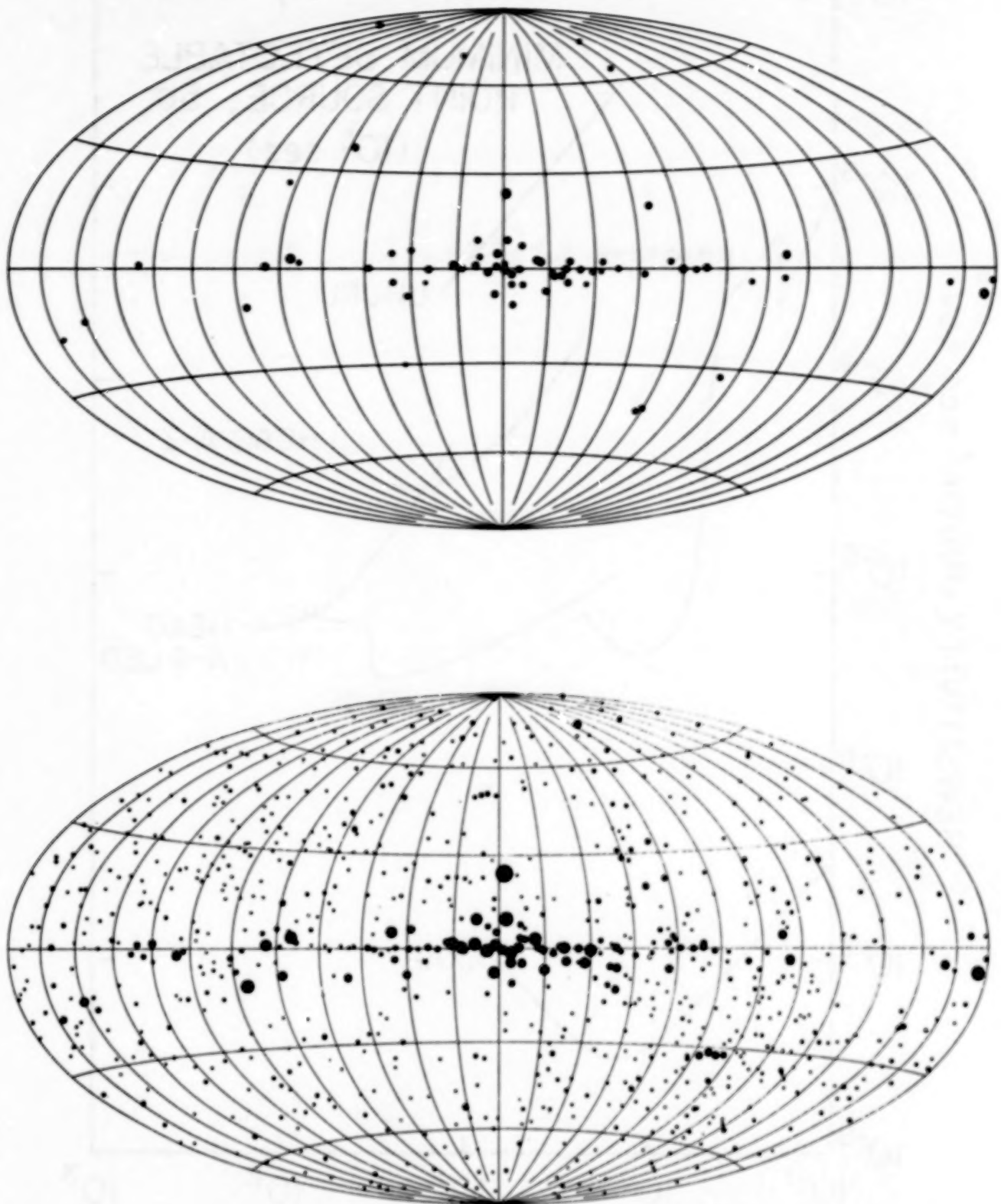
Figure 2. (Lower) HEAO A-1 catalog (0.5 to 25 keV), displayed in galactic coordinates.
(Upper) HEAO A-4 catalog (13 to 120 keV) displayed in same mode.
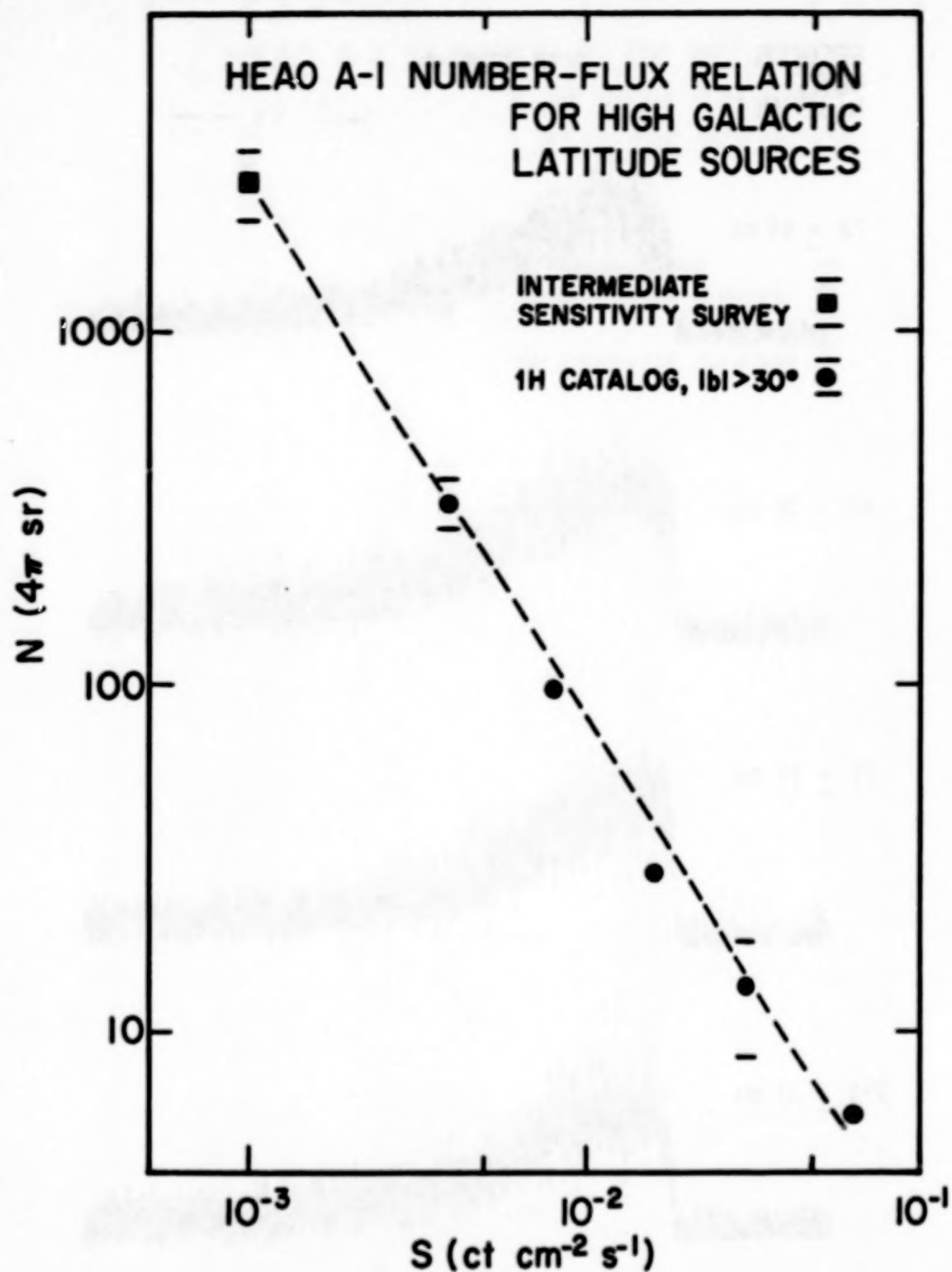
Figure 3. Source confusion, beam width, and flux limit: circles give source counts at several flux levels obtained with a 1 deg x 4 deg collimator. A finer collimator (1/2 deg x 1 deg) must be used below 3×10^{-3} ct cm^{-2} s^{-1}

Figure 4. X-ray burst time profiles. Large collecting area and high-time resolution are needed to follow spectral evolution during the rapid rise of the burst.

TABLE 1. P/OF X-RAY INSTRUMENT PERFORMANCE SUMMARY
(FOR ASTRONOMICAL OBSERVATIONS)

|	
Angular resolution	0.2 arc s
Field of view	1 deg
Total area	15 000 cm^2
Time resolution	1 ms
Energy range	2 to 120 keV
Sensitivity at 20 keV	10^{-5} ct cm^{-2} s^{-1} keV^{-1}
Sensitivity at 5 keV	0.03 μJy
Telemetry allocation	250 kbps

TABLE 2

ASTRO-C

Proportional Counter and All-Sky Monitor to Study Time Variations

1987 Launch
Proportional Counter: 5000 cm^2; 1 deg x 3 deg FOV
All-Sky Monitor Sensitive to 100 UFU

XTE

Proportional Counter, Scintillator, and All-Sky Monitor

1991 Launch
Proportional Counter: 10 000 cm^2; 1 deg x 1 deg FOV; 2 to 60 keV
Hard X-ray: 2000 cm^2
Monitor: Sensitivity to 10 UFU in Long Integrations
Rapid Response to Transients

ROSAT

Moderate Resolution Telescope for Sky Survey

1988 Launch
X-Ray Telescope: Wolter I; E < 3 keV; 500 cm^2 Limiting Area;
    Angular Resolution: 3 arc s

AXAF

High-Resolution Telescope

1991 Launch
X-Ray Telescope: Wolter I; E < 8 keV; 3000 cm^2 Limiting Area; Angular
    Resolution: 1/2 arc s within 3 arc min; 1 arc s within 1 deg

TABLE 3. NUMBER OF SOURCES IN FULL SKY ACCESSIBLE IN 10^4 s

E (keV)	Number (4π sr)
2	15000
4	12000
8	9000
16	2000
32	500
64	100

SUBPANEL SUMMARIES

● X-RAY PHYSICS

● CORONAL PHYSICS

X-RAY PHYSICS SUBPANEL SUMMARY

Robert P. Lin and Brian R. Dennis

The X-ray subpanel of the P/OF Workshop provided the opportunity to get input from a broad-based scientific community, including SMM experimenters and data analysts, solar flare theorists, and ground-based observers, on scientific and technical trade-offs involved in the X-ray instrumentation. The basic objective was to review the strawman payload set up for the Pinhole/Occulter Facility in the light of scientific developments of the last five years.

We began with a discussion of the spatial resolution of the X-ray system. The aspect system appears to limit the angular resolution that could be obtained with the Fourier-transform telescope. A knowledge of the relative pointing to ~20% of the desired resolution was required over time intervals of interest for flares. Thus, to achieve the diffraction-limit resolution of ~0.2 $''$, knowledge or relative pointing to ~0.04 $''$ would be required. The "alpha" or initial version of P/OF studied by MSFC would only provide ~0.3 $''$ knowledge, so the angular resolution would be limited to ~1.5 $''$. The Solar Disk Sextant – discussed as a "guide telescope" through its precise astrometry of the solar limb – may be able to provide the accuracy needed for solar X-ray measurements at 0.2 $''$. However, aspect determination at that level for cosmic X-ray measurements would still be a problem.

Ed Fenimore and Gordon Hurford briefly described the coded-aperture and Fourier-transform techniques, respectively. A lively discussion of these techniques ensued. It became clear that more simulations, using model images based on SMM and radio data or on theoretical models, are needed to help decide the trade-offs between sensitivity, image completeness, dynamic range in the image, etc.

The subpanel generally agreed that a wide energy range, extending from a few keV to well above 100 keV, was highly desirable. The Fourier-transform imager could easily be extended in energy to ~1 MeV by using NaI-scintillation Anger cameras behind the xenon proportional counters. For the coded-aperture imager, increasing the energy range to ~70 keV (and improving the energy resolution at the same time) may be possible through identification of the xenon fluorescence X-ray. Significant additional hardware is required for both these techniques. For a short Shuttle mission the extension to high energies may not be justified, as the likelihood of observing a large flare is small, but for long-term observations the extension to gamma-ray energies is scientifically very exciting.

Similar thoughts were expressed about the question of dynamic range – whether to plan for very large flares. Observation of these large flares would probably require movable shutters to cut down the flux. For a long-term mission, observations of these large flares would be a prime goal.

Many SMM observers argued for a larger field of view for the Fourier-transform telescope (presently 3 arc min) on the grounds that SMM, with a comparable field of view, missed all gamma-ray flares and parts of many other flares. P/OF, however, provides full Sun coverage at ~4 $''$ resolution with the coded-aperture imager, but only at energies below 30 keV (70 keV if the xenon fluorescence X-ray is identified). One suggestion was to provide a zoom capability by changing the mask-to-detector distance so that the field of view could be matched to the size of the active region.

We noted that the specifications for the X-ray instruments, as given in the P/OF description, need updating as indicated in the following table:

X-RAY IMAGING REQUIREMENTS FOR P/OF

	Coded-Aperture Imager	Fourier-Transform Imager
Angular resolution	4 arc s	0.2 arc s
Aspect knowledge		
(relative)	1 arc s	0.04 arc s
(absolute)	1 arc s	1 arc s
Field of view	Whole Sun (1 deg)	5 arc min (variable?) (function of energy)
Energy range	2 to 70 keV	2 keV to 1 MeV
Energy resolution ($\Delta E/E$ FWHM)		
at Fe^{55}	20%	20%
at 20 keV	10%	10%
at 100 keV	–	12%
at 662 keV	–	7%
Time resolution	1 ms	1 ms
Sensitive area	5000 cm^2	25 cm^2 x 100 subcollimators

CORONAL PHYSICS SUBPANEL SUMMARY

Richard H. Munro

The objectives of the coronal physics subpanel's discussions were to clarify the scientific background for the instrumentation of the Pinhole/Occulter Facility. There is continuing need for input into what we think of as the "strawman" payload, to reflect the growth of knowledge and capabilities since the original discussions of P/OF took place. In general we find that the major scientific objectives for the coronal instrumentation as presented in the original P/OF report (NASA Technical Paper 2168) remain valid. There are new scientific discoveries, however, together with an enhanced awareness of the potential capabilities of the Facility.

The SMM observations have expanded the scientific questions that the joint (X-ray and coronal) capabilities of the Pinhole/Occulter can attack. We would now like to push the coronal observations as close to the limb as possible; the SMM observations had intermediate resolution and sensitivity for hard X-rays, together with simultaneous observations at ultraviolet and visible wavelengths, and these were very productive even outside times of flare activity. Coronal flares – weak X-ray events without a detectable chromospheric response – may be the signature of magnetic reconnection. Pre-flare activity has been observed in bright points; are micro-flares the same physical phenomenon as the bright-point flares? Is it possible to resolve type III bursts with both kinds of instrumentation? Combining the high-resolution X-ray observations with the range of plasma diagnostics provided by the coronal instruments might provide the first direct astrophysical observations of magnetic reconnection.

It is not clear whether the physical properties of the coronal plasma are controlled by a continuous interaction with a non-radiative energy flux generated by sub-photospheric convection, or by a continuum of dynamic "explosive" phenomena such as spicules, macro-spicules, "coronal bullets," micro-flares, magnetic-field reconnection, etc. There are suggestions that bright points are heated by a sequence of minor stochastic events; this concept might extend to major active regions too, with present low-resolution observations simply integrating over a number of individual discrete energy releases. In either case, there is great need for observations that can diagnose the physical characteristics of these non-equilibrium plasmas. Because hard X-ray observations preferentially probe the tail of the electron energy distribution, complementary coronal measurements are required to determine the core of the distribution. This is most easily accomplished by observing line emission, where the production mechanism is more tightly coupled to the majority of the electrons. The specification of the pre-event conditions and the physical parameters of the flare environment would lead to a far deeper understanding of these energetic processes.

The determination of the direction and strength of the magnetic field as it expands into the corona has always been a major goal of solar observations. Both technical and theoretical difficulties have hampered this effort. The accurate specification of the polarization properties of emission and absorption lines has been compromised by stray-light and seeing. From the P/OF vantage point, polarimetry with high-spatial resolution might provide the key knowledge necessary to track the extension of the solar magnetic field into the corona.

Major technical concerns regarding the Facility still remain. If the instruments are to perform at the 1 arc s level under the current P/OF design, then each instrument must have some form of active image compensation to negate the imposed motion of the detector plane as it keeps the occulter steady. While X-ray detectors can time-tag single photon events, the flux in

the EUV and visible is normally too great for this to be done; one solution is to degrade the spatial resolution, but this has obvious disadvantages both in the absolute sense and for comparison with the high-resolution X-ray data. The use of array detectors without internal active image compression requires substantial data rates to produce a series of weakly exposed images to "freeze" the motion of P/OF. This then puts a strain on post-observation data processing to align the images for reconstruction to a suitable signal-to-noise level.

Another substantial technical problem, more difficult with P/OF than with the previous intermediate-resolution observations, is the angular co-alignment of X-ray and coronal observations. This problem may be more difficult still if the coronal instruments use some form of active optical compensation.

WORKSHOP SUMMARY

Hugh S. Hudson
UCSD

and

Einar Tandberg-Hanssen
NASA Marshall Space Flight Center

We desired most strongly at this Workshop to have an effective interaction between active developments in research — observational, analytical, theoretical — with the prospects for instrumentation on the Pinhole/Occulter Facility. The best avenue for this interaction was the communication among the participants who eminently represented these different perspectives. However, we also prepared a list of topics or questions to deal with, and requested that the subpanels in particular pay attention to these items. The following represents our view of the Workshop concensus response to these challenges.

1. Is the present P/OF science emphasis valid in the light of new developments?

Several new developments have taken place, as discussed above in the scientific papers and in the subpanel reports. Given the long delay between "strawman payload" identification — as early as 1979 — and actual implementation of P/OF — not before 1989 — it is rather obvious that changes have been taking place.

In the coronal area, the exploitation of P/OF's capability for observations near the limb now seems scientifically very exciting. This argues for a large separation between occulter and telescope: the longer this baseline, the closer to the limb one can view. Exploiting separations of 30 to 50 m seems entirely feasible from a technical point of view.

For high-energy observations, the basic difference in perception of P/OF goals seems to be in terms of energy range. The excellent γ-ray observations from SMM strongly impel us towards an imaging capability for high energies; the interesting coronal soft X-ray observations also from SMM simultaneously drive us towards lower energies. One can therefore anticipate that new kinds of high-energy instrumentation, not now represented in the strawman payload, will be proposed to use the Pinhole/Occulter Facility.

2. What programs are appropriate for P/OF deployment?

The basic idea of P/OF, the use of a long separation between an occulter and a detector, will work well in many applications. Our development to date has been for a Spacelab facility, analogous to the multi-telescope spar deployed from the Space Shuttle for the solar instruments of Spacelab 2 or for the comet observations (the Astro mission) of Spacelabs 4, 5, and 6. Such a facility would evolve in a natural way towards use in a solar observatory (the Advanced Solar Observatory) installed in a manned space station in the 1990's. With these large facilities, we could realize P/OF's promise of very high angular resolution.

On the other hand, smaller-scale opportunities may also be available. In a P/OF-like instrument installed on the MMS spacecraft now carrying SMM, for example, one could have a boom of 6 to 7 m length. While this would not give sub-arcsecond capability, it would still give

us a chance to make substantial improvements. The concensus of the Workshop was that although all opportunities for obtaining scientific observations should be followed up as energetically as possible, the ultimate goal remains the establishment of a true Pinhole/Occulter Facility using as long a baseline separation as is practical from an engineering point of view.

3. How do the present P/OF program and the strawman payload need to be altered in the presence of new data or second thoughts?

We have mentioned programmatic concerns above. Regarding the strawman payload, there is no doubt as to its incompleteness, but this is the nature of the "strawman payload" procedure. Below we give examples of new "detector plane" instruments that have been suggested since the strawman payload was created, and which would be likely to be proposed in response to an Announcement of Opportunity for facility use.

4. Are there good suggestions for new experiments that would use the Facility?

We have identified in the high-energy area the possibility of γ-ray and neutron imaging, soft X-ray imaging, and a concept for an X-ray emission-line imager with moderate (few arc s) angular resolution. In the coronal domain, the most powerful augmentation of P/OF scientific goals probably would not come from P/OF instruments beyond those in the strawman payload, but instead from coordinated instruments (see below).

5. What are the best coordinated experiments (including ground-based) to accompany P/OF?

As a general statement, P/OF as a facility needs to coordinate its observations with both wide field-of-view experiments and specialized forms of intermediate solar instrumentation. Simultaneous observation with SOT would be wonderful, both for high-resolution disk observations in comparison with the X-ray images from P/OF, and also near-limb observations for support of the coronal imaging. The same considerations apply to successful modern ground-based observations, such as those from a large optical telescope, a Stokes polarimeter capability, or other magnetographic system. The most powerful use of P/OF would certainly be as part of the Advanced Solar Observatory, in which second-generation solar space instrumentation could be brought to bear on a variety of problems through coordinated observing and analysis.

6. What developments of P/OF would we like to see for the year 2010?

The detector-plane and focal-plane instrumentation capability will certainly evolve, and P/OF should be able to keep pace with these developments. The Facility itself will inevitably appear to be too small or in the wrong place by this time – the Space Station should be approaching its third decade of use, for example, and the Advanced Solar Observatory may have long since been built, used, updated, and then installed on its own free-flying platform. A free-flying occulter is a natural extension of the P/OF concept, which would lead to much better angular resolution again if so desired.

In concluding these comments, and with them the proceedings of the Workshop, we would like again to thank all of those associated with planning for the Pinhole/Occulter Facility. The ideas presented here confirm the vitality of the scientific domain of P/OF, and the Facility itself has shown an ability to evolve even before its first implementation takes place. This is a healthy

sign, because space research programs often take so long a time to mature as to make initial concepts obsolete. We do not think that this will happen with the P/OF principle, which in one form or another is likely to become a prominent feature in future astrophysical investigations at the highest resolution.

1. REPORT NO. NASA CP-2421	2. GOVERNMENT ACCESSION NO.	3. RECIPIENT'S CATALOG NO.
4. TITLE AND SUBTITLE Solar Flares and Coronal Physics Using P/OF as a Research Tool		5. REPORT DATE April 1986
		6. PERFORMING ORGANIZATION CODE ES01
7. AUTHOR(S) Edited by Einar Tandberg-Hanssen, Robert M. Wilson, and Hugh S. Hudson		8. PERFORMING ORGANIZATION REPORT #
9. PERFORMING ORGANIZATION NAME AND ADDRESS George C. Marshall Space Flight Center Marshall Space Flight Center, Alabama 35812		10. WORK UNIT NO. M-523
		11. CONTRACT OR GRANT NO.
		13. TYPE OF REPORT & PERIOD COVERED
12. SPONSORING AGENCY NAME AND ADDRESS National Aeronautics and Space Administration Washington, D.C. 20546		Conference Publication
		14. SPONSORING AGENCY CODE

15. SUPPLEMENTARY NOTES
Einar Tandberg-Hanssen and Robert M. Wilson: Marshall Space Flight Center,
  Huntsville, Alabama.
Hugh S. Hudson: University of California, San Diego, La Jolla, California.

16. ABSTRACT

   This NASA Conference Publication contains the proceedings of the Workshop on
Solar High-Resolution Astrophysics Using the Pinhole/Occulter Facility held at NASA
Marshall Space Flight Center, Alabama, on May 8-10, 1985. These proceedings include
primarily the invited tutorial papers, extended abstracts of contributed poster
papers, and summaries of subpanel (X-Ray and Coronal Physics) discussions. Both
observational and theoretical results are presented. Although the emphasis of the
Workshop was focused primarily on topics peculiar to solar physics, one paper is
included that discusses the P/OF as a tool for x-ray astronomy.

17. KEY WORDS Solar Physics Sun Corona X-Ray Pinhole/Occulter Facility	18. DISTRIBUTION STATEMENT Unclassified--Unlimited Distribution Category: 92	
19. SECURITY CLASSIF. (of this report) Unclassified	20. SECURITY CLASSIF. (of this page) Unclassified	21. NO. OF PAGES 310	22. PRICE A14